THE EFFECT OF IRON CONCENTRATION ON THE STRUCTURAL, ELECTRICAL, MAGNETIC AND MAGNETOELECTRIC PROPERTIES OF MULTIFERROIC COMPOSITES

A DISSERTATION SUBMITTED TO THE UNIVERSITY OF DHAKA IN PARTIAL FULFILLMENT OF THE REQUIREMENTS FOR THE DEGREE OF DOCTOR OF PHILOSOPHY IN PHYSICS

By
SHARIFA NASRIN
Registration No. 140
Session: 2015-16
and
Registration No. 76
Session: 2020-21

DEPARTMENT OF PHYSICS
UNIVERSITY OF DHAKA
DHAKA 1000

JUNE, 2023

Dhaka University Institutional Repository

CERTIFICATE OF THE SUPERVISORS

We certify that the dissertation entitled "**THE EFFECT OF IRON CONCENTRATION ON THE STRUCTURAL, ELECTRICAL, MAGNETIC AND MAGNETOELECTRIC PROPERTIES OF MULTIFERROIC COMPOSITES**" submitted to the University of Dhaka with our permission in partial fulfillment of the requirements for the degree of doctor of philoshopy (Ph. D.) in Physics by Sharifa Nasrin is the documentation of the investigations conducted by her during the course of time from 2015-2016 academic year (Registration number: 140) through the 2020-2021 academic year (Reregistration Number: 76) under our direction and supervision, and that neither this university nor any other university or higher educational organization has utilized this work as the foundation for the awarding of any degree, diploma, associateship, fellowship.

…….

(Professor Dr. Md. Dalilur Rahaman)

Supervisor

Department of Physics

University of Dhaka

Dhaka-1000

Bangladesh

…….

(Professor Dr. A. K. M. Akther Hossain)

Joint-supervisor

Department of Physics

Bangladesh University of Engineering and Technology (BUET)

Dhaka-1000, Bangladesh

Dhaka University Institutional Repository

DECLARATION

I, Sharifa Nasrin, registration number 140 for the academic year 2015-2016 and re-registration number 76 for the academic year 2020-2021, thus certify that I conducted the research detailed in this dissertation throughout the academic year. Solid-state reaction technique derived composites were fabricated and investigated at the Solid-state Physics Lab of Bangladesh University of Engineering and Technology (BUET), Dhaka. Also, I hereby certify that I have not copied anything from any source other than those that I have cited because the quantity of plagiarism is within acceptable bounds. If the University of Dhaka's research guidelines have been broken in this dissertation, I could face disciplinary action in accordance with the university's plagiarism policies. The fact that no part of this dissertation-or any component of it-has been presented to another organization for consideration of a degree or diploma is also declared.

Sharifa Nasrin

Acknowledgements

Above all, I want to explicit my indebtedness to the Almighty Allah for guiding me along the right path and providing me with the stamina, bravery, and patience necessary to finish this task.

I owe my mentor, Dr. Md. Dalilur Rahaman, Professor of Physics Department at the Dhaka University, a debt of gratitude for his help in finishing my research project as well as for his unwavering encouragement, priceless counsel, and careful supervision while I finished the prerequisites for my Ph.D. I owe my co-mentor, Dr. A.K.M. Akther Hossain, Professor of Physics, Department of Physics at the Bangladesh University of Engineering and Technology (BUET), a debt of gratitude for his counsel throughout the trying times of my academic career that encouraged me to persevere.

I'm obliged to Chairman, Department of Physics, University of Dhaka, who provided the equipment and chemicals I needed to carry out my research. I am also appreciative of all the faculty members who provided the support and assistance I needed. I appreciate being able to use the XRD, FTIR, and SEM equipment at the Center for Advanced Researches in Sciences (CARS), Dhaka University.

I'd want to use this chance to express my gratitude to the instructors and personnel at BUET's Experimental Solid State Physics Lab for letting me use their facility for my research. I appreciate having had the opportunity to conduct structural, microstructural, and elemental investigations utilizing the XRD, SEM, and EDX thanks to the Glass and Ceramic Engineering department at BUET.

I want to explicit my appreciation for the generous assistance of the Atomic Energy Center, Dhaka, in executing the M-H hysteresis loop on a few samples.

Dhaka University Institutional Repository

Moreover, I'm grateful to the People's Republic of Bangladesh's government and the Secondary and Higher Secondary Division, Ministry of Education for granting me the required study leave for my Ph. D. research.

I also appreciate the University Grants Commission of Bangladesh for offering me a fellowship for my Ph. D. studies.

I would want to use this previlege to offer my deep gratitudes to my family and the lab members in particular for their love, support, and encouragement.

The Author

Sharifa Nasrin

ABSTRACT

In this dissertation, stoichiometric and non-stoichiometric nickel copper zinc ferrites and ferroelectromagnetic composite ceramics (FEMCCs) have been synthesized. Crystal structure, micromorphology, elastic, electric, and magnetic traits of stoichiometric and non-stoichiometric nickel copper zinc ferrites and phase structure, micromorphology, electromagnetic and magnetoelectric traits of FEMCCs have been investigated employing X-ray diffractometer (XRD), Fourier transform infrared spectrometer (FTIR), Scanning electron microscope (SEM), Vibrating sample magnetometer (VSM), and Impedance analyzer. Stoichiometric $Ni_{0.25}Cu_{0.13}Zn_{0.62}Fe_2O_4$ (NCZFO) ceramics were prepared adopting the solid-state reaction approach and annealed for 5h at various sintering temperatures (T_s). FTIR and XRD analyses reveal that the development samples possessed spinel skeleton cubic symmetry. Micromorphological (SEM) study revealed that the grain size increases with increasing T_s. The longitudinal, transversal, and mean elastic wave velocities, elastic moduli, Poisson ratio were estimated using FTIR data. The electric permittivity increases with T_s due to the partial transformation of Fe^{3+} to Fe^{2+}, and exhibits dispersive character due to interfacial polarization. Electrical conduction mechanism follows Jonscher's law and is governed by the small polaron hopping phenomenon. The magnetic permeability boosts with increasing T_s due to the enhancement in bulk density as well as grain diameter. The Q-factor declines while the frequency of resonance moves toward low frequency region with T_s. The magnetic traits exceedingly decline with increasing T_s due to the lack of sample's homogeneity and existence of intra-granular porosity. $Ni_{0.25}Cu_{0.13}Zn_{0.62}Fe_{2-x}O_{4-3x/2}$ ($NCZFe_{2-x}O_{4-3x/2}$) (x = 0.0; 0.04, 0.08; 0.12) ceramics were developed using the traditional solid state synthetic process and annealed for 5h at various T_s. XRD study ascertained the development of the spinel skeleton without having no detectable undesired phases. The lattice constant escalates in a linear fashion with iron-deficient non-stoichiometry (IDNS) content at 1100 ℃, while it alters non-systematically at 1150, 1200, and 1250 ℃. The elastic moduli, Poisson's ratio, longitudinal, transversal, and

mean elastic wave velocities have been determined using FTIR data. According to SEM study, the magnetic interplay in the midst of the component grains causes abnormal and agglomerated grain development. The enhanced densification and production of Fe^{2+} ions result in an enhancement in the dielectric characteristics on increasing the temperature of sintering. The investigation of ac electrical conductivity indicated that a small-polaron-based hopping mechanism governs the conduction process. Nyquist plots suggested that the effect of the grain border is mainly is responsible for electrical conduction in non-stoichiometric nickel copper zinc ferrites rather than grain. According to the amount of IDNS, changes in density, porosity, grain diameter, and magnetic anisotropy may be responsible for the observed alternations in magnetic permeability and magnetic loss tangent. (1-y) [BCZTO] + (y) [NCZFO] ($0 \leq y \leq 1.0$) FEMCCs were developed using the solid state reaction approach and annealed for 5h at various T_s. XRD and FTIR examinations reveal that no impurity phases formed during the production of the single-phasic NCZFO spinel skeleton and the BCZTO tetragonal perovskite. SEM investigation revealed that a quasi-spherical type microstructure with low voids or pores, insignificant aggregation, and reasonably homogenous grain diameter is generated. The incorporation of NCZFO generates irregular shape grain. The generation of irregular shape grain with the escalation of NCZFO amount is ascribed to the filling of pores and their segregation at the grain borders. The electric permittivity declines as NCZFO content escalates because of the effect of dilution whereas the electric permittivity enhances with T_s. Different models have been used to calculate the electric permittivity. The discrepancy in the midst of the theoretical and observed values of the electric permittivity is related to ion's diffusion and interplay in the midst of two phases. Porosity correction of experimental electric permittivity is performed. A close coincidence in the midst of the porosity corrected electric permittivity and observed electric permittivity is achieved. Electrical conduction is caused by the small-polaron hopping. Impedance study suggested that the grains have less impact on overall electrical traits than grain borders. The magnetic permeability improves while the resonant

frequency drops as NCZFO content escalates. The deterioration in resonant frequency is due to the increased domain wall motion. The magnetic permeability was calculated using different models and a comparison in the midst of experimental and calculated values is made. The difference in the midst of the theoretical and measured values of magnetic permeability is accounted to the interplay in the midst of two phases and ion diffusion. (1-*y*) [BCZTO] + (*y*) [$NCZFe_{2-x}O_{4-3x/2}$] (x = 0.0; 0.04; 0.08; 0.12, and y = 0.2; 0.5) FEMCCs were manufactured employing the solid state sintering technique and annealed for 5h at 1200 ℃. XRD and FTIR studies confirmed that the component phases existed simultaneously without any undesired phases. There are non-systematic variations in lattice constants, crystallite diameter, and cell dimensions as IDNS level escalates. SEM examination confirmed the development of polyhedral or irregular grains with insignificant agglomeration and porosity as IDNS escalates. Maxwell-Wagner's interfacial polarization is responsible for the low-frequency electric permittivity dispersion. The ac electrical conductivity act in accordance with Jonscher's law and is controlled by the charge transfer in the midst of the adjacent localized sites and small-polaron hopping. The combined effects of strongly conducting grain and poorly conducting grain border responses, according to Nyquist plots, are thought to be the cause of electrical conduction phenomena. The magnetic permeability improves in x = 0.04, depreciates on increasing IDNS amount in y = 0.2, and then escalates on increasing IDNS amount in y = 0.5. The elastic interplay in the midst of the component phases, which is mediated by strain, results in an optimal magnetoelectric coefficient of 0.17 V $cm^{-1}Oe^{-1}$ in x = 0.0; y = 0.5 FEMCC. Finally, it is concluded that the achieved results make a significant contribution in designing and developing the next generation multifunctional devices in near future.

Table of Contents

List of Figures

List of Tables

Chapter One: Introduction

1.1. General Introduction

To meet societal demand and bring about the fourth industrial revolution, materials science, solid-state science, and condensed matter physics have been identified as some of the key drivers of national development and economic prosperity. Through the development of computer technology, wireless correspondences, Internet, digital data storage, and widely used end user devices to the investigation and advancements in materials science, our society has been substantially impacted and revolutionized [1]. The relationship in the midst of science, technology, and society is illustrated in Figure 1.1, with a focus on the triangle that is currently prominent and which is actually driven by materials science [2].

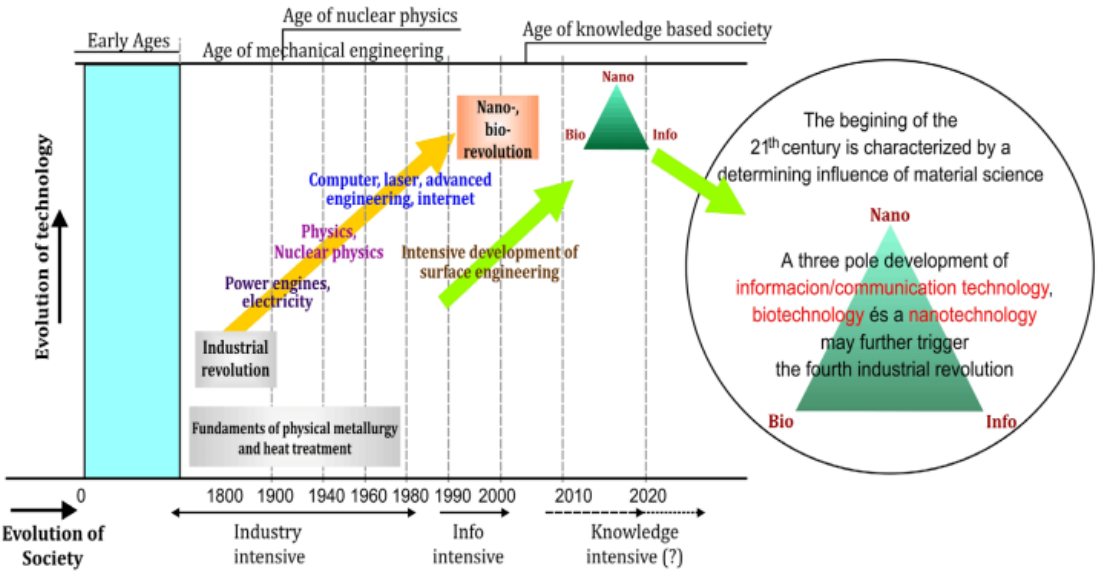

Figure 1.1: Interdependence amongst science, technology and society. Adapted from [2].

The intimate correlation in the midst of magnetic and electric traits, first invented by Oersted and unfolded in Faraday's investigations manifesting that electric current develop magnetic fields, is one of the indispensable presumptions of the fundamental theory of electromagnetism. Additionally, it has been demonstrated by Faraday's law, which connects magnetic flux with

electromotive force [3]. One of the decisive pieces of evidence that enabled Maxwell to formulate the equations that almost miraculously explain all physical phenomena controlled through the electromagnetic interplay, one of the four essential physical forces, was the pronouncement of such a correlation. Science and technology have been significantly influenced by this correlation in the midst of magnetic and electric traits. Magnetism in solid-state science thrives from electron's spin. The electrostatic Coulomb interplay is the predominant force, whereas magnetism is a second order, relativistic quantum mechanical phenomenon corroborated with the electron's spin and Pauli Exclusion Principle. The relativistic spin-orbit coupling, which links the spin of electron to the field produced that is created by its velocity, essentially accounts for the existence of the correlation in the midst of charge and spin, which is weak to some extent. Consequently, a weak correlation in the midst of magnetic and electric traits can be seen in the majority of materials that are ordered either electrically or magnetically [4]. In this connection, chemists, physicists, material scientists and electrical and electronic engineers have been put their synergistic efforts to design and development of materials possessing strong coupling in the midst of magnetic and electrical traits. Among the materials, solid-state magneto-electric-elastic multiferroic materials has been considered as one of best materials for studying the cross-correlation in the midst of the electrical and magnetic traits. Solid-state magneto-electric-elastic multiferroic materials are the materials which simultaneously manifest at least two ferroic orders from ferroelectricity, ferromagnetism, ferroelasticity, ferrotoroidicity, and non-primary ferroic antiferromagnetism [5] in the single-phase or composite [Figure 1.2] and linear magnetoelectric coupling effect. The interplay of several ferroic orders can lead to effects like the magneto-electric-elastic magnetoelectric effect that is schematically depicted in Figure 1.3 and Figure 1.4 (a, b).

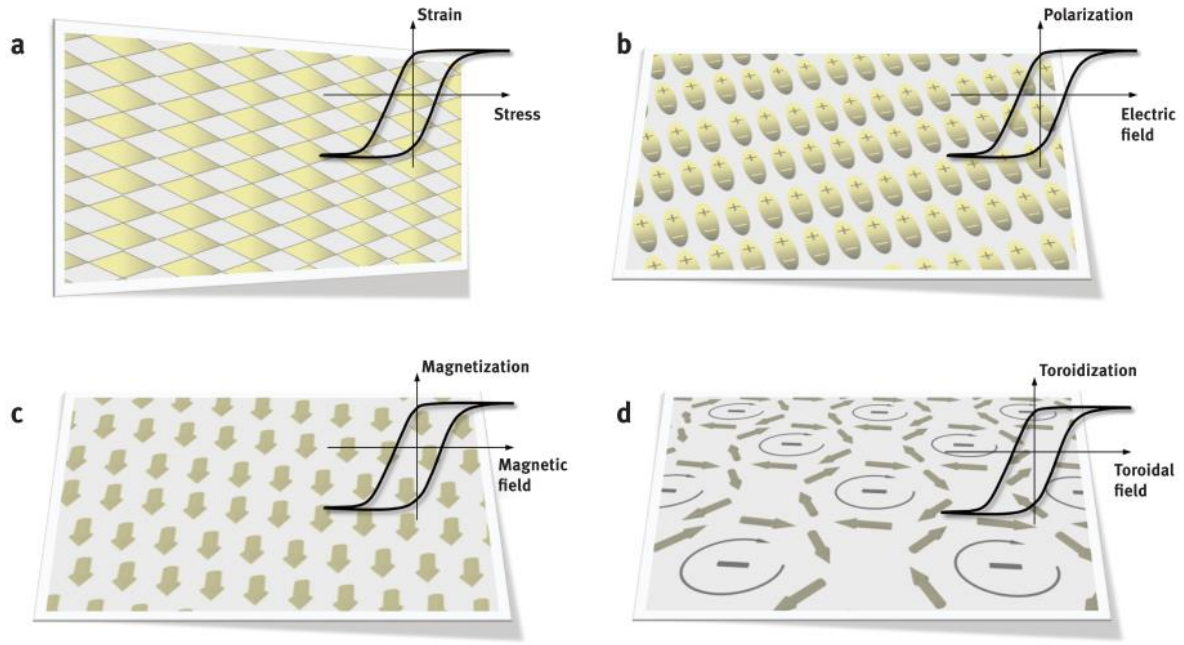

Figure 1.2: Four types of primary ferroic orders responsible for multiferroicity: (a) ferroelasticity, (b) ferroelectricity, (c) ferromagnetism, and (d) ferrotoroidicity. Adapted from [6].

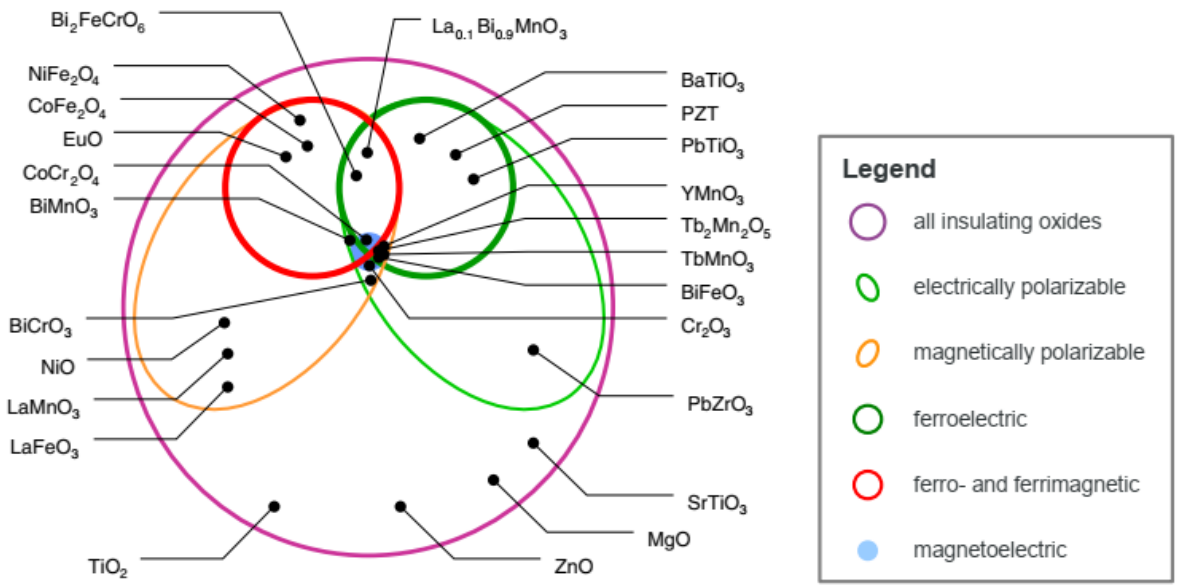

Figure 1.3: (a) Depiction of multiferroics and magnetoelectrics in a Venn diagram. Ferroelectric materials shown in the upper right circle, while ferromagnetic materials are displayed in the top left circle. Therefore, magnetoelectric materials are present in the area where these two circles overlap. The huge outer circle is made of ferrous or ferric materials. Adapted from [7-9].

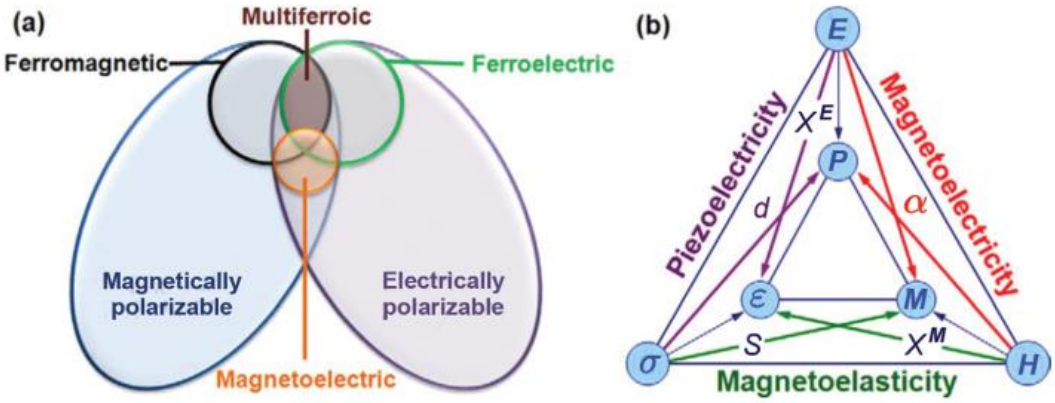

Figure 1.4: (a) Correlation in the midst of multiferroic materials. Notice that only a limited subset of materials is simultaneously multiferroics and magnetoelectrics. (b) Heckman diagram, which shows the physical correlations naturally eventuating materials and a design precept for new materials. Adapted from [10-12].

In the 19th century, the idea of rudimentary study on the magneto-electric effect was reported. Roentgen [13] asserted in 1888 that a moving dielectric material magnetized when exposed to a magnetic field while in 1894 Pierre Curie [14] had theorized the existence of an intrinsic magnetoelectric concept of (non-moving) solid crystals subject to the considerations of lattice symmetry. In the following years, the research on the concept of magnetoelectric started to get increasing attention. In 1926, Debye [15] introduced the terminology of the "magnetoelectric effect". In 1957, Landau and Lifshitz had noted that magnetoelectric phenomena may, in theory, occur in spin-ordered materials on the basis of thermodynamic and symmetry considerations rather than atomic mechanisms [16]. Subsequently, Dzyaloshinskii reported two proofs of the magnetoelectric phenomenon in 1959 that below Neel temperature (T_N): (i) an electric field induced magnetization and (ii) a magnetic field induced polarization in Cr_2O_3 [17], followed by related experimental and theoretical investigations reported by Astrov, Folen, Stadler and Rado [18-21]. Single-phase antiferromagnetic Cr_2O_3 magnetoelectric material revealed a magnetoelectric effect with Néel temperature T_N = 307° K and exhibited a magnetoelectric coefficient of 4.31 ps/m around 263° K [22]. In 1966, a nickel iodin boracite

($Ni_3B_7O_{13}I$) investigated and revealed weak ferromagnetic and ferroelectric orders at about 64º K [23]. In 1970, single-phase bismuth ferrite ($BiFeO_3$) was discovered to be distinctive among other magnetoelectric multiferroics due to its unusually high antiferromagnetic and ferroelectric transition temperatures (1103° K, and 643° K, respectively) far avove room temperature [24]. In an article that was published in 1962 [25] and a book that was published in 1970 [26], O'Dell provided summaries of the majority of the theoretical and experimental advancements made in the area of magneto-electric media to a maximum of that time-frame. In an article published in 1962 [25] and a book published in 1970 [26], O'Dell provided a comprehensive overview of the majority of theoretical and experimental advancements made in the field of magneto-electric media to a maximum of that time frame. The time-line of magnetoelectric coupling effect is presented in Figure 1.6 (a). In real-world, room-temperature single phase multiferroics are limited and exhibited weak magnetoelectric coupling and high permittivity loss tangent. The following issues may be responsible for the lack of single phase multiferroics at room temperature: (i) the exclusion of electric and magnetic sources. This means that the existence of the magnetic and electric orders must satisfy mutually exclusive criteria; magnetism needs partially filled $\boldsymbol{d}$ atomic orbitals (in transition metals) or partially filled $\boldsymbol{f}$ atomic orbitals (rare earth ions), but ferroelectricity typically needs empty $\boldsymbol{d}$ atomic orbitals [Fig. 1.5]. In addition, symmetry criteria are another consideration. There are 122 potential crystallographic point groups, but only 13 of them have been found to exhibit the multiferroic characteristic [1, 27], and (ii) significant fabrication challenges (iii) the appearance of the remnant magnetization appears at extremely low temperatures (low Neel temperature or Curie temperature). The elements responsible for magnetic and ferroelectric properties are highlighted in Figure 1.5.

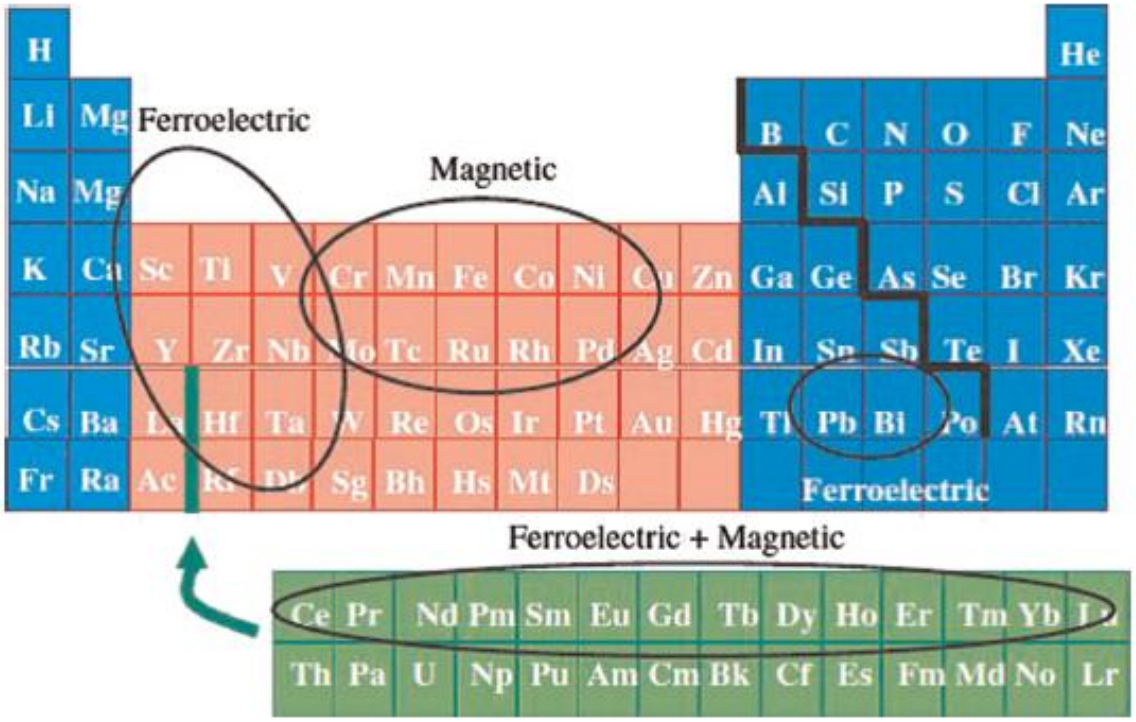

Figure 1.5: Periodic table of the elements emphasizing the elements responsible for magnetic and ferroelectric properties. Adapted from [28].

For the engineering of materials with the expected traits, J. Van Suchtelen [29] proposed two types of composites based on: (i) sum properties and (ii) product properties. In order to circumvent the the problems those allied the single-phase multiferroics, J. van Suchtelen [29] first recommended the conception of a "product tensor property" in biphasic composite materials in 1972. This notion refers to a property that results from the magneto-electric-elastic interplay of two phases with dissimilar properties [Figure 1.6 (a)]. The magnetoelectric response is one such product tensor property. A substantial magnetoelectric effect might be produced in such composites, according to research from Philips Laboratory [30-32], which was done shortly after the product magnetoelectric trait in the composite integrating magnetostrictive and piezoelectric phases was suggested. They produced ceramic composites of $BaTiO_3$ and $CoFe_2O_4$ by unidirectionally solidifying eutectic configurations in the quintant Fe-Co-Ti-Ba-O combination, and they achieved magnetoelectric response as large as 0.13 V/cm Oe at room temperature, which is approximately 100 times greater than single-phase

multiferroic ones.. However, unidirectional solidification of eutectic is challenging and necessitates exact compositional and processing control. This value was attained as a result of irregularities in the chemical reactions that took place during the sintering process, the magnetostrictive phase's low resistivity, and the induced eddy currents caused by the applied AC voltage. Additionally, there are issues with dispersion in composite materials, mechanical defects that limit mechanical coupling, and difficulties in aligning electric dipoles.

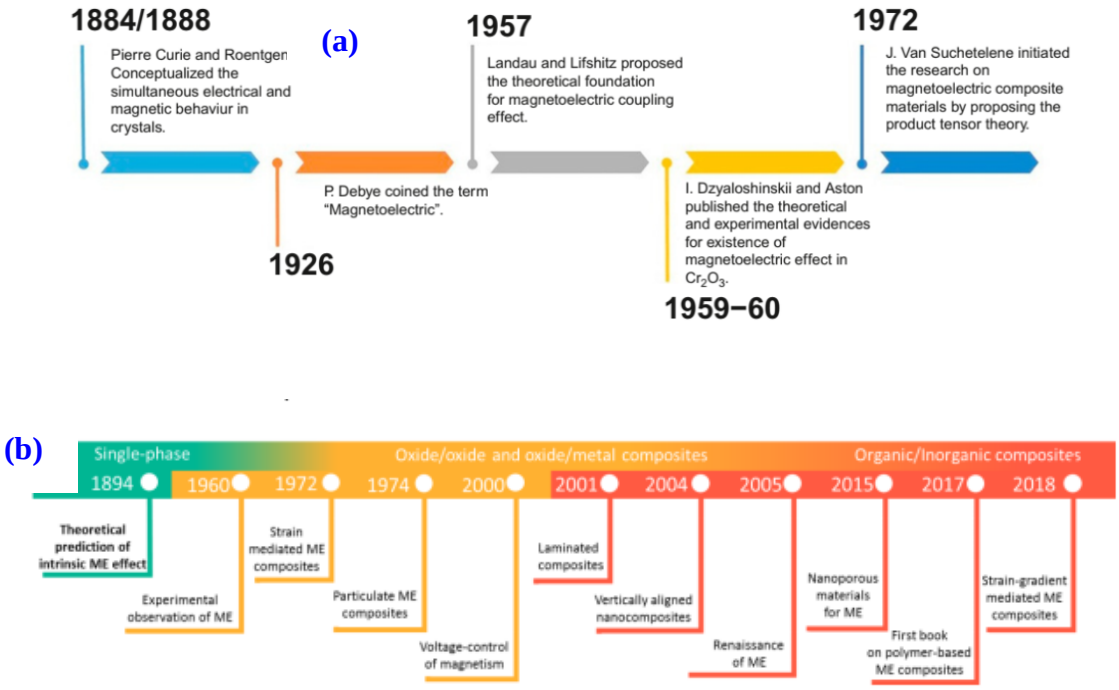

Figure 1.6: Research works on various types of magnetoelectric multiferroic materials from 1884 to 1972 and (b) from 1894 to 2018. Adapted from [33-35].

Early in the 1990s, Harshe et al. [36, 37] and Lopatin et al. [38] fabricated composite multiferroic materials using ferrites and either $BaTiO_3$ or $Pb(ZrTi)O_3$ (PZT) through a traditional sintering technique to address this issue. In comparison to eutectic composites, annealed ceramic composites were significantly simpler and less expensive to manufacture. They also offered the chance to combine phases with quite diverse crystal structures. However, compared to composites fabricated using a unidirectional eutectic method, these annealed composite multiferroic materials displayed weaker magnetoelectric couplings. The problem of

the strain-mediated magnetoelectric composites based on lead-based ferroelectric materials is that the lead-based ferroelectric materials is the brittleness and toxic. As a consequence, strain-mediated magnetoelectric composites based on lead-based ferroelectric materials are suitable soft-robotic and wearable or biomedical applications [11, 39]. In order to overcome the brittleness and toxicity of lead-based ferroelectric materials, polymer-based multiferroic composites have been fabricated and exhibited negligible magnetoelectric coupling strength [40-42] and a book published in 2017 [43] [Figure 1.6 (b)]. Most recently, the strain-gradient effect on magnetoelectric composites has been emerged as new technique to improve the magnetoelectric coupling strengths and still remained unrevealed [Figure 1.6 (b)]. In the 21st century (specially in the midst of 2005 and 2019), the number of research articles and patents on multiferroic magnetoelectric materials have rapidly increased toward the fabrication of next-generation energy efficient multifunctional magnetoelectric devices on all length and time scales [Figure 1.7 (a, b)].

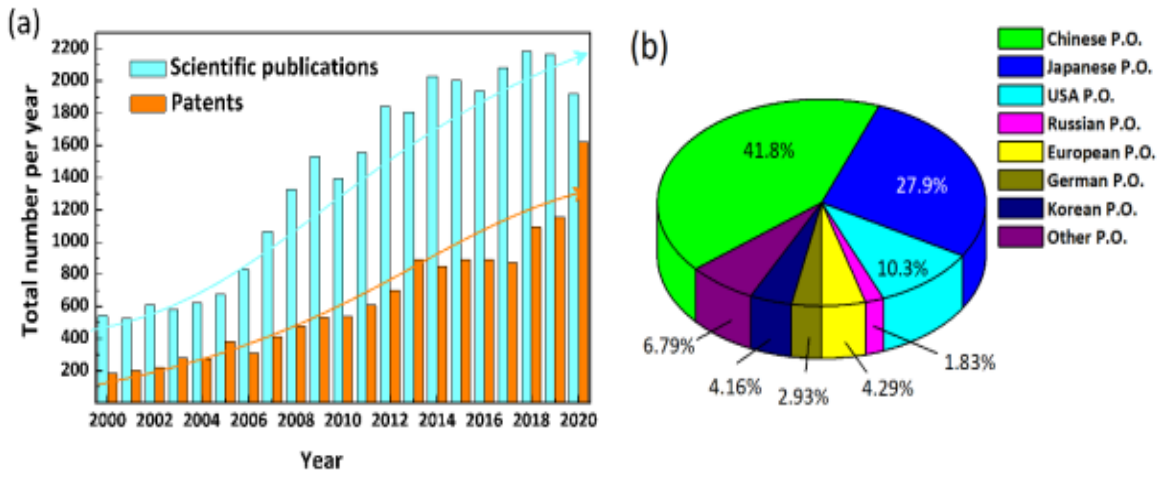

Figure 1.7: Development of the multiferroics and magnetoelectrics materials with respect to: (a) publications and (b) patents in the time-frame of 2000 to 2020 around the cross-country/region. Adapted from [35, 44-46].

So far, the investigated composites are the conventional multiferroic composites (strain mediated multiferroic composites). Thus, in the present investigation we were concentrated in fabricating the strain-mediated composite multiferroic materials based on the lead-free barium

calcium-zirconium-titanate ferroelectric and stoichiometric and non-stoichiometric nickel-copper-zinc ferrite to unravel the effect of iron-deficient non-stoichiometry on the magneto-electric-elastic coupling.

1.2. Motivation and selection of the component phases for composite multiferroic material

The demand of composite magnetoelectronics with high performance, low-cost and energy efficient has been increased day by day to meet the demand of human civilization and fourth industrial revolution. Composite magnetoelectrics and multiferroic materials intrinsically satisfy symmetry criteria concurrently, such as violating space inversion symmetry to display ferroelectricity and time-reversal symmetry to produce magnetism [47]. Specifically in single-phasic multiferroics, the material is comparably uncommon and imprecise due to a breakdown of both symmetries. The transition metal ions in ferroelectrics contain empty 'd^0' shells. In this instance, the positively charged ions form a molecule with the nearby anions, shifting the cations and anions in the crystal architecture to produce bulk electrical polarization. On the reverse hand, transition metals with the partially filled 'd^n' ($n = 1 - 9$) shell promote magnetism, where long-distance order of magnetism arises from the mutual interplay amongst the uncompensated spins of various ions and the virtual jumping of electrons amongst the ions. The two ordered states are mutually incompatible because they each need a different filling of the "d" shells for ferroelectricity and magnetism. Specifically, manipulating magnetization with an electric field and vice versa is accomplished by finding the magnetoelectric coefficient. This allows for the manipulation of one ferroic characteristic with the conjugate field of another [47]. In opposition to single-phasic multiferroic materials, magnetoelectric response in the composite magnetoelectronics does not establish an upper limit through the geometric mean of the electrical permittivity and magnetic permeability. It is possible to tailor the magnitude of magnetoelectric response by adusting the materials selected as well as the fabrication geometry and micromorphology of each individual material. The composite multiferroic materials

provide reasonable magnetoelectric coupling over the single-phase multiferroics at room temperature, but the realiziation of the composite magnetoelectrics with eloquent coupling amongst magnetic and electric orders and further enhacement in the magnetoelectric coupling is necessary to mitigate the demand of human civilization and fourth industrial revolution. In fact, there is a disparity in the midst of the desired value of the magneto-electric-elastic coupling coefficient and experimental value in composite multiferroic materials. The probable causes behind such disparity in magneto-electric-elastic coupling coefficient for composite multiferroic materials are: (i) presence of low resistive magnetostrictive phase, (ii) inevitable production of Fe^{2+} in the magnetostrictive phase enhances the material's leakage current (iii) formation of micro-cracks due to the discrepancy amongst the component phases' thermal expansion coefficients and (iv) porosity and unexpected phase generation [48]. Theoretically, it has been predicted that the composite multiferroic materials with equimolar component phase provide the optimum magneto-electric-elastic coupling coefficient. Thus, it is highly desirable to investigate experimentally the volume/mole fraction of magnetostrictive and ferroelectric phase's dependent magneto-electric-elastic response. Motivation of our work is to enhance the electromagnetic and magnetoelectric properties through the minimization of the above-mentioned problems using environmentally friendly piezoelectric phase and highly resistive piezomagnetic phase. The stoichiometric nickel copper zinc ferrites provide very low resistivity and high leakage current. It is therefore of interest to improve the resistivity and reduce the high leakage current of the stoichiometric nickel-copper-zinc ferrites. The iron-deficient non-stoichiometry in spinel ferrites can improve the resistivity of the spinel ferrites and reduce the leakage current. This motivated us to synthesize stoichiometric nickel-copper-zinc and iron-deficient non-stoichiometric nickel-copper-zinc ferrites separately and study their structural, elastic, thermodynamic and electromagnetic properties in details. The strain-mediated magneto-electric-elastic coupling coefficient in composite multiferroic materials is inversely connected with the relative electric permittivity and directly proportional to the

piezoelectric and piezomagnetic coefficients [49]. Thus, it is crucial to choose the proper ferroelectric and magnetostrictive materials that have outstanding piezoelectric and piezomagnetic coefficients in order to achieve the best strain-mediated magneto-electric-elastic coupling coefficient. We have selected barium-calcium-zirconium-titanate ferroelectric phase owing to its excellent piezoelectric properties near morphotropic phase border, and environmentally friendly. So, we have fabricated the particulate composites (perovskite-ferrite composites) having the component phases barium-calcium-zirconium-titanate (piezoelectric phase) and stoichiometric nickel-copper-zinc ferrite and non-stoichiometric nickel-copper-zinc ferrite (piezomagnetic phases) and studied the effect of sintering temperature and iron-deficient non-stoichiometric amount on structural, electromagnetic and magnetoelectric properties.

1.3. Goals of the current investigation

The goals of the present investigation are presented below:

i) To synthesize and characterize nickel copper zinc ferrites, $Ni_{0.25}Cu_{0.13}Zn_{0.62}Fe_2O_4$ (NCZFO) ferrites at various sintering temperatures (1000 to 1250 ºC; in step of 50 ºC) with an aim to unfold the impacts of sintering temperature on structure, micromorphological, elastic, and electromagnetic traits and to use as a component phase in fabricating composite multiferroic materials.

ii) To synthesize non-stoichiometric nickel copper zinc ferrites, $Ni_{0.25}Cu_{0.13}Zn_{0.62}Fe_{2-x}O_{4-3x/2}$ ($NCZFe_{2-x}O_{4-3x/2}$) (x = 0.00~0.12) at various sintering temperatures (1100 to 1250 ºC: in step of 50 ºC) with an objective to unravel the consequences of iron-deficient non-stoichiometric content and sintering temperature on structure, microstructure, elastic, and electromagnetic traits.

iii) To synthesize lead-free $Ba_{0.9}Ca_{0.1}Zr_{0.1}Ti_{0.9}O_3$ (BCZTO) ferroelectric phase with an objective to use as component phase in fabricating the multiferroic composite.

iv) To synthesize and characterize (1-*y*) [BCZTO] + (*y*) [NCZFO] (*y* = 0.0-1.0) composite multiferroic materials at various sintering temperature (1100 to 1250 ºC; in step of 50 ºC) with an aim to investigate the impacts of sintering temperatures on structure, microstructure, and electromagnetic traits.

v) To synthesize and characterize (1-*y*) [BCZTO] + (*y*) [$NCZFe_{2-x}O_{4-3x/2}$] (*x* = 0.0; 0.04; 0.08, 0.12 and *y* = 0.2; 0.5) composite multiferroic materials annealed at 1200 ºC with an aim to investigate the iron-deficient non-stoichiometric dependent structural, microstructure, electromagnetic, and magnetoelectric traits.

1.4. Framework of the Dissertation

The hierarchy of the current dissertation is given below.

Chapter one describes the general introduction, reason for the selection of the ferromagnetic and ferroelectric in fabricating the composite multiferroic materials, and objective of our present work**.**

Chapter two presents the brief literature review and important remarks of the relevant research work and a short description of composite multiferroic materials.

Chapter three presents the sample fabrication and various experimental techniques we used to investigate the different traits of stoichiometric and non-stoichiometric nickel-copper-zinc ferrites, and composite multiferroic materials.

Chapter four describes: (i) the investigation of the sintering temperature dependent crystallographic, elastic, electrical, and magnetic traits of NCZFO ceramics, (ii) the investigation on the impact of iron-deficient non-stoichiometry content on structure, microstructure, elastic and electromagnetic traits of $NCZFe_{2-x}O_{4-3x/2}$ ferrites at various sintering temperatures, (iii) investigation of the consequences of sintering temperature dependent microstructure, micromorphology and electromagnetic traits of (1-*y*) [BCZTO] + (*y*) [NCZFO]

(y = 0.0-1.0) composite multiferroic materials, and (iv) exploration of the iron-deficient non-stoichiometry dependent structure, microstructure, electromagnetic, and magnetoelectric traits of (1-y) [BCZTO] + (y) [$NCZFe_{2-x}O_{4-3x/2}$] (x = 0.0; 0.04; 0.08; 0.12 and y = 0.2; 0.5) composite multiferroic materials.

Chapter five describes the conclusions, recommendations for prospective works and novelty of the current research.

Chapter Two: Literature Reviews and Theoretical Features

In this chapter, we have reviewed the past and present studies on the ferroelectric phase, $Ba_{0.9}Ca_{0.1}Ti_{0.9}Zr_{0.1}O_3$, iron-deficient non-stoichimetric $Ni_{0.25}Cu_{0.13}Zn_{0.62}Fe_{2-x}O_{4-3x/2}$ (x = 0.0; 0.04; 0.08; 0.12), relavent studies on the composites of (1-y) $[Ba_{0.9}Ca_{0.1}Ti_{0.9}Zr_{0.1}O_3]$ + (y) $[Ni_{0.25}Cu_{0.13}Zn_{0.62}Fe_2O_4]$ (x = 0 to 1.0) and finally we reviewed the relevant studies on the effect on iron-deficient non-stoichiometric multiferroic composites of (1-y) $[Ba_{0.9}Ca_{0.1}Ti_{0.9}Zr_{0.1}O_3]$ + (y) $[Ni_{0.25}Cu_{0.13}Zn_{0.62}Fe_{2-x}O_{4-3x/2}]$ (x = 0.0; 0.04; 0.08; 0.12 and y = 0.2; 0.5) based on ferroelectric phase and ferromagnetic phase.

2.1. Literature review

2.1.1. Literature Review on Barium Calcium Titanium Zirconate Ferroelectric phase

Reyes-Montero et al. [50] prepared $Ba_{0.9}Ca_{0.1}Ti_{0.9}Zr_{0.1}O_3$ (BCTZO) ceramics using Pechini ursor process at 973 K for 1 h and were annealed at below 1573 K for 5h. They reported that the sample exhibited single-phase perovskite structure for all heat-treatments as provided in Figure 2.1. SEM analysis revealed that the sample annealed at 1473, 1523, and 1548 K for 5 h provided dense ceramics (95 %-98 % theoretical density) and the grain diameter was improved on increasing sintering temperatures as presented in Figure 2.2 (b-d) and their values were presented in Table 2.1. The ceramics annealed at 1548 K for 5 h exhibited the best ferro-piezoelectric characteristics: d_{33} = 390 pC/N, d_{31} = 143 pC/N, k_p = 50%, ε' = 2253 and tanδ = 0.06 (100 kHz) at room temperature, T_C = 112 ℃, $2P_r$ = 24 μC/cm^2 and $2E_C$ = 4.07 kV/cm. At 1250 ℃, dense ceramic (97% theoretical density) was achieved with average grain size ~5 μm, T_C = 115 ℃ and high ferro-piezoelectric properties (d_{33} = 340 pC/N, k_p = 49%). The high piezoelectric coefficent was ascribed to the high polarizability of the ceramics at local level. These values were provided in Table 2.1. At 1200 ℃, the presence of the tetragonal crystal structure and T_C = 118 ℃ indicated that Ca^{2+} substation took place at the A-sites of the perovskite structure.

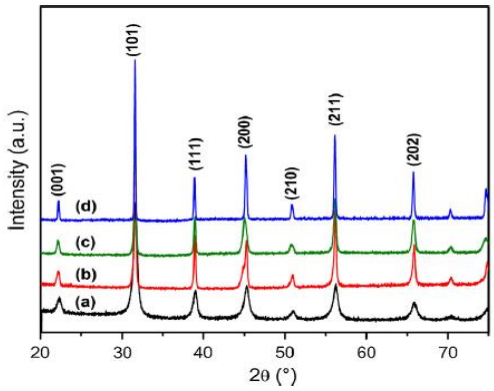

Figure 2.1: XRD patterns of BCTZO ceramics: (a) calcinated at 973 K for 1 h; and annealed at: (b) 1473 K, (c) 1523 K and (d) 1548 K for 5 h. Adapted from [50].

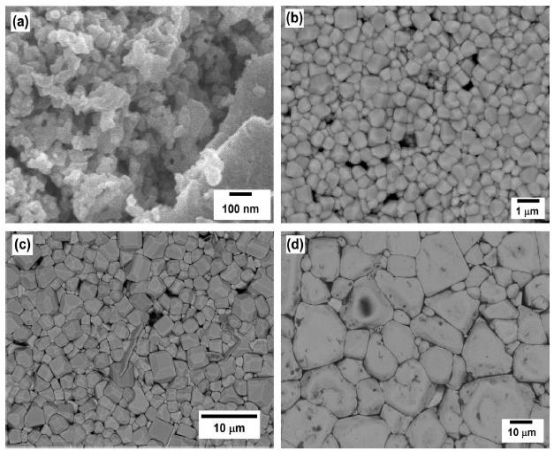

Figure 2.2: SEM images for BCTZO ceramics: (a) calcinated powders at 973 K for 1 h; annealed BCTZO: (b) 1473 K, (c) 1523 K and (d) 1548 K for 5 h. Adapted from [50].

Table 2.1. Density, d_{33}, Grain size, Permittivity loss tangent $(tan\delta_{\varepsilon})$of BCTZO annealed at different T_s. Adapted from [50].

T_s ºC	density (g/cm^3)	d_{33}	Grain size (μm)	$tan\delta_{\varepsilon}$
1473	5.49	45	0.4	0.016
1523	5.64	240	4.6	0.014
1548	5.70	390	15.2	0.012

Herrera-Pérez, et al. [51] prepared $Ba_{0.90}Ca_{0.10}Ti_{0.90}Zr_{0.10}O_3$ (BCTZO) ceramics by the adjusted Pechini technique with an objective to investigate electronic structure achieved via

Core-hole spectroscopies such as X-ray photoelectron spectroscopy and high-resolution electron energy loss spectroscopy. Raman spectra suggested that Ca^{2+} cations partly occupied the Ti^{4+} cations in the octaahedrally coordinated (B)-site with the tetragonal phase. A multiplet structure was achieved through X-ray photoelectron spectroscopy for Ti 2p and via high-resolution electron energy loss spectroscopy for Ca $L_{2,3}$ and Ti $L_{2,3}$ edges. Octahedral symmetry in the crystal field effects reproduced the local distortion of TiO_6 octahedra. The charge transfer effects were reproduced L_3-edge electron energy loss spectroscopy shoulders and the satellite in the Ti 2p X-ray photoelectron spectroscopy region. The crystal field and charge transfer parameters, charge transfer energy, and Coulomb repulsion energy were reported for future reference. The broadening of the Ti L_2-edge suggested the presence of the Coster-Kronig electron decay process.

Reyes-Montero et al. [52] prepared $Ba_{1-x}Ca_xTi_{0.9}Zr_{0.1}O_3$ (x = 0.10, 0.15) (BCTZ) powder via solid-state reaction method employing a lower thermal treatment at 1623 K (2 h) and various sintering temperatures (1573, 1623 and 1673 K for 2 h). They reported that a single-phase perovskite structure for both samples at different sintering temperatures were achieved by X-ray diffraction analysis as showed in Figure 2.3 (a-b). SEM analysis revealed homogeneous and dense (≥ 95%) microstructures having sub-10 μm grain size were achieved for all sintering temperatures and conditions as provided in Figure 2.4 (a-f). At 1673 K, ceramics exhibited excellent ferro-piezoelectric properties for x = 0.10: d_{33} = 300 pC/N, d_{31} = –150 pC/N, k_p = 0.48 and d_{33} = 410 pC/N, d_{31} = –154 pC/N, k_p = 0.50 for x = 0.15 due to an enhancement in average grain size. Howevere, they reported that a diffuse phase transition was observed at T_c = 100 °C (approx.) at 1 kHz.

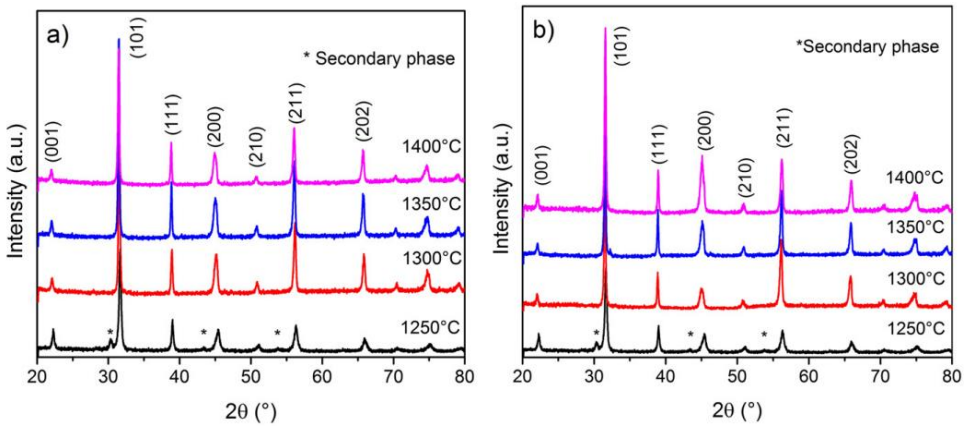

Figure 2.3: XRD profiles of BCTZO perovskite synthesized at 1523 K and annealed at 1573, 1623, 1673 K: (a) x = 0.10, and (b) x = 0.15. Adapted from [52].

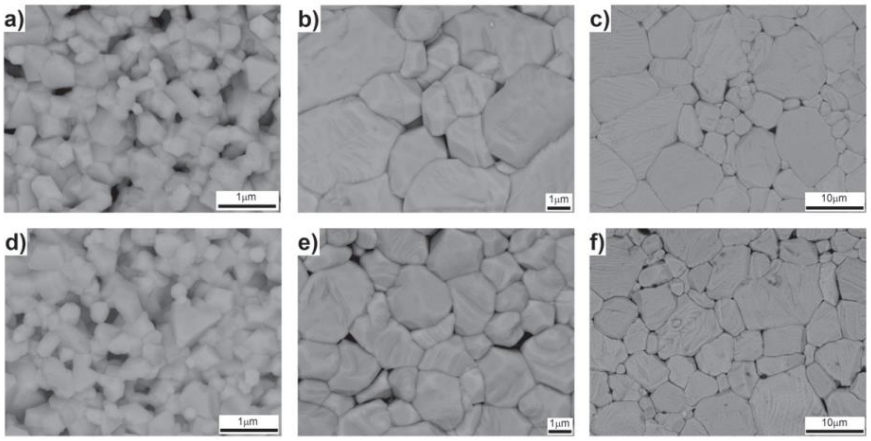

Figure 2.4: Micromorphological structures of BCTZO annealed ceramics: *x* = 0.10: (a) 1573 K, (b) 1623 K, and (c) 1673 K; *x* = 0.15: (d) 1573 K, (e) 1623 K, and (f) 1673 K. Adapted from [52].

Reyes-Montero et al. [53] prepared $Ba_{0.9}Ca_{0.1}Ti_{0.9}Zr_{0.1}O_3$ (BCTZ) lead-free ceramics by Pechini method and annealed at 1548 K for 5h to investigate the effect the electric field on the crystallographic, microstructural and electrical characteristics. They reported that electric field induced changes in rhombohedral-tetragonal relative content that facilitated polarization process. SEM analysis exhibited a mean grain diameter of 20 μm and complex ferroelectric domains. Ceramics displayed high piezoelectric coefficient of ~390 pC/N, high ferroelectric remnant polarization of 15.3 μC cm^{-2} and low field of coercivity of 1.5 kV cm^{-1} at room temperature.

Herrera-Pérez et al. [54] synthesized $Ba_{1-x}Ca_xTi_{0.90}Zr_{0.10}O_3$ (BCTZO) ceramics (x = 0, 0.1, 0.125, 0.15, 0.175, 0.20) via the adjusted Pechini process and annealed at 1673 K for 5 h. They reported that XRD patterns with narrow peaks suggested that crystallite sizes were in the micron scale as shown in Figure 2.5 (a-c). SEM micrographs reveals a nonhomogeneous rod polyhedral-type shapes and faceted quasi-cubs for $Ba_{0.9}Ca_{0.1}Ti_{0.90}Zr_{0.10}O_3$ as provided in Fig. 2.5 (d) while $Ba_{0.85}Ca_{0.15}Ti_{0.90}Zr_{0.10}O_3$ revealed a duplex morphology consisting of small grains and abnormally rod-large grains as illustred in Figure 2.5 (e).

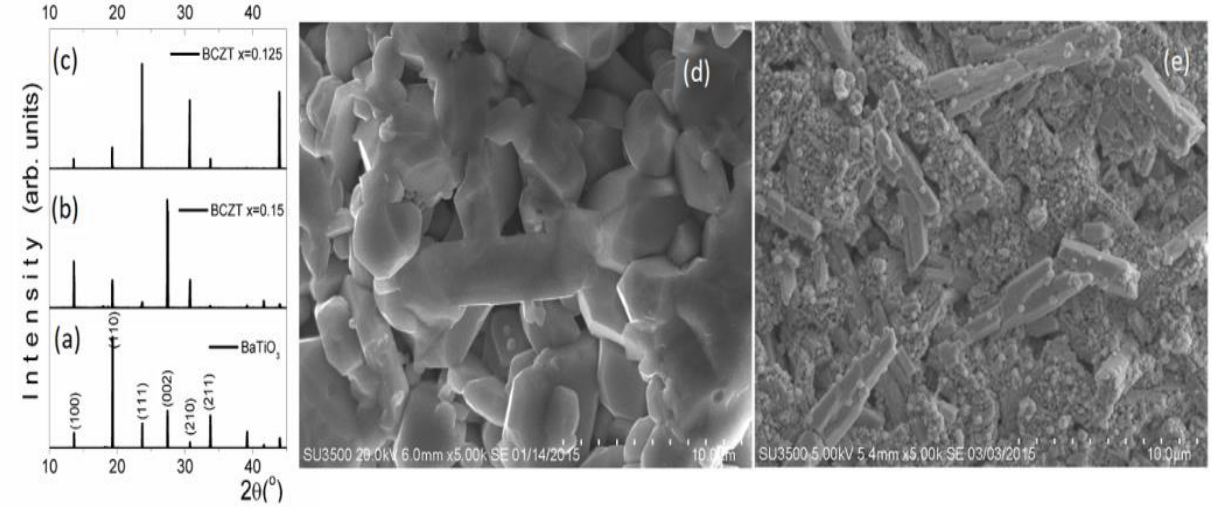

Figure 2.5: HR-XRD patterns for the: (a) reference compound $BaTiO_3$, (b) BCZT with x = 0.15, (c) BCZT with x = 0.125. SEM micrographs for: (d) BCZT with x = 0.1 (e) BCZT with x = 0.15. Adapted from [54].

Herrera-Pérez et al. [55] prepared $Ba_{0.90}Ca_{0.10}Ti_{0.90}Zr_{0.10}O_3$ (BCZTO) ceramic by using a modified Pechini method. They reported that the material crystallized in the tetragonal symmetry at 973 K for 1 h as delineated in Figure 2.6 (a). Figure 2.6 (b) and 2.6 (c) reveaked the TEM bright field micrograph for the powders heated at 973 K and the corresponding histogram for particle size distribution which was centered at ~ 30 nm.

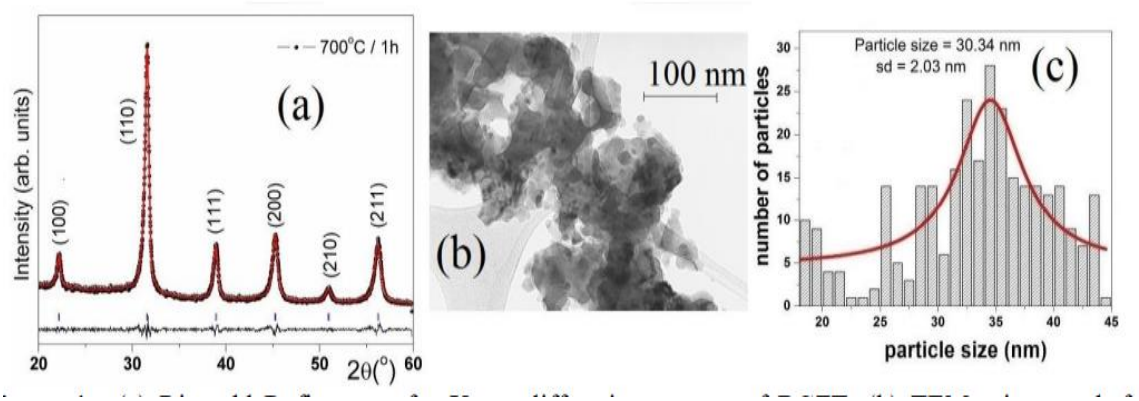

Figure 2.6: (a) Rietveld Refinement for XRD of BCZTO (b) TEM micrograph for powders samples calcinated at 973 K for 1 h. (c) Particle size distribution from TEM. Adapted from [55].

Herrera-Pérez et al. [56] fabricated $Ba_{0.9}Ca_{0.1}Ti_{0.9}Zr_{0.1}O_3$ (BCZTO) lead-free perovskites by the adjusted Pechini process followed by sintering at 1523 K for 5 h to determine the effective piezoelectric coefficient and the macro ferroelectric hysteresis behavior. They reported that the sample exhibited single-phase perovskite structure as was ascertained by XRD analysis with a slight degree of tetragonality of 1.0025. SEM analysis revealed a non-homogeneous terrace-type shape with a grain size distribution centered at 13 μm. The sample exhibited improved ferroelectric properties (piezoelectric coefficient: 232 pC/N, coercive field: 1.3 kV/cm and saturation polarization: 15.7 $\mu C/cm^2$) which were associated with the tetragonal distortion.

Herrera-Pérez et al. [57] prepared $Ba_{1-x}Ca_xTi_{0.9}Zr_{0.1}O_3$ (x = 0, 0.1 and 0.15) by the modified Pechini method and annealed in the midst of 1473 to a maximum of 1673 K for 5 h to inspect the connection in the midst of the crystal and electronic skeleton with the dielectric and piezoelectric traits. The high-resolution XRD examination suggested the simultaneousness of tetragonal symmetric and rhombohedral symmetric phases. The dielectric analysis indicated a relaxor feature with a Curie temperature in a range of 100-120 °C. Micro-X-ray absorption near edge spectroscopy was carried out to monitor possible changes of electronic structure profile due to the local distortions as Ca^{2+} increased.

2.1.2. Literature Review on Stoichiomteric and non-stoichiometric Ferromagnetic phase

Sujatha et al. [58] synthesized $Ni_{0.50}Cu_{0.05}Zn_{0.45}Fe_2O_4$ through the sol-gel method annealed at three different temperatures (1173, 1223 and 1303 K). They reported that the microstructures displayed homogeneous polyhedral shape grains and grain size was increased with sintering temperature (Figure 2.7). Magnetization was increased to a maximum of 1223 K and henceforth decreased at 1303 K due to the improved grain size and zinc evaporation. The cut-off frequency decreased as the magnetic permeability rose (Figure 2.8) with sintering temperature due to the combined effect of of improved magnetization and grain size.

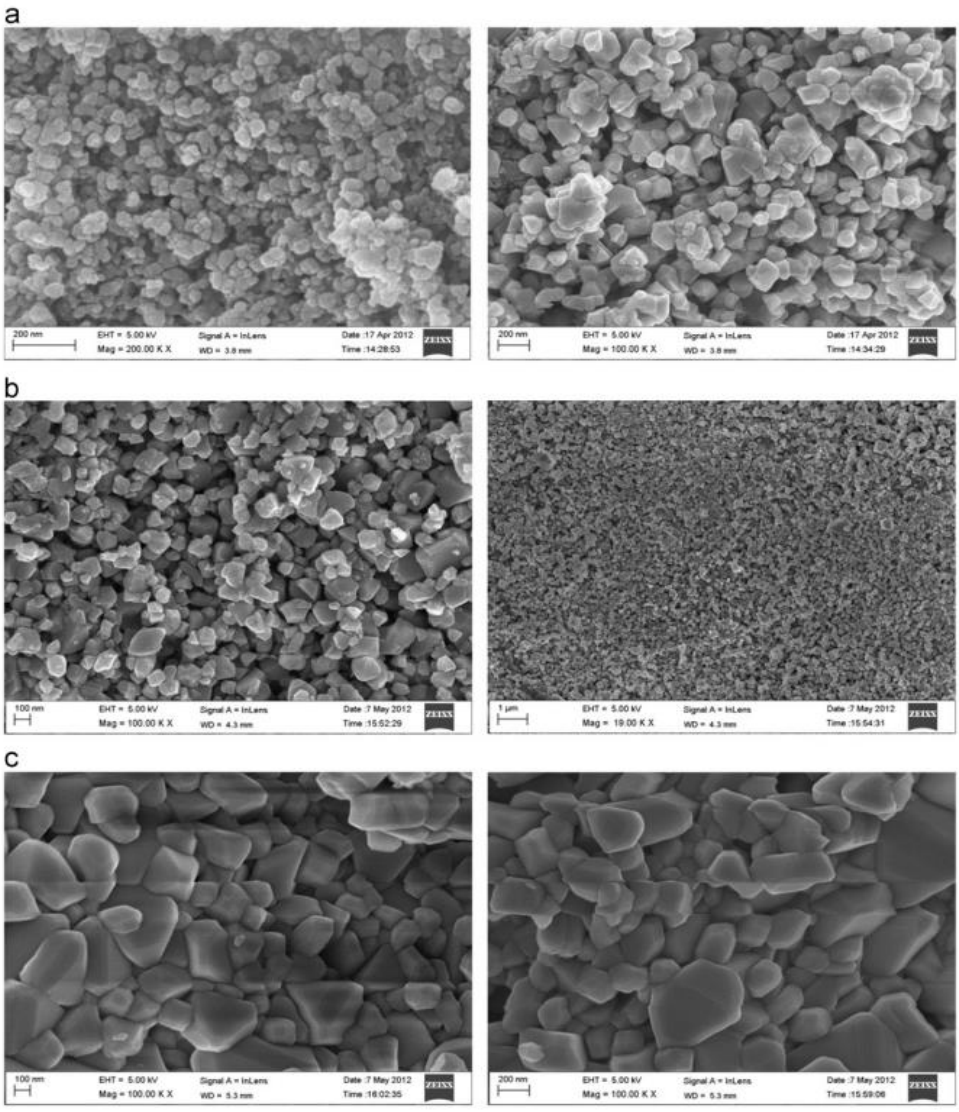

Figure 2.7: FESEM micrographs for $Ni_{0.50}Cu_{0.05}Zn_{0.45}Fe_2O_4$ ferrite annealed at: (a) 1173 K (b) 1223 K, and (c) 1303 K. Adapted from [58].

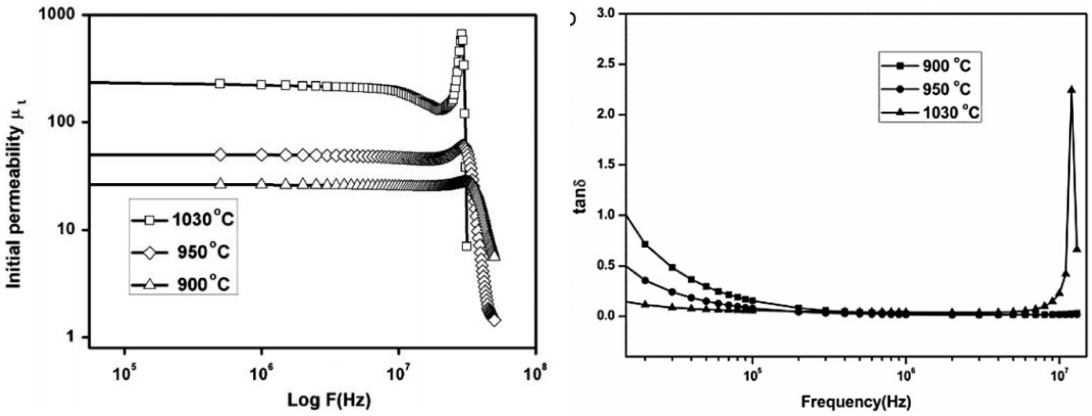

Figure 2.8: Frequency dependent: (a) magnetic permeability spectra and (b) magnetic loss tangent for $Ni_{0.50}Cu_{0.05}Zn_{0.45}Fe_2O_4$ ferrite annealed at 1173 K, 1223 K and 1303 K. Adapted from [58].

Gholizadeh et al. [59] successfully prepared $Ni_{0.3}Cu_{0.2}Zn_{0.5}Fe_2O_4$ using citrate precursor method and subsequently annealed at temperatures 473, 673, and 873 K for 2 h under air-, argon-, and carbon monoxide-ambient atmospheres to probe the consequences of sintering enviroment and temperature on crystallographic architecture, redistribution of Zn^{2+} and Fe^{3+} ions, the oxidation of Fe atoms in lattice, and magnetic properties. They claimed that in various sintering atmospheres, the crystallite size and unit cell parameter increased as the sintering temperature increased. The saturation magnetization was increases with sintering temperature and atmosphere due to the variation of ternary variables: magnetic core diameter, transposition variable and the alteration of Fe^{3+}-ion concentration due to the presence of Fe^{4+} and Fe^{2+} ions.

Murthy [60] synthesized $Ni_{0.65-x}Cu_xZn_{0.35}Fe_{2-x}O_4$ (x = 1, 4, 8, 12 and 14 mol%) applying the solid-state sintering technique and annealed at different temperatures (773 K-1273 K) in step of 283 K) for 10 h to investigate the magnetic, electrical and elastic properties. They claimed that the grain diameter increased as copper concentration and sintering temperature increased.. The saturation magnetization and permeabity were increased with increasing copper content. The enhancement in magnetic permeability was correlated with the enhancement in grain size. Young's and rigidity moduli increased on increasing sintering temperature to a maximum of 1173 K and declined at higher sintering temperatures. Additionally, the Young's and rigidity

moduli improved as the copper concentration increased to a maximum of 12 mol%, which showed an improvement in the atomic binding strength.

Su et al. [61] synthesized $Ni_{0.45}Cu_{0.20}Zn_{0.35}Fe_{2-x}O_{4-3/2x}$ (x = 0-0.25 in steps of 0.05) ferrites utilizing ball milling technique followed by a sintering at 1173 K to investigate the influence of iron-nonstoichiometry content on the microstructure, sintering behavior, saturation magnetization, magnetic permeability and electric permittivity spectra properties. They reported that the samples possessed spinel structucture with cubic symmetry without any impurity phase (Figure 2.9). In addition, the sintering density and linear shrinkage ratio were increased on upsurging the iron-deficient non-stoichiometric extent to a maximum of x = 0.10 and eventually remained almost constant with further enhancement in iron-nonstoichiometry content.

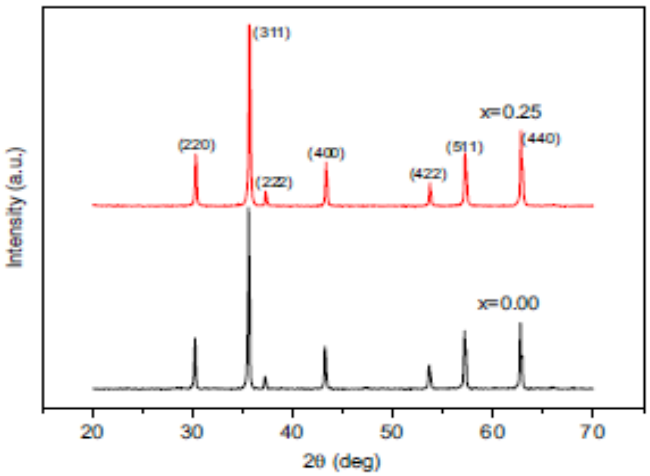

Figure 2.9: XRD patterns of $Ni_{0.45}Cu_{0.20}Zn_{0.35}Fe_{2-x}O_{4-3/2x}$ (x = 0, 0.25) cermaics. Adapted from [61].

Microstructures of the samples exhibited a skeleton-type structure having some point contacts in the midst of the grains (Figure 2.10 (a-f)) and the average grain size increased and some abnormal big grains appeared with increasing iron-nonstoichiometry. An archetypal binal micromorphology (small grains and some larger grains) was observed when the iron-nonstoichiometry was reached to a value of x = 0.15. The big grains disappeared and grain size changed very little when the iron-nonstoichiometry was greater than x = 0.15. The electric

permittivity monotonously increased with increasing iron-nonstoichiometry and the samples having iron-nonstoichiometry possessed relatively small permittivity loss tangent.

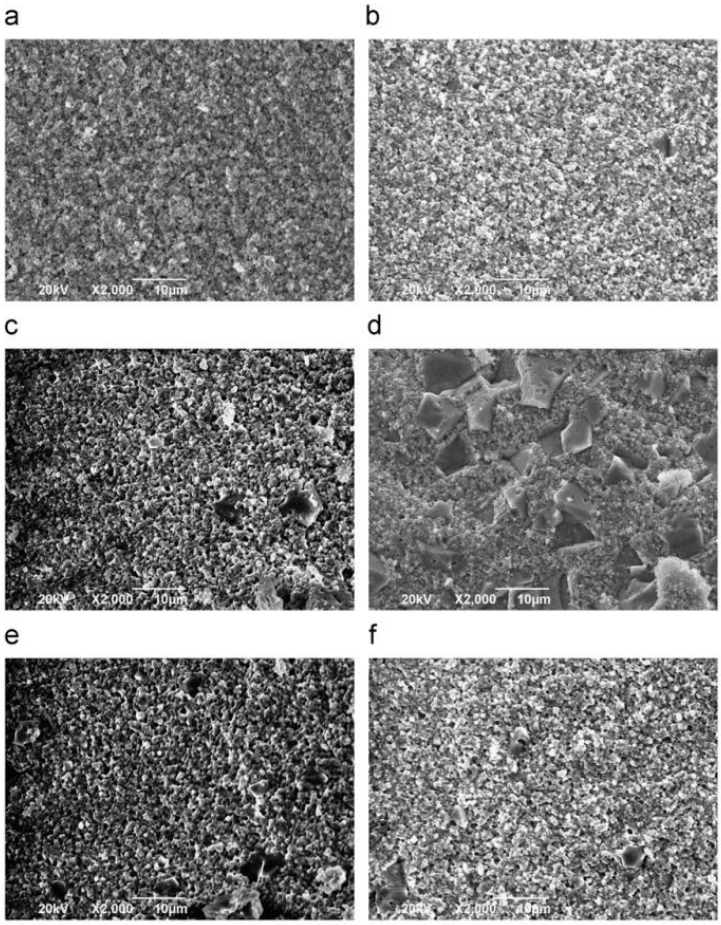

Figure 2.10: SEM photographs of the $Ni_{0.45}Cu_{0.2}Zn_{0.35}Fe_{2-x}O_{4-3/2x}$ ferrites with different Fe-deficiency (a) x = 0, (b) x = 0.05, (c) x = 0.10, (d) x = 0.15, (e) x = 0.20, and (f) x = 0.25. Adapted from [61].

The magnetic permeability, Snoek's product and saturation magnetization were increased on escalating iron-deficiency non-stoichiometric amount to a maximum of x = 0.10 and reduced with further increased in iron-deficient non-stoichiometry due to the sintering density and average grain size (Table 2.2) and optimum value of these parameters was accomplished at x = 0.10. The cut-off frequency was decreased on enhancing iron-deficient non-stoichiometry to a maximum of x = 0.10 and therafter gradually decreased.

Table 2.2. Magnetic permeability (μ_i'), cut-off frequency (f_r), Snoek's product and saturation magnetization (M_s) of the samples. Adapted from [61].

X	μ_i'	Cut-off frequency, f_r (MHz)	Snoek's product	M_s (emu/g)
0.00	24	227	5114	60.8
0.05	69	99	6735	61.5
0.10	82	93	7497	62.0
0.15	79	94	7265	61.9
0.20	76	96	7162	61.7
0.25	75	96	7181	61.6

Murbe et al. [62] successfully developed $Ni_{0.20}Cu_{0.20}Zn_{0.60+z}Fe_{2-z}O_{4-(z/2)}$ with ($0 \leq z \leq 0.06$) ferrites using standard ceramic route to investigate the shrinkage and magnetic permeability of sub-stoichiometric, iron-deficient ferrites. In addition, they investigated the effect of Bi_2O_3 addition to stoichiometric and sub-stoichiometric ferrites on the microstructure formation and magnetic permeability. The highest shrinkage rate's temperature changed taken away T = 1273 K for z = 0 to 1173 K for a sub-stoichiometric composition with $z \geq 0.02$. After firing at 1173 K dense samples were achieved for sub-stoichiometric ferrites (z > 0) only. At 1173 K, the sub-stoichiometric samples were decamped into stoichiometric sample and copper oxide. The presence of copper oxide enhanced the shrinkage significantly. At 1173 K, the non-stoichiometric samples (z > 0) exhibited dense characteristics. During sintering, the presence of CuO in non-stoichiometric samples supported the densification (Figure 2.11). At 1173 K, incorporation of 1 wt% Bi_2O_3 as liquid phase sintering aid into stoichiometric ferrite (z = 0) provided sufficient densification. At 1173 K, incorporation of 0.37 wt% Bi_2O_3 into non-stoichiometric sample (z = 0.02) resulted dense samples but the microstructure was predominated through the heterogeneous grain growth. The magnetic permeability was

enhanced from 230 for stoichiometric samples ($z = 0$) to $\mu = 430$ for non-stoichiometric sample ($z = 0.02$) (Figure 2.12).

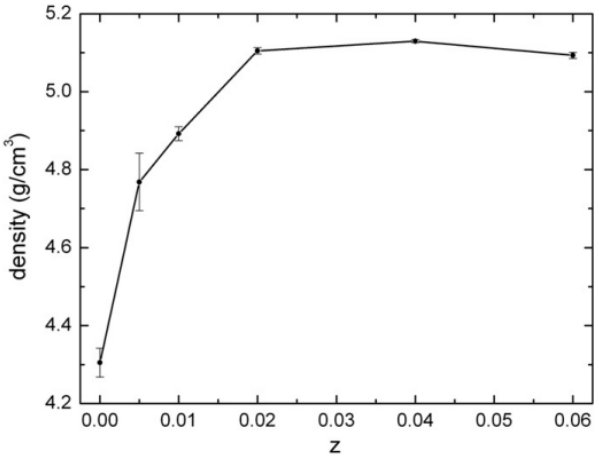

Figure 2.11: Density vs. compositions of $Ni_{0.2}Cu_{0.2}Zn_{0.6+z}Fe_{2-z}O_{4-(z/2)}$ ($0 \leq z \leq 0.06$) annealed at 1173 K for 2 h. Adapted from [62].

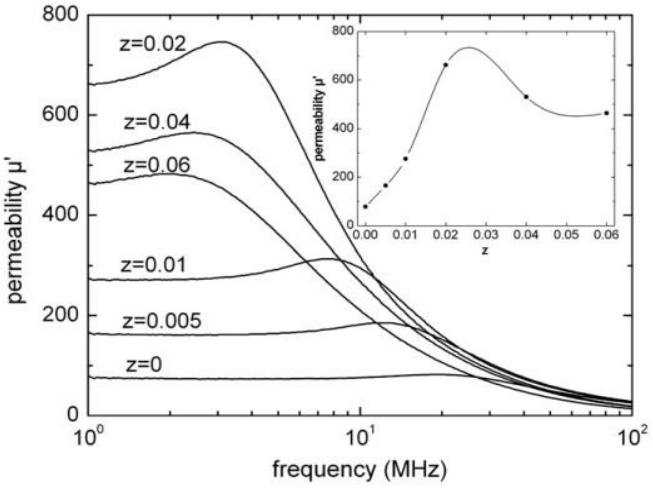

Figure 2.12: Magnetic permeability vs. frequency for $Ni_{0.20}Cu_{0.20}Zn_{0.60+z}Fe_{2-z}O_{4-(z/2)}$ (with $0 \leq z \leq 0.06$); inset: magnetic permeability at 1 MHz vs. compositions. Adapted from [62].

Khan et al. [63] successfully synthesized $Ni_{0.28}Cu_{0.10}Zn_{0.62}O(Fe_2O_3)_{1-x}$ (with $0 \leq z \leq 0.08$) using double sintering ceramic technique to examine the impact of Fe-deficiency and sintering temperature on the temperature and frequency dependent complex magnetic permeability and relevant parameters. They reported that the Curie temperature, magnetic permeability (Figure 2.13 (a, b)), and resonant frequency were increased with increasing Fe-deficiency due to the

enhancement in nickel/copper ratio. In addition, they also reported that the resonant frequency and Curie temperature were increased primarily with increasing Fe-deficieny and thereafter decreased and eventually achieved a maximum at x = 0.06.

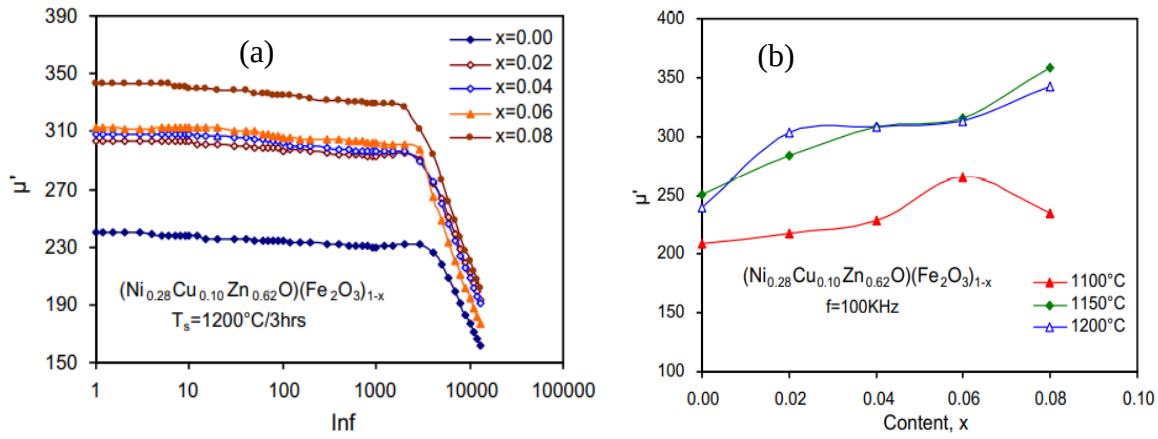

Figure 2.13: (a) Frequency dependence of μ_i' of $Ni_{0.28}Cu_{0.10}Zn_{0.62}O(Fe_2O_3)_{1-x}$ (with $0 \leq x \leq 0.08$) ferrites annealed at 1200 ºC; (b) Variation with Fe-deficient at different T_s. Adapted from [63].

Chen et al. [64] successfully synthesized $Ni_{0.56}Cu_{0.10}Zn_{0.34}Fe_{2-x}O_{4-3/2x}$ (with $0 \leq x \leq 0.12$) ferrites using conventional oxide ceramics process to probe the consequences of Fe-non-stoichiometry content on magnetic and Brillouin function characteristics. They noted that as the amount of Fe-deficiency increased, the average grain diameter steadily increased, and when the amount of Fe-deficiency reached x = 0.06, a characteristic dual microstructure with small grains and large grains was produced. (Figure 2.14). The discontinuous grain growth suggested an inhomogeneous distribution of the liquid phase and big grains were disappeared with increasing Fe-deficient content. The saturation magnetic induction was increased while the coercivity was decreased with increasing Fe-deficiency content. Based on the Néel molecular field theory, for the spinel ferrites which contained not only Fe^{3+} ions but also some other multiple magnetic ions (Ni^{2+} and Cu^{2+}), the non-linear fitting method was used to estimate the intrasublattice molecular field coefficients (ω_{aa} and ω_{bb}) and intersublattice molecular field coefficient ω_{ab} ($\omega_{ba} = \omega_{ab}$) and the Curie temperature formula were modified. The

molecular field coefficients ω_{aa} and ω_{bb} were increased while the value of ω_{ab} was decreased with increasing Fe-deficient content which resulted in reduction of Curie temperature. In addition, the fitting Curie temperatures values well consistent with the Curie temperatures achieved using the modified formula.

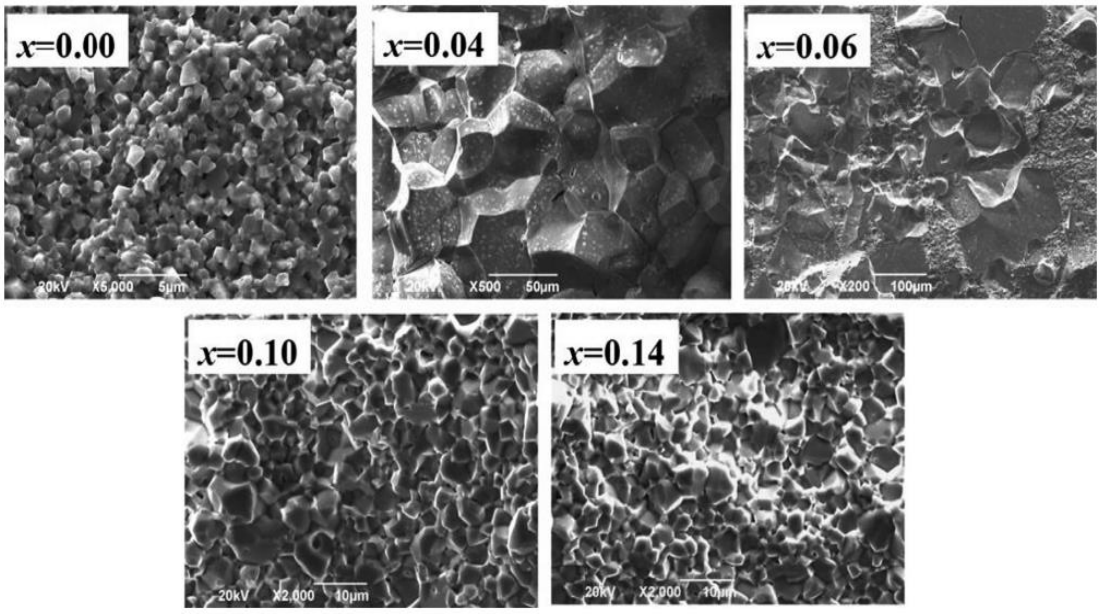

Figure 2.14: The SEM images of $Ni_{0.56}Cu_{0.10}Zn_{0.34}Fe_{2-x}O_{4-3/2x}$ (x = 0.0-0.12) with various Fe-deficiency. Adapted from [64].

Sun et al. [65] synthesized non-stoichiometric $Ni_{0.56+x/2}Zn_{0.34}Cu_{0.10}Fe_{2.0-x}O_{4-x}$ (with $0 \leq x \leq 0.12$) ceramics using solid-state synthetic technique to examine the ferromagnetic resonance linewidth characteristics and the physical, structural, cation distribution, and microstructural aspects. The results revealed that the lattice constant displayed descending trend with increasing iron-nonstoichiometry amount due to the lattice shrinkage resulted from the increasing iron-nonstoichiometry amount. The grain size was increased and maximized at x = 0.04, and afterwards revealed descending trend (Figure 2.15). The bulk density improved as the amount of iron-nonstoichiometry increased. The findings showed that when the amount of iron-deficient non-stoichiometry increased to x = 0.08 (approx.), the content of Fe^{3+} ions at the tetrahedrally coordinated (A)-site declined somewhat, while Ni^{2+} ions increased and the

content of Fe^{3+} ions rapidly decreased at the octaahedrally coordinated (B)-site. However, when the iron-deficient non-stoichiometric content is $x \leq 0.08$, the content of Fe^{3+} ions diminished dramatically at the tetrahedrally coordinated (A)-site and tends to decrease somewhat at the octaahedrally coordinated (B)-site. As the amount of iron-nonstoichiometry increased, the saturation magnetization upsurged to a maximum of $x = 0.04$ before decreasing. The saturation magnetization of stoichiometric samples was much lower than that of iron-deficient samples due to the superposition effect in the midst of molecule magnetic moment and bulk density. The porosity linewidth broadening was significantly larger than the anisotropy linewidth broadening.

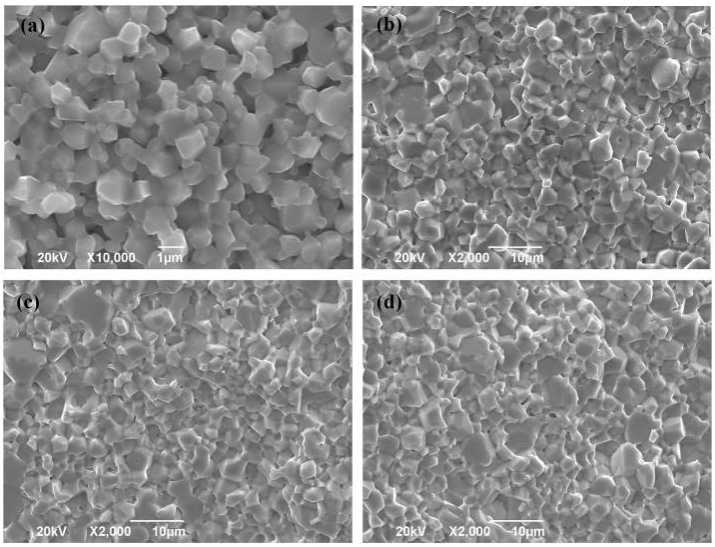

Figure 2.15: SEM micrographs of $Ni_{0.56+x/2}Zn_{0.34}Cu_{0.10}Fe_{2.0-x}O_{4-x}$ ferrites with various amounts of iron-nonstoichiometry: (a) $x = 0$, (b) $x = 0.04$, (c) $x = 0.08$, and (d) $x = 0.12$. Adapted from [65].

Priese et al. [66] successfully developed $Ni_{0.30}Cu_{0.20}Zn_{0.50+z}Fe_{2-z}O_{4-(z/2)}$ ($0 \leq z \leq 0.06$) using classic ceramic technique and annealed at various temperature (900-1150 ℃) to study the effect of sintering temperature in air atmosphere and oxygen partial pressessure on the phase formation, micromorphological, and magnetic traits. They reported that the single-phasic spinel architecture with some impurity was formed (Figure 2.16). The shrinkage rate was shifted from 1000 ℃ for $z = 0$ towards lower temperatures and reached its maximum rate at

900 °C for z = 0.02. Stoichiometric ferrites revealed regular growth of single-phase ferrite grains if annealed at $T_s \leq 1100$ °C. At 1150 °C appeared a small amount of Cu_2O which triggered exaggerated grain growth. The coexistence of nonstoichiometric ferrites ($z > 0$) form Cu-poor stoichiometric ferrites with a minority CuO phase retained after sintering at 900-1000 °C. At $T_s \geq 1050$ °C, CuO transformed into Cu_2O, and exaggerated grain growth was developed. The magnetic permeability was increased with increasing sintering temperature and at T_s = 1000 °C, the magnetic permeability reached a maximum value of 230 for z = 0 or 580 for z = 0.02, respectively. At higher sintering temperatures, the magnetic permeability was reduced due to the formation of intra-crystalline porosity and a non-magnetic CuO grain border phase.

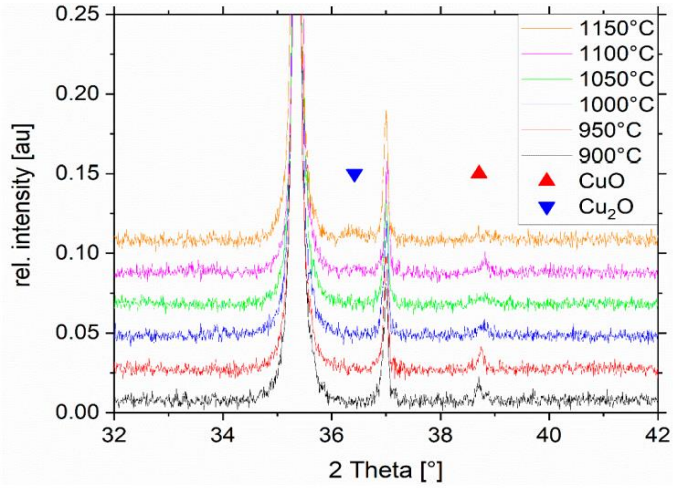

Figure 2.16: XRD patterns of z = 0.06 annealed at different T_s. Adapted from [66].

Bahiraei et al. [67] successfully synthesized $Mg_{0.3}Cu_{0.2}Zn_{0.5}Fe_{2-x}O_{4-3x/2}$ (with $0 \leq x \leq 0.04$) ferrites using sol-gel route and annealed at 1173 K for 4 h to investigate the consequence of iron ions on the microstructural and electromagnetic traits. The analysis of the samples' microstructures demonstrated the change in iron concentration has a substantial impact on densification and development of grains (Figure 2.17 (a-e)). The magnetic permeability was improved with rising Fe-deficiency content and achieved a maximum when x = 0.03 and the resonance frequency decreased. In addition, the magnetic permeability dramatically decreased

with further increasing Fe-deficiency content (Figure 2.18 (a)). The saturated magnetization and Curie temperature were decreased with increasing Fe-deficiency contnet (Fig. 2.18 (b)).

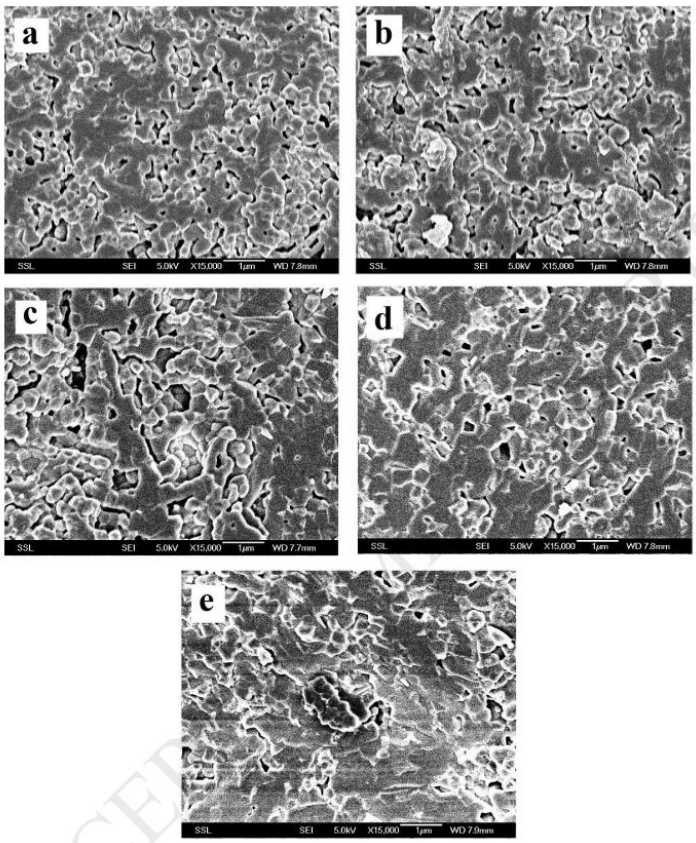

Figure 2.17: The SEM micromorphologies of annealed specimens with (a) x = 0, (b) x = 0.01, (c) x = 0.02, (d) x = 0.03, and (e) x = 0.04. Adapted from [67].

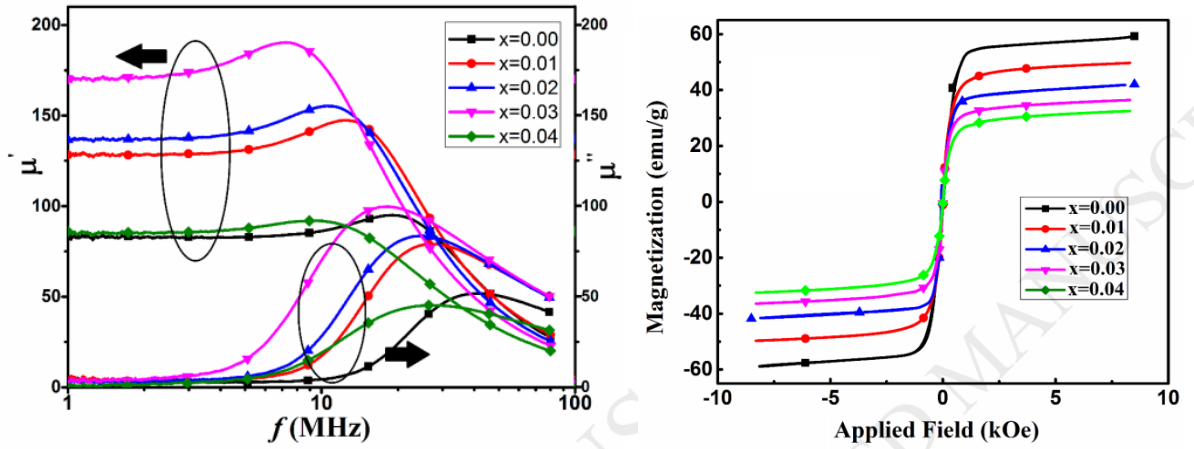

Figure 2.18: (a) Frequency-dependent real and imaginary components of magnetic permeability with different Fe deficient content and (b) M-H loops with different Fe deficiency content. Adapted from [67].

2.1.3. Literature Review on Barium Calcium Titanium Zirconate and Different stoichiometric Ferrite based Composite materials

Wang et al. [68] synthesized $Ba_{0.9}Ca_{0.1}Ti_{0.9}Zr_{0.1}O_3$ (BCZT) + $Co_{0.8}Ni_{0.1}Zn_{0.1}Fe_2O_4$ (CNZF) laminated composites (2-2 type composites) and particulate composites (0-3 type composites) via the solid state syntheic technique to study the dielectric, magnetic, and magnetoelectric traits. The simultaneous presence of the component phases were ascertained via XRD analysis as illustrated in Figure 2.19. They reported that the BCZT/CNZF laminated composites exhibited higher electric permittivity. The laminated composites provided the higher resistivities and lower leakage currents as compared to the particulate composites. The leakage current density increased on rising NCZFO content. The saturation polarization reduced on upsurging CNZF amount as a result of the descending of ferroelectricity. The laminated composites (2-2 type composites) exhibited an optimum magnetoelectric coefficient of 21.73 mV cm^{-1} Oe^{-1} at 1100 Oe, which was 20 times greater than that of the particulate composites (1.45 mV cm^{-1} Oe^{-1}) as observed in Figure 2.20.

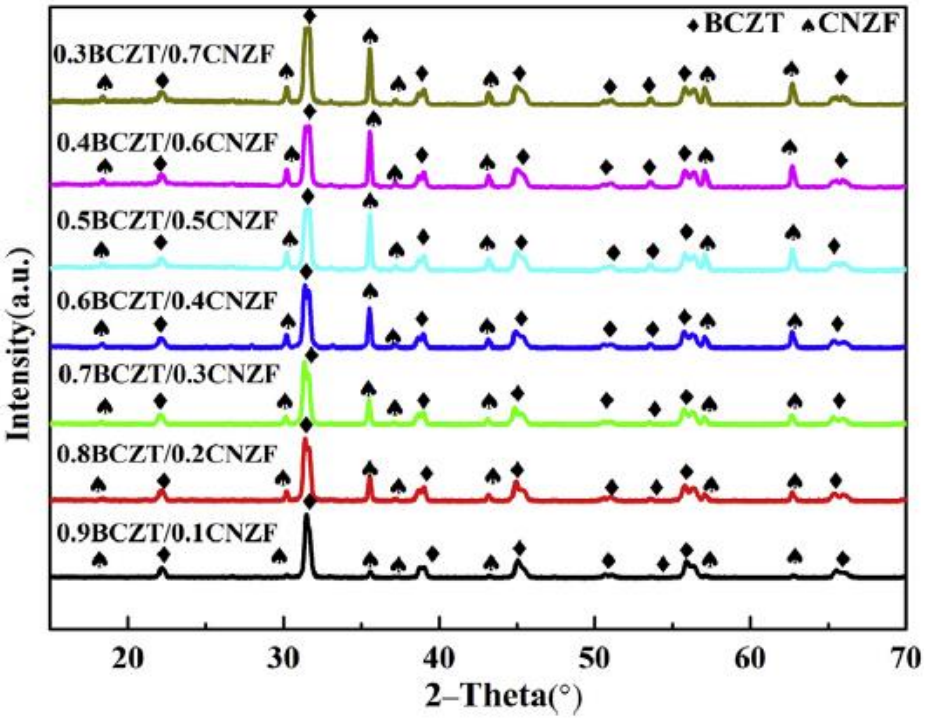

Figure 2.19: XRD patterns of (1-*x*) BCZTO/*x*CNZFO particulate composites (0-3 type composites) for *x* = 0.1; 0.2; 0.3; 0.4; 0.5; 0.6; 0.7. Adapted from [68].

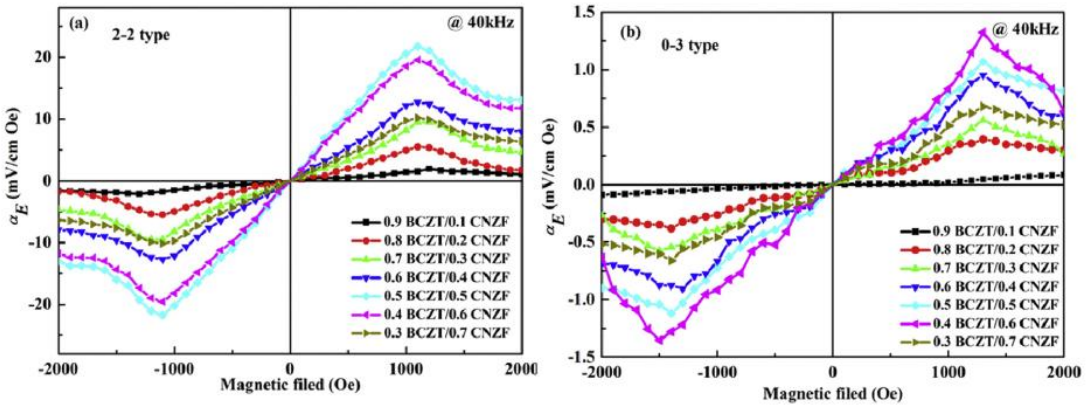

Figure 2.20: Transverse magnetoelectric coefficient α_E as a function of bias field measured at 40 kHz for the BCZT/CNZF composites with different contents of CNZF: (a) 2-2 type BCZT/CNZF composites and (b) 0-3 type BCZT/CNZF composites. Adapted from [68].

Wang et al. [69] fabricated $Ba_{0.90}Ca_{0.10}Ti_{0.90}Zr_{0.10}O_3/CoFe_2O_4$ (BCZT/CFO) layered composites employing the solid-state synthetic technique to investigate the ferroelectric, magnetic and magnetoelectric properties. They reported that the simultaneous presence of BCZT and CFO phases in the composites without any chemical reaction. The piezoelectric coefficient decreased on escalating CFO amount as shown in Figure 2.21 (a). The resistance of the composites decreased while the leakage current density increased with increasing CFO content. The composite with equal amount of the component phases exhibited the optimum magnetoelectric response of ~159 mV cm^{-1} Oe^{-1} at 1120 Oe (Figure 2.21 (b)).

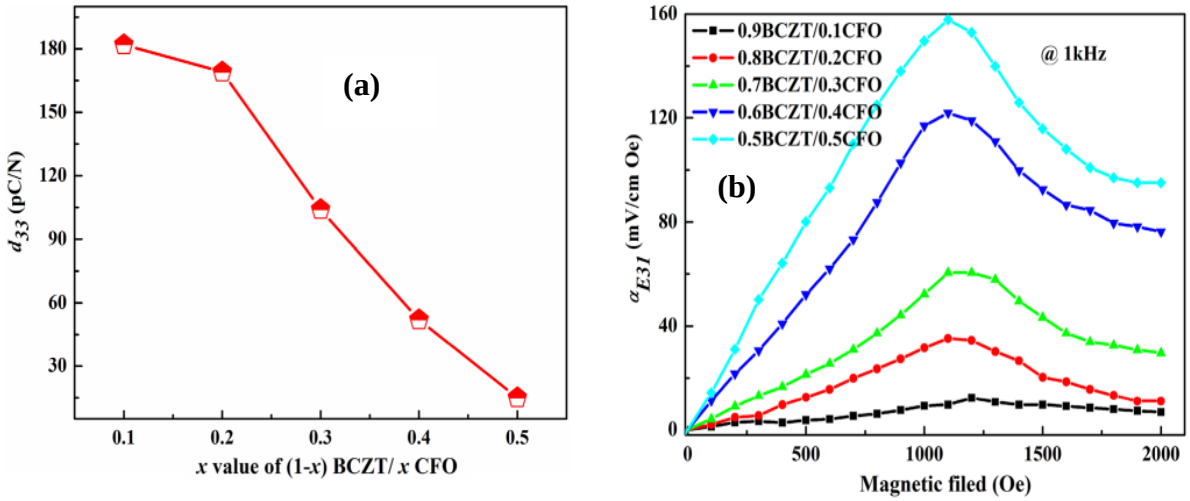

Fig. 2.21: (a) Piezoelectric coefficients (d_{33}) and (b) magnetoelectric voltage coefficient of the laminated (1-*x*) BCZT/*x* CFO composites with different contents of CFO. Adapted from [69].

Li et al. [70] prepared (*x*) [$Ni_{0.15}Cu_{0.25}Zn_{0.6}Fe_2O_4$] (NCZFO)-(1-*x*) [$Ba_{0.85}Ca_{0.15}Ti_{0.90}Zr_{0.10}O_3$] (BCTZO) (*x* = 0~1) composites by combining chemical co-precipitation method with sol-gel technique with an intent to study the microstructure, dielectric, ferroelectric, magnetic and multiferroic traits. The simultaneous presence of the NCZFO and BCTZO phases has been confirmed via XRD. Compacness of the most composites have been high enough and the NCZFO phase possessed larger grain size while BCTZO phase possessed smaller grain size. The electric permittivity and permittivity loss tangent change non-monotonically with increasing BCTZO phase due to relaxation polarization and thermally excited electrons. Composites exhibited apparent ferroelectric hysteresis loops due to leakage current. The remnant polarization and coercive field did not change monotonically with increasing BCTZO phase. The saturation magnetization changed monotonically with increasing NCZFO phase due to strong interfacial interaction in the midst of NCZFO and BCTZO phases. Strongest magnetoelectric coupling (relative polarization change 37%) for *x* = 0.2 was achieved at 1 mT. **Tanna et al.** [71] synthesized (*y*) [$Mn_{0.5}Cu_{0.5}Fe_2O_4$] (MCFO)-(1-*y*) [$Ca_{0.1}Ba_{0.9}Zr_{0.1}Ti_{0.9}O_3$] (CBZTO) (*y* = 25, 50, and 75 %) composites successfully using solid state method and annealed at 1200 ℃ for 12 h. In addition, the 25% MCFO-75% CBZTO composite was subjected to high-energy mechanical milling for 12, 18, and 30 h to unravel to the effect of milting time on the electromagnetic and magnetoelectric properties. The saturation magnetization and Curie temperature of 25% MCFO-75% CBZTO composite were decreased on upsurging the milling duration. Because of the strong granular coupling in the midst of the CBZTO phase and the MCFO phase, which resulted in spin disorganization and hindered long-distance magnetic super exchange connections in MCFO phase, the saturation magnetization was less than per-gram value. In Mossbauer spectra, a relaxed wide doublet with a dispersion of nuclear hyperfne fields suggested a strong connection in the midst of the component phases brought on by mechanical grinding. The magnetoelectric coupling coefficient increased with increasing milling duration due to the efficient coupling of MCFO and CBZTO phases (Figure 2.22 (a)).

The 25% MCFO-75% CBZTO composite milled for 18 h exhibited optimum magnetoelectric response of 382 μV cm^{-1} Oe^{-1} which was 2.5 times larger than the un-milled one (Figure 2.22 (a-b)).

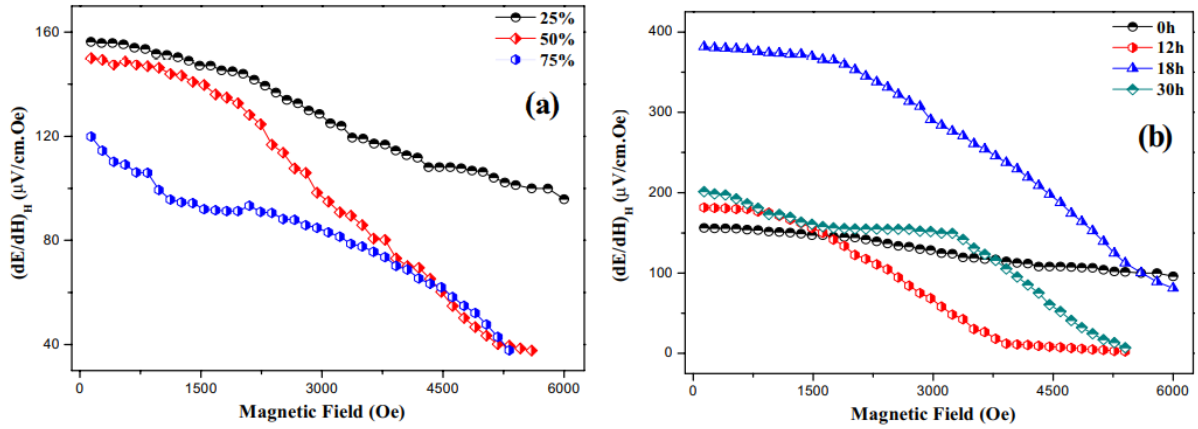

Figure 2.22: Variations in the magnetoelectric coefficient with respect to the magnetic field: (a) (y) [MCFO]-(1-y) [CBZTO] (y = 0, 0, and 75) and (b) milled MCFO-CBZTO composites. Adapted from [71].

Rani et al. [72] successfully synthesized (x) [$CoFe_2O_4$] (CFO)-(1-x) [$Ba_{0.85}Ca_{0.15}Zr_{0.1}Ti_{0.9}O_3$] (BCZT) (with $0.1 \leq x \leq 0.4$) composites employing solid state synthetic approach. The electric permittivity decreased with increasing CFO content. Temperature-dependent electric permittivity study exhibited two anomalies: one was close to ferroelectric to paraelectric phase transition of BCZT ceramic and another one lied near the magnetic transition temperature of CFO. Magnetocapacitance was increased and the saturation magnetization increased whereas the coercive field decreased with increasing CFO content. The composite with 40 % CFO exhibited an optimum magnetocapaciatance of 1.07.

Negi et al. [73] synthesized of (1-x) [$Ba_{0.85}Ca_{0.15}Ti_{0.9}Zr_{0.1}O_3$] (BCZT)-($x$) [$CoFe_2O_4$] (CFO) ($0.1 \leq x \leq 0.9$) synthesized by chemical solution method followed by a sintering at 1323 K for 2h to investigate the crystallographic architecture, ferroelectric, magnetic, dielectrical and magnetoelectric characteristics. BCTZ power was developed using sol-gel method while CFO was synthesized using metallo-organic decomposition method. The ferroelectric properties

were decreased while the ferromagnetic properties were increased with increasing CFO content. The composite with 10 wt. % of CFO phase exhibited excellent ferroelectric properties (high saturation polarization: ~ 5.1 μC/cm^2, high remanant polarization: ~ 1.4 μC/cm^2 and high coercive field: ~ 11.6 kV/cm). The composite having 90 wt. % of CFO phase exhibited improved ferromagnetic properties (saturation magnetization: ~ 32 emu/g, remanant magnetization: ~ 11.7 emu/g and coercivity: 504 Oe). The magnetic hyperfine field strength was reduced with increasing BCTZ amount. The electric permittivity was reduced on upsurging CFO amount. The composite with 10 wt. % of CFO phase provided maximum electric permittivity of ~ 678 at 1 MHz. The leakage current density was suppressed at lower CFO content. The magnetoelectric response was increased with increasing CFO content and the composite having 90 wt. % of CFO phase provided highest magnetoelectric response of ~1028 μV cm^{-1} Oe^{-1} at 9 kOe.

Praveen et al. [74] synthesized [$Ba_{0.85}Ca_{0.15}Zr_{0.1}Ti_{0.9}O_3$] (BCZT)-[$CoFe_2O_4$] (CFO) composites with two different connectivity schemes, particulate and laminates to investigate their structural and magnetoelectric properties. Furthermore, they reported that BCZT and CFO phases were synthesized by sol-gel and combustion techniques respectively. Particulate composite was fabricated through the mechanical mixing of BCZT and CFO phases with equal mass fraction. On the otherhand, the laminated composited (bilayer and trilayer) were prepared through the bonding BCZT with CFO layers using epoxy. The laminated composite exhibited optimum piezoelectric coefficients of ~ 630 pC/N, piezoelectric voltage coefficient of ~11 mV m/N, and magnetostricition coefficient of ~183 ppm. Trilayer laminated composites exhibited high magnetoelectric coefficient of ~803 mV cm^{-1} Oe^{-1} which was 8 times higher than that of the particulate composite with equal mass fraction of the component phases, magnetoelectric coefficient of ~ 104 mV cm^{-1} Oe^{-1}. Bilayer laminated composite provided a highest magnetoelectric response of ~ 615 mV cm^{-1} Oe^{-1}.

Praveen et al. [75] synthesized (1-*x*) [$Ba_{0.85}Ca_{0.15}Zr_{0.1}Ti_{0.9}O_3$] (BCZT)-(*x*)[$CoFe_2O_4$] (CFO) (mass fraction $0 \leq x \leq 1.0$) particulate composites via mechanical blending of the calcinated and milled component phases with desired mass portions followed by a sintering at 1573 K for 4h to investigate their structural and magnetoelectric properties. The component phases, BCZT and CFO were fabricated employing sol-gel auto combustion technique, respectively and calcinated at 1673 K. They reported that the component phases coexisted in the composites as revealed by XRD analysis. The composite with equal masst fraction of the component phases, i.e., 0.5BCZT-0.5CFO composite exhibited high saturation magnetization of 64 emu/g and large sensitivity to starin of 52×10^{-9} Oe^{-1}, whichever was commensurable to that of unadulterated CFO (50×10^{-9} Oe^{-1}). The composite with 20 % CFO exhibited large piezoelectric voltage constant of 8×10^{-3} V m/N. The composite with equal mass fraction of the component phases, i.e., 0.5BCZT-0.5CFO composite exhibited high magnetoelectric response of 6.85 mV cm^{-1} Oe^{-1} at 1 kHz, and at resonant frequency, highest magnetoelectric response of 115 mV cm^{-1} Oe^{-1}.

Haq et al. [76] synthesized [$Ba_{0.85}Ca_{0.15}Zr_{0.1}Ti_{0.9}O_3$] (BCZT)-0.15[$CoFe_2O_4$] (CFO) composite through solid-state reaction technique and annealed at 1573 K 6h. They reported that the low-frequency dielectric dispersion was mainly accounted to Maxwell-Wagner relaxation and the dielectric properties were partly affected by the contribution from the CFO phase. A sizeable magnetoelectric coefficient of 6.03 ps/m was perceived. They were also suggested that the intrinsic piezoelectric coefficient and the ratio in the midst of the ferroelectric and ferrimagnetic phase, microstructure: grain size, density of ceramics and quality of interfaces, and the difference in the midst of the stiffness parameters of BCZT and CFO might have significant impact on the magnetoelectric coefficient.

Mane et al. [77] synthesized (*x*) [$Co_{0.90}Ni_{0.10}Fe_2O_4$] (CNFO)-(1-*x*) [$Ba_{0.85}Ca_{0.15}Zr_{0.1}Ti_{0.9}O_3$] (BCZT) (*x* = 10, 20, 30 and 40 wt%) composited using a hydroxide coprecipitation method and

were subjected to sintering via the hybrid microwave sintering technique at 1473 K for 20 min. They reported that the constitutent phases coexistedb in the composites as ascertained by XRD analysis. SEM analysis confirmed the growth of ferrite in the ferroelectric-rich region. Two anomalies in the electric permittivity based on temperature study-one at 140 °C and the other at or above 500 °C proved the coexistence of the component phases with separate transition points. The CNFO phase exhibited excellent magnetic properties (saturation magnetization: ~80 emu/g, magnetic moment: ~3.37, remanant magnetization: ~19.05 emu/g and coercivity: ~599 Oe) and a high value of the magnetostriction coefficient of -118 ppm. The composite with 40% CNFO exhibited optimum linear magnetoelectric response of 21.6 mV cm^{-1} Oe^{-1} at 1 kHz.

Jain et al. [78] successfully fabricated (1-*x*) $Ba_{0.9}Sr_{0.1}Zr_{0.1}Ti_{0.9}O_3$ (BSZT)-(*x*) $NiFe_2O_4$ (NFO) ($0.0 \leq x \leq 0.30$) using mechano-chemical activation technique. They reported that SEM analysis revealed that microstructure showed inhomogeneous grains and the inhomogeneity enhanced with increasing NFO content as compared to the pristine BSZT sample. Dielectric studies showed that the composites exhibited a well-defined ferroelectric to paraelectric transition peak while the composite's diffuseness enhanced on rising NFO level. The composite with 0.05 NFO content exhibited superior ferroelectric properties and decreases with further increasing NFO content. A maximum dielectric breakdown strength was achieved for 0.05 NFO concentration. The saturation magnetization and coercive field increased gradually with increasing NFO content. The electric permittivity reduced on upsurging NFO amount. The piezoelectric properties did not reveal any enhancement over the pristine BSZT and were found to decline with NFO addition.

Jain et al. [79] successfully synthesized (1-*x*) $Ba_{0.9}Sr_{0.1}Zr_{0.1}Ti_{0.9}O_3$ (BCTZO)-(*x*) $CoFe_2O_4$ (CFO) ($0.0 \leq x \leq 0.30$) composites using mechanochemical activation method with an aim to investigate the effect CFO addition in BSZT on the microstructure, dielectric, ferroelectric, ferromagnetic and piezoelectric properties. They reported that the compsite having 0.05 CFO

extent revealed a remarkable enhancement in microstructure, dielectric, ferroelectric and piezoelectric properties over the pristine BSZT sample. This enhancement in electrical properties was attributed to larger grain size, improved density and easier ferroelectric domain wall motion inside the grain. The optimum dielectric breakdown strength was achieved 0.05 CFO concentration. The ferromangnetic properties improved substantially with increase in CFO content.

Sowmya et al. [80] successfully prepared (*x*) [0.5BZT-0.5BCT] -(100-*x*) $NiFe_2O_4$ (x = 90, 80, 70 wt %) particulate composites using sol-gel route to investigate the composition dependent magnetoelectric properties. They reported that the SEM micrograph the composites displayed uniform grains distribution and exhibited high electro-mechanical coupling coefficient in the range of 0.41 to 0.37. The saturation magnetization increased linearly with increasing ferrite concentration. An optimum magnetoelectric coefficient of 13.3 mV cm^{-1} Oe^{-1} at 420 Oe for 20 % ferrite content which was attributed to high piezoelectric, magnetic and adequate interface contact in the midst of the component phases.

Haq et al. [81] synthesized (1-*x*) [$Ba_{0.85}Ca_{0.15}Zr_{0.1}Ti_{0.9}O_3$] (BCZT)-(*x*) [$NiFe_2O_4$] (NFO) (*x* = 0.2, 0.3, 0.4, 0.5) composites using thesolid-state method. They reported that the composites exhibited extremely slim hysteresis loop and the saturation magnetization was increased with rising NFO concentration and the maximum saturated magnetization were achieved for the composite containing 50 % NFO content. In addition, they reported that the composite containing 30 % NFO phase exhibited a converse magnetoelectric coefficient which was approximately two times larger than that of $BaTiO_3$-$CoFe_2O_4$ composites. They explored the relationship in the midst of the phase connectivity within these composites and the magnetoelectric properties using the time-of-flight secondary ion mass microscopy.

Rani et al. [82] successfully fabricated (1-*x*) [$Ba_{0.85}Ca_{0.15}Zr_{0.10}Ti_{0.90}O_3$] (BCZTO) + (*x*) [$Ni_{0.8}Zn_{0.2}Fe_2O_4$] (NZFO), ($0 \leq x \leq 0.45$) by the solid state approach and annealed at 1250 °C/2

h to investigate structural, dielectrical, ferroelectric, magnetic and magnetoelectric characteristics. They reported that XRD patterns ascertained the developemnt of specimens having no impurity phase. Furthermore, temperature-dependent dielectric study reveled that the composites exhibited two dielectric inconsistencies: (i) first inconsistency at ~ 413 K corroborated with the ferroelectric transition of BZT-0.5BCT and (ii) second inconsistency at ~ 723 K associated with the magnetic transition of NZFO. The electric permittivity was decreased with increasing NZF concentration. The ferroelectric polarization was reduced on escalating NZFO amount as a result of the decrement in resistivity. The composite with 25 % NZFO provided optimum magnetoelectric response of ~12.95 mV cm^{-1} Oe^{-1} at 1 kHz and 254 mV cm^{-1} Oe^{-1} at 35 kHz at room temperature.

2.1.4. Literature Review on different Ferroelectrics and iron deficient non-stoichiometric Ferrites based composite materials

Sadhana et al. [83] successfully developed (*x*) [$Ni_{0.53}Cu_{0.12}Zn_{0.35}Fe_{1.88}O_4$] (NiCuZn ferrite) + (1-*x*) [$BaTiO_3$] (BTO) composites (*x* = 0~100 wt. %) using microwave-hydrothermal method followed by sintering at 900 °C/30 min. The simultaneous presence of the component phases in the composites were confirmed via XRD analysis (Figure 2.23 (a)). In addition, the formation of the component phases was also confirmed via FTIR analysis (Figure 2.23 (b, c)). The experimental density of the composites was increased on increasing BTO content. The grains of NiCuZn ferrite were increased while the grains of BTO were decreased continually with increasing NiCuZn extent. The grain diameters were seen to be in the midst of 72 to 92 nm. At 1 MHz, the magnetic permeability was decreased with increasing BTO content. The saturation magnetization was declined while the coercivity was enhanced on upsuring BTO amount and was illucidated through Braggeman theory. The magnetic permeability was increased with increasing ferrite content (Figure 2.24 (a)). The imaginary part of magnetic permeability (shown in Figure 2.24 (b)) was enhanced progressively on escalating the frequency of the applied field and took an optimum at a particular frequency, where the real

part of magnetic permeability rapidly declined. The resonant frequency was increased with decreasing ferrite content (Figure 2.24 (b)). The enhancement in resonant frequency was ascribed to the decrement in the interplay in the midst of ferrite particles due to the dilution effect of ferroelectric particles. The resonant frequency exhibited maximum value and shifted towards high frequency region with increasing BTO content.

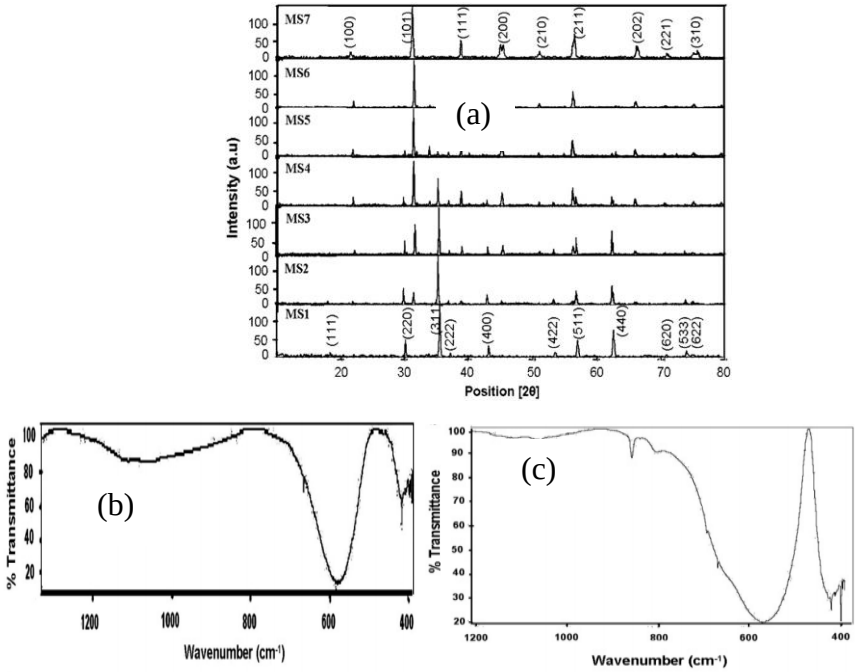

Figure 2.23: (a) XRD patterns of (x) [NiCuZn ferrite] + (1-x) [BTO] (x = 0~100 wt.%) composites, (b) and (c) FTIR spectra of NiCuZn ferrite and $BaTiO_3$ powders. Adapted from [83].

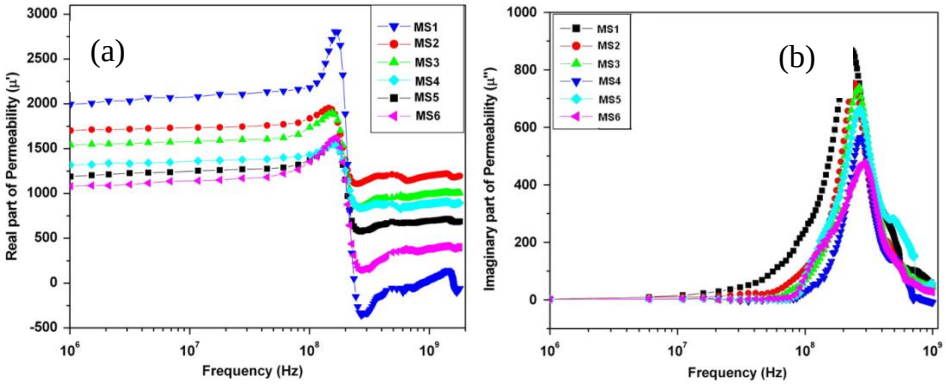

Figure 2.24: Evolution of (a) real component (μ_i') and (b) imaginary component (μ_i'') of magnetic permeability against frequency of (x) [NiCuZn-ferrite] + (1-x) [BTO] (x = 0~100 wt. %) composites. Adapted from [83].

Ling et al. [84] successfully prepared (1-*x*) [$Ni_{0.37}Cu_{0.20}Zn_{0.43}Fe_{1.92}O_{3.88}$] (NCZFO)-(*x*) [$BaTiO_3$] (BTO) (x = 5, 10, 15, and 20 wt. %,) (designated as S1 (x = 5 wt.%), S2 (x = 10 wt.%), S3 (x = 15 wt. %), and S4 (x = 20 wt. %)) composites using the usual ceramic technique combined with the sol-gel method followed by a sintering at 1173 K. XRD analysis was used to determine the development of the component phases and their coexistence in the composites (Figure 2.25). BTO powder exhibited fine and agglomerated grains with the size of 0.1-0.6 μm (Figure 2.26 (a)) while NCZFO powder exhibited relatively low porosity having larger grain size (> 5 μm) (Figure 2.26 (b)). The microstructures of the composites (S1-S4) were porous and the mean grain diameter was reduced on rising BTO level which was suggested that the BTO acted as grain growth inhibitor (Figure 2.26 (c-f)). The magnetic permeability was reduced due to the dilution effect while the peak value of the imaginary component of magnetic permeability was declined and shifted to the high frequency region with increasing BT amount. The electric permittivity was increased on increasing BT amount due to the improvement in the density of the samples.

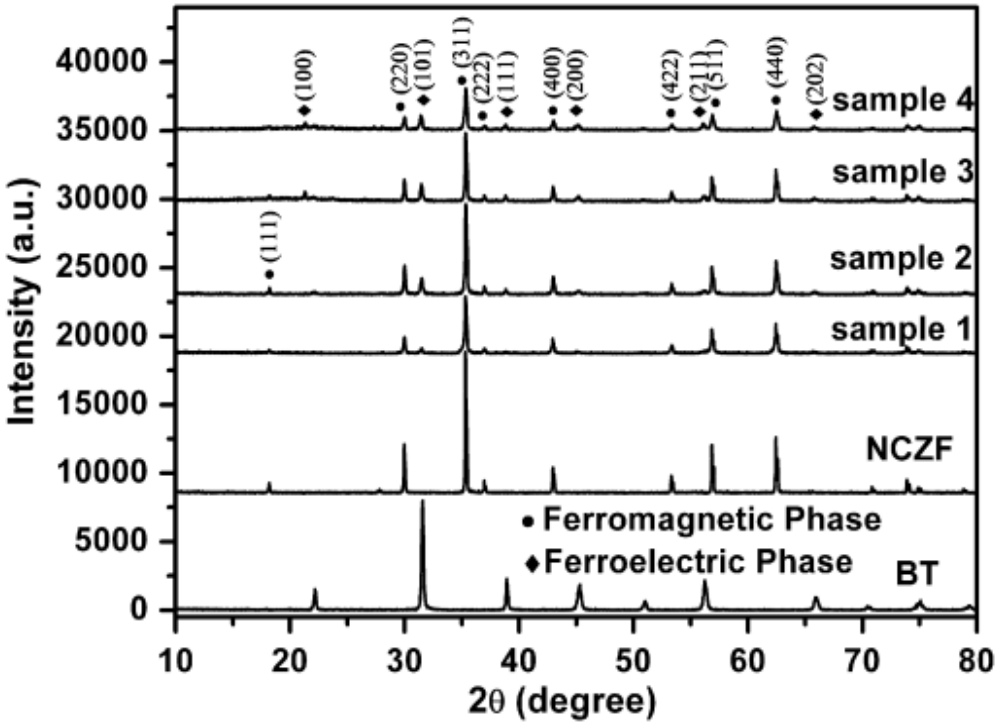

Figure 2.25: XRD patterns for NCZF, BT powder, and samples 1-4. Adapted from [84].

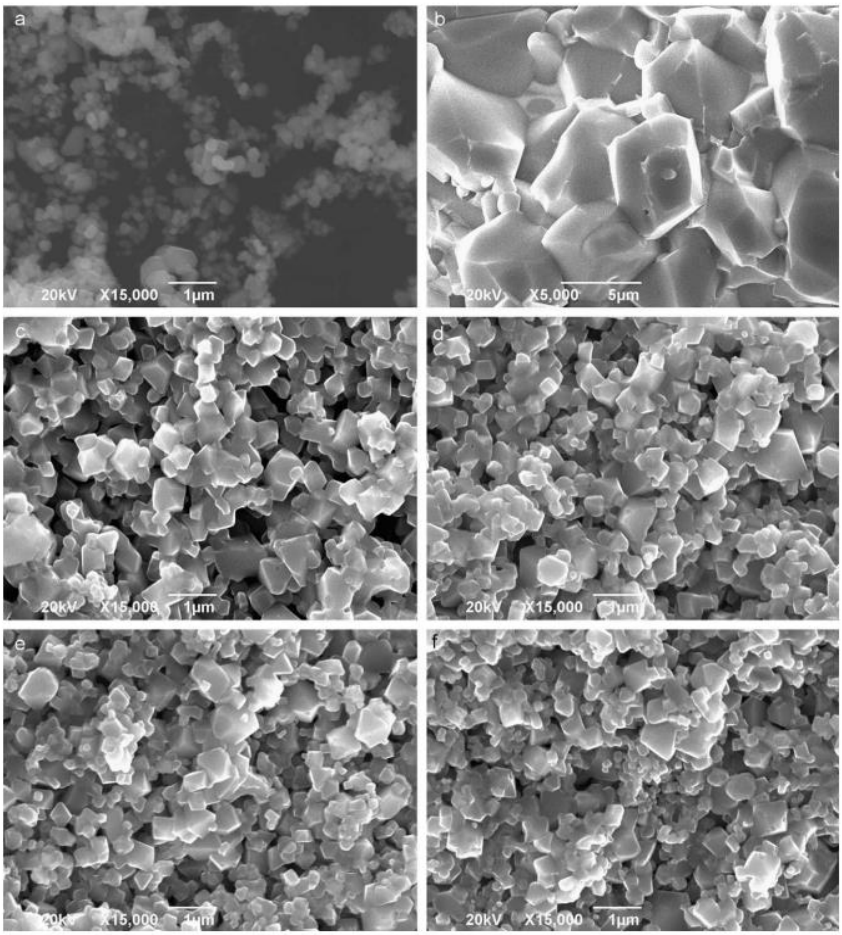

Figure 2.26: SEM micrographs of (a) BT powder, (b) NCZF, (c) S1, (d) S2, (e) S3 and (f) S4. Adapted from [84].

Lin et al. [85] prepared (1-*x*) [$BaFe_{0.5}Nb_{0.5}O_3$] (BFN) + (*x*) [$Ni_{0.37}Cu_{0.20}Zn_{0.43}Fe_{1.92}O_{3.88}$] (NiCuZn ferrite) (*x* = 20-80 wt. %) composites employing solid state synthetic process and annealed at 1223 K. The simultaneous presence of the component phases in the composites was ascertained through XRD analsysis (Figure 2.27). Homogeneous microstructures were observed with some pores for the composites (Figure 2.28 (a-d)). Additionally, because NiCuZn sinters at a lower temperature than BFN, microstructures get denser and denser when NiCuZn concentration is increased. The electric permittivity and permittivity loss tangent were increased with decreasing NiCuZn content because the electric permittivity and permittivity loss tangent of BFN were both higher than those of NiCuZn (Figure 2.29 (a)). The magnetic permeability was enhanced while the resonant frequency was declined on escalating NiCuZn amount due to the enhancement in saturation magnetization (Figure 2.29 (b)),

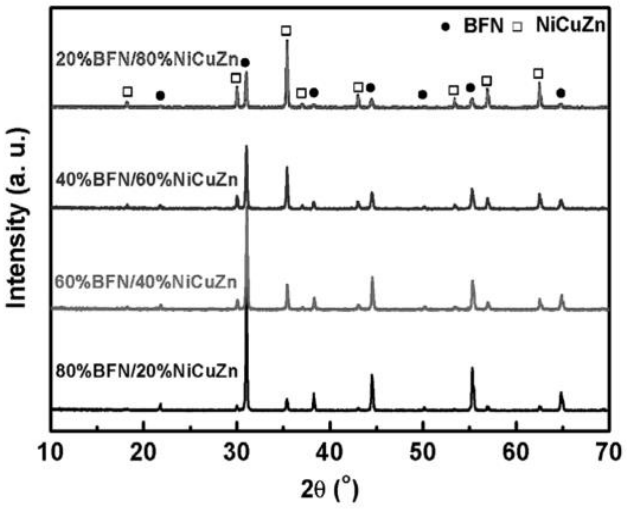

Figure 2.27: XRD patterns of the BFN/NCZF composites with different NCZF content. Adapted from [85].

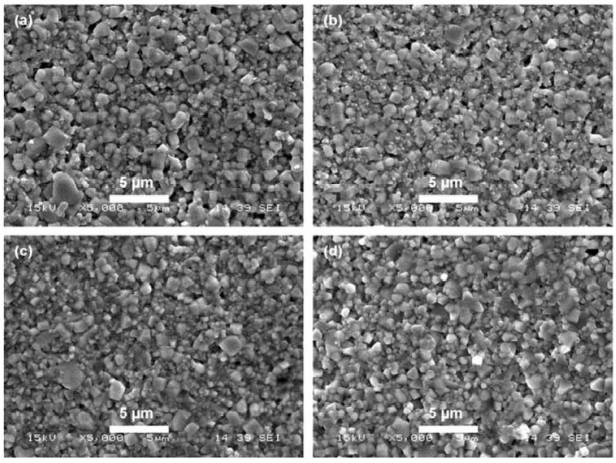

Figure 2.28: SEM micrographs of the BFN/NiCuZn composites with different NiCuZn content annealed at 950 ℃: (a) 20, (b) 40, (c) 60, and (d) 80 wt. %. Adapted from [85].

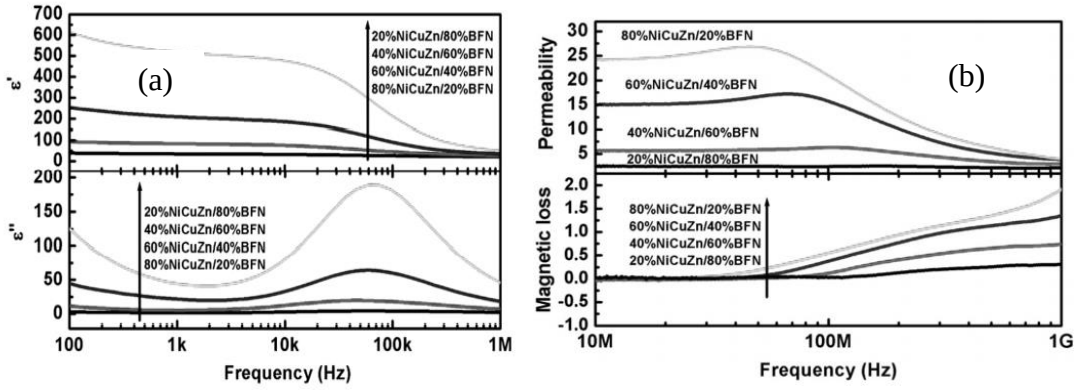

Figure 2.29: Frequency dependent: (a) complex electric permittivity and (b) magnetic properties of the BFN/NiCuZn composites with different NiCuZn contents. Adapted from [85].

Qi et al. [86] successfully synthesized (x) [$BaTiO_3$] + (1-x) [$Ni_{0.2}Cu_{0.2}Zn_{0.6}Fe_{1.96}O_4$] (NiCuZn ferrite) ($0 \leq x \leq 1.0$) composites using standard ceramics method with nanosized precursor powders. XRD analysis was used to confirm the simultaneous presence of the component phases in the composites (Figure 2.30). The saturation magnetization declined while the coercivity enhanced on rising BTO level. The initial permeablity was decreased while the resonant frequency was increased on upsurging BTO amount due to the pinning effect of domain wall dispalcement (Figure 2.31 (a)). The maximum value of the quality factor was shifted toward high frequency region (Figure 2.31 (b)).

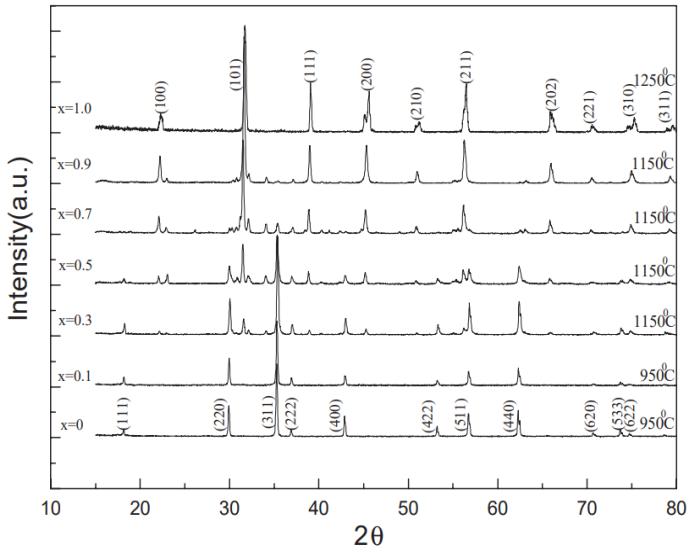

Figure 2.30: XRD profiles of annealed (x) [BTO] + (1-x) [NCZFO] ($0 \leq x \leq 1.0$) composites. Adapted from [86].

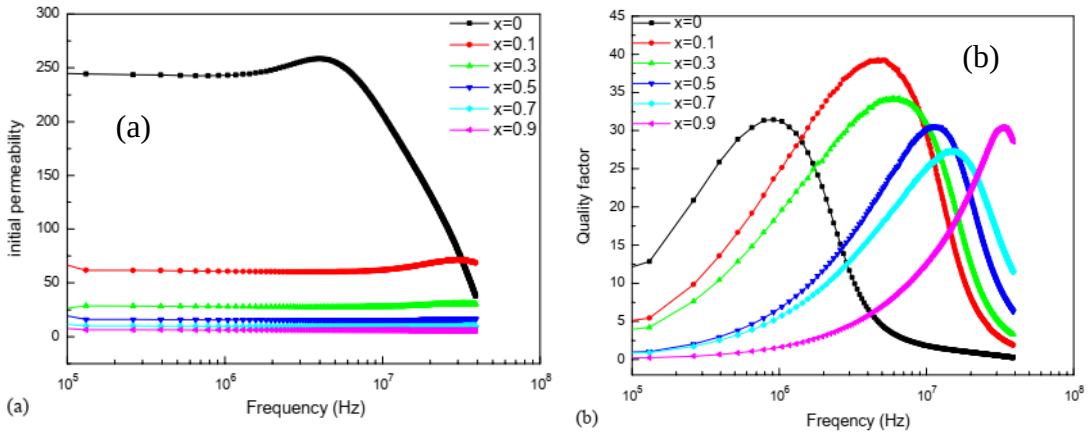

Figure 2.31: Frequency dependent: (a) magnetic permeability, and (b) quality factor of (x) [BTO] + (1-x) [NCZFO] ($0 \leq x \leq 1.0$) composites. Adapted from [86].

Su et al. [87] developed (1-x) [$Ni_{0.4}Cu_{0.2}Zn_{0.4}Fe_{1.96}O_4$] (NCZF) + (x) [$BaTiO_3$] (BTO) ($x$ = 0-40 wt. %) composites using standard ceramic method followed by a sintering at 1223 K. The coexistence of the component phases was affirmed by XRD pattern (Figure 2.32). The grain size was slowly reduced with increasing BTO content (Figure 2.33).

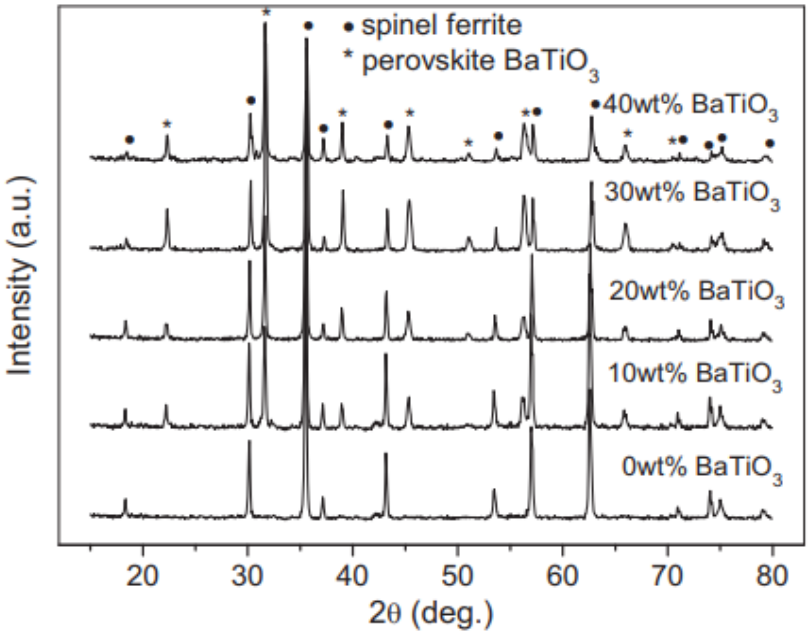

Figure 2.32: XRD patterns for (1-x) [NCZF] + (x) [BTO] (x = 0-40 wt. %) multiferroic composites. Adapted from [87].

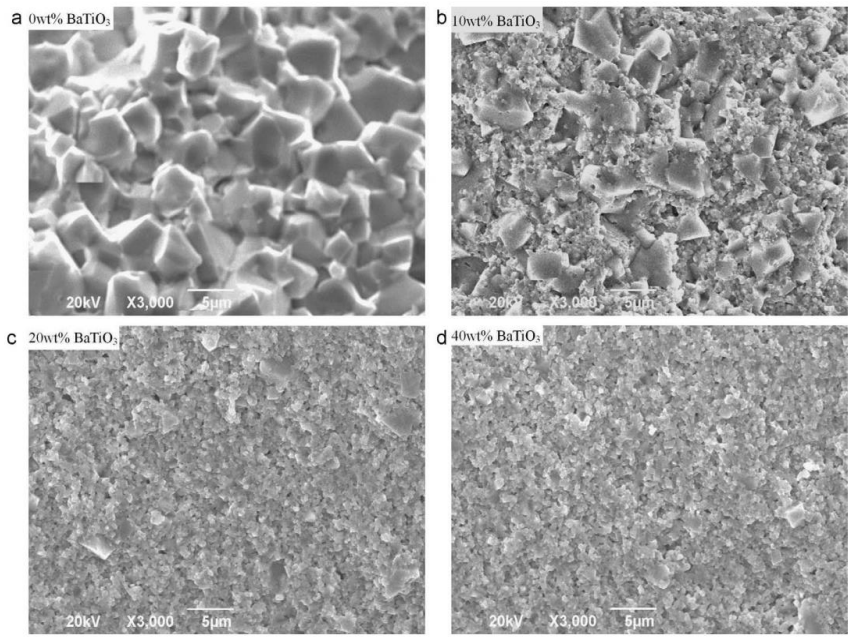

Figure 2.33: SEM photographs for (1-x) [NCZF] + (x) [BTO] (x = 0-40 wt. %) multiferroics: (a) x = 0, (b) x = 10, (c) x = 20, and (d) x = 40 wt. %. Adapted from [87].

The magnetic permeability was declined with increasing BTO content (Figure 2.34 (a)) due to the magnetic dilution effect. The quality factor was exhibited high values for x = 20-30 wt% (Figure 2.34 (b)). In addition, the electric permittivity was increased with increasing BTO content (Figure 2.34 (c)) and the composites exhibited a low permittivity loss tangent ≤ 100 MHz (Figure 2.34 (d)).

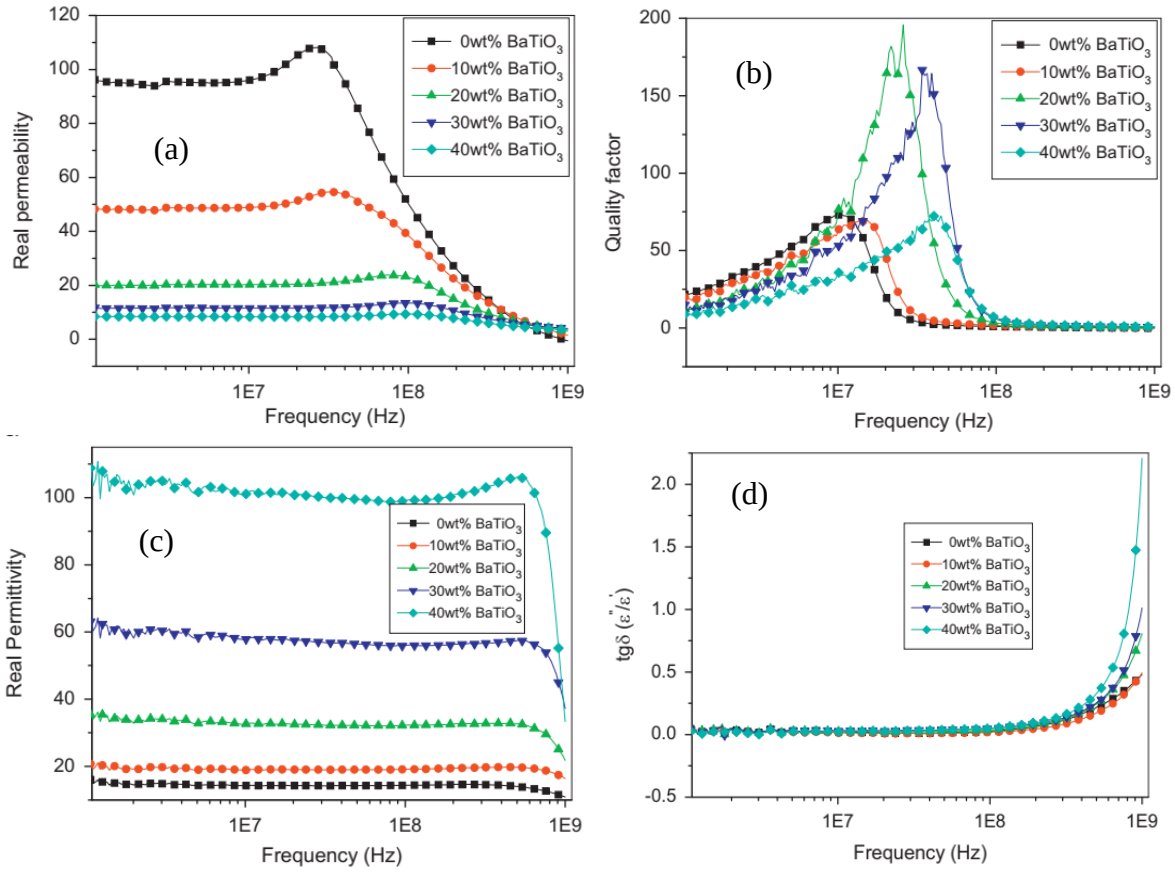

Figure 2.34: Frequency dependent (a) magnetic permeability, (b) quality factor, (c) electric permittivity, (d) permittivity loss tangent (1-*x*) [NCZF] + (*x*) [BTO] (*x* = 0~40 wt. %) composites. Adapted from [87].

Su et al. [88] synthesized (*x*) [$Ba_{0.6}Sr_{0.4}TiO_3$] (BST) + (1-*x*) [$Ni_{0.2}Cu_{0.2}Zn_{0.62}Fe_{1.96}O_{3.94}$] (NiCuZn ferrite) ($0 \leq x \leq 0.60$) composites with an addition of Bi_2O_3 sintering agent via solid-state reaction method to develop multilayer chip electromagnetic interference filters. The simultaneous presence of the component phases in the composites were confirmed by XRD patterns (Figure 2.35).

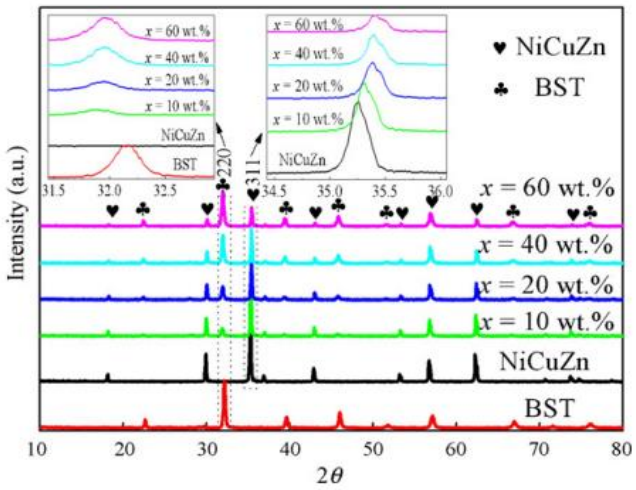

Figure 2.35: XRD profiles of (*x*) [BST] + (1-*x*) [NCZFO] (*x* = 0-60 wt. %) composites along with their component phases. Adapted from [88].

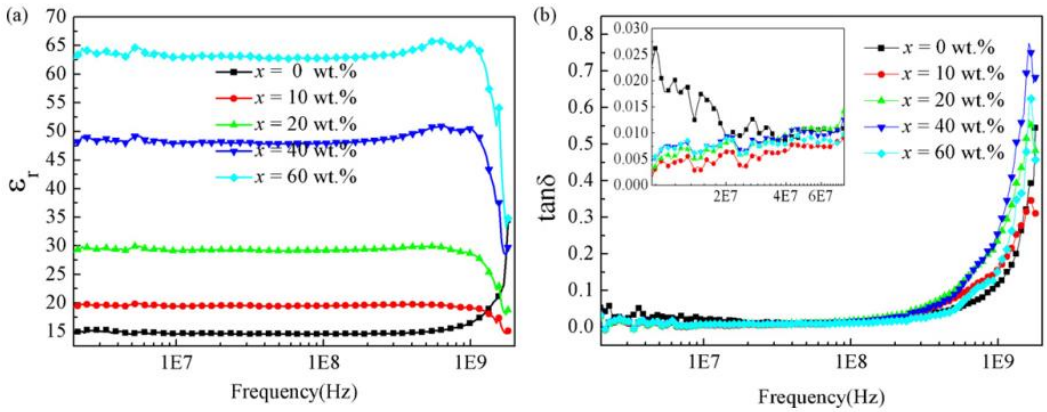

Figure 2.36: Frequency dependent: (a) permittivity constant, and (b) permittivity loss tangent of (*x*) [BST] + (1-*x*) [NCZF] (*x* = 0-60 wt. %) composites. Adapted from [88].

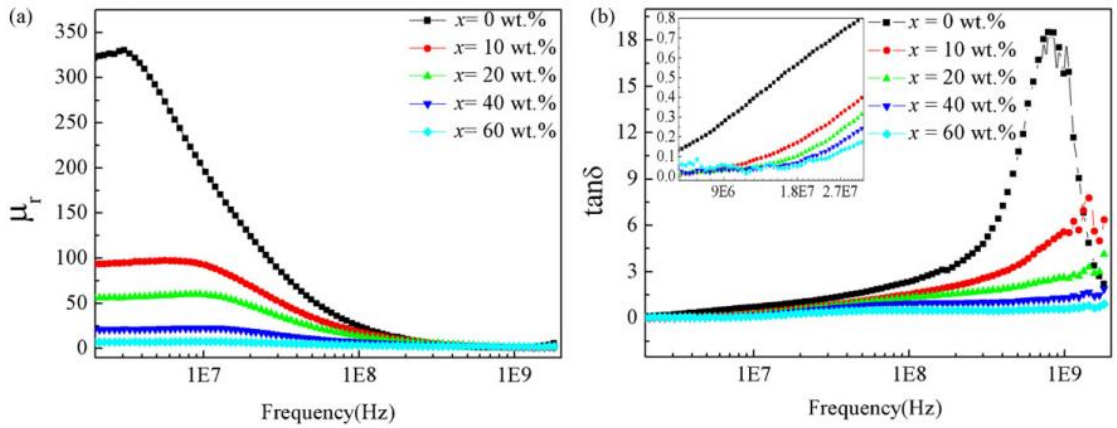

Figure 2.37: Frequency spectra of (a) magnetic permeability (μ_i') and (b) the magnetic loss tangent of (*x*) [BST] + (1-*x*) [NCZF] (*x* = 0-60 wt. %) composites. Adapted from [88].

The electric permittivity was increased with increasing BST content and exhibited excellent frequency stability to a maximum of 100 MHz, while the permittivity loss tangent was decreased below 100 MHz due to the decrement in permittivity loss tangent of BST (Figure 2.36 (a, b)) because some of Ni^{2+} or Cu^{2+} ions might substitute for Ti^{4+} in BST. The composite having 60 wt. % ferrite exhibited excellent electromagnetic properties (ε_r = 48, $tan\delta_{\varepsilon} = 0.01$, μ = 20.8, $tan\delta_{\mu/10MHz}$ = 0.03, f_r = 100 MHz). The magnetic permeability and magnetic loss tangent were declined on rising BST level due to the magnetic dilution consequence (Figure 2.37 (a, b)).

Jia et al. [89] successfully synthesized (*x*) $[Pb_{0.95}Sr_{0.05}Zr_{0.52}Ti_{0.48}O_3]$ (PZT) + (1-*x*) $[Ni_{0.24}Cu_{0.21}Zn_{0.55}Fe_{1.96}O_4]$ (NiCuZn-ferrite) (where *x* = 0~25 wt. %) employing solid-state reaction approach to investigate the phase compostion, densification, microstructural and electromagnetic characteristics. The simultaneous presence of the component phases in the composites were confimed using XRD analysis (Figure 2.38). The abnormal grain growth was achieved in the pristine sample and many pores were observed inside the large grains (Figure 2.39 (a)). On other hand, uniform microstructures were achieved in the composite sample (Figure 2.39 (c-d)). The grain diameter reduced on rising PZT level since PZT restrained the grain development.

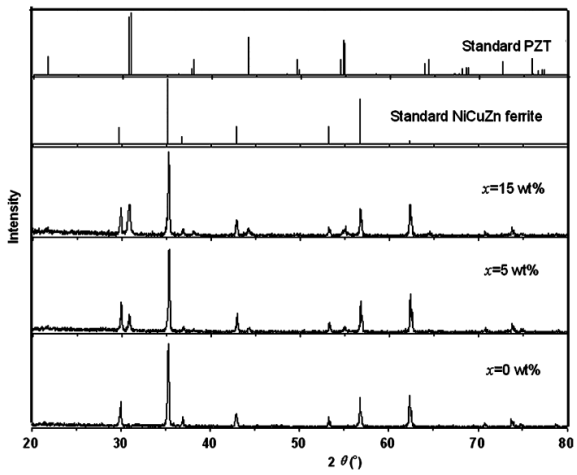

Figure 2.38: XRD profiles of (*x*) [PZT] + (1-*x*) [NiCuZn-ferrite] (x = 0, 5, 15 wt. %) composites. Adapted from [89].

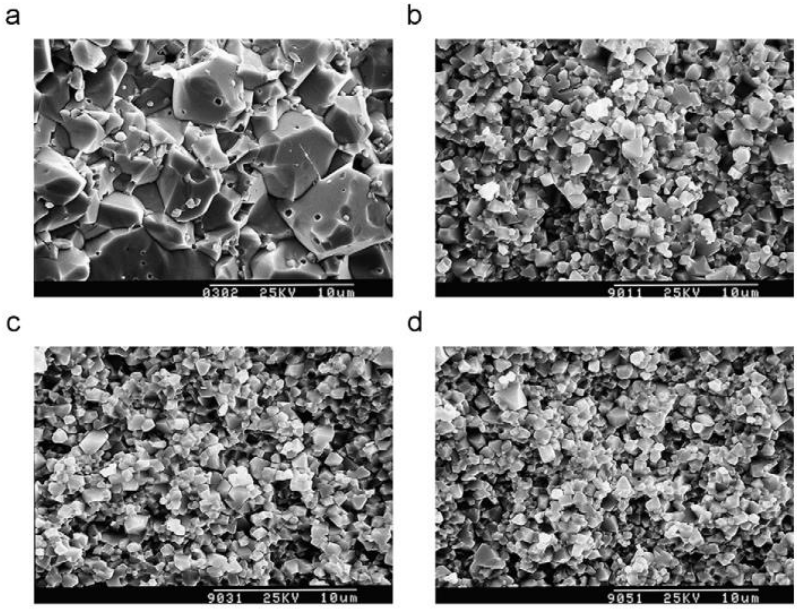

Figure 2.39: SEM photographs of (*x*) [PZT] + (1-*x*) [NiCuZn-ferrite] (*x* = 0~25 wt. %) composite materials: (a) *x* = 0, (b) *x* = 5, (c) *x* = 15, and (d) *x* = 25 wt%. Adapted from [89].

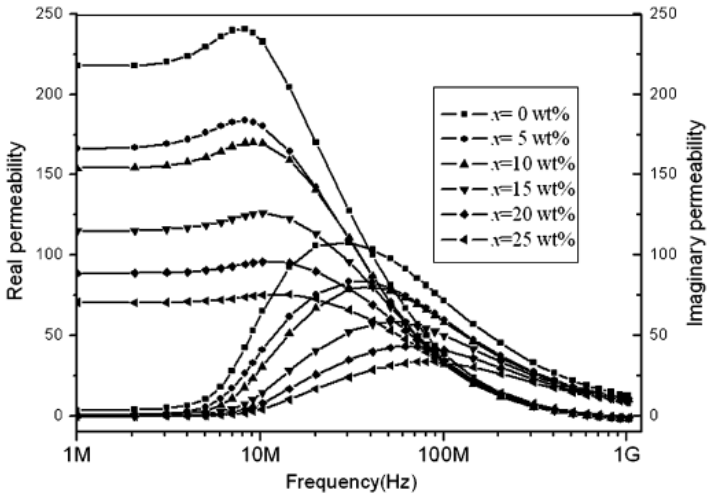

Figure 2.40: Effect of PZT on magnetic permeability (μ_i') of different composites. Adapted from [89].

At 1 MHz, the real and imaginary component of magnetic permeability was reduced progressively on upsurging PZT amount as a result of the decrement in magnetic moment (Fig. 2.40). The reduction in magnetic permeability was responsible for reduction in magnetic moment. The initial magnetic permeability decreased with increasing PZT concentration because the incorporation of PZT phase reduced the magnetic characteristic of the composites

as well as increased the magnetic block. The resonant frequency was shifted toward high frequency region with increasing PZT content (Figure 2.40).

Yang et al. [90] synthesized (1-x) [$Ba(Zn_{0.33}Nb_{0.67})O_3$] (BZN) + (x) [$(Ni_{0.37}Cu_{0.20}Zn_{0.43}O)$-$(Fe_2O_3)_{0.96}$] (NiCuZn) composites (x = 20-80 wt. %) employing solid state synthetic technique and annealed at 1223 K to investigate the electromagnetic properties. Dense and homogeneous microstructures were achieved (Figure 2.41 (a-d)). In the low frequency region, complex electric permittivity spectra were exhibited a Debye-like relaxation due to Maxwell-Wagner polarization (Figure 2.42 (a)). As the NiCuZn concentration increased, the resonant frequency and electric permittivity decreased, but the magnetic permeability increased in the high frequency zone (Figure 2.42 (b)).

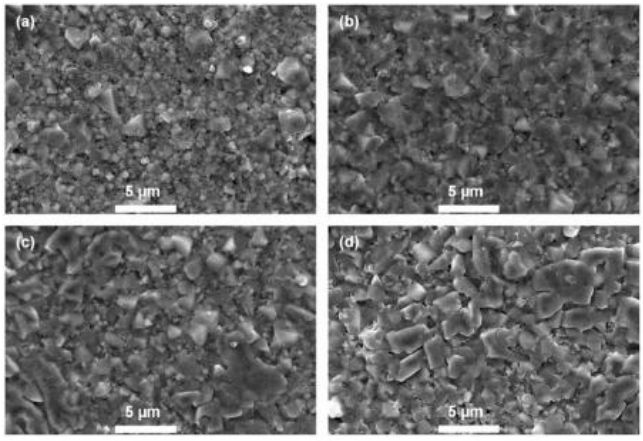

Figure 2.41: SEM micrographs of the BZN/NiCuZn composites with different NiCuZn contents annealed at 1223 K: (a) 20, (b) 40, (c) 60, and (d) 80 wt. %. Adapted from [90].

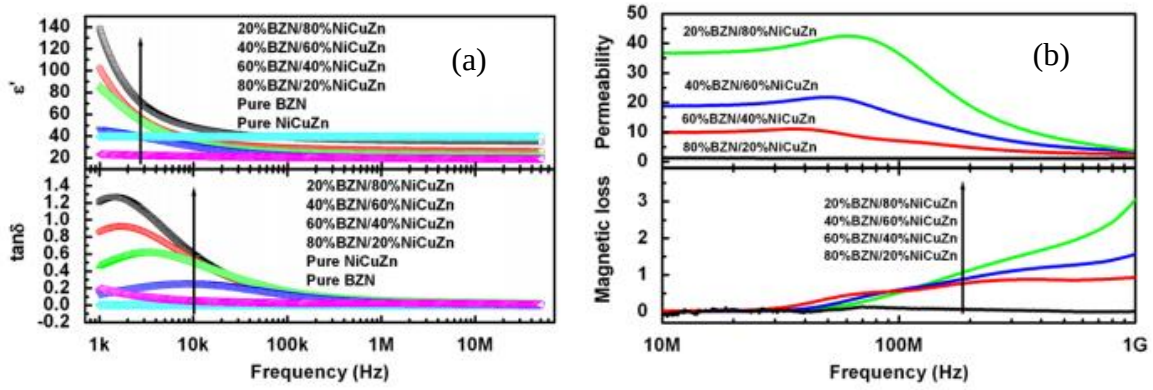

Figure 2.42: Frequency dependent: (a) dielectric traits, and (b) magnetic traits of the BZN/NiCuZn composites with different NiCuZn contents. Adapted from [90].

Yang et al. [91] prepared (*x*) [$Ba_{0.6}Sr_{0.4}TiO_3$] (BST) + (1-*x*) [$Ni_{0.37}Cu_{0.20}Zn_{0.43}Fe_{1.92}O_{3.88}$] (NiCuZn) (x = 20, 40, 60 and 80 wt.%) thick film composites successfully employing screen printing technique and annealed at 1153 K to investigate the electromagnetic properties. Dense microstructures were achieved (Figure 2.43 (a-d)). The electric permittivities were declined while the permittivity loss tangents were increased on upsurging BST amount as a result of the fact that the electric permittivity of BST is higher than that of NiCuZn while its permittivity loss tangent was lower than that of NiCuZn. The composite thick film having with 20 % NiCuZn displayed dielectric traits (ε' = 283 % and $\tan\delta_\varepsilon$ = 0.4 %) at 1 MHz, and 5% permiitivity tenability 5% (Figure 2.44 (a)). The saturation magnetization and remnant magnetization were declined with increasing BST contentis mainly due to the dilution effect and composite thick film with 20 wt. % NiCuZn displayed saturation magnetization and coercivity of 8 emu/g and 27.1 G (Figure 2.44 (b)).

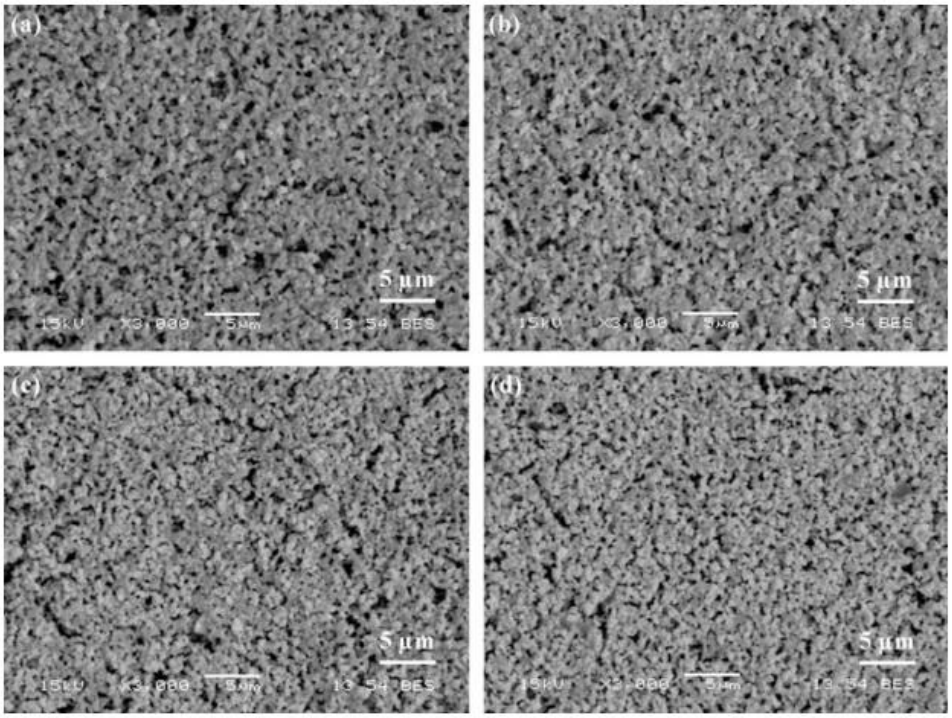

Figure 2.43: SEM micrographs of the natural surface of the NiCuZn/BST thick films with different concentration of BST: (a) 20, (b) 40, (c) 60, and (d) 80 wt. %. Adapted from [91].

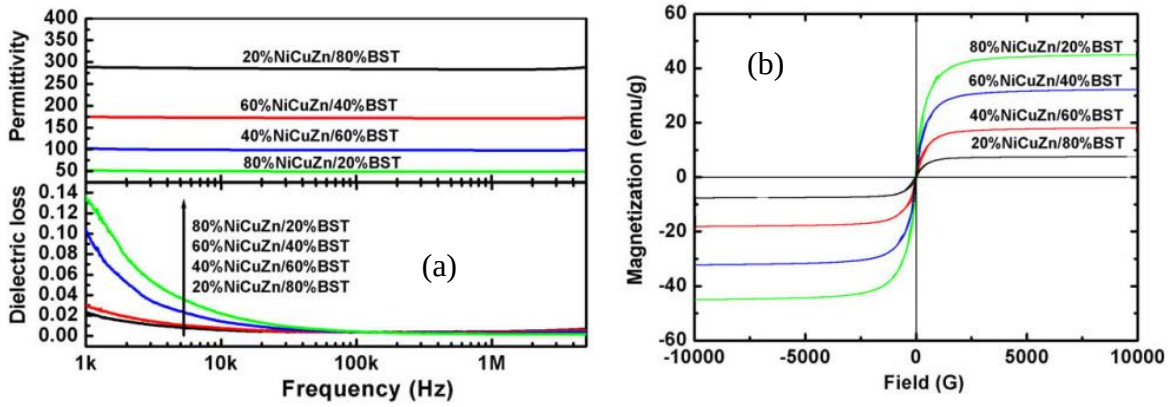

Figure 2.44: (a) Frequency dependency of the dielectric properties and (b) Magnetic hystereis of the NiCuZn/BST thick films with different concentration of BST. Adapted from [91].

Sadhana et al. [92] synthesized (x) [$BaTiO_3$] + (1-x) [$Ni_{0.53}Cu_{0.12}Zn_{0.35}Fe_{1.88}O_4$] (x = 0, 30, 50, 70 and 100 wt.%) composites fabricated via the microwave synthetic technique and annealed at 1183 K and they claimed that when $BaTiO_3$ concentration was raised, theoretical densitiy enhanced but magnetic properties (such saturation magnetization and coercivity) reduced. The magentic permeability of composites was found to be decreasing with increasing frequency (Figure 2.45 (a)) and randomly varied with increasing $BaTiO_3$ content. The Q_{max} values were achieved for all the composites at 250 kHz (Figure 2.45 (b)).

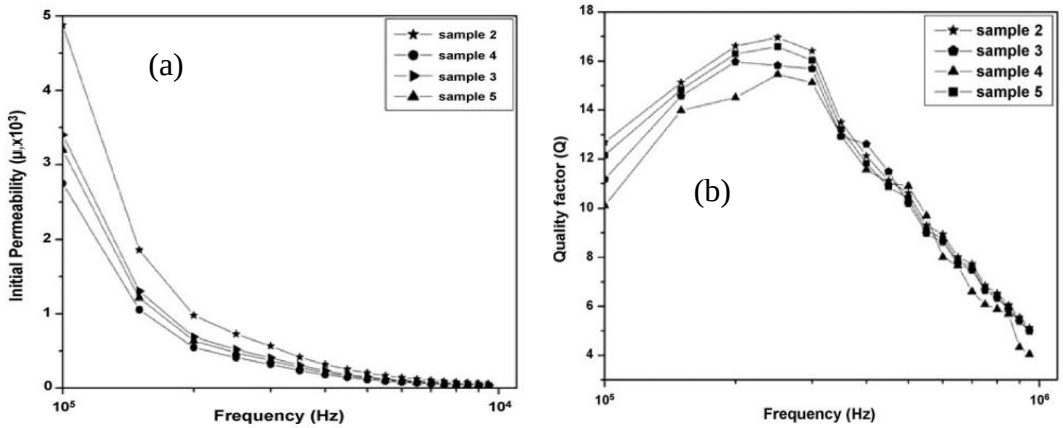

Figure 2.45: Frequency dependent: (a) magnetic permeability and (b) quality factor. Adapted from [92].

Liu et al. [93] successfully prepared $ZnTiO_3$-$Ni_{0.8}Cu_{0.12}Zn_{0.12}Fe_{1.96}O_4$ composites employing a limited shrinkage sintering technique and inspected the co-firing interface, inter-ionic diffusion in the midst of component phases, and dielectrical traits and claimed that the

interfacial interactions eventuated as a result of the stronger association of ferroelectric and ferromagnetic layers.

Lin et al. [94] synthesized (1-x) $[(K_{0.441}Na_{0.539})Li_{0.02}(Nb_{0.77}Ta_{0.18}Sb_{0.05})O_3]$ (LKNNTS) + (*x*) $[Ni_{0.37}Cu_{0.20}Zn_{0.43}Fe_{1.92}O_{3.88}]$ (NCZF) (x = 0.1, 0.2, 0.3, and 0.4) 2-2 type (laminated) and 0-3 type (particulate) composites employing solid state synthetic technique and annealed at 1353 K to optimize the electrical and magnetoelectric properties with the variation NCZF content. At low frequency region, the dielectric trait became weaker and weaker on upsurging NCZF amount due to dilution effect (Figure 2.46 (a, b)). At high frequency region, the electric permittivity displayed a step decrease at a certain frequency while the permittivity loss tangent revealed a relaxation peak. The permittivity loss tangent peaks shifted to lower frequency region and the relaxation time improved gradually.

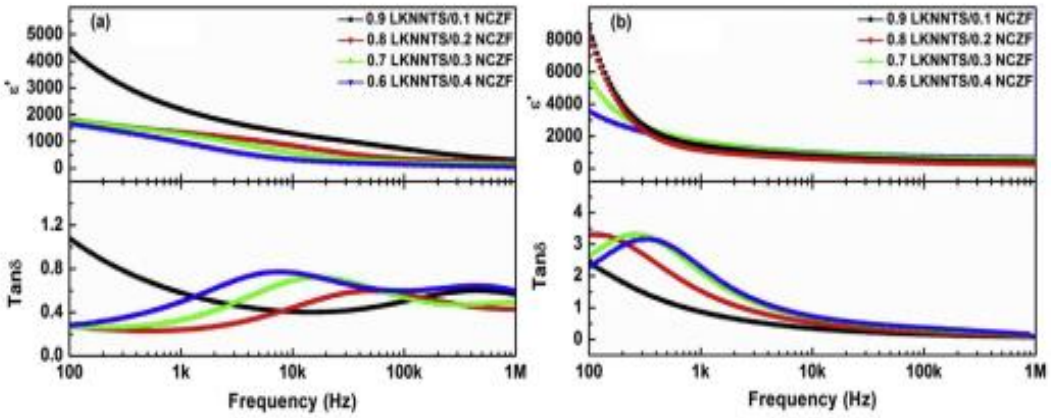

Figure 2.46: Variation of the dielectric traits of LKNNTS/NCZF composites against frequency: (a) 2-2 type; (b) 0-3 type. Adapted from [94].

At lower frequency region, frequency dependent transverse magnetoelectric coefficient (α_{E31}) became stronger and stronger with increasing NCZF content (Figure 2.47 (a-b)). The value of α_{E31} for laminated composites declined gradually and then tend to stable, which exhibited a maximum value at 1 kHz. The DC magnetic field dependent transverse ME coefficient (α_{E31}) varied non-monotonically with the magnetic field, and exhibited a peak at ~300 Oe (Figure 2.47 (c. d)). The 0.6LKNNTS/0.4NCZF laminated composite exhibited maximum α_{E31} of 133

mV/cm Oe which was more than four times as higher as that of the particulate composites (α_{E31} = 34 mV/cm Oe). This large disparity was accredited to the better coupling in the midst of component phases in the laminated composites.

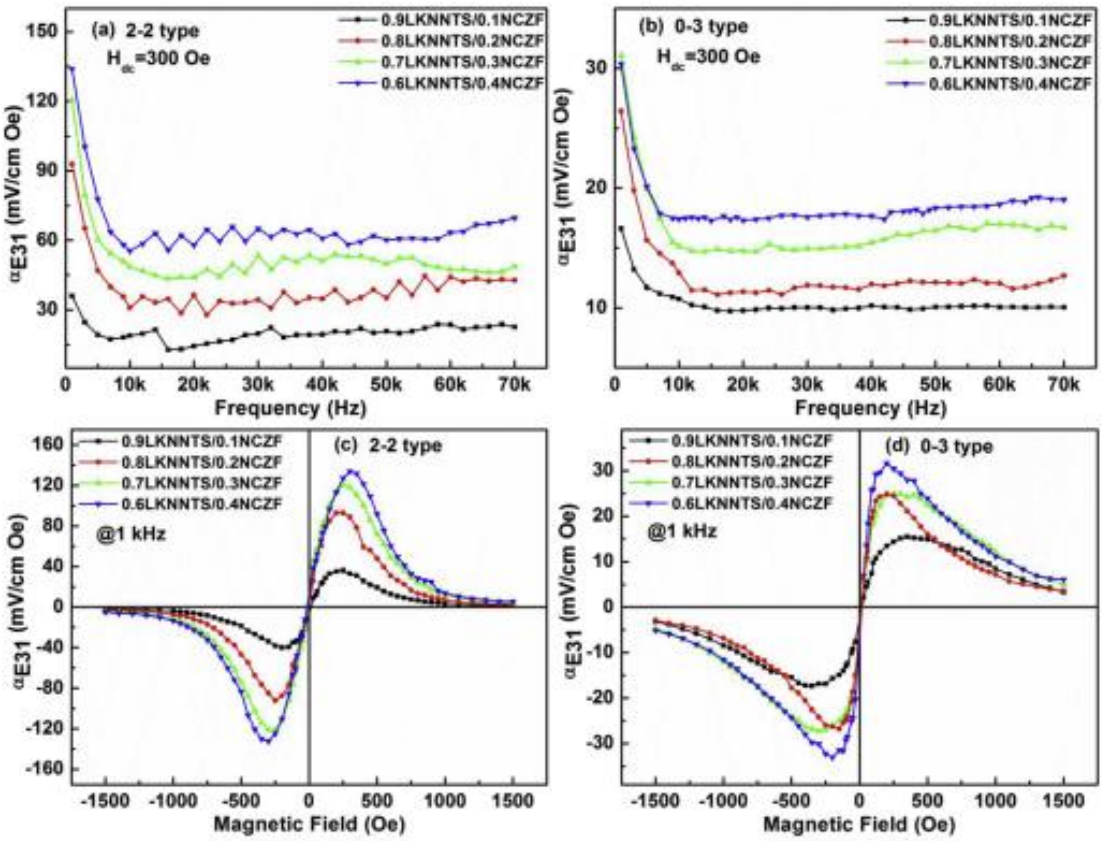

Figure 2.47: Transverse ME coefficient α_{E31} of the LKNNTS/NCZF composites as functions of frequency (a, b) at 300 Oe, and magnetic field (c, d) at 1 kHz. Adapted from [94].

The longitudinal magnetoelectric coefficient (α_{E33}) was enhanced significantly with increasing NCZF content and frequency for the laminated composites (Figure 2.48 (a)) while the value of α_{E33} for the particulate composites was declined firstly and then enhanced gradually (Figure 2.48 (b)). However, the valu of α_{E33} was enhanced with increasing the magnetic field and NCZF content (Figure 2.48 (c, d)). The value of α_{E33} varied feebly in the high magnetic field range due to saturated magnetostriction. The 0.6LKNNTS/0.4NCZF laminated composite exhibited maximum α_{E33} of 63 mV/cm Oe which was approximately two times larger than that of the particulate composites (α_{E33} = 38 mV/cm Oe).

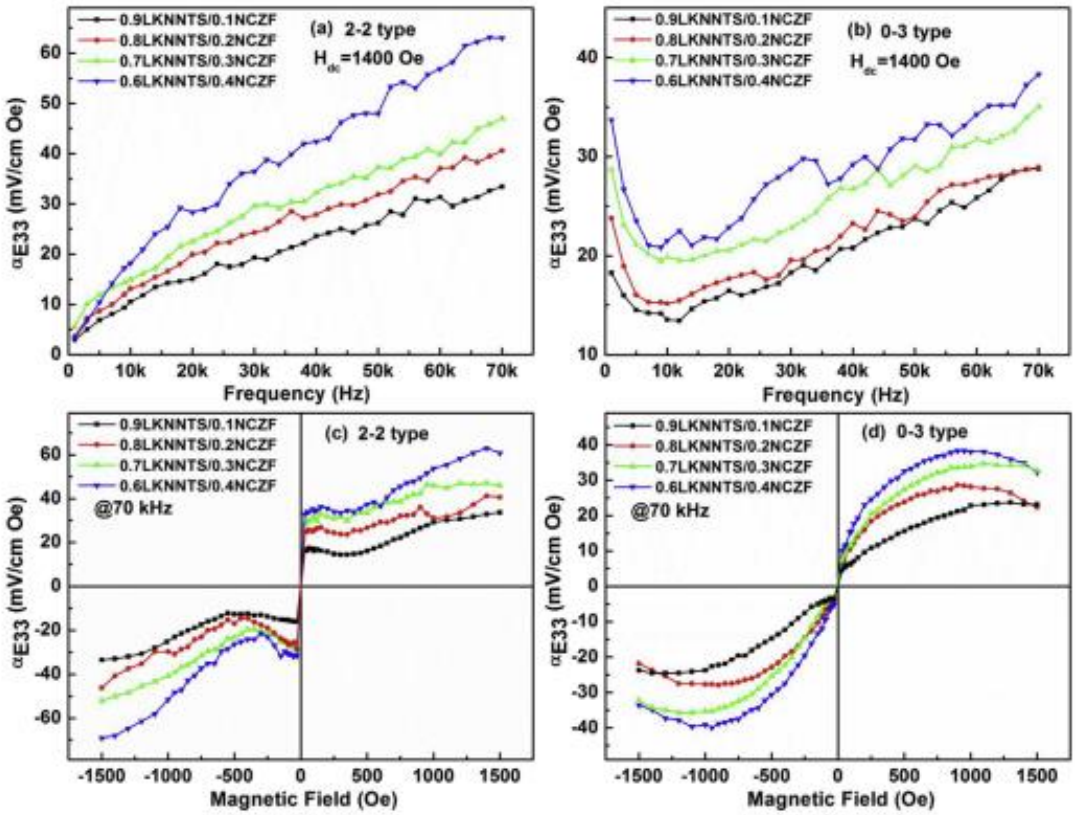

Figure 2.48: Longitudinal ME coefficient α_{E33} of the LKNNTS/NCZF composites as functions of frequency (a, b) at 1400 Oe, and magnetic field (c, d) at 70 kHz. Adapted from [94].

Yang et al. [95] synthesized (x) [$Bi_4Ti_3O_{12}$] (BTO) + (1-x) [$Ni_{0.37}Cu_{0.20}Zn_{0.43}Fe_{1.92}O_{3.88}$] (NiCuZn) (x = 0.2, 0.4, 0.6 and 0.8) composites successfully using the conventional solidstate reaction method and annealed at 950 ℃ to meet the demand of low-temperature co-fired ceramic technology. All composites were exhibited homogeneous microstructures without having no pores. The plate-like white grains of BTO were surrounded by quadrate-like dark grains of NiCuZn (Figure 2.49 (a-d)). The density of the composites was increased with increasing the NiCuZn content was attributed to lower sintering temperature of NiCuZn as compared to that of pure BTO. In the low frequency region, the BTO/NiCuZn composites exhibited giant electric permittivities. At low frequency window, the 40%BTO/60%NiCuZn composite possessed giant dielectric property and magnetic permeability of 60,000 and 25

(Figure 2.50 (a). On the contrary, in the low frequency region, the BTO/NiCuZn composites exhibited very high permeabilities (Figure 2.50 (b)).

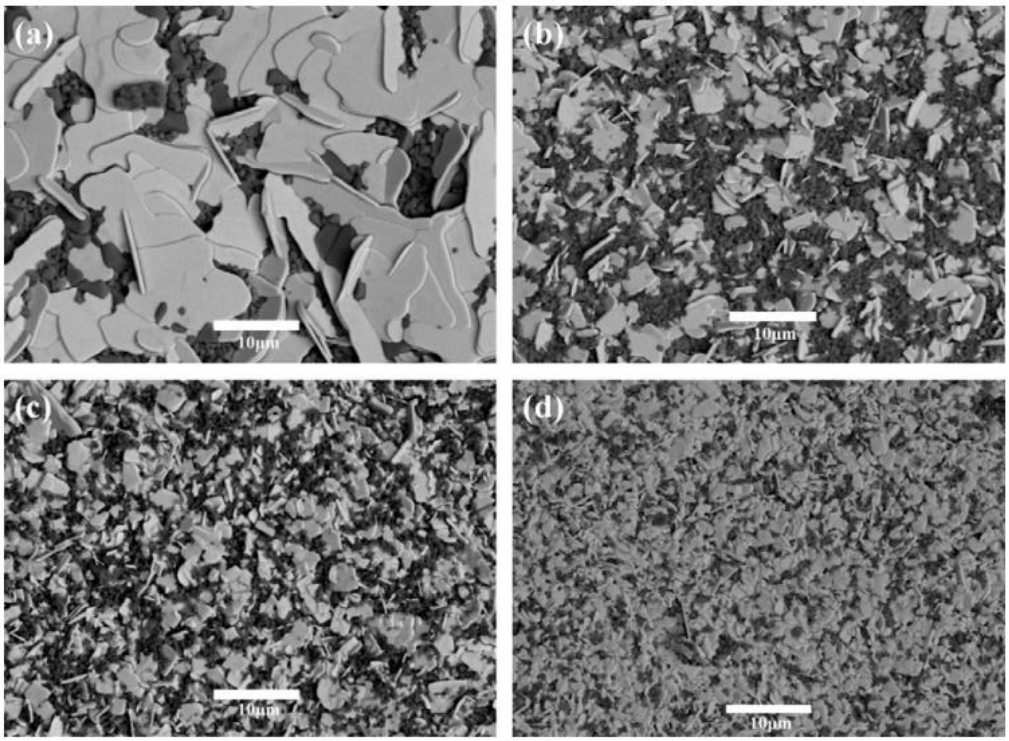

Figure 2.49: SEM micrographs of the BTO/NiCuZn composites with different NiCuZn extent: (a) x = 20, (b) x = 40, (c) x = 60, and (d) x = 80 wt. %. Adapted from [95].

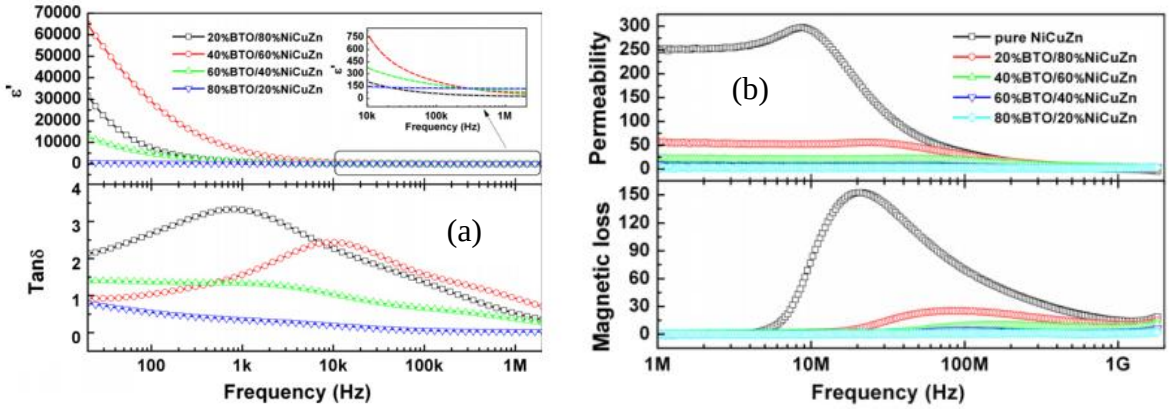

Figure 2.50: Frequency dependence of (a) the dielectric properties and (b) magnetic properties of the BTO/NiCuZn composites with different NiCuZn contents. Adapted from [95].

Yang et al. [96] fabricated (1-x) [$CaTiO_3$] (CTO) + (x) [$Ni_{0.37}Cu_{0.20}Zn_{0.43}Fe_{1.92}O_{3.88}$] (NiCuZn) composites (x = 20-80 wt. %) employing solid-state reaction technique and annealed at 1223 K to investigate the electromagnetic properties. The CTO/NiCuZn composites possessed high

electromagnetic properties. The electric permittivity was declined where as the permittivity loss tangent improved on upsuring NiCuZn amount (Figure 2.51). On the contrary, the magnetic permeability was improved whereas the resonant frequency was reduced on upsurging NiCuZn amount (Figure 2.52).

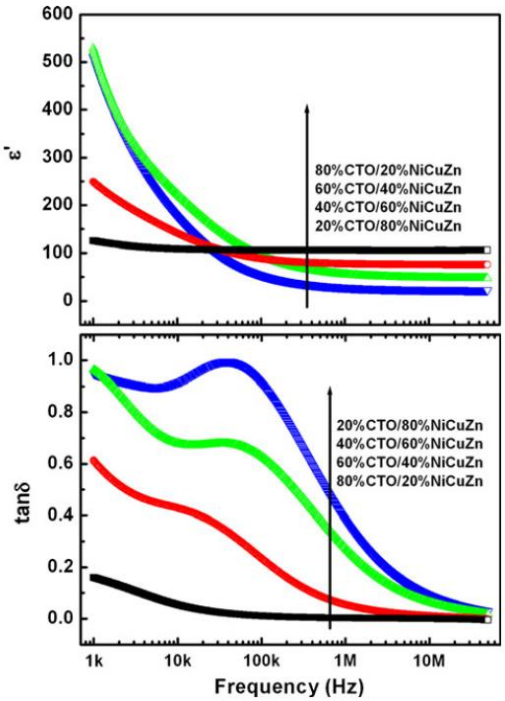

Figure 2.51: Frequency dependence of the dielectric traits of the CTO/NiCuZn composites with various NiCuZn amount. Adapted from [96].

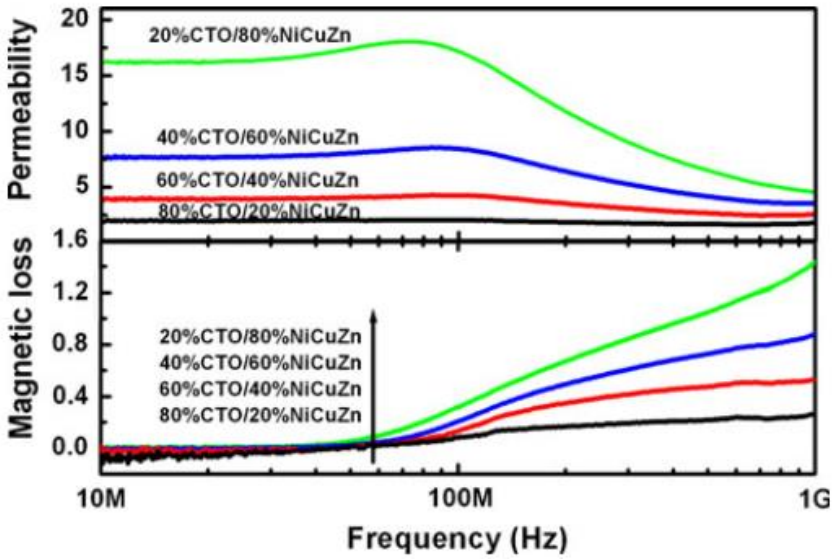

Figure 2.52: Frequency dependence of the magnetic traits of the CTO/NiCuZn composites with various NiCuZn amount. Adapted from [96].

Hsiang et al. [97, 98] successfully developed BaO. $(Nd_{0.8}Bi_{0.2})_2O_3.4TiO_2$ (BNBT) + Bi_2O_3-B_2O_3-SiO_2-ZnO (BBSZ)-$(Ni_{0.28}Cu_{0.12}Zn_{0.6}O)$-$(Fe_2O_3)_{0.99}$ (NiCuZn) composites via solid state synthetic technique and annealed at 1173-1223 K to investigate the effects of sintering behavior, microstructural feature, and electromagnetic characteristics and stated that as the material was sintering, any evidence of a chemical reaction could not be distinguished in the midst of the component phases and that it had excellent electromagnetic properties.

Peng et al. [99] synthesized three $Bi_2(Zn_{1/3}Nb_{2/3})_2O_7$ (BZN)/ $(Ni_{0.3}Cu_{0.1}Zn_{0.6}O)$-$(Fe_2O_3)_{0.8}$ (NiCuZn), $Pb(Ni_{1/3}Nb_{2/3})O_3$-$PbZrO_3$-$PbTiO_3$ (PNZT)/ $(Ni_{0.3}Cu_{0.1}Zn_{0.6}O)$-$(Fe_2O_3)_{0.8}$(NiCuZn), and $BaNd_2Ti_4O_{12}$ + ZnO-B_2O_3 (BNTZB)/ $(Ni_{0.3}Cu_{0.1}Zn_{0.6}O)$-$(Fe_2O_3)_{0.8}$ (NiCuZn) particulate composites and laminated composites via the solid state synthetic technique and annealed at 1173 K and found that having an effective sintering flux was one of the most important considerations in creating ferromagnetic-ferroelectric particulate composites or layered composites are capable of co-firing at a temperature that is similar to that of unadulterated ferromagnetic and ferroelectric substances. The electric permittivity and dieletric loss were declined with increasing frequency for the composites with 50-90 vol% ferrite while for the other composites the electric permittivity and permittivity loss tangent exhibited almost frequency independent behavior. The electric permittivity was initially increased to a maximum of 30 vol% ferrite content, but declined with further increase in ferrite content (Figure 2.53 (a, b)). Such behavior was acridated to the formation of a new crystalline phase of $Bi_{1.5}ZnNb_{1.5}O_7$, which possessed an electric permittivity of 170 much higher than those of $Bi_2Zn_{0.67}Nb_{1.33}O_7$ (electric permittivit = 585) and ferrite (electric permittivity = 520). At 1 kHz < f < 3 MHz, the magnetic permeability exhibited frequency independent behavior (Figure 2.54 (a)). A higher magentic permeability was perceived with increasing ferrite content. In Q value spectra, a peak value was observed at ~1 MHz for the composites having ferrite content higher than 70 vol% (Figure 2.54 (b)). At a given frequency, the Q value was enhanced with increasing ferrite content.

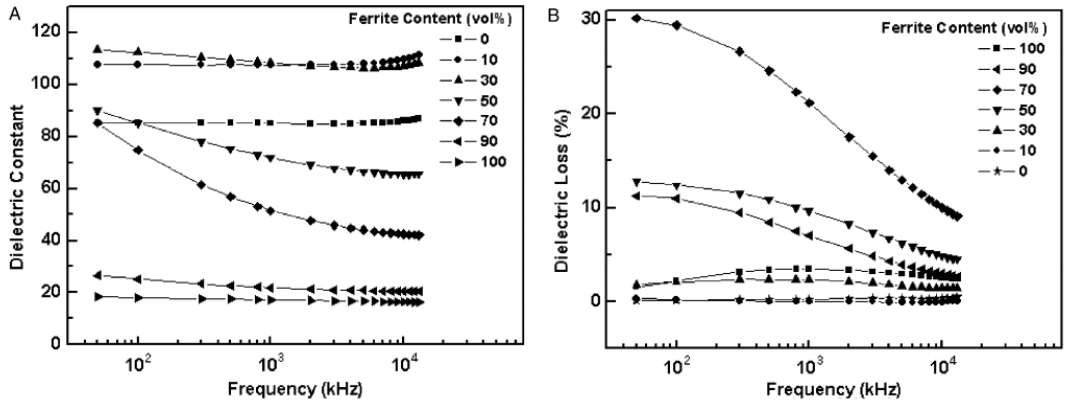

Figure 2.53: Effect of ferrite content and frequency on: (a) permittivity constant and (b) permittivity loss tangent for BZN + ferrite powder composite annealed at 1173 K for 2 h. Adapted from [99].

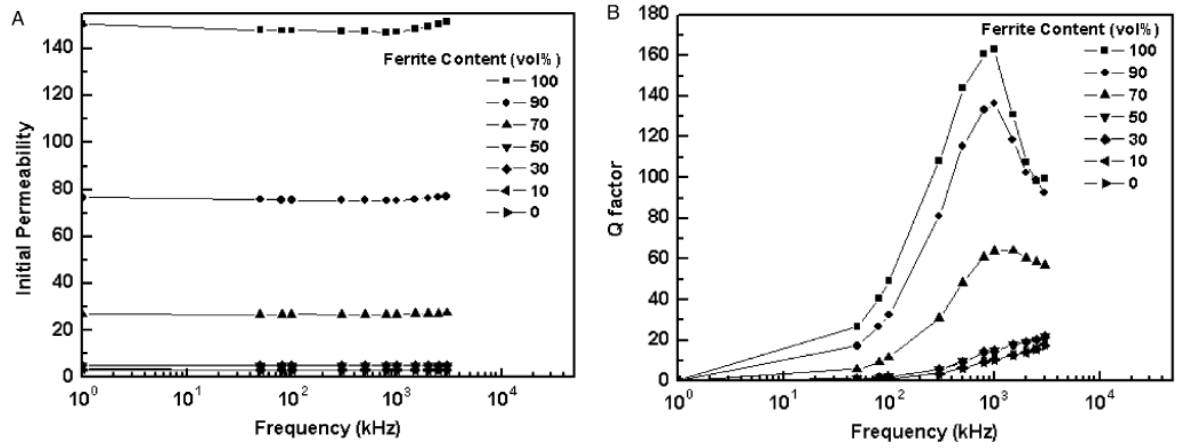

Figure 2.54: Effect of ferrite content and frequency on: (a) electric permittivity, and (b) Q factor against frequency for BZN + ferrite powder composite annealed at 1173 K for 2 h. Adapted from [99].

Ling et al. [100] successfully developed $CaTiO_3/(Ni_{0.60}Cu_{0.24}Zn_{0.16}O)_{1.02}(Fe_2O_3)_{0.98}$ and $BaTiO_3/ (Ni_{0.60}Cu_{0.24}Zn_{0.16}O)_{1.02}(Fe_2O_3)_{0.98}$ composites with molar ratio of ferrite to ceramic of 10:1 having 2 % Bi_2O_3 as fluxing agent via solid state synthetic technique and annealed at 1173-1223 K to investigate the effect of microstructure and gap criterion on the magnetic permeability. The magnetic model was maticulously compatible among the adjusted values of the gap criterion on the magnetic permeability. Maxwell-Garnett's model was used to study the dielectric characteristics, and it was discovered that the experimental and theoretical values did not match up due to the sintering behavior and inhomogeneousness of the composites.

Ling et al. [101] synthesized (1-x) [$BaTiO_3$] (BT) + (x) [$(Ni_{0.60}Cu_{0.24}Zn_{0.16}O)_{1.02}(Fe_2O_3)_{0.98}$] (NCZF) ($x$ = 10, 20, 30 and 40 wt.%) composites successfully by solid state synthetic technique annealed at 1173 K for 3 h and subsequently some of the samples were annealed in oxygen (0.06 MPa) at 1123 K for 2h to investigate the influence of annealing on electromagnetic properties. At 1 MHz, Q-factor at was enhanced amidst 10 and 20 weight percent of $BaTiO_3$ (Figure 2.55 (a)), whilst the product of Snoek was embellished amidst 10, 20, and 30 weight percent of $BaTiO_3$ whilst the composites were annealed in O_2 (Figure 2.55 (b)). The permittivity loss tangent was reduced at 1 MHz following annealing in O_2 with 10 weight percent $BaTiO_3$. For 30 weight percent of $BaTiO_3$, the permittivity constant was reduced from 49.4 to 30.8 at 1 MHz, while the permittivity loss tangent was reduced from 5.29 $\times 10^{-3}$ to 2.48 $\times 10^{-4}$ (Figure 2.56).

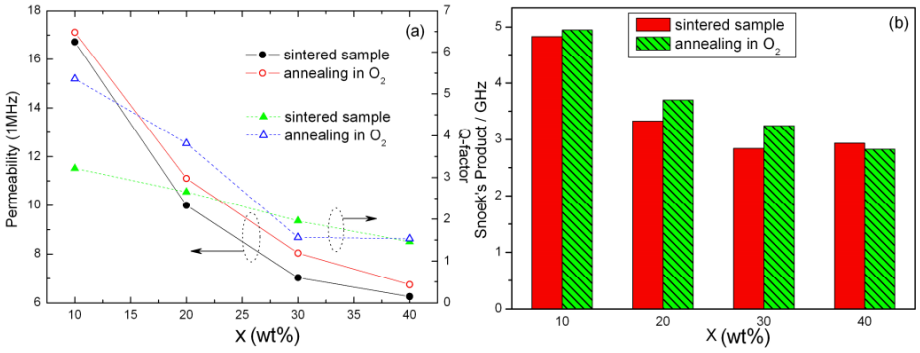

Figure 2.55: (a) Variation of magnetic permeability (μ') and Q-factor (measured at 1MHz) and (b) Variation of Snoek's product with mass ratio of BT/NCZF (x). Adapted from [101].

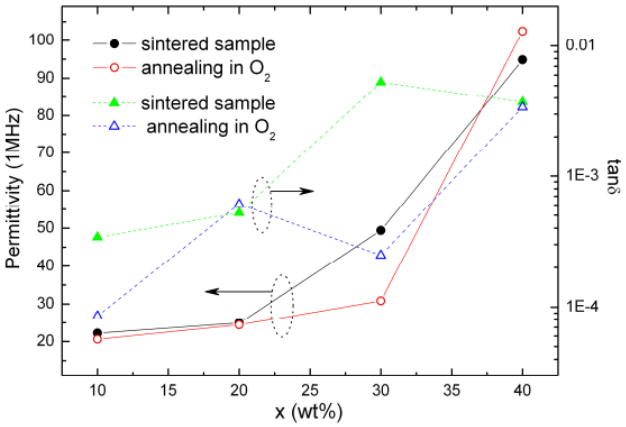

Figure 2.56: Variation of ε' and tanδ (measured at 1MHz) with mass ratio of BT/NCZF (x). Adapted from [101].

2.2. Ferroelectrics

Ferroelectrics are materials that display spontaneous polarization and a domain skeleton below the Curie point, and that may also be changed upon the applications of electric fields. Figure 2.57 illustrates a timetable from 300 BCE to the current day of advent significant occasions in the development of ferroelectrics.

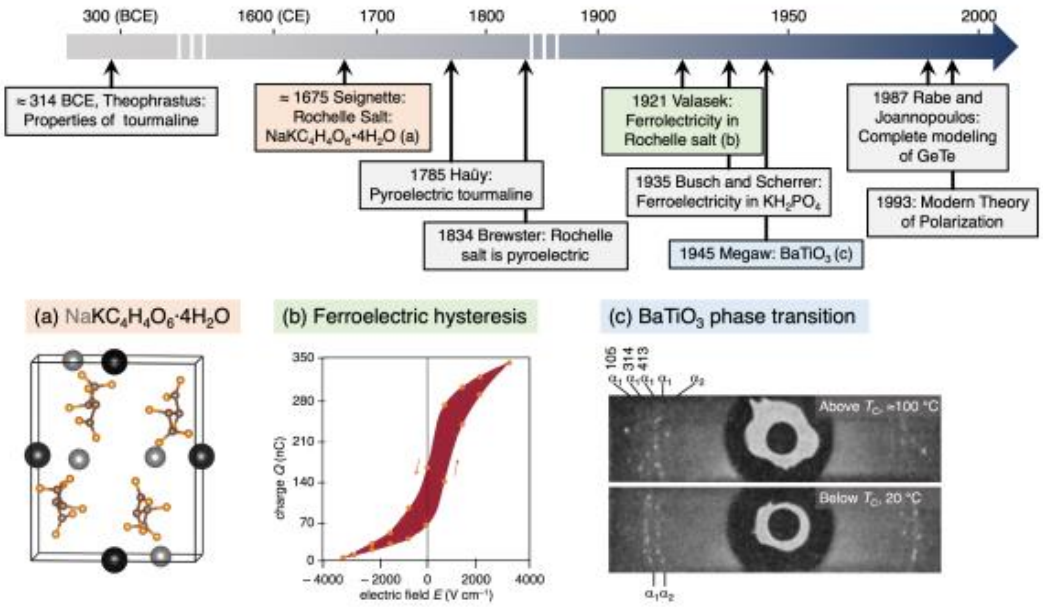

Figure 2.57: Top diagram: a timetable from 300 BCE to the current day of advent significant occasions in the development of ferroelectrics. (*a*) Paraelectric phase of Rochelle salt's crystal architecture. For simplicity, water molecules and hydrogen atoms have been disregarded. (*b*) Rochelle salt's ferroelectric hysteresis loop, as reported by Valasek in 1921. (*c*) Reproduction of the X-ray photographs of high-angle reflections in $BaTiO_3$ powders above and below the ferroelectric phase transition taken by Megaw using $Cu - K\alpha_1$ and $Cu - K\alpha_2$ radiation. Adapted from [102].

2.2.1. Crystal structure of barium titanate

Barium titanate ($BaTiO_3$) is the perovskite-structured ferroelectric and piezoelectric materials and is very stable chemically and mechanically. The perovskite structure's stoichiometry is ABO_3, where A stands for a big monovalent, bivalent, or tri-valency cation and B is often a smaller tri-valency, tetra-valency, or tri-valency cation. Ideal perovskite structures use the

cubic space group $Pm\bar{3}m$ with a face-centered cubic arrangement. A unit cell of perovskite is depicted in Figure 2.58.

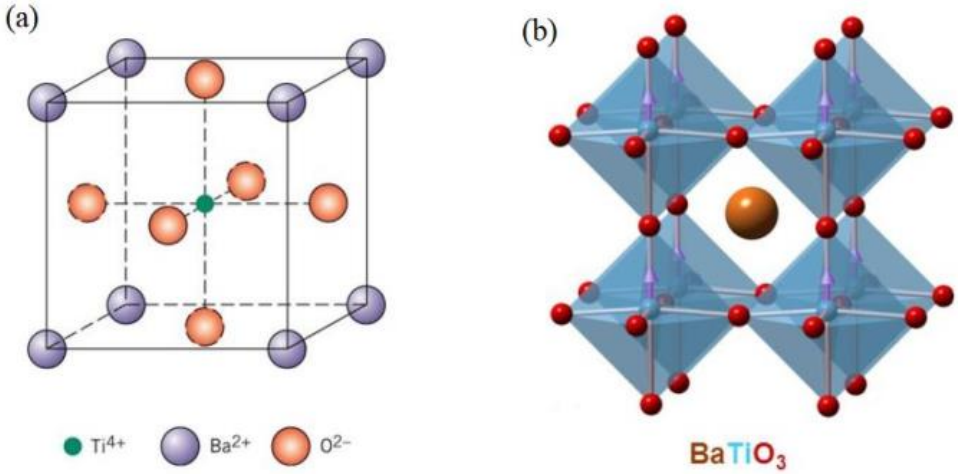

Figure 2.58: (a) The cubic phase for a unit cell of $BaTiO_3$. Here, the Ti^{4+} ion is in the middle of the composition, O^{2-} is in the middle of the phases, and Ba^{2+} ions are at the corner of the cube. (b) $BaTiO_3$ perovskite crystal structure in three dimensions. Adapted from [103].

With $BaTiO_3$, the oxygen ions form an octahedron with Ba^{2+} ions at the body center and Ti^{4+} ions at the B sites, which are located at the corners of the cube. $BaTiO_3$ exhibits a significant spontaneous polarization (~ 25 μC/cm^2) and a Curie temperature of 393 K. Figure 2.59 shows the various structural phase changes that $BaTiO_3$ goes through as the temperature drops. The term "polymorphic phase transition" (PPT) is used to describe each of these temperature-dependent phase changes. $BaTiO_3$ possesses cubic architecture and is paraelectric above its Curie temperature. The cubic structure becomes tetragonal as the temperature drops below its Curie point. The oxygen and titanium ions are moved away from the barium ions as a result of the c-axis broadening, which leads to ferroelectric polarization. At 290 K and 190 K, respectively, the structure shifts from tetragonal to cubic, then from rhombohedral to orthorhombic as the temperature drops [104].

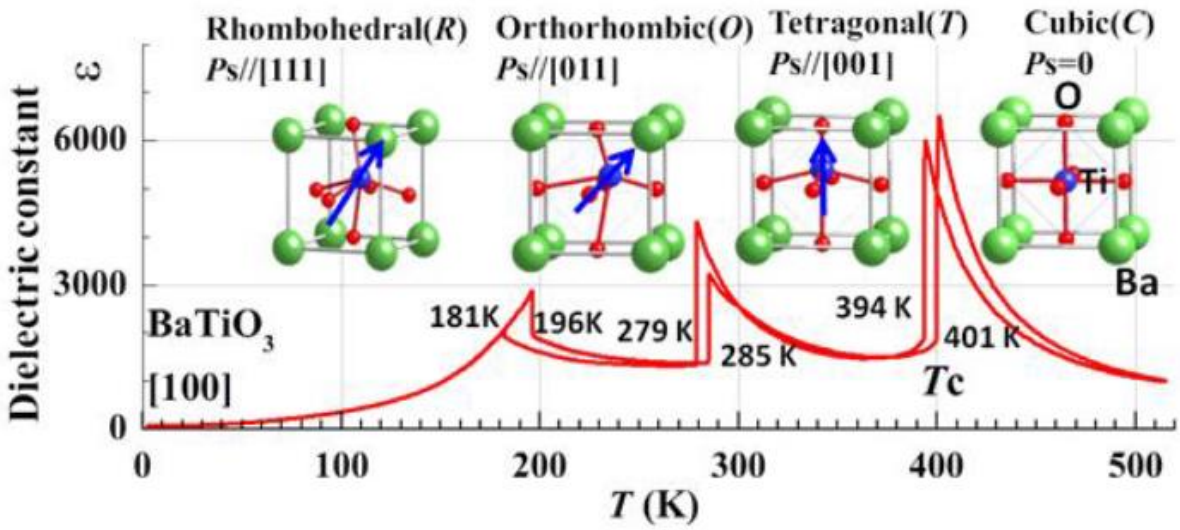

Figure 2.59: Phase transition of $BaTiO_3$ vs. temperature. Adapted from [104].

2.2.2. Barium Calcium Titanium Zirconate system

The current scientific goal is to find the lead-free ferroelectric materials with high piezoelectric properties for various technologies since the lead-based ferroelectric is toxic and harmful for atmosphere and human health. In this regard, it is essential to search, design and promote a new lead-free ferroelectric/piezoelectric ceramic material. Amid the lead-free ceramic materials, barium titanate ($BaTiO_3$) has widely investigated owing to its excellent dielectric and piezoelectric characteristics. However, $BaTiO_3$ reveals reasonably low electric permittivity and piezoelectric properties as compared to the lead-based perovskite ceramics. To surmount the drawback, there is now urgent need to modify the barium titanate. Substitution, doping and/or chemical modifications is one of the effective ways to tune the piezoelectric characteristics of piezoelectric materials. In doing so, divalent calcium (Ca^{2+}) and tetravalent zirconium (Zr^{4+}) can be incorporate into the crystal lattice of $BaTiO_3$ to replace Ba^{2+} and Ti^{4+}, respectively. The partial replacement of Ba^{2+} with Ca^{2+} in $BaTiO_3$ has been shown to be able to adjust the Curie point as well as the phase transition temperature from orthorhombic symmetry to tetragonal symmetry, making the tetragonal symmetric phase invariable across a large temperature spectrum [105]. On the contrary, Zr^{4+} replacement at the Ti^{4+} site allows for

fine-tuning of the skeletal and electrical characteristics of $BaTiO_3$. Additionally, Zr^{4+} is more chemically stable than Ti^{4+}. As a consequence, (Ba, Ca) (Ti, Zr)O_3 system becomes a significant ferroelectric and piezoelectric material due to its excellent electrical and piezoelectric traits and environmentally friendly nature. The prototype perovskite structure is shown in Figure 2.60, where the ions Ba^{2+} and Ca^{2+} are positioned in the A sites and Zr^{4+} and Ti^{4+} are present in the B sites.

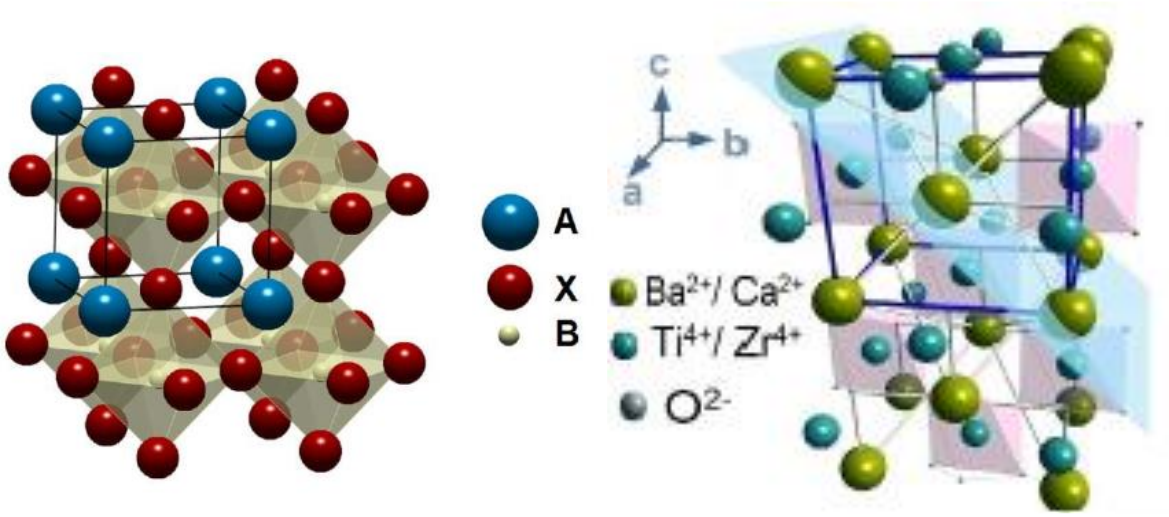

Figure 2.60: Schematic delineation of a perovskite architecture prototype, where A = Ba^{2+}, Ca^{2+}; B = Zr^{4+}, Ti^{4+}; X = O^{2-}. Adapted from [76, 106].

2.2.3. Phase diagram of barium calcium zirconium titanate

Phase diagram are effective way to visualize the crystal structure of a materials and characteristic over a specified range of compositions and/or temperatures. Figure 2.61 (a) depicts the structural phase diagram of lead-based ceramics. Figure 2.61 (b) illustrates the first structural phase diagram of the barium calcium zirconium titanate system is similar to lead-based ceramics which was established by Liu and Ren [107] in 2009 adopting an association of temperature-dependent XRD and dielectrical investigations. The phase diagram of BCTZO ceramic system has a convergence phase point (PCR) making of triple point of the cubic paraelectric (C, $Pm\bar{3}m$) phase, tetragonal ferroelectric (T, $P4mm$) and rhombohedral ferroelectric (R, $R3m$) phases based on the temperature-dependent dielectric characteristics, that was accountable for the large piezoelectricity at $x = 0.32$ and at temperature of 57 °C. A

morphotropic phase border (MPB) is present in the phase representation in the midst of ferroelectric rhombohedral phase (*R*3*m*) on the BZTO-rich edge and a tetragonal phase (*P*4*mm*) on the BCTO-rich edge. In contrast, according to Acosta, an association of low anisotropic energy, large polarization, and improved elastic softening results in the strongest piezoelectric coefficients near the border in the midst of ferroelectric phases with orthorhombic and tetragonal symmetries [108].

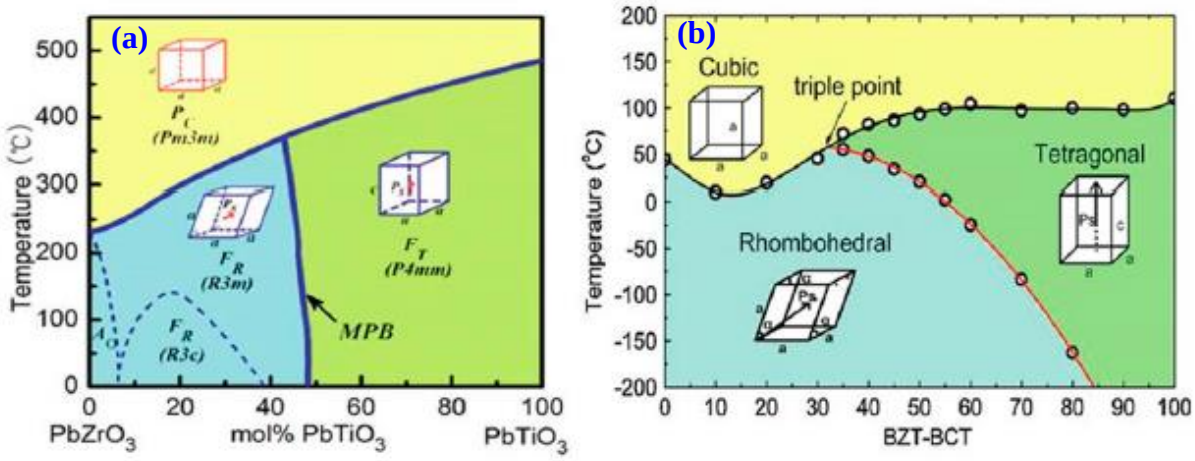

Figure 2.61: Phase diagram of (a) $PbZr_{1-x}Ti_xO_3$ system. Adapted from [109] and (b) $Ba_{0.85}Ca_{0.15}Zr_{0.1}Ti_{0.9}O_3$ (BZT-xBCT) system around MPB composition. Adapted from [107].

Subsequently, Keeble and Damjanovic [109-111] refined the structural phase diagram of BCTZO system employing high-resolution synchrotron X-ray diffraction methods and revealed that for compositions close to $x = 0.5$, an orthorhombic (O) phase is thought to exist as a transitional state in the midst of the R and T phases, as depicted in Figure 2.62 (a) with a distinctive quadruple point in in the midst of four phases and disappeared at the triple point. Figure 2.62 (b) represents the formation of the high instability gradient. Keeble and Damjanovic have been discussed triple phase changes, i.e., from R to O, from O to T, and from T to C in the proximity of room temperature. Additionally, they proposed that the polymorphism could permit a significant increase in piezoelectricity through processes for the rotation and extension of polarization associated with a flattened energy environment.

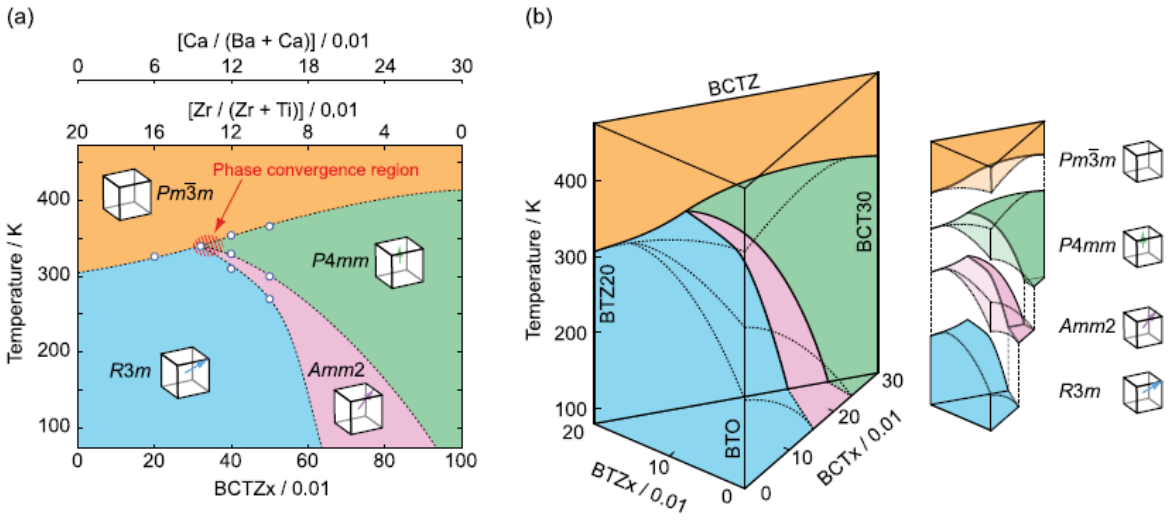

Figure 2.62: (a) Phase representation of BCTZO perovskite. In comparison to Liu and Ren workv [107] a persistent orthorhombic phase that reaches the area of phase convergence and (b) A 3D phase representation of BCTZO demonstrates how the two binary phases of BTZO and BCTO combine to generate the ternary BCTZO phase. Adapted from [109].

2.3. Piezoelectrics

Piezoelectric materials are a subset of dielectric materials which can be mechanically polarized when an electric field is applied (Figure 2.63). Piezoelectricity, or literally "pressure electricity," is the unusual characteristic displayed by a few dielectric materials. The two types of piezoelectric materials: (i) polar piezoelectrics (endowed with a net dipole moment) and (ii) non-polar piezoelectrics (endowed with dipole moments that add to a maximum of zero when added in various directions) [112].

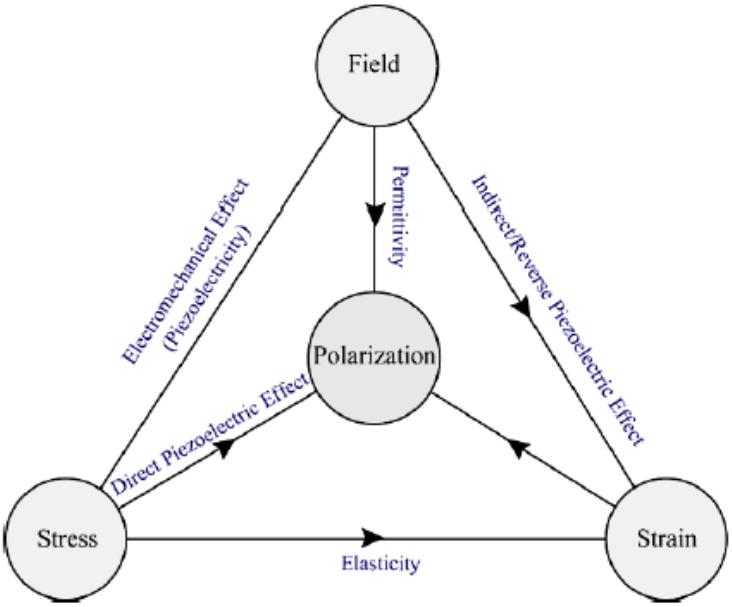

Figure 2.63: Piezoelectricity: the fusion of elastic and electric phenomena. Adapted from [112].

A conventional perovskite-structured piezoelectric ceramic is shown in Figure 2.64. Each of them is made up of a small metal ion possessing tetra-valency, generally Ti^{4+} or Zr^{4+}, arranged in a crystal lattice with heavier metal ions possessing bi-valency, typically Pb^{2+} or Ba^{2+}, and O2- ions. Each crystal possesses a dipole moment when the surrounding conditions result in tetragonal or rhombohedral symmetry for the crystals.

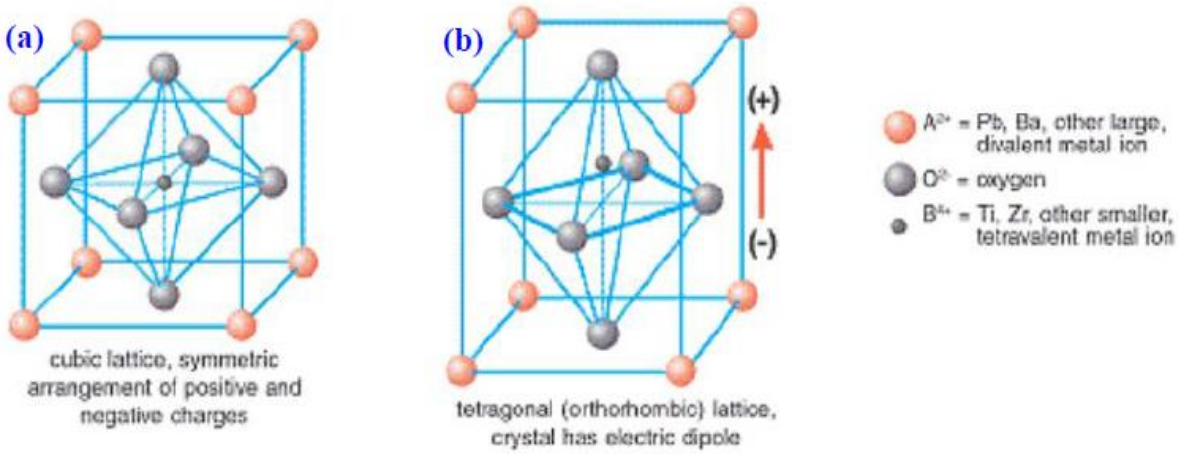

Figure 2.64: Crystal architecture of a conventional piezoelectric: (a) above Curie temperature and (b) below Curie temperature. Adapted from [113].

At a threshold temperature noted as the Curie temperature, respective crystal of perovskite in the annealed ceramic component displays a straightforward cubic arrangement without a moment of dipole (Figure 2.64 (a)). In contrast, respective crystal maintains tetragonal or rhombohedral arrangement and possesses moment of dipole below the Curie temperature (Figure 2.64 (b)). Domains are localized areas of alignment created by adjacent dipoles. The alignment results in a net polarization and a net dipole moment for the domain. However, the ceramic component has no complete polarization since the direction of polarization in nearby domains is random (Figure 2.65 (a)). A strong DC electric field is used to line up the domains in a ceramic element, typically below the Curie temperature (Figure 2.65 (b)). Through this polarizing process, the component elongates along the field's direction and domains that are predominantly lined up accompanying the electric field develop at the cost of domains which are not lined up with the field. Most of the dipoles are locked into a nearly aligned form when the electric field is withdrawn (Figure 2.65 (c)). The element is permanently elongated and has a residual polarization that is permanent.

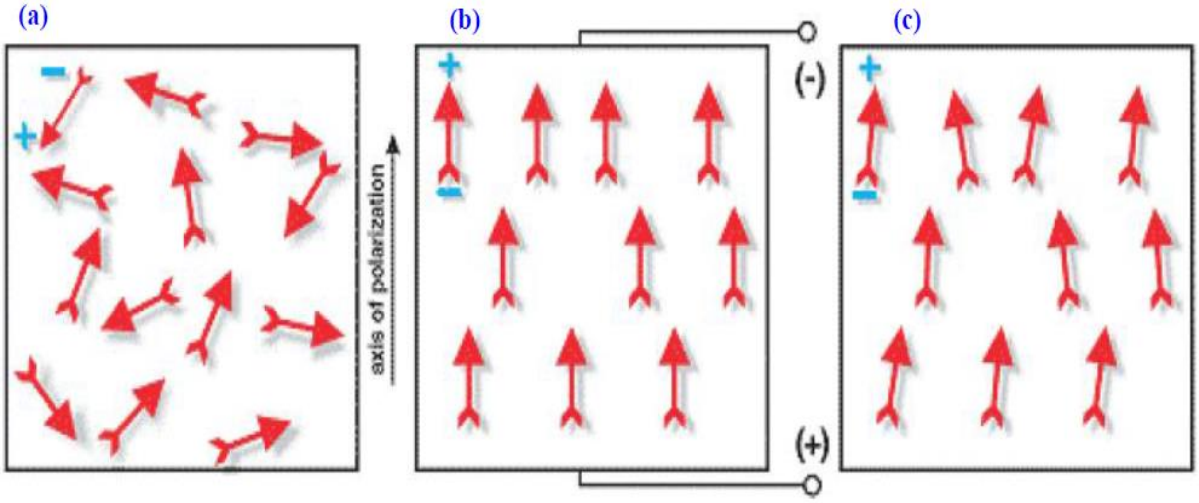

Figure 2.65: Piezoelectric ceramic polarization: (a) before polarization, a polar domain's orientation is random, (b) DC electric field polarization and (c) polarization that remains after the electric field is removed. Adapted from [113].

Figure 2.66 shows the timetable for the advancement of piezoelectric characteristics in lead-free piezoelectric materials as well as the conventional piezoelectric materials.

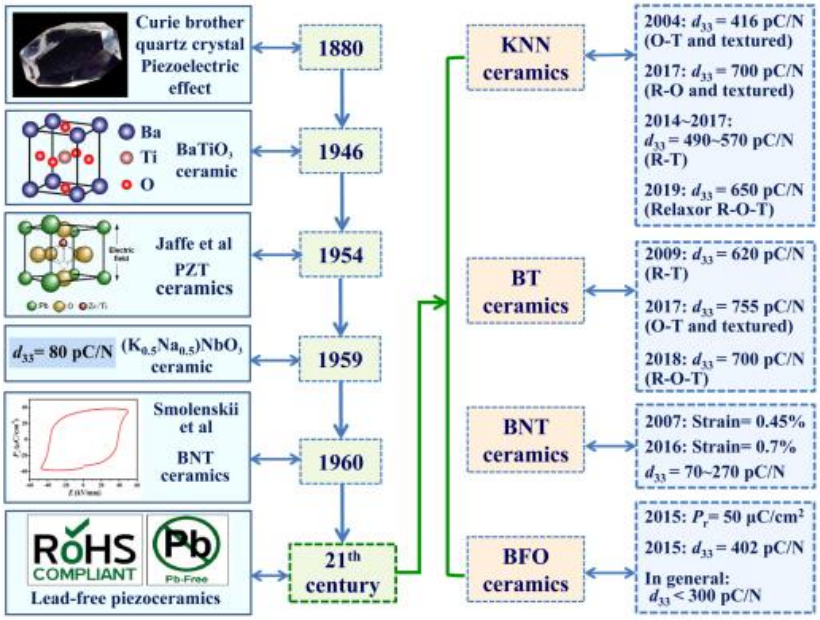

Figure 2.66: Timetable for the advancement of piezoelectric characteristics in lead-free piezoelectrics as well as the conventional piezoelectric materials. Adapted from [114].

2.3.1. Mechanism of Piezoelectricity

Piezoelectricity is the buildup of electric charge under mechanical stress in certain solid materials [114]. There are two types of piezoelectricity, namely direct piezoelectric response and converse or reverse piezoelectric response. Figure 2.67 illustrates direct and converse piezoelectric responses. Direct piezoelectric response (Figure 2.67 (a)) is the intrinsic creation of electric charge in response to the mechanically applied force, and the inverse or converse piezoelectric effect (Figure 2.67 (b)) is the internal creation of mechanical strain brought on by electric fields [115, 116].

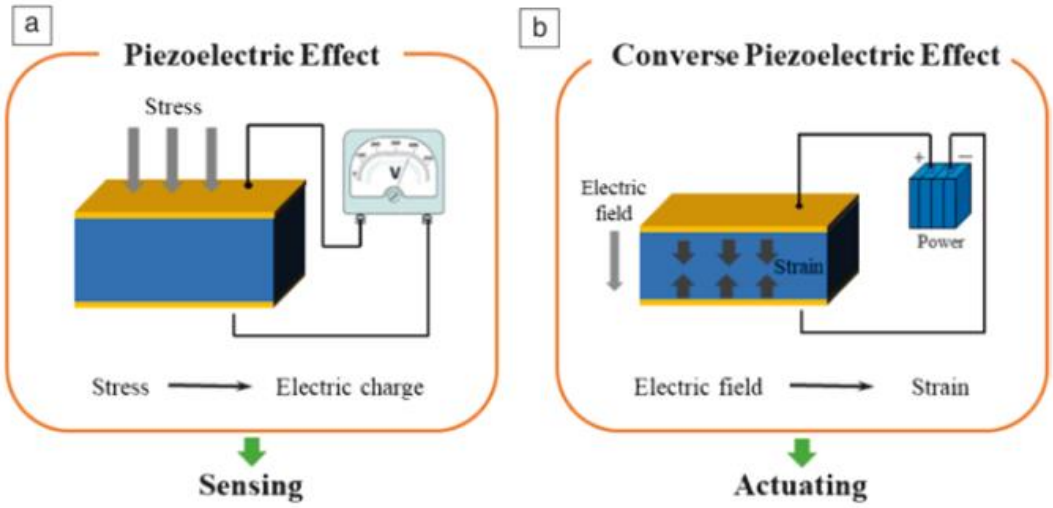

Figure 2.67: (a) The direct piezoelectric response generates an electrical charge when a mechanical stress is applied, while (b) the converse piezoelectric response illustrates the case where strain arises due to an applied electric field. Adapted from [117].

2.3.2. Molecular model of piezoelectricity

A straightforward molecular model is frequently used to explain the creation of electrical charge because of a force acting on a material is known as the piezoelectric effect (Figure 2.78) [112]. Each molecule's centers for the negative and positive charges line up before the material is put under external stress, resulting in electrically neutral molecules, as illustrated in Figure 2.68 (a). The internal network, however, deforms when an external mechanical stress is applied, separating the molecule's positive and negative centers and creating a small number of dipoles, as seen in Figure 2.68 (b). A fixed charge is thus appeared on the surface as a result of opposing poles within the material canceling one another out which is delineated in Figure 2.68 (c). This indicates polarization of the material, or what is known as a direct piezoelectric response [112]. The mechanical energy required to distort the material may be transformed into electrical energy using this polarization, which produces an electric field. The piezoelectric material in Figure 2.69 (a) has two metal electrodes placed on the opposing surfaces. A continuous charge density emerges onto the surface of the crystal in contact with the electrodes when a force is applied to the piezoelectric body's surface and a galvanometer is attached to the short-circuit wire to externally short-circuit the electrodes [112]. The conductor's free

charges flow as a result of this polarization's creation of an electric field. The free charges travel to the end, based on their sign, where the fixed charge produced by polarization has the opposite sign. Figure 2.69 (a) illustrates this free flow of charges until the free charges cancel out the polarization effect. Accordingly, no charge flows in a stable state or an unaltered condition independent of the existence of an external force. The polarization likewise vanishes when the force acting on the material is withdrawn, the free charge flow is then reversed, and the material finally reverts to its initial rest state (see Figure 2.69 (b)). A galvanometer is used to demonstrate this process by identifying two current peaks with the opposite sign. Current will flow and transform mechanical energy into electrical energy if the shorted wire is replaced with a resistor and load [112].

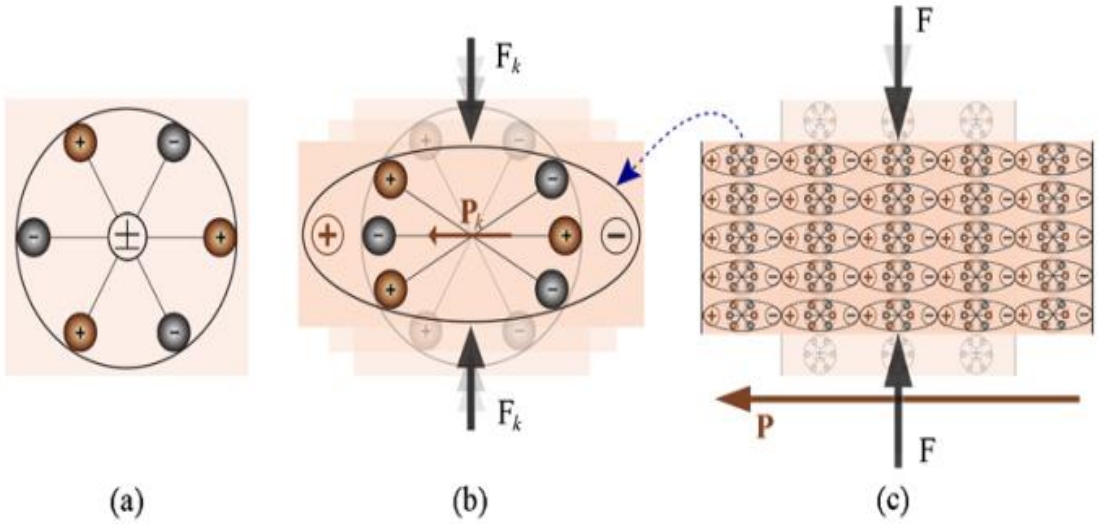

Figure 2.68: Piezoelectric response: a straightforward molecular model: (a) An unperturbed, non-polarized piezoelectric molecules (despite the possibility of preceding electric polarization); (b) The molecule was subjected to an external force (F_k), which produced electrical polarization (P_k), as shown; (c) the surface's polarizing reaction when piezoelectric material is forced by an external force. Adapted from [112].

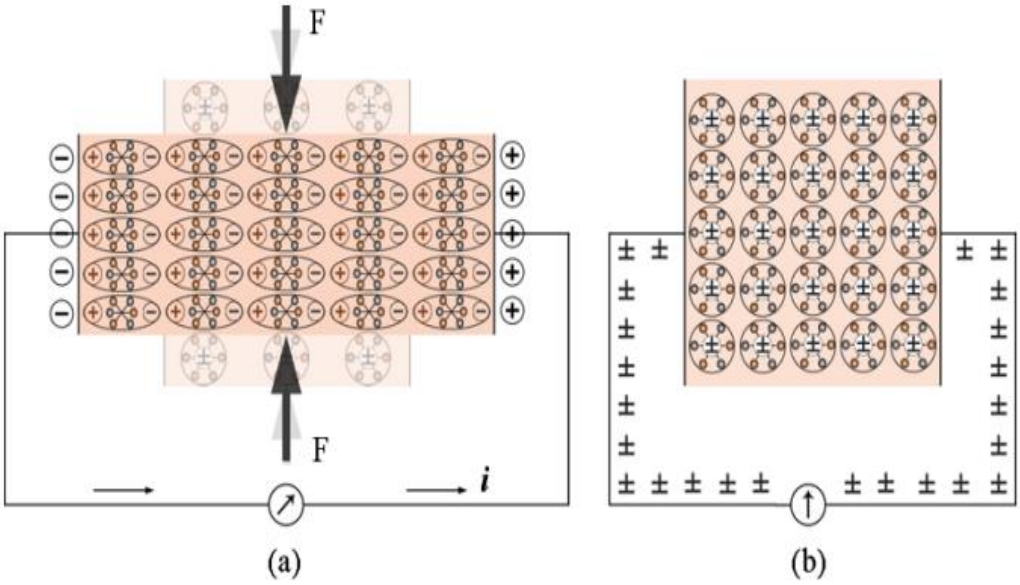

Figure 2.69: Phenomenon of piezoelectricity: (a) Neutralizing current flows when two terminals of a piezoelectric material subjected to an external force are shorted; (b) No current is flowing via the short-circuit when the material is unperturbed. Adapted from [112].

2.4. Electric permittivity, permittivity loss tangent and quality factor

In dielectric materials, the electric displacement vector (D) varies directly with the electric field (E) and the constant is known as the relative permittivity constant (ε_r). Mathematically, it can be expressed as [118]:

$$D = \varepsilon_r E_0 = \varepsilon_0 \varepsilon' E_0 \qquad [2.1]$$

Where D is the electrical displacement vector, E_0 is the electric field, ε' represents the real permittivity constant and ε_0 represents the permittivity constant in air. Using Eq. [2.1] and the capacitative illustrated in Figure 2.70 (a), the expressions for the real component of the permittivity constant (ε'), total charge Q and capacitance C for the material may be achieved using the following equation [118]:

$$\varepsilon' = \frac{D}{\varepsilon_0 E} = \frac{Q/A}{\varepsilon_0 V/d} \qquad [2.2]$$

Therefore,

$$Q = \varepsilon_0 \varepsilon' \frac{A}{d} V = CV \qquad [2.3]$$

where

$$C = \varepsilon_0 \varepsilon' \frac{A}{d} \quad [2.4]$$

$$C_0 = \varepsilon_0 \frac{A}{d} \quad [2.5]$$

And

$$\varepsilon' = \frac{C}{C_0} = \frac{\varepsilon}{\varepsilon_0} \quad [2.6]$$

A is the capacitive cell's area, d is the thickness of the capacitative cell, C_0 is the capacitance in air and C stands for the capacitance of the material, respectively, V is the voltage developed over the cell, and ε' is the electric permittivity of material.

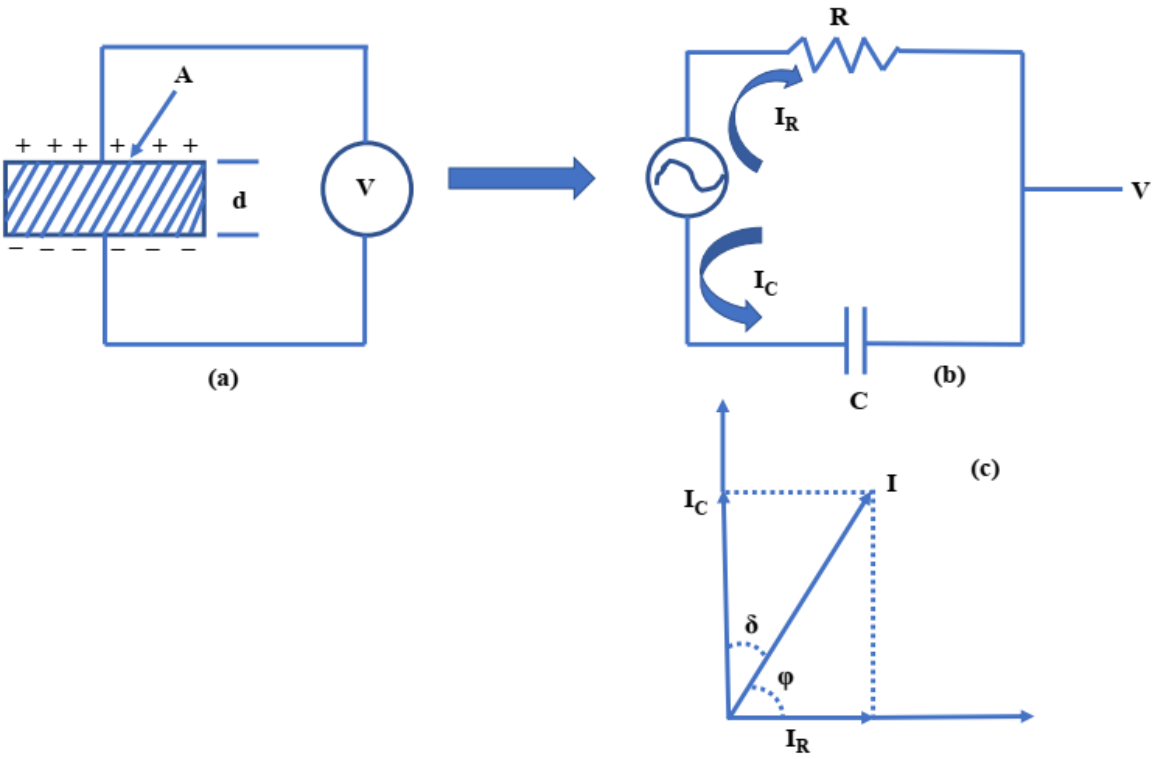

Figure 2.70: Equivalent electrical circuits: (a) cell of capacitor; (b) loss and charging current; (c) permittivity loss tangent for a conventional dielectric. Adapted from [118].

For the case of V being sinusoidal, Eq. [2.3] may be written as [118]:

$$Q = CVe^{i\omega t} \quad [2.7]$$

Therefore,

$$I = \frac{dQ}{dt} = i\omega CVe^{i\omega t} = i\omega C_0 \varepsilon' V \quad [2.8]$$

where I denotes the capacitive cell's discharge current in time t. However, in the case of a lossy dielectric, which is represented by the analogous circuit possessing a resistor and capacitor with parallel combination, the current I has vector components (I_C) and (I_R), as shown in Figure 2.70. A (wattles) current due to capacitance proportionate to the charge held in the capacitor is represented by the current I_C. It rely upon frequency and 90° degrees behind the voltage. The voltage (V) represent the energy or power loss of dielectric material, and the current (I_R), both indicate ac conduction currents that are in phase with one another. To deal with the loss current, this condition can be represented by a complex electric permittivity, as shown below [118]:

$$I = i\omega C_0(\varepsilon' - i\varepsilon'')V = i\omega C_0\varepsilon' V + i\omega C_0\varepsilon'' V = I_C + I_R \quad [2.9]$$

Thus, a dissipation factor, $tan\delta$, can be defined from the value of these currents as [118]:

$$tan\delta = \left|\frac{I_R}{I_C}\right| = \frac{\omega C_0\varepsilon'' V}{\omega C_0\varepsilon' V} = \frac{\varepsilon''}{\varepsilon'} \quad [2.10]$$

From Eq. [2.8], the permittivity loss tangent, ε'', is demonstrated to be the result of the material characteristics ε' and $tan\delta$. A quality factor Q, defined as [118]:

$$Q = \frac{1}{tan\delta} = \frac{average\ energy\ stored\ per\ cycle}{energy\ dissipated\ per\ cycle} \quad [2.11]$$

is often used as a design parameter for high-frequency dielectric use.

2.5. Electrical polarization

The four fundamental polarization types seen in dielectric materials are as follows:

2.5.1. Space charge polarization

The diffusion of ions across many interatomic distances makes it the slowest process. The fruitful ion jumps under the action of the applied field affect this process' relaxation time. In the kilohertz or even lower range of frequencies, space charge polarization frequently occurs. The process for the occurance of the space charge polarization is delineated in Figure 2.71.

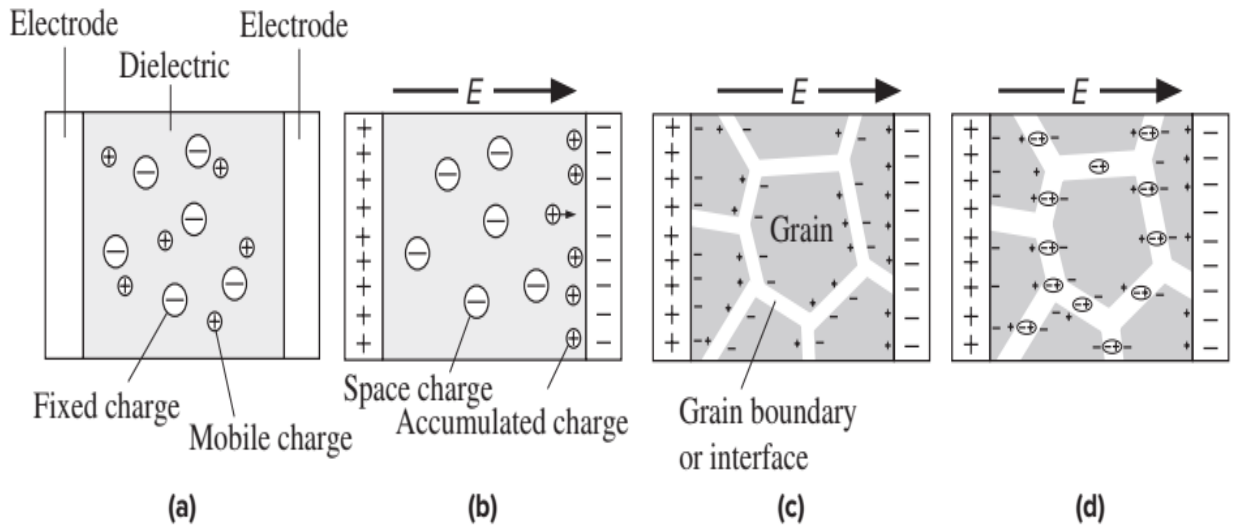

Figure 2.71: (a) A crystal that has an equal amount of fixed negative ions and movable positive ions. There is no net embarkation in the midst of all positive and negative charges when there isn't a field, (b) The mobile positive ions move toward and aggregate at the negative electrode when an electric field is persisted. Positive and negative charges in the dielectric are now generally separated. As a result, the dielectric displays interfacial polarization, (c) Interfacial polarization is typically caused by grain borders and interfaces in the midst of various materials. In this illustration, holes and electrons inside grains move aimlessly and get trapped at the grain borders, (d) Under the action of applied field, positive and negative ions inside a grain border can hop to nearby empty locations and create dipoles there. Adapted from [119].

2.5.2. Dipole/orientational polarization

It proceeds more slowly than ionic polarization. The rotation of molecular dipoles in the field causes the orientation polarization. In a liquid as opposed to a solid, polar molecules can more easily reorient themselves. Orientation polarization takes place when the applied voltage's frequency is in audio range. The process for the occurance of the dipolar polarization/orientation polarization is delineated in Figure 2.72.

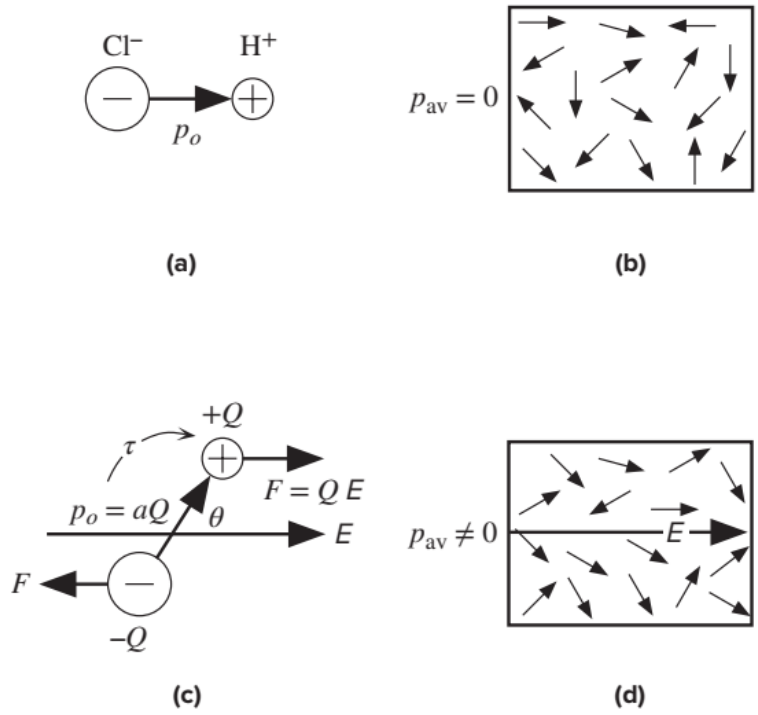

Figure 2.72: (a) The permanent dipole moment (P_0) of a molecule of hydrogen chloride, (b) Thermal unrest of the molecules produces net zero average molecule dipole moments when there is no external field, (c) When a dipole, e.g., hydrogen chloride, is positioned in a field, a torque attempts to rotate it so that P_0 is parallel to the field E, (d) The dipoles attempt to spin to line up with the applied field when thermal unrest is present. Now, each molecule along the field has an average net dipole moment. Adapted from [119].

2.5.3. Ionic (atomic) polarization

The comparative movement of cations and anions in an electric field is related to this mechanism. Since a much heavier ion is involved in this displacement than the electron cloud is, ionic polarization proceeds more slowly than electronic polarization. It will be possible to transfer ions over a small piece of the interatomic distance at a frequency that is similar to the lattice vibrational frequency (10^{13} Hz). An electric field with a frequency in the optical region (10^{15} Hz) has no effect on the ions at all, as an ion needs 100 times longer to complete one oscillation than the voltage's period. Therefore, ionic polarization is absent at optical frequencies. The process for the occurance of the ionic polarization is delineated in Figure 2.73.

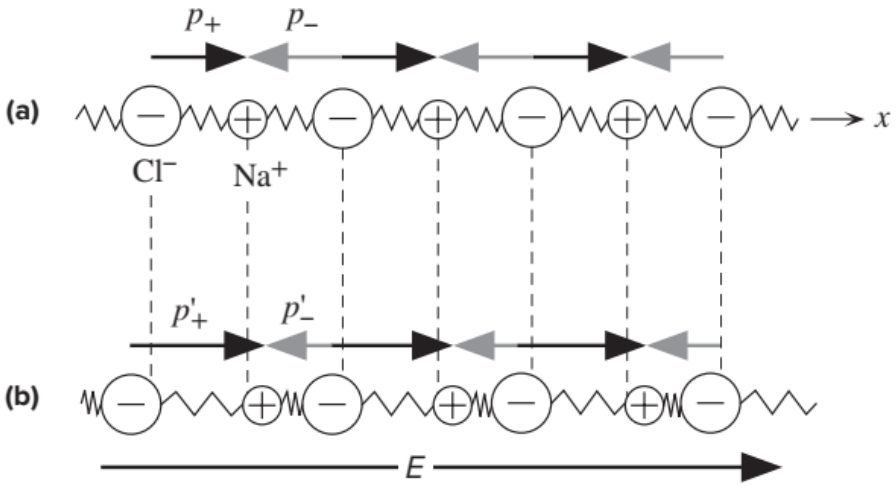

Figure 2.73: (a) Sodium chloride chain in sodium chloride crystal when the field is absent. There is no net or average dipole moment for an ion, (b) The ions are slightly displaced in the existence of an applied field, resulting in a net average dipole moment per ion. Adapted from [119].

2.5.4. Electronic polarization

This process takes place when the electric field moves the electron density away from the nucleus it surrounds in an atom. One can comprehend electronic polarization by imagining an atom as a tiny nucleus enclosed by the cloud of a spherical electron with a homogeneous charge density. Since electrons possess extremely low mass, they can follow high-frequency fields all the way to the optical range. It happens really quickly and is practically finished the moment the voltage is introduced. Electronic polarization takes place during each cycle of the applied voltage, even when the optical region's frequency is quite high (10^{15} Hz). The process for the occurance of the electronic polarization is delineated in Figure 2.74.

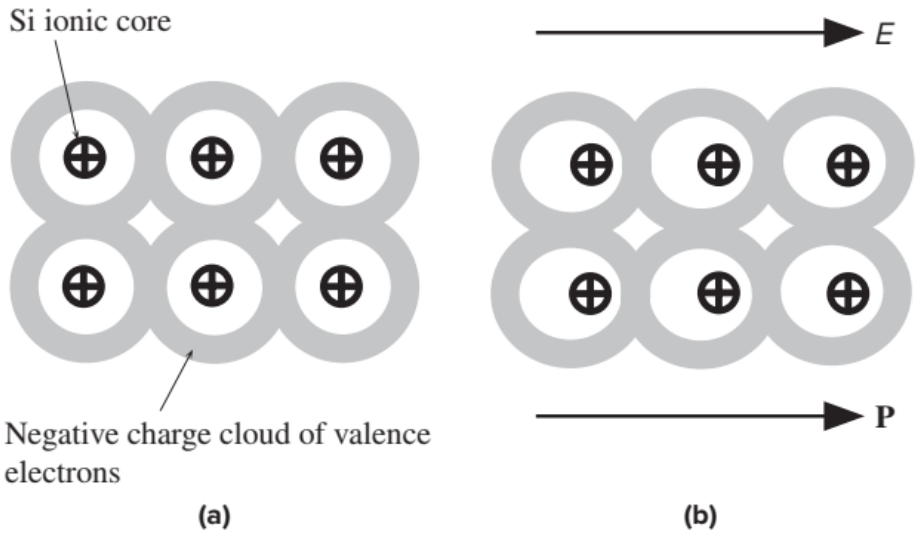

Figure 2.74: (a) Covalent bonds' valence electrons when the electric field is absent, (b) When a field is administered to a covalently bonded substance, the electrons in valence state within the covalent ties are very simply moved in relation to the cores of positive ions. The collective shift in the valence electrons' negative charge distribution causes the entire solid to become polarized. Adapted from [119].

2.5.5. Frequency-dependent dielectrical polarization

The time-dependent dielectrical polarization mechanism may be articulated as [120]:

$$P(t) = P_{max}\left[1 - exp\left(\frac{t}{t_r}\right)\right] \qquad [2.12]$$

where P is the highest degree of polarization that may be perceived when an electric field is introduced, and t_r is the length of time it takes for that process to completely relax. The length of time needed for a polarization mechanism to attain 63% of its optimum value is known as the time of relaxation (t_r).Various polarization processes cause a significant variation in the relaxation time. There are various polarization mechanisms as depicted in Figure 2.75. The most typical are listed below, starting with high frequencies [120].

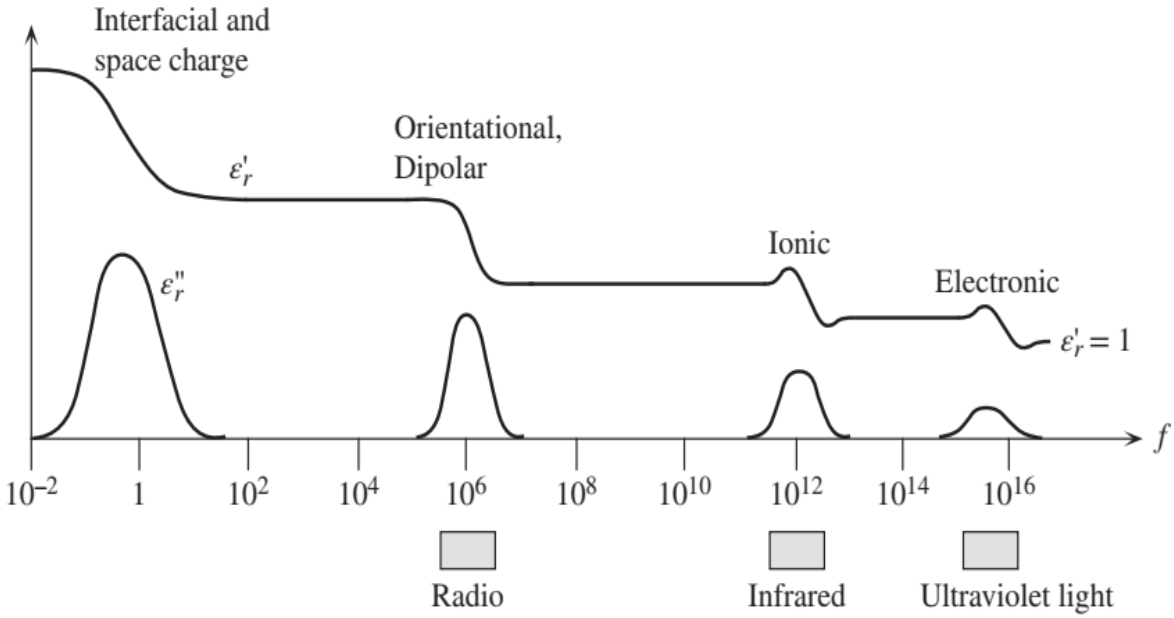

Figure 2.75: Frequency-dependent dielectric properties when interfacial, orientational, ionic, and electronic polarization mechanisms are present. Adapted from [119, 120].

2.6. Elastic characteristics

The elastic constants of a material define how it reacts to an applied stress or the stress needed to keep a specific deformation. The resilience of the materials to different strains is determined by the elastic characteristics of ferrites, making these features significant in industry. In fundamental research, the data are helpful for gaining understanding of the nature of the long-range and interatomic forces in solids. The elastic moduli are frequently utilized in engineering practice [121]. The Hook's law states that the stress-strain concept provides the basis for the correlation in the midst of the constants of stress (η_i), strain (ε_{ij}), and stiffness (C_{ij}) [122]. To explore the elastic properties of materials that meet the requirements of Born's mechanical stability, stiffness constants (C_{ij}) and compliance (S_{ij}) are utilized [123]. The x, y, and z axes are identical for the cubic symmetry of a material, resulting in stiffness constants like $C_{11} = C_{22} = C_{33};\ C_{12} = C_{21} = C_{13} = C_{31} = C_{23} = C_{32};\ C_{44} = C_{55} = C_{66}$. There are only three independent stiffness constants in the form of the cubic elastic stiffness tensor, namely C_{11}, C_{12} and C_{44}. The elastic constants (moduli) of a material are calculated using these three stiffness

constants. A material that has relatively greater stiffness constants C_{ij}'s is more resistant to compressions and shear deformations. The elasticity in length is represented by stiffness constant C_{11}, which changes with longitudinal strain, whereas the elasticity in shape is represented by stiffness constants C_{12} and C_{44}. Transverse strain causes the shape to change, while stretching forces parallel to all crystallographic axes with unequal amounts do not cause the volume or shape to change. In order to achieve symmetry in a cubic crystal, the stiffness parameters C_{11}, C_{22} and C_{33} must be of equal value. These are known as longitudinal elastic stiffness parameters, whilst the diagonal parameters with $i \geq 4$ are known as shear elastic parameters [124]. In determining stiffness constant (C_{11}), the two variables are crucial, e.g., (i) the strength of the bonds in the midst of nearby atoms and (ii) The relationship in the midst of the forces of attraction and repulsion in the midst of the atoms' positions, as well as the crystal architecture and direction [124]. If the forces of attraction and repulsion are of equal strength for all the sample's crystals, then only their excellent values can change the stiffness constant C_{11} [125].

The stiffness constants (C_{11} and C_{12}) is determined using the following formulae:

$$C_{11} = \frac{K_{av}}{a} \quad [2.13]$$

$$C_{12} = \frac{C_{11} \times \sigma}{(1-\sigma)} \quad [2.14]$$

where

$$K_{av} = \frac{K_A + K_B}{2} \quad [2.15]$$

The force constants for tetrahedrally coordinated (A)-site and octahedrally coordianted (B)-site are calculated using the vibrational band frequency through the following equation:

$$K_{A/B} = 4\pi^2 c^2 \nu_{A/B}^2 \mu \quad [2.16]$$

where K represents the force constant, c represents the speed of light, ν represents the vibrational band frequency of tetrahedrally coordinated (A)-or octahedrally coordinated (B)-sites and μ stands for the reduced mass for ferric and oxygen ions.

and

$$\sigma = 0.324(1 - 1.043 \times f) \quad [2.17]$$

The Poisson's ratio (σ) gives crucial details about the properties of the bonding nature. The Poisson ratio's value indicates the strength of covalent bond directionality in the sample. According to Frabtsevich et al. [126], the Poisson ratio is also used to study the material's brittleness and ductility. When the Poisson ratio is less than 0.26, the material is brittle; when it is greater than 0.26, the material is ductile.

The elastic moduli are computed using the following formulae:

$$\text{Young's modulus}, E = \frac{(C_{11}-C_{12})(C_{11}+2C_{12})}{(C_{11}+C_{12})} \quad [2.18]$$

$$\text{Rigidity modulus}, G = \frac{E}{2(1+\sigma)} \quad [2.19]$$

$$\text{Bulk modulus}, B = \frac{1}{3}(C_{11} + 2C_{12}) \quad [2.20]$$

The ratio B/G is regarded as a criterion by Pugh's rule [127] to examine the material's brittleness and ductility. When the ratio $B/G < 1.75$, the materials are brittle; otherwise, the materials reveal ductility nature. The relationship in the midst of the stiffness constant C_{11} and the longitudinal elastic velocity V_l through material density is achieved by

Longitudinal elastic velocity $$V_l = \sqrt{C_{11}/\rho_x} \quad [2.21]$$

Transversal elastic velocity $$V_t = \sqrt{G_0/\rho_x} \quad [2.22]$$

The mean elastic wave velocity is determined using:

$$V_m = \left[\frac{1}{3}\left(\frac{2}{V_t^3} + \frac{1}{V_l^3}\right)\right]^{-\frac{1}{3}} \quad [2.23]$$

2.7. Zero porosity correction to elastic moduli

To obtain the information about the maximum strength of the materials for practical applications, the zero porosity correction to elastic moduli should be carried out. There are three methods available for executing the zero-porosity corrections to elastic constants [128].

2.7.1. Hasselman and Fulrath theory

In this theory [128, 129], the assumption is that the pores were acknowledged as spherical ones and their arrangement in a material was compatible and possessed isotropic elastic traits. In this theory, the following observational relationships have been used to correct elastic constants to the pore-free state:

$$\frac{1}{E_0} = \frac{1}{E}\left[1 - \frac{3f(1-\sigma)(9+5\sigma)}{2(7-5\sigma)}\right] \quad [2.24]$$

$$\frac{1}{G_0} = \frac{1}{G}\left[1 - \frac{15f(1-\sigma)}{(7-5\sigma)}\right] \quad [2.25]$$

$$\sigma_0 = \left(\frac{E_0}{2G_0}\right) - 1 \quad [2.26]$$

$$B_0 = \left(\frac{E_0 G_0}{3(3G_0 - E_0)}\right) \quad [2.27]$$

2.7.2. Ledbetter and Datta theory

In this theory [128, 130], the assumption is that the spherical pores were distributed randomly and possessed zero obstruction to shear and dilation. The following empirical relations have been used to correct elastic constants in this model to the pore-free state:

$$G_0 = \left(\frac{1}{2A_1}\right)\left[-A_2 + (A_2^2 - 4A_1A_3)^{\frac{1}{2}}\right] \quad [2.28]$$

$$B_0 = \frac{(4G_0B)}{[4(1-f)G_0 - 3fB]} \quad [2.29]$$

$$E_0 = \frac{9B_0G_0}{3B_0 + G_0} \quad [2.30]$$

where,

$$A_1 = \left(\frac{8}{3}\right)(1-f) \quad [2.31]$$

$$A_2 = (3-2f)B - \left(\frac{8}{3} + 4f\right)G \quad [2.32]$$

$$A_3 = -3(1+f)BG \quad [2.33]$$

2.7.3. Elastic theory

In this theory [128, 131], it has been believed that the relationship in the midst of elastic moduli and porosity should be linear when the porosity is at a lower range ($f < 0.2$). The following

empirical formulae have been employed to correct elastic constants to the pore-free state in this model:

$$V_l = V_{l0}(1 - C_l f) \quad [2.34]$$

$$V_s = V_{s0}(1 - C_s f) \quad [2.35]$$

$$E = E_0(1 - C_E f) \quad [2.36]$$

$$G = G_0(1 - C_G f) \quad [2.37]$$

$$\sigma = \sigma_0(1 - C_\sigma f) \quad [2.38]$$

where C_l, C_s, C_E, C_G and C_σ are the material's constants. The material's non-porous elastic parameter is indicated by the subscript '0'. The following are the constants' precise expressions:

$$C_l = \frac{1}{2}\left\{\left|\frac{[C_E + 2C_\sigma\sigma_0^2(2-\sigma_0)]}{(1-\sigma_0)(1+\sigma_0)(1-2\sigma_0)-1}\right|\right\} \quad [2.39]$$

$$C_s = \frac{1}{3} \quad [2.40]$$

$$C_E = \left(\frac{1}{18}\right)(29 + 11\sigma_0) \quad [2.41]$$

$$C_G = \frac{5}{3} \quad [2.42]$$

$$C_\sigma = \left(\frac{5}{9}\right) + \left(\frac{11\sigma}{18}\right) - \left(\frac{1}{18}\sigma\right) \quad [2.43]$$

2.7.4. Debye Temperature

In problems requiring lattice vibrations in solid state and materials research, the Debye temperature is a crucial parameter. It is recognized that a solid's Debye temperature affects a number of physical characteristics, including mean square displacements, elastic constants, sound velocities, lattice instabilities, etc. [132]. The Debye temperature is the temperature of the crystal's highest normal mode of vibration. There two approaches are available to calculate the Debye temperature. Debye temperature (Θ_{DW}) is calculated using the Waldron formula [133]:

$$\Theta_{DW} = \frac{hcv_{av}}{k_B} \quad [2.44]$$

where, v_{av} is the average wave number, h expresses Planck's constant, k_B expresses Boltzmann constant and c is velocity of light. Therefore, Θ_{DW} is expressed as:

$$\Theta_{DW} = 1.438 \frac{v_T + v_O}{2} \quad [2.45]$$

(ii) Debye temperature 'Θ_{DA}' is calculated utilizing Anderson equation [134]:

$$\Theta_{DA} = \frac{hV_m}{k_B}\left(\frac{3d_{X-ray}qN_A}{4\pi M_w}\right)^{1/3} \times \left[\frac{1}{3}\left(\frac{2}{V_t^3} + \frac{1}{V_l^3}\right)\right]^{-1/3} \quad [2.46]$$

, where h represents Planck's constant, k_B stands for the Boltzmann constant, N_A represents the Avogadro's number, M_w is the molecular mass, q represents number of atoms per formula unit, d_{X-ray} represents theoretical density and V_m represents average velocity [135].

2.8. Magnetism and Magnetic materials

Generally speaking, the magnetism of materials is a result of the spin and orbital movement of electrons, and the magnetism traits are defined by the configuration of electron in the atoms and the crystal skeleton of the material. Distinct magnetic orders are produced by the arrangement of electrons and their exchange interplays, and these orders have distinct magnetic characteristics [136]. In turn, this allows us to categorize the material's magnetism into paramagnetism, diamagnetism, ferromagnetism, ferrimagnetism, antiferromagnetism, helimagnetism, and so forth, as illustrated in Figure 2.76 [136].

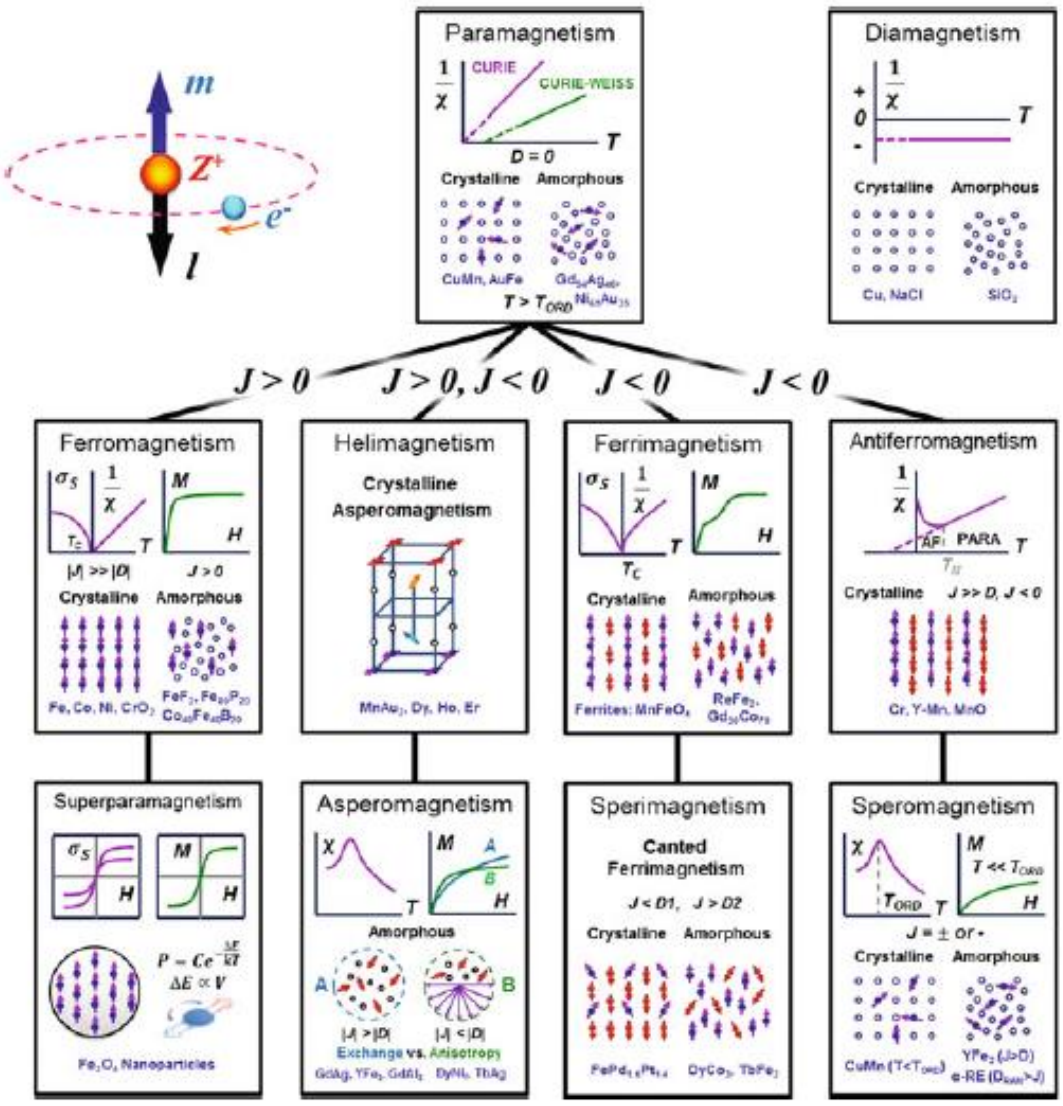

Figure 2.76: Classification of materials' magnetism based on its origin. Adapted from [137].

Ferromagnetism is a phenomenon wherein atoms' magnetic moments are lined up in the like orientation to create a type of ordering (spontaneous magnetization) without the use of an external magnetic field. Under a specific temperature (Curie's temperature), this type of magnetic order is created by the exchange interplay in the midst of electrons in various atoms. The magnetic moments are aligned parallel in the like orientation in the middle each of the small regions that make up the spontaneous magnetization in ferromagnetic materials, which are collectively known as magnetic domains. Due to the canceling effect in the midst of the various magnetic domains, the orientations of the material's spontaneous magnetization are irregular and distinct from one another, and the entire sample exhibits net zero magnetization

when there is no magnetic field. Each magnetic domain's magnetization tends to line up along the external magnetic field direction it is used, and the net magnetization can reach high values. The states of magnetization and magnetic domains are preserved when the magnetic field is eliminated, causing the magnetization and magnetic field (M-H) curve to exhibit hysteresis behavior, or the magnetic hysteresis loop, as seen in Figure 2.77.

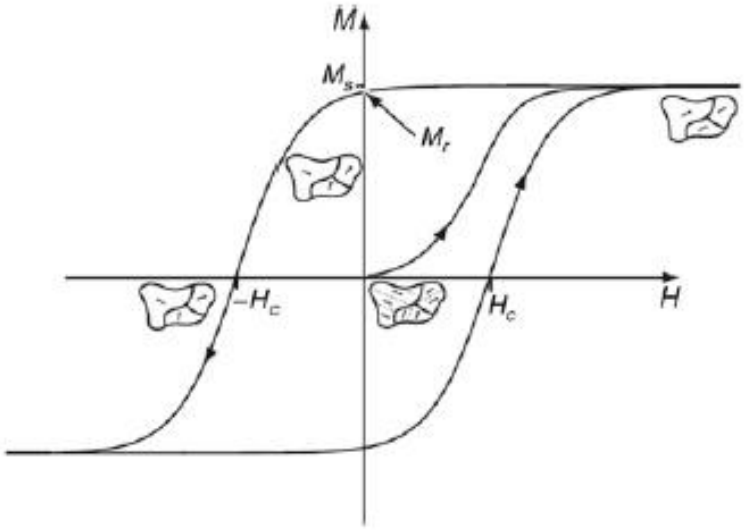

Figure 2.77: The magnetic hysteresis loop and domains in ferromagnetic materials. Adapted from [137].

When nearby spins align in opposite directions, a phenomenon known as antiferromagnetism occurs. This is a phenomenon where the atom's magnetic moments align in a regular fashion. Because the adjacent atomic magnetic moments cancel each other out, antiferromagnetic materials lack any macro magnetic characteristics and have magnetization curves with linear behaviour akin to paramagnetism. Antiferromagnetic materials typically have equivalent internal magnetic fields that are substantially bigger than the external magnetic field because it is difficult for a magnetic field that is utilized externally to affect the acclimatization of the antiferromagnetic magnetic moment. As a consequence, magnetic pinned layers made of antiferromagnetic materials are frequently employed in the exchange bias system. The phenomenon known as helimagnetism occurs when the atom's magnetic moments are organized in a helical shape with the nearby spins moving at an angle to one another. As a

consequence, in some of the provisions, the magnetic moments cancel with each other and the materials don't show any macro magnetic traits, even though in other provisions, the magnetic moments can't be completely cancelled out and the materials clearly show macro magnetic traits. Materials with 4f electron rare earth elements always exhibit helimagnetism [137].

2.8.1. Crystal Structure of Spinel Ferrites

In general, the family of spinel ferrites can normally be represented through the generic formula AB_2O_4, where A is commonly a bivalent cation, that resides at the middle points of tetrahedrally coordinated edges and B is mostly a trivalent cation that resides at the middle points of octahedral sites and the oxygen anion lies at the polyhedral vertexes (in normal spinel material). Typically speaking, the tetrahedrally coordinated (A)-site interstices typically have smaller sizes than octahedrally coordinated (B)-site interstices. The tetrahedrally coordinated (A)-sites are therefore preferred by cations with smaller radii, while the octahedrally coordinated (B)-sites are preferred by cations with larger radii. The oxygen anion typically assumes a 2^- oxidation state in the formula AB_2O_4. To assert the valence stability, the equivalent B cations may be in the 3^+ or 2^+ oxidation state, while A cations may be in the 2^+ or 4^+ oxidation state. Additionally, spinel materials can be categorized as: normal, inverse, and complex spinel materials depending on how their cations are distributed in the tetrahedrally and octahedrally coordinated positions. According to the formula $(A^{2+}{}_{th})(B^{3+}{}_{oh})O_4$, the A^{2+} cations reside the tetrahedrally coordinated positions while the B^{3+} cations reside the octahedrally coordinated positions in typical spinel materials. For instance, the Mg^{2+} cations reside at the middle points of the tetrahedrally coordinated (A)-sites whereas Al^{3+} resides at the octahedral sites normal spinel oxide $MgAl_2O_4$ (Figure 2.78 (a, d)). In inverse spinel materials, the B^{3+} cations are allotted in both tetrahedrally and octahedrally coordinated positions, with the expression $(A^{2+}{}_{oh})(B^{3+}{}_{th})(B^{3+}{}_{oh})O_4$. The A^{2+} cations occupy the octahedral sites. For instance, in the inverse spinel $NiFe_2O_4$ (Figure 2.78 (b)), Ni^{2+} ions and the other fifty percent of the Fe^{3+} cations take

over the tetrahedrally coordinated sites, while the remaining fifty percent of the Fe^{3+} cations reside at midpoints of the tetrahedrally coordinated sites. This material is denoted by the formula $Fe(NiFe)O_4$. With the formula $(A^{2+}_{th})(A^{2+}_{oh})(B^{3+}_{th})(B^{3+}_{oh})O_4$, complex spinel materials, which are characterized as being in-between the normal and inverse spinels. These spinel materials allow A^{2+} and B^{3+} cations to partially occupy both tetrahedrally and octahedrally coordinated sites. The complex spinel $CuAl_2O_4$ (Figure 2.78 (c)) is one such, in which the tetrahedrally and octahedrally coordinated sites are both partially occupied by the Cu^{2+} and Al^{3+} cations [138, 139].

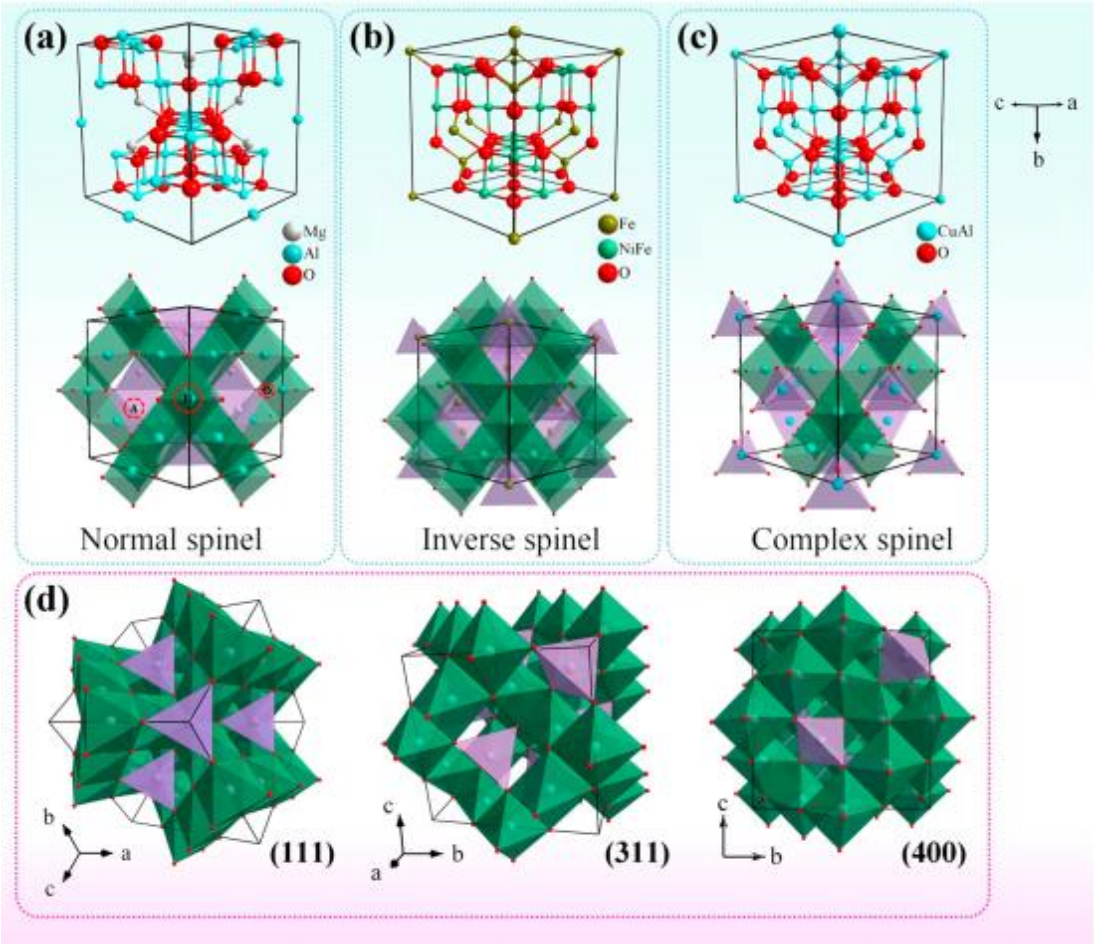

Figure 2.78: Typical architectures of spinel materials: (a) $MgAl_2O_4$ normal spinel material, (b) $NiFe_2O_4$ inverse spinel material, and (c) $CuAl_2O_4$ complex spinel material in various viewpoints and fashions. The octahedrally and tetrahedrally coordinated metal occupation locations are shown by the green and purple polyhedra, respectively. In panel a, typical A, B, and O defect sites in AB_2O_4 spinel are shown. (d) Directions for normal spinel ($MgAl_2O_4$) with (111), (311), and (400). Adapted from [138, 139].

2.8.2. Nickel copper zinc ferrite

Figure 2.79 illustrates the crystal architecture of the NiZnCu ferrites. Within the tightly packed network of O^{2-} ions, Ni^{2+}, Zn^{2+}, and Fe^{3+} reside the tetrahedrally coordinated interstices, whilst Cu^{2+} and Fe^{3+} reside the octahedral empty locations. Tetrahedrally and octahedrally coordinated sites, respectively, are represented by the areas colored in blue and pink. Overall, the unit cell contains 24 cations (8 of which are accommodated at tetrahedrally coordinated sites and 16 at octahedral sites) and 32 O^{2-} anions [140].

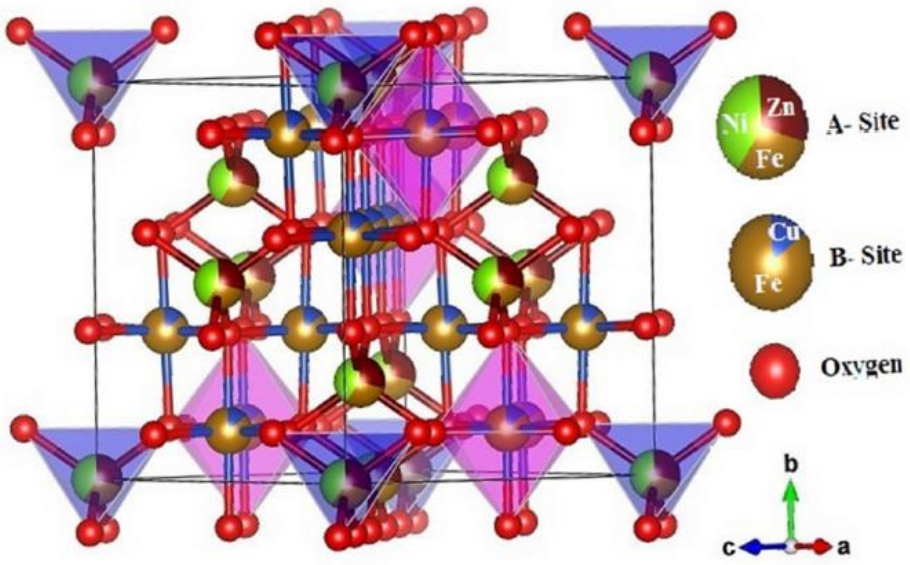

Figure 2.79: Crystal architecture of nickel-copper-zinc ferrite. Adapted from [140].

2.9. Multiferroic Materials

Materials known as multiferroic materials (ferroelectric, ferromagnetic, or ferroelastic) show at least two ferroic orders. In general, multiferroics are often classified into two groups: (i) single-phasic multiferroic material and (ii) composite multiferroic materials. Furthermore, in 2009, D. Khomskii first proposed a useful classification approach for multiferroics into so-called type-I and type-II multiferroics [141].

2.9.1. Single-phasic magnetoelectric multiferroic materials

Single-phasic multiferroic materials are materials which display both ferromagnetic and ferroelectric order. Hence, the material's multiferroicity is an intrinsic property. According to the physical process underlying ferroelectricity, D. Khomskii divided single-phase multiferroic materials into two major classes and other subgroups [141, 142].

2.9.1.1. Type-I single-phasic magnetoelectric multiferroic materials

In Type-I single-phasic magnetoelectric (ME) multiferroics, ferroelectricity and magnetism take place at various temperatures, which are recognized as Neel and Curie temperatures, and arise from different mechanisms and are significantly independent of one another, though there is some interplay in the midst of them; typically, they exhibit high polarization values and ferroelectricity develops due to structural distortion at much higher temperatures, and the magnetic ordering, which is typically antiferromagnetic, materializes due to ferroelectricity at much lower temperatures. It is clear from the disparity in the midst of the transition temperatures that both sequences involve a variety of energies and processes that lead to weak ME coupling. In turn, Type-I multiferroics are divided into a number of subgroups based on the ferroelectric mechanism that underlies them:

2.9.1.2. Ferroelectricity induced by lone-pair electrons

In $BiFeO_3$ and $PbVO_3$ multiferroics, the presence of one of the cations (i. e. Bi^{3+}, Pb^{2+}, . . .) generate ferroelectricity since these multiferroic materials possess two 6*s* outer electrons and also recognized as lone pairs or dangling bonds and do not take part in any chemical bonds, which can be orientated in one direction to enhance its polarizability as depicted in Figure 2.80 (a) [141].

2.9.1.3. Ferroelectricity induced by charge ordering

In compounds with comparable cations in the alike structural site but different valences, charge ordering can take place. The transition metal complexes show imbalanced sites and bonds (long and short bonds) once they become ordered. As a consequence, the structure can exhibit ionic polarizability [143]. Such example is $TbMn_2O_5$, Ca_3CoMnO_6 or $Pr_{1/2}Ca_{1/2}MnO_3$, respectively. A diagrammatic depiction of imbalanced sites is depicted in Figure 2.80 (c).

2.9.1.4. Geometric ferroelectricity

Manganites (ABO_3 with A = Y, Lu, etc.) having hexagonal symmetry are the most typical example of geometric ferroelectricity. Ferroelectricity eventuates in manganites having hexagonal symmetry since the MnO_5 polyhedron's tilting creates a tight packing. Thus, an electric dipole is created as the oxygen ions move toward the relatively small tetrahedrally coordinated (A)-site ions [Figure 2.80 (b)] [144].

2.9.1.5. Spin-driven mechanisms

In spin-driven ferroelectrics, its ferroelectric polarization is induced along the *c* axis by the inversion symmetry breaking due to a cycloidal spiral spin order through the antisymmetric Dzyaloshinskii-Moriya (DM) interplay. Three mechanisms, including exchange restriction, spin dependent p-d hybridization, and spin current (commonly referred to as the inverse DM interplay) are primarily responsible for the complex physics of spin-driven ferroelectricity [145]. Three mechanisms are diagrammatically depicted in Figure 2.80 (d).

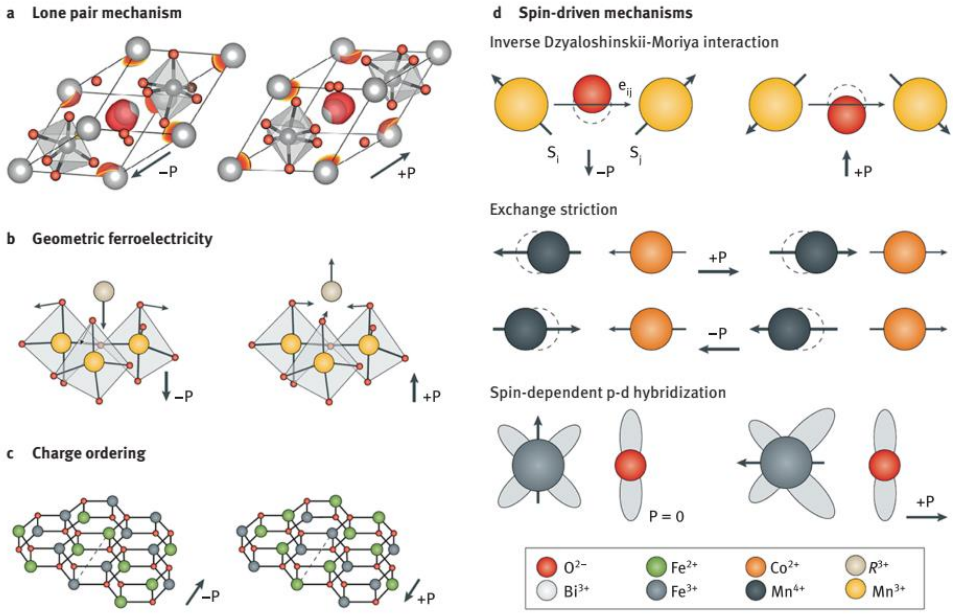

Figure 2.80: Phenomenon of multiferroicity. (a) Lone-pair phenomenon; (b) geometric ferroelectricity; (c) charge ordering phenomenon; (d) spin-driven phenomenon. Adapted from [145-147].

2.10. Single-phase Type-II magnetoelectric multiferroic materials

In materials known as type-II multiferroics, the magnetic order breaks the inversion symmetry, causing ferroelectricity, and there is a strong interaction in the midst of the two. They exhibit low levels of electric polarization, and ferroelectricity (always antiferromagnetic ordering) always manifests at lower temperatures than magnetic order. In this case the ordering temperatures for the two phenomena are identical. These are:

2.10.1. Spiral Type-II magnetoelectric multiferroic materials

Due to a specific form of magnetic spiral in this type, ferroelectricity manifests in the structure. This group includes the majority of Type-II multiferroics, which include $TbMnO_3$, $Ni_3V_2O_6$, $MnWO_4$, and $DyMnO_3$ [6, 148]. According to Figure 2.81 (a) below T_{N1} (= 41 K), $TbMnO_3$ exhibits a sinusoidal spin density wave with zero overall magnetism, indicating that it is antiferromagnetic. However, the DM interplay below T_{N2} (= 28 K) seen in Figure 2.81 (b) suggests that magnetically progressive Mn ions facilitate the magnetic response subject to noncollinear spin ordering [149]. This interplay results in the displacement of oxygen ligands

perpendicular to the spin wave, making it feasible for the structure to have a non-zero polarizability (P). When spiral spins are rotating perpendicular to the wave vector, as shown in Figure 2.81 (c), they can generate polarization parallel to the spin proliferation direction as opposed to cycloidal spins. Typically, delafossite-type oxides AMO_2, where A is a magnetic element like Cr or Fe and M is a magnetic component like Cu or Ag, have such magnetic architecture. One of the multiferroic materials, $CuFeO_2$, for instance, has a proper-screw-kind spin architecture possessing electric polarization together with its bond orientations [150].

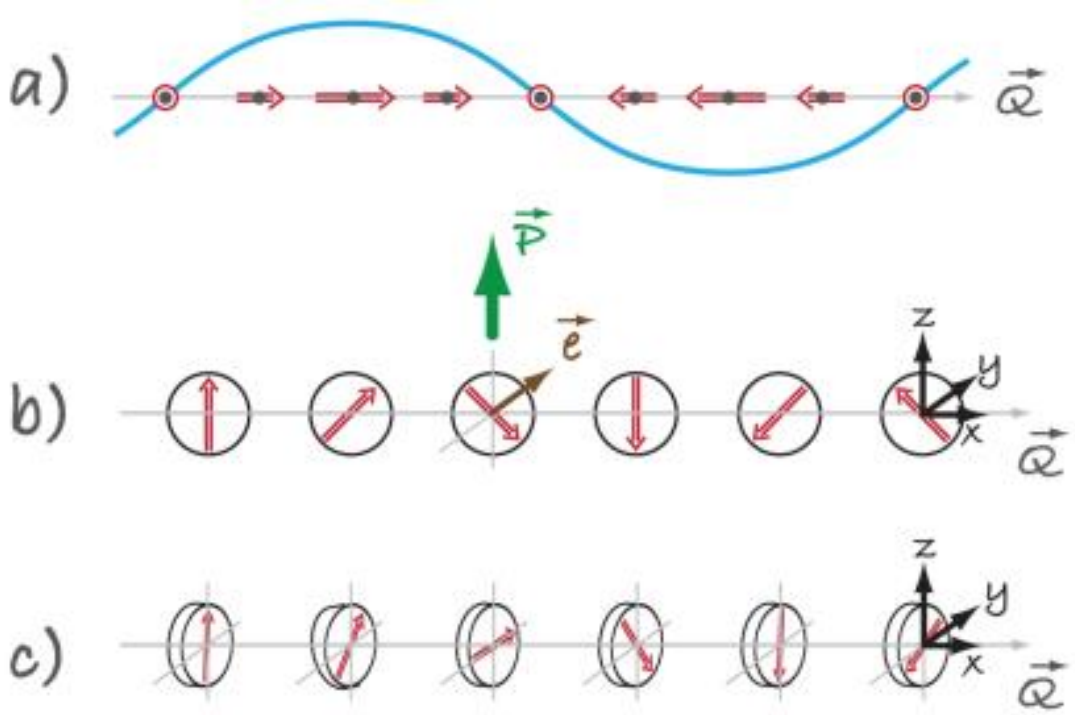

Figure 2.81: (a) A centrosymmetric sinusoidal spin-density wave having different degree, (b) Magnetism of the cycloidal spiral category with a positive polarization, and (c) Spin structures of the proper screw type, where spins rotate normal to the wave vector (Q). Adapted from [141].

2.10.2. Type-II Multiferroic Materials having Collinear Magnetic Configurations

There are also specific materials which display a collinear spin architecture having a positive electric polarization because of the violation of inversion symmetry, in addition to the spin-

orbit interplays in spiral type-II multiferroics. All magnetic moments in this category of Type-II multiferroics are acclimatized in the same direction, as illustrated in Figure 2.82. In Figure 2.82 (a), spins rotated in a plane do not result in polarizability, but Figure 2.82 (b) shows a comparable situation of cycloidal spin architecture that results in a net polarization (P) perpendicular to wave vector. On the other hand, as delineated in Figure 2.82 (c), the arrangement of dipole moments may vary relying on the strength of the Cu-tip's electric field if an electric field can be applied to the domain walls. For instance, the compound Ca_3CoMnO_6 exhibits up-up-down-down spin configuration with 1D chains of changing Co^{2+} and Mn^{4+} ions. Through the exchange of various bonds, this antiferromagnetic ordering disrupts inversion symmetry and drives ferroelectric polarization throughout the chains [151]. The orthorhombic perovskites $RMnO_3$, which typically contain small rare earth elements as Ho, Er, and Tm, also exhibit a similar process. Despite identical magnetic ions (Mn^{3+}) being present in the structure, the exchange restriction causes oxygen ions to move perpendicular to Mn-O-Mn bonds. This causes electric polarization which is often stronger than that of spin-orbit interplays [152].

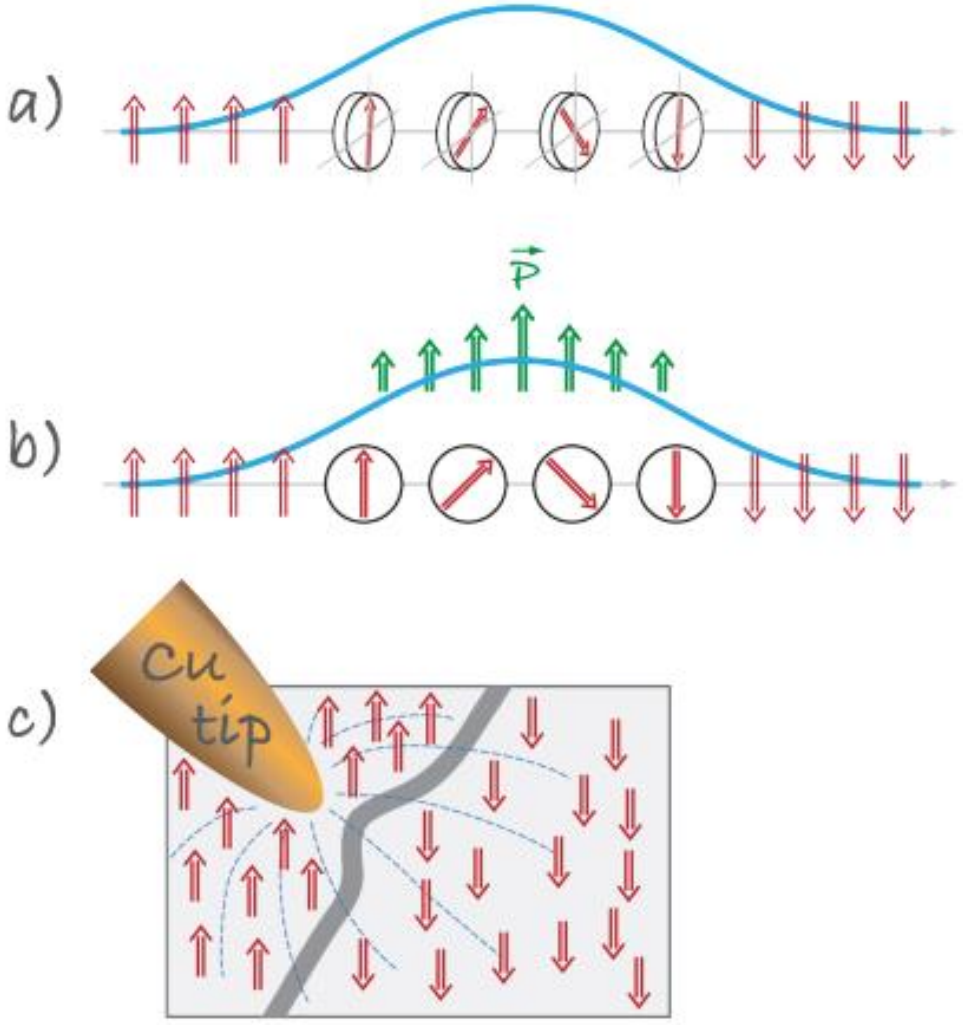

Figure 2.82: (a) The direction of rotation of spins is perpendicular to the wave vector, (b) Cycloidal spiral spins creating a comparable spontaneous polarization (P), and (c) Diagram showing the effect of the electric field on the arrangement of the dipole moment along Bloch walls. Adapted from [141].

To date, lot of single-phasic multiferroics have been investigated. Magnetoelectric coefficients in various single-phasic magnetoelectric multiferroics, characteristics of the ferroelectric-ferromagnetic, ferroelectric-antiferromagnetic-class single-phasic magnetoelectrics are presented in Table 2.3-2.5, respectively.

Table 2.3. Magnetoelectric coefficients in various single-phasic magnetoelectric multiferroics. Adapted from [153].

Material	α_{ij} (s/m)	Linear magnetoelectric effect?	Circumstance for investigation	Investigation temperature
Cr_2O_3 (single crystal in bulk)	4.13×10^{-12}	Yes	Magnetization is parallel to electric field	265º K
Cr_2O_3 (thin-film)	$(4.6 \pm 0.3)\times10^{-12}$	Yes	Magnetization is parallel to electric field	250º K
$TbPO_4$ (single crystal in bulk)	3×10^{-10}	Yes	Polarization is parallel to magnetic field intensity	4.2º K
$Ba_{0.52}Sr_{2.48}Co_2Fe_{24}O_{41}$ (bulk single crystal)	3.2×10^{-9} at 10.5 mT	No	Polarization is parallel to magnetic field intensity	305º K
$BiFeO_3$ (mono-domain bulk single crystal)	1.1×10^{-10} at 24 T	No	Polarization is perpendicular to magnetic field intensity	4.2º K
$TbMnO_3$ (single crystal in bulk)	1.1×10^{-9} at 5 T	No	Polarization is perpendicular to magnetic field intensity	9º K

Table 2.3. (continued)

Material	α_{ij}(s/m)	Linear magnetoelectric effect?	Circumstance for investigation	Investigation temperature
$TbMn_2O_5$ (single crystal in bulk)	2×10^{-9} at 1.1 T	No	Polarization is perpendicular to magnetic field intensity	3º K
$Ni_3B_7O_{13}I$ (single crystal in bulk))	1.6×10^{-9}	Yes	Polarization is perpendicular to magnetic field intensity	46º K

Table 2.4. Characteristics of the ferroelectric-ferromagnetic-class single-phasic magnetoelectrics. Adapted from [153].

Material	Type of multiferroics	Polarization	Magnetization	T_{FE}	T_C
$Ni_3B_7O_{13}I$	Type I	0.076 μC/cm^2 at 46º K	3.26 μ_B per Ni atom at 6º K	60º K	64º K
$BiMnO_3$	Type I	0.15 μC/cm^2 at 87º K	3.6 μ_B per manganese atom at 5º K	450-490º K	105º K
$LaBiMnO_3$	Type I	N/A	2.5 × 105 A/m at 10º K	N/A	90º K
Strained $EuTiO_3$	Type I	10 μC/cm^2 at 5º K	3 μ_B per europium atom at 1.8º K	250º K	4º K

Table 2.5. Characteristics of the ferroelectric-antiferromagnetic-class single-phasic magnetoelectrics. Adapted from [153].

Material	Type of multiferroics	Origin of ferroelectricity	Spontaneous polarization	T_{FE}	T_{AFM}
$Pb(Fe_{1/2}Nb_{1/2})O_3$	Type I	6 s lone-pair	11.5 $\mu C/cm^2$ at room temperature in ceramics	380º K	145-160º K (T_N)
$BiFeO_3$	Type I	6 s lone-pair	100 $\mu C/cm^2$ at room temperature in bulk single crystals, 55 $\mu C/cm^2$ at room temperature in epitaxial thin films	1098º K	643º K (T_N)
$YMnO_3$	Type I	Geometrically driven	5.5 $\mu C/cm^2$ at room temperature in bulk single crystals	570-990º K	70-130º K (T_N)
Hexagonal $LuFeO_3$	Type I	Geometrically driven	5 $\mu C/cm^2$ at room temperature in bulk single crystals	1050º K	T_N ~ 400º K in film, T_{WFM} ~ 100º K
$BaNiF_4$	Type I	Geometrically driven	6.7 $\mu C/cm^2$ at room temperature in bulk single crystals	1320º K (melts first)	50º K (T_N)
Cr_2BeO_4	Type II	Spin-driven (noncollinear spin ordering)	3×10^{-4} $\mu C/cm^2$ at 7º K at 0.6 MV/m in ceramics	28º K	28º K (T_N)
$TbMnO_3$	Type II	Spin-driven (cycloidal spin spiral)	0.08 $\mu C/cm^2$ at 10º K in bulk single crystals	27º K	T_N ~ 41º K, T_{CYCL} ~ 27º K
$CaMn_7O_{12}$	Type II	Spin-driven (noncollinear spin ordering)	0.287 $\mu C/cm^2$ at 15 K in bulk single crystals, 0.024 $\mu C/cm^2$ at 10º K in ceramics	90º K	90º K (T_N)

Table 2.5. (continued)

Material	Type of multiferroics	Origin of ferroelectricity	Spontaneous polarization	T_{FE}	T_{AFM}
$TbMn_2O_5$	Type II	Spin-driven (collinear spin ordering)	0.04 μC/cm^2 at 3º K in bulk single crystals	40º K	40º K (T_N)
$TbMnO_3$ under intense pressure (> 5 GPa)	Type II	Spin-driven (collinear spin ordering)	1 μC/cm^2 at 5º K at 5.2 GPa in single crystals (bulk)	20º K	20º K ($T_{E\text{-}AFM}$)
$CuCrO_2$	Type II	Spin-driven (p-d orbital hybridization)	0.03 μC/cm^2 at 5º K at 30 MV/m in single crystals (bulk)	24º K	24º K

Table 2.6. Characteristics of the ferroelectric-antiferromagnetic-class single-phasic magnetoelectrics. Adapted from [153].

Material	Type of multiferroics	Origin of ferroelectricity	Spontaneous polarization	Spontaneous magnetization	T_{FE}	T_C
Fe_3O_4	Type I	Charge order	5.0 μC/cm^2 at 4.2 K	4.0 μ_B per Fe atom @ 125 K	119-125º K	858º K
$(LuFeO_3)_9$/ $(LuFe_2O_4)_1$	Type I	Charge order	6.0 μC/cm^2 at room temperature	2.0 μ_B per Fe atom @ 50 K	>700º K	281º K

2.11. Composite magnetoelectric multiferroics

2.11.1. Connectivity of composite magnetoelectric multiferroics

The connectivity of composite ME multiferroics is a significant aspect because it influences the interfacial area in the midst of the constituent components and, consequently, the dominancy and efficiency of the ME effect [154]. Newnham et al. [155] was first developed the concept of connectivity and is now a widely accepted codification used to describe the way in which the constituent components are self-connected (continuous). Connectivity is explicated with reference to the number of dimensions in which the components are associated with one another. The geometry of composites can be designed based upon the connection schemes. Gnerally, the scheme can be achieved through the ratio $\frac{(n+3)!}{3!n!}$, where *n* is the quantity of phases. In diphasic composites, ten connectivity schemes are possible and those are delineated in Figure 2.83 using a cube as the basic building block. As a particulate type of composite, 0-3 connectivity denotes the presence of two phases, one of which is disseminated in the matrix as 0-3 structures. Geometry represented by 2-2 connection is stacked. Although not out of plane, the stages are related. In multilayer capacitors and laminated ME composites, this connectivity is most frequently used. A different kind of connectivity system is of the 1-3 types, which consists of 1D skeletons of one component embedded in a 3D matrix of the other component [155].

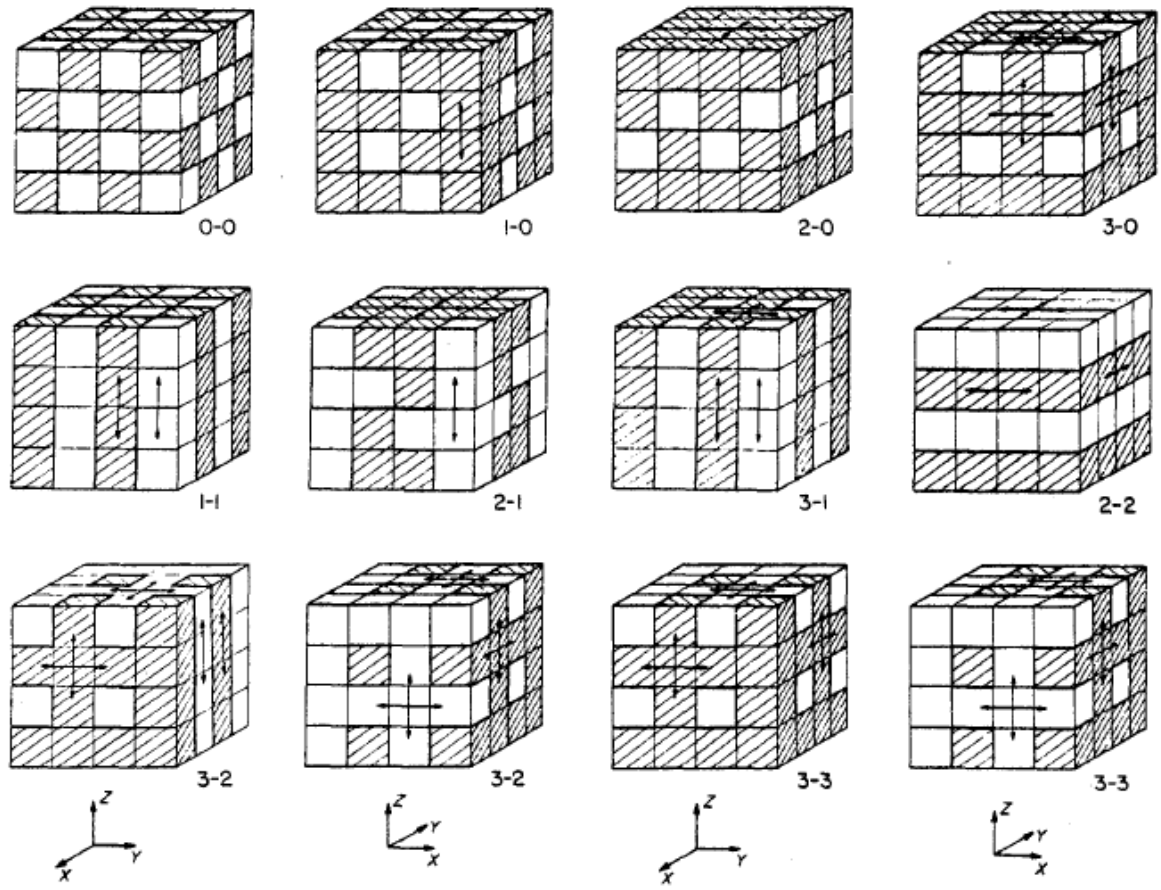

Figure 2.83: All the possible connectivity schemes of a biphasic composite. Adapted from [156].

Till to date, the most widely studied connectivity schemes of magnetoelectric composites in Figure 2.84

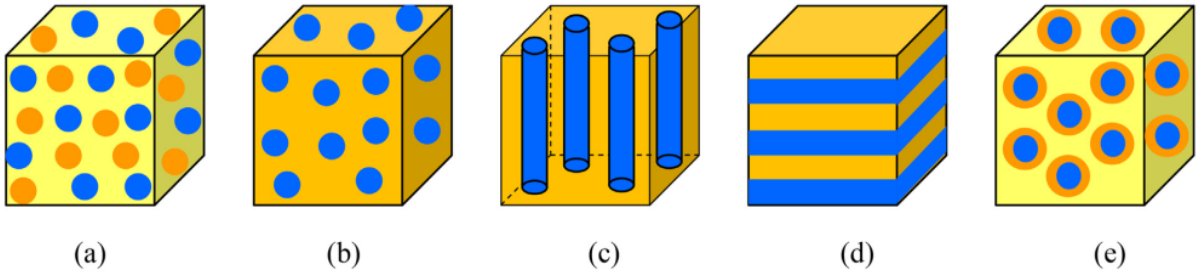

Figure 2.84: Composite ME materials of various types of connectivity schemes: (a) 0-0; (b) 0-3; (c) 1-3; (d) 2-2; (e) core-shell nanocomposite. Adapted from [157].

2.12. Composite Effects

The appropriate attributes of each phase can be used, depending on the application, to construct a composite with a sum property or a product property. These ideas are fundamentally significant.

2.12.1. Sum property or effect

Let's explain about a composite function that transforms an input parameter X into an output parameter Y in a diphasic system. The outcome Y^* of a composite material of phase 1 and phase 2 might be a number that is halfway in the midst of Y_1 and Y_2, ascertaining that Y_1 and Y_2 are the results from phase 1 and phase 2, respectively, in response to the input X. In the scenario where $Y_1 > Y_2$, Figure 2.85 (a) depicts the Y^* change with volume snippet of phase 2. The alteration may have a concave or convex type, but in a composite material, the average value does not go above Y_1 or below Y_2. Concisely, A composite's sum property or effect (Figure 2.85 (a)) is the total weighted attributions from each of its component phases, which are proportional to their weight fractions' volume in the composite (physical parameters like density and resistivity are sum effects).

2.12.2. Combination property or effect

A composite's combination property or effect (Figure 2.85 (b)) manifests itself in the following scenario. In some circumstances, the averaged output value of a composite, Y^*, does surmount Y_1 and Y_2. This improved output alludes to an impact Y/Z that is dependent on the two inputs Y and Z. The association value Y/Z will display an optimum value at an intermediate ratio of the phases if Y and Z, as shown in Figure 2.85 (b), exhibit concave- and convex-type sum effects, respectively.

2.12.3. Product property or effect

In the event where phase 1 displays an outcome Y with an input X and phase 2 displays an outcome Z with an input Y, one can anticipate that composite material will display an outcome Z with an input X. A "product effect" is a brand-new function that is developed for the composite structure (Figure 2.85 (c)).

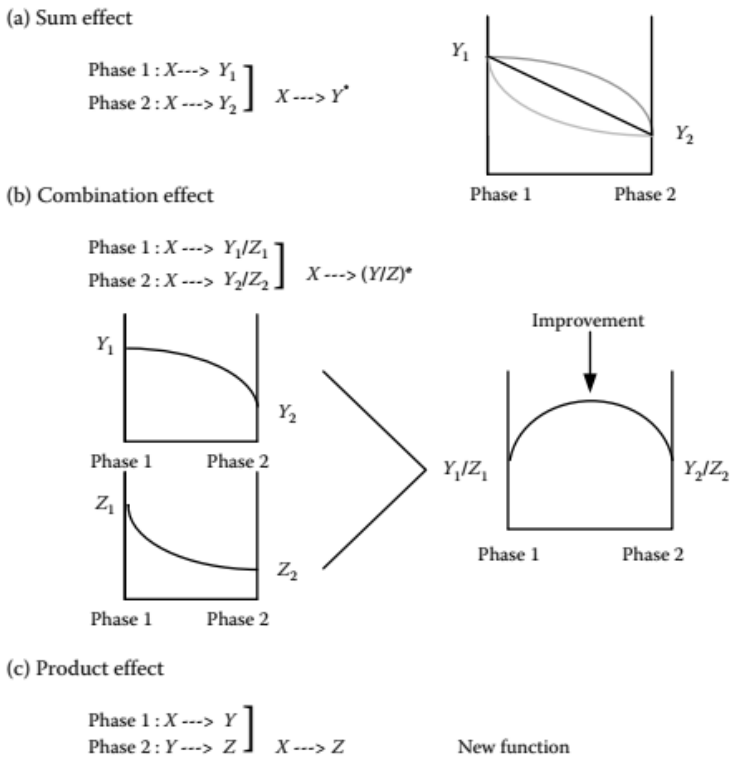

Figure 2.85: Composite properties: (a) sum property, (b) combination property, and (c) product property. Adapted from [158-160].

2.13. Magnetoelectric effect

The magnetoelectric effect is a consequence of the interaction in the midst of the magnetostriction event within the ferromagnetics and the piezoelectric reaction within the ferroelectrics. The magnetic and dielectric materials that make up magnetoelectric composites can interact in such a way that the magnetic material can be magnetically stimulated to modify the electrical response of the dielectric materials, and vice versa. In particular, employing a magnetic field (H) can modify electrical polarization (P), where $\Delta P = \alpha_H \Delta H$, or an electric field (E), $\varepsilon_0 \chi_e \Delta E = \alpha_H \Delta H$, where χ_e is the electrical susceptibility and ε_0 is the permittivity in air; in contrast, upon the application of an electric field, one can alter magnetization (M), $\mu_0 \Delta M = \alpha_E \Delta E$, where μ_0 stands for magnetic permeability in air; α_H and α_E represent the direct and converse ME effects, consequently. As a result, in the absence of an electric current, ME composites allow for the conversion of magnetic energy to electric energy [161]. By

making comparisons to other interaction phenomena in functional materials, such as those shown in Figure 2.86, it is possible to comprehend the magnetoelectric effect. On the basis of the piezoelectric effect-the interaction among the mechanical strain ($\boldsymbol{\varepsilon}$) and electric field ($\vec{E}$) or among electrical polarization ($\vec{P}$) and the mechanical stress ($\boldsymbol{\sigma}$), for instance, permit mutual transformation among mechanical energy and electric energy without the presence of any electrical current [153].

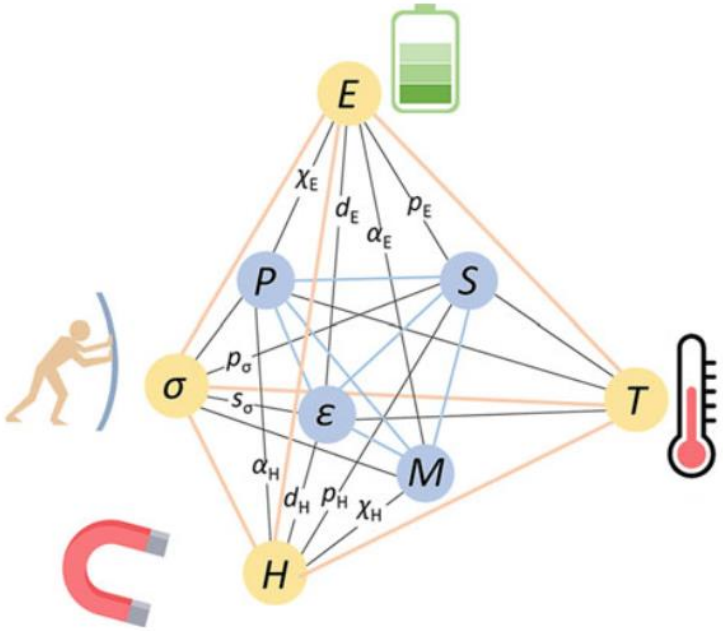

Figure 2.86: Coupling interactions in materials which allow for a solid-state conversion of energy, revealing ordered components (blue) and complementary fields (yellow), namely electric field ($\vec{E}$), magnetic field ($\overrightarrow{H}$), and temperature (T). Coupling coefficients are represented by additional symbols. Adapted from [153].

2.13.1. Direct magnetoelectric coupling

A sujection of magnetic field to the composite results in mechanical stress/strain in the magnetostrictive (ferromagnetic) phase in a direct ME effect. The mechanical input from this stress and strain causes the piezoelectric (ferroelectric) phase to produce a voltage and an electric field proportionate to (and with the same frequency as) the input magnetic field (Figure 2.87).

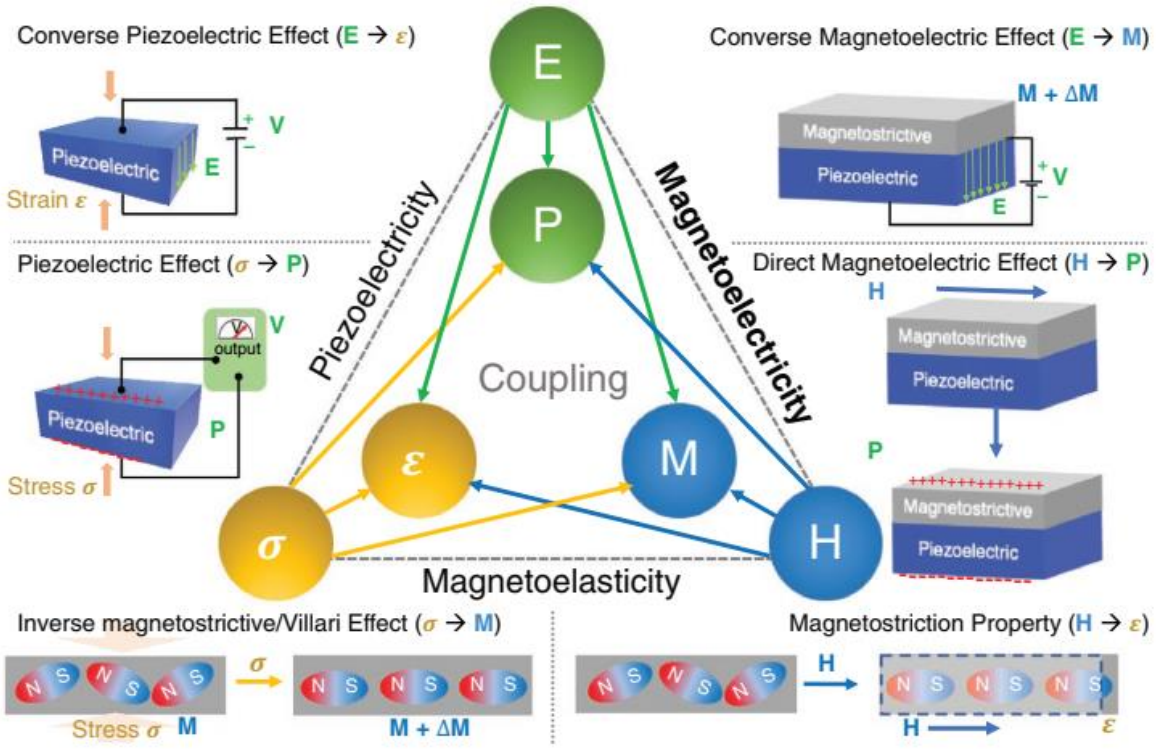

Figure 2.87: Schematics of coupling multiferroic and magnetoelectric materials. Adapted from [162].

2.13.2. Converse magnetoelectric coupling

When a ME composite is exposed to an external electric field, the inverse electrostrictive/piezoelectric action causes strain in the ferroelectric phase. Using the inverse magneto-strictive/piezomagnetic (mechanical/magnetic) effect, this strain that is created in the ferroelectric phase and transferred to the magnetic phase can switch and adjust the magnetization. The name of the coupling is converse ME coupling (Figure 2.87). This coupling occurs by an elastic interplay in the midst of the ferroelectric and magnetic phases [163]. Hence, the following equation [164] can be used to generically represent these two ME couplings:

$$\text{Megnetoelectric effect} = \underbrace{\frac{\text{Electric Output/Input}}{\text{Mechanical Input (transfer from/to)}}}_{\substack{\text{Piezoelectric/}\\ \text{Magnetostrictive}\\ \text{Effect}}} \times \underbrace{\frac{\text{Mechanical Output (transfer to/from)}}{\text{Magnetic Input/Output}}}_{\substack{\text{Magnetostrictive/}\\ \text{Piezoelectric}\\ \text{Effect}}} \quad [2.47]$$

2.13.3. Thermodynamics of linear magnetoelectric effect

It is particularly desirable to describe multiferroic materials thermodynamically since it provides a number of distinct benefits, including the following [1]:

(i) The multiferroic phase's microscopic origins and its related couplings are not mentioned in the thermodynamic description, which takes into account macroscopic variables. This property is notably useful because the ME interplay in multiferroic materials, specifically in single-phasic multiferroic materials, is not described by a single universal mechanism.

(ii) It is impossible to create a microscopic theoretical model that encompasses both forms of multiferroics since they are divided into single-phase and composites. Thermodynamic equations are true whether we discuss single-phasic or composite multiferroics since the thermodynamic approach is generally applicable. Consequently, delinquent of its single-phasic or composite skeleton, a multiferroic material refers to a single entity in the thermodynamic approach that follows.

Assume that the material is a multiferroic. Also, one can believe that two ordered phases display linear combination phenomena like piezoelectric and magnetoelectric coupling; higher-order coupling phenomena are not taken into account in this method. Thermodynamics can be used to express the material's connection of its thermal, electric, magnetic, and elastic properties.

If the strain, entropy, electric polarization, and magnetization of the multiferroic system are all changed slightly, the differential modification in the internal energy (dU) of the system, is expressed as [1]:

$$dU = TdS + \sigma_{ij}dx_{ij} + E_i dP_i + H_i dM_i \qquad [2.48]$$

where T is the temperature, σ_{ij} is the second rank tensor of the externally applied mechanical stress, E_i represents the applied electric field, and H_i stands for applied magnetic field. Tensor subscripts will not be included in the subsequent treatment for the sake of simplicity. Using the Legendre transformation, one can convert the thermodynamic potential $U(S, x, P, M)$ to Gibbs

free energy $G(T, s, E, H)$ as we typically operate at fixed temperature and adoption the externally activated fields and stress as unallied parameters [1]:

$$G = U - TS - \sigma x - EP - HM \quad [2.49]$$

Differentiating Eq. [2.49] and combining with [2.48], we obtain:

$$dG = dU - TdS - SdT - \sigma dx - xd\sigma - EdP - PdE - HdM - MdH$$

$$dG = TdS + \sigma dx + EdP + HdM - TdS - SdT - \sigma dx - xd\sigma - EdP - PdE - HdM - MdH$$

$$dG = -SdT - xd\sigma - PdE - MdH \quad [2.50]$$

Since $G = G(T, \sigma, E, H)$, the differential relation for the Gibbs free energy can be also expressed as [1]:

$$dG = \left(\frac{\partial G}{\partial T}\right)_{\sigma,E,H} dT + \left(\frac{\partial G}{\partial \sigma}\right)_{T,E,H} d\sigma + \left(\frac{\partial G}{\partial E}\right)_{\sigma,T,H} dE + \left(\frac{\partial G}{\partial H}\right)_{\sigma,E,T} dH \quad [2.51]$$

The differential formulas for a multiferroic system's entropy, stress, electrical polarization, and magnetization in terms of its overall Gibbs free energy are achieved through identification by combining relations [2.50] and [2.51]:

$$\left.\begin{aligned} S &= -\left(\frac{\partial G}{\partial T}\right)_{\sigma,E,H} \\ x &= -\left(\frac{\partial G}{\partial \sigma}\right)_{T,E,H} \\ P &= -\left(\frac{\partial G}{\partial E}\right)_{\sigma,T,H} \\ M &= -\left(\frac{\partial G}{\partial H}\right)_{\sigma,E,T} \end{aligned}\right\} \quad [2.52]$$

The electrical polarization (P), magnetization (M), and strain (x) may all have the same set of unallied parameters because the Gibbs free energy contains (T, σ, E, H) as independent variables. As a result, we can distinguish them from their independent variables (T, σ, E, H), leading to useful relations and coefficients that describe coupling effects [1]:

$$dS = \underbrace{\left(\frac{\partial S}{\partial T}\right)_{\sigma,E,H} dT}_{\text{Heat capacity coefficient}} + \underbrace{\left(\frac{\partial S}{\partial \sigma}\right)_{T,E,H} d\sigma}_{\text{Piezo-caloric effect}} + \underbrace{\left(\frac{\partial S}{\partial E}\right)_{\sigma,T,H} dE}_{\text{Electro-caloric effect}} + \underbrace{\left(\frac{\partial S}{\partial H}\right)_{\sigma,E,T} dH}_{\text{Magneto-caloric effect}}$$

[2.53]

$$dx = \underbrace{\left(\frac{\partial x}{\partial T}\right)_{\sigma,E,H} dT}_{\text{Thermal expansion coefficient}} + \underbrace{\left(\frac{\partial x}{\partial \sigma}\right)_{T,E,H} d\sigma}_{\text{Elastic compliance coefficient}} + \underbrace{\left(\frac{\partial x}{\partial E}\right)_{\sigma,T,H} dE}_{\text{Converse piezo-electric coefficient}} + \underbrace{\left(\frac{\partial x}{\partial H}\right)_{\sigma,E,T} dH}_{\text{Magneto-striction coefficient}}$$

[2.54]

$$dM = \underbrace{\left(\frac{\partial M}{\partial T}\right)_{\sigma,E,H} dT}_{\text{Pyro-magnetic effect}} + \underbrace{\left(\frac{\partial M}{\partial \sigma}\right)_{T,E,H} d\sigma}_{\text{Piezo-magnetic effect}} + \underbrace{\left(\frac{\partial M}{\partial E}\right)_{\sigma,T,H} dE}_{\text{Magneto-electric effect}} + \underbrace{\left(\frac{\partial M}{\partial H}\right)_{\sigma,E,T} dH}_{\text{Magnetic susceptibility}}$$

[2.55]

$$dP = \underbrace{\left(\frac{\partial P}{\partial T}\right)_{\sigma,E,H} dT}_{\text{Pyro-electric effect}} + \underbrace{\left(\frac{\partial P}{\partial \sigma}\right)_{T,E,H} d\sigma}_{\text{Direct piezo-electric effect}} + \underbrace{\left(\frac{\partial P}{\partial E}\right)_{\sigma,T,H} dE}_{\text{Dielectric susceptibility}} + \underbrace{\left(\frac{\partial P}{\partial H}\right)_{\sigma,E,T} dH}_{\text{Magneto-electric effect}}$$

[2.56]

Under the linear approximation, each partial derivative in Eqs. [2.53] to [2.56] denotes a physical response, as noted beneath each term giving description of a coupling coefficient. These coefficients, sometimes known as "compliances," offer a gauge of the coupling in the midst of fields. Eqs. [2.54] to [2.56] can be rewritten in integral form and linear approximation for isothermal ($dT = 0$) and adiabatic ($dS = 0$) piezo-multiferroic systems as follows [1]:

$$\left.\begin{aligned} x &= s\sigma + d^{e}E + d^{m}H \\ P &= d^{e,c}\sigma + \chi^{e}E + \alpha^{m}H \\ M &= d^{m,c}\sigma + \alpha^{e}E + \chi^{m}H \end{aligned}\right\} \qquad [2.57]$$

where tensor subscripts have been purposefully ignored, the superscripts e and m stand for the electric and magnetic phase, correspondingly, s stands for the elastic compliance (tensor possessing rank of fourth), $d^{e,m}$ and $d^{e,m,c}$ represent the direct and converse piezoelectric and piezomagnetic coefficients (tensors possessing rank of third), $\alpha^{e,m}$ represent the magnetoelectric coupling coefficient (second rank tensor) and $\chi^{e,m}$ stand for dielectric or magnetic susceptibility (second rank tensor). Equation [2.57] is referred to as one of the multiferroic system's constitutive linear equations of state. The compliances in equation [2.57], along with the factors, represent tensors possessing different ranks as a consequence of the partial derivatives shown in [2.54] to [2.57], which are as follows [1]:

$$s_{ijkl} = \left(\frac{\partial x_{ij}}{\partial \sigma_{kl}}\right)_{T,E,H}; \qquad d^{e}_{kij} = \left(\frac{\partial P_k}{\partial \sigma_{ij}}\right)_{T,E,H} = d^{e,c}_{ijk} = \left(\frac{\partial x_{ij}}{\partial E_k}\right)_{\sigma,T,H}; \qquad \chi^{e}_{ij} = \left(\frac{\partial P_i}{\partial E_j}\right)_{\sigma,T,H} \alpha^{e}_{ij} =$$

$$\left(\frac{\partial M_i}{\partial E_j}\right)_{T,\sigma,H} = \alpha^{m}_{ij} = \left(\frac{\partial P_i}{\partial H_j}\right)_{T,\sigma,E}; \; d^{m}_{kij} = \left(\frac{\partial M_k}{\partial \sigma_{ij}}\right)_{T,E,H} = d^{m,c}_{ijk} = \left(\frac{\partial x_{ij}}{\partial H_k}\right)_{\sigma,T,E};$$

$$\chi^{m}_{ij} = \left(\frac{\partial M_i}{\partial H_j}\right)_{\sigma,T,E}. \qquad [2.58]$$

2.13.4. Magnetoelectric coupling in composites and single-phase multiferroics

In matter, the ME effect is a cross-conjugation in the midst of electric and magnetic fields, which allows for the interaction amongst electric and magnetic states [165]. The ME effect is typically quantitatively characterized through the linear magnetoelectric coupling coefficient (MECC), which is the major coupling part, even if this coupling might have non-linear components. The presence of numerous long-range ferroic ordering in multiferroic materials increases the constitutional magnetic and electric fields, which in turn results in strong ME coupling effects. Additionally, in materials that exhibit piezo-effects, the ME coupling may be stress-mediated, particularly although the two ferroic materials are distinctly distinct, as in laminated multiferroics or composite materials. The ME effect in this instance is explained through a device's effective MECC (α_{eff}), which combines the linear direct ME effect and stress-treated part. Suppose that the electric (E) and magnetic (M) phases of a multiferroic

material are present. Assume also that the two ordered phases show ME coupling, piezoelectric effects, and piezoelectric coupling effects. Thermodynamics can be used to express the material's connection of its thermal, electric, magnetic, and elastic properties. In order to measure macroscopic material parameters under various experimental circumstances, this will offer relationships in the midst of those parameters. It is helpful to use the Gibbs free energy $G(T, \sigma, H, E)$ as the thermodynamic potential because in every case one can operate at fixed temperature T and account the externally applied fields and stress as unallied parameters. This thermodynamic potential can be expressed for this multiferroic system as follows [165]:

$$-G(T, \sigma, E, H) = ST + \frac{1}{2} s_{ijkl}\sigma_{kl}\sigma_{ij} + d^{e}_{ijk}\sigma_{ij}E_k + d^{m}_{ijk}\sigma_{ij}H_k + \pi_{ijkl}E_iH_j\sigma_{kl} + \frac{1}{2}\varepsilon_{ij}E_iE_j + \frac{1}{2}\mu_{ij}H_iH_j + \alpha_{ij}E_iH_j + \cdots \quad [2.59]$$

where: S stands for system's entropy; s_{ijkl} is the fourth rank tensor of elastic compliance; σ_{kl} represents the externally applied mechanical stress tensor; d^{e}_{ijk}stands for piezoelectric coefficient (third rank tensor); d^{m}_{ijk} represents piezomagnetic coefficient (third rank tensor); π_{ijkl} represents piezoelectric coupling constant (fourth rank tensor); ε_{ij} represents electric permittivity tensor; μ_{ij} stands for magnetic permeability tensor; α_{ij} represents linear MECC. The $\alpha_{ij}E_iH_j$ represents the ME energy part, at the same time higher order non-linear coupling parts are not taken into account in this case. From equation [2.59] we can calculate the system's overall strain (x):

$$x_{ij} = -\left(\frac{\partial G}{\partial \sigma_{ij}}\right)_{T,E,H} = s_{ijkl}\sigma_{kl} + d^{e}_{ijk}E_k + d^{m}_{ijk}H_k + \pi_{ijkl}E_kH_l \quad [2.60]$$

where the first term denotes the strain caused by an externally applied stress, the second part stands for the piezoelectrical strain generated through the operation of an electric field (E), the third component represents the ferromagnetic strain generated through the operation of a magnetic field (H), and the fourth component represents a piezoelectric coupling strain generated through mutual piezoelectrical and ferromagnetic responses. The common

formulation for electrical polarization and magnetization of a multiferroic material gives rise to the following results when standard thermodynamic differentiation of [2.59] is performed:

$$P_i = -\left(\frac{\partial G}{\partial E_i}\right)_{\sigma,T,H} = \varepsilon_{ij}E_j + d^e_{ijk}\sigma_{jk} + \alpha_{ij}H_j + \pi_{ijkl}H_j\sigma_{kl} \quad [2.61]$$

$$M_i = -\left(\frac{\partial G}{\partial H_i}\right)_{\sigma,T,E} = \mu_{ij}H_j + d^m_{ijk}\sigma_{jk} + \alpha_{ij}E_j + \pi_{ijkl}E_j\sigma_{kl} \quad [2.62]$$

which, in condensed matrix notation, may be expressed as::

$$P_i = \varepsilon_{ij}E_j + d^e_{im}\sigma_m + \alpha^{eff}_{ij}H_j \quad [2.63]$$

$$M_i = \mu_{ij}H_j + d^m_{in}\sigma_n + \alpha^{eff}_{ij}E_j \quad [2.64]$$

where: i, j = 1, 2, 3 and m, n = 1, 2, 3, 4, 5, 6 and

$$\alpha^{eff}_{ij} = \alpha_{ij} + \pi_{ijkl}\sigma_{kl} \quad [2.65]$$

where α^{eff} is the device's effective MECC, which comprises the piezo-coupling (or stress-mediated) magnetoelectric effect ($\pi\sigma$) and the linear ME coupling effect (α). The effective MECC is the same as the linear magnetoelectric coefficient ($\alpha^{eff} = \alpha$) when the piezoelectric coupling is absent in the system (i.e., $\pi = 0$) or no piezoelectric responses. In this regard, nevertheless, the eqs. [2.63] and [2.64] are expressed likewise aside from the α^{eff} is retrieved by α. As a result, using the relationships [2.63] and [2.64], the electrically [2.66] and magnetically [2.67] activated ME couplings are articulated likewise for direct ME coupling, strain-mediated ME coupling, or even a ME coupling that involves a combination of the two.

$$\alpha_E = \frac{\partial M}{\partial E} \quad [2.66]$$

$$\alpha_H = \frac{\partial P}{\partial H} \quad [2.67]$$

where the matrix indexes were removed. A multiferroic device or sensor will objectively function in like manner inconsiderate of the form of ME coupling exhibited, which has the following implications: (i) direct or strain mediated MECCs are mathematically explained

likewise; (ii) experimental evaluations of the MECC can be designed likewise for all type of ME coupling [165].

2.13.5. Theory of magnetoelectric effect in single-phase multiferroics

The Landau theory of phase transitions provides a macroscopic explanation for the interaction in the midst of the material's stress tensor (σ), electric field ($\vec{E}$), and magnetic field ($\vec{H}$). According to the thermodynamics, the magnetoelectric response could be comprehended in the context of Landau theory, solicited via the extension of free energy for a magneteoectric structure [166-168], i.e.

$$F(\vec{E},\vec{H},T) = F_0 - P_i^S E_i - M_i^S H_i - \frac{1}{2}\varepsilon_0\varepsilon_{ij}E_iE_j - \frac{1}{2}\mu_0\mu_{ij}H_iH_j - \alpha_{ij}E_iH_j - \frac{1}{2}\beta_{ijk}E_iH_jH_k - \frac{1}{2}\gamma_{ijk}H_iE_jE_k - \frac{1}{6}\delta_{ijk}E_iE_jE_k - \frac{1}{6}\eta_{ijk}H_iH_jH_k - \cdots \quad [2.68]$$

where F_0 represents the ground-state free energy, (i,j,k) stands for the triple parts of a parameter in spatial coordinate, E_i stands for electric field component and H_i represents the magnetic field component, P_i^S represents the part of spontaneous electrical polarization and M_i^S is the part of spontaneous magnetization, ε_0 and μ_0 represent the electric permittivity and magnetic permeability in air, ε_{ij} stands for electric permittivity tensor (second-order rank), μ_{ij} represents the magnetic permeability tensor (second-order rank), β_{ijk} and γ_{ijk} represent the tensor coefficients of third-order and, most significantly, α_{ij} stands for the elements of linear ME response tensor and refers to the polarization or magnetization consecration by a magnetic or electric field, respectively. The remaining components in the aforementioned equations are the high-order ME responses parameterized by tensors β and γ. The Eq. [2.68] is legitimate since the external applied fields are minimal in comparison to the internal field. Since the 4-dimensional constitutive law of electromagnetism requires that these terms occur in addition to the ones with β_{ijk} and γ_{ijk}, we added the final two terms in Eq. [2.68], with third rank tensors, δ_{ijk} and η_{ijk} [169]. For the sake of benefit, $1/6$ factors are introduced in Eq. [2.68].

All of these third rank tensors' indices are completely symmetric, i.e., $\delta_{ijk} = \delta_{ikj} = \delta_{jki} = \delta_{jik} = \delta_{kij} = \delta_{kji}$, and $\eta_{ijk} = \eta_{ikj} = \eta_{jki} = \eta_{jik} = \eta_{kij} = \eta_{kji}$. Thus, for a crystal with triclinic symmetry, there are only 10 independent components remaining out of a total of 27 components for each tensor [167]. It is possible to realize the components of total electrical polarization by differentiating the free energy equation [2.68] with regard to the electric field in the form [168, 170]:

$$P_i(\vec{E}, \vec{H}, T) = -\frac{\partial F}{\partial E_i} = P_i^S + \varepsilon_0 \varepsilon_{ij} E_j + \alpha_{ij} H_j + \frac{1}{2}\beta_{ijk} H_j H_k + \gamma_{ijk} H_i E_j + \cdots \quad [2.69]$$

Magnetic field-induced total electrical polarization in the absence of applied electric field ($E = 0$) is given by [168, 170]:

$$P_i = \alpha_{ij} H_j + \frac{1}{2}\beta_{ijk} H_j H_k \quad [2.70]$$

The Eq. [2.70] describes the induced electrical polarization as a results of direct ME effect. The inverse ME effect, which is a subset of total magnetization, may be achieved by differentiating free energy Eq. [2.68] with respect to the magnetic field in the form [168, 170]:

$$M_i(\vec{E}, \vec{H}, T) = -\frac{\partial F}{\partial H_i} = M_i^S + \mu_0 \mu_{ij} H_j + \alpha_{ij} E_j + \beta_{ijk} H_j E_i + \frac{1}{2}\gamma_{ijk} E_j E_k + \cdots \quad [2.71]$$

When there is no external magnetic field (H = 0), electric field-activated total magnetization is expressed as [168, 170]:

$$M_i = \alpha_{ij} E_j + \frac{1}{2}\gamma_{ijk} E_j E_k \quad [2.72]$$

These two Eqs. [2.71] and [2.72] are the basic equations for experimental calculation of MECC. Additionally, the ME response is restricted by the equation $\alpha_{ij}^2 < \chi_{ii}^s \chi_{ii}^m$ where χ^s and χ^m represent the electric and magnetic susceptibilities. This means that the ME effect can only be large in ferroelectric and/or ferromagnetic materials [171]. It is further shown that the ME response can be described by the following [13]:

$$\alpha_{ij}^2 < \chi_{ii}^e \chi_{jj}^m \quad [2.73]$$

where χ_{ii}^{e} and χ_{jj}^{m} are the electric and magnetic susceptibilities. From Equation [2.73] it is logically possible to draw the following two inferences: (i) the magnetoelectric responses can only be significant in in ferroelectric (or ferromagnetic) materials with high relative electric permittivity (or magnetic permeability) and (ii) significant magnetoelectric responses may manifest in materials that are both ferroelectric and ferromagnetic [153]. There is no cross-conjugation in the midst of electric and magnetic traits for the majority of materials. This can be elucidated by investigating the impact of time and spatial inversion procedures on the system. Under spatial inversion, the electric polarization and electric field change sign, but remain unchanged when time is turned around. On the other hand, during spatial inversion, the magnetization and magnetic field are invariant and change sign. A material having inversion symmetry has an invariant ME susceptibility tensor. If we use the electric polarization as an example (only focusing on the cross-coupling factor), $\vec{P} = \alpha\vec{H}$, then applying spatial inversion results in $-\vec{P} = \alpha\vec{H}$. This can only be invariable with the initial state if $\alpha = 0$.

No ME coupling may exist in such a material because the same outcome is achieved when time or spatial inversion procedures are applied to the polarization or the magnetization, respectively. Only a material that violates both time and spatial inversion symmetry can have a non-zero value for (Figure 2.88).

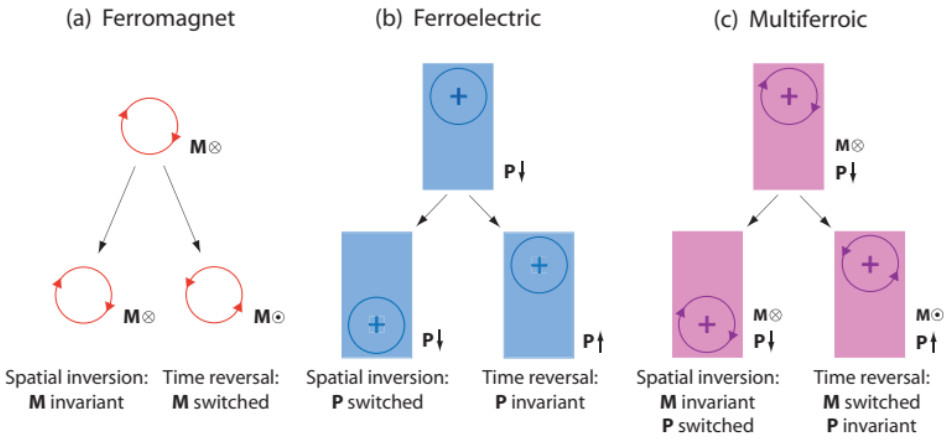

Figure 2.88: The impact of time reversal and spatial inversion on: (a) ferromagnetic materials, (b) ferroelectric materials and (c) multiferroic materials. Adapted from [172].

2.13.6. Magnetoelectric coupling coefficient

According to thermodynamic theory, materials having the coexistence of ferroelectric and ferromagnetic phases experience the ME effect [164]. Magnetoelectric coupling facilitates the modification of net magnetization under an external electric field, and magnetoelectric coupling facilitates the modification of electric polarization under an external magnetic field. The effect is explained mathematically by the MECC of α [173]. The change in the sample's magnetic induction (B) brought on through the operation of an electric field (E) which is known as the MECC.

$$\alpha_{ij}^{E} = \left(\frac{\partial B_i}{\partial E_j}\right) \quad [2.74]$$

or magnetically activated, expressing the alteration in the electrical polarization (P) as a result of applying a magnetic field (H):

$$\alpha_{ij}^{H} = \left(\frac{\partial P_i}{\partial H_j}\right) \quad [2.75]$$

The $\alpha^{E} = \frac{\partial M}{\partial E}$, can also be used to express relation [2.74], depending on the independent thermodynamic variables chosen. The ME susceptibility second rank tensor, α_{ij}, has nine components and is the real representation of the MECC in any case:

$$\alpha_{ij} = \begin{pmatrix} \alpha_{11} & \alpha_{12} & \alpha_{13} \\ \alpha_{21} & \alpha_{22} & \alpha_{23} \\ \alpha_{31} & \alpha_{32} & \alpha_{33} \end{pmatrix} \quad [2.76]$$

The electrically and magnetically activated ME coefficients are thermodynamically equal, according to the Maxwell equations [1]:

$$\alpha_{ij}^{E} = \left(\frac{\partial B_i}{\partial E_j}\right) = \left(\frac{\partial P_i}{\partial H_j}\right) = \alpha_{ij}^{H} = \alpha_{ij} \quad [2.77]$$

Despite having nine components, just one of the ME tensor's nine components is non-zero in the majority of studies. This depends on the symmetries of the samples and crystals, the sample geometry, and the geometry of the external fields that are being used. Typically, only one of the non-diagonal α_{31} and α_{13} or diagonal α_{11}, α_{22}, and α_{33} components is non-zero for a given experimental geometry. Let's now look at the MECCs that are induced by electrical and magnetic fields.

$$\alpha_{ij} = \left(\frac{\partial P_i}{\partial H_j}\right) = \varepsilon_0 \varepsilon_{ii} \left(\frac{\partial E_i}{\partial H_j}\right) \quad [2.78]$$

where we applied the equation $P_i = \varepsilon_0 \chi E_i \cong \varepsilon_0 \varepsilon_{ii} E_i$ having the approximation $\chi = \varepsilon_{ii} - 1 \cong \varepsilon_{ii}$. We now introduce the relationship $B_i = \mu_0 \mu_{jj} H_j$ in Eq. [2.78], leading to

$$\alpha_{ij} = \left(\frac{\partial P_i}{\partial H_j}\right) = \varepsilon_0 \varepsilon_{ii} \left(\frac{\partial E_i}{\partial H_j}\right) = \varepsilon_0 \mu_0 \varepsilon_{ii} \mu_{jj} \left(\frac{\partial E_i}{\partial B_j}\right) \quad [2.79]$$

Substituting Eq. [2.78] in Eq. [2.79] one can perceive the following relation:

$$\alpha_{ij}^2 = \varepsilon_0 \mu_0 \varepsilon_{ii} \mu_{jj} \quad [2.80]$$

Or

$$\alpha_{ij} = \sqrt{\varepsilon_0 \mu_0 \varepsilon_{ii} \mu_{jj}} \quad [2.81]$$

Eq. [2.81] reveals that all elements of the MECC tensor should be positive subsequently no materials prevail possessing negative electric permittivity and magnetic permeability, while the electric permittivity and magnetic permeability are positive in nature in air. Equation [2.81] is inscribed in non-tensor fashion as:

$$\alpha \leq \sqrt{\varepsilon_0 \mu_0 \varepsilon_r \mu_r} = \sqrt{\varepsilon \mu} \quad [2.82]$$

where $\underline{\varepsilon_r}$, μ_r denote the relative dielectric permittivity and magnetic permeability. Equation [2.82] can be derived in part by using the relationship in the midst of the refractive index n ($n = \sqrt{\varepsilon_r \mu_r}$) and the speed of light c ($c = 1/\sqrt{\varepsilon_0 \mu_0}$). Equation [2.82] is changed to:

$$\alpha = \sqrt{\varepsilon_0 \mu_0 \varepsilon_r \mu_r} = \frac{n}{c} \qquad [2.83]$$

It, once more, only permits positive values of the ME coupling and provides the coupling coefficient in SI units, [s/m]. The n/c term in Equation [2.83] can be understood as the reciprocal of velocity of electromagnetic radiation propagation in a multiferroic system, where $\alpha = \frac{n}{c} = \frac{1}{v}$. Using Einstein's Special Relativity postulate, we may then force velocity to be less than the velocity of light ($v \leq c$), resulting in $v \cdot n \leq c$. Now dividing the both sides of the equation $v \cdot n \leq c$ by the velocity of light, one can realize $v \cdot \frac{n}{c} \leq 1$, that leads to the Eq. [2.82], $a \leq \sqrt{\varepsilon \mu}$. The MECC can therefore only have positive values in the range $\alpha \in (0, \sqrt{\varepsilon \mu}]$. One can enumerate that the abovementioned prescription is legitimate for single-phasic multiferroics. There have been accounts of negative coupling parameters, but these are only true for composite multiferroics where negative coupling parameters are permitted and the ME coupling (MEC) is strain/elastically mediated. A closer examination demonstrates the opportunity to maneuver Eq. [2.78] additionally. The subsequent equation for the magnetically activated ME effect is established:

$$\alpha_{ij}^{H} = \left(\frac{\partial P_i}{\partial H_j}\right) = \varepsilon_0 \varepsilon_{ii} \left(\frac{\partial E_i}{\partial H_j}\right) = \frac{\varepsilon_0 \varepsilon_r}{t} \left(\frac{\partial V}{\partial H}\right) = \alpha_V^H \varepsilon_0 \varepsilon_r \qquad [2.84]$$

where α_V^H stands for the magnetically activated ME voltage coefficient specified as [174]:

$$\alpha_V^H = \left(\frac{\partial E}{\partial H}\right) = \frac{1}{t} \left(\frac{\partial V}{\partial H}\right) \qquad [2.85]$$

[s/m] units can be used to express α^H and α^E. The more useful ME voltage coefficient, however, is connoted by the units VA^{-1} in SI and $Vcm^{-1}Oe^{-1}$ in CGS [168, 175, 176].

2.14. The potential application of multiferroic composites

In electronic industries, ME composites are applicable in radiofrequency coil, switching, and microwave devices, tunable inductors, bandstop filters, tunable resonators, high-density magnetic recording, computer memory chips, magnetic freezers [177], isolators, catalysts, ME random access memory (MeRAM), ME antennas, ME gyrator, filter, phase shifter, attenuator and delay line [158], transformer cores, spintronics, ME magnetic sensor, energy harvester, ME current sensor. In Spintronics, information is supported by the orientation of spin of an electron instead of charge. Each electron occurs in one of the two positions- spin up or spin down. In logical operation 0 and 1 is the two possible spin states. In biomedical research, ME composites are advantageous for color imaging, tissue engineering, ME effect for brain stimulation, magnetically controlled drug delivery methods such as optogenetics, bio-magnetic separation, cell separation, tumor hyperthermia, magnetic resonant imaging, catalysis, magnetic drug administration and release, drug targeting, etc [8]. In brief, some important applications of ME composites are illustrated in Figure 2.89

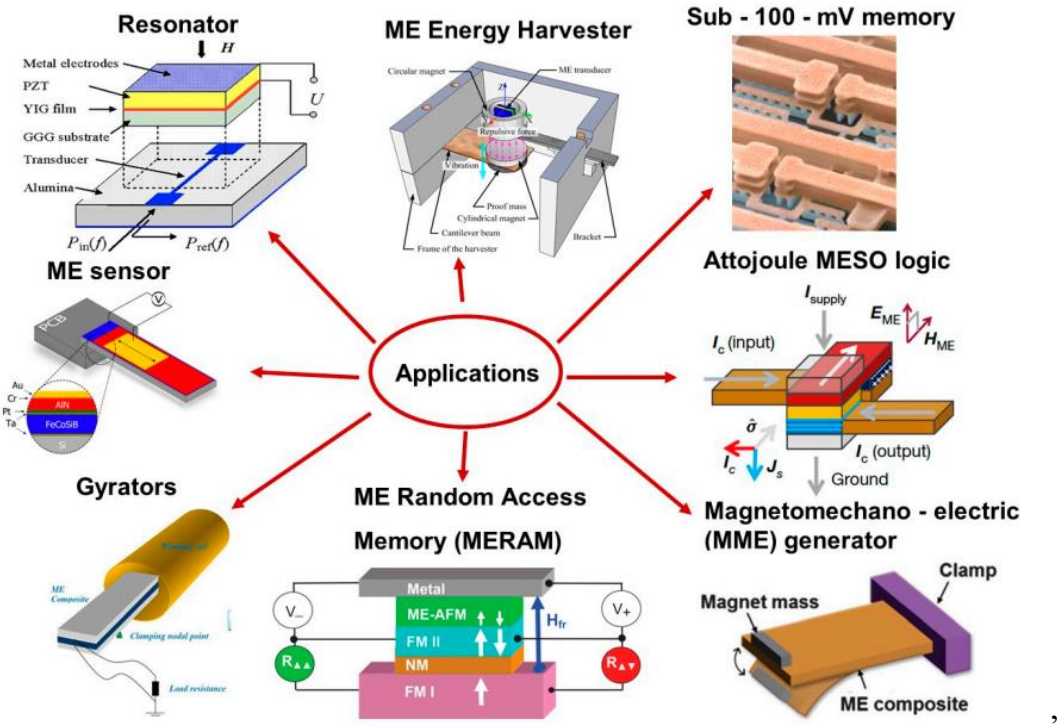

Figure 2.89: Various applications of magnetoelectric (ME) composites. Adapted from [164].

Chapter Three: Material Fabrication and Experimental Procedures

In this chapter, the fabrication technique of stoichiometric nickel-copper-zinc, non-stoichiometric nickel-copper-zinc ferrites, and ferroelectromagnetic ceramic composites are described briefly. Various methods/techniques to characterize their structural, microstructural, elastic, dielectric, electrical, magnetic and magnetoelectric properties are also presented herein.

3.1. Material fabrication

3.1.1. Traditional Solid State synthetic approach

A solid state synthetic technique (also known as ceramic route) is the most reliable and versatile synthetic route to develop new material by heating two or more materials together at elevated temperatures (1000-1400 ℃) and the final products are thermodynamically stable [178].

3.1.2. Mechanism of solid-state synthetic technique

Figure 3.1 illustrates the formation of AB_2O_4 spinel skeleton through the solid-state synthetic route (SSSR) of bivalent and trivalent oxides with the nominal formulas AO and B_2O_3. With the proceeding of the reaction in the midst of AO and B_2O_3, a product layer having the chemical composition AB_2O_4 is developed and it develops over time as it is heated. Reactants are unable to diffuse through the product layer for additional reaction due to the development of the specific threshold thickness of the product layer and as a result, the reaction either ceases or becomes extremely low. As a consequence, the majority of SSSRs act in accordance with a parabolic rate law, that interprets why the SSSRs rate starts out quickly before slowing down over time until it ultimately ceases at the point where the product layer is sufficiently thick to prevent reactant diffusion. Hence the fitful grinding was employed in order to assure the unreacted reactants come across the contact with one another and to destroy the product layer. Therefore, SSSR with fitful grinding always provides high-grade controller of homogeneity. The kinetics of SSSRs become accelerated when one of the reactants melts at or under the reaction temperature, due to easiness of the ion's diffusion in the molten state [178].

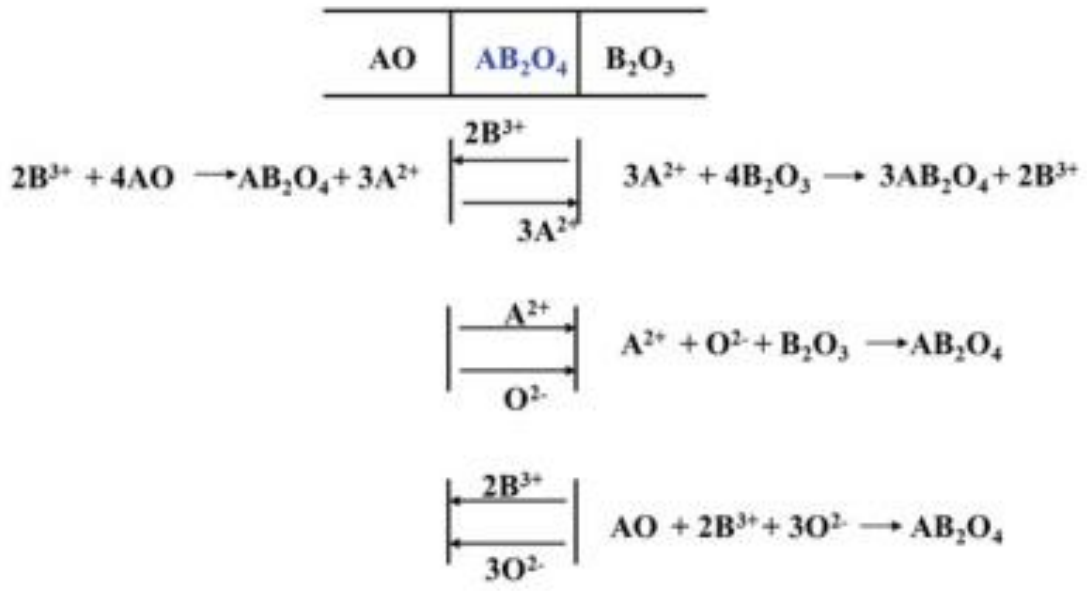

Figure 3.1: Mechanism of a solid-state synthetic route. Adapted from [178].

In SSSR, the electrical-neutrality state must be maintained. According to Figure 3.1 it can be seen that there are three forms where ions diffuse at the time of reaction such a one that the electroneutral state of the samples was maintained. To interpret this, we can consider a classic example of the fabrication of a spinel AB_2O_4 from the reactants AO and B_2O_3. $3A^{2+}$ and $2B^{3+}$ ions counter-diffuse in the opposite directions, or an A^{2+} ions diffuse to B_2O_3 with an O^{2-} ions, or $2B^{3+}$ ions with $3O^{2-}$ ions diffuse through the AO reagent to assert the electroneutrality. These three combinations of ion diffusion will preserve the local electroneutrality. These three types of ions diffusion depend on the type of the reactants [178].

3.1.3. Brief discussion on the steps in solid-state synthetic technique

3.1.3.1. Starting material

The starting materials used to develop the samples were in analytical grade. Details are recorded in Table 3.1.

Table 3.1. List of the basic ingredients those were employed to fabricate the samples

Name of ingredients	Empirical formula	Purity grade	Supplier
Barium carbonate	$BaCO_3$	99.9 %	SRL Pvt. Ltd., India
Calcium carbonate	$CaCO_3$	99.8 %	do
Titanium oxide	TiO_2	99.9 %	do
Zirconium oxide	ZrO_2	99.9 %	do
Nickel (II) oxide	NiO	99.9 %	do
Copper (II) oxide	CuO	99.9 %	do
Zinc (II) oxide	ZnO	99.9 %	do
Iron (III) oxide	Fe_2O_3	99.9 %	Sigma-Aldrich, Germany

3.1.3.2. Weighing

The weight percentage of the oxide was calculated using the formula:

$$\text{Weight percent of oxide} = \frac{\text{Molecular mass of oxide} \times \text{desired mass of the specimen}}{\text{Sum of molecular mass of each oxide in a specimen}}$$

[3.1]

3.1.3.3. Grinding and Mixing

After weighing the starting materials according to Equation [3.1], they were mixed and ground using a mortar and pestle in acetone media for 6h for homogenizing the samples. During grinding and mixing, the acetone was gradually volatilized and completely evaporated within 10-15 minutes.

3.1.3.4. Powder calcination

Calcination is the process of heating the reactants to break them down and get the appropriate products. During this procedure, the gaseous byproducts generated by the heating the reactants and eventually evaporates. For the calcination process, a proper atmosphere is necessary.

Reactions occurred during the calcination process are most often carried out near the thermal decomposition temperature or at the phase transition temperature. In thermodynamics, the temperature of calcination is the lowest temperature wherein the fundamental free energy due to Gibbs phenomenon of a specific SSSR reaches zero [178].

3.1.3.5. Compacting/Pressing

The calcinated powders of the samples were mixed with binder (10 wt. % PVA) to avoid the brittleness of the samples and pressed into small cylindrical pellet specimens and toroids using a uniaxial using a hydraulic press with 4.41×10^{7} N/m^{2} pressure.

3.1.3.6. Solid-state Sintering

Sintering is the thermal technique by which powders are transformed into a solid by heating directly under the melting point of the solid mass of the components, as a result, the material basically endures solid during the whole of the process and acquires the appropriate annealed density. In sintering, the atoms or ions diffusion from one side to other of the physical borders of the component particles takes place, resulting in the fusion of small particles into a larger one, more well-dense solid. Figure 3.2 describes the stages that occur during the sintering process [179, 180]. Generally, four basic steps are involved to sinter and to densify the samples during the sintering technique. (i) Physical contact in the midst of sample particles directed by employing pressure to the calcining samples, (ii) establishment of concave sinter necks in the midst of abutting particles, which increase the interface in the midst of particles, (iii) development and grain borders diffusion and sinter necks (necks and pores develop and diffuse through and gather at the grain borders), and (iv) finally, the pores are eradicated and detached and closed pores generate. The contact area of grain border in the midst of grains gradually enhances and compaction takes place amid sintering.

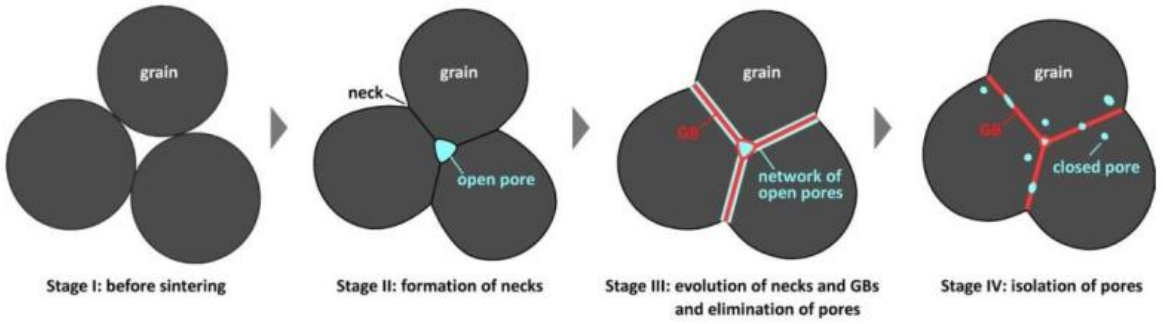

Figure 3.2: Different stages in solid-state sintering. Adapted from [181].

3.1.3.7. Sample fabrication of $Ba_{0.9}Ca_{0.1}Ti_{0.9}Zr_{0.1}O_3$

The $Ba_{0.9}Ca_{0.1}Zr_{0.1}Ti_{0.9}O_3$ (BCZTO) powders were fabricated by the conventional SSSR. The starting ingredients were $BaCO_3$, $CaCO_3$, TiO_2, and ZrO_2, respectively. The stoichiometric raw powders were mixed for 6 h using pestle and mortar in acetone media and then calcinated at a temperature of 950 °C for 5h. At the time of calcination process, chemical reaction takes place as: $0.9BaCO_3 + 0.1CaCO_3 + 0.1ZrO_2 + 0.9TiO_2 \rightarrow Ba_{0.9}Ca_{0.1}Zr_{0.1}Ti_{0.9}O_3$ (BCTZO) + $CO_2\uparrow$. To produce uniform and fine powder, the calcinated powder was reground for 3 h. The calcinated powder was used to investigate the phase formation, lattice constant, and crystalline size, respectively. The flowchart of samples fabrication is delineated in Figure 3.3.

3.1.3.8. Sample fabrication of $Ni_{0.25}Cu_{0.13}Zn_{0.62}Fe_2O_4$

The $Ni_{0.25}Cu_{0.13}Zn_{0.62}Fe_2O_4$ (NCZFO) powders were fabricated by the conventional SSSR. The starting ingredients were NiO, CuO, ZnO, and Fe_2O_3, respectively. The stoichiometric raw powders were mixed for 6 h using pestle and mortar in acetone media and then calcinated at temperature of 950 °C for 5h. To produce uniform and fine powder, the calcinated powder was reground for 3 h. The calcinated powder was used to investigate the phase formation, lattice constant, and crystalline size. The flowchart for the fabrication of samples is delineated in Figure 3.4.

3.1.3.9. Sample fabrication of $Ni_{0.25}Cu_{0.13}Zn_{0.62}Fe_{2-x}O_{4-3x/2}$

Samples were fabricated using conventional SSSR. The starting ingredients were NiO, CuO, ZnO, and Fe_2O_3, respectively. The powders were measured in accordance with the stoichiometric ratio and mixed using pestle and mortar for 6h in acetone media and calcinated at temperature of 950 °C for 5h. To produce uniform and fine powder, the calcinated powder was reground for 3 h. The homogeneous powders were characterized to investigate the phase formation, lattice constant, and crystalline size, respectively. The flowchart for the fabrication of samples is delineated in Figure 3.5.

3.1.3.10. Sample fabrication of (1-y) [BCZTO] + (y) [NCZFO]

The calcinated powders of BCZTO and NCZFO was measured in accordance with the stoichiometric ratio and mixed using pestle and mortar for 6 h in acetone media. Subsequently, the powders were mixed with binder (5 wt% PVA) and compacted into pellet specimens and toroids using the uniaxial pressing machine. The pellet specimens and toroidal specimens were annealed under different temperatures of 1100 ℃-1250℃ for 5h. Finally, the samples were subjected to different characterizations for evaluating the structural, microstructural, and electromagnetic properties. The flowchart for the fabrication of samples is delineated in Figure 3.6.

3.1.3.11. Sample fabrication of (1-y) [BCZTO] + (y) [$NCZFe_{2-x}O_{4-3x/2}$]

The BCZTO and $NCZFe_{2-x}O_{4-3x/2}$ powders were measured in accordance with the stoichiometric ratio and mixed using pestle and mortar for 3h in acetone media. The powders were mixed with small amount of binder (5 wt% PVA) and pressed into pellet specimens and toroidal specimens using the uniaxial pressing machine and finally annealed for 5h at 1200 ℃. The flowchart for the fabrication of samples is delineated in Figure 3.7.

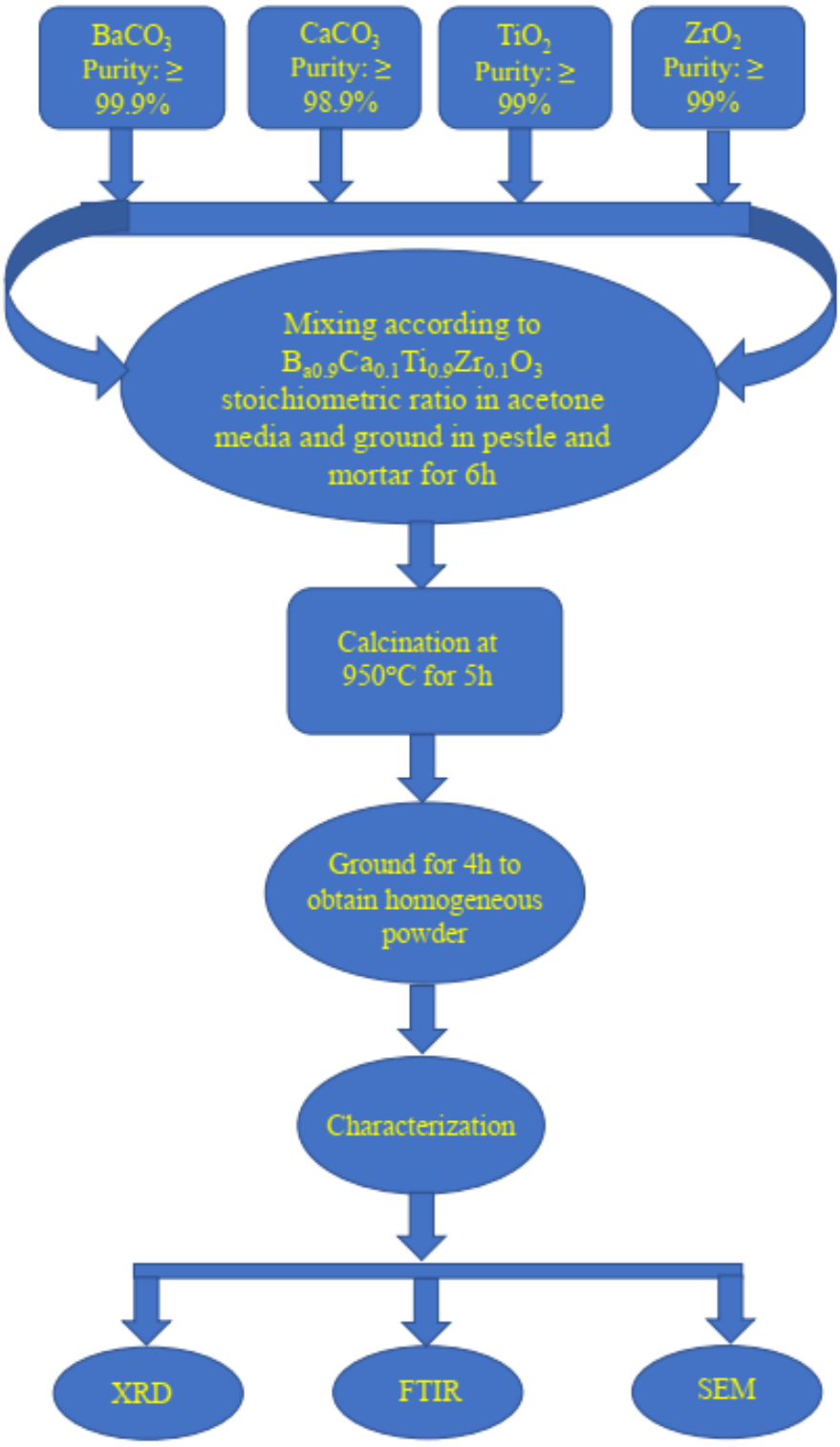

Figure 3.3: Pictorial representation or flow chart for the synthesis of stoichiometric barium calcium titanium zirconate ($Ba_{0.90}Ca_{0.10}Ti_{0.90}Zr_{0.10}O_3$).

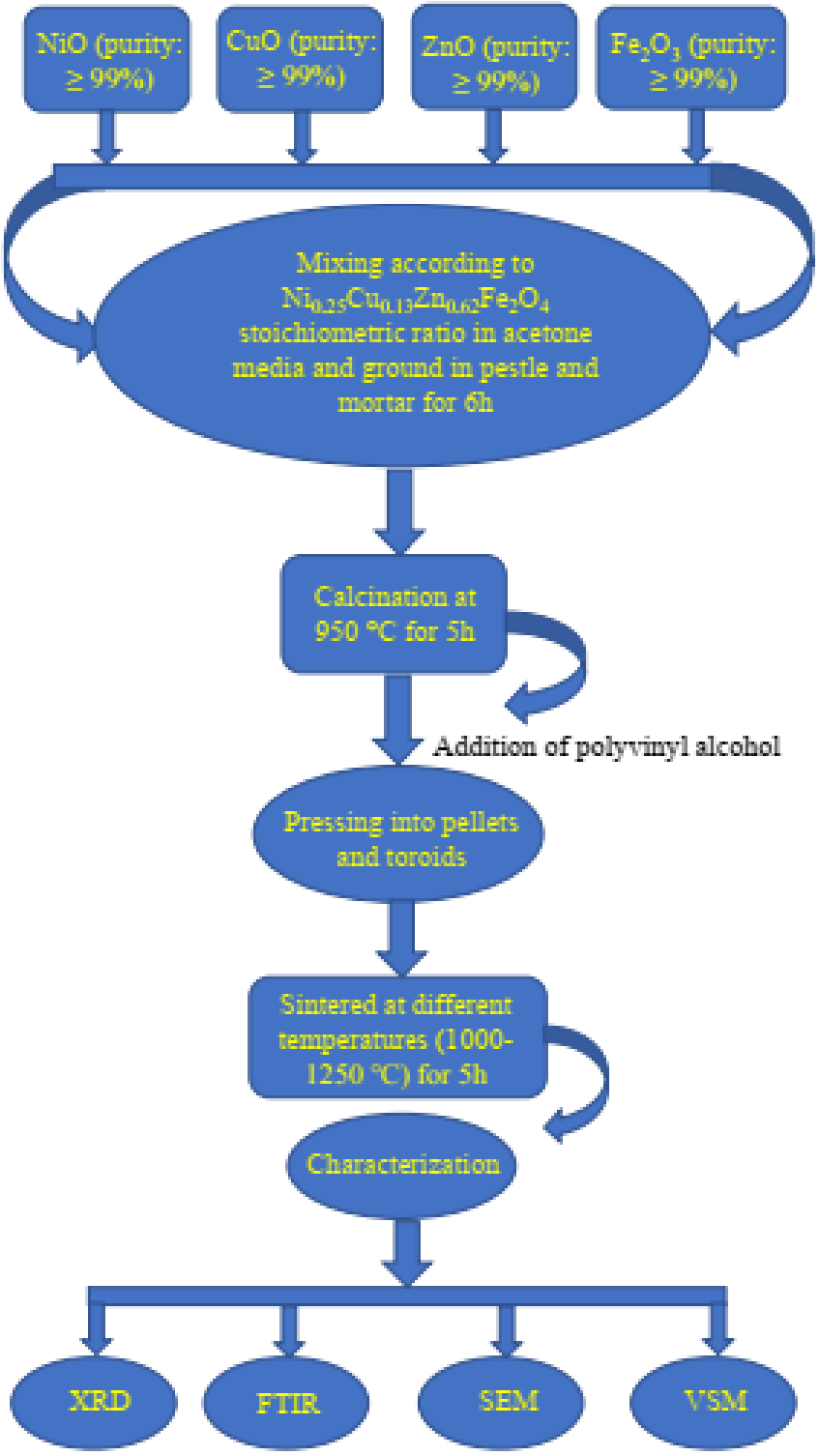

Figure 3.4: Pictorial representation or flow chart for the synthesis of stoichiometric nickel-copper-zinc ferrite ($Ni_{0.25}Cu_{0.13}Zn_{0.62}Fe_2O_4$).

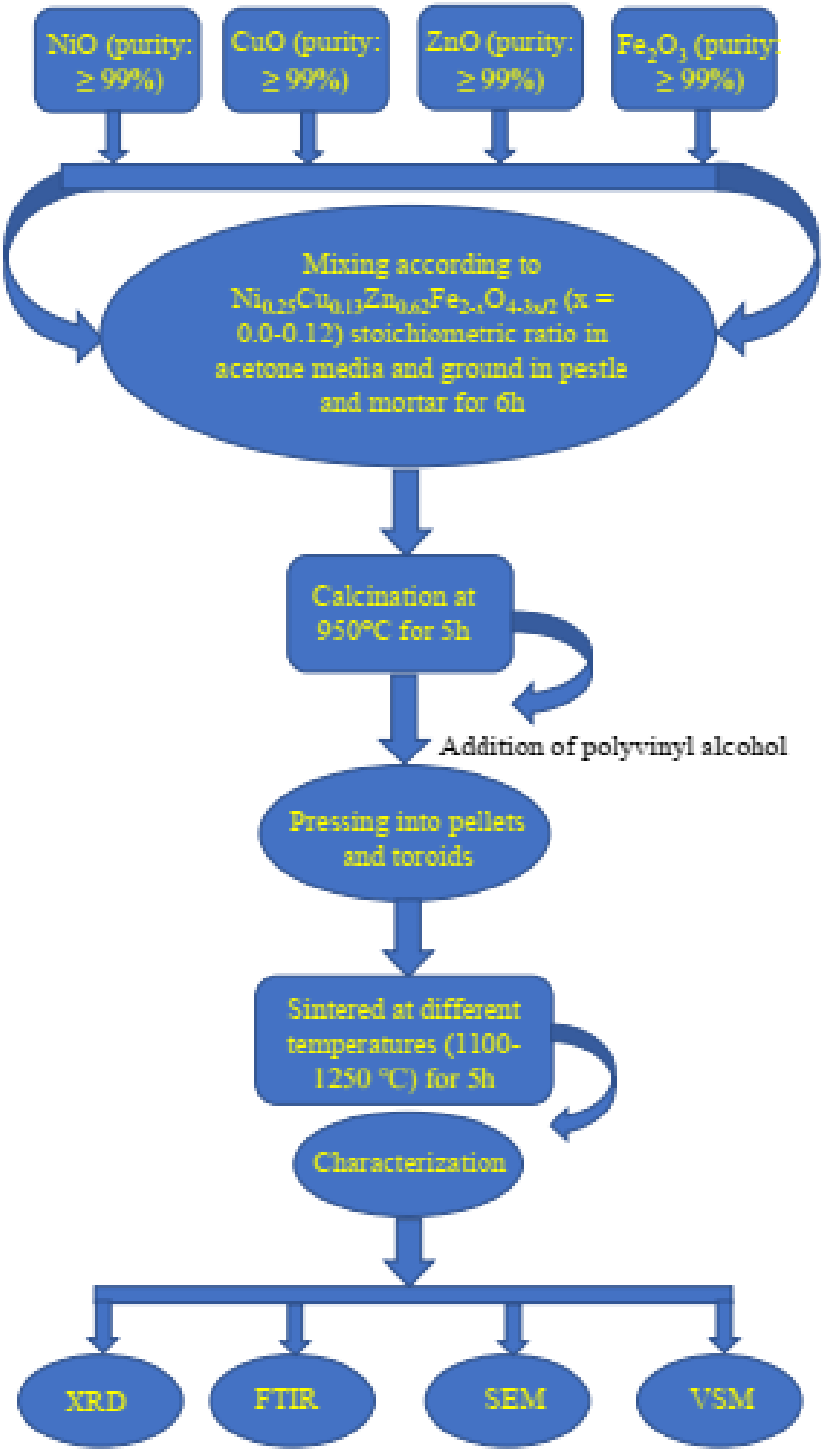

Figure 3.5: Pictorial representation or flow chart for the synthesis of non-stoichiometric nickel-copper-zinc ferrite ($Ni_{0.25}Cu_{0.13}Zn_{0.62}Fe_{2-x}O_{4-3x/2}$).

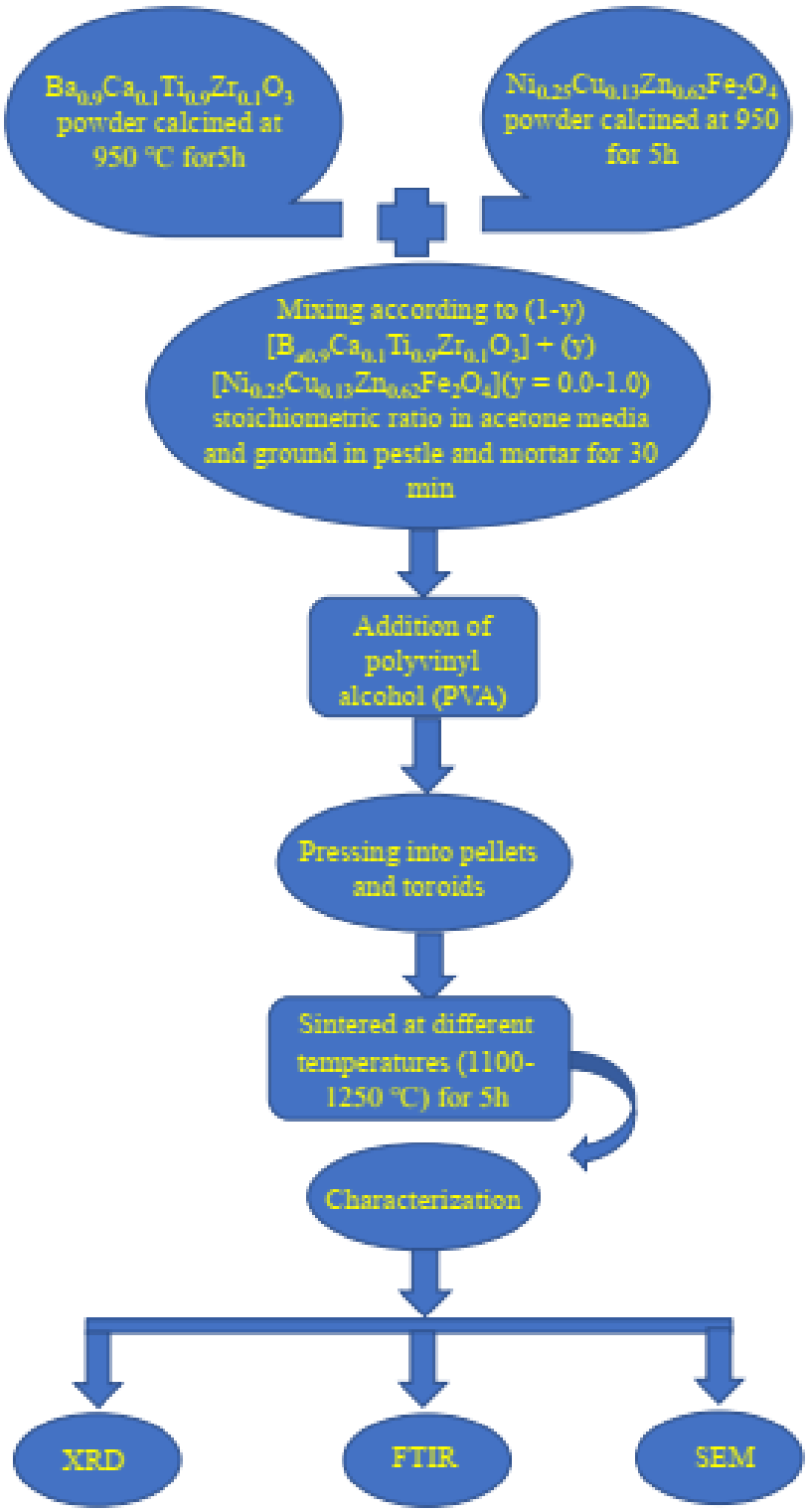

Figure 3.6: Pictorial representation or flow chart for the synthesis of (1-*y*) $[Ba_{0.90}Ca_{0.10}Ti_{0.90}Zr_{0.10}O_3]$ + (*y*) $[Ni_{0.25}Cu_{0.13}Zn_{0.62}Fe_2O_4]$ (*y* = 0.0 to 1.0) multiferroic composites.

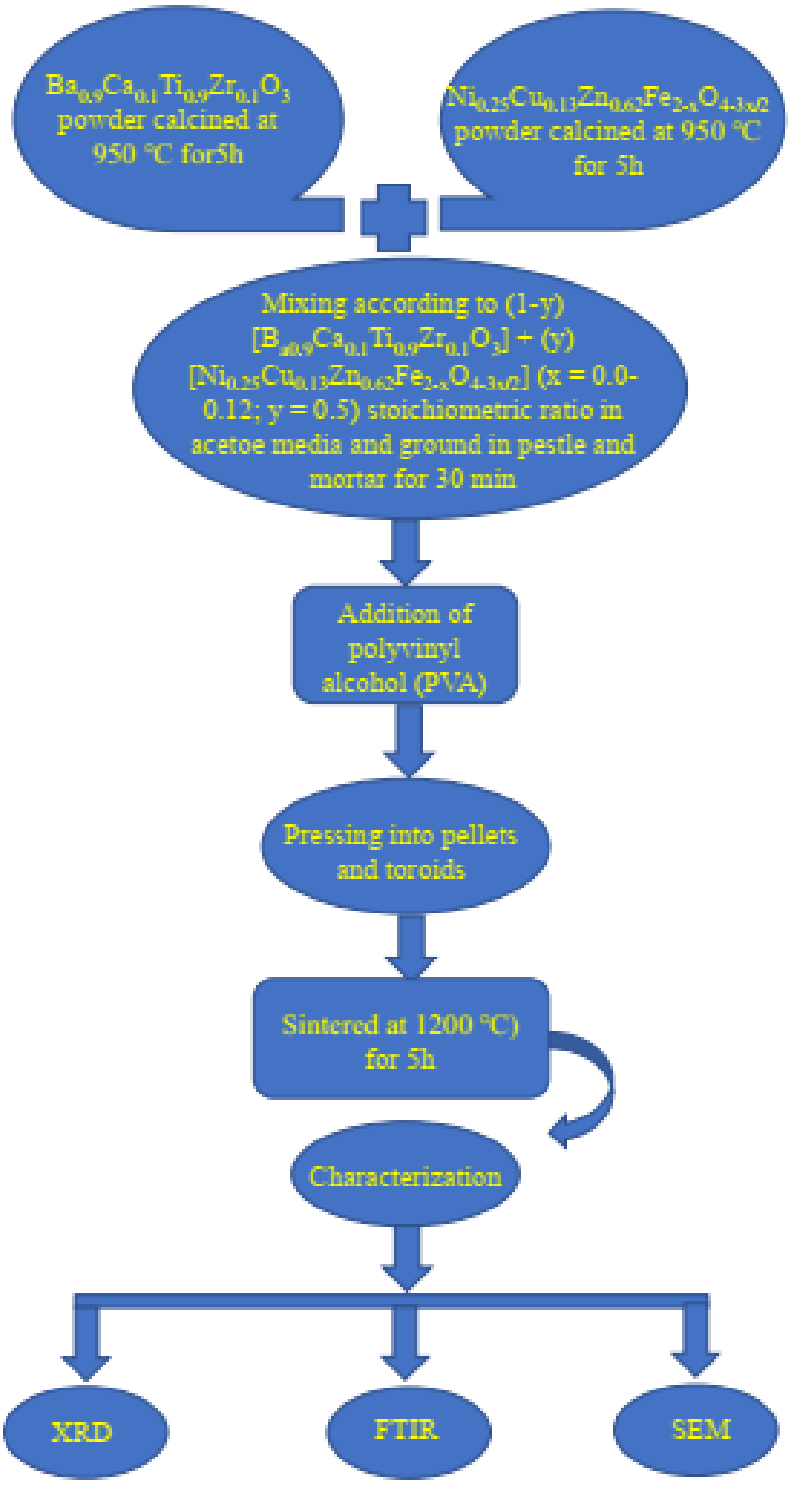

Figure 3.7: Schematic diagram showing synthesis of (1-*y*) $[Ba_{0.9}Ca_{0.1}Ti_{0.9}Zr_{0.1}O_3]$ + (*y*) $[Ni_{0.25}Cu_{0.13}Zn_{0.62}Fe_{2-x}O_{4-3x/2}]$ (x = 0.0; 0.04; 0.08; 0.12; y = 0.2, 0.5) multiferroic composites.

3.2. Characterization and property measurements

In this section, we have explained, in brief, the basic principles and experimental procedures for investigating the developed samples. X-ray diffractometer (XRD) was utilized to clarify the architecture of the generated samples. Micromorphological study and compositional analysis of the generated samples were carried out using a scanning electron microscope (SEM) and energy dispersive X-ray spectroscopy (EDXS).

3.2.1. X-ray diffractometer

To elucidate the crystallographic structure of the samples and the information achieved from XRD patterns were used for qualitative and quantitative analyses, unit cell lattice constant determination, crystallite size and strain evaluation X-ray diffraction (XRD) is a powerful approach. Figure 3.8 (a) represents a schematic illustration of a diffractometer and Figure 3.8 (b) illustrates photograph of X-ray diffractometer. X-ray diffractometer has the four fundamental components: an X-ray source (cathode ray tube), incident beam optics or collimator, sample holder, and a CCD detector (the number of scattered X-rays by the sample is counted). In the cathode ray tube, X-rays are produced by heating a tungsten filament that emanates electrons at that moment. A voltage is applied to accelerate the emanated electrons toward the target material for the bombardment of the target material. When emanated electrons possess significant amout energy to extricate electrons from the target material's inner shell (consisting of copper), X-rays are generated. The collimator makes these X-rays parallel to each other (Figure 3.8 (a)) and focused on the sample. When a parallel beam of monochromatic X-rays (single wavelength) irradiates the sample, the sample's lattice serves as a 3D diffraction grating, resulting the X-ray beams to diffract at specific angles and satisfying the Bragg's diffraction equation [182, 183] as depicted in Figure 3.9:

$$2d_{hkl}sin\theta_{hkl} = n\lambda\ (n\ =\ 1, 2, 3, \dots\dots) \qquad [3.2]$$

, where, d_{hkl} denotes the interplanar distance, θ_{hkl} represents the angle of diffraction and λ represents X-ray's wavelength. When the Bragg's diffraction law is fulfilled, a constructive interference takes place and a peak in intensity develops. Since the testing sample and CCD detector are swiveled around the test sample, the detector records strength of the reflected X-rays and processes the signal of X-rays and transforms the signal of X-rays into a count rate.

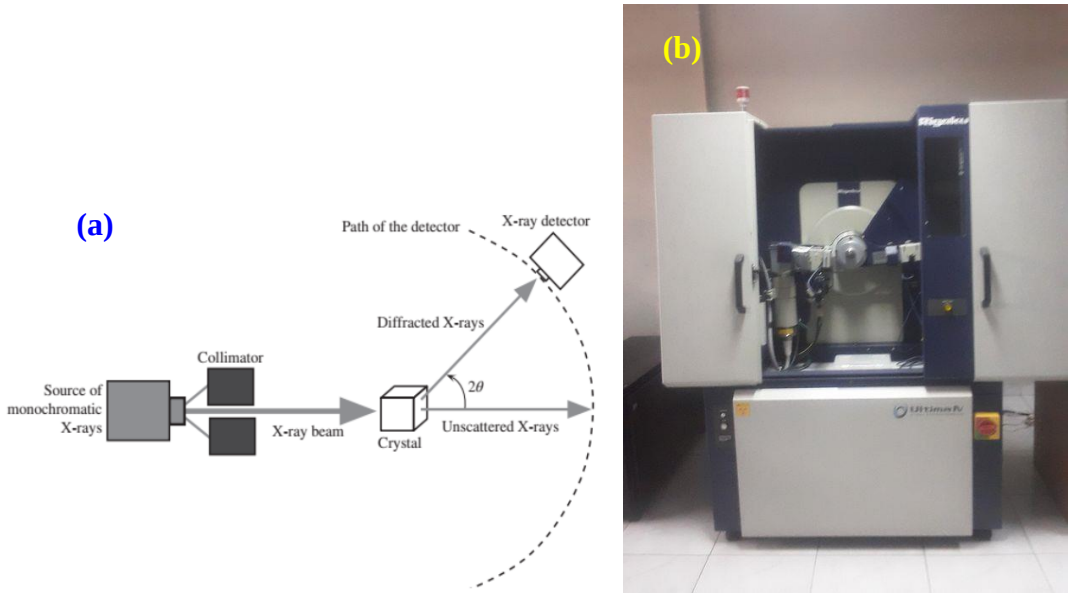

Figure 3.8: (a) A schematic illustration of a diffractometer for X-ray diffraction investigation of samples. Adapted from [119] and (b) Photograph of the RIGAKU Ultima IV X-ray diffractometer.

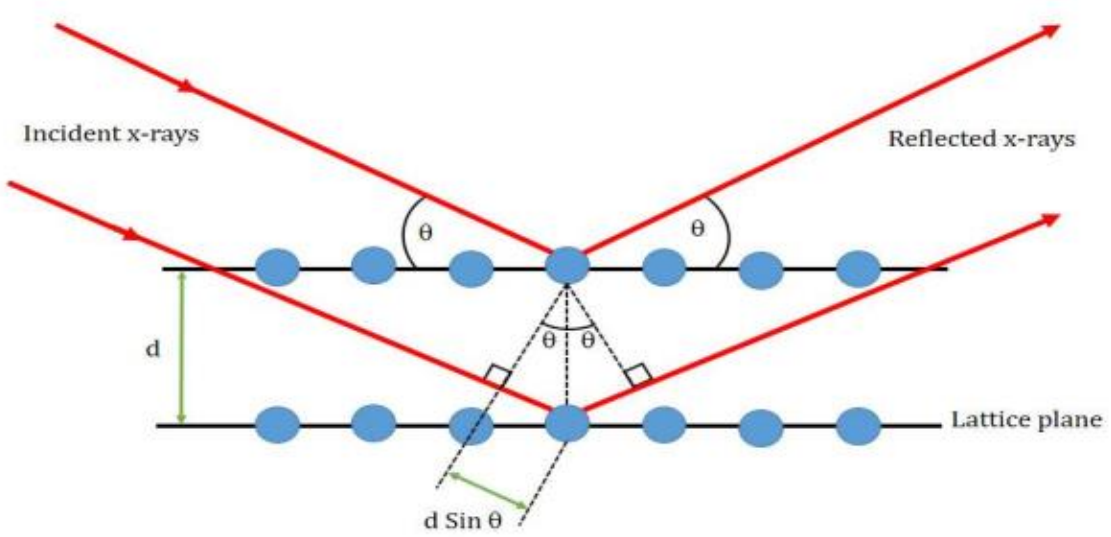

Figure 3.9: Bragg's diffraction law. Adapted from [109, 184].

3.2.1.1. The lattice constants

The lattice constants of the ferromagnetic phase possessing cubic symmetry and ferroelectric phase possessing tetragonal symmetry is determined using the relations [185]:

$$a^2 = (\lambda^2/4sin^2\theta_{hkl}) \times (h^2 + k^2 + l^2) \quad [3.3]$$

and

$$sin^2\theta_{hkl} = \frac{\lambda^2(h^2+k^2)}{4a^2} + \frac{\lambda^2 l^2}{4c^2} \quad [3.4]$$

where, hkl represents the Miller's indices, λ reprents the X-ray's wavelength (Cu-Kα = 1.5406 Å) and θ_{hkl} is the angle of diffraction for each Bragg reflection plane.

3.2.1.2. Structural parameters of ferromagnetic phases

The X-ray parameters, i.e., the hopping lengths in the midst of magnetic ions at tetrahedrally-tetrahedrally coordinated site (L_{A-A}), octahedrally-octahedrally coordinated site (L_{B-B}), tetrahedrally-octahedrally coordinated site (L_{A-B}), tetrahedrally-octahedrally coordinated sites radii (r_A and r_B), tetrahedrally coordinated bond length (d_{AX}), octahedrally coordinated bond length (d_{BX}), tetrahedrally coordinated edge (d_{AXE}), shared octahedrally coordinated edge (d_{BXE}) and unshared octahedrally coordinated edge (d_{BXEU}) were determined using lattice constant (a) the positional parameter of oxygen ($u = 0.381$Å), ionic radius of oxygen ions ($R_O = 1.32$ Å) were determined using the equations outlined in Table 3.2.

Table 3.2. Formulae of the jumping lengths in the midst of magnetic ions at tetrahedrally-tetrahedrally cordinated site (L_{A-A}), octahedrally-octahedrally coordinated site (L_{B-B}), tetrahedrally-octahedrally coordinated site (L_{A-B}), tetrahedrally-octahedrally coordinated sites radii (r_A and r_B), tetrahedrally coordinated bond length (d_{AX}), octahedrally coordinated bond length (d_{BX}), tetrahedrally coordinated edge (d_{AXE}), shared octahedrally coordinated edge (d_{BXE}) and unshared octahedrally coordinated edge (d_{BXEU}) [186].

Hopping length in the midst of magnetic ions at tetrahedral-tetrahedral site (L_{A-A}) (Å)	$L_{A-A} = \frac{a\sqrt{3}}{4}$
Hopping length in the midst of magnetic ions at octahedral-octahedral site (L_{B-B}) (Å)	$L_{B-B} = \frac{a\sqrt{2}}{4}$
Hopping length in the midst of magnetic ions tetrahedral-octahedral site (L_{A-B}) (Å)	$L_{A-B} = \frac{a\sqrt{11}}{8}$
Interstial radius for tetrahedral site (r_A) (Å)	$r_A = \left(u - \frac{1}{4}\right)a\sqrt{3} - R_O$
Interstial radius for octahedral site (r_B) (Å)	$r_B = (0.625 - u)a - R_O$
Shared tetrahedral edge length (d_{AXE}) (Å)	$d_{AXE} = a\sqrt{2}(2u - 0.5)$
Shared octahedral edge length (d_{BXE}) (Å)	$d_{BXE} = a\sqrt{2}(1 - 2u)$
Unshared octahedral edge lengths (d_{BXEU}) (Å)	$d_{BXEU} = a\left[4u^2 - 3u + \left(\frac{11}{16}\right)\right]^{1/2}$
Tetrahedral bond length (d_{AX}) (Å)	$d_{AX} = a\sqrt{3}(u - 0.25)$
Octahedral bond length (d_{BX}) (Å)	$d_{BX} = a\left[3u^2 - \left(\frac{11}{4}\right)u + \left(\frac{43}{64}\right)\right]^{1/2}$

The interionic distances in the midst of the cations (b, c, d, e, and f), interionic distances in the midst of the cation and anion (p, q, r and s), and the bond angles (θ_1, θ_2, θ_3, θ_4, and θ_5) were determined using the equations outlined in Table 3.3 [187].

Table: 3.3. Formulae of the interionic distances (b, c, d, e, f) in the midst of cations, (p, q, r, s) in the midst of cations and anions, and bond angles (θ_1, θ_2, θ_3, θ_4, θ_5)

Parameters	Interaction in the midst of sublattices	Formula
b (Å)	*Oct-Oct*	$(a/4)\sqrt{2}$
c (Å)	*Tet-Oct*	$(a/8)\sqrt{11}$
d (Å)	*Tet-Tet*	$(a/4)\sqrt{3}$
e (Å)	*Tet-Oct*	$(3\,a/8)\sqrt{3}$
f (Å)	*Oct-Oct*	$(a/4)\sqrt{6}$
p (Å)	*Oct-O*	$a(5/8-u)$
q (Å)	*Tet-O*	$a(u-1/4)\sqrt{3}$
r (Å)	*Tet-O*	$a(u-1/4)\sqrt{11}$
s (Å)	*Oct-O*	$a(u/3+1/8)\sqrt{3}$
θ_1 (degree)	*Tet-O-Oct*	$cos^{-1}[(p^2+q^2-c^2)/2pq]$
θ_2 (degree)	*Tet-O-Oct*	$cos^{-1}[(p^2+r^2-e^2)/2pr]$
θ_3 (degree)	*Oct-O-Oct*	$cos^{-1}[(2p^2-b^2)/2p^2]$
θ_4 (degree)	*Oct-O-Oct*	$cos^{-1}[(p^2+s^2-f^2)/2ps]$
θ_5 (degree)	*Tet-O-Tet*	$cos^{-1}[(r^2+q^2-d^2)/2rq]$

3.2.1.3. Bulk density, theoretical density and porosity

The bulk density (ρ_{bulk}) of ferroelectric and ferromagnetic phases and ferroelectromagnetic ceramic composites were was using the equation [186]:

$$\rho_{bulk} = \frac{mass}{volume} = \frac{m}{\pi r^2 h} \qquad [3.5]$$

, where m represents the pellet specimen's mass, r represents the pellet specimen's radius, and h represents the pellet specimen's thickness.

The theoretical density (ρ_{X-ray}) of ferromagnetic phases was evaluated using the equation [186]:

$$\rho_{X-ray\ (\text{Ferromagnetic})} = \frac{Z \times M_{w(\text{Ferromagnetic})}}{N_A \times V_{\text{Ferromagnetic}}} \quad [3.6]$$

where, Z represents the number of atoms in a single cell (for ferromagnetic phase, $Z = 8$), $M_{w(\text{Ferromagnetic})}$ represents the molecular mass of the ferromagnetic phase, N_A stands for Avogadro's number, $V_{\text{Ferromagnetic}} = a^3$ expresses the volume of unit cell of ferromagnetic phase, and a expresses the lattice constant of ferromagnetic phase. The theoretical density (ρ_{X-ray}) of ferroelectric phase was estimated using the equation [185]:

$$\rho_{X-ray\ (\text{Ferroelectric})} = \frac{Z \times M_{w(Ferroelectric)}}{N_A \times V_{Ferroelectric}} \quad [3.7]$$

where Z represents the number of atoms in a single cell (for BCZTO phase $Z = 1$), $M_{w(Ferroelectric)}$ represents the molecular mass, $V_{Ferroelectric} = a^2c$ represents the ferroelectric phase unit cell volume, a and c are the lattice constants of the ferroelectric phase, and N_A is Avogadro's number. The theoretical density of ferroelectromagnetic ceramic composites was determined utilizing the equation [59, 71]:

$$\rho_{X-ray\ (\text{Composite})} = (1-y)\left[\frac{M_{w(Ferroelectric)}}{N_A \times V_{Ferroelectric}}\right] + (y)\left[\frac{8 \times M_{w(\text{Ferromagnetic})}}{N_A \times V_{\text{Ferromagnetic}}}\right] \quad [3.8]$$

, where $M_{w(FE)}$ and $M_{w(F)}$ are the molecular mass of ferromagnetic and ferroelectric phases. The porosity (P %) of the developed samples was achieved using the equation:

$$\text{porosity}\ (P\ \%) = \frac{\rho_{X-ray} - \rho_{bulk}}{\rho_{X-ray}} \times 100 \quad [3.9]$$

, where ρ_{bulk} and ρ_{X-ray} are the bulk and X-ray densities of the samples.

3.3. Fourier transform infrared spectrometer and working principle

Fourier transform infrared (FTIR) spectrometer operates on the basis of Michelson interferometer [188] and schematically delineated in Figure 3.10 (a) and on the other hand, a photograph of FTIR spectrophotometer (Model: IRPrestige-21) is depicted Figure 3.10 (b)

delineates. FTIR spectrometer which consists of infrared radiation source, collimating mirror, beam splitter (BS) (which is designed to transmit half of the infrared radiation incident upon it and reflect half of the infrared radiation incident upon it), static mirror, movable mirror, sample cell and detector [189]. First a beam of infrared source falls on the collimating mirror which makes the beam of infrared source parallel and afterward a beam of infrared source falls on the BS where the half (50 %) of the radiation is reflected to the static mirror and half (50 %) of the radiation is transmitted to the movable mirror. Again, from the static mirror and movable mirror, the radiation is reflected back to the BS. Then from the BS, it is transmitted through the sample, and eventually reached to the detector. When the distance in the midst of movable mirror to the BS and from stationary mirror to the BS is constant. The condition is called the zero-path difference which means that there is no path difference. At this condition constructive in phase pattern occurs and maximum signal reaches to the detector. When the movable mirror moves $\lambda/2$ then two wavelengths are out of phase with each other and destructive interference takes place. At this condition, minimum or no signal reaches to the detector. Since the infrared radiation sources are polychromatic in nature therefore each wavelength produces cosine wave. In practice, as moving mirror progresses, the net signal falling on the detector is a cosine wave. At detector, cosine waves are summed up and finally the interferogram (intensity versus optical path difference plot) is produced. The interferogram basically holds the spectral information in time domain and a Fourier transformation is then applied to obtain spectral information in frequency domain (intensity versus wavenumber plot) [190].

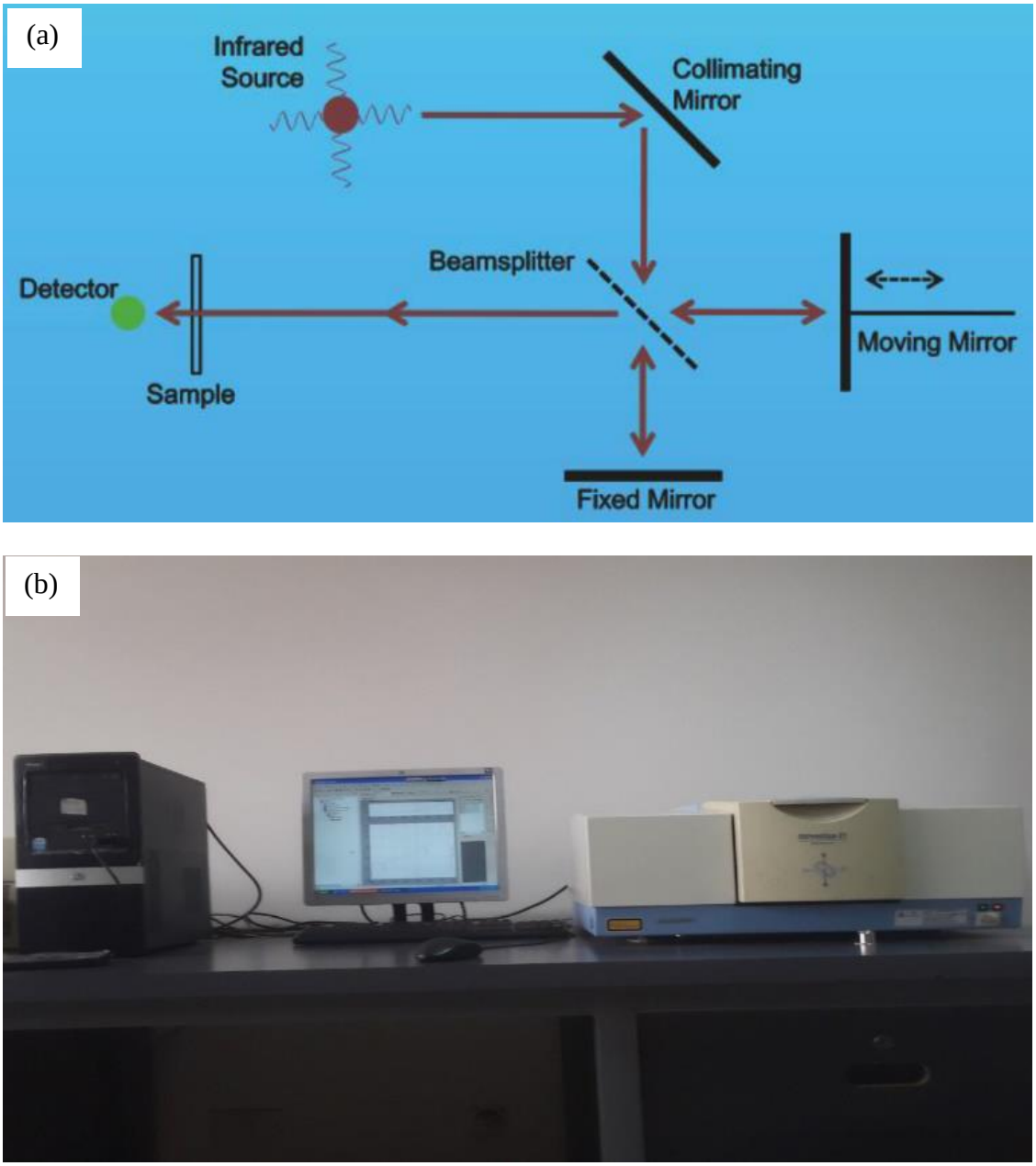

Figure 3.10: (a) Schematic illustration of an FTIR spectrometer. Adapted from [189] and (b) Photograph of the SHIMADZU FTIR spectrophotometer (IR Prestige-21).

3.4. Scanning Electron Microscope

To investigate microstructures of the samples, is a scientific instrument such as scanning electron microscope (SEM) is used. The major components of SEM are delineated in Figure 3.11 (a). An electron beam is generated in the electron gun, which is situated at the top of the column and contains a filament. The filament is a thin tungsten loop which serves as the cathode. Typically, voltage of 30 kV is applied to heat up the tungsten loop. The anode, which

is positive with regard to the filament, generates strong attractive forces for electrons that causes the electrons to move more quickly towards the anode. The anode attracts the electrons, which are then condensed by one or more condenser lenses and focused as a sharp point by the objective lens on the sample. In the electron optical column, the electrons beam passes via the paired scanning coils or paired deflector plates. By adjusting the voltage generated by the scan generator, the scan coils are energized and produce a magnetic field that deflects the beam both horizontally and vertically as it scans over a rectangular region of the sample surface [191]. Figure 3.11 (b) illustrates the photograph of SEM with major components identified. When the primary electrons interplay with the atoms of the sample they produce various signals e.g., secondary electrons, backscattered electrons, Auger electrons, X-rays, cathodoluminescence are produced (Figure 3.12) [192]. Among the various signal, three signals are important e.g., secondary electrons, backscattered electrons, and emitted X-rays. The secondary electrons play prime role to detect the microstructure of the sample. The backscattered electrons, which interact with the positively charged nucleus of the sample and scattered at lager angles, give compositional information. As the secondary electrons arrive at and penetrate the detector, they strike a scintillator. The scintillator emits flashes of light that are transformed into an electric current via photomultiplier and send to the cathode ray tube as a signal which creates a viewable and photographable image in monitor.

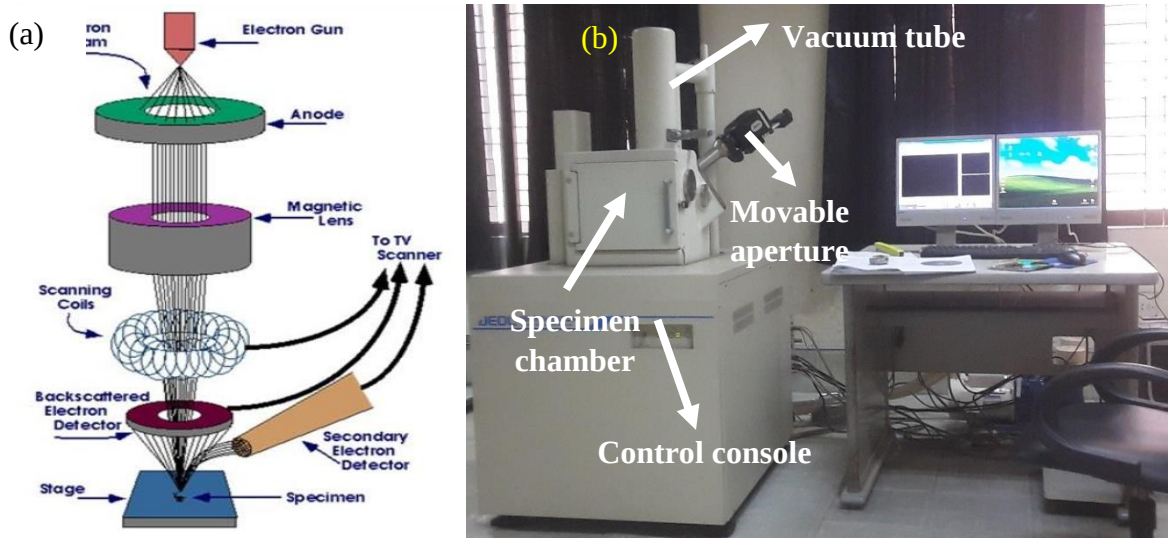

Figure 3.11: (a) Schematic diagram of electron gun column. Adapted from [191] and (b) Photograph of the JEOL SEM with major components identified.

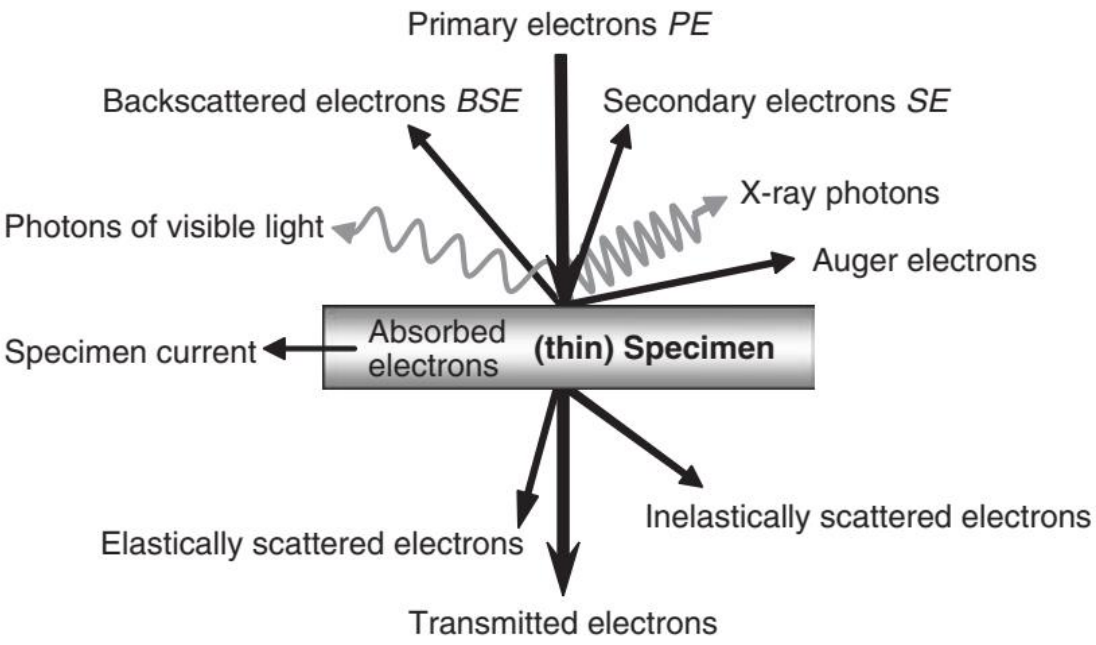

Figure 3.12: Schematic depiction of the emitted signals from the surface of the sample. Adapted from [192].

3.5. Electrical Characterization

3.5.1. Dielectric permittivity characteristics

The dielectric traits of ferroelectric and ferromagnetic phases and ferroelectromagnetic ceramic composites were investigated using high precision LCR meter (Figure 3.13). The complex electric permittivity of the samples was determined using the equation:

$$\varepsilon^* = \varepsilon' + j\varepsilon'' \quad [3.10]$$

, where ε' and ε'' the real and imaginary component of electric permittivity. The electric permittivity (ε') was otained employing the equation:

$$\varepsilon' = \frac{c_p \times t}{A \times \varepsilon_0} \quad [3.11]$$

, where c_p is the capacitance, t is the pellet specimen's thickness and A stands for electrode's cross-area.

Figure 3.13: Photograph of precision impedance analyzer (Wayne-Kerr, Model: 6500B)

3.5.2. AC electrical conductivity

AC conductivity of the samples has been achieved by the equation:

$$\sigma_{ac} = 2\pi f \varepsilon_0 \varepsilon' tan\delta \quad [3.12]$$

where ε_0 denotes the vacuum electric permittivity, $\varepsilon_0 = 8.854 \times 10^{-12} F/m$, f is the applied frequency, ε' stands for the real electric permittivity, and $\tan\delta$ is permittivity loss tangent represent by $tan\delta = \varepsilon''/\varepsilon'$.

3.5.3. Impedance and dielectrical modulus spectroscopy

The complex impedance of ferromagnetic and ferroelectric phases has been determined by the equation:

$$Z^* = Z' + iZ'' \quad [3.13]$$

, where Z' and Z'' represent the real and imaginary component of impedance.

The dielectrical modulus of ferromagnetic and ferroelectric phases has been calculated through the relation:

$$M^* = M' + iM'' = \frac{\varepsilon'}{\varepsilon'^2+\varepsilon''^2} + i\frac{\varepsilon''}{\varepsilon'^2+\varepsilon''^2} = \frac{1}{\varepsilon'(1+tan^2\delta)} + i\frac{tan\delta}{\varepsilon'(1+tan^2\delta)} \quad [3.14]$$

, where M' and M'' are the real and imaginary component of dielectrical modulus.

3.6. Magnetic characteristic characterization

3.6.1. Magnetic permeability and magnetic loss tangent

The magnetic properties (permeability, magnetic loss tangent, and Q-factor) of ferromagnetic phase and ferroelectromagnetic ceramic composites were also investigated using high precession impedance analyzer. The magnetic permeability (μ_i') is calculated using both the inductance (L) and inductance of the air core (L_0) by the relation: $\mu_i' = L/L_0$, L_0 is determined using the following equation [193]:

$$L_0 = \frac{\mu_0 N^2 t}{2\pi} ln\left(\frac{OD}{ID}\right) \quad [3.15]$$

where N represents the no. of wire turns on toroid samples, t is the toroid's thickness, μ_0 represents the magnetic permeability in air ($1.26 \times 10^{-6}\, H/m$), OD and ID are the outer and inner diameters of toroid samples. The magnetic loss tangent ($tan\delta_\mu$) is determined through the equation:

$$tan\delta_{\mu} = \mu_i''/\mu_i' \quad [3.16]$$

The Q-factor is estimated by the following equation:

$$\text{Q} - \text{factor} = \frac{1}{tan\delta_{\mu}} \quad [3.17]$$

, where $tan\delta_{\mu}$ is the magnetic loss tangent.

3.7. Vibrating Sample Magnetometer

To characterize magnetic traits of a material subject to Faraday's law of induction, a vibrating sample magnetometer (VSM) is used [194]. When a material is lodged in a uniform magnetic field (UMF) originated by an electromagnet, material vibrates within a UMF and the UMF magnetizes the material by tuning the various magnetic spins or magnetic domains with the field. The magnetization becomes greater as the uniform field becomes convalescent. The sample's magnetic dipole moment generates a magnetic field (magnetic stray field (MSF)) throughout the sample. As the sample is moved up and down, this MSF alters with time and could be detected by a group of pick-up coils which are mounted on the pole faces of the magnet. The alternating magnetic field of the pick-up coils produces an electric field in accordance with Faraday's law of induction. The magnetization of the sample is directly proportional to this induced current. So, the value of the induced current increases with magnetization. The illustrative depiction of a VSM is delineated in Figure 3.14 (a). The vibrating sample is vibrated in the magnetic field using a vibrator mechanism. Detection coils generates the signal voltage as a result of the changing flux coming from the vibrating sample. As sketched in Figure 3.14 (b), the sample is mounted onto a non-magnetic sample holder (glass rod). The sample plane is normal to the z-axis when measuring the in-plane hysteresis loop and normal to the x-axis when measuring the perpendicular hysteresis loop. Sample

becomes magnetized in the x-direction when revealed to an external magnetic field while vibrating in the z-direction. The time dependent flux was detected via a set of pick-up coils. A transimpedance amplifier and lock-in amplifier both amplify the induced current. A computer interface is connected to the various components. When a full cycle in the midst of a positive and negative saturating field is completed by the sweeping magnetic field, a hysteresis loop is produced. From the hysteresis loop, the magnetic properties are extracted [195].

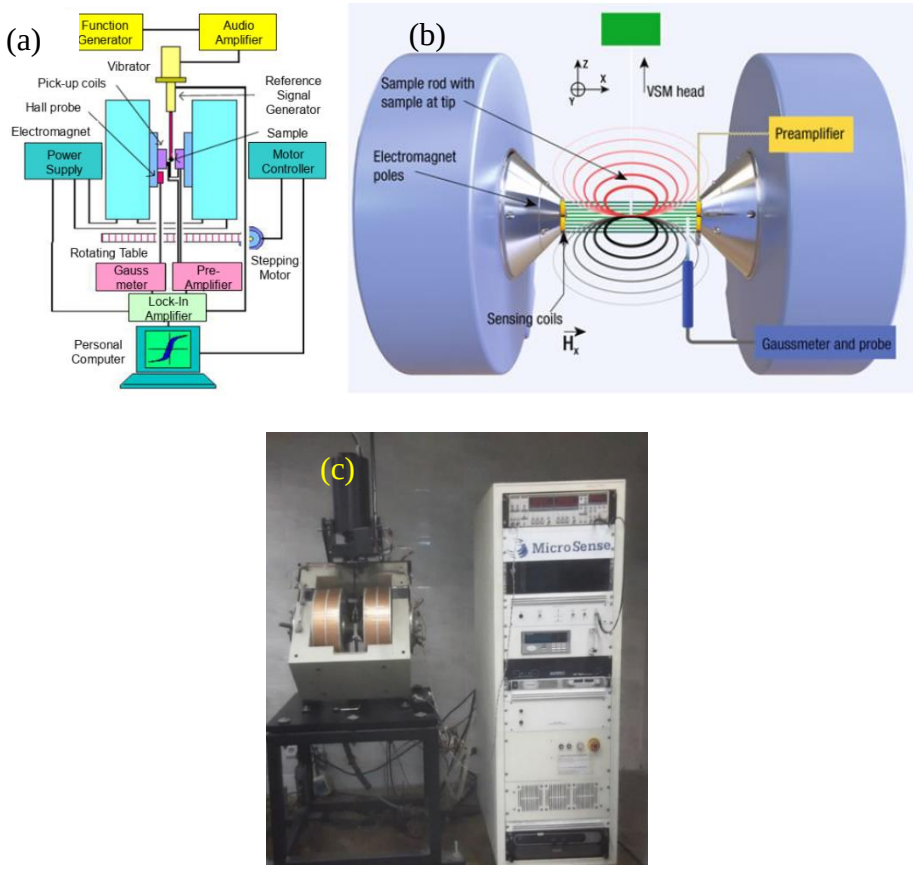

Figure 3.14: (a) System illustrative of a vibrating sample magnetometer. Adapted from [196], (b) Enlarged view showing the alignment (in-plane) of sample with respect to the magnets). Adapted from [195], and (c) Photograph of Micro-Sense Vibrating Sample Magnetometer (VSM).

3.8. Magnetoelectric characterization

The study of the magnetoelectric voltage coupling coefficient is an important parameter for fabricating the next generation multifunctional devices. Figure 3.15 depicts the experimental

set-up for measuring the magnetoelectric voltage coupling coefficient (α_{ME}). An electromagnet was used to develop DC magnetic of 8 kOe for biasing. The time dependent DC magnetic field was achieved using a DC power source. A Hall probe was used to determine the DC magnetic field. AC magnetic field of 8 Oe was overlapped onto the DC field. A Helmholtz coil used to produce AC field. Keithley 2000 multimeter was used to measure the AC magnetic field's value. The sample was lodged in the magnetic field with either its surface parallel to or perpendicular to the magnetic field's direction contigent upon whether the measurement was longitudinal or transverse [197]. A voltage (V) develops when ferroelectromagnetic ceramic composites are exposed to a magnetic field (H) [197]. Supposing

$$V = f(H) = Const. + \alpha H + \beta H^2 + \gamma H^3 + \delta H^4 + \cdots \quad [3.18]$$

$$\frac{dV}{dH} = \alpha + 2\beta H + 3\gamma H^2 + 4\delta H^3 + \cdots \quad [3.19]$$

When a small AC magnetic field $h = h_0 sin\omega t$ is overlapped with a DC bias field (H), the total field is [197]:

$H_{total} = H + h_0 sin\omega t$. Then $V = Const. + \alpha\,(H + h_0 sin\omega t) + \beta(H + h_0 sin\omega t)^2 + \gamma(H + h_0 sin\omega t)^3 + \delta(H + h_0 sin\omega t)^4 + \cdots = \frac{1}{8}[(Const. + 4\beta h_0^2 + 3\delta h_0^4 + 8\alpha H + 12\gamma h_0^2 + 8\beta H^2 + 24\delta h_0^2 H^2 + 8\gamma H^3 + 8\delta H^4) + (8\alpha h_0 + 6\gamma h_0^3 + 16\beta h_0 H + 24\delta h_0^3 H + 24\gamma h_0 H^2 + 32\delta h_0 H^3 sin\omega t) + (-4\beta h_0^2 - 4\delta h_0^4 - 12\gamma h_0^2 H - 24\delta h_0^2 H^2) cos2\omega t + (-2\gamma h_0^3 - 8\delta h_0^3 H) sin3\omega t + \delta h_0^4 cos4\omega t + \cdots]$. [3.20]

The lock-in amplifier output voltage V_{out} is [197]:

$V_{out} = \frac{1}{8}(8\alpha h_0 + 6\gamma h_0^3 + 16\beta h_0 H + 24\delta h_0^3 H + 24\gamma h_0 H^2 + 32\delta h_0 H^3) = \frac{H^4}{8}\left[\frac{8\alpha}{H^3}\left(\frac{h_0}{H}\right) + \frac{6\gamma}{H}\left(\frac{h_0}{H}\right)^3 + \frac{16\beta}{H^2}\left(\frac{h_0}{H}\right) + 24\delta\left(\frac{h_0}{H}\right)^3 + \frac{24\gamma}{H}\left(\frac{h_0}{H}\right) + 32\delta\left(\frac{h_0}{H}\right)\right]$ [3.21]

When $\left(\frac{h_0}{H}\right) \ll 1$, we can neglect the high order terms in $\left(\frac{h_0}{H}\right)$, and the output voltage becomes:

$$V_{out} = \frac{H^4}{8}\left(\frac{8\alpha}{H^3} + \frac{16\beta}{H^2} + \frac{24\gamma}{H} + 32\delta\right)\left(\frac{h_0}{H}\right) = h_0(\alpha + 2\beta H + 3\gamma H^2 + 4\delta H^3)$$

$$= h_0\left(\frac{dV}{dH}\right) \quad [3.22]$$

Therefore, the magnetoelectric voltage coupling coefficient is [197]:

$$\alpha_{ME} = \frac{dE}{dH} = \frac{1}{d}\frac{dV}{dH} = \frac{V_{out}}{h_0 \times d} \quad [3.23]$$

, where d is the thickness of the sample.

Therefore, by checking the output voltage (V_{out}) that is generated across the ferroelectromagnetic ceramic composites, we were determined the magnetoelectric voltage coupling coefficient [197].

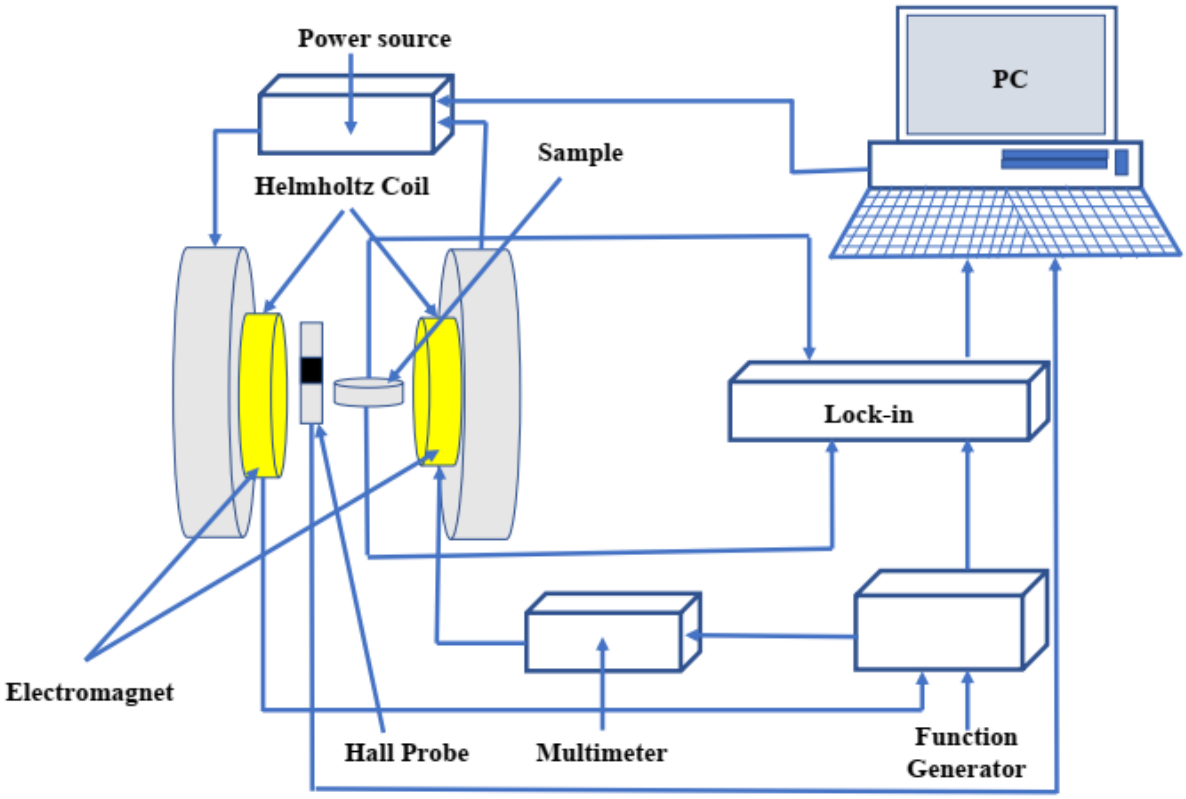

Figure 3.15: Block diagram of the experimental setup of the magnetoelectric measurement. Adapted from [197].

Chapter Four: Experimental Results and Discussions

4.1. Probing the effects of sintering temperature on the electromagnetic traits of $Ni_{0.25}Cu_{0.13}Zn_{0.62}Fe_2O_4$ system

In this section, the sintering temperature (T_s) dependent structural, microstructural, elastic, and electrical, magnetic characteristics of $Ni_{0.25}Cu_{0.13}Zn_{0.62}Fe_2O_4$ (NCZFO) ferrites are desciphered.

4.1.1. Crystallographic characteristics

Figure 4.1 (a) depicts the XRD profile of the $Ni_{0.25}Cu_{0.13}Zn_{0.62}Fe_2O_4$ (NCZFO) ceramic annealed at various T_s. It is possible to say that the annealed samples possess diffraction peaks related to the (111), (220), (311), (222), (400), (422), (511), and (440) planes, which is associated with the emergence of a spinel skeleton of a space group $Fd\bar{3}m$ with no any undesirable phases and legitimately coincides with the standard ICSD-Inorganic Crystal Structure Database (01-081-8134). It is apparent that as T_s increases, the peaks broaden. To clarify the impact of T_s on the crystallite diameter (D_{hkl}), we calculate the crystallite diameter (D_{hkl}) employing the Debye-Scherrer equation [183]:$D_{hkl} = \frac{0.9\lambda}{\beta_{hkl} \times cos\theta_{hkl}}$, where λ denotes the X-ray's wavelength, θ_{hkl} denotes the diffraction angle, β_{hkl} denotes the full width at half maximum (FWHM). Table 4.1 displays the crystallite diameter (D_{hkl}) values for samples annealed at T_s. The diameter of the crystallites initially drops at 1050 °C, then grows at 1100 °C, then drops further to a maximum of 1200 °C, and lastly grows at 1250 °C. Particle coalescence via solid-state diffusion is believed to have led to the rise in crystallite diameter at 1100 and 1250 °C. By reducing the surface area of the particles in this system, the free energy is diminished. The size of the crystallite is bigger when T_s is lower than when it is large. This demonstrates unequivocally that when T_s rises, crystal formation is reduced. Therefore, it may be claimed that a high Ts enhances crystallinity while also reducing crystallite diameter. The

lattice constant (a) is calculated employing the formula: $a = d_{hkl}(h^2 + k^2 + l^2)^{1/2}$, where h, k, and l denote the Miller indices and d_{hkl} denotes interplanar spacing.

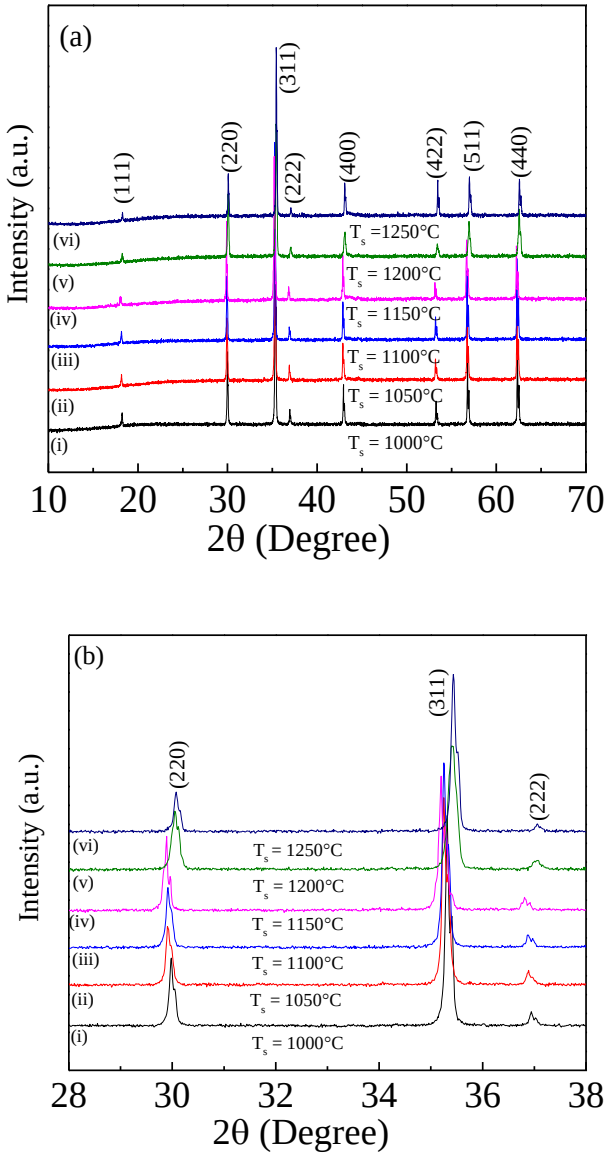

Figure 4.1: (a) XRD profiles of NCZFO ceramics, and (b) Local enlargement XRD peaks of NCZFO ferrites annealed for 5 h at various T_s: (i) 1000, (ii) 1050, (iii) 1100, (iv) 1150, (v) 1200, and (vi) 1250 ºC.

The location of the strongest peak (311), as seen in Figure 4.1 (b), changes marginally to smaller 2θ values to a maximum of 1150 °C before rising to greater 2θ values at 1200 and 1250 °C. It demonstrates how T_s changes the lattice constant. Table 4.1 displays the value of the lattice constants with T_s. Table 4.1 shows that when the T_s rises from 1000 to 1050 °C, the

lattice constant drops. The crystallization development continues modestly at low T_s. Thus, the lattice may experience surface flaws which lead to shrinkage of the lattice. Additionally noticed is the reality that the lattice constant rises at 1100 °C and then drops as T_s goes from 1150 to 1250 °C. The oxidation-reduction procedure, the cation's reallocation amongst the tetrahedrally and octahedrally coordinated sites, and zinc depletion from the sample are the root cause of an increase and reduction of the lattice constant with the T_s [198]. Because the Fe^{2+} ions have a greater ionic radius (0.76 Å) than the Fe^{3+} ion (0.64 Å), the curtailment of iron from ferric to ferrous throughout the course of sintering might be responsible for an increase in the lattice constant at 1100 °C. The development of Ni^{3+} (0.62 Å), leading to the lattice constant to drop, essentially leads the lattice constant to be reduced at higher T_s. The bulk density was determined using the formula: $\rho_{bulk} = \frac{mass}{mr^2t}$, where t and r express the thickness and radius of the manufactured pellet specimens and shown in Table 4.1. As can be recognized from Table 4.1, the value of ρ_{bulk} is inversely related to the T_s. The ρ_{bulk} value always rises with rising T_s to a maximum of 1150 °C, and then ρ_{bulk} drops with growing T_s after that. As T_s rises the value of ρ_{bulk} reduces, which corresponds to the enhanced intragranular porosity driven on by irregular grain development. The theoretical density (ρ_{X-ray}) at various T_s was computed using formula: $\rho_{X-ray} = \frac{8M_W}{N_A \times a^3}$, where M_W denotes the molecular mass and N_A denotes the Avogadro's number and shown in Table 4.1. The value of ρ_{X-ray} is seen to initially rise at 1050 °C, then drop at 1100 °C, and then enhance more with rising T_s. The lattice constant, which drops around 1050 °C, is responsible for the rise in ρ_{X-ray} value. The lattice constant may also be responsible for the rise in ρ_{X-ray}. It is evident that the annealed samples' ρ_{X-ray} value is higher than that of the comparable bulk. The existence of holes within the annealed samples is the root cause of the disparity in the midst of the ρ_{X-ray} and ρ_{bulk} [199]. The porosity is determined employing the formula: $P(\%) = \frac{\rho_{X-ray} - \rho_{bulk}}{\rho_{X-ray}} \times 100\%$ and is

shown in Table 4.1. It is also obvious that lowering porosity while raising T_s results in a rise in ρ_{bulk} value. This is due to the simple reason that when T_s rises, grain development takes place segregating the intergranular gaps and results in a denser sample [200]. Figure 4.2 illustrates how P (%),ρ_{X-ray}, and ρ_{bulk} rely on T_s. With rising T_s, it has been found that the values of ρ_{bulk} and P (%) exhibit opposing patterns. This demonstrates the sintering process' rapid densification quite clearly. The development of grains and the density are closely connected, according to Lange and Kellet [201]. The occurrence of pores inside the grains or at grain borders is believed to be the root cause of the drop in density in the midst of the 1200 and 1250 °C. The jump lengths in the midst of the magnetically active ions at the tetrahedrally coordinated (A)-site and octahedrally coordinated [B]-site at various T_s were determined using the formulae: $L_A = \frac{a\sqrt{3}}{4}$ and $L_B = \frac{a\sqrt{2}}{4}$, where L_A denotes the hop length of the tetrahedrally coordinated sites and L_B denotes the hop length of the octahedrally coordinated sites. Table 4.1 displays the values of L_A and L_B at various T_s. The tetrahedrally coordinated (A) site radii (r_A), octahedrally coordinated (B) site radii (r_B), tetrahedrally and octahedrally coordinated bond lengths (d_{AX} and d_{BX}), tetrahedrally coordinated edge, shared and unshared octahedrally coordinated edge (d_{AXE} , d_{BXE} , d_{BXEU}) were determined utilizing the lattice constant 'a', oxygen positional factor 'u' (u = 0.381Å), radius of O^{2-} ion radius R_O (1.32Å) and the formulae [202, 203]: $r_A = (u - 0.25)a\sqrt{3} - R_O$, $r_B = (0.625 - u)a - R_O$, $d_{AX} = a\sqrt{3}(u - 0.25)$, $d_{AXE} = a\sqrt{2}(2u - 0.5)$, $d_{BX} = a\left[3u^2 - \left(\frac{11}{4}\right)u + \left(\frac{43}{64}\right)\right]^{1/2}$, $d_{BXE} = a\sqrt{2}(1 - 2u)$, and $d_{BXEU} = a\left[4u^2 - 3u + \left(\frac{11}{16}\right)\right]^{1/2}$. The determiend tetrahedrally coordinated (A)-site radius (r_A), octahedrally coordinated (B)-site radius (r_B), tetrahedrally and octahedrally coordinated bond lengths (d_{AX} and d_{BX}), tetrahedrally coordinated edge, shared and unshared octahedrally coordinated edge (d_{AXE} , d_{BXE} , d_{BXEU}) are shown in Table 4.2. It can be identified from Table 4.2 that the parameters associated with the structure such as tetrahedrally

coordinated (A) site radius (r_A), octahedrally coordinated (B) site radius (r_B), tetrahedrally and octahedrally coordinated bond length d_{AX} and d_{BX}, tetrahedrally coordinated edge, shared and unshared octahedrally coordinated edges (d_{AXE} , d_{BXE} , d_{BXEU}) boosts with T_s. The shrinking distance in the midst of magnetic ions is the factor that causes the declining trend of r_A and r_B with T_s.

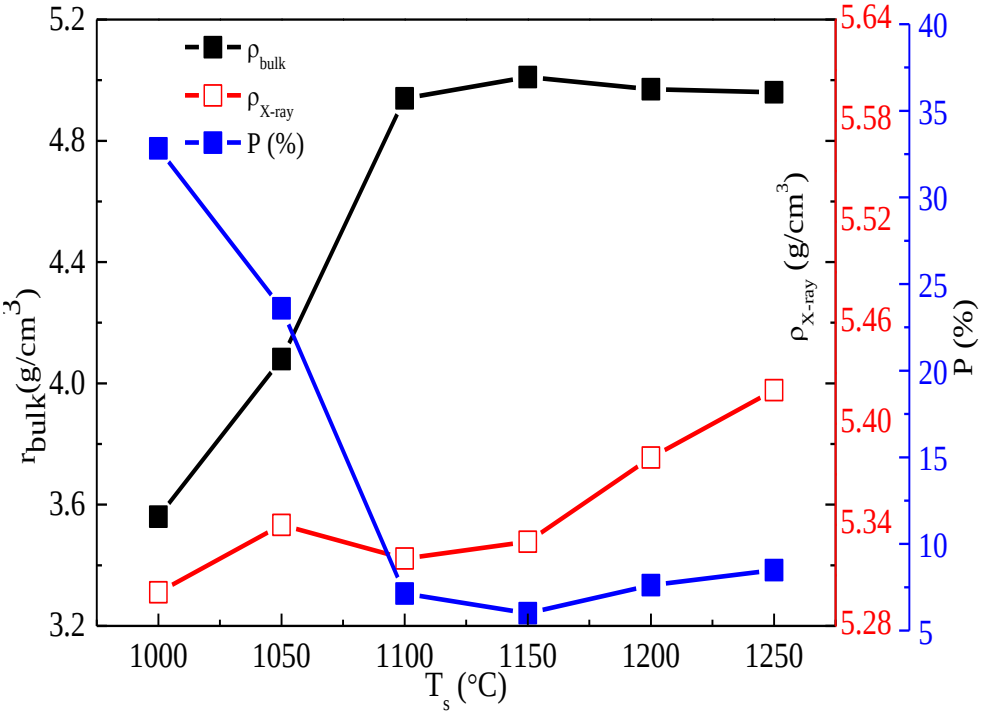

Figure 4.2: Evolution of bulk density (ρ_{bulk}), theoretical density (ρ_{X-ray}), and porosity (P) with T_s of NCZFO ferrites.

Table 4.1. Lattice constant (a), cell volume (V), crystallite diameter (D), bulk density (ρ_{bulk}), theoretical density (ρ_{X-ray}), porosity P (%), grain diameter and jumping lengths (L_A and L_B) of NCZFO ferrite annealed at various T_s.

T_s(ºC)	a (Å)	V (Å^3)	D_{311} (nm)	ρ_{bulk} (g/cm^3)	ρ_{X-ray} (g/cm^3)	P %	D_{SEM} (µm)	L_A (Å)	L_B (Å)
1000	8.4324	599.59	71	3.56	5.30	33	0.98	3.65	2.98
1050	8.4110	595.04	54	4.08	5.34	24	1.74	3.64	2.97
1100	8.4230	597.59	69	4.94	5.32	7	2.80	3.65	2.98
1150	8.4141	595.69	58	5.01	5.33	6	6.08	3.64	2.98
1200	8.3873	590.02	28	4.97	5.38	8	15.58	3.63	2.97
1250	8.3707	586.52	53	4.96	5.42	9	82.40	3.63	2.96

Table 4.2. Tetrahedrally and octahedrally coordinated site radii (r_A and r_B), tetrahedrally and octahedrally coordinated bond lengths (d_{AX} and d_{BX}), tetrahedrally coordinated edge, shared and unshared octahedrally coordinated edges (d_{AXE}, d_{BXE}, d_{BXEU}) of NCZFO ferrite annealed at various Ts

(T_S)	r_A (Å)	r_B (Å)	d_{AX} (Å)	d_{BX} (Å)	d_{AXE} (Å)	d_{BXE} (Å)	d_{BXEU} (Å)
1000	0.5933	0.7375	1.9133	2.0587	3.1244	2.8382	2.9830
1050	0.5884	0.7323	1.9084	2.0535	3.1165	2.8310	2.9755
1100	0.5912	0.7352	1.9112	2.0565	3.1209	2.8350	2.9797
1150	0.5891	0.7330	1.9091	2.0543	3.1176	2.8320	2.9765
1200	0.5831	0.7265	1.9031	2.0477	3.1077	2.8230	2.9671
1250	0.5793	0.7225	1.8993	2.0437	3.1015	2.8174	2.9612

4.1.2. Micromorphological and elemental investigation

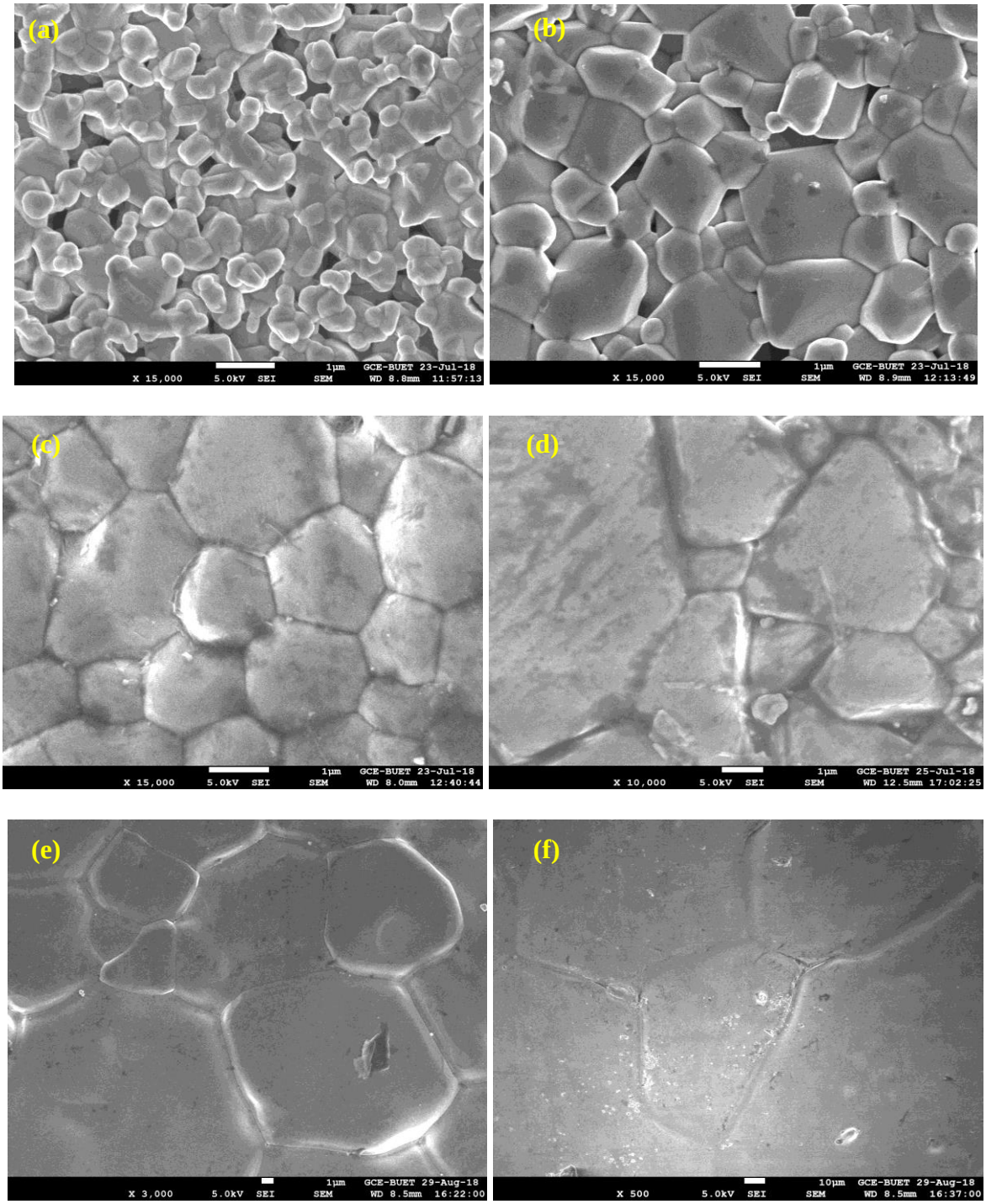

Figure 4.3: Micromorphological structures of NCZFO ferrites annealed for 5 h at various T_s: (a) 1000, (b) 1050, (c) 1100, (d) 1150, (e) 1200, and (f) 1250 ºC.

Effects of sample's mean grain diameter along with grain form on magnetic characteristics can be explored in part using micromorphological structures investigations. Figure 4.3 (a-f) displays representative SEM pictures of NCZFO ferrites annealed for 5 h each at the following T_s: 1000, 1050, 1100, 1150, 1200, and 1250 °C. At 1000 °C, the microstructure of a sample is readily apparent in the SEM picture [Figure 4.3 (a)] as having tiny grains and open porosity, proving that this temperature is insufficient for effectively generating the structure. In comparison to 1000 °C, the sample's SEM pictures at 1050 °C revealed a higher grain diameter with open porosity (inter-particle porosity). It becomes sense to infer that the drop in bulk density is triggered by the open pores. A clearly established crystal skeleton [Figure 4.3 (c)] could be observed by SEM at 1100 °C, and the microstructure was well-homogenized having an even distribution of grain diameters. SEM micromorphology unfolded unusual grain development with closed holes (intragranular pores) when T_s ascended from 1150 to 1200 °C and larger [Figure 4.3 (d, e)]. Due to the emergence of the liquid phase, abnormal grain development was more noticeable for closed pores at 1250 °C [Figure 4.3 (f)]. Multiple intragranular pores could serve as a substantial demagnetization source, aggravating the domain wall movement circumstances inside the NCZFO ferrite grain volume. As a result, saturation magnetization deteriorates when there are closed pores [204]. It is evident that several grains have been combined into one big grain [205]. Mean grain diameter was determined using the formula [206]: $D_{SEM} = \frac{1.5 \times L}{M \times N}$, where L denotes the absolute distance of the examination line, M denotes the enlargement and N denotes the whole amount of intercepts in the SEM images and shown in Table 4.1. With raising T_s, it is shown that the grain diameter continually rises, going from < 1 micrometer at 1000 °C to > 82 micrometer at 1250 °C. It can be anticipated that the grain diameter would rise as we increase T_s in the solid-phase sintering procedure because the coefficient of diffusion enhances with rising T_s, generating fast grain border movement and encouraging grain expansion [207]. The diffusion of oxygen vacancies is the primary basis for the ferrite densification process [208]. According to the literature, Fe^{3+}

ions are converted to Fe^{2+} ions at higher sintering temperatures, which creates oxygen vacancies and causes enhanced densification with bigger grains [209]. Fe^{2+} ions also rapidly diffuse, which promotes grain formation [210]. All of these variables affect the grain diameter of samples annealed at 1150, 1200, and 1250 °C through affecting the microstructure of the samples. The discrepancies in the midst of the crystallite diameter estimated from the XRD data and the grain diameter persuaded by the SEM picture employing the linear intercept approach is plainly visible. This indicates that the grain diameter derived from the SEM pictures is larger than the crystallite diameter derived from the XRD data. Due to internal stresses or structural flaws, the particles are made up of many crystallites, which accounts for the anomalous in the midst of these two parameters [211]. The chemical constitution at various T_s is clarified using energy dispersive X-ray analysis (EDX). Figure 4.4 (a-f) displays a typical EDAX spectrum NCZFO. According to the original stoichiometry, the spectrum solely exhibits the peaks associated with the components Ni, Cu, Zn, Fe, and O, with pure NCZFO ferrites forming without appreciable component loss or evidence of extra elements within detection limits [212]. The figure inset of Figure 4.4 (a-f) displays the masses of the chemical composition and atomic percentages of the Ni, Cu, Zn, Fe, and O ions in the investigated samples.

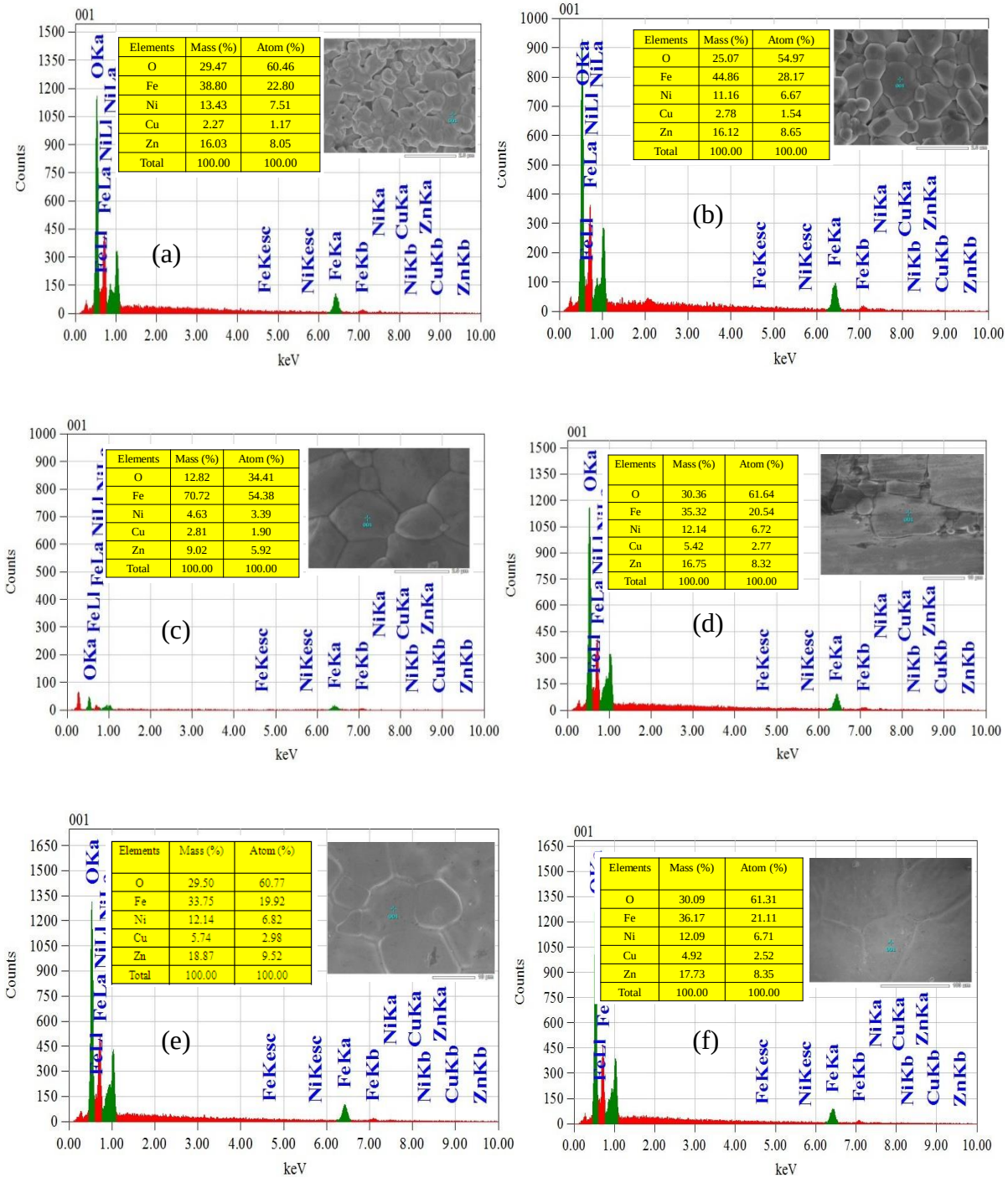

Figure 4.4: EDS spectra of NCZFO ferrites annealed for 5 h at various T_s: (a) 1000, (b) 1050, (c) 1100, (d) 1150, (e) 1200, and (f) 1250 °C.

4.1.3. Fourier transform infrared spectroscopic investigation

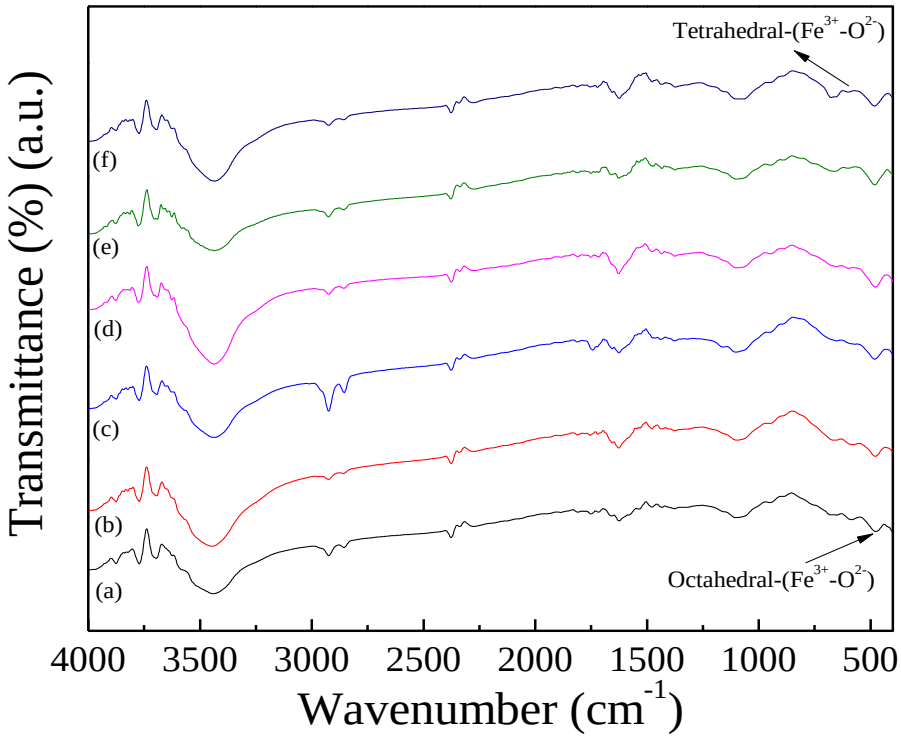

Figure 4.5: FTIR spectra of NCZFO ferrites annealed for 5 h at various T_s: (a) 1000, (b) 1050, (c) 1100, (d) 1150, (e) 1200, and (f) 1250 °C.

Figure 4.5 displays the room-temperature 400-4000 cm^{-1} Fourier transform infrared (FTIR) spectra of the NCZFO system annealed at different T_s. The wavenulongmber band showing at 600 cm^{-1}, which is higher wavenumber band (ν_1), has been attributed to the stretching forms of the oxygen-tetrahedron and Fe^{3+}-O^{2-}, whilst the wavenumber band showing at 400 cm^{-1}, which is lower wavenumber band (ν_2), is related to the vibrations caused by bending of the oxygen-octahedron and Fe^{3+}-O^{2-} [134, 213]. Table 4.3 displays the higher wavenumber band (ν_1) and lower wavenumber band (ν_2) values for samples annealed at various T_s. In the current instance, the bands ν_1 are close together at different T_s of 588.29 cm^{-1} for 1000 °C, 580.57 cm^{-1} for 1050 °C, 570.93 cm^{-1} for 1100 °C, 596.62 cm^{-1} for 1150 °C, 595.38 cm^{-1} for 1200 °C, and 600.00 cm^{-1} for 1250 °C, which demonstrates a change of ν_1 toward higher wavenumber with a further rise in T_s.

The lower wavenumber band ν_2 seems close to at 478.35 cm^{-1} for 1000 °C, 478.35 cm^{-1} for 1050 °C, 480.28 cm^{-1} for 1100 °C, 478.35 cm^{-1} for 1150 °C, 482.20 cm^{-1} for 1200 °C and 482.20 cm^{-1} for 1250 °C that stays unchanged for 1050 °C and afterwhich it boosts for 1100 °C and reduces for 1150 °C and ultimately it stays unchanged for 1200 and 1250 °C. The improvement in crystallization of the sample is clearly seen by the movement of ν_1 and ν_2 toward higher frequency with T_s [214]. Since the manufacturing procedure, grain diameter, Ts, and the arrangement of cations at octahedrally and tetrahedrally coordinated sites are all strongly influenced by T_s, the fluctuation of the bands ν_1 and ν_2 with T_s is predicted [215]. In general, the disparity in bond length that exists in the midst of the octahedrally coordinated site (0.199 nm) and the tetrahedrally coordinated site (0.189 nm) is the factor that creates the mismatch in the higher wavenumber band (ν_1) and the lower wavenumber band (ν_2) absorption [216]. The out of plane bending vibrational modes of the O-H stretched absorbed water molecules are what cause the pronounced band to form at 1101.35 cm^{-1} for 1000 °C, 1097.50 cm^{-1} for 1050 °C, 1101.35 cm^{-1} for 1100 °C, 1097.50 cm^{-1} for 1150 °C, 1099.43 cm^{-1} for 1200 °C, and 1070.49 cm^{-1} for 1250 °C [217]. The peak for the C = C stretched bond is seen at 1751.36 cm^{-1} for 1000 °C, 1747.20 cm^{-1} for 1050 °C, 1741.72 cm^{-1} for 1100 °C, 1747.20 cm^{-1} for 1150 °C, 1751.36 cm^{-1} for 1200 °C, and 1753.29 cm^{-1} for 1250 °C [218]. The stretching and bending vibrational modes of the H-O-H bonding are accountable for the wavenumbers which correspond to 1624.06 cm^{-1} for 1000 °C, 1625.99 cm^{-1} for 1050 °C, 1625.99 cm^{-1} for 1100 °C, 1625.99 cm^{-1} for 1150 °C, 1625.99 cm^{-1} for 1200 °C, and 1625.99 cm^{-1} for 1250 °C. The chemical adsorption of H_2O on the surfaces has been shown here [219-221]. The extremely faint band in the vicinity of 2376.30 cm^{-1} for 1000 °C, 2376.30 cm^{-1} for 1050 °C, 2376.30 cm^{-1} for 1100 °C, 2376.30 cm^{-1} for 1150 °C, 2378.23 cm^{-1} for 1200 °C, and 2376.30 cm^{-1} for 1250 °C suggests the existence of adsorbed or ambient CO_2. Hydrogen bonding is believed to be the reason for the low intensity frequency band that could be seen at 2924.09 cm^{-1} for 1000 °C, 2924.09 cm^{-1} for 1050 °C, 2924.09 cm^{-1} for 1100 °C, 2924.09 cm^{-1} for 1150 °C, 2926.01 cm^{-1}

for 1200 °C, and 2929.09 cm^{-1} for 1250 °C [222]. The vibrations caused by the stretched absorbed water upon the specimen's surface are accountable for the existence of the broad bands at 3439.08-3874.99 cm^{-1} for 1000 °C, 3448.72-3974.99 cm^{-1} for 1050 °C, 3435.22-3772.76 cm^{-1} for 1100 °C, 3437.15-3774.69 cm^{-1} for 1200 °C, and 3433.29-3772.76 cm^{-1} for 1250 °C. It is widely recognized that the force constant (K) and the vibration frequency are inversely related. As a result, band shifts at the frequencies of ν_1 and ν_2 suggest the force constants are shifting. The force constants (K_T and K_O) for the tetrahedrally coordinated (A) site and the octahedrally coordinated (B)-site were determined using the formula [223, 224]: $K_{T/O} = 4\pi^2 c^2 \nu_{1/2}^2 \mu$, where K denotes the force constant, c denotes the speed of light, ν denotes the tetrahedrally or octahedrally coordinated sites vibrational frequency and μ is the reduced mass [225] and are shown in Table 4.3. The Debye temperature (Θ_{DW}) due to Waldron model at various T_s was determined using the formula [226-228]:

$$\Theta_{DW} = \frac{\hbar c \nu_{mean}}{k_B} = 1.438 \nu_{mean},$$

where, h expresses Planck's constant, c expresses the spped of light and $\nu_{mean} = \frac{\nu_1 + \nu_2}{2}$ is the mean frequency of the main band positioned at tetrahedrally and octahedrally coordinated sites, and is shown in Table 4.3.

Table 4.3. FTIR wavenumber bands, force constants (K_T and K_O) and ($\nu_1 - \nu_2$) difference and Debye temperature based on Waldron (Θ_{DW}) of NCZFO ferrite at various T_s.

T_s(°C)	ν_1 (cm^{-1}) (A-site)	ν_2 (cm^{-1}) (B-site)	ν_{mean} (cm^{-1})	$K_T \times 10^5$ (dynes/cm)	$K_O \times 10^5$ (dynes/cm)	$K_{mean} = \frac{K_T + K_O}{2}$ $\times 10^5$ (dynes/cm)	$\nu_1 - \nu_2$ (cm^{-1})	Θ_{DW} (K)
1000	588.29	478.35	533.32	2.54	1.68	2.11	109.94	767
1050	580.57	478.35	529.46	2.47	1.68	2.08	102.22	761
1100	570.93	480.28	525.61	2.39	1.69	2.04	90.65	756
1150	596.62	478.35	537.49	2.61	1.68	2.15	118.29	773
1200	595.38	482.20	538.79	2.60	1.70	2.15	113.18	775
1250	600.00	482.20	541.10	2.64	1.70	2.17	117.18	778

4.1.4. Elastic characteristics

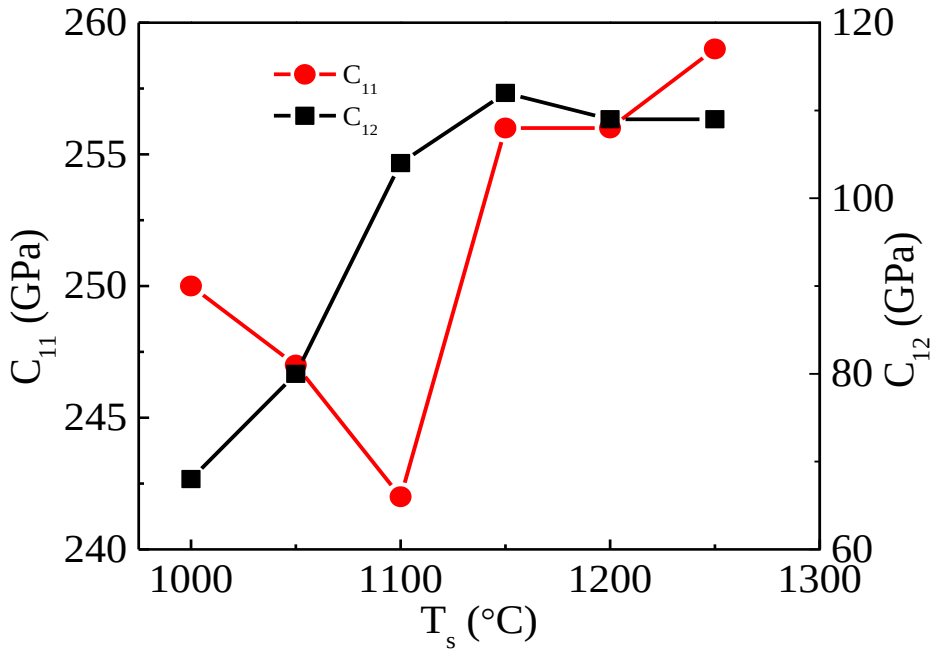

Figure 4.6: Evolution of the stiffness constants (C_{11} and C_{12}) with T_s of NCZFO ferrite.

The FTIR technique may be applied to figure out the elastic traits of NCZFO ferrites annealed at various T_s. The stiffness constants (C_{11} and C_{12}) were determined using the formulae [226]: $C_{11} = \frac{K_{average}}{a}$ and $C_{12} = \frac{C_{11} \times \sigma}{(1-\sigma)}$, where $K_{average}$ denotes the mean force constant ($K_{average} = \frac{K_T + K_O}{2}$), a denotes the lattice constant, σ denotes the Poisson ratio: $\sigma = 0.324(1 - 1.043 \times P)$, P denotes the porosity. Table 4.4 provides the magnitudes of the elastic stiffness constants C_{11} and C_{12} at various T_s. Figure 4.6 shows how the elastic stiffness constants C_{11} and C_{12} change with T_s. The stiffness constant C_{11} may be shown to drop to a maximum of 1100 °C and then improve as Ts rises further, while the stiffness constant C_{12} may rise to a maximum of 1150 °C and then drop as T_s rises further. The changing process, during which the lattice's volume grows, may be the root cause of the decline in C_{11} and C_{12}values [229]. C_{11} and C_{12} value changes strongly suggest that the crystallization process improves as T_s changes. In general, stiffness constants are significantly influenced by the characteristics of both of the components, such as the atomic bond strength and force constant.

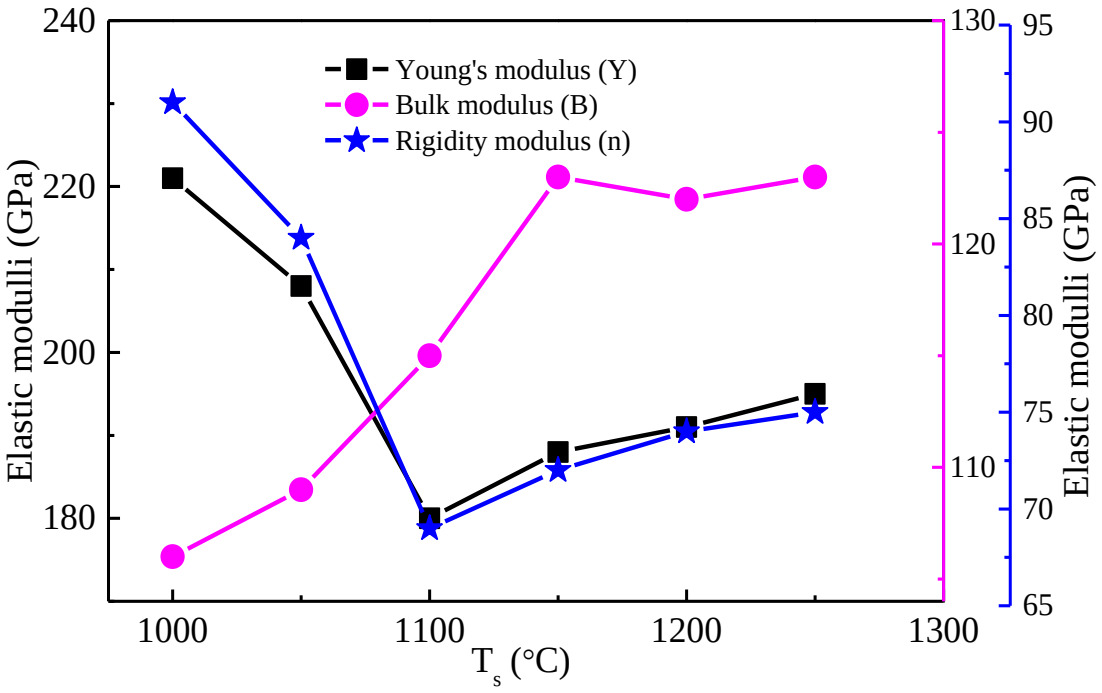

Figure 4.7: Evolution of the elastic constants with T_s of NCZFO ferrite.

The reducing strength of atomic bonds in the midst of Ni^{2+}, Cu^{2+}, Zn^{2+}, Fe^{3+}, and O^{2-} ions with rising T_s can be utilized to clarify the reduction in C_{11} and C_{12} values [229].Young's modulus (Y), rigidity modulus (n) and bulk modulus (B) with various T_s were determined using the formuale [226, 230]: $Y = \frac{(C_{11}-C_{12})(C_{11}+2C_{12})}{(C_{11}+C_{12})}$, $n = Y/2(1+\sigma)$, and $B = (C_{11}+2C_{12})/3$, and are shown in Table 4.4. Figure 4.7 depicts the fluctuation of elastic constants with T_s. Table 4.4 and Fig. 4.7 show that the elastic and rigidity modulus values drop to a maximum of 1100 °C and rise when T_s is raised further. On the reverse hand, when the T_s rises, the bulk modulus value rises. A boost in atomic bonding strength is what generates a boost in moduli of elasticity [231]. The longitudinal velocity (V_l) and transversal velocity (V_s) were determined employing the formulae [232]: $V_l = \left(C_{11}/\rho_{X-ray}\right)^{1/2}$ and $V_s = \left(n_0/\rho_{X-ray}\right)^{1/2}$ where n_0 denotes the pore-free rigidity modulus and shown in Table 4.4.

The density of the ferrite substance has a significant impact on the moduli of elasticity. The achieved moduli of elasticity of the sample having pores are less than those of the sample having no pores because the ferrite under examination was porous. It is necessary to take into consideration for zero porosity while computing the moduli of elasticity. Zero porosity coorection of the moduli of elasticity was done employing the formulae of Hasselman and Fulrath [130] and Ledbetter and Datta [131]: $\frac{1}{Y_0} = \frac{1}{Y}\left[1 - \frac{3P(1-\sigma)(9+5P)}{2(7-5P)}\right]$, $B_0 = \frac{Y_0 n_0}{3(3n_0 - Y_0)}$, $\sigma_0 = \frac{Y_0}{2n_0} - 1$, and $\frac{1}{n_0} = \frac{1}{n}\left[1 - \frac{15P(1-\sigma)}{(7-5P)}\right]$ and $n_0 = \left(\frac{1}{2A_1}\right)\left[-A_2 + (A_2^2 - 4A_1A_3)^{\frac{1}{2}}\right]$, $B_0 = \frac{(4n_0B)}{[4(1-P)(n_0-3PB)]}$, and $Y_0 = \frac{9B_0n_0}{3B_0+n_0}$; where $A_1 = \left(\frac{8}{3}\right)(1-P), A_2 = (3-2P)B - \left(\frac{8}{3} + 4P\right)n$ and $A_3 = -3(1+P)Bn$. Table 4.5 provides zero-porosity corrected moduli of elasticity (Y_0), B_0, n_0), and Poisson ratio (σ_0). As seen in Table 4.5, the modulus of elasticity values drop as T_s rises. The mean elastic wave velocity (V_m) was achieved using the formula [233]: $V_m = \left[\frac{1}{3}\left(\frac{2}{V_s^3} + \frac{1}{V_l^3}\right)\right]^{-1/3}$. Figure 4.8 illustrates how elastic wave velocities (V_l , V_s and V_m) vary as T_s rises. It can be seen that these wave velocities reduce as T_s rises to a maximum of 1100 °C and then grow as T_s keeps rising.

Table 4.4. Elastic stiffness constants (C_{11} and C_{12}), longitudinal velocity (V_l), transversal velocity (V_s) and mean wave velocity (V_m), moduli of elasticity (Y, B, n), Poisson's ratio (σ) and Debye temperature (Θ_{DA}) of NCZFO ferrite at various T_s.

T_s (°C)	C_{11} (GPa)	C_{12} (GPa)	V_l (m/s)	V_s (m/s)	V_m (m/s)	Y (GPa)	B (GPa)	n (GPa)	σ	Θ_{DA} (K)
1000	250	68	6868	7040	6981	221	106	91	0.21	943
1050	247	80	6801	5399	5737	208	109	84	0.24	777
1100	242	104	6745	3880	4309	180	115	69	0.30	583
1150	256	112	6930	3910	4349	188	123	72	0.30	589
1200	256	109	6898	4001	4440	191	122	74	0.30	603
1250	259	109	6913	4071	4512	195	123	75	0.30	614

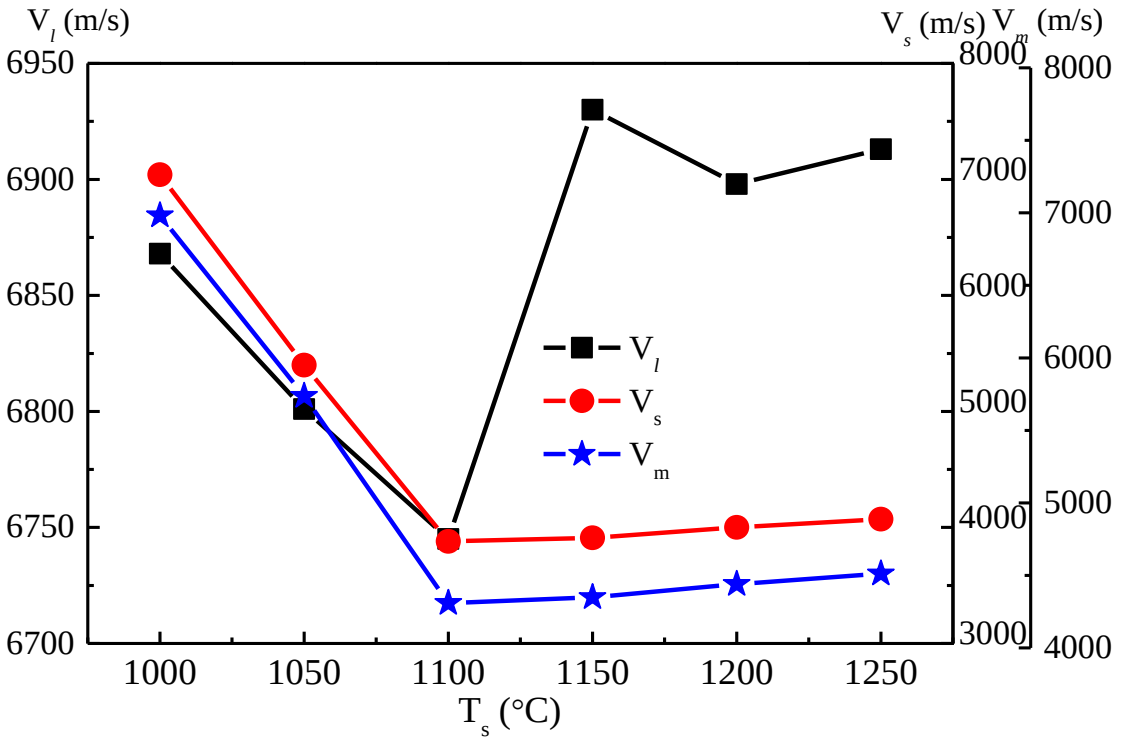

Figure 4.8: Evolution of the longitudinal velocity (V_l), transversal velocity (V_s) and mean wave velocity (V_m) with T_s of NCZFO ferrite.

Debye temperature (Θ_{DA}) was determined using the formula [232, 234]: $\Theta_{DA} = (hV_m/k_B)\left(3\rho_{X-ray}qN_A/4\pi M_w\right)^{1/3}$ where h denotes Planck's constant, k_B denotes Boltzmann constant), N_A denotes the Avogadro's number, M_w denotes the molecular mass, q denotes the number of atoms per unit formula (q = 7), ρ_{X-ray} denotes the theoretical density, V_m denotes the mean wave velocity. Figure 4.9 displays the fluctuation of Θ_{DA} with T_s. With a rise in T_s, it is seen that the value of Θ_{DA} drops to a maximum of 1100 °C before rising to a maximum of 1250 °C. It is feasible to interpret changes in the Θ_{DA}value by employing the concept of specific heat [225, 233]. The conduction electrons' fractional heat absorption is the mechanism that leads Θ_{DA} to drop to a maximum of 1100 °C. It is apparent that a rise in the Θ_{DA} in the 1150-1250 °C temperature range correlates to a reduction in the number of electrons that conduct and a rise in the number of conduction holes.

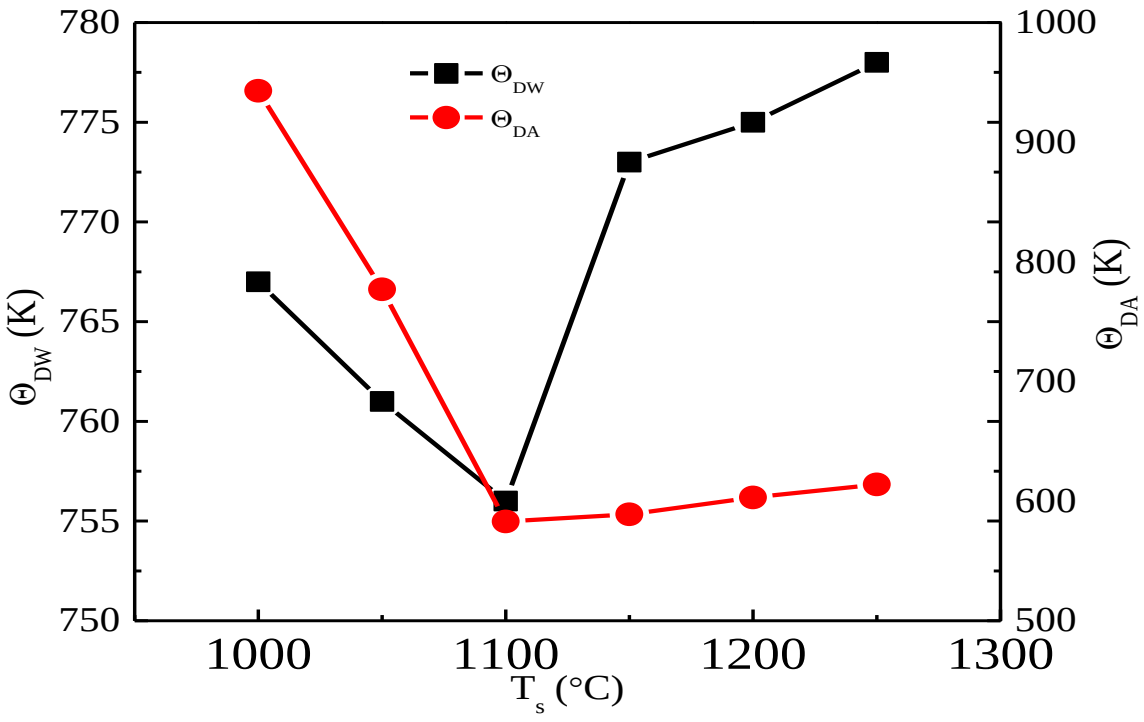

Figure 4.9: Evolution of the Debye temperature (Θ_{DW} and Θ_{DA}) with T_s of NCZFO ferrite.

Table 4.5. Zero-porosity corrected moduli of elasticity (Y_0,B_0,n_0) and Poisson's ratio (σ_0) of NCZFO ferrite annealed at various T_s employing different models.

Model	T_s (°C)	Y_0 (GPa)	B_0 (GPa)	n_0 (GPa)	σ_0
Hasselmann-Fulrath	1000	645	396	263	0.23
	1050	395	284	156	0.27
	1100	210	184	80	0.31
	1150	214	190	81	0.31
	1200	226	197	86	0.31
	1250	235	203	90	0.31
Ledbetter-Datta	1000	469	369	182	0.29
	1050	357	331	135	0.32
	1100	208	180	80	0.31
	1150	211	179	81	0.30
	1200	224	195	85	0.31
	1250	233	206	89	0.31

4.1.5. Electrical characteristics

4.1.5.1. Dielectric permittivity and permittivity loss tangent analsysis

Figure 4.10 (a, b) show how the real (ε') and imaginary (ε'') part of the permittivity of NCZFO ferrites evolve with frequency annealed at various T_s.

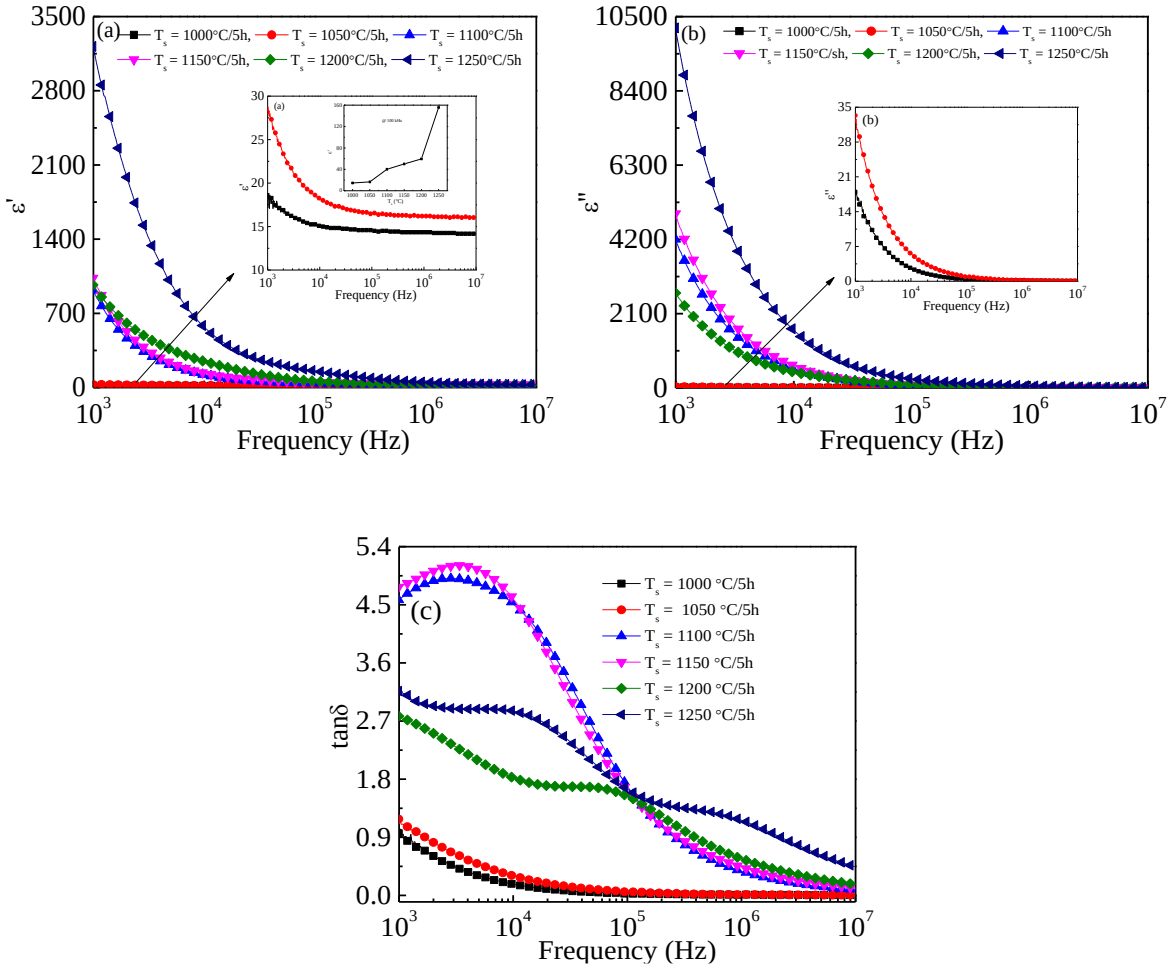

Figure 4.10: Evolution of (a) real component (ε'), (b) imaginary component (ε'') of permittivity, and (c) permittivity loss tangent (tanδ) with frequency of NCZFO ferrites sintering at various T_s.

The ε' value diminishes against frequency that goes to a maximum of 10 kHz at 1000 and 1050 °C, as displayed in Figure 4.10 (a). The ε' value develops into a frequency invariant value over 10 kHz. On the opposite hand, at 1100, 1150, and 1200 °C, the value of ε'declines on rising frequency below 100 kHz. The ε' value develops into a frequency invariant value over 100

kHz. Last but not least, the value of ε' declines with frequency that goes to a maximum of 1 MHz at 1250 °C. The ε' value develops into a frequency invariant value above 1 MHz. The value of ε'' for all T_s drops with frequency that goes to a maximum of 1 MHz, while the value of ε'' is not affected by frequency above 1 MHz, as is also demonstrated in Figure 4.10 (b). Based on the Koop's notion [235] and the Maxwell-Wagner's notion, it could be done to clarify the noticed dispersion that characterizes the electric permittivity. The ferrite may be thought of as an arrangement composed of extremely conducting grains divided by conducting borders of grains of poor conductivity, based to the concept put forward by Koop. Because grain edges have an elevated resistance, while an electric field is put on it, the electrons jump to the grain edges and congregate there, generating interfacial polarization. As an outcome, the low frequency zone has a higher level of the electric permittivity. As an outcome, the likelihood that electrons will cross the border of the grain drops and the polarization follows line. The inset of Figure 4.10 (a) displays the change in permittivity with T_s at specific frequencies. We are able to see that when the T_s rises, the value of ε'gets higher. Because of the boosted grain development and substantial transformation of Fe^{3+} to Fe^{2+} that takes place at higher T_s, the value of ε' increases. As the oxygen partial pressure that occurs during the process of sintering is adjustable, some of the Fe^{3+} is transformed to Fe^{2+} in accordance to the formula [236, 237]:

$$2Fe^{3+} + \frac{3}{4}V_A' + O^{2-} \overset{K(T)}{\longleftrightarrow} 2Fe^{2+} + \frac{1}{2}O_2(g).$$

As an outcome, the value of ε' improves as we raise T_s [238, 239]. The evolution of permittivity loss tangent ($tan\delta$) with frequency at various T_s is depicted in Figure 4.10 (c). The value of $tan\delta$ drops with a higher frequency in the midst of 1000 and 1050 °C. At 1100 and 1150 °C, nevertheless, the value of $tan\delta$ indicates a resonant peak, rises as it increases frequency, and then steadily falls. On overall, the $tan\delta$ peak comes when the dielectric relaxation time and applied field's time is harmonized and the condition $\omega\tau = 1$ is met, where $\omega = 2\pi f$, f denotes the applied frequency and τ denotes the relaxation time; these two quantities are connected by

the formula: $\tau = p/2$ to the hopping chance per unit time, i.e., the maximum frequency (f_{max}) is correlated to the hopping chance [240, 241]. The electron interchange in the midst of Fe^{2+} and Fe^{3+} ions need greater energy at lower frequencies, that is connected with an elevated resistance (because of the grain border), leading to increased permittivity loss tangents ($tan\delta$). The losses thus become substantial. The energy needed for the transfer of electrons in the midst of Fe^{2+} and Fe^{3+} ions at the octahedrally coordinated sites is lower at higher frequencies, which correlates to a lower resistance (because of to the grains). The losses thus become minimal. It has been shown that when T_s rises, the value of $tan\delta$ grows. The different dimensions of grains are the reason for variations in $tan\delta$ value.

4.1.5.2. Electrical conductivity analysis

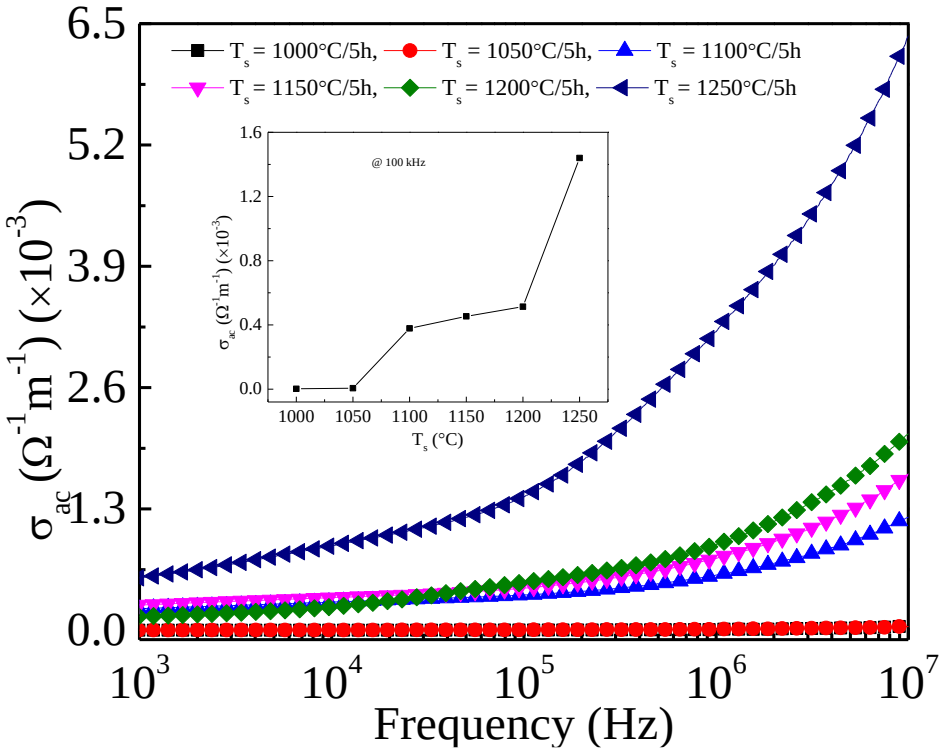

Figure 4.11: Evolution of ac conductivity (σ_{ac}) with frequency of NCZFO ferrites annealed at various T_s. Inset represents the evolution of σ_{ac} with T_s at 100 kHz.

Figure 4.11 displays how the ac conductivity evolves with frequency and T_s throughout the frequency interval from 1 kHz to 10 MHz. To a maximum of a particular frequency (≥ 10 kHz), it appears that the electrical conductivity is steady at low frequencies. This frequency-invariant

characteristic correlates to dc conductivity and is linked to grain borders, which are better at low frequencies due to elevated resistance. However, it starts to grow right away following a specific frequency (≥ 10 kHz) and achieves its peak around 10 MHz. The conducting grains are increasingly active as the frequency rises, boosting the jumping of electron from ferric to ferrous ions at the octahedrally coordinated A-site. As a result, the electrical conductivity rises. Therefore, the universal power law [242, 243]: $\sigma_{ac} = \sigma_{dc}(\omega = 0) + A\omega^n$ regulates how the ac conductivity of the sample annealed various T_s changes, where $A\omega^n$ is the pure σ_{ac} as a result of the jumping mechanism at octahedrally coordinate (B)-site, σ_{dc} signifies the dc conductivity, and it relies upon temperature and frequency invariant variable. The power, n, that is a moderate dependence on frequency, must be computed for all compositions despite the fact A is only moderately influenced by temperature and $\omega = 2\pi f$ denotes the frequency at which the electrical conductivity is determined [243]. The quantity of Fe^{3+} conversion to Fe^{2+} and the T_s have a significant impact on the quantity of ferric/ferrous ion pairs in ferrite material. The change in σ_{ac} as a result of T_s at a chosen frequency (1 MHz) is displayed in the inset of Figure 4.11. It can be shown that σ_{ac} rises as T_s rises. Because there are more Fe^{2+} ions present at the octahedrally coordinated location, there is a boost in $\sigma_{ac}$with T_s.

4.1.5.3. Impedance spectroscopic investigation

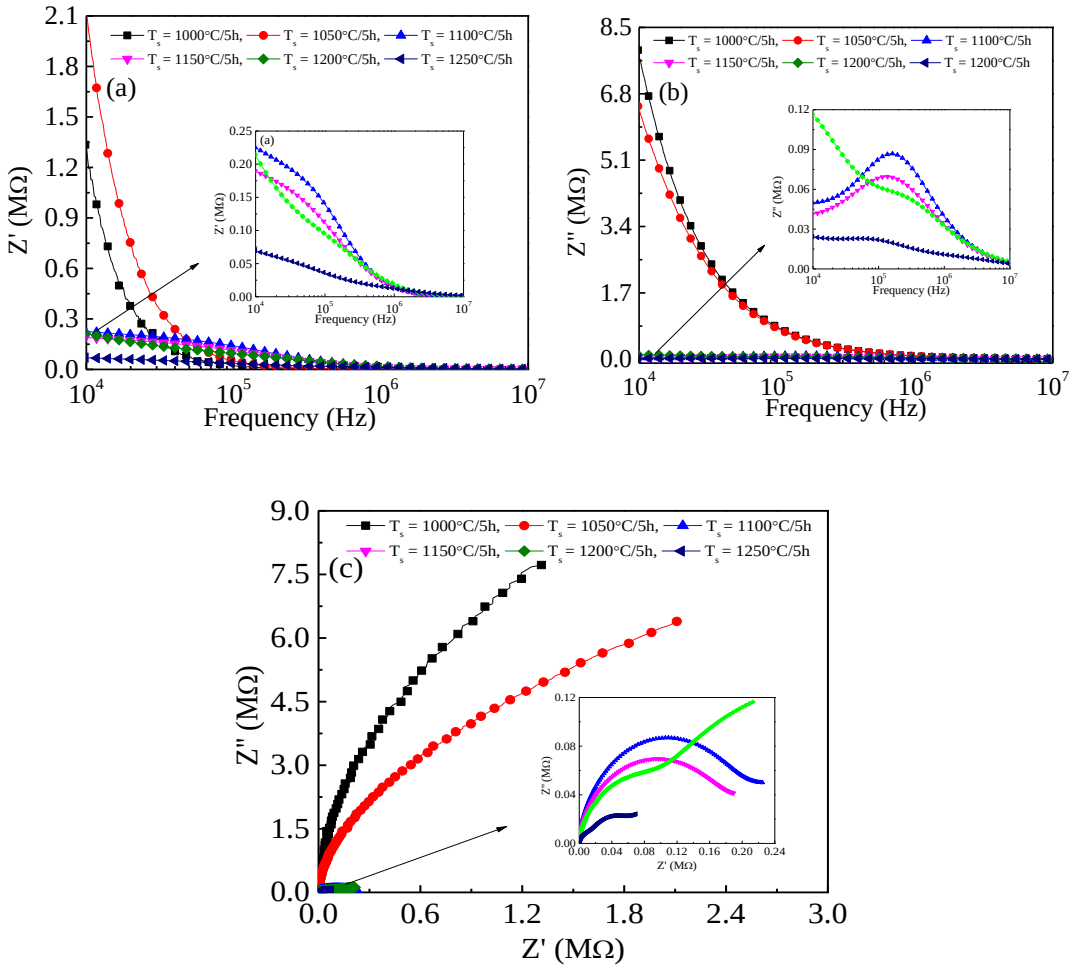

Figure 4.12: Evolution of (a) real component (Z'), (b) imaginary component (Z'') of impedance as a function of frequency, and (c) Nyquist plots of NCZFO ferrites annealed at various T_s.

Figure 4.12 (a) shows how the real part (Z') of the impedance evolves with frequency annealed at various T_s. It is evident from Figure 4.12 (a) that the value of Z' drops as the frequency rises. The fact that the Z' value is declining as the frequency changes demonstrates that the sample's AC conductivity is rising. The Z' value, on the other hand, becomes zero at higher frequencies, suggesting activity that is frequency invariant. Due of the high frequency range's smaller space charge relaxation period, quicker recombination, and reduced polarization of space charge, every curve appears to converge on the high frequency edge [244]. Figure 12 (b) shows how the imaginary component (Z'') of impedance changes with frequency annealed at various T_s. It

is evident that the Z' values decrease repeatedly with frequency in respect to the polarization diminution, that is unable to maintain up with the frequency modification, and the specimens annealed at 1100 and 1150 °C demonstrate a maximum at a specific frequency. The Cole-Cole plots are shown in Figure 4.12 (c) at various T_s. The Cole-Cole plots may produce two semicircles, according to the electrical characteristics of the substance being investigated. The grain border resistance plays a role in the first semicircle's existence at lower frequencies. The grain's resistance or bulk characteristics are the factors that cause the second semicircle to show up in the high frequency band. In certain circumstances, extremely small semi-arcs of sufficiently low frequency can exist in addition to these two semi-arcs of grain and borders of grain that may be triggered by electrodes or interfaces [245]. For each T_s, just one semicircle was identified in the current examination, and as T_s grew, both its maximum value and diameter dropped, referring exactly to a dominating relaxing process.

4.1.6. Investigation of magnetic characteristics

4.1.6.1. Magnetization

The hysteresis loop characteristics of NCZFO ferrite annealed at various T_s are shown in Figure 4.13 (a). The M-H loop was clearly visible in the loops, indicating that the chemicals used to synthesize materials are arranged soft ferromagnetic in character. The M-H is used to derive the magnetic characteristics, such as saturation magnetization (M_s), coercivity (H_c), retentivity (M_r), squareness ratio (M_r/M_s). The magnetic moment per (n_B) was persuaded using the formula: $n_B = \frac{M_w \times M_s}{5585}$, where n_B denotes the magnetic moment, M_w denotes the molecular mass and M_s denotes the saturation magnetization. The anisotropic constant (K) was determined using the formula [246]: $H_c = \frac{0.96 \times K}{M_s}$, where H_c denotes the coercivity. The determined values of M_s, M_r, M_r/M_s, H_c, n_B and K are shown in Table 4.6.

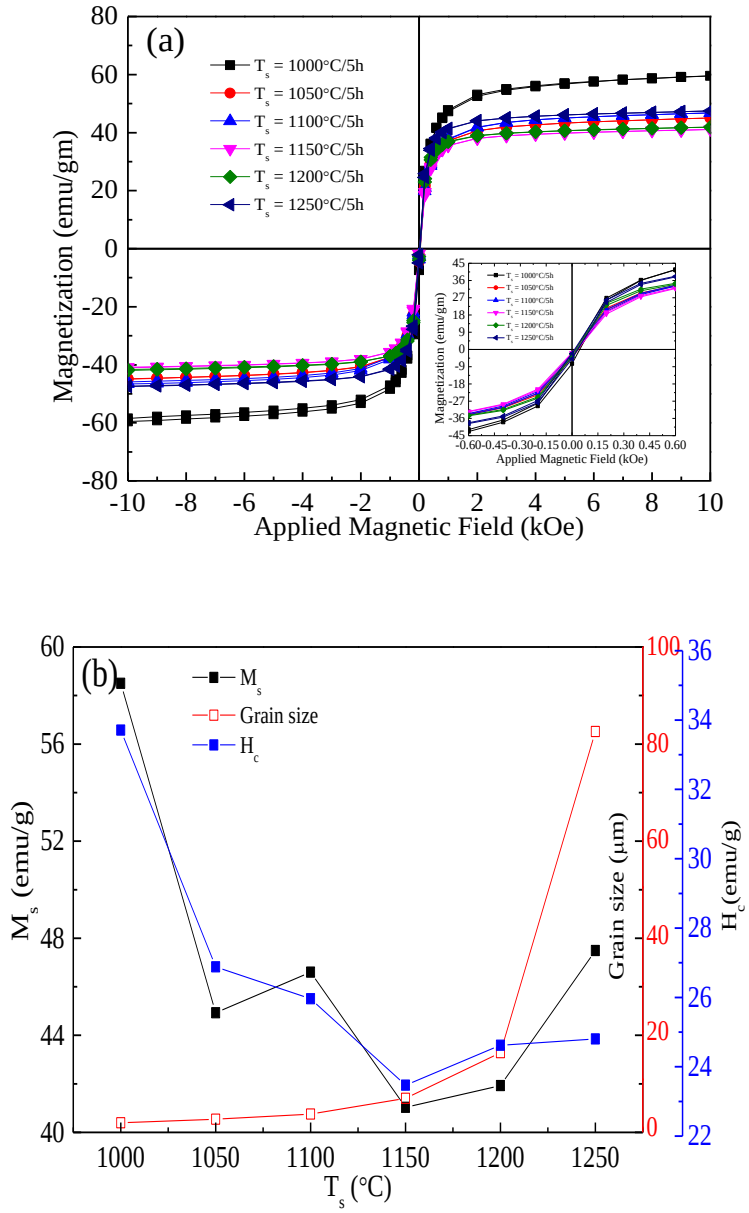

Figure 4.13: (a) M-H loops of NCZFO ferrites and (b) evolution of the coercivity, saturation magnetization and remanence with various T_s.

Figure 4.13 (b) shows how the values of M_s, M_r and H_c change as a result of Ts. The value of M_s is seen to initially fall at 1050 °C, afterwhich inconsiderably rise at 1100 °C, drop again at 1150 °C, and then rise as T_s rises further to a maximum of 1250 °C. Since high T_s promotes the diffusion of ions throughout sintering and leads to the development of intragranular porosity with a rise in T_s and restricts domain wall movement within the grain structure, the value of M_s drops as you increase T_s, which can be related to the sample heterogeneity [204, 205]. Fe^{2+}-

Cr nano-ferrites have been seen to produce a comparable magnetic outcome based on T_s [247]. The fluctuation of the lattice constant's value with T_s, on the opposite hand, may be responsible for the fluctuation of M_s with T_s. The value of M_s has been demonstrated to have an inverse relationship with the ferrite materials' cubic lattice constant [248]. The improvement in the mean magnetic domain area is what generates the rise in M_s at 1150 °C. To a maximum of 1150 °C, the value of M_r and H_c falls as T_s rises and then rises as T_s rises more. Since bigger grains often contain more domain barriers, it is predicted that the value of H_c will decrease as T_s increases. A smaller amount of energy is needed for generating magnetization due to domain wall movement than to produce magnetization due to domain rotation [249]. Wall movement contributes more to magnetization than domain rotation because there are more walls as grain diameter rises. Therefore, it is predicted that samples with bigger grains will have a lower value of H_c.

Table 4.6. Magnetic parameters (saturation magnetization(M_s), remanence (M_r), coercivity (H_c), magnetic moment (n_B), anisotropic constant (K)) of NCZFO ferrite annealed at various T_s.

T_s (°C)	Crystallite size (nm)	M_s (emu/g)	M_r (emu/g)	M_r/M_s	H_c (Oe)	n_B (μ_B)	K (erg/g)
1000	0.98	58.50	5.40	0.092	34	2.51	2054
1050	1.74	44.93	3.34	0.074	27	1.92	1258
1100	2.80	46.60	3.03	0.065	26	1.99	1260
1150	6.08	41.03	2.44	0.059	24	1.76	1003
1200	15.58	41.93	3.27	0.078	25	1.80	1075
1250	82.40	47.49	3.54	0.075	25	2.03	1227

4.1.6.2. Magnetic permeability and magnetic loss tangent analysis

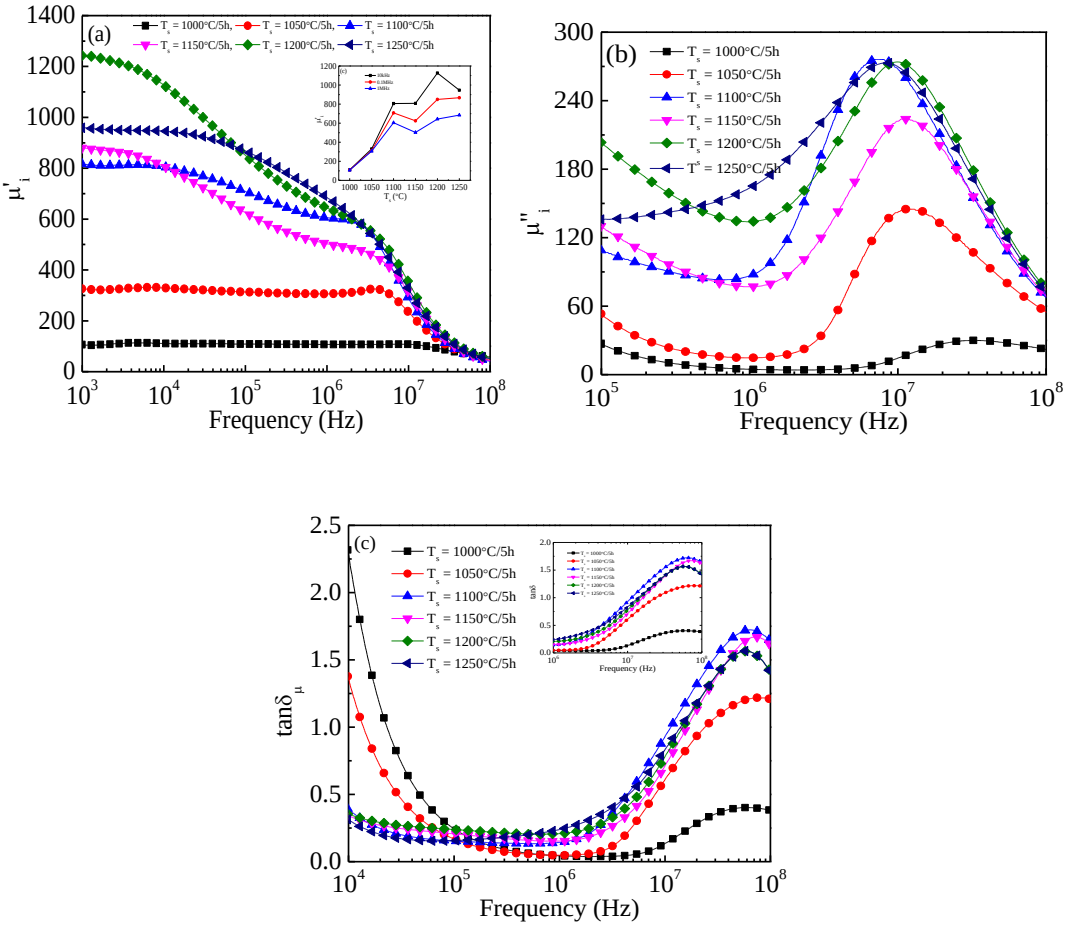

Figure 4.14: Evolution of (a) real component (μ_i'), (b) imaginary component (μ_i'') of magnetic permeability and (c) magnetic loss tangent ($tan\delta_\mu$) with frequency of NCZFO ferrites annealed at various T_s.

Figure 4.14 (a) and (b) shows how the real component (μ_i') and imaginary component (μ_i'') of magnetic permeability evolves with frequency of NCZFO ferrite annealed at various T_s. The value of μ_i' at 1000 and 1050 °C was very stable to a maximum of 6.31 and 1.30 MHz, before ferromagnetic resonance occurred. At higher frequencies, it began to diminish, and with a further rise in frequency, it lowers as a result of domain wall relaxation [250]. Resonance, a phenomenon seen in ferromagnetic materials owing to the hermonization of domain wall oscillational frequency and applied frequency, causes a modest increase in the value of μ_i' at 4.45 MHz at 1050 °C. At 1100, 1150, 1200, and 1250 °C, the value of μ_i' also steadily drops as the frequency rises. Table 4.7 displays the magnetic permeability, resonant frequency, and

magnetic loss tangent at several chosen frequencies at various T_s. Figure 4. 14 (a) shows the fluctuation of μ_i' at a few frequencies with T_s. The value of μ_i' grows to a maximum of 1200 °C and afterwhich decreases at 1250 °C, at 1 kHz, according to Table 4.7 and Figure 4.14 (a). At 1 MHz, the μ_i' value ascends to a maximum of 1100 °C and then significantly drops around 1150 °C. Thereafter, the value of μ_i' rises as T_s rises further. The following elements contributed to the improvement in the value of μ_i' with T_s: enhanced densification and grain diameter, as well as a lowered magnetocrystalline anisotropic constant. By lowering the internal stress and crystal anisotropy, a rise in T_s causes an improvement in grain diameter and densification as well as a drop in the magnetocrystalline anisotropic constant [251, 252]. The resistance to domain wall movement can be reduced to a minimal by a small crystal anisotropy constant, resulting in greater magnetic permeability as T_s rises [251, 252]. It is logical to infer that the grain border and pores might restrict the mobility of the domain wall. Larger T_s results in smaller pores and grain boundaries, which promotes domain wall movement and provides high magnetic permeability. At 1 kHz and 1 MHz, this decline takes place around 1200 and 1150 °C. This is presumably because the pinning action that happens when the magnetic pores within the crystal take shape caused the grain width to rise whilst the magnetic permeability dropped. Although grain diameter reduces with development, the resultant pores enlarge [253-255]. It is noticeable from Figure 4.14 (b) that the μ_i'' value continuously reduces to a maximum of 1 MHz, then gradually rises with frequency increase until reaching a maximum at a particular frequency. The ferromagnetic resonance is accountable for the development of peaks in all samples at particular frequencies. In Table 4.7, the resonant frequency is calculated from the maximum value of μ_i''. Figure 4.14 (c) shows how the magnetic loss tangent ($tan\delta_\mu$) evolves with frequency annealed at various T_s. The value of $tan\delta_\mu$ drops to a maximum of 1 MHz in the midst of 1000 and 1050 °C with increasing frequency. From 1100 to 1150 °C to a maximum of 1 MHz, the value of $tan\delta_\mu$ is nearly frequency invariant. For all T_s, starting at 1 MHz, the

$tan\delta_\mu$ value continuously rises as the frequency rises, culminating at a fixed frequency. The occurrence of ferromagnetic resonance is responsible for this [256].

4.1.6.3. Quality factor analysis

Figure 4.15 (a) depicts how the quality factor (Q-factor) evolves with frequency of NCZFO ferrite for various T_s. There are peaks at 2.13 MHz for 1000 °C, 1 MHz for 1050 °C, 0.54 MHz for 1100 °C, 0.89 MHz for 1150 °C, 0.67 MHz for 1200 °C, and 0.071 MHz for 1250 °C, which drop as the frequency rises. To a maximum of 1100 °C, the peak Q-value gradually changes to the lower frequencies. When compared to 1100 °C, the peak moves to higher frequencies at 1150 °C. When compared to 1150 °C, the peak Q-value translocates to the lower frequencies in the midst of 1200 and 1250 °C. The change in peak Q-factor value is the result of actual magnetic permeability rising. Interestingly, samples annealed at 1000 °C had the greatest Q-factor. The microstructure of small grains is probably responsible for the formation of the maximum Q-factor at 1000 °C, since the small grains function as catalysts to lessen $tan\delta_\mu$in ferrite. The change of the Q-factor as a result of T_s is shown in Figure 4.15 (b) for a set of frequencies, and it is apparent that the Q-factor drops as T_s changes. Given that big grains often possess a low Q-factor, the fast growth of grains could be a result of the Q-factor reduction by T_s [257].

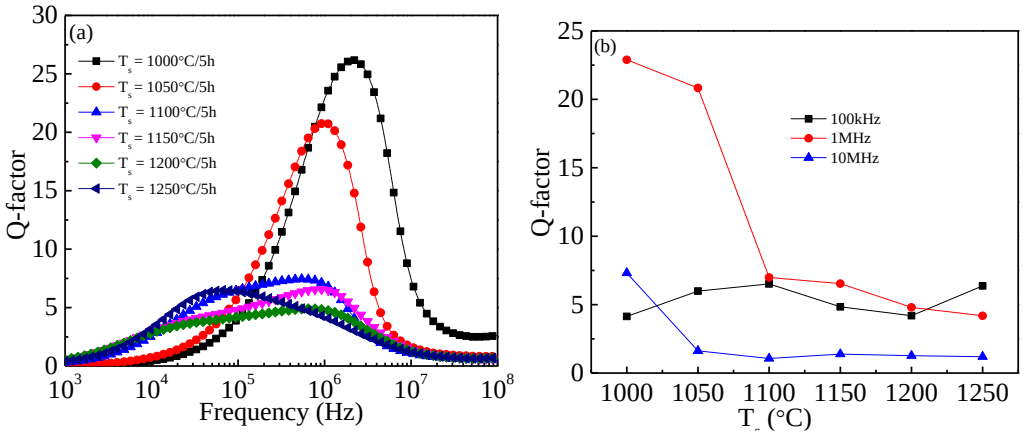

Figure 4.15: (a) Evolution Q-factor with frequency and (b) Q-factor at specific frequencies of NCZFO ferrite annealed at various T_s.

Table 4.7. Magnetic permeability (μ_i'), resonant frequency (f_r), magnetic loss tangent ($tan\delta_\mu$) and maximum quality factor (Q_{max}) of NCZFO ferrite at specific frequencies annealed at various T_s.

T_s (°C)	μ_i' at				f_r (MHz)	$\mu_i' \times f_r$ at 10 kHz	μ_i'' at				$tan\delta_\mu$				Q_{max}
	10 kHz	0.1 MHz	1 MHz	100 MHz			10 kHz	0.1 MHz	1 MHz	100 MHz	10 kHz	0.1 MHz	1 MHz	100 MHz	
1000	111	109	107	58	32	3585	253	26	5	15	2.28	0.24	0.04	0.14	26
1050	330	313	306	45	12	3927	447	52	15	143	1.36	0.17	0.05	0.62	21
1100	806	708	605	41	8	6069	313	109	87	267	0.39	0.15	0.14	0.94	7
1150	808	625	503	43	11	9130	275	129	77	222	0.34	0.21	0.15	0.72	7
1200	1126	849	643	53	10	11039	398	203	134	274	0.35	0.24	0.21	0.79	5
1250	947	867	684	51	8	7780	293	136	164	269	0.31	0.16	0.24	0.84	7

4.2. Evaluation the impacts of iron-nonstoichiometry on the characteristics of $Ni_{0.25}Cu_{0.13}Zn_{0.62}Fe_{2-x}O_{4-3x/2}$ system

This section explores the effects of iron-nonstoichiometry on the crystallographic structure, microstructure, elastic, electric, and magnetic characteristics of $Ni_{0.25}Cu_{0.13}Zn_{0.62}Fe_{2-x}O_{4-3x/2}$ ($NCZFe_{2-x}O_{4-3x/2}$) ceramics manufactured using the solid state synthetic technique and annealed at various T_s (1100 to 1250 °C).

4.2.1. Crystallographic characteristics

Figure 4.16 shows the XRD profiles of $Ni_{0.25}Cu_{0.13}Zn_{0.62}Fe_{2-x}O_{4-3x/2}$ ($NCZFe_{2-x}O_{4-3x/2}$) ferrites at various T_s: (a) 1100, (b) 1150, (c) 1200, and (d) 1250 ℃. The fact that all samples at all T_s exhibit a single-phasic cubic spinel architecture without incorporating any foreign phases demonstrated that the crystal architecture of manufactured ferrites wouldn't modify as the degree of iron-nonstoichiometry changed. The rise in peak sharpness and intensity with growing T_s is an indication that the material's crystallinity is becoming stronger. With rising Ts, it is viewed that the strongest peak (311) develops, narrows, and sharpens. This results from the internal strains being released and the particle development. The lattice constant (a) was determined employing the formula [183]: $a = \frac{\lambda}{2sin\theta}\sqrt{h^2 + k^2 + l^2}$, where a denotes the lattice constant, λ denotes is the wavelength of X-ray, and h, k, and l denote Miller's indices. The results are given in Table 4.8-4.9. At 1100 °C, it is found that the distinctive peak (311) moves toward the lower 2θ value as the iron-nonstoichiometry quantity rises that indicates that the crystal lattice extends as the degree of iron-nonstoichiometry rises. As a result, at 1100 °C, it appears that the lattice constant rises as the level of iron-nonstoichiometry rises. At 1150 °C, it turns out that the distinctive peak (311) moves toward the higher 2θ value in x = 0.04, afterwhich to a lower 2θ value in x = 0.08, and lastly to the higher 2θ value in x = 0.12. When the iron-nonstoichiometry level goes to a maximum of x = 0.08 at 1200 °C, it appears that the distinctive peak (311) moves towards the lower 2θ value, and at x = 0.12 it shifted toward the

higher 2θ value. At 1250 °C, the distinctive peak (311) first shifted toward the 2θ value in x = 0.04, afterwhich moved toward the higher 2θ value in x = 0.08, and at last it was perceived to move toward the smaller 2θ value in x = 0.12. The drifting of diffraction peaks to smaller 2θ value indicates a rise in the lattice constant [258]. The little variation in diffraction peak strength in the midst of samples can be attributed to the varying ionic radii. The shift in cations allocation may be utilized to clarify the reduction in the lattice constant [259].

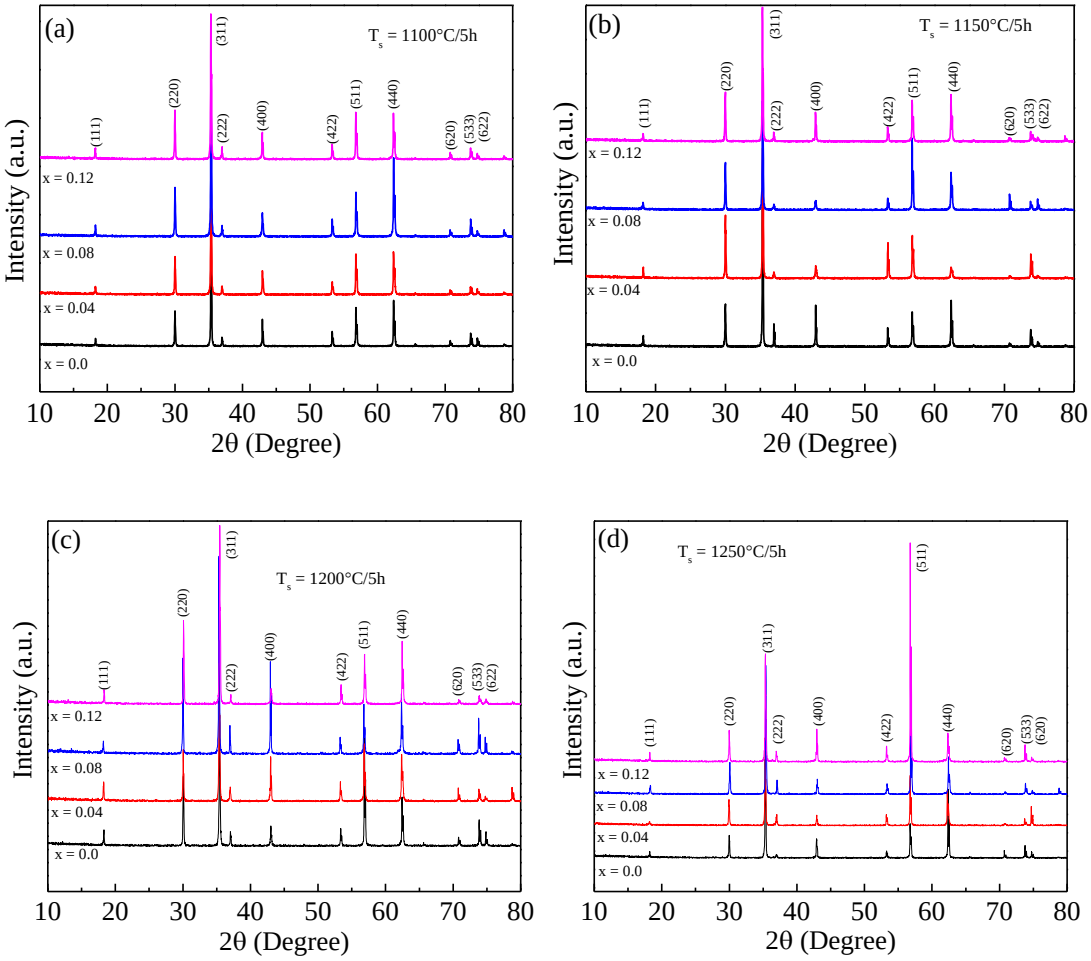

Figure 4.16: XRD profiles of NCZFe$_{2-x}$O$_{4-3x/2}$ system annealed for 5 h at (a) 1100, (b) 1150, (c) 1200 and, (d) 1250 °C.

It is also important to note that, as well to the adjustment in cation allocation, imperfections in structure and oxygen defects may trigger the metal oxide bonds to bend [259]. The change of the lattice constant is therefore noticed. In contrast to the Zn^{2+} (0.074 nm), Ni^{2+} (0.069 nm), and Cu^{2+} (0.073 nm) ions, which are more likely to move into the tetrahedrally coordinated

(A)-site more strongly, the Fe^{3+} (0.0645 nm) ions possess no affinity for any site due to their zero crystal field stabilizing energy [260-263]. The Ni^{2+} ions (0.069 nm) from octaahedrally coordinated (B)-sites are often replaced with an equivalent amount of Fe^{3+} ions. The Ni^{2+} ion has a radius of 0.069 nm, which is bigger than the Fe^{3+} ion's radius of 0.0645 nm. The XRD peaks migrate toward the greater 2θ value as a result of the replacement of Ni^{2+} (0.069 nm) ions for Fe^{3+} (0.0645 nm) ions. As an outcome, it appears that the lattice constant drops as the level of iron-nonstoichiometry rises. The iron-deficient non-stoichiometric nickel-copper-zinc ferrite's oxygen vacancies might be the reason of the XRD peaks proceeding toward the lower diffraction angle. As an outcome, it is noticed that the lattice constant grows as the level of iron-nonstoichiometry rises. The lattice constant is viewed to expand when the iron-nonstoichiometry quantity rises at 1100 °C, as demonstrated in Table 4.8-4.9. The lattice constant appears to go up in x = 0.08 at 1150 and 1250 °C, then it turns out to decrease in x = 0.12 at such temperatures. When the iron-nonstoichiometry quantity rises to 1200 °C, the lattice constant continues gradually increasing to a maximum of x = 0.08 until suddenly dropping at x = 0.12. In addition, in x = 0.0 and 0.04, the lattice constant appears to be increasing first at 1150 °C, then to drop at 1200 °C, and lastly to rise at 1250 °C. At 1150 °C, the lattice constant appears to grow initially in x = 0.08; but, when the T_s increases more, the lattice constant begins to decline. The lattice constant is viewed to slowly decrease with growing T_s to a maximum of 1200 °C until it finally rises at 1250 °C in x = 0.12. The mean crystallite diameter (D_{hkl}) has been determined employing Debye-Scherrer's formula [183] and the results are given in Table 4.8-4.9. As seen in Table 4.8-4.9, the quantity of iron-nonstoichiometry has been shown to have an impact on D_{hkl} value. The variance in ionic radius in the midst of the replacement ion such as Ni^{2+} (0.69 Å), Cu^{2+} (0.73 Å), Zn^{2+} (0.74 Å), and Fe^{3+} (0.645 Å), is believed to be the reason for the modification in D_{hkl} [264]. At 1100 °C, the value of D_{hkl} appears to firstly fall at x = 0.04, and then it begins to rise as the iron-nonstoichiometry level rises. The value of D_{hkl} appears to be stable at 1150 °C to a maximum of x = 0.04, afterwhich it appears to drop in x =

0.08, and then it turns out to rise in x = 0.12. The value of D_{hkl} began to rise at 1200 °C and continued to do so until x = 0.08 before eventually starting to decrease at x = 0.12. The value of D_{hkl} is shown stays the same at 1250 °C as the iron-nonstoichiometry level rises. The coarsening of grains and grain border wall movement that pushes collectively the tinier grains resulting in bigger grains, may be connected to a rise in D_{hkl} with growing T_s [264]. Additionaly, we calculated the mean lattice strain using Stoke-Wilson's formula, $\epsilon = \frac{1}{4} \times \frac{FWHM}{tan\theta}$ [265, 266] and are displayed in Table 4.8-4.9. At 1100 °C, the value of ϵ is shown to grow at the beginning in x = 0.04 before it turns out to drop when the iron-nonstoichiometry level rises further. At 1150 °C, it turns out that the value of ϵ holds constant until x = 0.04, rises in x = 0.08, and then begins to drop in x = 0.12. The value of ϵ is shown to go down to a maximu of x = 0.08 at 1200 and 1250 °C, and then it appears to rise in x = 0.12. Dislocations in the ferrite lattice may serve as immobilize centers, restrict the the domain wall movement, and also have an impact on coercivity. The number of dislocations per volume, was determined using the formula $\delta = \left(\frac{\beta cos\theta}{0.9\lambda}\right)^2$ [247] and shown in Table 4.8-4.9, is determined by the length of the dislocation lines. At 1100 °C, the value of δ is demonstrated to expand first in x = 0.04, and then it begins to fall as the iron-nonstoichiometry level rises more. At 1150 °C, the value of δ is observed to be stable to a maximum of x = 0.04 before rising in x = 0.08 and beginning to drop in x = 0.12. If the iron-nonstoichiometry level is raised further, the value of δ is noted to develop at 1200 °C after initially dropping in x = 0.04. The value of δ is displayed to remain steady at 1250 °C as the level of iron-nonstoichiometry rises. The drop in δ in x = 0.04 at all T_s indicates to a reduction in defect density, which improves crystallinity [267]. The occurrence of a sample defect is displayed by the larger values of δ in x = 0.08 and 0.12 at all T_s. Due to the fact that the dislocation amount per volume is inversely correlated to the square of the mean crystallite diameter, a pattern of rising and falling dislocation amount per volume with iron-nonstoichiometry level is predicted. The jumping length in the midst of the magnetic ions at

tetrahedrally coordinated (A) and octahedrally coordinated (B)-sites has been determined utilizing the formulae [268]: $L_A = \frac{a\sqrt{3}}{4}$ and $L_B = \frac{a\sqrt{2}}{4}$ Å . The polaron radius (R_p) was determined quantitatively utilizing the formula [268]: $R_p = \frac{1}{2}\left[\frac{\pi}{6N}\right]^{1/3}$, where N denotes the number of sites per unit volume ($N = 96/a^3$). Table 4.10-4.11 provide an overview of the assessed values of L_A and L_B. At 1100 °C, the value of L_A and L_B begins to rise as the iron-nonstoichiometry level rises. The value of L_A and L_B is found to drop at the beginning in x = 0.04 at 1150 and 1250 °C, rise in x = 0.08, and subsequently decline in x = 0.12, respectively. With an increase in iron-nonstoichiometry degree to a maximum of x = 0.08 at 1200 °C, the value of L_A and L_B is noticed to steadily grow until decreasing at x = 0.12. Since the values of L_A and L_B vary directly with the lattice constant, the increasing and reducing character of L_A and L_B with the iron-nonstoichiometry degree can be credited to the modification of the lattice constant. The redistribution of cations in the midst of the tetrahedrally coordinated (A) and octahedrally coordinated (B)-sites could also be responsible for the rise in L_A and L_B with growing iron-nonstoichiometry levels. The depletion of Fe^{3+} ions on the octahedrally coordinated (B)-site could be responsible for the drop in L_A and L_B by reducing the distance in the midst of the magnetic ions. The electron hopping in the midst of ions at the tetrahedrally coordinated (A) and octahedrally coordinated (B)-sites is less likely than that in the midst of the octahedrally-octahedrally coordinated (B-B)-sites, as can be shown from Table 4.10-4.11. The value of R_p is seen to remain constant at 1100 °C to a maximum of x = 0.04 before rising when the iron-nonstoichiometry level rises higher. The value of R_p seems to drop in x = 0.04 at 1150 and 1250 °C, rise in x = 0.08, and then drop in x = 0.12 at these temperatures. At 1200 °C, the value of R_p begins to progressively rise to a maximum of x = 0.08, and then it starts to fall in x = 0.12. The X-ray parameters such tetrahedrally coordinated (A)-site radii (r_A), octahedrally coordinated (B)-site radii (r_B), d_{AX} (the shortest speration in the midst of the metal-oxygen cation-anion at tetrahedrally coordinated (A)-site) and d_{BX} (the smallest

seperation amongst the metal-oxygen cation-anion at octahedrally coordinated B-site), tetrahedrally coordinated edge, shared and unshared octahedrally coordinated edges (d_{AXE}, d_{BXE} and d_{BXEU}) were determined employing lattice constant 'a', oxygen positional factor 'u' (u = 0:381A˚) and ionic radius of oxygen ion R_O (1.32 Å) and entering into the formulae [269, 270]: $r_A = (u - 0.25)a\sqrt{3} - R_O,\ r_B = (0.625 - u)a - R_O,\ d_{AX} = a\sqrt{3}(u - 0.25),\ d_{BX} = a\left[3u^2 - \left(\frac{11}{4}\right) + \left(\frac{43}{64}\right)\right]^{\frac{1}{2}},\ d_{AXE} = a\sqrt{2}(2u - 0.5),\ d_{BXE} = a\sqrt{2}(1 - 2u),\ d_{BXEU} = a\left[4u^2 - 3u + \left(\frac{11}{16}\right)\right]^{\frac{1}{2}}$ and is shown in Table 4.10-4.11. The disparity in the values of r_A and r_B that can be seen in Table 4.10-4.11 can be associated with the transfer of ferric ions from tetrahedrally coordinated (A)-site to octahedrally coordinated (B)-site. In simple terms, this characteristic is explained by the fact that the tetrahedrally coordinated (A)-site and the octahedrally coordinated (B)-site have more covalent bonds than one another [271]. The value of r_A and r_B begins to rise at 1100 °C as the iron-nonstoichiometry level rises. The value of r_A and r_B is seen to drop initially in x = 0.04, rise in x = 0.08, and subsequently fall in x = 0.12 at 1150 and 1250 °C. The r_A and r_B values are recognized to drop in x = 0.12 at 1200 °C after starting to rise with a rise in iron-nonstoichiometry degree to a maximum of x = 0.08. The site radius r_B appears to be bigger than r_A. As seen in Table 4.10-4.11, the depletion of Fe^{3+} ions at octahedrally coordinated (B)-sites is the reason why the value of d_{AX} is lower than that of d_{BX}. At 1100 °C, the value of d_{AX} is seen to grow as the iron-nonstoichiometry level increases to a maximum of x = 0.08, after which it drops in x = 0.12. In contrast, the value of d_{BX} is shown to rise as the iron-nonstoichiometry level rises. At 1150 and 1250 °C, it turns out that the value of d_{AX} and d_{BX} drops first in x = 0.04, then rises in x = 0.08, and ultimately falls in x = 0.12. If the iron-nonstoichiometry level rises to a maximum of x = 0.08 at 1200 °C, the value of d_{AX} and d_{BX} starts to rise, and at x = 0.12 it begins to fall. At 1100 °C, it is seen that the values of d_{AXE}, d_{BXE}, and d_{BXEU} grow when the iron-nonstoichiometry level rises. The values of d_{AXE},

d_{BXE}, and d_{BXEU} are found to fall initially in x = 0.04, rise in x = 0.08, and then decline in x = 0.12 for 1150 and 1250 °C. At 1200 °C, d_{AXE}, d_{BXE}, and d_{BXEU} values start to drop in x = 0.12 and then imprives as the iron-nonstoichiometry level rises to a maximum of x = 0.08. The depletion of ferric ions at the octahedrally coordinated (B)-site and the allocation of ferric in the midst of the tetrahedrally coordinated (A)-site and octahedrally coordinated (B)-site are responsible for the decline in d_{AXE}, d_{BXE}, and d_{BXEU}. Additionally, using lattice constant and oxygen positional factor (u), the interionic lengths in the midst of the cations (Me-Me) (b, c, d, e, and f) and amongst the cation and anion (Me-O) (p, q, r, and s) were determined using the formulae [272]: $b = \left(\frac{a}{4}\right)\sqrt{2}$, $c = \left(\frac{a}{8}\right)\sqrt{11}$, $d = \left(\frac{a}{4}\right)\sqrt{3}$, $e = \left(\frac{3a}{8}\right)\sqrt{3}$, $f = \left(\frac{a}{4}\right)\sqrt{6}$, $p = a\left(\frac{5}{8} - u\right)$, $q = a\sqrt{3}\left(u - \frac{1}{4}\right)$, $r = a\sqrt{11}\left(u - \frac{1}{4}\right)$, and, $s = a\sqrt{3}\left(\frac{u}{3} + \frac{1}{8}\right)$,where b, c, d, e, f, p, q, r, and s express the factors of ion pair lengths concurrent with the angle θ_1 to θ_5 and are shown in Table 4.12-4.13. At 1100 °C, the values of b, c, d, e and f begin to rise as the iron-nonstoichiometry level rises. The values of b, c, d, e and f at 1150 and 1250 °C are first shown to drop in x = 0.04, aftewhich it grows in x = 0.08, and lastly it appears to be decreasing in x = 0.12. The iron-nonstoichiometry degree grows to a maximum of x = 0.08 at 1200 °C, and then the values of b, c, d, e and f begin to drop at x = 0.12. Because the surrounding cations are not being blocked by any intermediate anions, the values of b are relatively minimal among all interionic distances in the midst of the cations-cations for all samples at all T_s. The values of p, q, r and s are seen to rise at 1100 °C as the level of iron-nonstoichiometry rises. At 1150 and 1250 °C, the values of p, q, r and s begin to fall in x = 0.04 before rising in x = 0.08 and then dropping in x = 0.12. At 1200 °C, it became apparent that the values of p, q, r and s improved with a rise in iron-nonstoichiometry level to a maximum of x = 0.08 before beginning to drop at x = 0.12. The alterations in the iron-nonstoichiometric nickel-copper-zinc ferrite brought on by the reduction of iron-nonstoichiometry degree might be the cause of the rise in (b, c, d, e, and f) and (p, q, r and s)

as one raises the iron-nonstoichiometry degree. Because interionic lengths rely on the lattice constant directly, the decreasing and growing pattern of $b, c, d, e,$ and f and p, q, r and s is in good alignment with the modification of the lattice constants. Additionally, the bond angles in the midst of cations-cations and cations-anions were calcuated utilizing the trigonometric formulae [272]: $\theta_1 = cos^{-1}\left(\frac{p^2+q^2-c^2}{2pq}\right)$, $\theta_2 = cos^{-1}\left(\frac{p^2+r^2-e^2}{2pr}\right)$, $\theta_3 = cos^{-1}\left(\frac{2p^2-b^2}{2p^2}\right), \theta_4 = cos^{-1}\left(\frac{p^2+s^2-f^2}{2ps}\right)$, and $\theta_5 = cos^{-1}\left(\frac{r^2+q^2-d^2}{2rq}\right)$ and are shown in Table 4.14-4.15. The bond angles are almost identical to the conventional bond angles, as can be seen from Table 4.14-4.15. At 1100 °C, the value of θ_1 appears to be decreasing in x = 0.04, and then it turns out to stay unchanged as the iron-nonstoichiometry degree rises. In contrast, the value of θ_2 appears to stay unchanged as the iron-nonstoichiometry level boosts to a maximum of x = 0.08, after which it is went down in x = 0.12. The values of θ_1 and θ_2 are shown to be stable at 1150 °C up until x = 0.08, after which it appears to drop until x = 0.12. At 1200 °C, the value of θ_1 appears to stay steady as the degree of iron-nonstoichiometry rises, but θ_2 turns out to rise in x = 0.04, drop in x = 0.08, and then rise in x = 0.12. At 1250 °C, θ_1 value began to rise as the iron-nonstoichiometry level raised to a maximum of x = 0.08, and then it initiated that it grew in x = 0.12. In contrast, the value of θ_2 was noticed to be unchanged to a maximum of x = 0.04, afterwhich dropped in x = 0.08, and in the end it rised in x = 0.12. The value of θ_3 appears to drop until x = 0.04 at 1100 °C, afterwhich it stayed steady until x = 0.12. The value of θ_3 is observed to hold steady at 1150 °C as the iron-nonstoichiometry level rises. The value of θ_3 is recognized to grow at x = 0.12 at 1200 °C after being steady to a maximum of x = 0.08 at this temperature. At 1250 °C, it appears that the value of θ_3 remains steady to a maximum of x = 0.04, rises in x = 0.08, and then stays same in x = 0.12. At 1100 and 1150 °C, the value of θ_4 appears to drop in x = 0.04, rise for x = 0.08, and afterwhich hold stable in x = 0.12. The value of θ_4 is recognized to drop in x = 0.04, begin to rise in x = 0.08, and afterwhich it drops in x = 0.12 for 1200 °C. The θ_4 value holds steady at 1250 °C as the iron-nonstoichiometry level

rises. At all T_s, it turns out that the value of θ_5 stays steady as the iron-nonstoichiometry level rises. According to the decrease and increase in the pattern of the bond angles depending on iron-nonstoichiometry levels for various T_s, the cationic interactions with cations and anions are reducing and enhancing, respectively [273, 274].

4.2.2. Densification and porosity investigation

In ferrites, the densification process is primarily associated with the diffusion of oxygen vacancies [208]. Table 4.16-4.17 lists the magitudes of porosity (P), theoretical density (ρ_{X-ray}), and bulk density (ρ_{bulk}). The value of ρ_{bulk} appears to be falling in x = 0.04 in Table 4.16-4.17, and it then begins to rise when the iron-nonstoichiometry degree increases at 1100 and 1150 ºC. At 1200 °C, the value of ρ_{bulk} is shown to reduce as the iron-nonstoichiometry level rises to a maximum of x = 0.08, and then it is recognized to rise in x = 0.12. The value of ρ_{bulk} tends to rise at 1250 °C in x = 0.04, and then it is noted to drop when the iron-nonstoichiometry level is raised. In other words, in x = 0, 0.08, and 0.12, the value of ρ_{bulk} begins to rise to a maximum of 1150 °C, and then it shows a decline as T_s rises further. At 1150 °C, the value of ρ_{bulk} is displayed to enhance in x = 0.04; nevertheless, when T_s keeps on increasing, it occurs to essentially stay steady. The reduction in bulk temperature at 1200 and 1250 °C may be due to holes in the materials. Oxygen vacancies have been credited for the increase in ρ_{bulk} value. Some Fe^{3+} ions frequently get turned to Fe^{2+} ions at higher T_s, which results in oxygen vacancies. As a result, larger grains have a greater value for ρ_{bulk} [209]. According to equation $ZnO \rightarrow Zn + (1/2)O_2$ [275] and the occurrence of intragranular voids, which may act as confined pores within the grains due to the fast grain development, pores are formed at higher T_s [276]. The value of ρ_{X-ray} is shown to decrease as the level of iron-nonstoichiometry grows in Table 4.16-4.17, which is most likely results from the increase in cell volume. As the volume of a cell is inversely related to the magnitude of ρ_{X-ray}. The lattice constant and volume of unit cell are shown to rise substantially as the iron-

nonstoichiometry level is raised. The reducing pattern of the molecular mass of subsequent compounds from 239.16 to 229.57 g/mol may also be the cause of the reduction in the value of (ρ_{X-ray} as the iron-nonstoichiometry levels. The value of ρ_{X-ray} consequently declines. Table 4.16-4.17 shows that in x = 0, 0.04, and 0.12, the value of ρ_{X-ray} increases with rising T_s to a maximum of 1200 °C before beginning to fall at 1250 °C. In x = 0.08, the value of ρ_{X-ray} is seen to decrease with rising T_s to a maximum of 1200 °C before increasing at 1250 °C. ρ_{bulk} is worth less than ρ_{X-ray}, which is worth more. It makes sense since the annealed sample may include pores, voids, and fractures at the microscopic scale as well as vacancies at the atomic level. As a result, these defects cannot be circumvented through calculating ρ_{bulk} using the mass/volume relation. In contrast, by precisely determining the lattice constant, the cell volume, as well as the number of atoms per unit cell, one can figure out ρ_{X-ray}, which indicates the proportion of the unit cell's volume to its atoms' mass [277] with data from XRD. According to Table 4.16-4.17, the porosity appears to decrease according to rising iron-nonstoichiometry levels at 1100, 1150, and 1200 °C while remaining constant in x = 0.04. However, at 1250 °C, the porosity appears to rise with rising iron-nonstoichiometry levels. Additionally, the porosity starts to fall with an increase in the iron-nonstoichiometry level to a maximum of 1150 °C. In x = 0, 0.08, and 0.12, it is apparent that the porosity rises in the midst of 1200 and 1250 °C. The porosity escalates in x = 0.04 at 1200 °C, and afterwhich it was dropped in x = 0.04 at 1250 °C.

Table 4.8. Interplanar distance (d_{311}), lattice constant (a), crystallite diameter (D_{311}), cell volume (V_{cell}), dislocation density (δ), and lattice strain (ϵ) of NCZF$e_{2-x}O_{4-3x/2}$ (x = 0, 0.04) system annealed at various T_s.

Iron-nonstoichiometry (x)	T_s (˚C)	d_{311} (Å)	a (Å)	D_{311} (nm)	V_{cell} (Å^3)	δ (× 10^{-4} nm^{-2})	ϵ (× 10^{-3})
0.0	1100	2.54	8.4145	95.0	595.79	1.11	1.19
	1150	2.54	8.4169	110.0	596.28	0.83	1.03
	1200	2.53	8.4027	46.0	593.28	4.73	2.46
	1250	2.54	8.4217	50.0	597.31	4.00	2.24
0.04	1100	2.54	8.4150	79.0	595.89	1.60	1.44
	1150	2.54	8.4162	110.0	596.13	0.83	1.03
	1200	2.54	8.4085	48.0	594.51	4.34	2.34
	1250	2.54	8.4248	51.0	597.97	3.84	2.20

Table 4.9. Interplanar distance (d_{311}), lattice constant (a), crystallite diameter (D_{311}), cell volume (V_{cell}), dislocation density (δ), and lattice strain (ϵ) of NCZFe$_{2-x}$O$_{4-3x/2}$ (x = 0.08, 0.12) system annealed at various T$_s$.

Iron-nonstoichiometry (x)	T$_s$ (˚C)	d_{311} (Å)	a (Å)	D_{311} (nm)	V_{cell} (Å^3)	δ (× 10^{-4} nm^{-2})	ϵ (× 10^{-3})
0.08	1100	2.54	8.4160	87.0	596.09	1.32	1.30
	1150	2.54	8.4208	91.0	597.12	1.21	1.25
	1200	2.54	8.4197	51.0	596.88	3.84	2.20
	1250	2.53	8.4038	51.0	593.51	3.84	2.20
0.12	1100	2.54	8.4199	99.0	596.92	1.02	1.14
	1150	2.54	8.4195	96.0	596.84	1.09	1.18
	1200	2.53	8.3935	45.0	591.33	4.94	2.48
	1250	2.54	8.4202	51.0	596.99	3.84	2.22

4.2.3. Micromorphological investigation

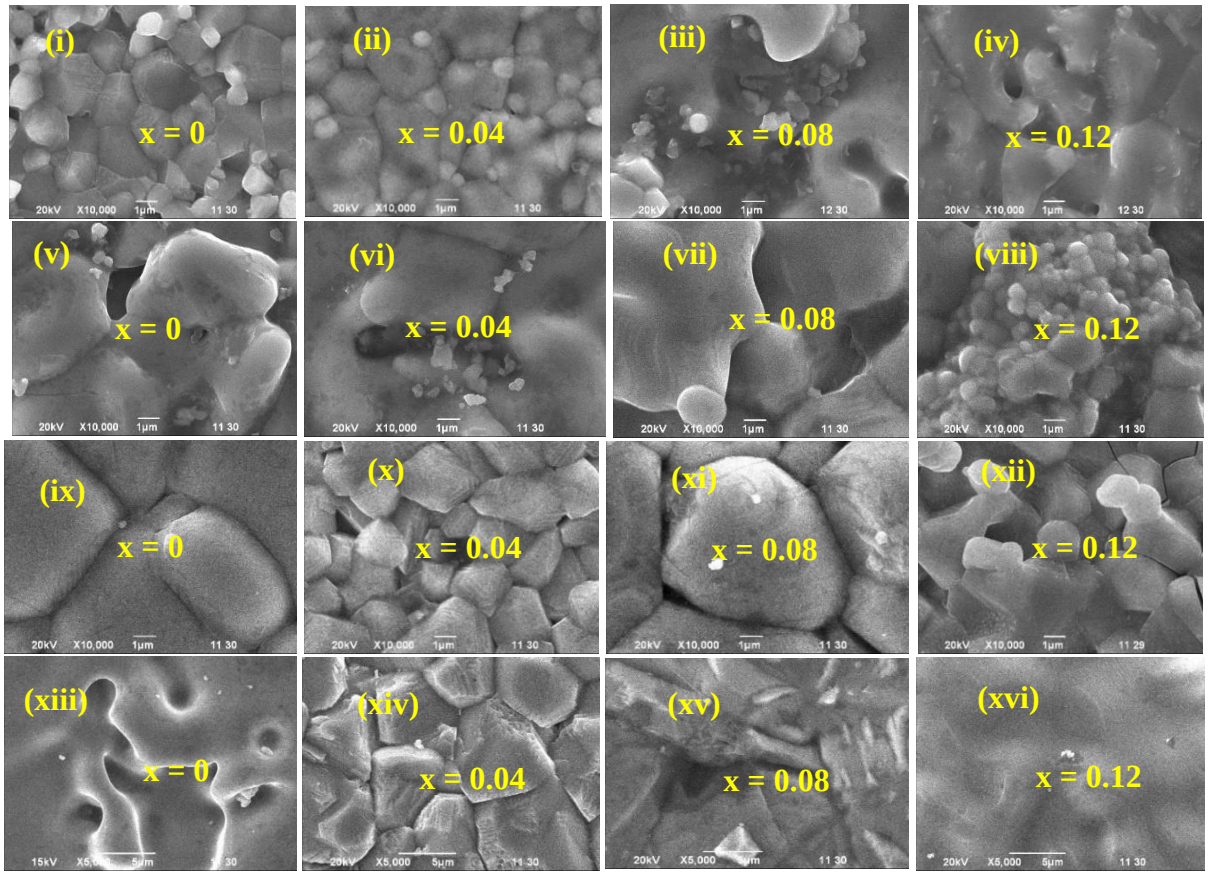

Figure 4.17: Micromorphological structures of $NCZFe_{2-x}O_{4-3x/2}$ system annealed for 5 h at (i-iv) 1100, (v-viii) 1150, (ix-xii) 1200 and, (xiii-xvi) 1250 ºC.

Figure 4.17 shows the micromorphological structures of $NCZFe_{2-x}O_{4-3x/2}$ system: (i-iv) annealed at 1100 ℃, (v-viii) annealed at 1150 ℃, (ix-xii) annealed at 1200 ℃, and (xiii-xvi) annealed at 1250 ℃. As can be seen in Figure 4.17 (i-iv), (v-viii), (ix-xii), and (xiii-xvi), the micromorphologies suggest that T_s and deficiency of iron have a significant impact on grain diameter and porosity. In x = 0.0 and 0.04, the microstructure at 1100 °C shows basically uniform grain diameter as well as some degree of agglomeration. In samples with x = 0.08 and 0.12, irregular growth of grains with some intergranular pores progressively occurs, and homogeneity declines, which may be explained by the production of a liquid phase through the process of sintering [278]. Increasing the iron-nonstoichiometry level to a maximum of x = 0.08 caused the unusual grain to form at 1150 °C with some intergranular holes, and x = 0.12

caused aggregation of small granules to be seen. With rising iron-nonstoichiometry levels, polyhedral granules are seen at 1200 °C. As the level of iron-nonstoichiometry rises, irregular grain development is seen at 1250 °C along with some intragranular holes. The disruption of the equilibrium in the midst of grain development and grain-border diffusion may be the cause of the emergence of some unusual grains with pores [279-281]. In contrast to other specimens (annealed at 1100, 1150, and 1250 °C), the morphology alterations annealed at 1200 °C indicate a distinct growth pattern. This characteristic suggests that the most suitable T_s for the formation of iron-deficient non-stoichiometric nickel-copper-zinc ferrite is 1200 °C. Table 4.16-4.17 lists the average grain diameter together with the level of iron-nonstoichiometry and T_s. As can be seen from Table 4.16-4.17, there is a large difference amongst the mean grain diameter persuaded from SEM micrographs through the line intercept approach and the mean crystallite diameter/mean particle diameter determined from XRD data amploying Debye-Scherrer's formula. It is a known fact that the SEM's resolution is not as important as that of the XRD to clearly differentiate particles, but it may still give growth in grains with substituent amount. However, the XRD strength correlates precisely with the square of the volume. In another word, the mean crystallite diameter that was persuaded was the result of weighing the data on average by a factor of six times the crystal radius. As a result, the signals are varied in strength with respect to particle radii and heavily rely on sample dispersion. The mean diameter of a crystallite or mean particle diameter measured by XRD data should thus never be greater than that determined by SEM [282-284]. Table 4.8 shows that when the level of iron-nonstoichiometry increases at 1100 °C, the mean grain diameter increases as well. At 1150, 1200, and 1250 °C, however, the mean diameter of the grains is shown to grow in x = 0.08, fall in x = 0.12, and then start growing again in x = 0.04. In addition, in x = 0.04 and 0.08, the mean diameter of the grains is seen to rise to a maximum of 1150 °C, then it turns out to drop at 1200 °C, and lastly demonstrated to grow at 1250 °C. At 1150 °C, the mean diameter of the grains begins to shrink, and in x = 0.12, it is subsequently shown to expand with rising T_s. The

dissimilar development of particles and the pore creation with rising T_s may be responsible for the growing and decreasing pattern of mean grain diameter as T_s increases the iron-nonstoichiometry degree. It is also conceivable to use the fluctuation of the lattice constant to explain the growing and decreasing pattern of mean grain diameter with increasing iron-nonstoichiometry level. Table 4.8 shows that above 1100 °C, the lattice constant in x = 0.0 rapidly rises. As a result, the apparent activation energy decreases while the internal tension rises and the action of ferrite powders rises. As a result, the advancement of the grains is promoted, and as a result, the micromorphology has been improved. On the other hand, at 1150, 1200, and 1250 °C, the lattice constant varies nonlinearly with the extent of iron-nonstoichiometry. The improvement in the lattice constant shows that the internal tension rises and the action of ferrite powder increases at 1150, 1200, and 1250 °C. The decrease in perceived activation energy is therefore noticeable. So, when grain develops, it becomes more elaborate, which enhances the microstructure. At 1150, 1200, and 1250 °C, the lattice constant falls, but a rise in internal stress and a reduction in the activity of ferrite powders causes a rise in perceived activation energy. As a result, the growth of grains is slowed, which causes the diameter of the grains to shrink. By lowering the sintering activation energy and enhancing crystalline development, it may be deduced that the proper iron-nonstoichiometry degree in ferrite is advantageous for boosting the solid-state response. The mean diameter of the grains is shown to grow as you increase T_s, as can be seen in Table 4.16-4.17. The advancing of the boundaries of grains closer to one another as far as the combination of distinct small particles into a distinct big particle is believed to be the cause of the increase in mean diameter of grains with rising T_s [281, 282, 285]. To put it another way, the increase in diffusion coefficient which leads in a rapid shift of boundaries of grains and the stimulation of the growth of grains may be the cause of the rise in the diameter of grains with T_s [207].

Table 4.10. Jumping lengths (L_A and L_B), tetrahedrally and octahedrally coordinated sites radii (r_A and r_B), tetrahedrally coordinated bond length (d_{AX}), octahedrally coordinated bond length (d_{BX}), tetrahedrally coordinated shared edge (d_{AXE}), octahedrally coordinated shared edge (d_{BXE}), and octahedral coordinated unshared edge (d_{BXEU}) of $NCZFe_{2-x}O_{4-3x/2}$ (x = 0, 0.04) system annealed at various T_s.

Iron-nonstoichiometry (x)	T_s (˚C)	Hopping lengths		Interstitial radii		d_{AX} (Å)	d_{BX} (Å)	Tetrahedrally coordinated edge	Octahedrally coordinated edge	
		L_A (Å)	L_B (Å)	r_A (Å)	r_B (Å)			d_{AXE} (Å)	d_{BXE} (Å)	d_{BXEU} (Å)
0.00	1100	3.6436	2.9750	0.5892	0.7331	1.9092	2.0544	3.1178	2.8322	2.9767
	1150	3.6446	2.9758	0.5898	0.7337	1.9098	2.0550	3.1187	2.8330	2.9775
	1200	3.6385	2.9708	0.5866	0.7303	1.9066	2.0515	3.1134	2.8282	2.9725
	1250	3.6467	2.9775	0.5909	0.7349	1.9109	2.0561	3.1204	2.8346	2.9792
0.04	1100	3.6438	2.9752	0.5894	0.7333	1.9094	2.0545	3.1180	2.8323	2.9769
	1150	3.6443	2.9756	0.5896	0.7336	1.9096	2.0548	3.1184	2.8327	2.9773
	1200	3.6410	2.9729	0.5879	0.7317	1.9079	2.0529	3.1156	2.8302	2.9746
	1250	3.6480	2.9786	0.5916	0.7357	1.9116	2.0569	3.1216	2.8356	2.9803

Table 4.11. Jumping lengths (L_A and L_B), tetrahedrally and octahedrally coordinated sites radii (r_A and r_B), tetrahedrally coordinated bond length (d_{AX}), octahedrally coordinated bond length (d_{BX}), tetrahedrally coordinated shared edge (d_{AXE}), octahedrally coordinated shared edge (d_{BXE}), and octahedral coordinated unshared edge (d_{BXEU}) of $NCZFe_{2-x}O_{4-3x/2}$ (x = 0.08, 0.12) system annealed at various T_s

iron-nonstoichiometry (x)	T_s (˚C)	Hopping lengths		Interstitial radii		d_{AX} (Å)	d_{BX} (Å)	Tetrahedrally coordinated edge	Octahedrally coordinated edge	
		L_A (Å)	L_B (Å)	r_A (Å)	r_B (Å)			d_{AXE} (Å)	d_{BXE} (Å)	d_{BXEU} (Å)
0.08	1100	3.6442	2.9755	0.5896	0.7335	1.9096	2.0547	3.1183	2.8327	2.9772
	1150	3.6463	2.9772	0.5907	0.7347	1.9107	2.0559	3.1201	2.8343	2.9789
	1200	3.6458	2.9768	0.5904	0.7344	1.9104	2.0556	3.1197	2.8339	2.9785
	1250	3.6390	2.9712	0.5868	0.7305	1.9068	2.0518	3.1138	2.8286	2.9729
0.12	1100	3.6459	2.9769	0.5905	0.7345	1.9105	2.0557	3.1198	2.8340	2.9786
	1150	3.6458	2.9767	0.5904	0.7344	1.9104	2.0556	3.1196	2.8339	2.9785
	1200	3.6345	2.9676	0.5845	0.7280	1.9045	2.0493	3.1099	2.8251	2.9693
	1250	3.6461	2.9770	0.5905	0.7345	1.9105	2.0558	3.1199	2.8341	2.9787

Table 4.12. Interionic distances (p, q, r, s, b, c, d, e and f) of NCZFe$_{2-x}$O$_{4-3x/2}$ (x = 0, 0.04) system annealed at various T$_s$.

Iron-nonstoichiometry (x)	T$_s$ (˚C)	Interatomic distances in the midst of cations (Me-Me)					Interatomic distances in the midst of cations-anions (Me-O)			
		b (Å)	c (Å)	d (Å)	e (Å)	f (Å)	p (Å)	q (Å)	r (Å)	s (Å)
0.00	1100	2.9750	3.4885	3.6436	5.4654	5.1528	2.0531	1.9092	3.6559	3.6727
	1150	2.9758	3.4895	3.6446	5.4669	5.1543	2.0537	1.9098	3.6570	3.6738
	1200	2.9708	3.4836	3.6385	5.4577	5.1456	2.0503	1.9066	3.6508	3.6676
	1250	2.9775	3.4915	3.6467	5.4701	5.1572	2.0549	1.9109	3.6590	3.6758
0.04	1100	2.9752	3.4887	3.6438	5.4657	5.1531	2.0533	1.9094	3.6561	3.6730
	1150	2.9756	3.4892	3.6443	5.4665	5.1538	2.0536	1.9096	3.6567	3.6735
	1200	2.9729	3.4860	3.6410	5.4615	5.1491	2.0517	1.9079	3.6533	3.6710
	1250	2.9786	3.4927	3.6480	5.4721	5.1591	2.0557	1.9116	3.6604	3.6772

Table 4.13. Interionic distances (p, q, r, s, b, c, d, e and f) of NCZFe$_{2-x}$O$_{4-3x/2}$ (x = 0.08, 0.12) system annealed at various T$_s$.

Iron-nonstoichiometry (x)	T$_s$ (˚C)	Interatomic distances in the midst of cations (Me-Me)					Interatomic distances in the midst of cations-anions (Me-O)			
		b (Å)	c (Å)	d (Å)	e (Å)	f (Å)	p (Å)	q (Å)	r (Å)	s (Å)
0.08	1100	2.9755	3.4891	3.6442	5.4664	5.1537	2.0535	1.9096	3.6566	3.6734
	1150	2.9772	3.4911	3.6463	5.4695	5.1567	2.0547	1.9107	3.6587	3.6755
	1200	2.9768	3.4906	3.6458	5.4688	5.1560	2.0544	1.9104	3.6582	3.6750
	1250	2.9712	3.4830	3.6390	5.4584	5.1463	2.0505	1.9068	3.6513	3.6681
0.12	1100	2.9769	3.4907	3.6459	5.4689	5.1561	2.0545	1.9105	3.6583	3.6751
	1150	2.9767	3.4905	3.6458	5.4686	5.1559	2.0544	1.9104	3.6581	3.6749
	1200	2.9676	3.4798	3.6345	5.4517	5.1399	2.0480	1.9045	3.6468	3.6636
	1250	2.9770	3.4908	3.6461	5.4691	5.1563	2.0545	1.9105	3.6584	3.6752

4.2.4. Fourier transform infrared spectroscopic investigation

Figure 4.18 shows the FTIR spectra of $NCZFe_{2-x}O_{4-3x/2}$ system at various T_s: (a) 1100, (b) 1150, (c) 1200, and (d) 1250 °C. The vibrations of the intrinsic stretching absorption spectra of the octahedrally coordinated (B) sites (ν_2 band) are at 479.18-452.79 cm^{-1} and the vibrations of the tetrahedrally coordinated (A) sites (ν_1 band) are at 602.35-814.37 cm^{-1}, as shown in Table 4.18-4.19.

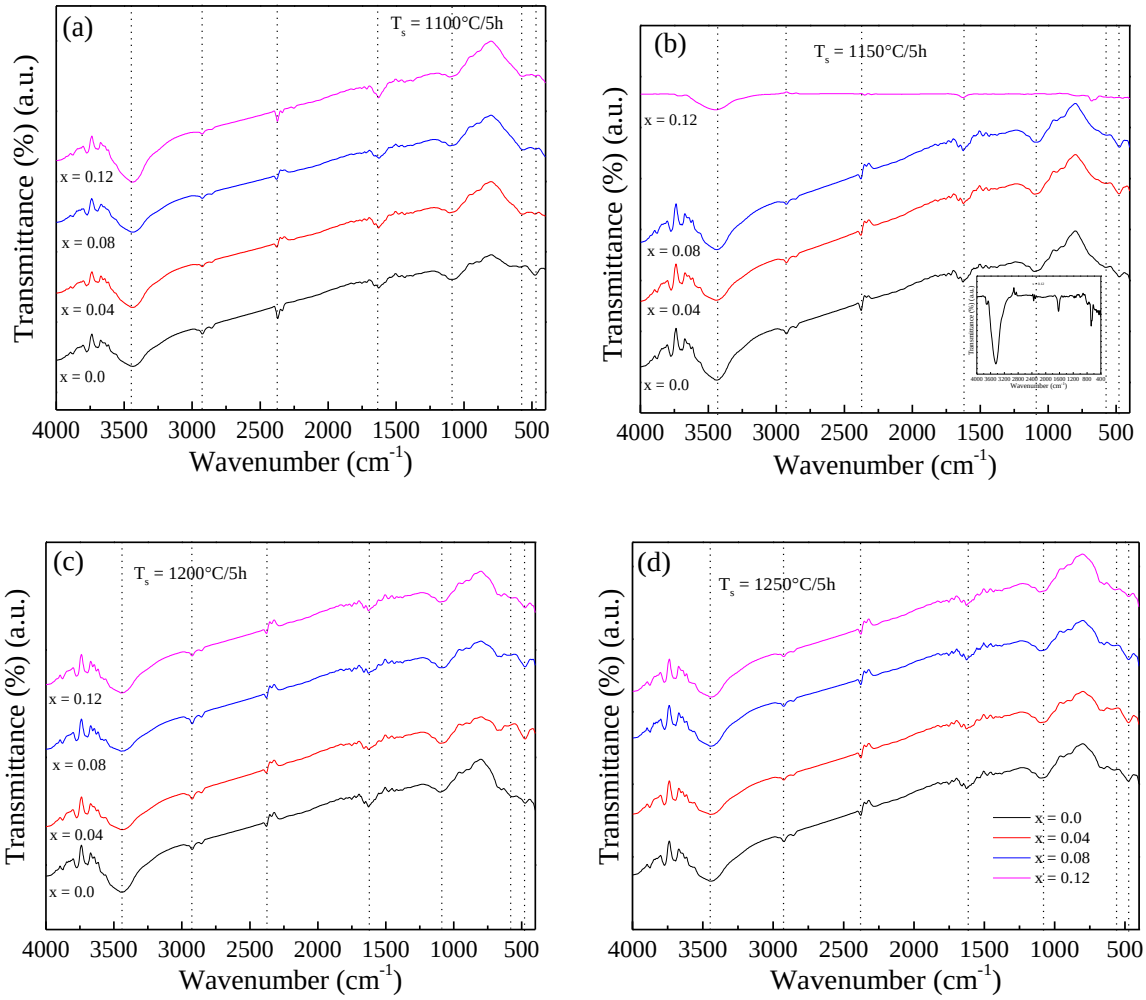

Figure 4.18: FTIR spectra of $NCZFe_{2-x}O_{4-3x/2}$ system annealed at (a) 1100, (b) 1150, (c) 1200, and (d) 1250 °C.

Two bands, ν_1 (590 from 610 cm^{-1}) and ν_2 (400 to 420 cm^{-1}) are the result of the elongation of cation-anion bonds at the tetrahedrally and octahedrally coordinated (A and B)-sites, according to Waldron's classification [134]. Consequently, it may be assumed that the manufactured ferrites are of the spinel type with cubic symmetry [286]. Table 4.18-4.19 provide an overview of the disparity amongst ν_1 and ν_2 bands with iron-nonstoichiometry level at different T_s. The mean metal-oxygen lengths, electronegativity, ionic radii, and force constants at the tetrahedrally and octahedrally coordinated (A and B)-sites, respectively, are often accountable for discrepancies in the positions of two bands [287]. According to Evans and Hafner's prediction that the bonding distance of the Fe^{3+}-O^{2-} groups at the tetrahedrally coordinated-A site (1.890-1.879Å) is lessened than that of the octahedrally coordinated (B)-site (1.982 to 1.970 Å), the discrepancy in the midst of the band positions can be explained by the variation in bond length [226]. This means that the normal vibrational modes of the tetrahedrally coordinated (A)-site groups is larger than that of the octahedrally coordinated (B)-site groups [234, 288] or that the metal-oxygen groups at the tetrahedrally coordinated (A)-site have more covalence than those at the octahedrally coordinated (B)-site [289]. Table 4.18-4.19 show that, at 1100 °C, the value of ν_1 shifts toward the higher wavenumber band in x = 0.04, then toward a low frequency band in x = 0.08, and finally shifts toward the higher wavenumber band in x = 0.12, while the value of ν_2 shifts toward the lower wavenumber band at x = 0.04, afterwhich it stays invariant in x = 0.08, and lastly, when x = 0.12, it changes to the higher wavenumber band. At 1150 °C, it is discovered that the value of ν_1 and ν_2 is unaffected by increasing the iron-nonstoichiometry level to a maximum of x = 0.08, and that progress to low wavenumber band in x = 0.12. At 1200 °C, the value of ν_1 shifts toward the high wavenumber band as the iron-nonstoichiometry level increases to a maximum of x = 0.08; after that, it shifts toward the low wavenumber band in x = 0.12; meanwhile, the value of ν_2 shifts toward the low wavenumber band in x = 0.04 and is recognized to remain the same as iron-nonstoichiometry degree rises. At 1250 °C, the ν_1 value changes toward the higher wavenumber band at x = 0.04,

and then it turns out to move toward the low wavenumber band on rising iron-nonstoichiometry degree. In contrast, the value of ν_2 stays constant with raising iron-nonstoichiometry degree. The reallocation of Ni/Zn/Cu and Fe cations amongst the tetrahedrally and octahedrally coordinated (A and B)-sites may be connected to the shifting of ν_1 and ν_2 to the high frequency and low frequency band, respectively. Since it is well known that a smaller site radius increases the basicfrequency, the center frequency should be moved to the higher wavenumber band. In x = 0.0 and 0.08, it is noticed that the absorption (ν_1) band shifts toward the lower wavenumber band as T_s rises to a maximum of 1200 °C before shifting to the higher wavenumber band at 1250 °C. With growing T_s to a maximum of 1200 °C, the absorption (ν_1) band is shown to move toward the higher wavenumber band in x = 0.04; at 1250 °C, it is then shifted toward the lower wavenumber band. In x = 0.12, the absorption (ν_1) band is seen to stay unaffected to a maximum of 1250 °C after shifting toward the lower wavenumber band at 1150 °C. The bending vibrational modes of the O-H of the absorbed water molecules result in the strong wavenumber band at 1084.46 cm^{-1} for 1100 °C, 1084.46 cm^{-1} for 1150 °C, 1084.46 cm^{-1} for 1200 °C, and 1077.42 cm^{-1} for 1250 °C [218]. The bending vibrations of the H-O-H bond are responsible for the wavenumbers corresponding to 1628.15 cm^{-1} for 1100 °C, 1621.11 cm^{-1} for 1150 °C, 1621.11 cm^{-1} for 1200 °C, and 1614.08 cm^{-1} for 1250 °C. The physical adsorption of H_2O on the surfaces is demonstrated here [219-221]. The existence of a faint band around the numbers 2372.43 cm^{-1} for 1100 °C, 2379.47 cm^{-1} for 1150 °C, 2379.47 cm^{-1} for 1200 °C, and 2379.47 cm^{-1} for 1250 °C might be attributed to the minute amount of ambient CO_2 that has been adsorbed [290]. Hydrogen bonding is attributed with causing the low intensity wavenumber band to exist around 2921.41 cm^{-1} (at 1100 °C), 2928.45 cm^{-1} for 1150 °C, 2928.45 cm^{-1} for 1200 °C, and 2928.45 cm^{-1} for 1250 °C [290]. The H-O-H stretching pattern is responsible for the broad band with the center points of 3438.71 cm^{-1} at 1100 °C, 3428.15 cm^{-1} for 1150 °C, 3442.23 cm^{-1} for 1200 °C, and 3442.23 cm^{-1} for 1250 °C, that can be taken as proof of free (or absorbed) water [287]. The force constants (K_T and K_O) of tetrahedrally

and octahedrallly coordinated sites were determined using the formula [134, 204]: $K_{T/O} = 4\pi^2 c^2 \nu_{1/2}^2 \mu$, where c denotes the speed of velocity; $\nu_{1/2}$ denotes FTIR wavenumber peak at the tertrahedrally and octahedrally coordinated sites; μ denotes the reduced mass and are shown in Table 4.18-4.19. Table 4.18-4.19 show that the value of K_O is lower than K_T. This variation is caused by variations in a band that spans ν_1 and ν_2 bands. At 1100 °C, the value of K_T drops as the iron-nonstoichiometry degree increases to a maximum of x = 0.08; however, then improves until x = 0.12; in contrast, the value of K_O drops at x = 0.04, and then it stays invariant until x = 0.08; and ultimately, it declines. The values of K_T and K_O are found at 1150 °C to be unchanged to a maximum of x = 0.08 and thereafter drops until x = 0.12. At 1200 °C, the value of K_T rises to a maximum in x = 0.08 and afterwhich it drops until x = 0.12, while the value of K_O is shown stays constant as the iron-nonstoichiometry level rises. At 1250 °C, the value of K_T improves in x = 0.04 and then begin to fall when the iron-nonstoichiometry degree is increased further. In contrast, the value of K_O seems to stay stable as the iron-nonstoichiometry amount is raised. Additionally, it is seen that there is a little shift in the force constants as the iron-nonstoichiometry level rises, which may be related to a slight fluctuation in the molecular mass of the cations at the sites [202]. The cationic redistribution could be responsible for the decreasing and growing trends in K_T and K_O with iron-nonstoichiometry amounts at different T_s [291]. The Debye temperature (Θ_{Dw}) due to Waldron [134] was determined using the formula [134]: $\Theta_{Dw} = \frac{\hbar c \nu_{av}}{k_B} = 1.438\, \nu_{av}$, where k_B denotes Boltzmann constant, h denotes the Planck's constant, c expresses the speed of light and $\nu_{av} = \frac{\nu_1 + \nu_2}{2}$ denotes the mean frequency. The computed values of Θ_{Dw} are shown in Table 4.18-4.19. In Table 4.18-4.19, the calculated values of Θ_{Dw} are displayed. At 1100 °C, the value of Θ_{Dw} is shown to reduce when iron-nonstoichiometry level rises to a maximum of x = 0.08, and afterwhich improves in x = 0.12. When iron-nonstoichiometry level is increased to a maximum of x = 0.08 at 1150 °C, the value of Θ_{Dw} appears to stay constant. At x = 0.12 it begins to

increase. The value of Θ_{Dw} is shown to increase with increasing iron-nonstoichiometry extent to a maximum of x = 0.08 at 1200 °C and thereafter to fall in x = 0.12. The value of Θ_{Dw} enhances in x = 0.04 at 1250 °C, and afterwhich it drops with more enhancement in the degree of the iron-nonstoichiometry. The decreasing tendency of Θ_{Dw}value that occurs as iron shortage increases may be related to a reduction in vibrational frequencies [292, 293].

4.2.5. Elastic characteristics

The investigation of elastic characteristics is required to clarify the class of the bonding attractions in solid materials and to comprehend the thermal characteristics of solid materials. Using the XRD and FTIR data, it is possible to compute the samples' elastic properties and Debye temperature. The stiffness constants $C_{11}$and C_{12} have been derived using the relationships [234]: $C_{11} = \frac{K_{average}}{a}$ and $C_{12} = \frac{\sigma C_{11}}{(1-\sigma)}$, where $K_{average} = (K_T + K_O)/2$ denotes the mean force constant, a denotes the lattice constant, and σ denotes the Poisson ratio that is relied upon the pore fragment (Porosity P) [294]: $\sigma = 0.324(1 - 1.043\ P)$. Table 4.20-4.21 provide a summary of $C_{11}$and C_{12} and σ at various Ts. In contrast to shear, the Poisson ratio (σ) is typically used to gauge how stable a crystal is, and the superior the Poisson ratio, the superior the plasticity [233]. Poisson ratio is determined to have a value in the midst of 0.28 and 0.32, as shown in Table 4.4.20-4.21. The reported magnitudes of σ range from -1 to 0.5 that is in line with the isotropic elastic notion of [295] and implies acceptable plasticity and elasticity character of iron-deficient non-stroichiometric nickel-copper-zinc ferrite [233]. The value of C_{11} is outlined to decrease gradually on rising the iron-nonstoichiometry degree to a maximum of x = 0.08, and afterwich it stayed unaltered in x = 0.12, according to Table 4.20-4.21, whereas the value of C_{12} progressively drops in x = 0.04, and afterwhich it escalates in x = 0.08, and aftewhich stayed unaltered in x = 0.12 for 1100 °C. At 1100 °C, C_{11} value stays unaltered to a maximum of x = 0.08 and then to fall in x = 0.12, whereas the value of C_{12} is recognized to drop in x = 0.04, afterwhich it improves in x = 0.08, and lastly drops in x = 0.12.

The value of C_{11} and C_{12} steadily improves to a maximum of x = 0.08 at 1200 °C, afterwhich it drops till x = 0.12. At 1250 °C, the value of C_{11} rises in x = 0.04, and as the iron-nonstoichiometry level rises, it is discovered to fall. The fluctuation of the lattice constant is directly related to the increasing and decreasing pattern of the elastic stiffness constants with iron-nonstoichiometry amount. When the cation-oxygen bond length is found to grow, less energy is required to break longer bonds, which causes a decrease in the attraction and C_{11} and C_{12} [296]. The moduli of elasticity of the iron-deficient nickel-copper-zinc ferrites have been determined employing the formulae [179, 226]:

$$B = \frac{1}{3}(C_{11} + 2C_{12}),$$

$$E = \frac{(C_{11}-C_{12})(C_{11}+2C_{12})}{(C_{11}+C_{12})}$$

$$n = \frac{E}{2(\sigma+1)}.$$

The longitudinal (V_l) and shear (V_s) wave velocities were determined through the formulae [294]:

$$V_l = \sqrt{\frac{C_{11}}{D_x}},$$

$$V_t = \frac{V_l}{\sqrt{3}}\ [294].$$

The average velocity (V_m) was determined from V_l and V_s values through the formula:

$$\frac{3}{V_m^3} = \frac{1}{V_l^3} + \frac{2}{V_t^3}.$$

The Debye temperature (Θ_{DA}) was determined using Anderson's formula [294]:

$$\Theta_{DA} = \frac{h}{k_B}\left[\frac{3D_{X-ray}qN_A}{4\pi M_w}\right]^{1/3} \times V_m,$$

where h represents Planck's constant, k_B denotes Boltzmann's constant, M_w denotes molecular mass, q denotes the number of atoms per formula unit and V_m denotes average wave velocity. Table 4.20-4.21 lists the elastic stiffness constants (C_{11} and C_{12}), wave velocities (V_l and V_s), and mean (V_m), moduli of elasticity (E, B, G), Poisson ratio (σ), and Debye temperature (Θ_{DA}) annealed at various T_s. As shown in Table 4.20-4.21, the value of E is found to be stable at 1100 °C in x = 0.12 after declining with increasing the iron-nonstoichiometry level to a maximum of x = 0.08. The value of E improves in x = 0.04 at 1150 °C, and afterwhich it drops as the iron-nonstoichiometry level increases. The value of E is found to grow to a maximum of x = 0.08 and thereafter drops till x = 0.12 at 1200 °C. The value of E steadily drops with increasing iron insufficiency quantity around 1250 °C. Similar to this, at 1100 °C, B value is shown to drop in x = 0.04, rise in x = 0.08, and then remain unchanged in x = 0.12. The value of B drops at 1150 °C in x = 0.04; afterwhich it grows in x = 0.08; and ultimately, it drops in x = 0.12. The value of B steadily improves to a maximum of x = 0.08 at 1200 °C, and then it drops until x = 0.12. The value of B enhances in x = 0.04 at 1250 °C, and then it drops as the iron-nonstoichiometry level increases. On the other hand, G value is discovered to remain stable until x = 0.12 at 1100 °C, when it is detected to decrease steadily to a maximum of that point. The value of G begins to rise in x = 0.04 at 1150 °C, and when the iron-nonstoichiometry degree rises, it is then shown to fall. The value of G steadily enhances to a maximum of x = 0.08 at 1200 °C and then it drops till x = 0.12. The value of G drops at 1250 °C as the iron-nonstoichiometry degree rises. As seen in Table 4.20-4.21, the value of B is more than that of G (i.e., $B > G$), indicating that the modulus of rigidity has a substantial impact on the stability and robust ability of nickel-copper-zinc ferrite to resist deformation. The noticed fluctuation of the moduli of elasticity with the degree of iron-nonstoichiometry and the variation of the lattice constant exhibit strong correlations. The observed increasing and decreasing characteristics of the moduli of elasticity with the iron-nonstoichiometry degree at various T_s imply that the

interatomic interaction amongst the component atoms in iron-deficient non-stoichiometric nickel-copper-zinc ferrite is strengthening and weakening [126, 297]. As shown in Table 4.20-4.21, the value of V_l is found to rise in x = 0.12 at 1100 ºC after declining with increasing the iron-nonstoichiometry level to a maximum of x = 0.08. The value of V_l enhances to a maximum of x = 0.08 at 1150 °C, and thereafter it drops till x = 0.12. The value of V_l enahnces to a maximum of x = 0.08 at 1200 °C before beginning to decrease till x = 0.12. The value of V_l improves at 1250 °C in x = 0.04, and afterwhich it drops as the iron-nonstoichiometry level increases. The value of V_s begins to decrease around 1100 °C as the extent of iron-nonstoichiometry rises. The value of V_s enhances in x = 0.04 at 1150 °C, but it then seems to decrease as the iron-nonstoichiometry level increases. The value of V_s enhances to a maximum of x = 0.08 at 1200 °C, afterwhich it drops till x = 0.12. At 1250 °C, the value of V_s drops in x = 0.04, remain constant in x = 0.08, and afterwhich it enhances in x = 0.12. Since the samples have varied densities, the fluctuation of the moduli of elasticity and wave velocity is attributed to the change in the density admist the iron-nonstoichiometry level at various T_s [298]. The value of V_m is shown to decrease at 1100 °C as the iron-nonstoichiometry degree rises. The value of V_m begins to increase in x = 0.04 at 1150 °C, and when the iron-nonstoichiometry level increases, it is then shown to decrease. The value of V_m is shown to escalate to a maximum of x = 0.08 at 1200 °C, and then it is discovered to decrease till x = 0.12. When the iron-nonstoichiometry degree is increased to a maximum of x = 0.08 at 1250 °C, the value of V_m begins to decrease. However, once x = 0.12 is reached, it is discovered to grow.

Table 4.14. Bond angles in the midst of the cations and cation-anion (θ_1, θ_2, θ_3, θ_4 and θ_5) of NCZFe$_{2-x}$O$_{4-3x/2}$ (x = 0, 0.04) system annealed at various T_s.

Iron-nonstoichiometry (x)	T_s (˚C)	bond angles in the midst of the cations and cation-anion (º)				
		θ_1 (degree)	θ_2 (degree)	θ_3 (degree)	θ_4 (degree)	θ_5 (degree)
0.00	1100	123.35	144.95	92.86	125.92	74.48
	1150	123.34	144.94	92.85	125.92	74.48
	1200	123.34	144.94	92.85	125.92	74.48
	1250	123.34	144.95	92.85	125.92	74.48
0.04	1100	123.34	144.95	92.85	125.91	74.48
	1150	123.34	144.94	92.85	125.91	74.48
	1200	123.34	144.95	92.85	125.87	74.48
	1250	123.33	144.95	92.85	125.92	74.48

Table 4.15. Bond angles in the midst of the cations and cation-anion (θ_1, θ_2, θ_3, θ_4 and θ_5) of $NCZFe_{2-x}O_{4-3x/2}$ (x = 0.08, 0.12) system annealed at various T_s.

Iron-nonstoichiometry (x)	T_s (˚C)	bond angles in the midst of the cations and cation-anion (º)				
		θ_1 (degree)	θ_2 (degree)	θ_3 (degree)	θ_4 (degree)	θ_5 (degree)
0.08	1100	123.34	144.95	92.85	125.92	74.48
	1150	123.34	144.94	92.85	125.92	74.48
	1200	123.34	144.45	92.85	125.92	74.48
	1250	123.28	144.94	92.86	125.92	74.48
0.12	1100	123.34	144.94	92.85	125.92	74.48
	1150	123.33	144.94	92.85	125.92	74.48
	1200	123.34	144.94	92.86	125.91	74.48
	1250	123.34	144.95	92.86	125.92	74.48

Table 4.16. Bulk density (ρ_{bulk}), theoretical density (ρ_{X-ray}), pore fraction (f), porosity (P), and grain diameter (D_{SEM}) of NCZFe$_{2-x}$O$_{4-3x/2}$ (x = 0, 0.04) system annealed at various T$_s$.

Iron-nonstoichiometry (x)	T$_s$ (˚C)	ρ_{bulk} (g/cm^3)	ρ_{X-ray} (g/cm^3)	pore fraction (f)	P (%)	D_{SEM} (μm)
0.0	1100	4.94	5.33	0.07	7	1.58
	1150	5.03	5.33	0.06	6	3.50
	1200	4.94	5.36	0.08	8	4.50
	1250	4.57	5.32	0.14	14	9.58
0.04	1100	4.86	5.26	0.08	8	1.88
	1150	4.93	5.26	0.06	6	2.42
	1200	4.91	5.27	0.07	7	2.10
	1250	4.91	5.24	0.06	6	6.02

Table 4.17. Bulk density (ρ_{bulk}), theoretical density (ρ_{X-ray}), pore fraction (f), porosity (P), and grain diameter (D_{SEM}) of $NCZFe_{2-x}O_{4-3x/2}$ (x = 0.08, 0.12) system annealed at various T_s.

Iron-nonstoichiometry (x)	T_s (˚C)	ρ_{bulk} (g/cm^3)	ρ_{X-ray} (g/cm^3)	pore fraction (f)	P (%)	D_{SEM} (μm)
0.08	1100	4.92	5.19	0.05	5	2.13
	1150	4.95	5.18	0.04	4	4.38
	1200	4.88	5.18	0.06	6	3.94
	1250	4.82	5.21	0.08	8	9.37
0.12	1100	4.94	5.11	0.03	3	2.92
	1150	4.97	5.11	0.03	3	1.20
	1200	4.93	5.16	0.05	5	2.02
	1250	4.66	5.11	0.09	9	7.45

Table 4.18. FTIR wavenumber bands, average wavenumber bands, force constants (K_T and K_0), average force constant, ($\nu_1 - \nu_2$), and Debye temperature due to Waldron method (Θ_{DW}) of $NCZFe_{2-x}O_{4-3x/2}$ (x = 0, 0.04) system annealed at various T_s.

Iron-nonstoichiometry (x)	T_s (˚C)	ν_1 (cm^{-1}) (A-site)	ν_2 (cm^{-1}) (B-site)	ν_{mean} (cm^{-1})	$K_T \times 10^5$ (dynes/cm)	$K_0 \times 10^5$ (dynes/cm)	$K_{av} = (K_T + K_O)/2 \times 10^5$ (dynes/cm)	$\nu_1 - \nu_2$ (cm^{-1})	Θ_{DW} (K)
0.0	1100	590.03	479.18	534.61	2.55	1.68	2.12	110.85	768.76
	1150	575.95	479.18	527.57	2.43	1.68	2.06	96.77	758.64
	1200	568.33	473.93	521.13	2.37	1.65	2.01	94.40	749.38
	1250	575.95	473.90	524.93	2.43	1.65	2.04	102.05	754.84
0.04	1100	568.91	473.90	521.41	2.37	1.65	2.01	95.01	749.78
	1150	575.95	479.18	527.57	2.43	1.68	2.06	96.77	758.64
	1200	595.31	473.90	534.61	2.60	1.65	2.13	121.41	768.76
	1250	595.31	473.90	534.61	2.60	1.65	2.13	121.41	768.76

Table 4.19. FTIR wavenumber bands, average wavenumber bands, force constants (K_T and K_0), average force constant, ($\nu_1 - \nu_2$), and Debye temperature due to Waldron method (Θ_{DW}) of $NCZFe_{2-x}O_{4-3x/2}$ (x = 0.08, 0.12) system annealed at various T_s.

Iron-nonstoichiometry (x)	T_s (˚C)	ν_1 (cm^{-1}) (A-site)	ν_2 (cm^{-1}) (B-site)	ν_{mean} (cm^{-1})	$K_T \times 10^5$ (dynes/cm)	$K_0 \times 10^5$ (dynes/cm)	$K_{av} = (K_T + K_O)/2 \times 10^5$ (dynes/cm)	$\nu_1 - \nu_2$ (cm^{-1})	Θ_{DW} (K)
0.08	1100	561.88	473.90	517.89	2.31	1.65	1.98	87.98	744.73
	1150	575.95	479.18	527.57	2.43	1.68	2.06	96.77	758.64
	1200	602.35	473.90	538.13	2.66	1.65	2.16	128.45	773.82
	1250	582.99	473.90	528.45	2.49	1.65	2.07	109.09	759.90
0.12	1100	568.91	479.18	524.05	2.37	1.58	1.98	89.73	753.58
	1150	514.37	452.79	483.58	1.94	1.50	1.72	61.58	695.39
	1200	568.91	473.90	521.41	2.37	1.65	2.01	95.01	749.78
	1250	568.91	473.90	521.41	2.37	1.65	2.01	95.01	749.78

Table 4.20-4.21 show that the value of V_l is greater than the V_s value (i.e., $V_l > V_s$). This might be clarified through the notion that as a wave goes through a substance, it brings its particles to vibrate. When exposed to vibrating particles, additional particles may vibrate as a result of the energy transfer. The energy of ultrasonic waves is lowered as a result. Compared to longitudinal waves, shearing waves take more energy to get nearby particles to vibrate when they are vibrated. The parallel vibrating of particles in longitudinal waves requires less energy than the vibration of an adjacent particle perpendicular to to the way the waves are moving. As a result, shearing or transversal velocity is lower than longitudinal velocity [299, 300]. The value of Θ_{DA} is seen to decrease as the iron-nonstoichiometry level increases at 1100 °C. At 1150 °C, the value of Θ_{DA} enhances in x = 0.04 and afterwhich begins to fall as the iron-nonstoichiometry level rises. The value of Θ_{DA} is found to increase to a maximum of x = 0.08 and thereafter drops till x = 0.12 at 1200 °C. At 1250 °C, Θ_{DA} value drops in x = 0.04 and afterwhich it improves as the iron-nonstoichiometry dgree increases. For all T_s, the iron-nonstoichiometry level is linearly related to the value of Θ_{DA} and mean velocity. According to the highest Debye temperature, the sample's strongest covalent bond is present. The Debye temperature increases and decreases depending on the level of iron-nonstoichiometry at different T_s, and this behavior is correlated with the persistence of all lattice vibration modes and the stiffness constants of the samples. Unless the observed elastic moduli are adjusted to a void-free state, they are meaningless. As a result, the porosity adjustment is obligatory for elastic characteristics in industrial uses. In order to ascertain the moduli of elasticity without pores or voids of our manufactured materials, we have used three approaches that are now available: (i) Hassselman and Fulrath model (HF model) [130]. This notion assumes that the pores are spherical and are dispersed across a homogenous, isotropic elastic material. These empirical formulae:

$$\frac{1}{E_0} = \frac{1}{E}\left[1 - \frac{3(1-\sigma)(9+5\sigma)}{2(7-5\sigma)}\right],$$

$$\frac{1}{G_0} = \left[1 - \frac{15(1-\sigma)}{(7-5\sigma)}\right],$$

$$\sigma_0 = \left(\frac{E_0}{2G_0}\right) - 1,$$

$$\text{and } B_0 = \left(\frac{E_0 G_0}{3(3G_0 - E_0)}\right)$$

were utilized, (ii) The Ledbetter and Datta model (LD model) [130] used the assumption that the spherical voids were dispersed at random and possessed no resistance to either dilation or shear. These formulae: $$G_0 = \left(\frac{1}{2A_1}\right)\left[-A_2 + (A_2^2 - 4A_1A_3)^{\frac{1}{2}}\right],$$

$$B_0 = \frac{(4G_0B)}{[4(1-f)G_0 3fB]},$$

$$\text{and } E_0 = \frac{9B_0G_0}{3B_0+G_0},$$

where $A_1 = \left(\frac{8}{3}\right)(1-f)$, $A_2 = (3-2f)B - \left(\frac{8}{3} + 4f\right)G$, and $A_3 = -3(1+f)BG$ were used, and (iii) The elastic hypothesis [129, 132] anticipated that when the pore fraction is $f < 0.2$, there will be a linear relationship in the midst of elastic moduli as a function of porosity. These formulae: $V_l = V_{l0}(1 - C_lP)$, $V_t = V_{t0}(1 - C_tP)$, $E = E_0(1 - C_EP)$, $n = n_0(1 - C_nP)$ and $\sigma = \sigma_0(1 - C_\sigma P)$ were used, where C_l, C_t, C_Y, C_n and C_σ are material's constants. The non-porous elastic constants of the substance are represented by the subscript '0'. The constants (C_l, C_t, C_Y, C_n and C_σ) are determined using the formulae:

$$C_l = \frac{1}{2}\left\{\left|\frac{[C_Y + 2C_\sigma\sigma_0^2(2-\sigma_0)]}{(1-\sigma_0)(1+\sigma_0)(1-2\sigma_0)-1}\right|\right\},$$

$$C_t = \frac{1}{3},\ C_E = \left(\frac{1}{18}\right)(29 + 11\sigma_0),$$

$$C_n = \frac{5}{3} \text{ and}$$

$$C_\sigma = \left(\frac{5}{9}\right) + \left(\frac{11\sigma}{18}\right) - \left(\frac{1}{18}\sigma\right).$$

Zero-porosity corrected moduli of elasticity (E_0, G_0, B_0), and Poisson ratio (σ_0) using elastic theory, Hassselman and Fulrath, Ledbetter and Datta models and preseneted in Table 4.22-

4.23, 4.24-4.25, and 4.26-4.27. It has been demonstrated that the change of the zero-porosity-corrected elastic parameters with iron-nonstoichiometry level at variousT_s (Table 4.22-4.23, 4.24-4.25, 4.26-4.27) is comparable to that of the uncorrected elastic constants at various T_s (Table 4.20-4.21). The elastic parameters without zero-porosity correction are less than the zero-porosity adjusted elastic parameters, as shown in Table 4.22-4.23, 4.24-4.25, and 4.26-4.27. These findings imply that the porosity has an impact on the iron-deficient non-stoiochiometric nickel-copper-zinc ferrite's elastic characteristics. Because interatomic interaction has improved in strength, the elastic parameters are shown to rise with rising T_s. Because of the persistent inter-atomic bonding in the midst of the different atoms in the samples, the moduli of elasticity decrease with the extent of iron-nonstoichiometry. The (B/G) ratio must be studied in order to determine if a material is brittle or ductile like synthetic materials. Pugh [128] has already stated that materials are brittle when the B/G ratio is below the crucial value (1.75), and are ductile when the ratio of B/G is more than 1.75. We additionally investigated the fragility and flexibility of ferrite materials through investigation of the Poisson ratio (σ) in line with Frabtsevich [126]. If the Poisson ratio is 0.26, the Poisson formula determines whether a material is brittle or ductile [301]. According to our research, the B_0/G_0 ratio falls in the midst of 1.98 and 2.44 (HF model) (Table 4.20-4.21) and 2.84 and 4.54 (LD model) (Table 4.22-4.23) at all T_s. As can be seen in Table 4.22-4.23, 4.24-4.25, and 4.26-4.27, the Poisson ratio (σ) is in the range of 0.28-0.32 with iron-nonstoichiometry level at different T_s. Since the manufactured iron-deficient non-stoichiometric ferrite displays ductile character with iron-nonstoichiometry degree at various T_s, it can be concluded that they meet Pugh and Frabtsevich's criteria.

Table 4.20. Elastic stiffness constants (C_{11} and C_{12}), longitudinal (V_l), transversal (Shear) (V_s) and mean (V_m) wave velocities, moduli of elasticity (E, B,G), longitudinal modulus (L), Poisson's ratio (σ), and Debye temperature according to to Anderson method (Θ_{DA}) of NCZFe$_{2-x}$O$_{4-3x/2}$ (x = 0, 0.04) system annealed at various T$_s$.

Iron-nonstoichiometry (x)	T$_s$ (˚C)	C_{11} (GPa)	C_{12} (GPa)	V_l (m/s)	V_s (m/s)	V_m (m/s)	E (GPa)	B (GPa)	G (GPa)	L (GPa)	σ	Θ_{DA} (K)
0.0	1100	252	108	6876	3909	4345	187	156	72	252	0.30	588
	1150	245	110	6780	3738	4165	177	155	68	245	0.31	564
	1200	239	102	6678	3807	4231	178	148	68	239	0.30	574
	1250	242	94	6745	4283	4710	189	143	74	242	0.28	637
0.04	1100	239	102	6741	3834	4262	178	148	68	239	0.30	577
	1150	245	105	6825	3842	4275	182	152	70	245	0.30	579
	1200	253	108	6929	3913	4352	188	156	72	253	0.30	589
	1250	253	108	6949	3905	4345	188	156	72	253	0.30	587

Table 4.21. Elastic stiffness constants (C_{11} and C_{12}), longitudinal (V_l), transversal (Shear) (V_s) and mean (V_m) wave velocities, moduli of elasticity (E, B, G), longitudinal modulus (L), Poisson's ratio (σ), and Debye temperature according to Anderson method (Θ_{DA}) of $NCZFe_{2-x}O_{4-3x/2}$ (x = 0.08, 0.12) system annealed at various T_s.

Iron-nonstoichiometry (x)	T_s (˚C)	C_{11} (GPa)	C_{12} (GPa)	V_l (m/s)	V_s (m/s)	V_m (m/s)	E (GPa)	B (GPa)	G (GPa)	L (GPa)	σ	Θ_{DA} (K)
0.08	1100	235	106	6729	3689	4113	169	149	65	235	0.31	557
	1150	245	110	6877	3753	4185	177	155	68	245	0.31	566
	1200	257	110	7044	3937	4382	191	159	73	257	0.30	593
	1250	246	105	6871	3905	4341	183	152	70	246	0.30	588
0.12	1100	235	106	6781	3660	4085	169	149	65	235	0.31	553
	1150	204	96	6318	3319	3712	143	132	54	204	0.32	502
	1200	239	107	6806	3705	4133	173	151	66	239	0.31	561
	1250	239	102	6839	3936	4371	178	148	68	239	0.30	591

Table 4.22. Zero porosity corrected moduli of elasticity (E_0, B_0, G_0), longitudinal modulus (L_0), bulk modulus to rigidity modulus ration (B_0/G_0), and Poisson's ratio (σ_0) of NCZFe$_{2-x}$O$_{4-3x/2}$ (x = 0, 0.04) system annealed at various T$_s$ employing Hasselmann and Fulrath model

Iron-nonstoichiometry (x)	T$_s$ (˚C)	E_0 (GPa)	B_0 (GPa)	G_0 (GPa)	L_0 (GPa)	B_0/G_0	σ_0
0.0	1100	209	160	81	268	1.98	0.28
	1150	192	152	74	251	2.05	0.29
	1200	201	161	78	265	2.06	0.29
	1250	242	156	98	287	1.59	0.24
0.04	1100	200	160	77	263	2.08	0.29
	1150	200	156	78	260	2.00	0.29
	1200	208	166	81	274	2.05	0.29
	1250	207	166	80	273	2.08	0.29

Table 4.23. Zero porosity corrected moduli of elasticity (E_0, B_0, G_0), longitudinal modulus (L_0), bulk modulus to rigidity modulus ration (B_0/G_0), and Poisson's ratio (σ_0) of NCZFe$_{2-x}$O$_{4-3x/2}$ (x = 0.08, 0.12) system annealed at various T$_s$ employing Hasselmann and Fulrath model

Iron-nonstoichiometry (x)	T$_s$ (˚C)	E_0 (GPa)	B_0 (GPa)	G_0 (GPa)	L_0 (GPa)	B_0/G_0	σ_0
0.08	1100	182	144	71	239	2.03	0.29
	1150	189	151	73	248	2.07	0.29
	1200	208	170	80	277	2.13	0.30
	1250	205	163	79	268	2.06	0.29
0.12	1100	177	143	68	234	2.10	0.29
	1150	148	136	56	211	2.44	0.32
	1200	184	155	71	250	2.18	0.30
	1250	204	161	79	266	2.04	0.29

Table 4.24. Zero porosity corrected moduli of elasticity (E_0, B_0, G_0), bulk modulus to rigidity modulus ration (B_0/G_0), and Poisson's ratio (σ_0) of $NCZFe_{2-x}O_{4-3x/2}$ (x = 0, 0.04) system annealed at various T_s employing Ledbetter and Datta model

Iron-nonstoichiometry (x)	T_s (˚C)	A_1	A_2	A_3	E_0 (GPa)	B_0 (GPa)	G_0 (GPa)	B_0/G_0	σ_0
0.0	1100	2.47	232	-36163	227	287	83	3.46	0.37
	1150	2.52	251	-33400	206	251	76	3.30	0.36
	1200	2.46	218	-32559	217	287	79	3.63	0.37
	1250	2.29	150	-36222	272	440	97	4.54	0.40
0.04	1100	2.46	220	-32487	216	281	79	3.56	0.37
	1150	2.50	233	-33921	215	254	79	3.22	0.36
	1200	2.49	235	-35997	224	274	82	3.34	0.36
	1250	2.50	238	-35819	221	261	81	3.22	0.36

Table 4.25. Zero porosity corrected moduli of elasticity (E_0, B_0, G_0), bulk modulus to rigidity modulus ration (B_0/G_0), and Poisson's ratio (σ_0) of $NCZFe_{2-x}O_{4-3x/2}$ (x = 0.08, 0.12) system annealed at various T_s employing Ledbetter and Datta model

Iron-nonstoichiometry (x)	T_s (˚C)	A_1	A_2	A_3	E_0 (GPa)	B_0 (GPa)	G_0 (GPa)	B_0/G_0	σ_0
0.08	1100	2.53	245	-30566	195	232	72	3.22	0.36
	1150	2.55	258	-33024	200	225	74	3.04	0.35
	1200	2.51	247	-36837	221	255	82	3.11	0.36
	1250	2.47	226	-34311	221	285	81	3.52	0.37
0.12	1100	2.58	255	-30023	186	196	69	2.84	0.34
	1150	2.59	239	-21970	153	168	57	2.95	0.35
	1200	2.55	252	-31232	194	220	72	3.06	0.35
	1250	2.43	213	-32852	2227	316	80	3.95	0.38

Table 4.26. Zero porosity corrected longitudinal velocity (V_{l0}), transversal velocity (V_{s0}), mean velocity (V_{m0}), moduli of elasticity (E_0, n_0), Poisson's ratio (σ_0) of the NCZFe$_{2-x}$O$_{4-3x/2}$ (x = 0, 0.04) system annealed at various T$_s$ employing elastic theory.

Iron-nonstoichiometry (x)	T$_s$ (˚C)	V_{l0} (m/s)	V_{s0} (m/s)	V_{m0} (m/s)	E_0 (GPa)	n_0 (GPa)	σ_0 (GPa)	C_l	C_Y	C_σ
0.0	1100	7742	4007	4485	215	82	0.32	1.53	1.81	0.72
	1150	7410	3809	4266	197	75	0.32	1.51	1.81	0.73
	1200	7584	3909	4377	207	78	0.32	1.52	1.81	0.72
	1250	8621	4494	5029	253	97	0.31	1.54	1.80	0.71
0.04	1100	7625	3934	4404	206	78	0.32	1.53	1.81	0.72
	1150	7552	3924	4392	205	78	0.31	1.54	1.80	0.72
	1200	7739	4004	4482	214	81	0.32	1.53	1.80	0.72
	1250	7693	3989	4465	212	80	0.31	1.54	1.80	0.72

Table 4.27. Zero porosity corrected longitudinal velocity (V_{l0}), transversal velocity (V_{s0}), mean velocity (V_{m0}), moduli of elasticity (E_0, n_0, σ_0), Poisson's ratio (σ_0) of the NCZFe$_{2-x}$O$_{4-3x/2}$ (x = 0.08, 0.12) system annealed at various T$_s$ employing elastic theory.

Iron-nonstoichiometry (x)	T$_s$ (˚C)	V_{l0} (m/s)	V_{s0} (m/s)	V_{m0} (m/s)	E_0 (GPa)	n_0 (GPa)	σ_0 (GPa)	C_l	C_Y	C_σ
0.08	1100	7304	3754	4204	187	71	0.32	1.51	1.81	0.73
	1150	7374	3809	4265	192	73	0.32	1.52	1.81	0.73
	1200	7733	4014	4493	213	81	0.31	1.54	1.80	0.72
	1250	7758	4005	4484	212	80	0.32	1.53	1.81	0.72
0.12	1100	7144	3701	4143	180	69	0.32	1.53	1.81	0.73
	1150	6589	3350	3754	150	57	0.33	1.50	1.81	0.73
	1200	7300	3761	4211	188	71	0.32	1.52	1.81	0.73
	1250	7894	4055	4542	212	80	0.32	1.52	1.81	0.72

4.2.6. Dielectric permittivity analysis

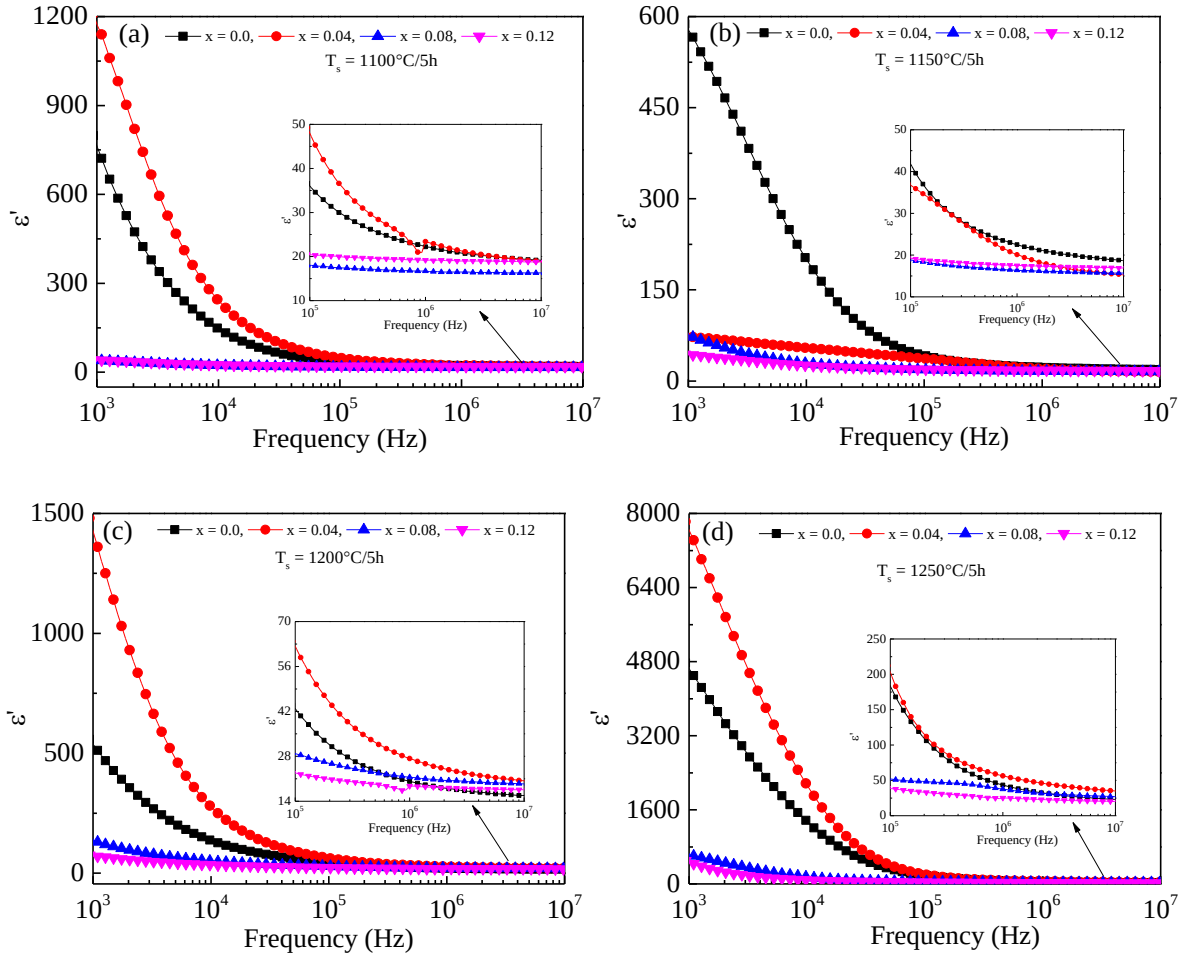

Figure 4.19: Evolution of the real component (ε') of electric permittivity with frequency of $NCZFe_{2-x}O_{4-3x/2}$ system annealed at various T_s: (a) 1100, (b) 1150, (c) 1200 and, (d) 1250 ℃.

Figure 4.19 shows how the real component (ε') of electric permittivity evolves with frequency of $NCZFe_{2-x}O_{4-3x/2}$ system at various T_s: (a) 1100, (b) 1150, (c) 1200, and (d) 1250 ℃. The electric permittivity (ε') is shown to drastically decline to a maximum of 10 kHz, then gradually decline, afterwhich it became frequency invariant. Maxwell-Wagner interfacial polarization [302, 303], that is supported by the hypothesis of Koop [235], is responsible for the dispersion of ε'at 10 kHz. The assumption that dielectric substances are constituted of two different layers has previously been made in the Maxwell-Wagner theory of heterogeneous double-layered solid structures; the first layer is made up of grains with strong conductivity apportioned by a thin layer that is made up of grain borders with weak conductivity. This causes the dielectric

material to become inhomogeneous, which allows for the local buildup of charge when an electric field is present. While highly conducting grains prove to be more efficient at higher frequencies, grain borders dominate at lower frequencies. The electrons typically travel through the jumping process to the grain border while being affected by the applied field. Due to the high resistance of grain borders, localized electron buildup takes place there, which causes the polarization of the space charge. As a result, ε' has a high value at lower frequenciese. The electrons can swiftly change their direction of travel as the frequency is increased, though. The polarization diminishes as a result, and the likelihood of an electron reaching the grain borders reduces considerably [304]. Consequently, as the frequency is rised, the value of ε' declines. It is also plausible to shed light on the frequency-invariant electric permittivity employing the Rabinkin and Novikova hypothesis regarding polarization that is linked to the electrical conducting pathway. Electrical polarization is caused by electrons repeatedly and continuously moving amongst the ferrous and ferric ions. Eventually, the continual and repetitive electron hopping in the middle of Fe^{2+} and Fe^{3+} causes localization of electrons in exactly the alike orientation as the electric field that is applied, which can be utilized to assess the level of polarization in the substances. Because the quick variation of the field that is used is unable to be accompanied by the speed of exchanging electrons among Fe^{2+} and Fe^{3+} over a particular frequency, the polarization diminishes and becomes frequency-independent at higher frequencies [305]. It is caused by the high number of ferrous ions, oxygen voids, piledup interfacial dislocation, grain borders responses, voids or pores, etc. [306]. The aforementioned problems may only have a small impact on polarization in the high frequency domain. As a result, the value of ε' is small. It is noticeable that ε' value drops with rising iron-nonstoichiometry level, which may be mostly due to the reduction of Fe^{2+} ions. Because Fe^{2+} ions are more polarized than Fe^{3+} ions, their production always contributes to the high value of ε' [307]. The value of ε' is small at 1100 °C. It is possible for reducing ions to exist at lower T_s in many oxidation states, which lowers the likelihood of charge carriers jumping [256].

Furthermore, the value of ε' is shown to grow with rising T_s, that may be imputed to an intensification in the ferric/ferrous ion amount at octahedrally coordinated (B)-site. According to the equation [275]:

$$ZnO \rightarrow Zn + (1/2)O_2,$$

zinc partly volatilizes at higher T_s and produces unsaturated oxygen ions and cation vacancies. The extra electrons subsequently begin to form bonds with nearby Fe^{3+} ions as a result of electrostatic contact, producing Fe^{2+} ions [308]. As a result, the ferric/ferrous ions ratio increases as a result of zinc's volatilization at higher T_s. The relationship [237]:

$$2Fe^{3+} + \frac{3}{4}V_A' + O^{2-} \overset{K(T)}{\longleftrightarrow} 2Fe^{2+} + \frac{1}{2}O_2(g)$$

results in some of Fe^{3+} ions being partly transformed to Fe^{2+} ions while the sintering process is in operation. As a result, it is shown that the value of ε' grows as T_s increases [238]. Additionally, when T_s rises, the rise in ε' value may be due to an improvement in the grain-to-grain border thickness ratio [309, 310]. Since the increase in density reduces porosity, which results in a greater number of polarizing species per unit volume [256], it is also probable that this factor has increased.

4.2.7. Permittivity loss tangent analysis

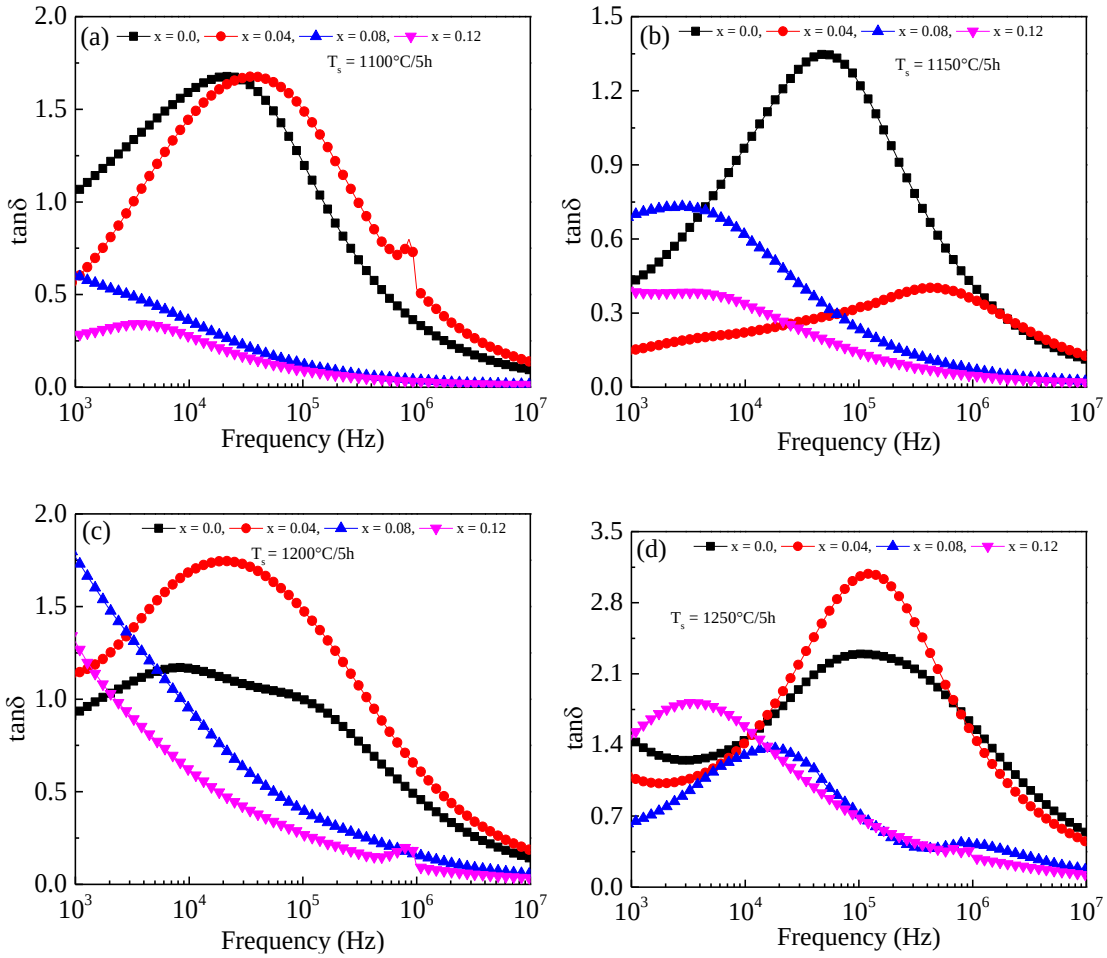

Figure 4.20: Evolution of the permittivity loss tangent ($tan\delta$) with frequency of $NCZFe_{2-x}O_{4-3x/2}$ system annealed at various T_s (a) 1100, (b) 1150, (c) 1200 and, (d) 1250 ℃.

Figure 4.20 shows how the permittivity loss tangent ($tan\delta$) evolves with frequency of $NCZFe_{2-x}O_{4-3x/2}$ system annealed at various T_s: (a) 1100 (b) 1150, (c) 1200, and (d) 1250 ℃. The permittivity loss tangent ($tan\delta$) is responsible for the polarization's lag behind the applied field. The main cause of the lagging of polarization in the midst of the applied fields is the existence of impurities, defects, imperfections, and inhomogeneous structure. In other words, a number of variables, including the stoichiometry percentage, fabrication process, the amount of Fe^{2+}, and the auxiliary homogeneity, may be related to the permittivity loss tangent ($tan\delta$). As seen in Figure 4.20, $tan\delta$ value is found to first grow with upturning frequency and display a maximum at a particular frequency, afterwhich it dropped with enhancing frequency for all T_s.

At 1100 °C, $tan\delta$ value is found to progressively rise with rising frequency, reaches a maximum at a particular frequency in x = 0, 0.04, and 0.12, and then begin to fall at higher frequencies. Additionally, it is discovered that when x = 0.08, $tan\delta$ value stays virtually invariant at the higher frequencies, declining gradually with increasing frequency. At 1150 °C, $tan\delta$ value is shown to progressively grow with increasing frequency, disclose a peak in x = 0, 0.04, and 0.08 at a specific frequency, and eventually be found to fall at higher frequencies. Additionally, it is discovered that when x = 0.12, $tan\delta$ value stays virtually invariant at the higher frequencies, drops gradually with increasing frequency. The $tan\delta$ value grows at 1200 °C in x = 0.0 and 0.04, first with rising frequency, then reveals a maximum at a specific frequency, and ultimately it dropped at higher frequencies. Meanwhile, it is discovered that in x = 0.08 and 0.12, $tan\delta$ value steadily drops with rising frequency and becomes frequency-invariant at higher frequencies. At 1250 °C, $tan\delta$ value escalates initially with rising frequency, achieves a maximum at a specific frequency, and afterwhich declines for all compositions at higher frequencies. In addition, two peaks in $tan\delta$ value are seen at x = 0.08 that ascribed to the grain and the grain border responses. As depicted in Figure 4.20 (a, b), the location of the maximum moved toward the lower frequencies, with the exception of x = 0.04; also, the peak's height dropped with rising iron-nonstoichiometry level. The location of maximum at 1100 and 1150 °C changes to the higher frequencies in x = 0.04.The location of peaks is also shown to shift towards the lower frequencies, as seen in Figure 4.20 (c, d). The decreasing conductivity and the number of Fe^{3+} ions on the octahedrally coordinated site may be responsible for the shifting of peaks towards the lower frequencies. Furthermore, it has been found that when T_s [311] increases, the severity of the relaxation peaks decreases. The $tan\delta$ value has a high value at lower frequency sides and a low value at higher frequency sides. Because the low conducting grain borders are electrically stronger at lower frequencies, a greater amount of energy is required for electrons transfer amongst Fe^{2+} and Fe^{3+} ions at the octahedrally coordinated (B)-site [311]. Therefore, there is a significant permittivity loss

tangent. Because the highly conducting grains are energetically reactive at higher frequencies, an insignificant quantity of energy required for the exchange of electron in the midst of ferrous and ferric ions at the octahedrally coordinated (B)-site [312]. The value of $tan\delta$ as a result is small. We may better understand the existence of the peak in $tan\delta$ spectra by using the Rezlescu model [313] and the relaxation process. For dielectric substances, the emergence of a peak in $tan\delta$ should meet the essential requirement: $\omega\tau = 1$, where $\omega = 2\pi f_{max}$ and τ are the respective angular frequency and relaxation time. The highest amount of energy is transmitted to the oscillating dipoles in this situation, which results in power loss [305]. The jumping probability of electrons per unit time (P) and the relaxation time (τ) are strongly related and can be stated by the equation [306]: $\tau = 1/3p$ or $f_{max} = 2P$. It follows that the jumping chance per unit time and the relaxation frequency are directly related. According to the Rezlescu model, the peaks' emergence is connected to the synchronization of the oscillating external field's frequency and the localized electric charge carriers' natural hopping frequency.

4.2.8. Electrical conductivity analysis

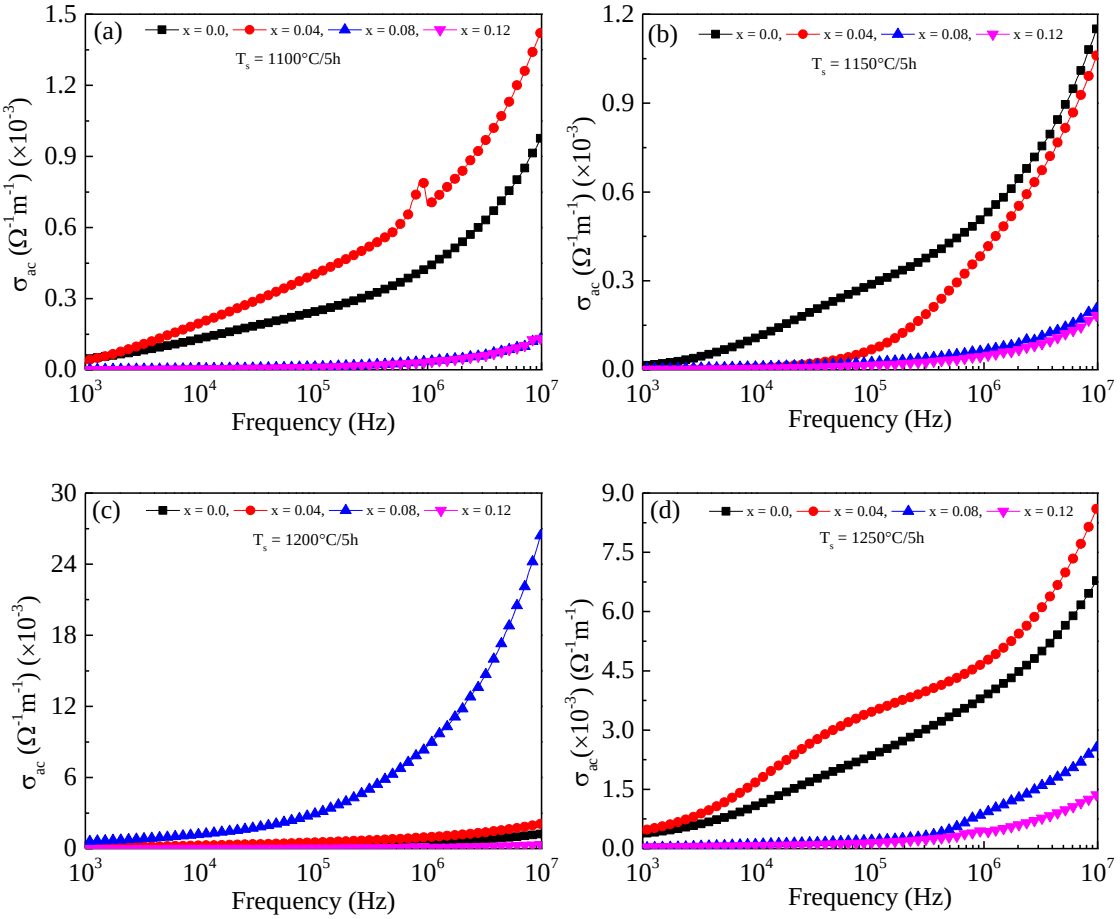

Figure 4.21: Evolution of ac conductivity (σ_{ac}) with frequency of NCZFe$_{2-x}$O$_{4-3x/2}$ system annealed at various T$_s$: (a) 1100, (b) 1150, (c) 1200 and, (d) 1250 ℃.

Figure 4.21 shows how the ac conductivity (σ_{ac}) with frequency of NCZFe$_{2-x}$O$_{4-3x/2}$ system annealed at various T$_s$: (a) 1100, (b) 1150, (c) 1200, and (d) 1250 ℃. The graph makes it very evident that all of the samples being studied have increasing conductivities with frequency. There are two distinct regions in the σ_{ac} spectrum that can be seen: (i) at low frequencies, σ_{ac} is seen to have grown nearly frequency standalone, which is ascribed to both grain borders and direct current conductivity because the unpredictable charge carrier's distribution; and (ii) at higher frequencies, σ_{ac} is shown to grow, which is explained by the improvement associated with carrier jumping amongst Fe^{2+} and Fe^{3+} ions at the octahedrally coordinated (B)-site and grain response as well [314]. Because grain borders have high resistivity, the charge carrier is typically not allowed to hop in the midst of Fe^{2+} and Fe^{3+} ions at the grain border walls at low

frequencies. As a result, the value of σ_{ac} is small. The distinctive feature for iron-deficient ferrites that has been noticed obeys Jonscher's power law: $\sigma_{ac}(f) = \sigma_{dc}(\omega = 2\pi f = 0) + A(2\pi f)^n$ where n $(0 < n < 1)$, where $\sigma_{dc}(\omega = 0)$ denotes dc conductivity that is connected to the permittivity relaxation of the bound charge species and it allows the long-distance electrical transportation, $A(\omega)^n$ denotes the ac conductivity that is concurrent with the jumping action in translation (short-distance jumping), ω denotes the angular frequency, A is temperature-dependent factor which is expressed as $A = \frac{\pi N^2 e^2}{6k_B T(2\alpha)}$, where N is the number of locations among which the jumping occurs, e is the electron's charge, T denotes the temperature, α denotes the polarizability, and n is a factor that varies 0 for perfect ionic solids and 1 for perfect dipolar Debye dielectric solids [315-319], and it indicates the level of interaction in the midst of mobile ions and the surroundings around them. As can be observed, at temperatures of 1100, 1150, and 1250 °C, the value of σ_{ac} is shown to decrease as the degree of iron-nonstoichiometry increases. At 1200 °C, σ_{ac} grows with rising iron-nonstoichiometry degree to a maximum of x = 0.08, and afterwhich it drops in x = 0.12. The decrease in charge carriers may be the cause of the decline in σ_{ac} value that occurs when iron-nonstoichiometry level rises. On the other hand, in x = 0, 0.04, and 0.12, it is discovered that the value of σ_{ac} grows as T_s increases. Additionally, the value of σ_{ac} in x = 0.08 is seen to rise to a maximum of 1200 °C before declining around 1250 °C. The increase in T_s speeds up the transformation of Fe^{2+} ions to Fe^{3+} ions, which may be explained by the increasing degree of charge carrier hopping in the midst of ferrous and ferric ions at the octahedrally coordinated (B)-site. The resistivity, however, decreases as the quantity of Cu^{1+} ions oxidized to Cu^{2+} increases on rising T_s [320]. As a result, it is shown that the value of σ_{ac} grows as T_s increases. Because the increased grain diameter has fewer grain borders (which restrict the electrons from flowing in the midst of the neighboring sites), the increase in grain diameter with rising T_s is another explanation for the improvement in σ_{ac} value [308]. We plotted $log(\sigma_{ac})$ vs. $log(\omega)$ graphs

to match the σ_{ac} results employing Jonscher's power law. Evolution of ac conductivity (σ_{ac}) with angular frequency (ω) of NCZFe$_{2-x}$O$_{4-3x/2}$ system annealed at various T$_s$ (a) 1100, (b) 1150, (c) 1200 and, (d) 1250 ℃. The varied values of A were found from the intercept component equal to $log(\sigma_{ac})$ on the y-axis $lo\,g(\omega) = 0$, and the various values of 'n' were achieved utilizing Jonscher's power law. The linear correlation coefficient (R^2) squared values for all samples at various T$_s$ are typically compared to determine the fit quality (see Table 4.28-4.29). A perfect linear graph in x = 0 and 0.04 for 1100 and 1150 ºC, is no longer visible at the dependency of $log(\sigma_{ac})$ vs. $log(\omega)$ [Figure 4.22 (a)]. A virtually identical linear curve is present at 1200 ºC [Figure 4.22 (c)]. We lose the linearity of the curve at 1250 °C [Fig. 4.22 (d)]. In Table 4.28-4.29, the values of A and 'n' are given. The value of 'n' is shown to be influenced by the degree of iron-nonstoichiometry, as can be seen in Table 4.28-4.29. The fluctuation of 'n' as a function of the degree of iron-nonstoichiometry is depicted in the inset of Figure 4.22 (a-d). With rising iron-nonstoichiometry degree at 1100 °C, the value of 'n' grows. At 1150 °C, 'n' quickly enhances in x = 0.04, afterwhich suddenly reduces in x = 0.08, and then sharply rises in x = 0.12. The 'n' at 1200 °C dramatically declines in x = 0.04 before rising to x = 0.12. The frequency exponent 'n' at 1250 °C grows to a maximum of x = 0.08 before decreasing till x = 0.12. The exponent 'n' has been noted to have values in the midst of 0 and 1 by Pike [321] and Elliott [322]. Additionally, according to Funke [323], when 'n' is less than 1, the electron jumping movement includes a short-distance translated jumping motion supported by a small polaronic process with an unexpected hop, while 'n' is larger than 1, the movement entails restricted or reorientational jumping driven by a large polaronic process in the midst of the adjacent sites. The process of ac conductivity in the synthetic iron-deficient non-stoichiometric nickel-copper-zinc ferrite relies upon frequency and controlled by the polaron jumping process, as can be shown from the values of 'n' being smaller than unity

[324]. When the $log(\sigma_{ac})$ vs. $log(\omega)$ figure deviates from linearity, the ac conduction is caused by mixed polaron jumping (small polaron jumping and big polaron jumping) [325].

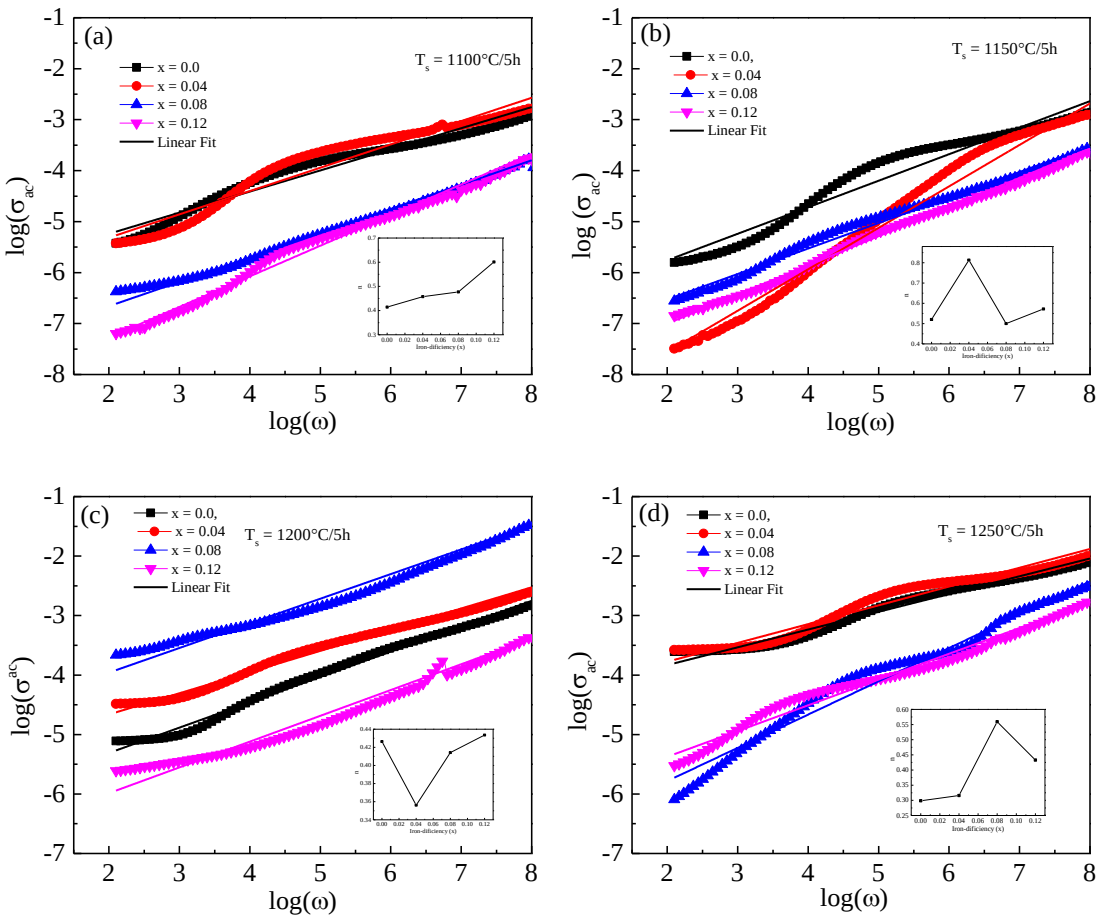

Figure 4.22: Evolution of ac conductivity (σ_{ac}) with angular frequency (ω) of NCZFe$_{2-x}$O$_{4-3x/2}$ system annealed at various T$_s$ (a) 1100, (b) 1150, (c) 1200 and, (d) 1250 °C.

Table 4.28. Extracted parameters from Jonscher's power law of $NCZFe_{2-x}O_{4-3x/2}$ (x = 0, 0.04) system annealed at various T_s.

Iron-deficiency, x	T_s °C	n	$log\ A$	A	R^2
0.00	1100	0.4143	- 6.06777	8.555×10^{-7}	0.9517
0.00	1150	0.5205	- 6.80017	1.5844×10^{-7}	0.9562
0.00	1200	0.4264	- 6.16341	6.8642×10^{-7}	0.9866
0.00	1250	0.2986	- 4.42965	3.7183×10^{-5}	0.9795
0.04	1100	0.4575	- 6.23042	5.8827×10^{-7}	0.9439
0.04	1150	0.8131	- 9.18752	6.4935×10^{-10}	0.9803
0.04	1200	0.3562	- 5.37446	4.2222×10^{-6}	0.9773
0.04	1250	0.3158	- 4.40725	3.9152×10^{-5}	0.9616

Table 4.29. Extracted parameters from Jonscher's power law of $NCZFe_{2-x}O_{4-3x/2}$ (x = 0.08, 0.12) system annealed at various T_s.

Iron-deficiency, x	T_s °C	n	$log\ A$	A	R^2
0.08	1100	0.4771	- 7.61403	2.4320×10^{-8}	0.9498
0.08	1150	0.5002	- 7.52857	2.9609×10^{-8}	0.9656
0.08	1200	0.4142	- 4.78762	1.6307×10^{-5}	0.9411
0.08	1250	0.5592	- 6.90130	1.2552×10^{-7}	0.9781
0.12	1100	0.6008	- 8.47260	3.3682×10^{-9}	0.9698
0.12	1150	0.5721	- 8.14673	7.1330×10^{-9}	0.9818
0.12	1200	0.4336	- 6.85369	1.4006×10^{-7}	0.9559
0.12	1250	0.4329	- 6.24021	5.7516×10^{-7}	0.9814

4.2.9. Cole-Cole plot

Figure 4.23 shows the Cole-Cole plots of $NCZFe_{2-x}O_{4-3x/2}$ system annealed at various T_s: (a) 1100, (b) 1150, (c) 1200, and (d) 1250 °C. The quantity of semicircular arcs identifies the type of electrical process in which the material is employed. The Nyquist plot usually displays three successive semicircles, subject to the number of relaxation mechanisms that exist in the substance: an incomplete semicircle at higher frequencies is related to grain bestowal; the grain border bestowal holds responsibility for forming the second semicircle at intermediate frequencies; and the third semicircle at lower frequencies is related to the electrode response [326]. The number of grains and grain diameters in the sample determine the semicircular arc's size.

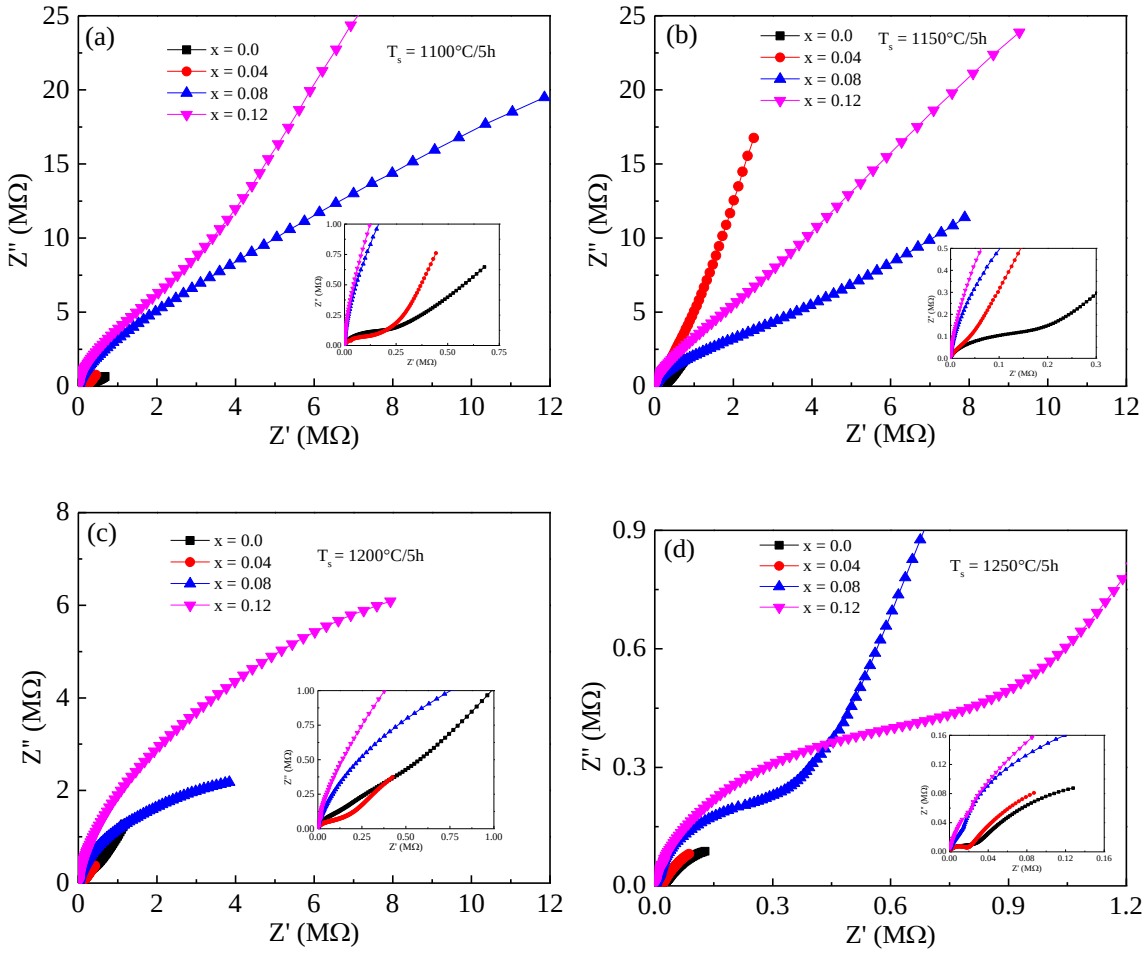

Figure 4.23: Cole-Cole plots of $NCZFe_{2-x}O_{4-3x/2}$ system annealed at various T_s: (a) 1100, (b) 1150, (c) 1200, and (d) 1250 °C.

As shown in Figure 4.23 (a-d), every sample exhibits a significant slope, a straight line, or a partially semicircular arc, that corresponds to the impact of the grain border. As a result, it is declared that the grain border's impact explains the majority of the conductivity of electricity phenomenon. Since it asserts a frequency range over the frequency spectrum of our measuring device, the impact of the grain core to the conductivity of electricity is entirely concealed [327]. The low concentration of ferric ions, enhanced surface-to-volume proportion, porosity, and disorganized atomic organization close to the grain border may all contribute to an elevated value associated with the grain border. Owing to the heterogeneity in grain size [328], the polydispersive non-Debye sort dielectric relaxing processes hallmark is clearly discernible as the center of semicircular arcs is somewhat beneath the (Z')-axis. At all T_s, the diameter of a semicircle tends to grow as the degree of iron-nonstoichiometry rises, indicating that the sample's resistivity has gotten better. On the opposite hand, it comes to light that the diameter of the semicircle drops as T_s grows, which indicates a drop in the resistance of the substance [329]. The fact that the impedance is linearly proportional to the total amount of grains can be credited to this property. With rising T_s, it becomes apparent that the smaller grains interact to generate bigger grains. As a result, it turns out that there are fewer grains in the specimens.

4.2.10. Magnetic permeability and magnetic loss tangent analysis

Figure 4.24 shows how magnetic permeability (μ_i') evolves with frequency of NCZ$Fe_{2-x}O_{4-3x/2}$ system annealed at various T_s: (a) 1100 ℃, (b) 1150 ℃, (c) 1200 ℃, and (d) 1250 ℃. The magnetic permeability of ferrites is generally influenced by different parameters: (i) intrinsic parameters, such as saturation magnetization, magnetostriction, and anisotropic constant; (ii) extrinsic parameters, such as micromorphology, grain diameter, porosity, and stress; and (iii) the integrated consequence of bifurcate distinct magnetization procedures, such as magnetization due to spin rotation and domain wall movement [330]. In contrast to spin rotation, the domain wall displacment has had a greater impact on magnetic permeability at

lower frequencies. Nakamura has already claimed that the domain wall motion is mostly responsible for the magnetic permeability below 100 MHz [330]. Typically, Globus' model is used to explain magnetic permeability brought on by domain wall displacement. The magnetic permeability (μ_i') caused by the displacement of the domain wall may be described as follows in Globus' model: $(\mu_i' - 1) = \frac{3\pi M_s^2 D}{4E_w}$ and the resonant frequency is determined by $f_r = \frac{16E_w}{\pi\beta D^2}$, where, E_w represents the domain wall's energy, β denotes the coefficient of damping, M_s denotes saturation magnetization, and D denotes grain diameter [285, 331-333].

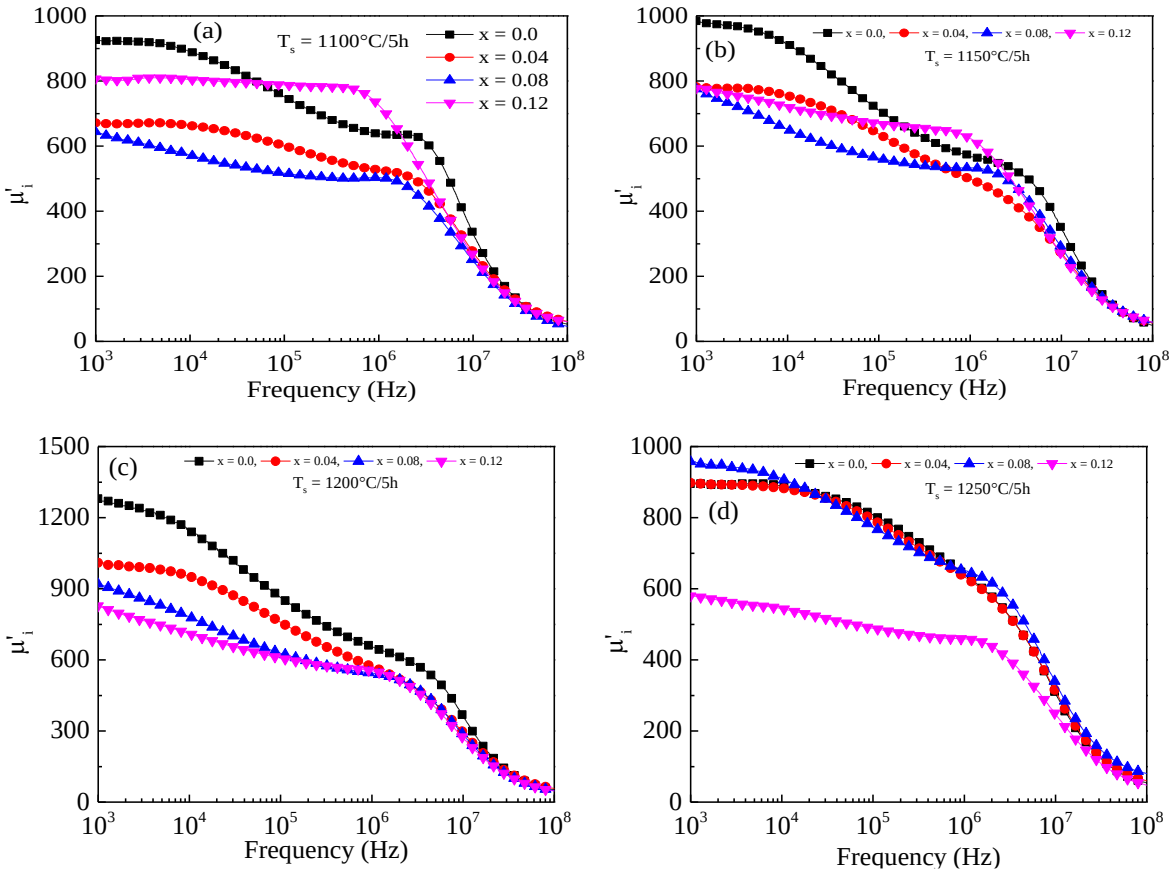

Figure 4.24: Evolution of magnetic permeability (μ_i') with frequency of NCZFe$_{2-x}$O$_{4-3x/2}$ system annealed at various T$_s$: (a) 1100, (b) 1150, (c) 1200 and, (d) 1250 ℃.

Table 4.30-4.31 list the μ_i' value at various chosen frequencies and $f_r$value as a function of the degree of iron-nonstoichiometry and T_s. With the exception of the x = 0.12 sample, all T_s exhibit a progressive reduction in μ_i' value as applied frequency rises at 1100 °C. The μ_i' value is seen to be constant at 1100 °C to a maximum of a specific frequency in x = 0.12, after which it begins to abruptly decline to a minimal value. Following Snoek's relation $\mu_i' \times f_r = constant$ [334], it can be shown that increased magnetic permeability correlates to lower resonant frequency (f_r). Table 4.30-4.31 provide an overview of the Snoek product at 1 MHz. Table 4.30-4.31 show that Snoek's product is practically constant, supporting Snoek's rule. As shown in Table 4.30-4.31, the value of μ_i' is shown to grow in x = 0.12 at 1100, 1150, and 1200 °C after initially decreasing with increasing iron-nonstoichiometry degree to maximum of x = 0.08. At 1250 °C, the value of μ_i' begins to decrease as the iron-nonstoichiometry degree rises. On the other hand, in x = 0, 0.04, and 0.08, it is shown that the value of μ_i' increases with rising T_s, as shown in Table 4.30-4.31. The improvement in bulk density and grain diameter is responsible for the increase in μ_i' value with increasing T_s in x = 0, 0.04, and 0.08. The increase in annealed density causes the volume portion of magnetic particles to increase, which in turn causes a rise in magnetic permeability [335]. Because there are more domain walls and fewer grain borders in big grain, the bulging or bending of the domain wall, whichever mostly attributes to the μ_i' value is greatly enhanced. During grain expansion, the pores that prevent the domain wall from moving because the wall is pinned would shrink [336]. As a result, it is shown that the value of μ_i' grows as T_s increases. Additionally, it has been shown that when T_s increases, magnetocrystalline anisotropic consatnt is seen to decrease due to a reduction in internal stress and crystal anisotropy [336, 337]. The orbit-lattice contact brought on by the surrounding ions would be the primary cause of the spin-orbit coupling, which is where the magnetocrystalline anisotropy would have its origins [291]. The value of μ_i' is seen to rise with rising T_s [251] because the reduction in magnetocrystalline anisotropic constant would aid in

the creation of movable and adjustable domain barriers. In addition, when x = 0.12, the μ_i' value begins to decrease on rising T_s. In x = 0.12, the decrease in μ_i' value with rising T_s may be attributed to the development of aberrant grain borders and excessively wide pores inside the grain borders [254]. The peak μ_i'' value [338] was used to establish the resonant frequency (f_r). The energy absorption caused by the synchronization in the midst of the magnetic dipoles' oscillational frequency and the applied frequency is what is responsible for the f_r value that associates to the maximum of μ_i''value. For the purpose of orienting the magnetic dipoles, the crystal lattice receives energy from the magnetic field at this frequency [331]. Table 4.30-4.31 contains a list of the resonant frequency. Table 4.30-4.31 show that for all T_s, the value of f_r is shown to slowly diminish as the level of iron-nonstoichiometry increases. Figure 4.25 shows how the magnetic loss tangent ($tan\delta_\mu$) with frequency of NCZ$Fe_{2-x}O_{4-3x/2}$ system annealed at various T_s: (a) 1100, (b) 1150, (c) 1200, and (d) 1250 °C. As becomes apparent, at lower frequencies (≤ 10 kHz), the $tan\delta_\mu$ value is shown to diminish, and at frequencies amongst 100 kHz and 1 MHz, it becomes almost frequency-invariant. At ≥ 1 MHz, $tan\delta_\mu$ is shown to increase with rising frequency, exhibit a peak at a particular frequency, and then begin to fall at higher frequencies. The resonance develops when there is synchronization in the midst of the applied field's frequency and the electron spin's Larmor precession; in this situation, energy from the magnetic field is transmitted to the system, aiding in the orientation of the magnetic dipoles. The values of $tan\delta_\mu$ measured at several chosen frequencies are shown in Table 4.30-4.31. Table 4.30-4.31 show that the value of $tan\delta_\mu$ begins to increase in x = 0.04 initially, afterwhich drops in x = 0.08, and improves again in x = 0.12 for 1100-1200 °C. The $tan\delta_\mu$ value drops as the iron-nonstoichiometry degree increases at 1250 °C. Additionally, the improvement in grain diameter causes the value of $tan\delta_\mu$ to grow with increasing T_s. There are a lot of domain walls inside grains when the grain diameter is huge. As a result, the domain walls could be easily capable of shifting along the grain and a significant quantity of eddy

current is generated. If the grain diameter is scanty, there are several grain borders inside the grain that block the movement of the eddy current. Big grains have a tendency to produce more magnetic domains, which causes losses brought on by the lag in domain wall motion [335, 339].

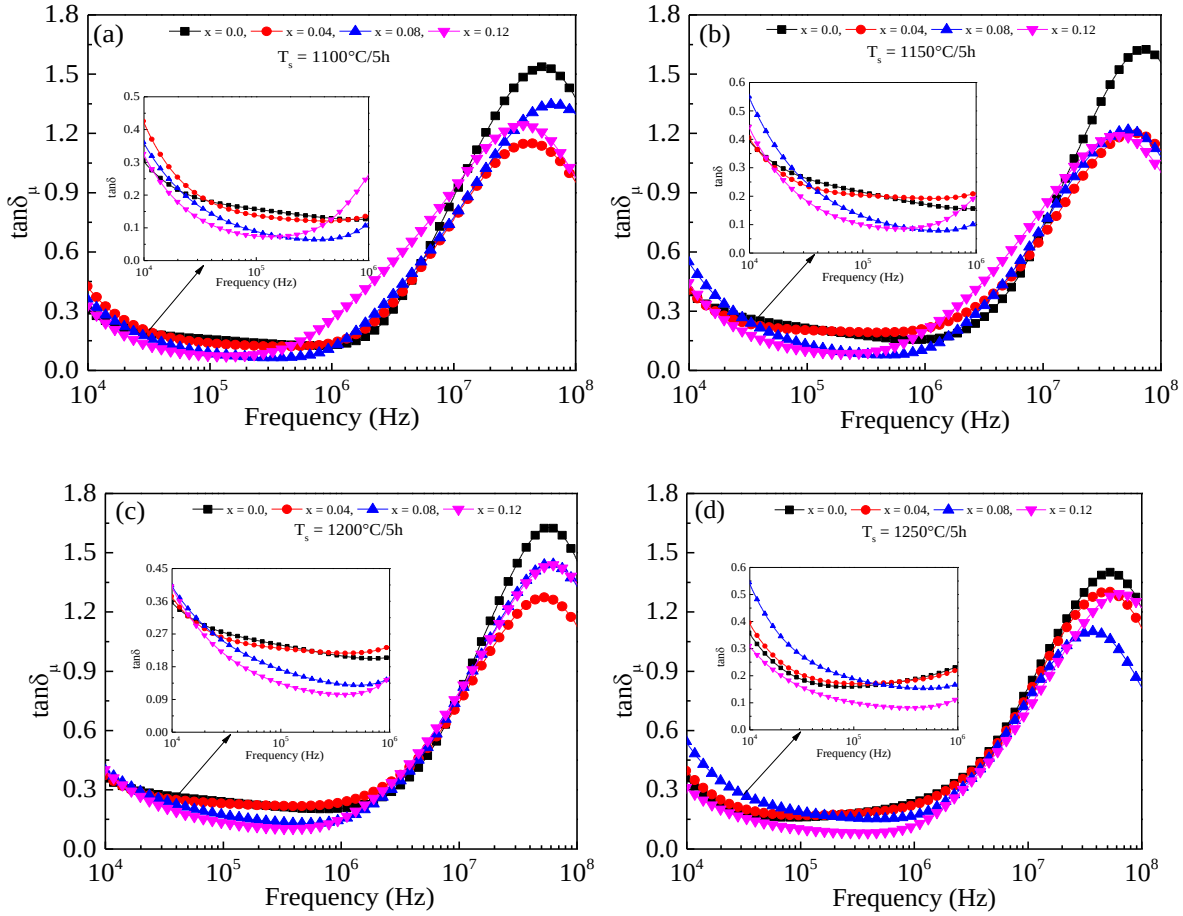

Figure 4.25: Evolution of magnetic loss tangent ($tan\delta_\mu$) with frequency of NCZFe$_{2-x}$O$_{4-3x/2}$ system annealed at various T$_s$: (a) 1100, (b) 1150, (c) 1200 and, (d) 1250 ℃.

Table 4.30. Magnetic permeability (μ_i'), resonant frequency (f_r), Snoek's product, and magnetic loss tangent ($tan\delta_\mu$) at specific frequencies of $NCZFe_{2-x}O_{4-3x/2}$ (x = 0, 0.04) system annealed at various T_s.

Composition (x)	T_s (˚C)	μ_i' at					f_r (MHz)	Snoek's product ($\mu_i' \times f_r$) (@ 1 MHz)	$tan\delta_\mu$ at				
		10 (kHz)	100 (kHz)	1 (MHz)	10 (MHz)	100 (MHz)			10 (kHz)	100 (kHz)	1 (MHz)	10 (MHz)	100 (MHz)
0.0	1100	890	751	637	328	53	7.67	4886	0.30	0.16	0.13	0.89	1.37
	1150	913	711	570	346	49	10.7	6099	0.39	0.21	0.16	0.73	1.56
	1200	1150	862	655	359	52	9.80	6419	0.36	0.24	0.21	0.79	1.46
	1250	888	808	640	304	54	8.37	5357	0.35	0.16	0.24	0.82	1.22
0.04	1100	663	600	527	272	61	7.27	3831	0.42	0.14	0.14	0.77	0.95
	1150	755	636	499	269	56	9.97	4975	0.40	0.20	0.21	0.69	1.11
	1200	952	758	571	291	57	8.37	4779	0.37	0.23	0.24	0.75	1.13
	1250	883	793	633	309	60	8.52	5393	0.39	0.17	0.22	0.79	1.12

Table 4.31. Magnetic permeability (μ_i'), resonant frequency (f_r), Snoek's product, and magnetic loss tangent ($tan\delta_\mu$) at specific frequencies of $NCZFe_{2-x}O_{4-3x/2}$ (x = 0.08, 0.12) system annealed at various T_s.

Composition (x)	T_s (˚C)	μ_i' at					f_r (MHz)	Snoek's product ($\mu_i' \times f_r$) (@ 1 MHz)	$tan\delta_\mu$ at				
		10 (kHz)	100 (kHz)	1 (MHz)	10 (MHz)	100 (MHz)			10 (kHz)	100 kHz	1 (MHz)	10 (MHz)	100 (MHz)
0.08	1100	572	516	503	245	46	6.55	3295	0.36	0.09	0.12	0.78	1.30
	1150	652	562	533	286	59	8.22	4381	0.54	0.13	0.11	0.74	1.08
	1200	781	627	544	282	48	8.08	4396	0.40	0.17	0.15	0.79	1.33
	1250	910	773	650	332	80	8.37	5441	0.54	0.19	0.17	0.76	0.81
0.12	1100	805	788	725	262	60	3.80	2755	0.32	0.08	0.26	0.92	0.97
	1150	721	669	623	265	59	5.22	3252	0.44	0.10	0.20	0.83	0.999
	1200	710	607	554	268	47	7.80	4321	0.397	0.13	0.15	0.80	1.34
	1250	544	489	459	245	48	8.98	4122	0.31	0.10	0.12	0.71	1.22

4.3. Elucidating the impacts of sintering temperature on the behavior of (1-*y*) [$Ba_{0.9}Ca_{0.1}Zr_{0.1}Ti_{0.9}O_3$] + (*y*) [$Ni_{0.25}Cu_{0.13}Zn_{0.62}Fe_2O_4$] composite multiferroics

In this section, the results on the impacts of T_s on electromagnetic characteristics of (1-*y*) [$Ba_{0.9}Ca_{0.1}Zr_{0.1}Ti_{0.9}O_3$] (BCZTO) + (*y*) [$Ni_{0.25}Cu_{0.13}Zn_{0.62}Fe_2O_4$] (NCZFO) composite multiferroics developed employing the solid-state synthetic technique route annealed for 5 h at four distinctive temperatures (1373-1523 K; in steps of 323 K) have been discussed.

4.3.1. Crystallographic characteristics

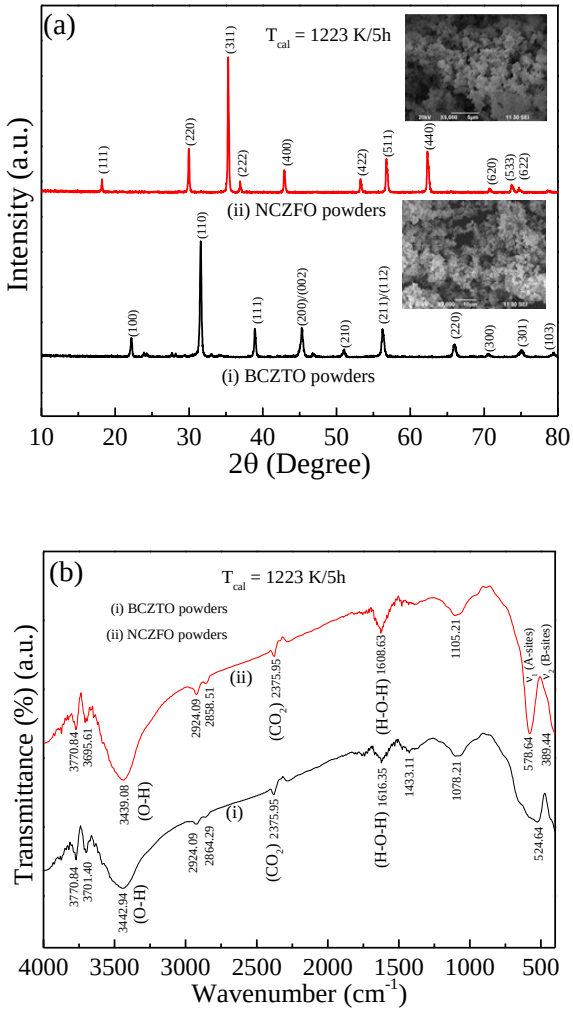

Figure 4.26: (a) XRD profiles and (b) FTIR spectrum of BCZTO and NCZFO powders are calcinated at temperature of 1223 K for 5h.

Figure 4.26 (a) shows the XRD profiles of (i) BCZTO and (ii) NCZFO powders that were calcinated for 5 h at 1223 K. The key peaks associated with the BCZTO and NCZFO phases may all be seen within the visual resolution limit, as shown in Figure 4.26 (a). The lower diffraction peaks were recognized as (100), (110), (111), (002), (102), (211), (301), and (311) reflections of BCZTO with tetragonal symmetry, whilst the top peaks were listed to (220), (311), (222), (400), (422), (333), (440), (622) and (444) reflections of NCZFO with cubic symmetry. The emergence of the BCZTO phase with tetragonal symmetry was supported by the wide peaks (200/002) and (211/112). There is no indication of the impurity phases' existence at the resolution limit of XRD. The absence of peaks in the XRD spectrum corresponding to the impurity phase shows how pure each phase is. This indicates that the Ca^{2+} and Zr^{4+} ions were successfully incorporated into the $BaTiO_3$ lattice's tetrahedrally and octahedrally coordinated (A and B)-sites to create a homogeneous solid solution. The lattice constants of the BCZTO and NCZFO phases were calculated using the interplanar distance (d_{hkl}) seen in the XRD spectra.Using the following formulae, the lattice constants of the NCZFO and BCZTO phases were calculated [185, 340]:

(i) $$a^2 = \left(\frac{\lambda^2}{4sin^2\theta_{hkl}}\right) \times (h^2 + k^2 + l^2)$$

and (ii) $sin^2\theta_{hkl} = \frac{\lambda^2(h^2+k^2)}{4a^2} + \frac{\lambda^2 l^2}{4c^2}$

where, *hkl* denote the Miller's indices, λ represents to X-ray's wavelength and θ_{hkl} denotes diffraction angle. The BCZTO has lattice constant, $a = b$ = 4.0034 Å and c = 4.0066 Å possessing tetragonal ratio c/a of 1.0008 whilst the NCZFO has the lattice constant of (8.4263 ± 0.0027) Å. The cell volume of BCZTO and NCZFO has been estimated employing the equations: $V_{cell}\ (BCZTO) = a^2c$ and $V_{cell}\ (NCZFO) = a^3$, where a and c denote the lattice constant of BCZTO and NCZFO. The cell volume of BCZTO and NCZFO is 64.2146 $Å^3$ and (598.2904 ± 0.5704) $Å^3$. The crystallite diameter (D_{hkl}) of calcinated BCZTO and NCZFO

powders was separately determined using Debye-Scherrer's formula [183] using the strongest peak of BCZTO (110) and the strongest peak of NCZFO (311). The calcinated BCZTO has a small crystallite diameter (39.3 nm), whilst the calcinated NCZFO has a large crystallite diameter (57.9 nm). The inset of Figure 4.26 (a) shows the micromorphological structures of BCZTO powder (underneath panel) and NCZFO powder (top panel) calcinated for 5 h at 1223 K. Both BCZTO and NCZFO powders were found to be highly agglomerated with small primary particle diameters. Figure 4.26 (b) shows the FTIR spectra of (i) BCZTO and (ii) NCZFO powders calcinated for 5 h at 1223 K. In Figure 4.26 (i), only one broad higer wavenumber band is detected at 524.64 cm^{-1}, proving the development of a perovskite framework.

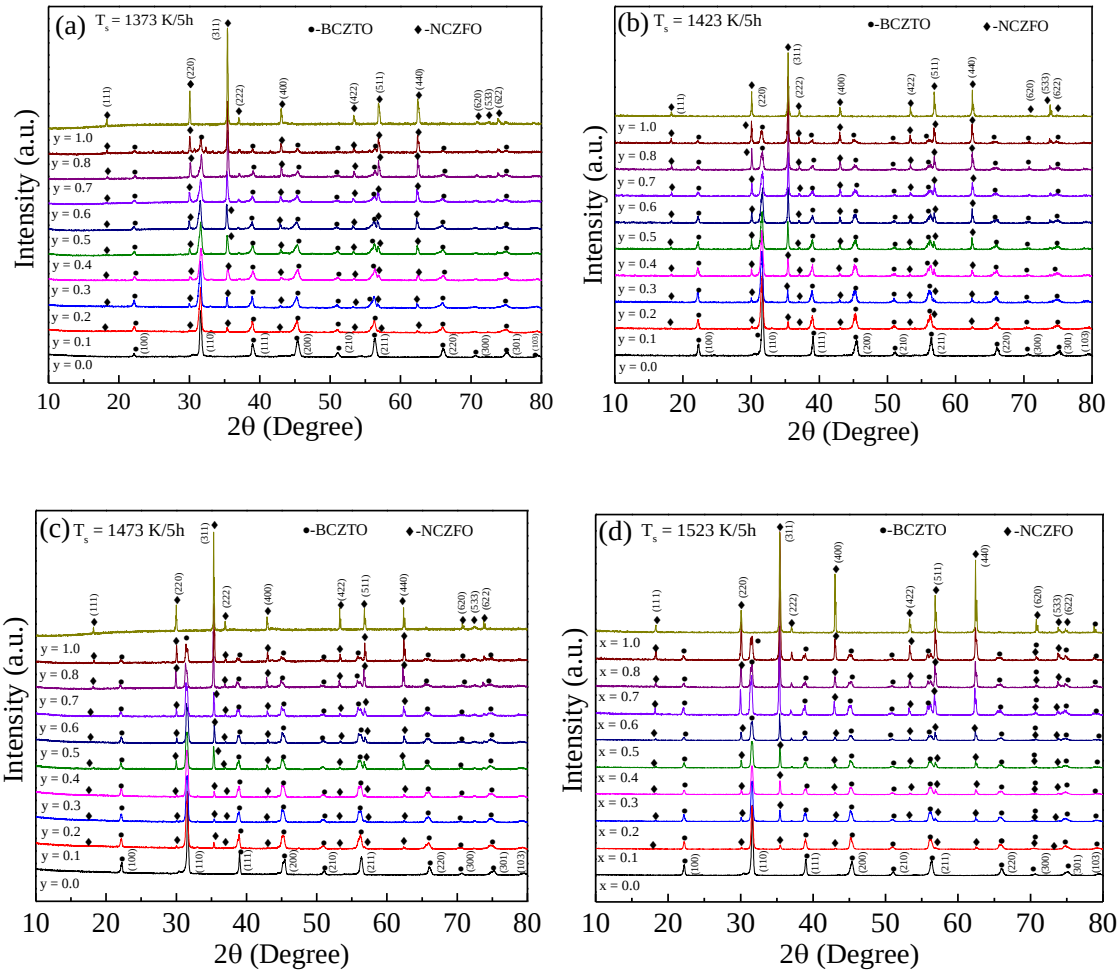

Figure 4.27: XRD profiles of (1-y) [BCZTO] + (y) [NCZFO] (y = 0-1.0) composite multiferroics annealed for 5 h at: (a) 1373, (b) 1423, (c) 1473 and, (d) 1523 K.

The two strong wavenumber bands can bee seen in Figure 4.26 (ii) for the calcinated powder associated with the cubic spinel ferrite. The presence of a high wavenumber band (ν_1) at 578.64 cm^{-1} indicates to the tetrahedrally coordinated (A)-site whilst the presence of a low wavenumber band (ν_2) at 389.44 cm^{-1} is associated with the octahedrally coordinated (B)-site. These two distinctive bands result from the stretching and bending vibrational modes resulting from interplay among the atoms of oxygen and cations within the limits of the tetrahedrally coordinated (A) and octahedrally coordinated (B)-sites, accordingly. We may thus draw the conclusion that the evolution of the cubic spinel architecture has been shown. The Fe^{3+}-O^{2-} lengths at the A-site (1.865 Å) and the B-site (2.02 Å), respectively, vary, which accounts for the variation in band locations [341]. Consequently, the FTIR spectra demonstrate that the calcinated powder has entirely changed into a ferrite skeleton. In response to the H-O-H bending vibrational mode of free or adsorbed water, a wide band was seen between 1616.35 cm^{-1} due to BCZTO and 1608.63 cm^{-1} due to NCZFO. Water adsorption may be connected to the component phases' high volume to surface ratios [342]. The existence of residual adsorbed or ambient CO_2 can be confirmed by an intense wavenumber band seen at 2375.95 cm^{-1} due to BCZTO and 2375.95 cm^{-1} due to NCZFO. Owing to the CH_2 vibration, two additional wavenumbers that occur at 2924.09 cm^{-1} and 2864.29 cm^{-1} due to BCZTO and 2924.09 cm^{-1} and 2858.51 cm^{-1} due to NCZFO are attributed to asymmetrical and symmetrical carbon chains, accordingly. Due to O-H stretching from the condensing items, the wide bands at 3442.94 cm^{-1} due to BCZTO and 3439.08 cm^{-1} due to NCZFO have been seen [343]. Figure 4.27 displays the XRD profiles of (1-y) [BCZTO] + (y) [NCZFO] composite multiferroics annealed at 1373 K in (a), 1423 K in (b), 1473 K in (c), and 1523 K in (d), over the course of five hours. As shown in Figure 4.27 (a-d), the composite multiferroics' XRD spectrum is able to be listed by the expected BCZTO [represented by solid circles (•); intense peak is (110)] and NCZFO [represented via a diamond (♦); for importance, just the strongest (311) peak] peak, and no additional contamination phases can be listed, demonstrating that each of the component phases

may exist together and demonstrate the anticipated chemical suitability instead of a response amongst the two phases during the process of crystallization and nucleation. This is crucial for the manufacture of magnetoelectric composite multiferroics in order to prevent a decline in the dielectric and magnetic characteristics of the component phases during sintering. The phase proportion in the compounds affects the strength of the strongest peaks, such as (311) NCZFO and (110) BCZTO. A precise examination of the composite multiferroics' XRD patterns discloses that as NCZFO concentrations rise, so do the NCZFO phase's peak intensity and number. For instance, the primary peaks [(220), (311), (400), (511), and (440)] related to the NCZFO escalate slowly as you raise the NCZFO amount from y = 0.0 to y = 1.0 subsequently, the primary peaks [(110), (111), (200), (210), (211), and (220) related to the BCZTO drop over time to eventually accomplish pristine BCZTO.

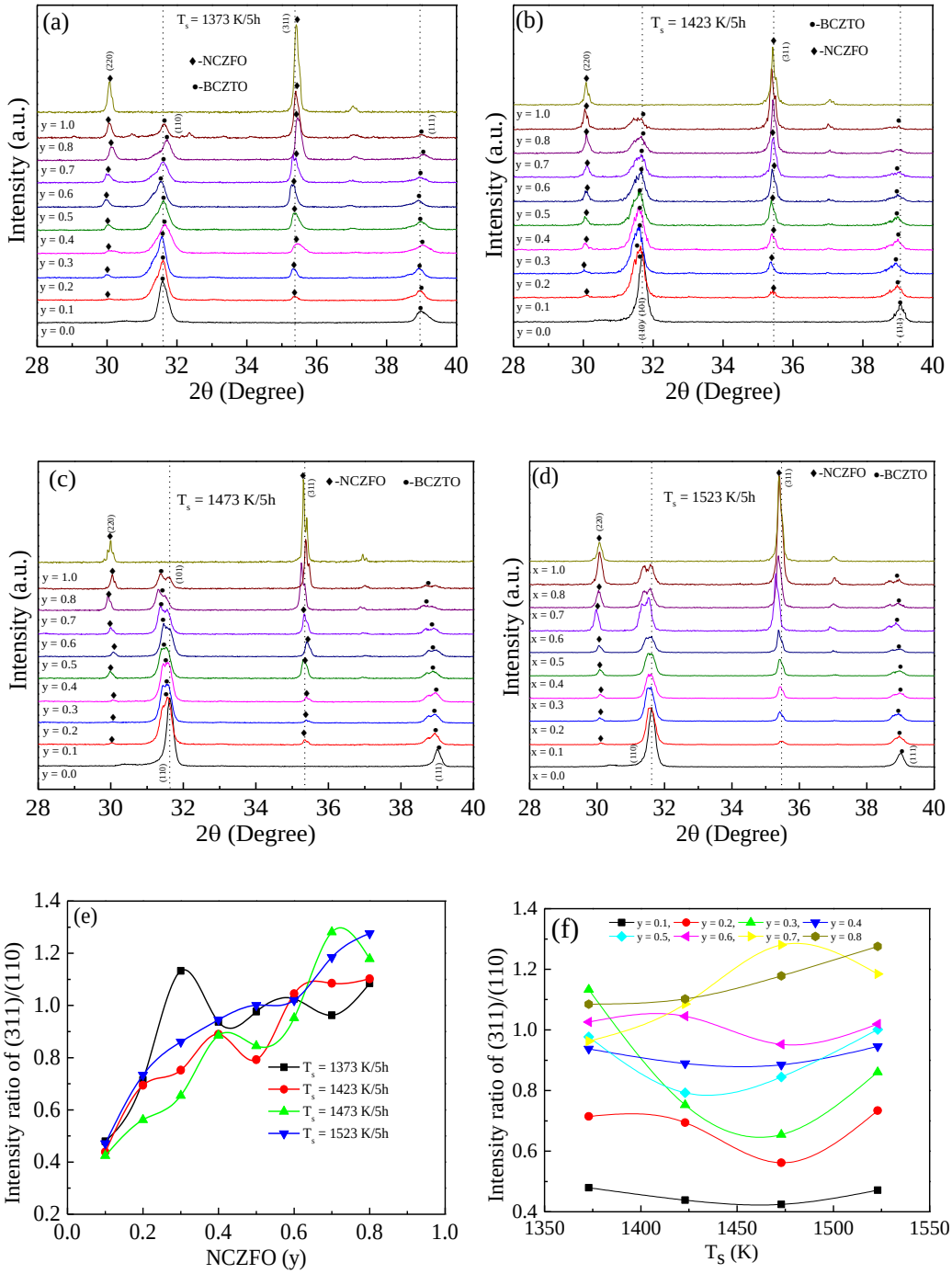

Figure 4.28: Partial enlargement of (110) and (311) peaks of (1-*y*) [BCZTO] + (*y*) [NCZFO] (*y* = 0-1.0) composite multiferroics in the midst of 2θ = 30°-36° annealed for 5 h at: (a) 1373, (b) 1423, (c) 1473 and, (d) 1523 K, and (e, f) shows composition and T_s dependent intensity ratio of (311)/(110).

This increase in the strength that corresponds to NCZFO indicates a boost in the crystal architecture of the material, and it is supported by the fact that BCZTO-NCZFO composite multiferroics with distinct NCZFO amounts. Exact locations of the cations Cu^{2+} (0.73 Å,

coordination number, CN = 6), Zn^{2+} (0.74 Å, CN = 6), Ca^{2+} (1.34 Å, CN = 12), and Zr^{4+} (0.72 Å, CN = 6). The ionic radius and valence of the constituent elements can be used to identify the lattice. The ionic radius of Cu^{2+} (0.73 Å, CN = 6), Zn^{2+} (0.74 Å, CN = 6), Ni^{2+} (0.69 Å, CN = 6), Ca^{2+} (1.34 Å, CN = 12), Ba^{2+} (1.35 Å, CN = 6), Zr^{4+} (0.72 Å, CN = 6) and Ti^{4+} (0.605 Å, CN = 6). Therefore, Cu^{2+} (0.73 Å, CN = 6), Zn^{2+} (0.74 Å, CN = 6), Ca^{2+} (0.99 Å, CN = 6) and Zr^{4+} (0.72 Å, CN = 6) mainly reside Ni^{2+} (0.69 Å, CN = 6), Ba^{2+} (1.35 Å, CN = 6) and Ti^{4+} (0.605 Å, CN = 6) cations [344]. Therefore, it may be said that the composite multiferroics that were created satisfy the rules of combining. From Fig. 4.28 (a-f), it is noticeable that the strongest peak (110) of the BCZTO is nearly retained at y = 0.1, 0.4, and 0.6 at 1373 K. At y = 0.2, y = 0.5, the strong peak (110) changes towards smaller angle, while at y = 0.3, 0.6, 0.7, and 0.8, the strongest peak (110) moves to larger angle. At the identical time, the strongest peak (311), that correlates to the NCZFO, changes towards higher angles in y = 0.3, 0.4, 0.6, 0.7, and 0.8 and towards lower angles in y = 0.2 and 0.5. As the level of NCZFO rises, the strongest maximum (110) connected with the BCZTO phase changes to smaller angles at 1423 K. At 1423 K, as the level of NCZFO rises, the strogest maximum (311) correlating to the NCZFO as well moves to lower angle. As the level of NCZFO is raised, the strongest maximum (110) connected with the BCZTO phase changes to lower angle. On raising NCZFO volume at 1473 K, the sharpest maximum (311) correlating to NCZFO as well changes toward lower angle. The strongest maximum (110) at 1523 K, which correlates to the BCZTO phase, changes toward lower angle while the NCZFO volume is raised. At 1373 K, the strogest maximum (311) associated with the NCZFO likewise changes towards a lower Bragg diffraction angle as the quantity of the NCZFO escalates. The splitting of the BCZTO (002/200) peak at $2\theta \sim 45°$ was seen in both pure BCZTO and composite multiferroics, confirming the tetragonal geometry of BCZTO. It's also important to note that the (002)/(200) splitting gets progressively worse when the NCZFO phase content of the composite rises. The electrostatic attraction between the 3d electrons of Ti^{4+} and the 2p electrons of O^{2-}ions is the mechanism that creates the resulting

splitting (002/200) characteristic peak [345, 346]. The crystallite diameter is also calculated employing Debye-Scherrer's relationship [183]. Table 4.32-4.35 lists the lattice constants, crystallite diameter, and tetragonality for each phase in all T_s. From Table 4.32-4.35, it is easy to see that the average crystallite diameter of each phase alters in a non-systematically on upsuring NCZFO amount and T_s. This diverse fluctuation in crystallite diameter may be assigned to the juxtaposition effect caused by two components, such as (1) alterations in the cell volume (the lattice constant), and (2) tensions and microstrains that stemmed from defects in the structure of the crystal, such as stacking faults, dislocations, vacancies, etc. [296]. Additionally, the composite multiferroics' combined powders' nano-characteristics may be seen. As compared to each of the component phases, i.e., NCZFO and BCZTO, the lattice constants of the component phases of the composite multiferroics are marginally different. A number of chemical interactions occur in a portion of the BCZTO phase while sintering. At first, the chemical bonds of Ba^{2+}-O^{2-}-Ba^{2+}, Ca^{2+}-O^{2-}-Ca^{2+}, Zr^{4+}-O^{2-}-Zr^{4+}, Ti^{4+}-O^{2-}-Ti^{4+}, Ba^{2+}-O^{2-}-Ti^{4+}, Ca^{2+}-O^{2-}-Ti^{4+}, Ba^{2+}-O^{2-}-Zr^{4+}, Ca^{2+}-O^{2-}-Zr^{4+} decomposes because some of O^{2-} is excited. Then, the ions Ba^{2+} (1.35 Å), Ca^{2+} (0.99 Å) and $Zr4^{+}$ (0.72 Å) and Ti^{4+} (0.605 Å) substitute the Fe^{3+} ion (0.645 Å) at tetrahedrally and octahedrally coordinated (A and B)-sites ions of NCZFO architecture [347]. This alteration might be attributable to a shift in the ionic radii of the metal ions; for example, Ni^{2+} ion (0.69 Å), Cu^{2+} ion (0.73 Å), Zn^{2+} ion (0.74 Å) ion have higher radii than Fe^{3+} ions (0.645 Å), Ba^{2+} (1.35 Å), Ca^{2+} (0.99 Å), Zr^{4+} (0.72 Å) and Ti^{4+} ions (0.605 Å), which are available in composite multiferroics [344]. Table 4.32-4.35 shows that (c/a) declines on rising NCZFO amount. The decrease in (*c*/*a*) ratio is attributed to the overlap of the (002/200) peaks on escalating NCZFO amount [348]. It is evident that when the NCZFO amount rises, the peak strength ratio rises as well. The intensity ratio was observed to decline to a maximum of 1473 K in the composite multiferroics with y = 0.1-0.4 and 0.6 and showed a rising feature at 1523 K. In y = 0.5, the intensity ratio was reduced at 1423 K, and after which, it was observed to improve with further increase in T_s. The ratio of intensity peak

in $y = 0.7$ was enhanced to a maximum of 1473 K and decrease at 1523 K. It is obsereved that the ratio of intensity peak in $y = 0.8$ increases with increasing T_s. The changed connection of the NCZFO phase is the factor that leads the peak ratio to rise. The proportion of the component phases in the composite multiferroics is determiend employing the following formula: % of NCZFO/BCZTO $= \frac{\text{Area under the spinel peak (311)/area under the perovskite peak \{(110)+(101)\}}}{\text{area under the perovskite peak \{(110)+(101)\}+Area under the spinel peak (311)}} \times 100\%$ [349]. The achieved phase fractions for each phase correspond roughly to the fractions originally used in the synthesis and are summarized in Table 4.32-4.35. This also confirms the simultaneous existence of the component phases within the composite.

4.3.2. Micromorphological and densification investigation

Figure 4.29 (i-x) and (xi-xx) show the micromorphological structures of (1-*y*) [BCZTO] + (*y*) [NCZFO] composite multiferroics annealed for 5 h at 1373 K and 1423 K. On the other hand, Figure 4.30 (i-x) and (xi-xx) represent the micromorphological structures for the composite multiferroics annealed for 5 h at 1473 K and 1523 K. The micromorphological structures of BCZTO (Figure 4.29 (i) annealed at 1373 K and (xi) annealed at 1423 K and Figure 4.30 (i) annealed at 1473 K and (xi) annealed at 1523 K phase and NCZFO (Fig. 4.29 (x) annealed at 1373 K and (xx) annealed at 1423 K and 4.30 (x) annealed at 1473 K and (xx) annealed at 1523 K phase exhibits a quasi-spherical like micrstructures with generally uniform grain diameter, few holes or pores, and little agglomeration. The incorporation of NCZFO to BCZTO displays the grain's asymmetrical form. The emergence of the grain's irregular form as the NCZFO concentration rises may be attributed to the NCZFO particles' segregation at the grain borders and their filling of pores in the midst of BCZTO grains. The line intercept approach [350] was used to calculate the grain diameter of the component phases and the composite multiferroics, and the results are shown in Table 4.32-4.35.

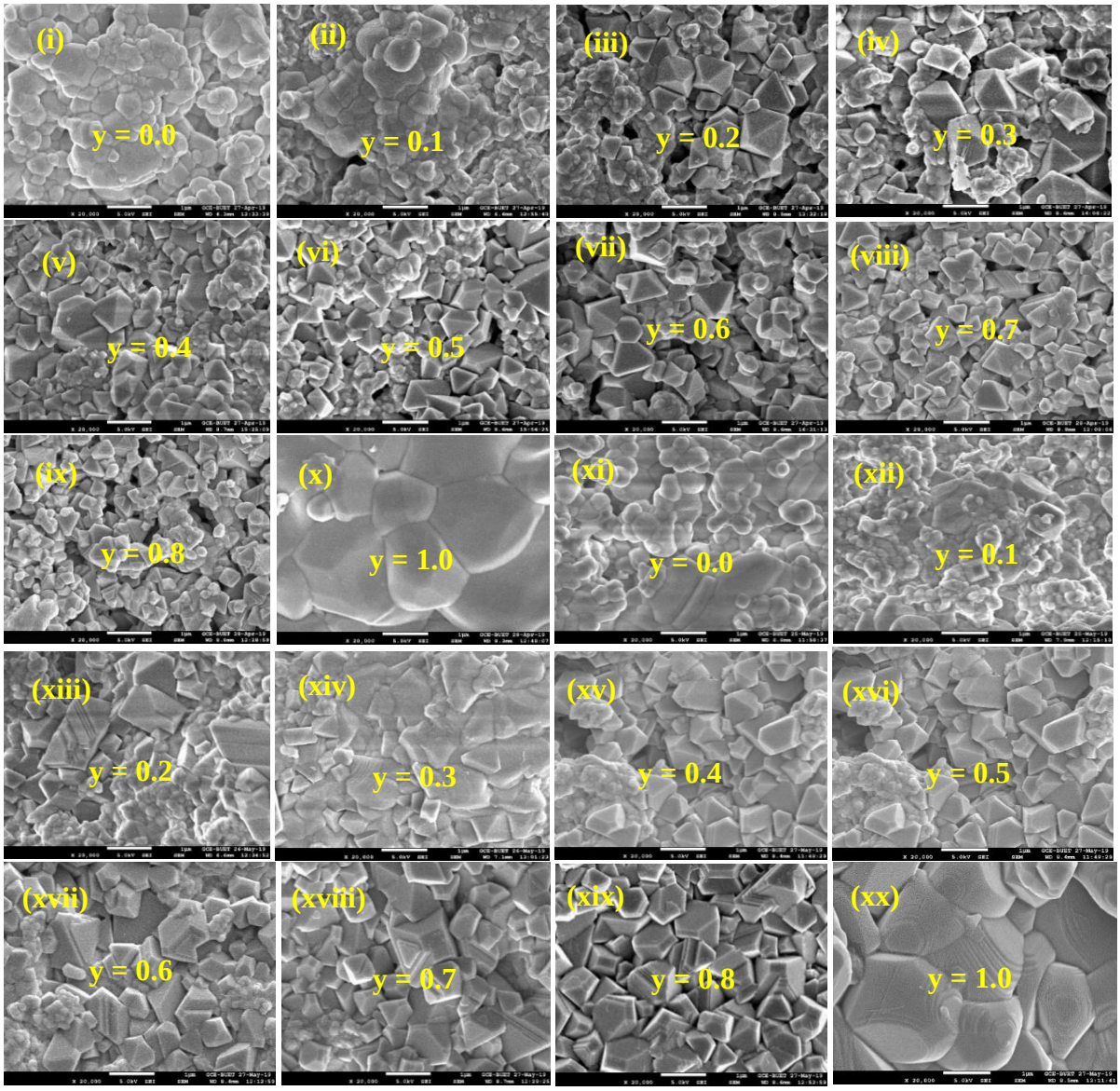

Figure 4.29: Micromorphological structures of (1-*y*) [BCZTO] + (*y*) [NCZFO] (*y* = 0-1.0) composite multiferroics (i) *y* = 0 (pure BCZTO), (ii) *y* = 0.1, (iii) *y* = 0.2, (iv) *y* = 0.3, (v) *y* = 0.4, (vi) *y* = 0.5, (vii) *y* = 0.6, (viii) *y* = 0.7, (ix) *y* = 0.8, (x) *y* = 1 (pure NCZFO) annealed at 1373 K for 5h and (xi) *y* = 0 (pure BCZTO), (xii) *y*=0.1, (xiii) *y* = 0.2, (xiv) *y* = 0.3, (xv) *y* = 0.4, (xvi) *y* = 0.5, (xvii) *y* = 0.6, (xviii) *y* = 0.7, (xix) *y* = 0.8, (xx) *y* = 1 (pure NCZFO) annealed at: 1423 K for 5h.

The NCZFO has bigger grains than the BCZTO, as seen in Table 4.32-4.35. This phenomenon is attributed to the BCZTO and NCZFO's different formation temperatures [349]. Another way to explain this characteristic is as follows: the heavier and larger component atoms in BCZTO may be responsible for the difference in grain diameter in the midst of the component phases,

and less mass transport during phase formation may have resulted in smaller grains compared to NCZFO grains [351]. Due to the discrepancy in the midst of the component phases' thermal expansion coefficients and rates of densification, it is impossible to prevent internal stress in composite multiferroics [352, 353]. It is conceivable that stress is the cause of the formation of the irregular micromorphology alongside varying grain diameters, as evidenced by the modification in the grain architecture on rising NCZFO concentration [352, 353]. The observed reduction in composite grain diameter on rising NCZFO concentration can be ascribed to the distinct grain diameters of the component phases. Due to the NCZFO phase's potential to impede grain growth, the reduction in grain diameter that occurs with increased NCZFO concentration may also be attributed to the BCZTO phase's grain growth being slowed. As the amount of NCZFO in the grain increases, the electron's mean free path is improved, which improves the composite multiferroics' resistivity and magnetoelectric properties [368]. With rising T_s, it is seen that the grain diameter steadily increases. This is due to the fact that the diffusion coefficient rises as T_s rises [354], which causes the grain border to shift quickly and encourages grain expansion [207]. It is important to note that the grain diameter determined from FESEM micrographs using the linear intercept approach is larger than the crystallite diameter determined from XRD patterns employing the Debye-Scherrer's prescription. The difference amongst these two characteristics is that the crystallite grain diameter is what is determined by XRD patterns, while the particle diameter is determined by FESEM micrographs.

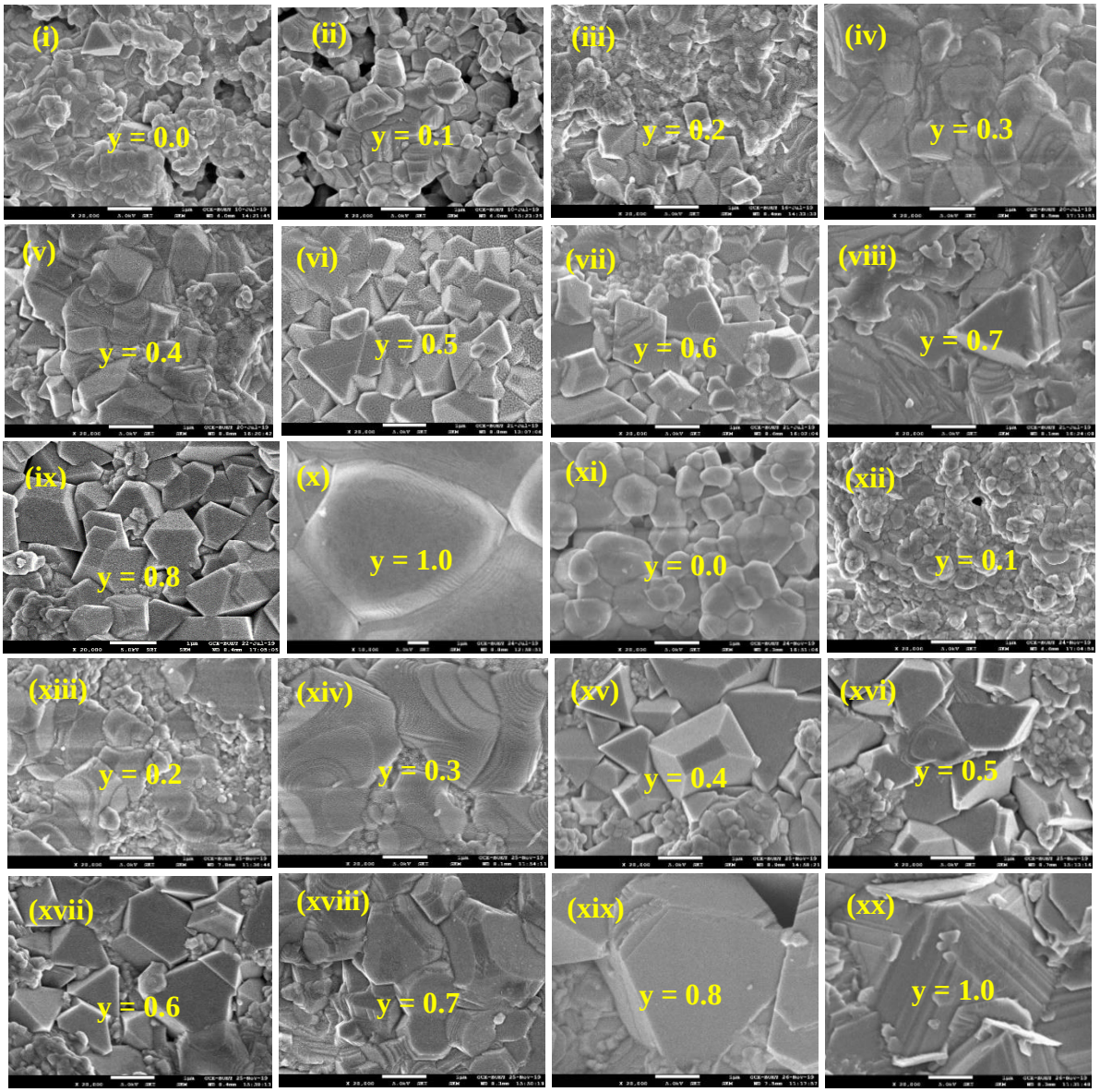

Figure 4.30: Micromorphological structures of (1-*y*) [BCZTO] + (*y*) [NCZFO] (*y* = 0-1.0) composite multiferroics (i) *y* = 0 (pure BCZTO), (ii) *y* = 0.1, (iii) *y* = 0.2, (iv) *y* = 0.3, (v) *y* = 0.4, (vi) *y* = 0.5, (vii) *y* = 0.6, (viii) *y* = 0.7, (ix) *y* = 0.8, (x) *y* = 1 (pure NCZFO) annealed at 1473 K for 5h and (xi) *y* = 0 (pure BCZTO), (xii) *y* = 0.1, (xiii) *y* = 0.2, (xiv) *y* = 0.3, (xv) *y* = 0.4, (xvi) *y* = 0.5, (xvii) *y* = 0.6, (xviii) *y* = 0.7, (xix) *y* = 0.8, (xx) *y* =1 (pure NCZFO) annealed for 5 h at: 1523 K.

It is essential to note that because a single particle may include more than one crystalline grains, the crystalline grain diameter may be less than the particle diameter. Since the crystallite diameters of the grains in composite multiferroics are not totally equal, the results derived from the Debye-Scherrer formula represent the genuine mean of crystallite grains with various diameters. Additionally, because the crystalline grain is not spherical, its thickness varies in

various directions, meaning that the diameter of the crystalline grain achieved by distinct diffraction peaks is frequently variable [355]. The component phases' and composite multiferroics' bulk densities (ρ_{bulk}) were calculated using the following relation: $\rho_{bulk} = \frac{mass}{volume} = \frac{m}{\pi r^2 h}$, where m represents the mass of the component phases, and the composite multiferroics, r denotes the pellet specimen's radius and h denotes the thickness of the pellet specimens. Table 4.32-4.35 provides a brief summary of the composite multiferroics' ρ_{bulk} values. It is noticeable from Figure 4.31 that, with the exception of the composite with y = 0.1, the ρ_{bulk} value rises on escalating NCZFO level at 1373 K. when anticipated, when the NCZFO concentration rises, so does the ρ_{bulk} value for the composite multiferroics. In the beginning, the ρ_{bulk} value is increaseed owing to the enhanced grain development and decreased porosity, and afterwards, the ρ_{bulk} value is changeed little considering the ideal grain compactness. It is also important to note that high T_s may result in increased sample density, which can be attributed to grain expansion via advancement of grain border motion [356]. When the NCZFO content is increased further, the value of ρ_{bulk} is shown to grow to a maximum of y = 0.2, then decrease to y = 0.4, and then increase once more. The ρ_{bulk} value at 1473 K steadily rises as NCZFO content rises. When the NCZFO amount is increased at 1523 K, the ρ_{bulk} value is seen to grow to maximum of y = 0.7 and then diminishes at y = 0.8. When the NCZFO content is increased, the value of ρ_{bulk} is seen to steadily grow at 1373 K, however at 1473 K, the value of ρ_{bulk} is seen to decrease. Additionally, the value of ρ_{bulk} for the composite multiferroics at 1473 K is less than that of ρ_{bulk} at 1423 K. The elevated grain growth may be responsible for the decrease in ρ_{bulk} value. Here, the intergrain gaps are made larger due to the increased grain diameter [357]. When compared to 1373 K, the value of ρ_{bulk} is less at 1423 K. The dissolution or interdiffusion in the midst of the BCZTO and NCZFO phases appears to be the primary cause of this decline. From 1373 to 1523 K, the density of the NCZFO rises. Since the T_s of the NCZFO is smaller than that of the BCZTO, the

densification at elevated T_s is attributed to the creation of the liquid phase, a decrease in activation energy, and encouragement of grain development. The exchange interactions amongst Fe^{3+} and Zr^{4+}, Ti^{4+} through O^{2-} ions may be responsible for the rise in ρ_{bulk} value. Component phases' and composite multiferroics' X-ray densities (ρ_{X-ray}) were estimated using the relationships [358, 359]:

(i) $\rho_{X-ray}(BCZTO) = \frac{ZM_W(BCZTO)}{N_A a^2 c}$,

(ii) $\rho_{X-ray}(NCZFO) = \frac{ZM_W(NCZFO)}{N_A a^3}$,

and

(iii) $\rho_{X-ray}(Composite) = \frac{m(NCZFO)+m(BCZTO)}{m(NCZFO)\times\rho_{X-ray}(NCZFO)+m(BCZTO)\times\rho_{X-ray}(BCZTO)}$,

where Z denotes number of atom per unit cell ($Z = 1$ for BCZTO and $Z = 8$ for NCZFO) M_w(BCZTO) and M_w(NCZFO) are the molecular mass, a and c are the lattice constants of BCZTO and NCZFO, and N_A denotes the Avogadro's number, m(NCZFO) and m(BCZTO) are the masses of NCZFO and BCZTO, ρ_{X-ray}(NCZFO), ρ_{X-ray}(BCZTO), and ρ_{X-ray}(composite) the $\rho_{X-ray}$of NCZFO, BCZTO, and composite multiferroics. Table 4.32-4.35 provides a summary of the value of ρ_{X-ray} for the composite multiferroics for all T_s. Table 4.32-4.35 makes it clear that the value of the ρ_{X-ray} displays a declining pattern with increasing NCZFO concentration. The large value of the NCZFO phase's lattice constant may be to blame for this descendent behavior. Additionally, compared to Ni^{2+} (8.91 g/cm^3), Cu^{2+} (8.96 g/cm^3), Zn^{2+} (7.14 g/cm^3) and Fe^{3+} (7.874 g/cm^3), has higher density than that of Ba^{2+} (3.51 g/cm^3), Ca^{2+} (1.55 g/cm^3), Zr^{4+} (6.52 g/cm^3) and Ti^{4+} (4.51 g/cm^3), which also causes the reduction in ρ_{X-ray} for all T_s. [360]. According to Table 4.32-4.35, there is a pronounced difference in the midst of the values of the ρ_{bulk} and ρ_{X-ray}, indicating that the value of the ρ_{bulk} is much less than the ρ_{X-ray}. The existence of the pores created during manufacturing

and sintering in the composite multiferroics [345] is explicitly indicated in this discrepancy. The component phases (BCZTO and NCZFO) and composite multiferroics' porosity were estimated using: (%) porosity = $\frac{theoretical\ density - experimental\ density}{theoretical\ density} \times 100$ and presented in Table 4.32-4.35. Two significant elements, such as intergranular porosity (P_{inter}) (at the point where grains converge) and intragranular porosity (P_{intra}) (within a grain), are responsible for the porosity in ceramics [313]. As a result, the total porosity ($P\ (\%) = P_{inter} + P_{intra}$) is the combination of P_{inter} and P_{intra}. To totally eradicate intragranular porosity is actually extremely challenging. Additionally, P_{inter} is said to rely on grain diameter, whereas P_{intra} is said to depend on T_s [313, 361]. The grain diameter is seen to vary randomly when NCZFO content rises. Because of this, when NCZFO concentration rises, P_{intra} has a greater effect whereas the attribution of P_{inter} fluctuates randomly [362]. A convincing justification for the NCZFO phase's ability to successfully accelerate the densification of the composite multiferroics can be seen in Table 4.32-4.35, which shows that the porosity drops on rising NCZFO level. Moreover, when T_s increases, the porosity decreases. This decrease of porosity with various T_s is associated with the observation that the component grains get bigger and close together, enhancing the grain-to-grain contact [363]. More mobile magnetic domains are created as a result of reduced porosity, which has a substantial impact on magnetic permeability.

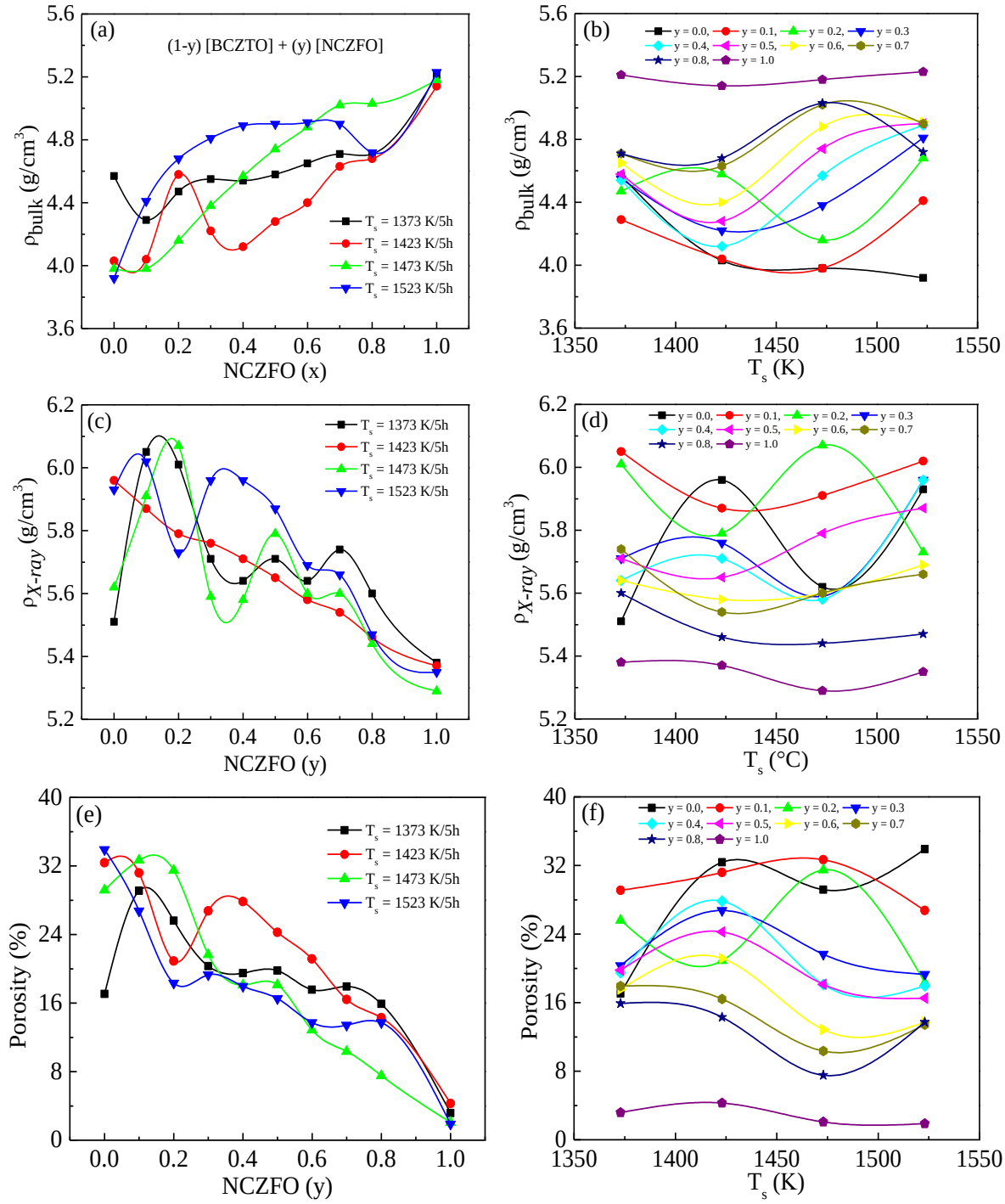

Figure 4.31: Evolution of: (a, b) bulk density (ρ_{bulk}), (c, d) theoretical density (ρ_{X-ray}) and (e, f) with composition and T_s of (1-*y*) [BCZTO] + (*y*) [NCZFO] (*y* = 0-1.0) composite multiferroics.

Table 4.32. Lattice constants, proportion of the component phases, bulk density (ρ_{bulk}), theoretical density (ρ_{X-ray}), porosity (P), grain diameter (D_{SEM}), and crystallite diameter (D_{hkl}) of (1- y) [BCZTO] + (y) [NCZFO] composite multiferroics annealed at 1373 K

T_s (°C)	Composition (x)	Lattice constant (Å)				% of component phases		ρ_{bulk} (g/cm^3)	ρ_{X-ray} (g/cm^3)	D_{SEM} (μm)	P(%)	D_{hkl} (nm)	
		NCZFO	BCZTO			NCZFO	BCZTO					NCZFO	BCZTO
		a	a	c	c/a								
1373	0	-	3.9863	4.3206	1.0838	-	100	4.57	5.51	0.45	17	-	25.9
	0.1	8.4191	4.0064	3.8436	0.9699	8.58	91.427	4.29	6.05	0.45	29	41.9	21
	0.2	8.4237	4.0394	3.7476	0.9278	20.92	79.08	4.47	6.01	0.46	26	49.1	21.2
	0.3	8.4159	3.9810	4.0624	1.0181	29.24	70.76	4.55	5.71	0.40	20	25.3	17.2
	0.4	8.4138	4.0083	4.0299	1.0054	38.81	61.19	4.54	5.64	0.46	20	38	19.3
	0.5	8.4143	4.0181	3.8553	0.9595	47.14	52.86	4.58	5.71	0.46	20	43	21.4
	0.6	8.4201	4.0229	3.8220	0.9501	56.02	43.98	4.65	5.64	0.51	18	36.8	23.9
	0.7	8.3856	4.0618	3.4961	0.8607	64.40	35.60	4.71	5.74	0.51	18	43.4	28.1
	0.8	8.3993	4.0707	3.4721	0.8530	71.07	28.93	4.71	5.60	0.40	16	48.2	40
	1.0	8.3888	-	-	-	100	-	5.21	5.38	1.89	3	52.7	-

Table 4.33. Lattice constants, proportion of the component phases, bulk density (ρ_{bulk}), theoretical density (ρ_{X-ray}), porosity (P), grain diameter (D_{SEM}), and crystallite diameter (D_{hkl}) of (1- y) [BCZTO] + (y) [NCZFO] composite multiferroics annealed at 1423 K

T_s (°C)	Composition (x)	Lattice constant (Å)				% of component phases		ρ_{bulk} (g/cm^3)	ρ_{X-ray} (g/cm^3)	D_{SEM} (μm)	P(%)	D_{hkl} (nm)	
		NCZFO	BCZTO			NCZFO	BCZTO					NCZFO	BCZTO
		a	a	c	c/a								
1423	0	-	3.9909	3.9820	0.9978	-	100	4.03	5.96	0.44	32	-	37.2
	0.1	8.4066	4.0014	3.9846	0.9958	5.46	94.54	4.04	5.87	0.22	31	52.8	22.9
	0.2	8.4136	4.0048	3.9959	0.9978	13.92	86.08	4.58	5.79	0.39	21	77.9	33
	0.3	8.4047	4.0058	3.9757	0.9925	17.71	82.29	4.22	5.76	0.56	27	81.8	22.6
	0.4	8.4053	4.0008	3.9765	0.9939	27.04	72.96	4.12	5.71	0.32	28	65.1	22.4
	0.5	8.4013	3.9977	3.9894	0.9979	35.88	64.12	4.28	5.65	0.48	24	77.2	21.8
	0.6	8.3980	3.9962	4.0069	1.0027	47.95	52.05	4.40	5.58	0.54	21	73.2	21.3
	0.7	8.3974	4.0019	3.9745	0.9932	58.88	41.12	4.63	5.54	0.61	16	91.6	21.3
	0.8	8.4033	4.0136	3.97753	0.9905	69.87	30.13	4.68	5.46	0.81	14	86	20.4
	1.0	8.3974	-	-	-	100	-	5.14	5.37	1.32	4	103	-

Table 4.34. Lattice constants, proportion of the component phases, bulk density (ρ_{bulk}), theoretical density (ρ_{X-ray}), porosity (P), grain diameter (D_{SEM}), and crystallite diameter (D_{hkl}) of (1- y) [BCZTO] + (y) [NCZFO] composite multiferroics annealed at 1473 K

T_s (°C)	Composition (x)	Lattice constant (Å)				% of component phases		ρ_{bulk} (g/cm^3)	ρ_{X-ray} (g/cm^3)	D_{SEM} (μm)	P (%)	D_{hkl} (nm)	
		NCZFO	BCZTO			NCZFO	BCZTO					NCZFO	BCZTO
		a	a	c	c/a								
1473	0	-	3.9888	4.2320	1.061	-	100	3.98	5.62	0.38	29.18	-	10
	0.1	8.4212	4.0077	3.9381	0.9826	10.14	89.86	3.98	5.91	0.49	32.66	74.4	7.58
	0.2	8.4046	4.0376	3.7164	0.9204	16.46	83.54	4.16	6.07	0.49	31.47	106	29.2
	0.3	8.4011	4.0012	4.1516	1.0376	30.99	69.00	4.38	5.59	0.43	21.65	81.6	27.5
	0.4	8.4320	4.0134	4.0692	1.0139	39.56	60.44	4.57	5.58	0.66	18.10	59	29.3
	0.5	8.4093	4.0407	3.7117	0.9186	43.66	56.34	4.74	5.79	0.54	18.13	65.4	29.6
	0.6	8.4283	4.0428	3.8331	0.9481	59.29	42.71	4.88	5.60	0.82	12.86	70.6	28.8
	0.7	8.4439	4.1015	3.5399	0.8631	66.55	33.45	5.02	5.60	1.06	10.36	76.4	33.5
	0.8	8.4180	4.0257	3.9582	0.9832	72.25	27.75	5.03	5.44	1.04	7.54	83.4	30.4
	1.0	8.4365	-	-	-	100	-	5.18	5.29	7.51	2.08	95.7	-

Table 4.35. Lattice constants, proportion of the component phases, bulk density (ρ_{bulk}), theoretical density (ρ_{X-ray}), porosity (P), grain diameter (D_{SEM}), and crystallite diameter (D_{hkl}) of (1- y) [BCZTO] + (y) [NCZFO] composite multiferroics annealed at 1523 K

T_s (°C)	Composition (x)	Lattice constant (Å)				% of component phases		ρ_{bulk} (g/cm^3)	ρ_{X-ray} (g/cm^3)	D_{SEM} (μm)	P (%)	D_{hkl} (nm)	
		NCZFO	BCZTO			NCZFO	BCZTO					NCZFO	BCZTO
		a	a	c	c/a								
1523	0	-	4.0000	3.9909	0.9975	-	100	3.92	5.93	0.67	33.90	-	38.5
	0.1	8.4098	4.0196	3.8445	0.9564	9.16	90.84	4.41	6.02	0.27	26.74	65.0	29.6
	0.2	8.4026	4.0095	4.0411	1.0079	22.32	77.68	4.68	5.73	1.26	18.32	77.8	39.5
	0.3	8.4010	4.0272	3.7510	0.9314	32.93	67.07	4.81	5.96	0.93	19.30	82.2	52.6
	0.4	8.3969	4.0344	3.6609	0.9074	42.42	57.58	4.89	5.96	0.63	17.95	79.2	38.3
	0.5	8.4061	4.0361	3.6373	0.9012	57.77	42.23	4.90	5.87	0.34	16.52	99.0	39.2
	0.6	8.4259	4.0324	3.7243	0.9236	62.95	37.05	4.91	5.69	0.66	13.71	79.2	54.5
	0.7	8.4081	4.0459	3.6250	0.8960	72.48	27.52	4.90	5.66	0.97	13.43	69.7	25.4
	0.8	8.4007	4.1859	3.6571	0.8737	83.76	16.24	4.72	5.47	1.21	13.71	75.1	43.1
	1.0	8.4047	-	-	-	100	-	5.23	5.35	1.45	1.87	95.7	-

4.3.3. Dielectric permittivity analsyis

Figure 4.32 how the real component (ε') of electric permittivity evolves with respect to frequency of (1 - y) [BCZTO] + (y) [NCZFO] composite multiferroics annealed for 5 h at various T_s: (a) 1373, (b) 1423, (c) 1473, and (d) 1523 K. The ε' value is often dependent on a number of factors, including stoichiometry, density, and uniform skeleton, porosity, and particle diameter. The ε' value in spectra decreases sharply at lower frequencies before evolving towards a frequency-independent value at higher frequencies. Maxwell-Wagner's theory [364] and Koop's theory [235] may both be used to explain this phenomenon. Pursuant to Maxwell-Wagner model, dielectric materials are widely recognized to have two layers, one of which is a highly conductive layer made up of grains and one more of which is a weakly conductive layer made up of grain borders. The contribution of the grain borders is substantial at lower frequencies, and as a result, grain border resistance is significantly high. As a result, space charges are prevented from emigrating and gathering at grain borders. This buildup of space charge helps to polarize the space charge, producing an extremely high ε'value. Due to the electron hopping Fe^{2+} and Fe^{3+} ions, Zr^{3+} and Zr^{4+} ions, and Ti^{3+} and Ti^{4+} ions, dipolar polarization becomes more prevalent as the applied frequency rises. The electron exchange in the midst of the ions may be used to explain how the dipoles move, and as a result, the dipoles align with the field that is active. However, the possible impediment in the midst of Fe^{2+} and Fe^{3+}, Zr^{3+} and Zr^{4+} and Ti^{3+} and Ti^{4+} ions will trigger the motion of the charge carriers to become inactive, leading to a relaxation of polarization. As a consequence, at higher frequencies, the polarization begins to recede behind the field. As a result, with rising frequency, the ε' value diminishes until it eventually becomes frequency independent [365]. Table 4.36-4.39 lists the values of ε' at various T_s and chosen frequencies. At 1373 and 1523 K, the NCZFO exhibits maximum ε' in contrast to the BCZTO at lower frequencies ($\leq$ 1 kHz). The spontaneous shift of the oxidation state in the midst of Fe^{2+} and Fe^{3+} at the tetrahedrally and octahedrally coordinated (A and B)-sites, which takes place without causing the crystal's

energy state to alter, is what causes an anomalous rise in ε' in the NCZFO [346, 366, 367]. The value of ε' is maximal for the NCZFO and least in y = 0.8 and 0.0, since the availability of space charge polarization for the NCZFO phase is greatest near the grain borders. The mean free route of the electron is increased for the NCZFO phase by the largest grain diameter and lowest grain border region, and as a result, ε' becomes maximal for the NCZFO phase. In the earlier trial [368], comparable outcomes were noted.

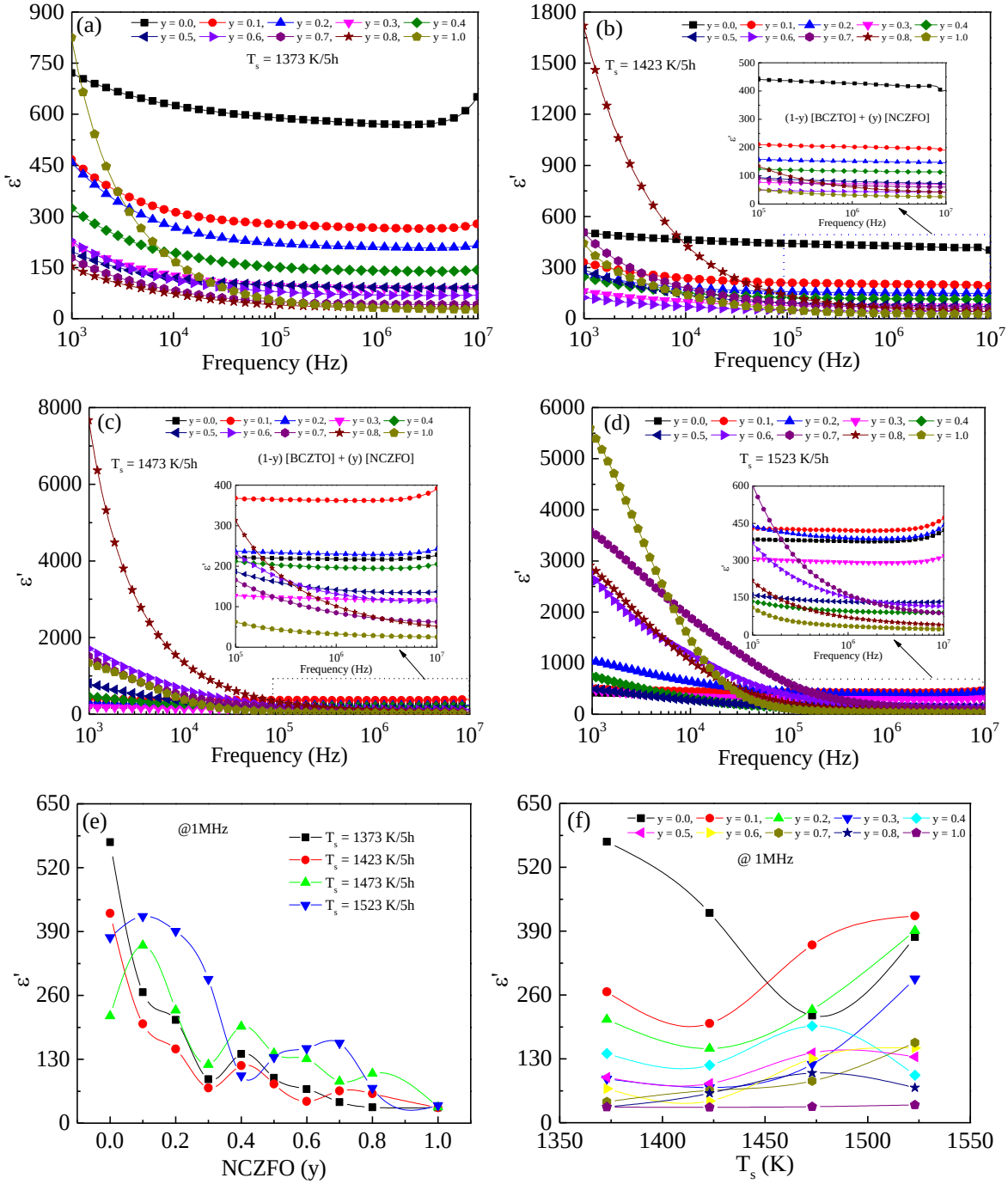

Figure 4.32: Evolution of real component (ε') of electric permittivity with frequency of (1-*y*) [BCZTO] + (*y*) [NCZFO] (*y* = 0-1.0) composite multiferroics annealed for 5 h at: (a) 1373, (b) 1423, (c) 1473 and, (d) 1523 K, and (e. f) shows composition and T_s dependent ε' at 1MHz.

The y = 0.8 composite demonstrates optimum ε' in comparison to BCZTO at 1423 K and 1473 K at the lower frequencies (≤ 1 kHz), whereas the y = 0.6 and 0.3 composite multiferroics reveal lowest ε'. The mobile charges' substantial density is where these improved dispersive properties come from [369]. Since the value of ε' for the NCZFO is greater than that of ε' for

the BCZTO [368], it is found that the ε' value at lower frequencies increases with increasing NCZFO concentration for only 1523 K. The ε' value is seen to diminish with increased NCZFO concentration at higher frequencies, as is readily apparent. The following variables could be the cause of the decrease in ε': (1) the lack of a percolation outcome and the disembodiment of component phases, (2) the NCZFO's ε' value is less than the BCZTO phase's ε' value (i.e., the dilution outcome), and (3) Verwey's class electronic interchange polarization [370, 371]. However, it has been found that when T_s rises, the value of ε' grows. The improvement in grain diameter with rising T_s and the increase in Fe^{2+} ions are both responsible for this increase in the value of ε'. Through the use of the following equations, the experimental findings were compared to the theoretical results [372, 373]:

(i) sum rule: $\varepsilon'(composite) = (1-x)\varepsilon'(BCZTO) + (x)\varepsilon'(NCZFO)$,

(ii) Lichtenecker equation [374]:
$ln\varepsilon'(\text{composite}) = (1-y)ln\varepsilon'(\text{BCZTO}) + (y)ln\varepsilon'(\text{NCZFO})$,

(iii) Looyenga's mixing formula [375, 376]:
$\varepsilon'^{1/3}(composite) = (1-y)\varepsilon'^{1/3}(BCZTO) + (y)\varepsilon'^{1/3}(NCZFO)$,

(iv) Maxwell-Wagner model [377]:
$$\varepsilon'(composite) = \varepsilon'(BCZTO)\left[\frac{2\varepsilon'(BCZTO)+\varepsilon'(NCZFO)+2y\left(\varepsilon'(NCZFO)-\varepsilon'(BCZTO)\right)}{2\varepsilon'(BCZTO)+\varepsilon'(NCZFO)-y\left(\varepsilon'(NCZFO)-\varepsilon'(BCZTO)\right)}\right],$$

(v) Bruggeman model [378]:
$$(1-y)\frac{\varepsilon'(BCZTO)-\varepsilon'(composite)}{\varepsilon'(BCZTO)+2\varepsilon'(composite)} + (y)\frac{\varepsilon'(NCZFO)-\varepsilon'(composite)}{\varepsilon'(NCZFO)+2\varepsilon'(composite)} = 0$$
and

(vi) Clausius-Mossotti law [379]:
$$\frac{\varepsilon'(composite)-1}{\varepsilon'(composite)+1} = (1-y)\frac{\varepsilon'(BCZTO)-1}{\varepsilon'(BCZTO)+2} + (y)\frac{\varepsilon'(NCZFO)-1}{\varepsilon'(NCZFO)+2},$$

where y is the volume percent of the NCZFO phase and $\varepsilon'(composite)$, $\varepsilon'(BCZTO)$ and $\varepsilon'(NCZFO)$ are the permittivities of the composite. Figure 4.33 compares the estimated value

of ε' with NCZFO content to the measured value (collected at 1 MHz) annealed for 5 h at various T_s: (a) 1373 K, (b) 1423 K, (c) 1473 K, and (d) 1523 K.

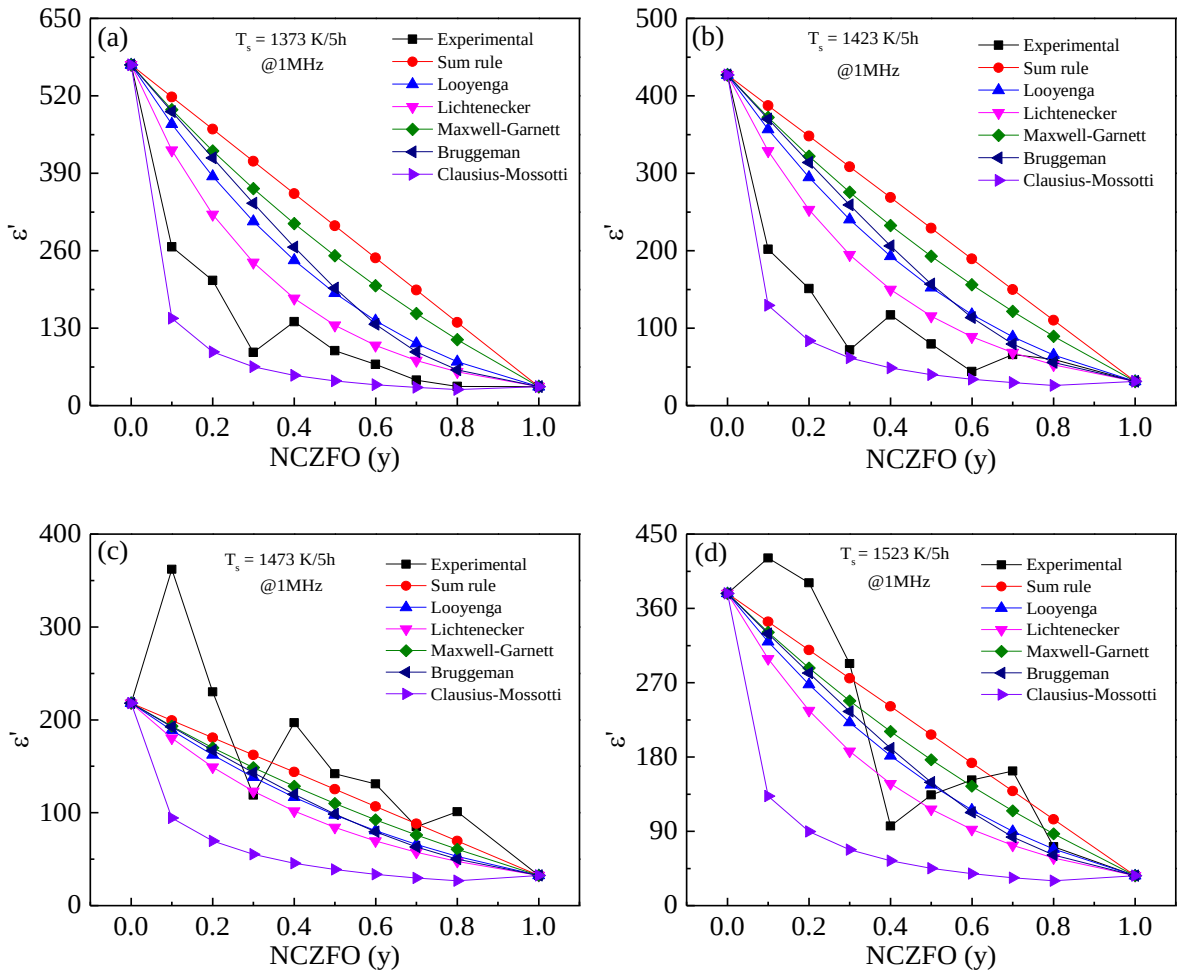

Figure 4.33: NCZFO content dependent experimental and predicted electric permittivity at 1MHz of (1-*y*) [BCZTO] + (*y*) [NCZFO] (*y* = 0-1.0) composite multiferroics annealed for 5 h at: (a) 1373, (b) 1423, (c) 1473 and, (d) 1523 K.

The discrepancy amongst the estimated and experimental values proves that composite multiferroics were effectively created and that it is impossible to avoid the consequence of ionic diffusion on ε' value amongst two separate phases [379, 380]. It is crucial to research the porosity adjustment for the experimental ε' value in order to eliminate the type of porosity that exists in composite multiferroics. In order to identify the existence of open porosity in the composite multiferroics, we utilized Rushman and Strivens' equation: $\varepsilon'(\text{corrected}) = \varepsilon'(measured) \times \frac{2+P}{2\times(1-p)}$, where $\varepsilon'(measured)$ denotes the measured electric permittivity

and P represents the porosity [381, 382]. Figure 4.34 shows the porosity corrected ε' value at 1 MHz with respect to NCZFO level annealed at (a) 1373, (b) 1423, (c) 1473, and (d) 1523 K. One observation was that the measured electric permittivity and the porosity adjusted electric permittivity extremely closely resemble one other. It is confirmed that the composite multiferroics have minimal porosity thanks to the similarity in the midst of the observed electric permittivity and the porosity adjusted electric permittivity [383].

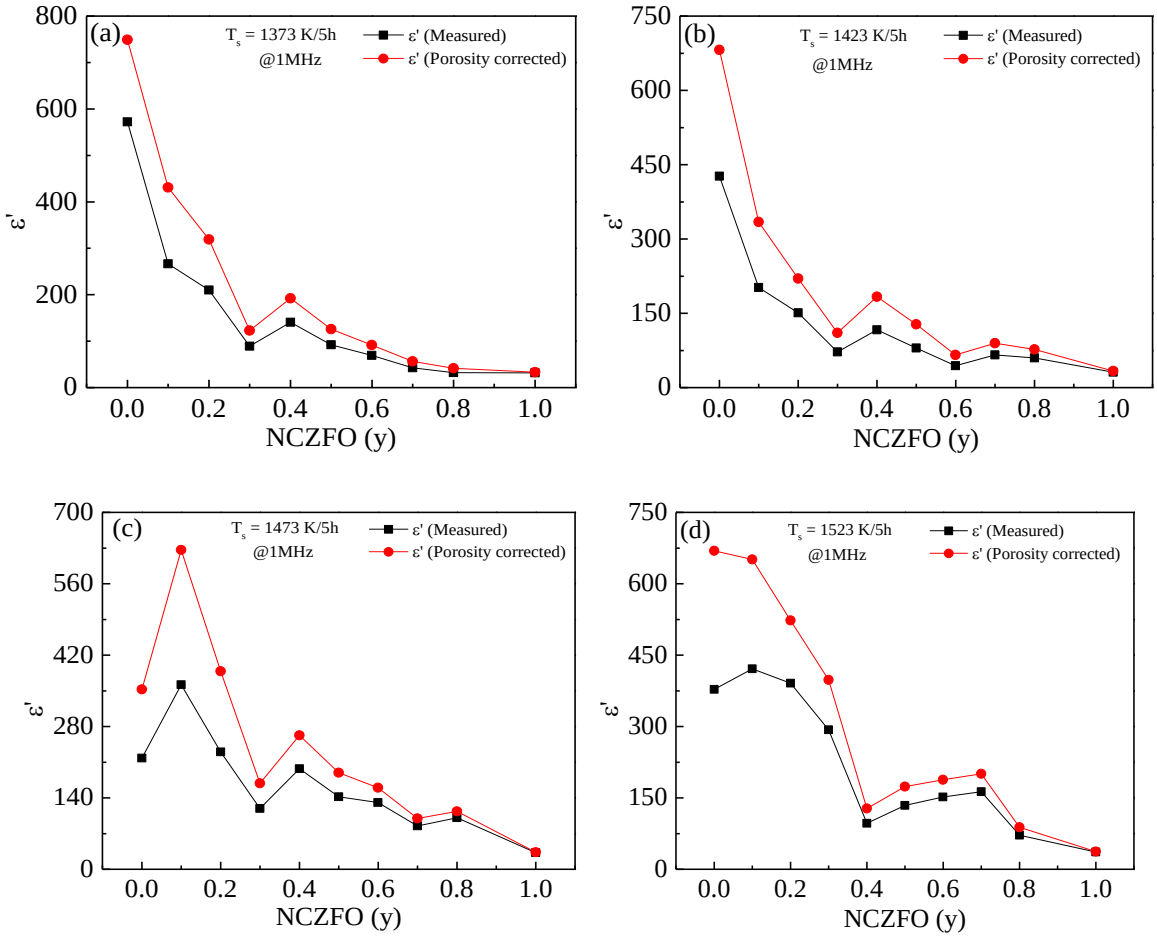

Figure 4.34: Porosity corrected electric permittivity (at 1MHz) of (1-y) [BCZTO] + (y) [NCZFO] (y = 0-1.0) composite multiferroics with NCZFO content annealed for 5 h at: (a) 1373, (b) 1423, (c) 1473 and, (d) 1523 K.

4.3.4. Permittivity loss tangent analysis

Figure 4.35 shows how the permittivity loss tangent ($tan\delta_\varepsilon$) evolves with respect to frequency of (1 - *y*) [BCZTO] + (*y*) [NCZFO] composite multiferroics annealed at: (a) 1373, (b) 1423, (c) 1473, and (d) 1523 K. $tan\delta_\varepsilon$, generally speaking, is a dielectric substance's capacity to convert electrical energy into thermal energy, which causes the material to produce heat [384]. Because of the presence of grain borders, contaminants, and defects in the crystal lattice, there is a lag amongst the polarization and applied field that causes the development of $tan\delta_\varepsilon$ [385]. The proportion of each phase, the stoichiometric ratio, the concentration of Fe^{2+} ions, and structural homogeneity are a few factors that affect the $tan\delta_\varepsilon$ value, which in turn relies on composition and T_s [239]. The $tan\delta_\varepsilon$ value drastically reduced at lower frequencies because of the strong resistance of the composite multiferroics, which reflects the grain border's bestowal. The $tan\delta_\varepsilon$ value is elevated, but at higher frequencies, $tan\delta_\varepsilon$ is weak, which relates the composite's low resistance, which is associated to grain's composition. Due to the considerable resistance offered by the composite multiferroics, transport of electrons inside the composite multiferroics will be challenging, and a significant amount of energy is needed for an electron transfer to take place amongst Fe^{2+} and Fe^{3+}, Ti^{3+} and Ti^{4+} and Zr^{3+} and Zr^{4+} ions. Due to the composite multiferroics' low internal resistance, transferring electrons in the midst of Fe^{2+} and Fe^{3+}, Ti^{3+} and Ti^{4+} and Zr^{3+} and Zr^{4+} ions will need less energy due to easier electron movement within the composite multiferroics. Table 4.36-4.39 lists the values of $tan\delta_\varepsilon$ for a selection of frequencies and T_s. The $tan\delta_\varepsilon$ value diminishes against frequency on a frequency-dependent trend in the midst of 1373 K and 1423 K. Tan at 1473 K revealed a maximum for NCZFO in the midst of 1 and 100 kHz (y = 1.0). The $tan\delta_\varepsilon$ value exhibited a maximum in all composite multiferroics in the midst of 10 kHz and 1 MHz at 1523 K. When the frequency of jumping of the electron interchange amongst Fe^{2+} and Fe^{3+}, Ti^{3+} and Ti^{4+} and Zr^{3+} and Zr^{4+} approaches the applied frequency [346], a maximum is seen in the $tan\delta_\varepsilon$ spectrum. The grain-grain border

contribution, which accounts for the peak's appearance, may be explained by the resonance of the domain wall, which, in accordance with the Debye relaxation theory [240, 386], corresponds to the equation below: $\omega_{max}\tau = 1$, where $\omega_{max} = 2\pi f_{max}$ denotes the angular frequency and τ stands for the relaxation period of time, that relates the jumping chance per unit time. The oscillating ions get the most energy during this process, and the value of $tan\delta_{\varepsilon}$ increases at resonant frequency [386]. When the NCZFO concentration is increased, the peak at 1523 K is shown to shift toward the higher frequencies, indicating that composite multiferroics containing the ion pairs Fe^{2+}/Fe^{3+}, Ti^{3+}/Ti^{4+}, and Zr^{3+}/Zr^{4+} would relax more quickly. When the relaxation period is longer than the applied field's fluctuation duration (high-frequency zone), the $tan\delta_{\varepsilon}$ value would be minimal, and vice versa [368]. With rising T_s and NCZFO concentration, respectively, the degree of $tan\delta_{\varepsilon}$ is shown to grow.

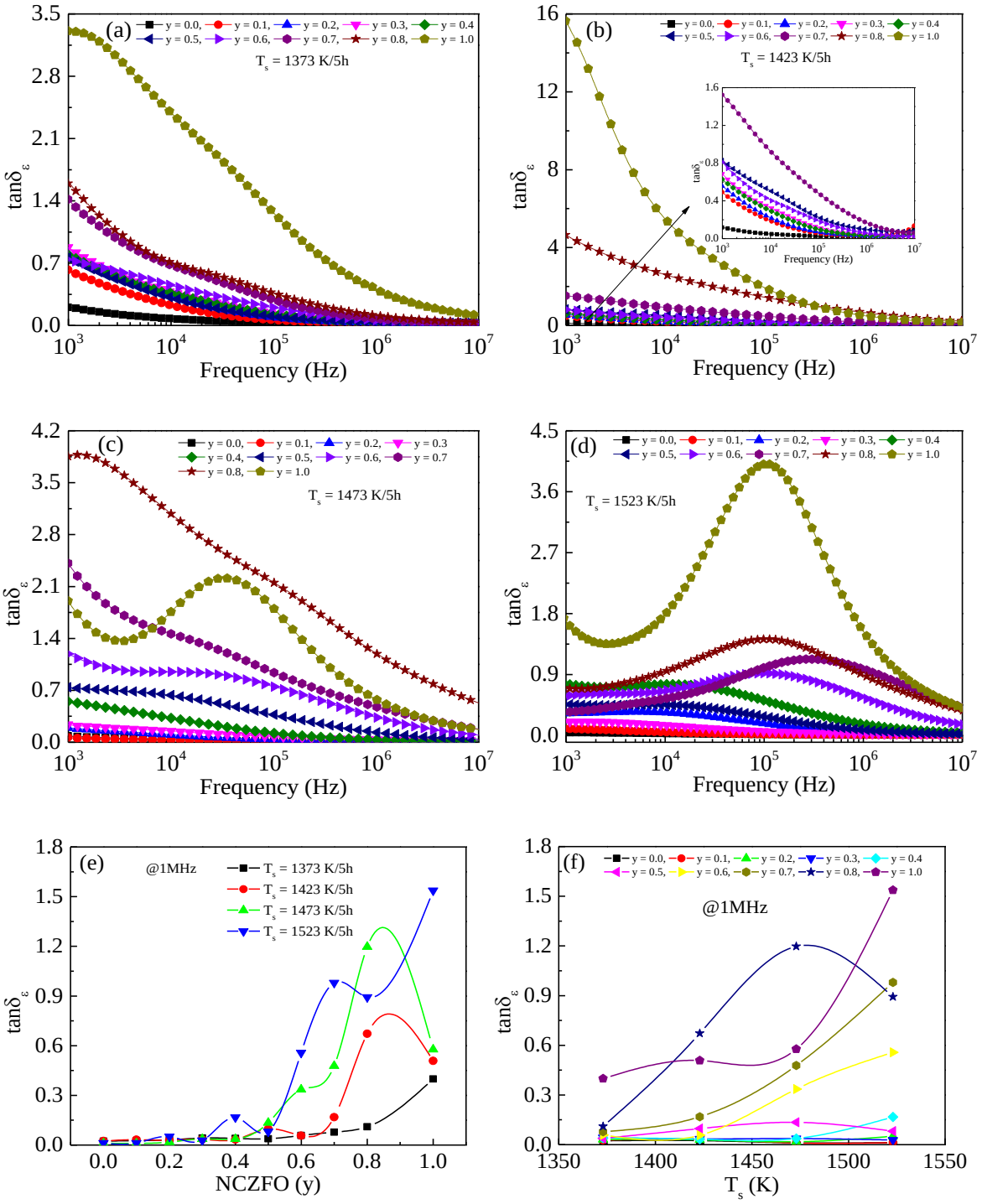

Figure 4.35: Evolution of permittivity loss tangent ($tan\delta_\varepsilon$) with frequency of (1-*y*) [BCZTO] + (*y*) [NCZFO] (*y* = 0-1.0) composite multiferroics annealed for 5 h at (a) 1373, (b) 1423, (c) 1473 and, (d) 1523 K, and (e, f) shows composition and T_s dependent $tan\delta_\varepsilon$ value at 1MHz.

Table 4.36. Electric permittivity (ε'), permittivity loss tangent ($tan\delta_\varepsilon$), and ac conductivity (σ_{ac}) of (1-*y*) [BCZTO] + (*y*) [NCZFO] composite multiferroics annealed at 1373 K.

T_s (K)	Composition	ε' at				$tan\delta_\varepsilon$ at				σ_{ac} ($\Omega^{-1}m^{-1}$)			
	(y)	10kHz	100kHz	1MHz	10MHz	10kHz	100kHz	1MHz	10MHz	10kHz	100kHz	1MHz	10MHz
1373	0	626	590	572	659	0.08	0.03	0.02	0.04	2.63×10^{-5}	1.09×10^{-4}	7.34×10^{-4}	1.43×10^{-2}
	0.1	314	277	266	280	0.23	0.06	0.03	0.03	3.98×10^{-5}	9.75×10^{-5}	3.94×10^{-4}	4.35×10^{-3}
	0.2	269	221	210	216	0.33	0.09	0.03	0.03	5.03×10^{-5}	1.18×10^{-4}	3.67×10^{-4}	3.33×10^{-3}
	0.3	127	97	89	89	0.38	0.14	0.04	0.03	2.68×10^{-5}	7.37×10^{-5}	2.09×10^{-4}	1.33×10^{-3}
	0.4	194	151	141	144	0.37	0.12	0.04	0.03	4.00×10^{-5}	1.06×10^{-4}	3.11×10^{-4}	2.37×10^{-3}
	0.5	120	98	92	92	0.31	0.10	0.04	0.03	2.09×10^{-5}	5.64×10^{-5}	1.93×10^{-4}	1.45×10^{-3}
	0.6	113	79	69	69	0.45	0.19	0.06	0.01	2.92×10^{-5}	9.06×10^{-5}	2.25×10^{-4}	5.34×10^{-4}
	0.7	83	50	42	41	0.68	0.29	0.08	0.03	3.13×10^{-5}	8.07×10^{-5}	1.85×10^{-4}	6.74×10^{-4}
	0.8	73	41	32	31	0.71	0.36	0.11	0.03	2.86×10^{-5}	8.20×10^{-5}	1.99×10^{-4}	6.05×10^{-4}
	1.0	171	54	32	27	2.39	1.26	0.40	0.11	2.27×10^{-4}	3.83×10^{-4}	7.09×10^{-4}	1.69×10^{-3}

Table 4.37. Electric permittivity (ε'), permittivity loss tangent ($tan\delta_\varepsilon$), and ac conductivity (σ_{ac}) of (1-*y*) [BCZTO] + (*y*) [NCZFO] composite multiferroics annealed at 1423 K.

T_s (K)	Composition	ε' at				$tan\delta_\varepsilon$ at				σ_{ac} ($\Omega^{-1}m^{-1}$)			
	(y)	10kHz	100kHz	1MHz	10MHz	10kHz	100kHz	1MHz	10MHz	10kHz	100kHz	1MHz	10MHz
1423	0	463	441	427	404	0.05	0.03	0.02	0.12	1.27×10^{-5}	6.89×10^{-5}	5.81×10^{-4}	2.75×10^{-2}
	0.1	237	210	202	191	0.19	0.06	0.03	0.14	2.48×10^{-5}	6.86×10^{-5}	3.66×10^{-4}	1.53×10^{-2}
	0.2	182	158	151	147	0.22	0.07	0.03	0.07	2.25×10^{-5}	6.24×10^{-5}	2.43×10^{-4}	5.39×10^{-3}
	0.3	98.3	76.7	71.8	69.6	0.33	0.12	0.03	0.03	1.80×10^{-5}	5.03×10^{-5}	1.38×10^{-4}	1.27×10^{-3}
	0.4	152	124	117	113	0.29	0.10	0.03	0.05	2.51×10^{-5}	6.84×10^{-5}	2.20×10^{-4}	3.35×10^{-3}
	0.5	142	93.5	79.6	71.8	0.51	0.23	0.10	0.08	4.03×10^{-5}	1.19×10^{-5}	4.32×10^{-5}	3.33×10^{-3}
	0.6	70.7	49.8	44.1	42.6	0.41	0.18	0.06	0.03	1.62×10^{-5}	5.17×10^{-5}	1.41×10^{-4}	7.37×10^{-4}
	0.7	180	90.8	65.8	60	0.93	0.48	0.17	0.06	9.32×10^{-5}	2.45×10^{-4}	6.19×10^{-4}	2.11×10^{-3}
	0.8	434	133	59.8	41.5	2.61	1.45	0.67	0.22	6.31×10^{-4}	1.09×10^{-3}	2.25×10^{-3}	5.14×10^{-3}
	1.0	140	51.4	31.2	25.7	5.46	1.94	0.51	0.13	4.28×10^{-4}	5.61×10^{-4}	8.88×10^{-4}	1.94×10^{-3}

Table 4.38. Electric permittivity (ε'), permittivity loss tangent ($tan\delta_\varepsilon$), and ac conductivity (σ_{ac}) of (1-*y*) [BCZTO] + (*y*) [NCZFO] composite multiferroics annealed at 1473 K.

T_s (K)	Composition	ε' at				$tan\delta_\varepsilon$ at				σ_{ac} ($\Omega^{-1}m^{-1}$)			
	(y)	10kHz	100kHz	1MHz	10MHz	10kHz	100kHz	1MHz	10MHz	10kHz	100kHz	1MHz	10MHz
1473	0	228	221	218	228	0.04	0.02	0.01	0.02	4.76×10^{-6}	2.04×10^{-5}	1.41×10^{-4}	2.08×10^{-3}
	0.1	378	367	362	392	0.03	0.01	0.01	0.02	6.37×10^{-6}	2.84×10^{-5}	1.93×10^{-4}	4.58×10^{-3}
	0.2	257	237	230	243	0.10	0.04	0.02	0.02	1.46×10^{-5}	5.07×10^{-5}	2.26×10^{-4}	2.45×10^{-3}
	0.3	147	127	119	118	0.15	0.07	0.04	0.03	1.24×10^{-5}	5.23×10^{-5}	2.45×10^{-4}	1.74×10^{-3}
	0.4	274	212	197	118	0.32	0.12	0.04	0.02	4.96×10^{-5}	1.47×10^{-4}	4.05×10^{-4}	2.54×10^{-3}
	0.5	345	186	142	137	0.63	0.37	0.13	0.04	1.22×10^{-4}	3.90×10^{-4}	1.07×10^{-3}	3.27×10^{-3}
	0.6	639	231	131	115	0.95	0.75	0.34	0.10	3.38×10^{-4}	9.74×10^{-4}	2.46×10^{-3}	6.22×10^{-3}
	0.7	481	165	85	62.3	1.46	0.94	0.48	0.18	3.92×10^{-4}	8.74×10^{-4}	2.27×10^{-3}	6.26×10^{-3}
	0.8	1350	310	101	51.3	3.08	2.15	1.20	0.53	2.31×10^{-3}	3.76×10^{-3}	6.77×10^{-3}	1.53×10^{-2}
	1.0	376	62	32.5	25.2	1.76	1.80	0.58	0.17	3.69×10^{-4}	6.28×10^{-4}	1.05×10^{-3}	2.42×10^{-3}

Table 4.39. Electric permittivity (ε'), permittivity loss tangent ($tan\delta_\varepsilon$), and ac conductivity (σ_{ac}) of (1-*y*) [BCZTO] + (*y*) [NCZFO] composite multiferroics annealed at 1523 K.

T_s (K)	Composition	ε' at				$tan\delta_\varepsilon$ at				σ_{ac} ($\Omega^{-1}m^{-1}$)			
	(y)	10kHz	100kHz	1MHz	10MHz	10kHz	100kHz	1MHz	10MHz	10kHz	100kHz	1MHz	10MHz
1523	0	397	385	378	423	0.03	0.02	0.01	0.01	6.72×10^{-6}	3.69×10^{-5}	2.51×10^{-4}	3.40×10^{-3}
	0.1	447	429	421	473	0.05	0.02	0.01	0.01	1.29×10^{-5}	5.03×10^{-5}	2.88×10^{-4}	3.56×10^{-3}
	0.2	630	436	391	444	0.34	0.17	0.05	0.03	1.24×10^{-4}	4.48×10^{-4}	1.11×10^{-3}	6.54×10^{-3}
	0.3	352	307	293	319	0.15	0.06	0.03	0.03	3.07×10^{-5}	1.11×10^{-4}	4.65×10^{-4}	5.86×10^{-3}
	0.4	307	134	96	92.7	0.75	0.51	0.17	0.04	1.33×10^{-4}	4.01×10^{-4}	9.00×10^{-4}	2.05×10^{-3}
	0.5	271	161	134	135	0.45	0.28	0.08	0.02	7.11×10^{-5}	2.60×10^{-4}	6.12×10^{-4}	1.78×10^{-3}
	0.6	1150	359	152	117	0.67	0.92	0.56	0.16	4.42×10^{-4}	1.94×10^{-3}	4.74×10^{-3}	1.07×10^{-2}
	0.7	1870	582	163	88	0.55	1.01	0.98	0.41	5.93×10^{-4}	3.47×10^{-3}	8.94×10^{-3}	2.06×10^{-2}
	0.8	1030	209	71	41	0.95	1.42	0.89	0.37	5.67×10^{-4}	1.75×10^{-3}	3.55×10^{-3}	8.66×10^{-3}
	1.0	1420	105	36	24	1.81	4.01	1.54	0.41	1.48×10^{-3}	2.48×10^{-3}	3.08×10^{-3}	5.49×10^{-3}

4.3.5. Electrical conductivity analysis

Figure 4.36 shows how the ac conductivity (σ_{ac}) evolves with respect to frequency of (1-*y*) [BCZTO] + (*y*) [NCZFO] composite multiferroics annealed at: (a) 1373, (b) 1423, (c) 1473, and (d) 1523 K. It is evident from Figure 4.36 (a-d) that the σ_{ac} spectrum distinguishes in the midst of two regions: (i) the plateau region at the lower ferquencies, and (ii) the dispersion zone at the higher frequencies. In the first region, the value of σ_{ac} is essentially constant, but in the second zone, it is substantially frequency dependent. The bulk conductivity, which developed because of the the charge carrier's movement, is often attributed to the plateau area and is connected with the direct current conductivity (σ_{dc}) [387]. The linear increase in frequency that is seen in the dispersion area is attributed to the improvement of the mobile charge carriers. The jumping frequency is demonstrated to move toward higher frequencies as NCZFO content and T_s rise [346], is the frequency that the dispersion of σ_{ac} is expected to take place. The observed properties of σ_{ac} follow Jonscher' power law, which is expressed as: $\sigma_{ac}(\omega = 2\pi f) = \sigma_{dc}(\omega = 2\pi f = 0) + A(2\pi f)^n$, where n $(0 < n < 1)$ is a temperature-dependent exponent that describes how migrating ions interplay with the neighboring lattice [316]. The Verwey-De Boer [388] process, which involves the electron exchange in the midst of the same element's ions that are dispersed randomly throughout the corresponding crystallographic lattice sites, may be used to interpret the conduction process. The hole amongst Ni^{3+} and Ni^{2+} (according to $Ni^{3+} \leftrightarrow Ni^{2+} + e^+$ (hole)), Cu^{2+} and Cu^{1+} (according to $Cu^{2+} \leftrightarrow Cu^{1+} + e^+$ (hole)), Zn^{3+} and Zn^{2+} (according to $Zn^{3+} \leftrightarrow Zn^{2+} + e^+$ (hole)), Ba^{3+} and Ba^{2+} (according to $Ba^{3+} \leftrightarrow Ba^{2+} + e^+$ (hole)) and Ca^{3+} and Ca^{2+} (according to $Ca^{3+} \leftrightarrow Ca^{2+} + e^+$ (hole)) are in charge of the p-type charge carriers and the transfer of electrons amongst Fe^{2+} and Fe^{3+} (according to $Fe^{2+} \leftrightarrow Fe^{3+} + e^-$ (electron)), Ti^{3+} and Ti^{4+} (according to $Ti^{3+} \leftrightarrow Ti^{4+} + e^-$ (electron)) and Zr^{3+} and Zr^{4+} (according to $Zr^{3+} \leftrightarrow Zr^{4+} + e^-$ (electron)) is in charge of the n-type charge carriers, which are in charge of conduction of electricity. It is evident that when T_s and NCZFO

content rises, the value of σ_{ac} is shown to grow as well. The improvement in σ_{ac} on rising T_s may be explained as follows: on raising T_s, the porosity reduces, enabling the component grains to look like they are touching one another, while the mean grain diameter grows, acting as a source to reduce the grain border. Due to these two reasons, the composite multiferroics' overall resistance decreases as their cross-sectional area increases. Additionally, it is discovered that when T_s increases, the quantity of Fe^{2+} ions increase, facilitating hopping-type conduction in the midst of Fe^{2+} and Fe^{3+}, Ti^{3+} and Ti^{4+} and Zr^{3+} and Zr^{4+}. It is widely recognized that the process of conduction happens to be carried out by two distinct kinds of polarons, small polaron and large polaron. When the electrical conductivity starts to decrease as one increases frequency, the big polaron hypothesis is favored; however, the small polaron concept is acceptable when the conductivity seems to go up linearly against frequency rise [389] as evidenced in Fig. 4.37. Table 4.36-4.39 lists the values of σ_{ac} for various T_s and specific frequencies.

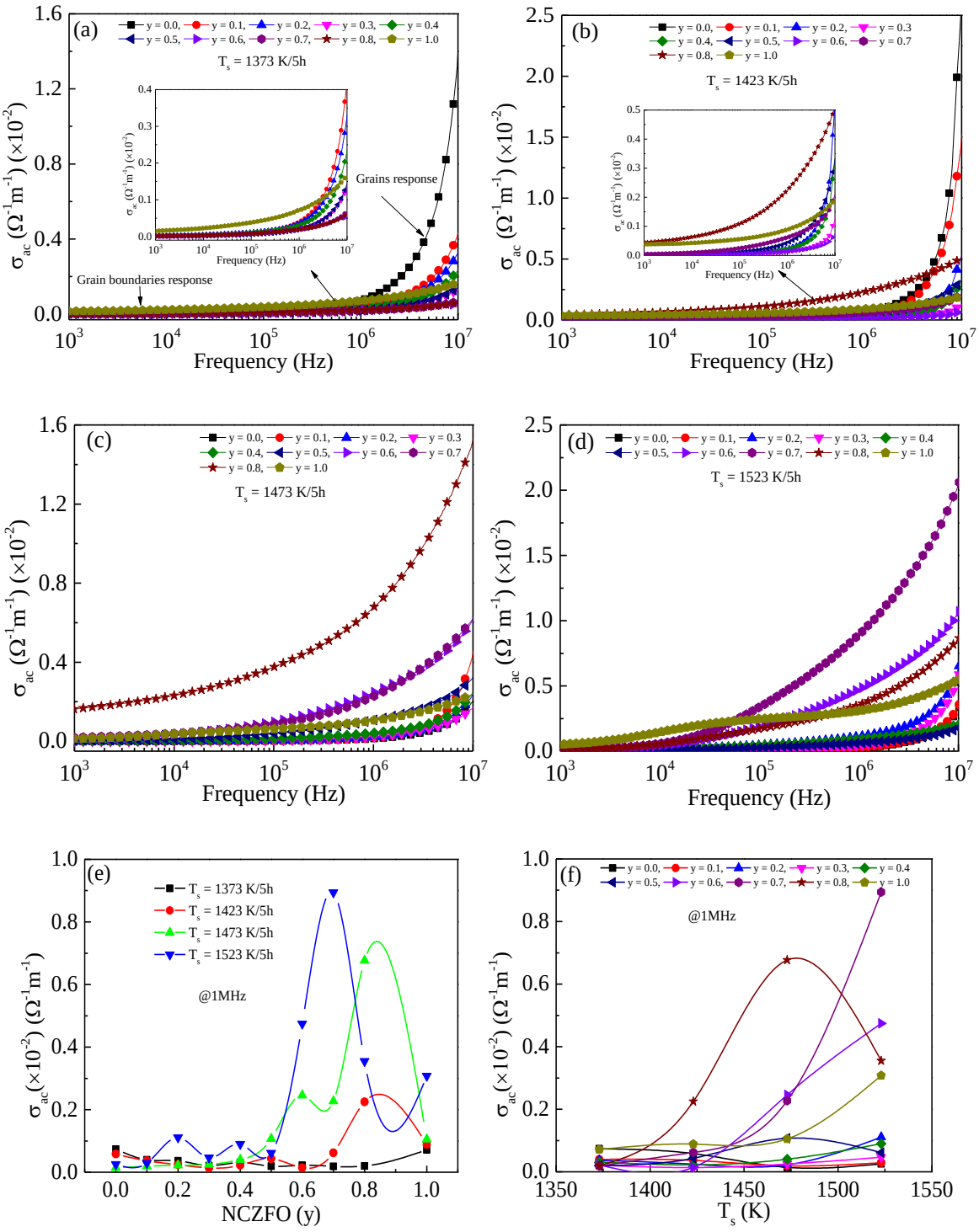

Figure 4.36: Evoluation of the ac conductivity (σ_{ac}) with frequency of (1-*y*) [BCZTO] + (*y*)[NCZFO] (*y* = 0-1.0) composite multiferroics annealed for 5 h at (a)1373, (b) 1423, (c) 1473 and, (d) 1523 K, and (e, f) shows composition and T_s dependent σ_{ac} at 1MHz.

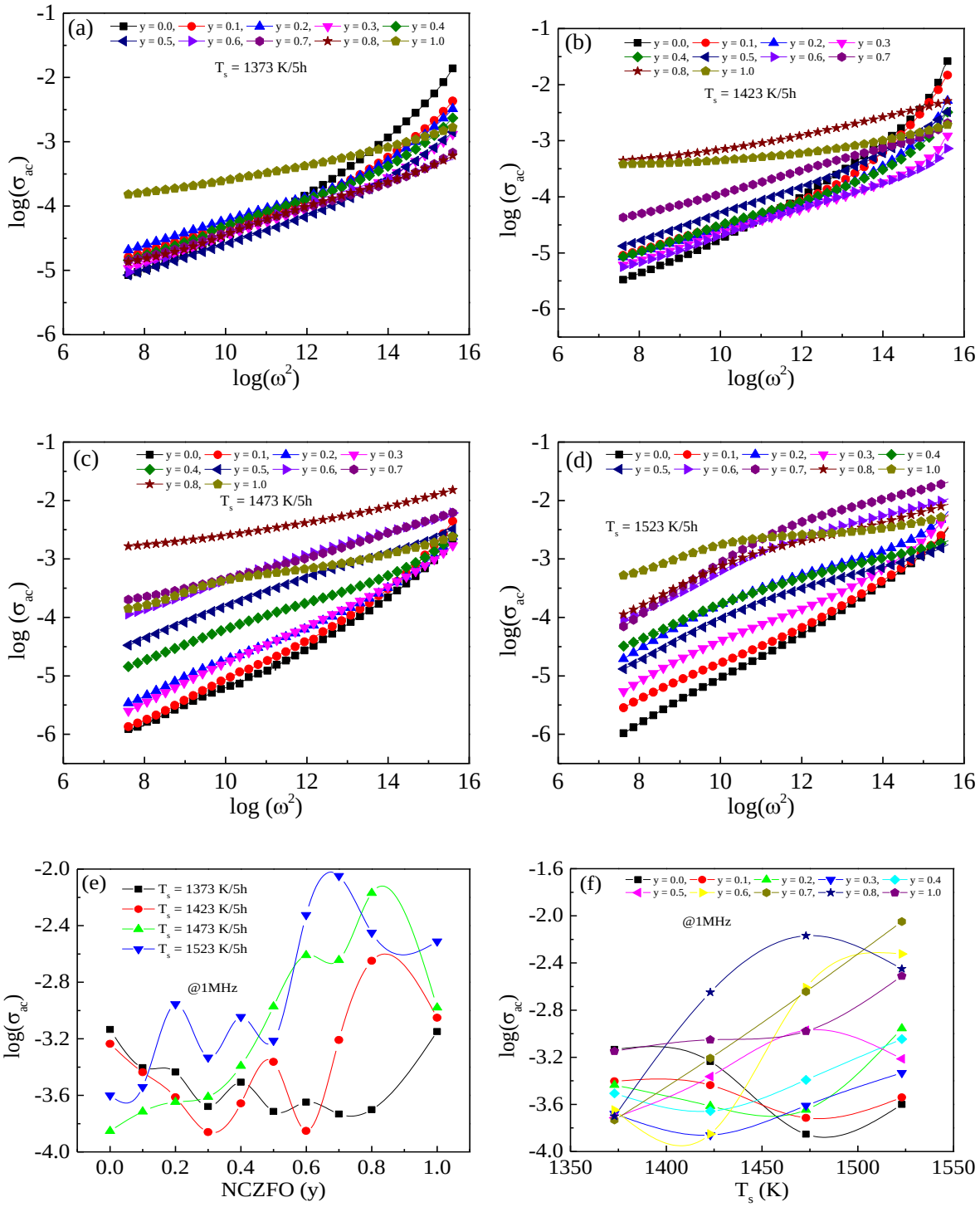

Figure 4.37: Evolution of the ac conductivity (σ_{ac}) with angular frequency of (1-*y*) [BCZTO] + (*y*) [NCZFO] (where *y* = 0-1.0) composite multiferroics annealed for 5 h at (a) 1373, (b) 1423, (c) 1473 and, (d) 1523 K, and (e, f) shows composition and T_s dependent σ_{ac} at 1MHz.

4.3.6. Impedance spectroscopic analysis

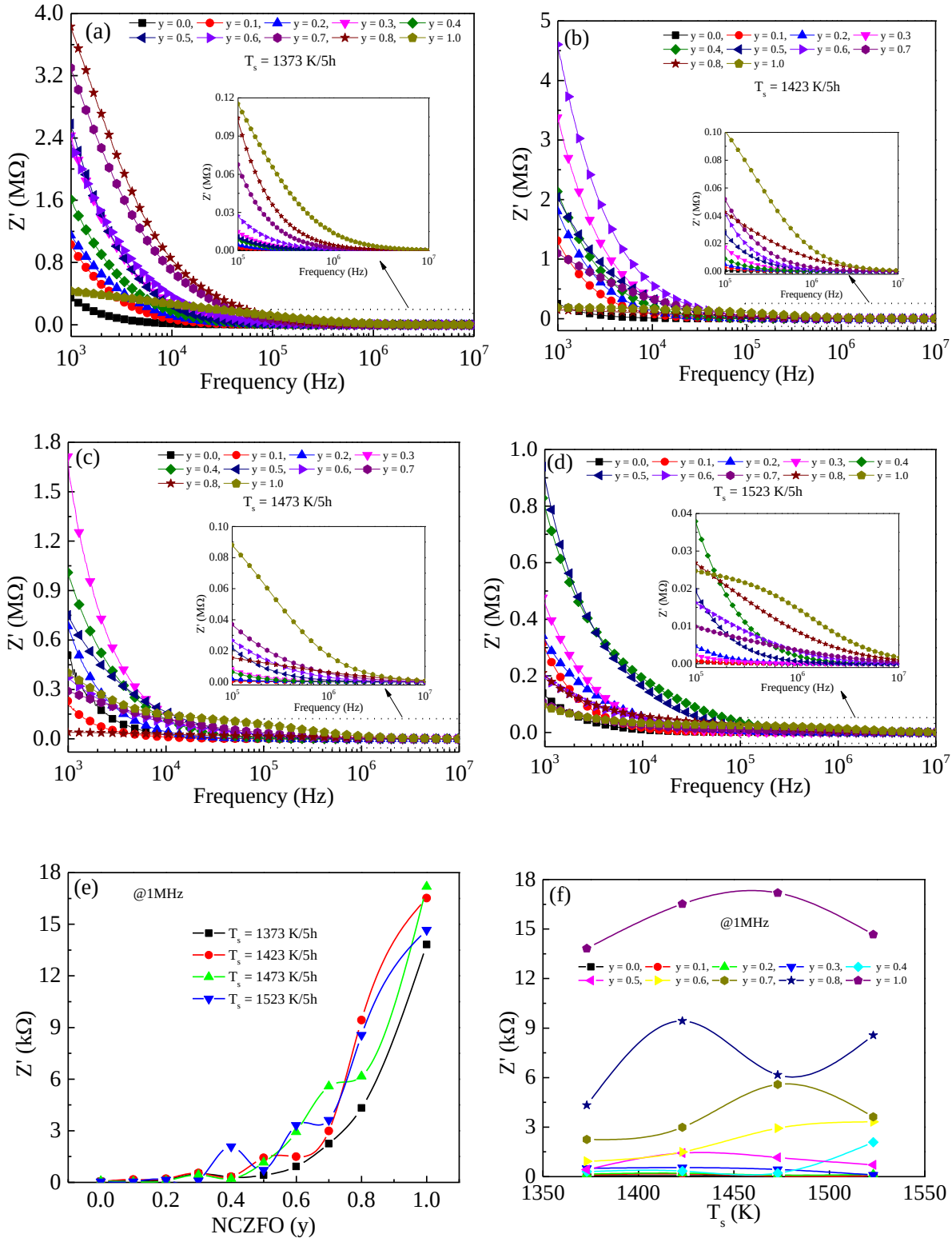

Figure 4.38: Evolution of the real component (Z') of impedance with frequency of (1-y) [BCZTO] + (y) [NCZFO] (y = 0-1.0) composite multiferroics annealed for 5 h at (a) 1373, (b) 1423, (c) 1473 and, (d) 1523 K, and (e, f) shows composition and T_s denpendent Z' at 1MHz.

Figure 4.38 shows how the real component (Z') of impedance depends on frequency for pristine BCZTO, NCZFO phases and (1-*y*) [BCZTO] + (*y*) [NCZFO] **(**where y = 0.1-0.8) composite multiferroics annealed at: (a) 1373, (b) 1423, (c) 1473 and, (d) 1523 K. The Z' value, which counts the space charge polarization at the intersection due to differences in permittivity, is high at low applied frequency windows, debilitates continuously to a maximum of a certain frequency, and bunches up at high applied frequency windows regardless of the NCZFO content. The rise in σ_{ac} value is supported by the falling Z' characteristic that descends more often [390, 391]. The fact that the formed charge carriers near the phase borders have enough energy to overcome the barrier is what is responsible for the increase in σ_{ac} value with the decrease in impedance [392]. The bunching togetherness property of Z' at a high frequency regime can be connected to the release of the space charges that have collected at the interface and the ensuing reduction of the potential barrier [393]. Additionally, the quantity of NCZFO affects how frequently space charges are released. The frequency at which Z' values cluster together and become frequency independent is shown to evolve toward a higher frequency with increasing NCZFO concentration, illuminating the potential of a frequency relaxation process [394]. Recombination occurs more quickly in a high-frequency window because the space charges have less time to relax. The composition- and sintering-dependent Z' value at a certain frequency of 1 MHz is delineated in Figure 4.38 (e, f). Figure 4.38 (e) delineates how the Z' value increases as the NCZFO concentration rises. Furthermore, the Z' value rose with T_s, as seen in Fig. 4.38 (f). Fig. 4.39 shows how the imaginary component (Z'') of impedance, which is connected to capacitance ($Z'' = 1/j\omega C$) at various T_s: (a) 1373, (b) 1423, (c) 1473, and (d) 1523 K. It is clear from the frequency domain that as the frequency rises, the Z'' value drops, supporting the claim that this also accounts for the rise in σ_{ac} value. The pure NCZFO and the x = 0.8 composite show relaxation in the low-frequency window at 1373 K. If there is no peak, it is possible that the peak is there but at a very low frequency window. The following

equation describes the genesis of a Debye peak: $Z'' = R[\omega RC/(1 + \omega RC^2)]$, where C represents the composite's capacitance in air, and electrodes with an air gap are utilized in its stead, and ω is the angular frequency. The formula $Z''(f) = R_{bulk}[\omega\tau/(1 + \omega^2\tau^2)]$ clarifies that the peak heights are proportional to the bulk resistance (R_{bulk}). [395]. Due to the stationary relaxation species/electron in the composite, the relaxation process is absent. Figure 4.39 (e, f) shows the composition and T_s dependent Z'' at a specific frequency of 1 MHz, respectively. According to Figure 4.39 (f), the value Z'' shows a declining trend as T_s increases. The value of Z'' rises in proportion to the NCZFO concentration.

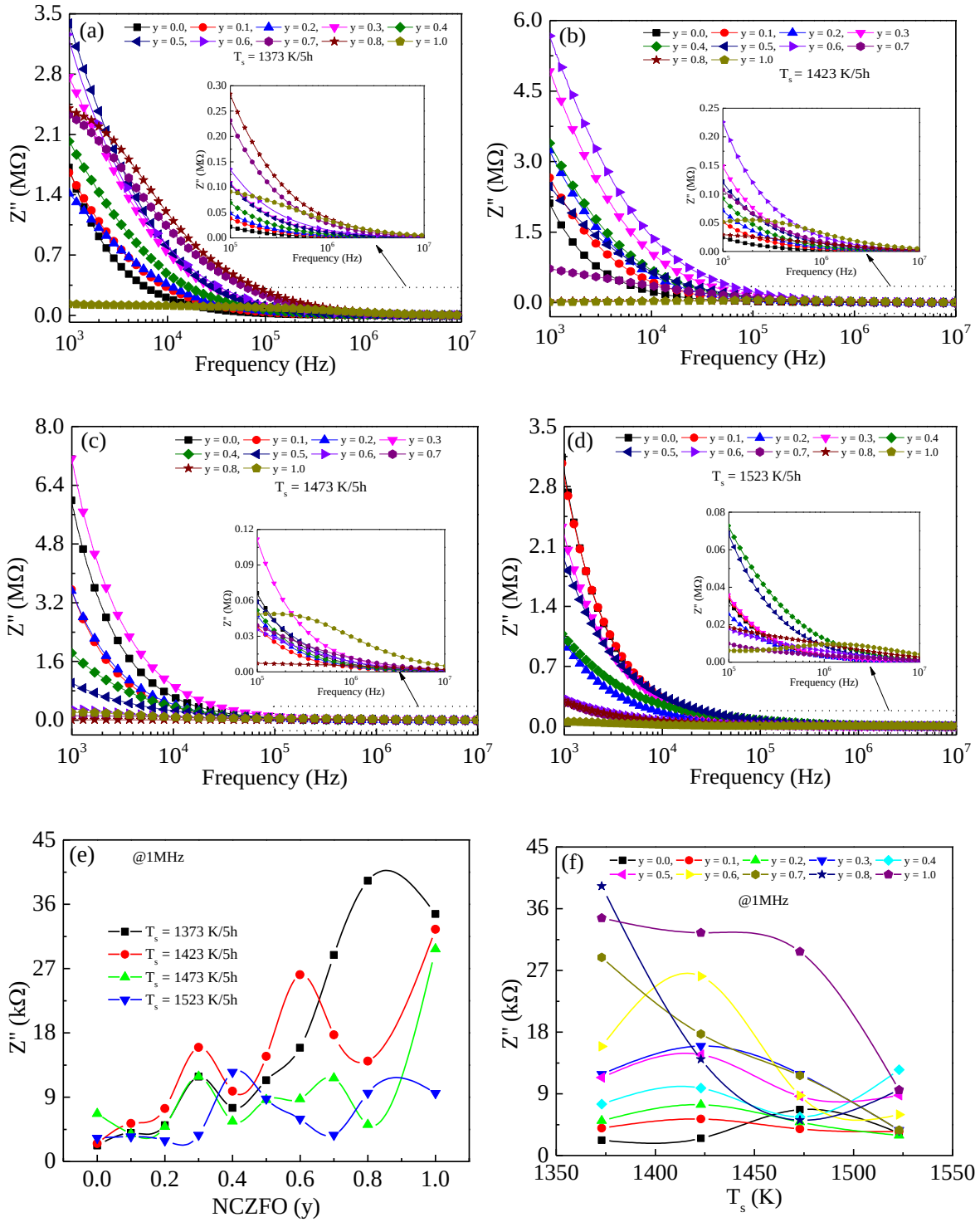

Figure 4.39: Evolution of the imaginary component (Z'') of impedance with frequency of (1-*y*) [BCZTO] + (*y*) [NCZFO] (*y* = 0-1.0) composite multiferroics annealed for 5 h at (a) 1373, (b) 1423, (c) 1473 and, (d) 1523 K, and (e, f) shows composition and T_s dependent Z'' at 1MHz.

4.3.7. Cole-Cole plots

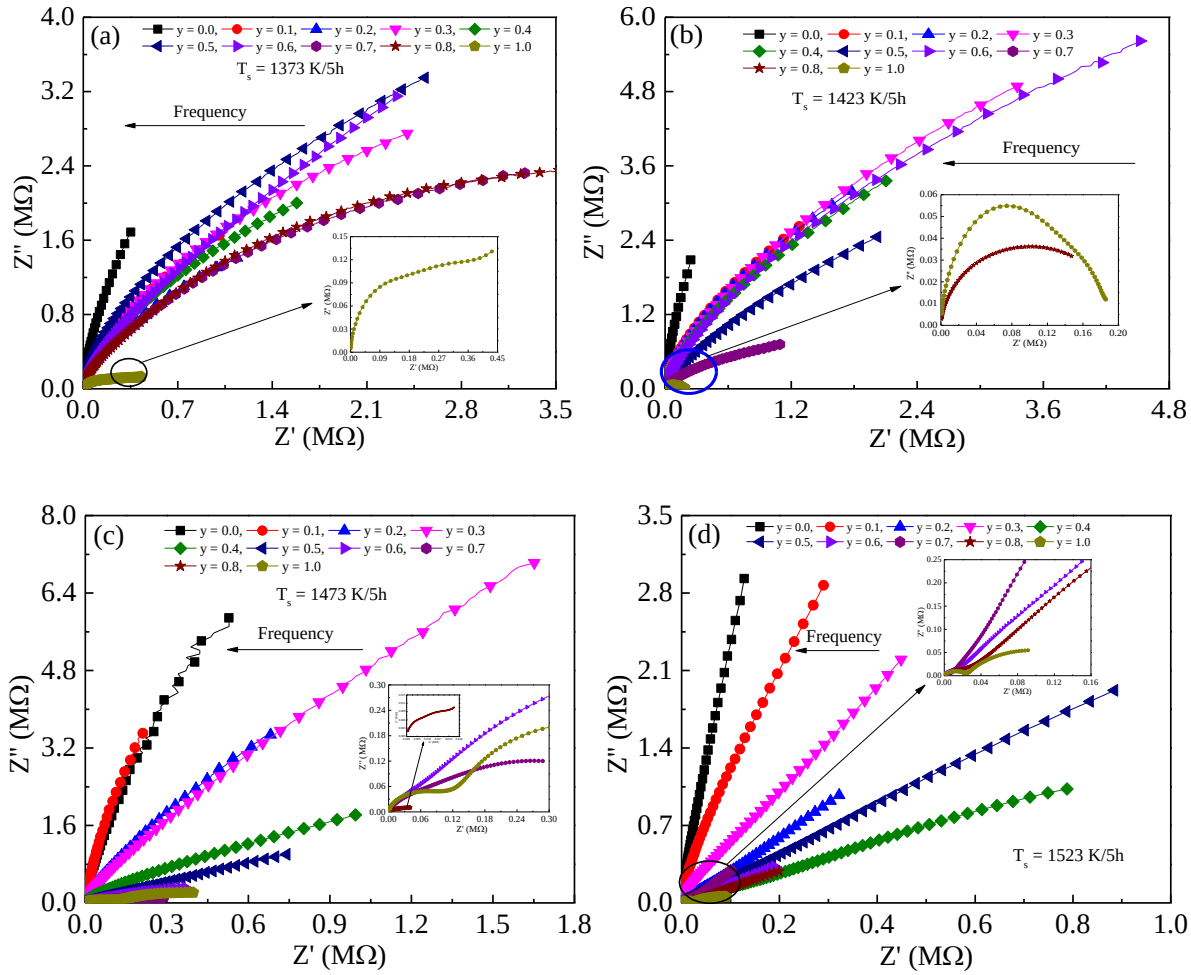

Figure 4.40: Cole-Cole plots of (1-*y*) [BCZTO] + (*y*) [NCZFO] (*y* = 0-1.0) composite multiferroics annealed for 5 h at (a) 1373, (b) 1423, (c) 1473, (d) 1523 K.

Figure 4.40 shows the Cole-Cole curves of (1-*y*) [BCZTO] + (*y*) [NCZFO] composite multiferroics annealed at: (a) 1373, (b) 1423, (c) 1473, and (d) 1523 K. An arrow's movement signifies a frequency enhancement was employed. The Cole-Cole diagram must originally include three successive semicircles that vary based on the electrical characteristics of the substances or the appropriate proportions for their time of relaxation. The initial one, which exists in certain substances at the lowest applied frequency range and correlates to the aggregate of grain and grain border resistance, is associated with a large polarization of the electrode effect. The second kind that could be detected in the intermediate region of the applied

frequency has connections to the resistance-significantly benefiting from the grain border action. A third type emerges obvious, that substantially raises the grain's effect on resistance at higher frequencies. [395]. The alignment of the real Z' axis at its beginning and higher frequencies creates an perfect Debye-kind, in accordance with Debye's hypothesis, that anticipates that uniform substances having only one relaxation duration will create a perfect semicircle where the center is located along the Z' axis [396, 397]. Single semicircular arcs may be seen in the complex impedance spectra, indicating strong dielectric and conductive property homogeneity, and many components can be seen, indicating local heterogeneity [398]. The center of the semicircle beneath the Z' axis, however, represents the distribution of relaxation time in the current research because of the uneven distribution of grains. This distinguishing quality unequivocally states that the non-Debye class relaxing impact is seen [399]. A number of variables, such as grain diameter allocation, grain acclimatization, atomic allocation, grain borders, and others [400], may contribute to the development of the non-ideal feature. At 1423 K, it can be shown that the composite multiferroics display comparable properties and lack the semicircle form in y = 0.0-0.7. Only the high-frequency semicircle is visible in y = 0.8 indicating that the grain resistance is lower and the grain border resistance is outside of the mesurement. Two semicircular arcs, one for the impact of grain and the other for the grain border impact respectively, can be seen in the NCZFO phase at 1473 K. It is discovered that at 1373 K, the composite multiferroics only display a single semicircular arc that elucidate both the bulk and grain border's impacts. There is a propensity for two semicircular arcs to emerge in NCZFO. A single semicircle with a center below the Z' axis is visible in y = 0.8 and NCZFO at 1423 K. The two semicircular arcs are seen around 1473 K for NCZFO. The grain border impsct is attributed with the low frequency arc, whereas the high frequency arc is credited with the grain impact. At 1523 K, the two semicircular arcs are visible in y = 0.8 and NCZFO. A single semicircle is seen in the current system, which solely shows the influence of grains [401]. Plots show that the arc's radius likewise lowers as NCZFO level

varies, indicating that resistance diminishes as NCZFO content rises. The NCZFO phase produces a small amount Ni, Cu, Zn, or Fe ions that interact with the BCZTO lattice, which is what causes the BCZTO phase's falling resistance [402].

4.3.8. Dielectrical modulus spectroscopic analysis

Figure 4.41 shows how the real component of dielectrical modulus (M') with frequency of pure BCZTO and NCZFO phases and (1-*y*) [BCZTO] + (*y*) [NCZFO] **(**where y = 0.1-0.8) composite multiferroics annealed at various T_s: (a) 1373, (b) 1423, (c) 1473 and, (d) 1523 K. It was noticed M' exhibits an increasing character to a maximum of a certain value before becoming practically constant as a result of the relaxing process. The M' variation may be separated into three sections, as shown in this Figure 4.41: (i) at the low-frequency window, the M' values are extremely low (pretty close to zero), claiming that the polarization of the electrodes (dipoles) makes a negligibly small contribution or disproving the existence of the polaron hopping in the composite multiferroics [403, 404]. Insufficiency of the restoration force, which controls how charge carriers advance when an electric field is formed, might potentially account for this phenomenon [405]. As a result of the insufficient restoring force needed to avert the movement of charge carriers while the produced electric field is present, the M' value advances very small at lower frequencies. This pattern supports charge carriers' long-distance movement in the context of a generated electric field. An exponential rise in M' values is seen at intermediate frequencies. At high frequencies, the magnitudes of M' have a propensity to become saturated at the highest asymptotic figure. This might be as a result of charge carriers' short-range mobility while being affected by a generated electric field [236, 406]. Furthermore, a sigmoidal rise in the M' value on rising frequency eventually reaching to infinity may be utilized to describe the conduction phenomena brought on by the short-distance movement of charge carriers (especially ions).

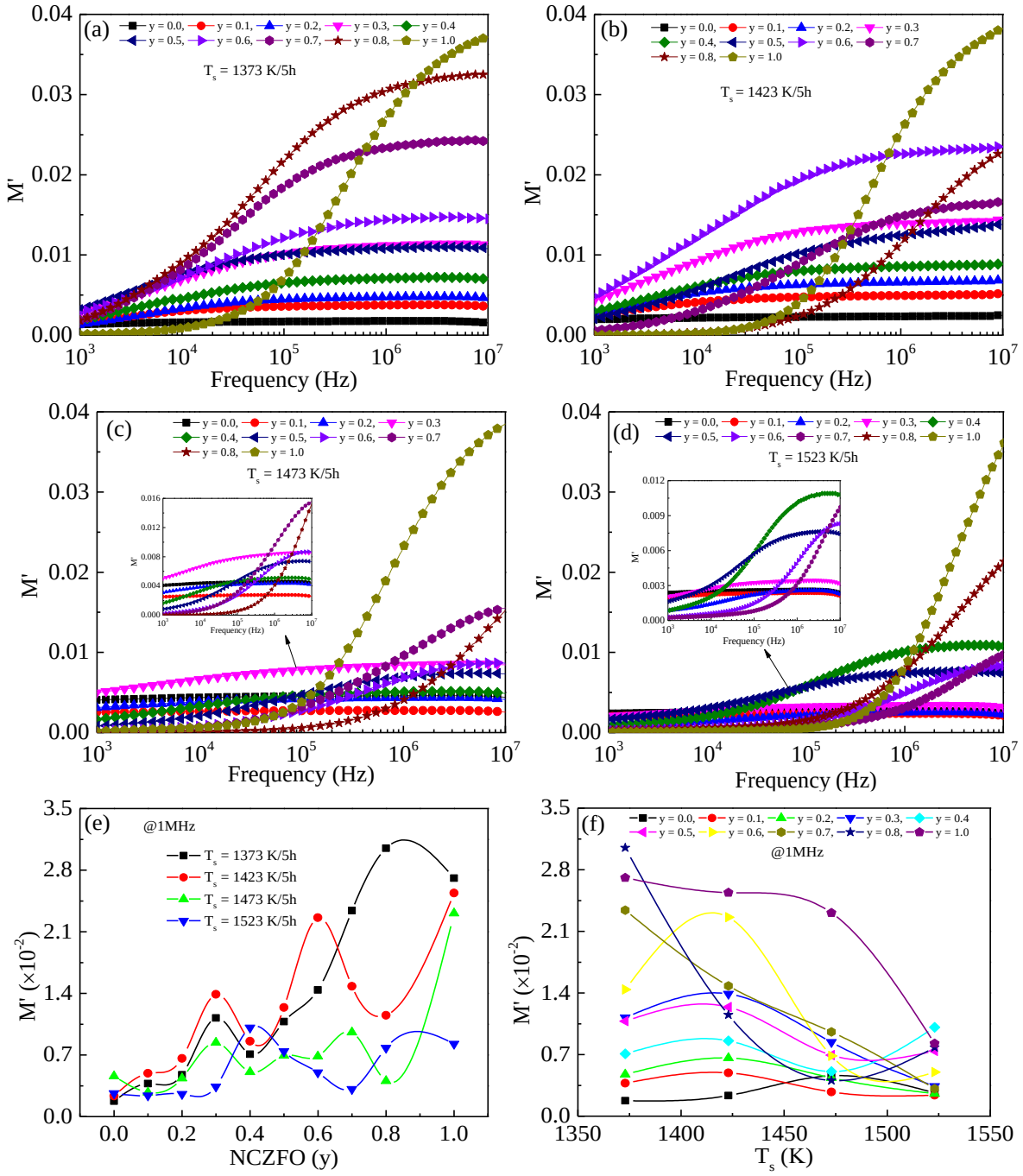

Figure 4.41: Evolution of the real component (M') of dielectrical modulus with frequency of (1-*y*) [BCZTO] + (*y*) [NCZFO] (*y* = 0.0-1.0) composite multiferroics annealed for 5 h at (a) 1373, (b) 1423, (c) 1473 and, (d) 1523 K, and (e, f) shows composition and T_s dependent M' at 1 MHz.

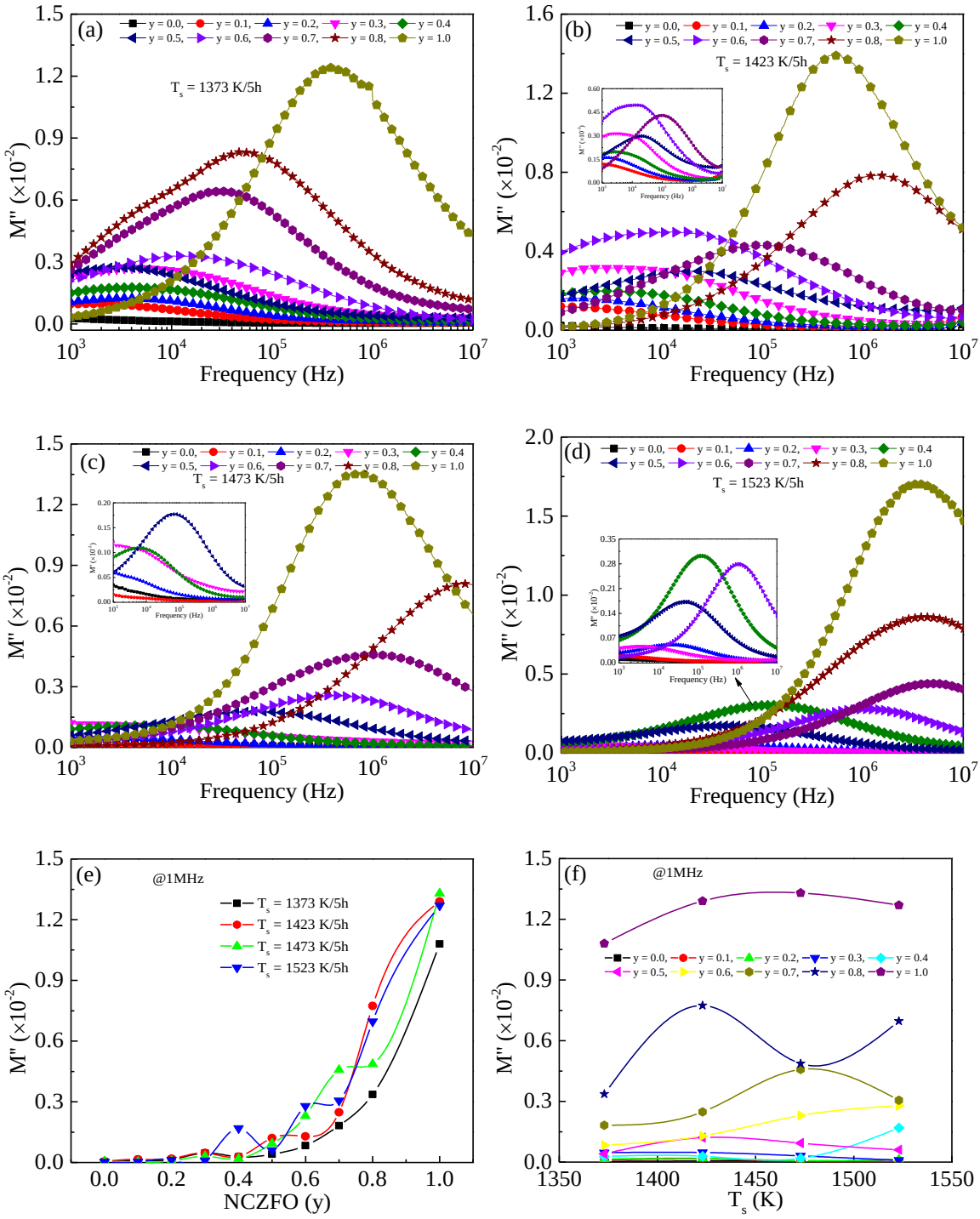

Figure 4.42: Evolution of the imaginary component (M'') of dielectrical modulus with frequency of (1-*y*) [BCZTO] + (*y*) [NCZFO] (*y* = 0.0-1.0) composite multiferroics annealed for 5 h at (a) 1373, (b) 1423, (c) 1473 and, (d) 1523 K, and (e, f) shows composition and T_s dependent M''at 1 MHz.

On escalating NCZFO level, the resonant frequency at which M' shifted from a constant low value to higher values. The fluctuation of M' in relation to the composition of the NCZFO

content and T_s at the chosen frequency are depicted in Figure 4.41(e, f). The M' value was discovered to rise as NCZFO content rose. The fluctuation of M'' for composite multiferroics annealed at (a) 1373, (b) 1423, (c) 1473, and (d) 1523 K is shown in Figure 4.42. For each T_s, it is discernible that M'' displayed traits that were comparable. As a matter of fact, at the beginning, M'' rises with applied frequency till reaching its maximum at relaxation frequency ($f_{M''}^{max}$). The M'' value then starts to decline with an increase in applied frequency. The resonant or relaxation frequency, which distinguishes in the midst of charge carriers moving over long distances and those moving over short distances, produces a relaxation peak at that frequency. When the applied and oscillating dipole frequencies synchronize, the relaxation peak has been reached. The reciprocal of the grain border capacitance and grain capacitance determines the maximum M'' values. In comparison to grain borders, the capacitances of the grains are smaller. As a result, in the M'' spectra, the maximum value associated with the grain is significantly stronger than that of grain border capacitances [407]. Additionally, when the NCZFO concentration increases, the sites of the maximums progressively shift to a higher frequency domain. Such a feature suggests that the rise in NCZFO content is connected to the relaxing process. Additionally, the positioning variation of M''_{max} with NCZFO concentration is connected to the alteration in composite multiferroics' resistivity. The formulas $2\pi f_{max}\tau = 1 \rightarrow \tau = \frac{1}{2\pi f_{max}}$ [408] are used to compute the relaxation time from the greatest peak of M''_{max} at frequency. The shift toward the high-frequency side shortens the relaxing period. The shift from short-range to long-distance mobility is proposed at the peak location (at lower frequency), where ions are free to move locally rather than being restricted to long-distance motion (in the high-frequency area) [409]. In addition, the asymmetric spreading of maximum demonstrates the distribution of relaxing phenomena over various time constants, which tangibly signals the presence of a non-Debye class relaxing tendency [410]. The non-uniform microstructure or the charge carriers' diffusive mobility in composite multiferroics are the

causes of the emergence of the non-Debye type relaxation [411]. The lower frequency regime on the left side of the relaxation peak shows the frequency range for which the conducting charge carriers (polarons) are capable of moving over a long distance, indicating that they can easily perform hopping from one site to a neighboring site and exhibit commensurate dc conductivity. The conducting charge carriers only move locally within their potential wells and remain spatially constrained by them in the higher frequency domain on the right side of the relaxation peak [412], which is comparable with ac conductivity [413]. The relaxation frequency, which is the complimentary frequency to the relaxation peak, corresponds to the change from dc to ac in the electrical conduction process. The increase in dc conductivity caused by the maximum M'' peak shifting into higher frequency areas as the NCZFO rises is consistent with the theory's prediction that the maximum M'' peak is travelling in that direction: In the formula, $\sigma_{dc} = \frac{\varepsilon_0}{M_\infty \tau}$, where ε_0 denotes the permittivity in air, M_∞ denotes the inverse of the high-frequency permittivity, and τ denotes the relaxation time [414]. However, as NCZFO content increases, the relaxation peak's intensity increases and it shifts to higher frequencies. This phenomenon may be explained by the increased interfacial region that results from adding more NCZFO content, which facilitates the movement and accumulation of free charges at the interface region and maintains the frequency change. Additionally, when NCZFO concentration rises, the relaxation peak of the composite multiferroics broadens. These relaxation patterns suggest that adding NCZFO material to the composite strengthens the interfacial polarization [415]. Figure 4.43 displays the Cole-Cole curves for the composite multiferroics annealed at various T_s: (a) 1373, (b) 1423, (c) 1473, and (d) 1523 K. This figure illustrates the presence of a single semicircle with a different radius, which confirms the grain's predominant contribution. Their centers of semicircles lying below the real axis show the spread of relaxation with various time constants. A jump mechanism for electrical conduction and non-Debye dielectric relaxation in the system is therefore suggested by the

characteristics of the dielectrical modulus spectra. It is evident that when the NCZFO quantity rises, the curve regions get larger.

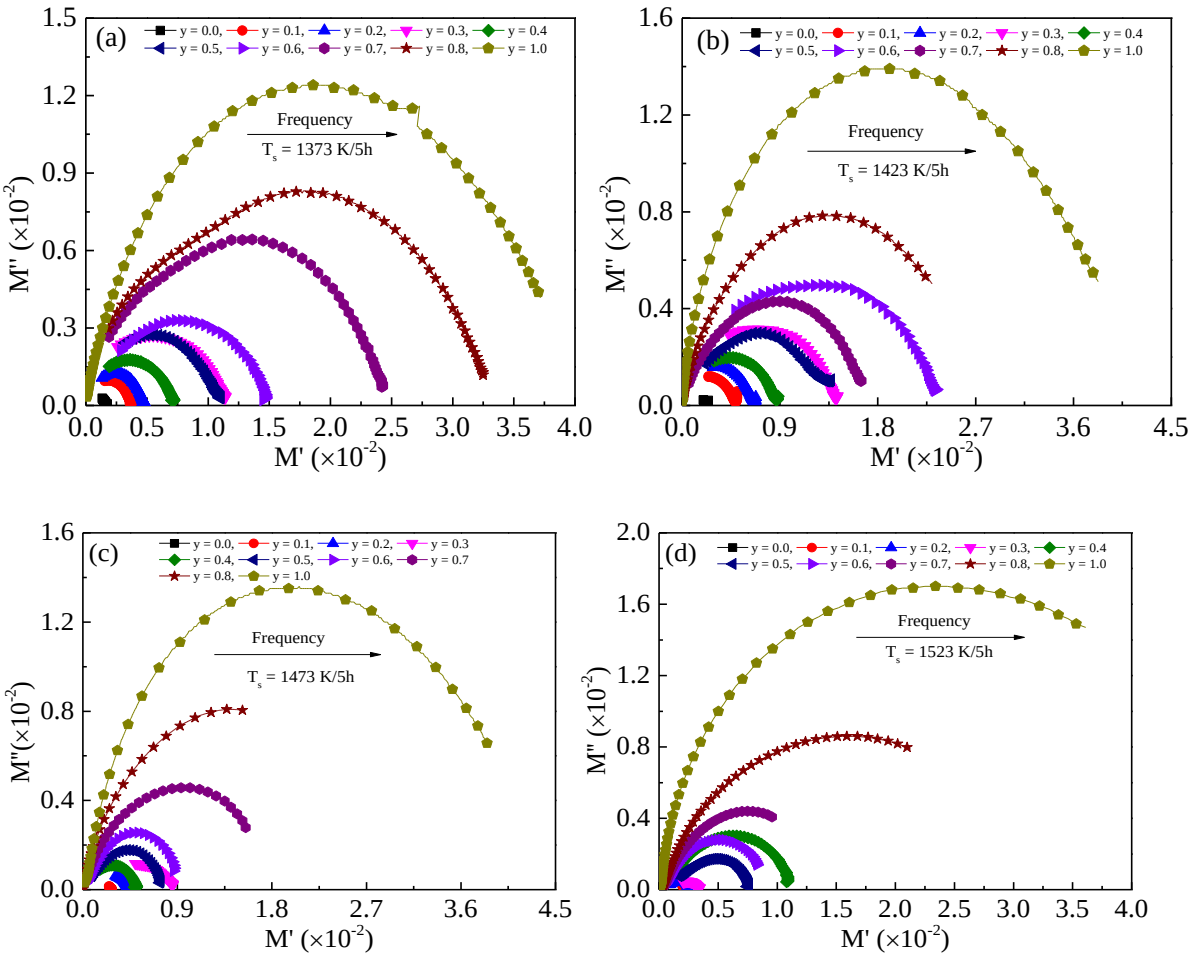

Figure 4.43: Cole-Cole plots of (1-*y*) [BCZTO] + (*y*) [NCZFO] (*y* = 0.0-1.0) composite multiferroics annealed for 5 h at: (a) 1373, (b) 1423, (c) 1473 and, (d) 1523 K.

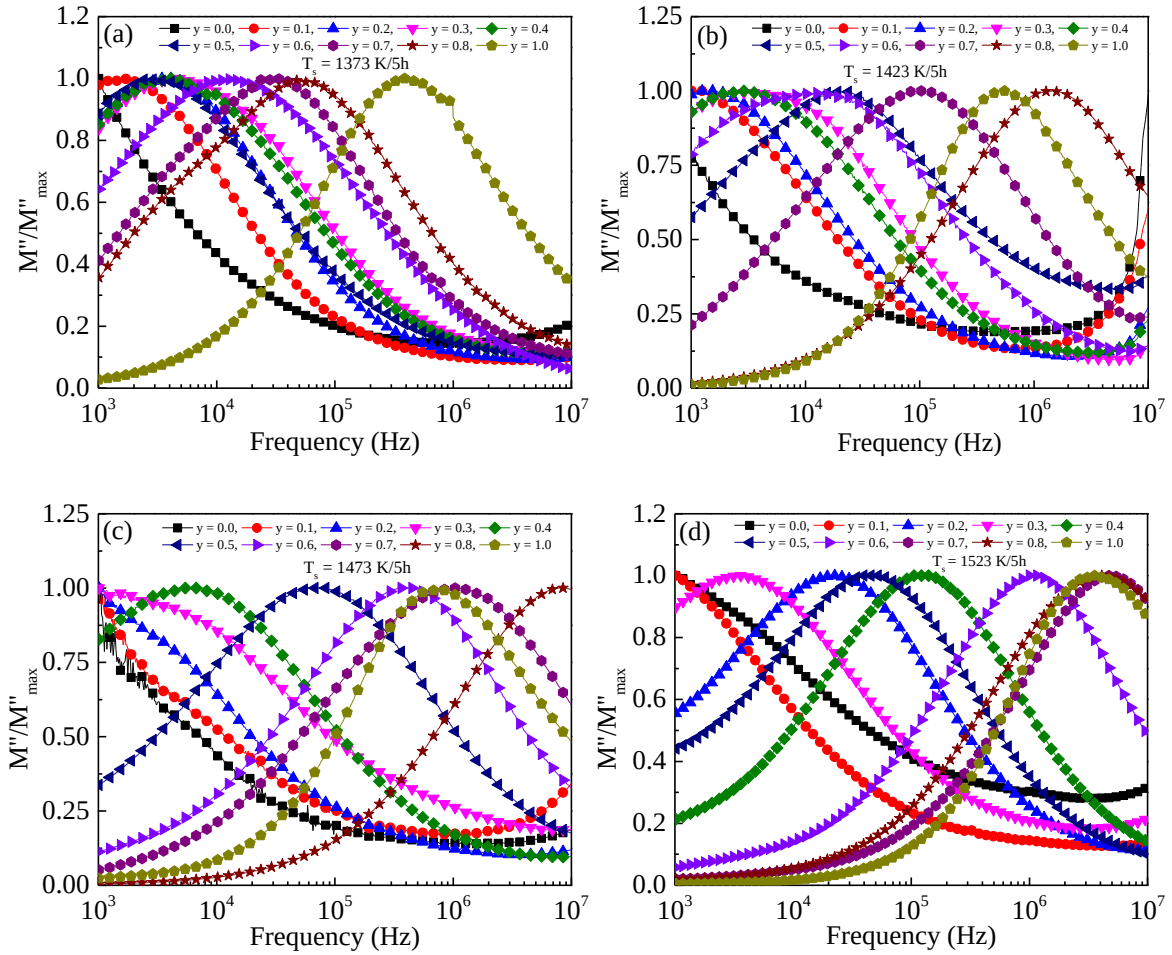

Figure 4.44: Evolution of the scaling characteristics (M''/M''_{max}) with frequency of (1-*y*) [BCZTO] + (*y*) [NCZFO] (*y* = 0-1.0) composite multiferroics annealed for 5 h at (a) 1373, (b) 1423, (c) 1473 and, (d) 1523 K.

The total capacitance supplied by the grain is shown by the intercept of the first semicircle on the real M'' axis, and the grain border effect's total capacitance contribution is shown by the intercept of the second semicircle [416]. As shown in Figure 4.44, we plot the modulus plots scaling behavior (M''/M''_{max}) for composite multiferroics with respect to frequency annealed at (a) 1373, (b) 1423, (c) 1473 and, (d) 1523 K to clarify whether the relaxation is dominated by long- or short-distance charge carrier's movement in the composite multiferroics. The differences in NCZFO content in the composite multiferroics may be seen as a disagreement amongst the curves. The relaxation peaks of M''/M''_{max} spectra show a perfect separation feature, demonstrating that the charge carrier's local hopping process dominates the dielectric

relaxation. The normalized plot of M''/M''_{max} vs f/f_{max} for composite multiferroics annealed at various T_s is shown in Figure 4.45 (a-d). The spectrum reveals three significant features, including (i) the presence of a slight amount of peak pattern shifting, (ii) basically identical form and layout with minor changes in full width at half maximum depending on NCZFO content, and (iii) the emergence of an asymmetric peak, denoting a non-Debye characteristic of the conductivity relaxation. As proof of delocalized or long-range relaxation, M''/M''_{max} curves' overlapping peak positions are shown [417].

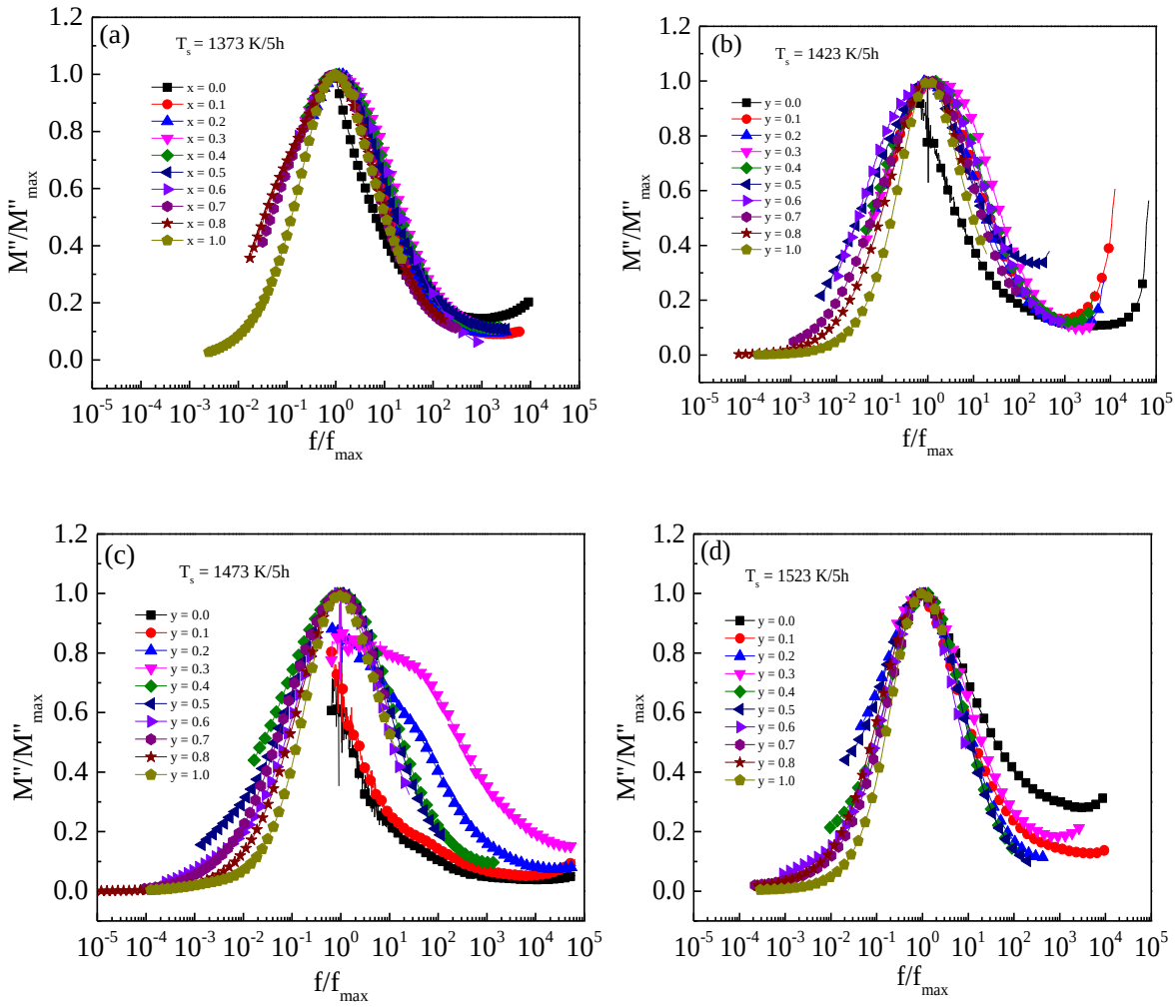

Figure 4.45: Modulus master curves ($M''(f)/M''_{max}(f)$ vs. f/f_{max}) of (1-*y*) [BCZTO] + (*y*) [NCZFO] (y = 0-1.0) composite multiferroics annealed for 5 h at (a) 1373, (b) 1423, (c) 1473 and, (d) 1523 K.

4.3.9. Magnetic permeability and magnetic loss tangent analysis

Figure 4.46 displays how the real component of magnetic permeability (μ_i') depends on frequency of (1 - *y*) [BCZTO] + (*y*) [NCZFO] composite multiferroics annealed at various T_s: (a) 1373 K, (b) 1423 K, (c) 1473 K and (d) 1523 K. The value of μ_i' in composite materials depends on a number of factors, including stoichiometry, phase composition, grain diameter, impurity level, intragranular porosity, saturation magnetization, magnetostriction, crystal anisotropy, porosity, reversible displacement of domain walls, and bulging of domain walls [185]. The value of μ_i' for the NCZFO phase is found to drop gradually with frequency, although the rate of decline accelerates at higher frequencies in the midst of 1 and 100 MHz for all Ts. The value of μ_i' is shown to be rather constant at 1373 K to a maximum of several MHz, then it starts to rise somewhat at a certain frequency before falling off quickly, which indicates the onset of ferromagnetic resonance. Contrarily, in composite multiferroics annealed at 1373-523 K, the value of μ_i' is found to be gradually declining after being rather steady to a maximum of several MHz without displaying any peak at a particular frequency. The range of utility, which may be applied in real-world situations, is defined as the frequency range to a maximum of which the value of μ_i' stays frequency-independent. It is discovered that when the NCZFO concentration rises, the stability of μ_i' is seen to diminish. The peak's presence at 1373 K can be interpreted in the fashion that follows. When the harmonization amongst the applied frequency and the Larmor precession frequency is detected, this peak often appears in the midst of the magnetic dipoles. When this happens, a particular amount of energy from the input field is transmitted to the moving magnetic dipoles at a specific frequency. As a result, magnetic dipoles exhibit high orientation and high velocity, which increases the domain wall's velocity. As a result, at the peak location, magnetic permeability achieves its greatest value.

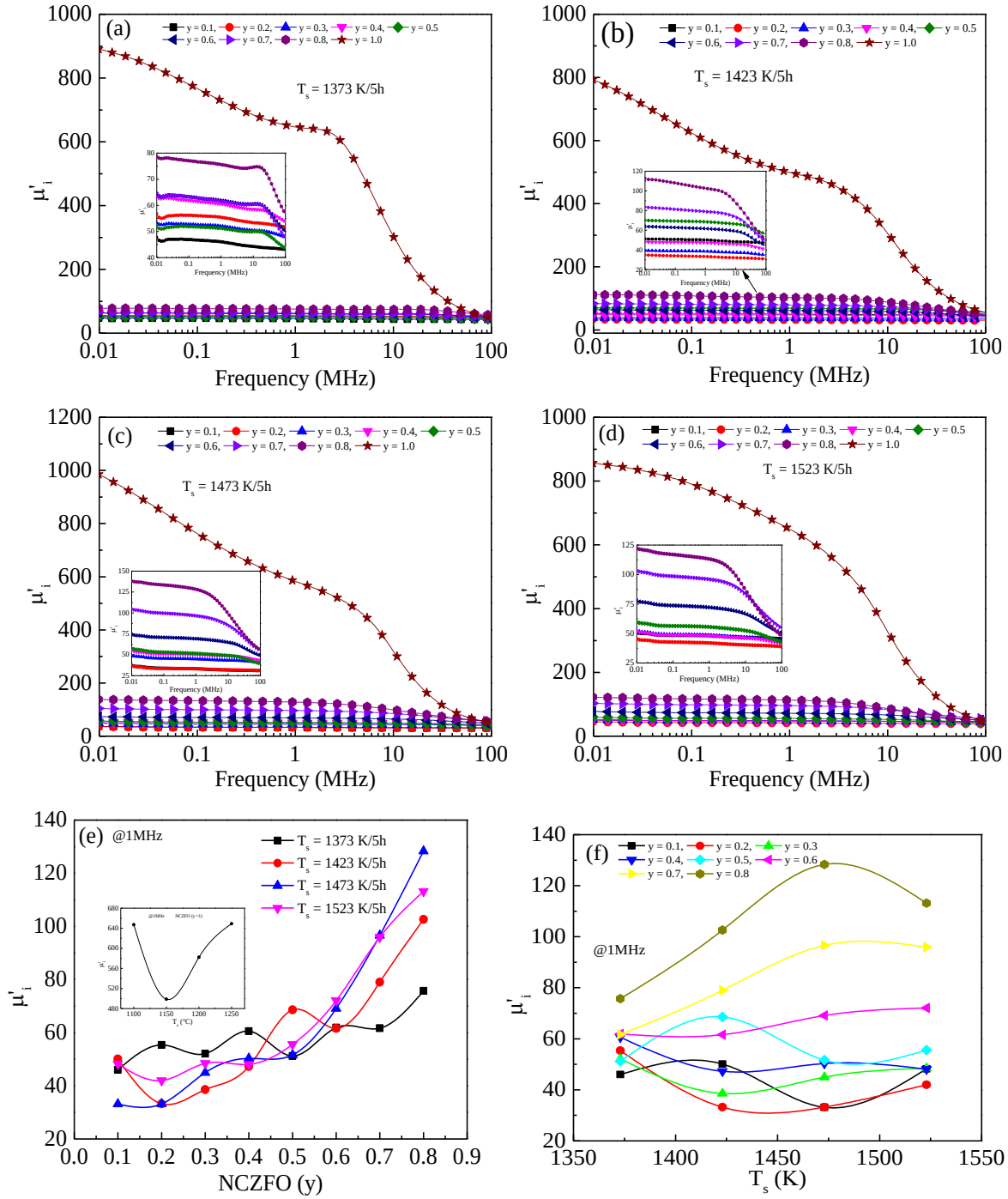

Figure 4.46: Evolution of the magnetic permeability (μ_i') with respect to frequency of (1-*y*) [BCZTO] + (*y*) [NCZFO] (*y* = 0.1-1.0) composite multiferroics annealed for 5 h at (a) 1373, (b) 1423, (c) 1473 and, (d) 1523 K, and (e-f) shows composition and T_s dependent μ_i' at 1 MHz.

The change in magnetic permeability (μ_i') can be explained by the formula [185]: $\mu_i' \propto \frac{\mu_0 M_S^2 D_m}{\left[K_1+\frac{3}{2}\lambda_s\sigma\right]\beta^{\frac{1}{3}}\delta}$, where μ_0, M_s, D_m, K_1, λ_s, σ, β, and δ are magnetic permeability in air, saturation magnetization, grain diameter, anisotropic constant, constant of saturated magnetostriction,

stress, impurity amount, and domain wall thickness, respectively. According to reports, the domain wall movement is mostly responsible for the μ_i' value down from 100 MHz [236]. As previously mentioned, according to our study's findings, the domain wall movement is the cause of magnetic permeability [83]. Increasing the percentage of NCZFO causes the value of μ_i' to rise, which is connected to the enhancement of the continuation and engagement of magnetic grains. A considerable contribution from domain wall movement and an improvement in saturated magnetization are the relevant causes of this improvement in μ_i' value with T_s. Because the higher Ts increases the activation energy, it is excellent for initiating grain development [280, 418, 419]. Small moveable domain barriers are present because of the minor quantity of grain borders and diminishing grain borders present in large grains. Pore density decreases during grain expansion, which also contributes to an improvement in μ_i' value. The domain wall is often restricted in its mobility by the pores, which also serve as a barrier to this movement. The value of μ_i' therefore shrinks. Additionally, when T_s increases, the magnetic anisotropy decreases due to a reduction in intrinsic tension and anisotropy in crystals that declines the resistance to domain wall movement [420, 421]. Table 4.40-4.43 display the μ_i' values for various T_s at various frequencies. To evaluate and compare the measured magnetic permeability, Maxwell-Garnett and Bruggeman approximation approaches were utilized according to the relationships [422-424]:

(i) $\mu_i'(composite) = \mu_i'(BCZTO)\left(1 + \frac{3f_{NCZFO}\beta}{1-f_{NCZFO}\beta}\right)$,

(ii) $\beta = \frac{\mu_i'(NCZFO)-\mu_i'(BCZTO)}{\mu_i'(NCZFO)+2\mu_i'(BCZTO)}$, and

(iii) $(1-y)\left(\frac{\mu_i'(BCZTO)-\mu_i'(composite)}{\mu_i'(BCZTO)+2\mu_i'(composite)}\right) + (y)\left(\frac{\mu_i'(NCZFO)-\mu_i'(composite)}{\mu_i'(NCZFO)+2\mu_i'(composite)}\right) = 0$,

where y is the proportion of NCZFO phase, $\mu_i'(composite)$ represents the magnetic permeability of composite, $\mu_i'(BCZTO)$ and $\mu_i'(NCZFO)$ express the magnetic permeability of component phases. Due to the BCZTO phase's non-magnetic nature, the value of $\mu_i'(BCZTO)$

is unity. It is generally known that the MG model applies when the filler content is negligible, but the Bru model is appropriate when each phase is equally important. The fluctuation of the measured and predicted permeabilities for composite multiferroics including NCZFO annealed at various T_s: (a) 1373, (b) 1423, (c) 1473, and (d) 1523 K are shown in Figure 4.47, accordingly. The outcomes of the experiment and the calculations are found to differ. This outcome might be attributed to how the component phases interacted. The fluctuation of magnetic loss tangent ($tan\delta_\mu$) with frequency annealed at (a) 1373, (b) 1423, (c) 1473, and (d) 1523 K is shown in Figure 4.48.

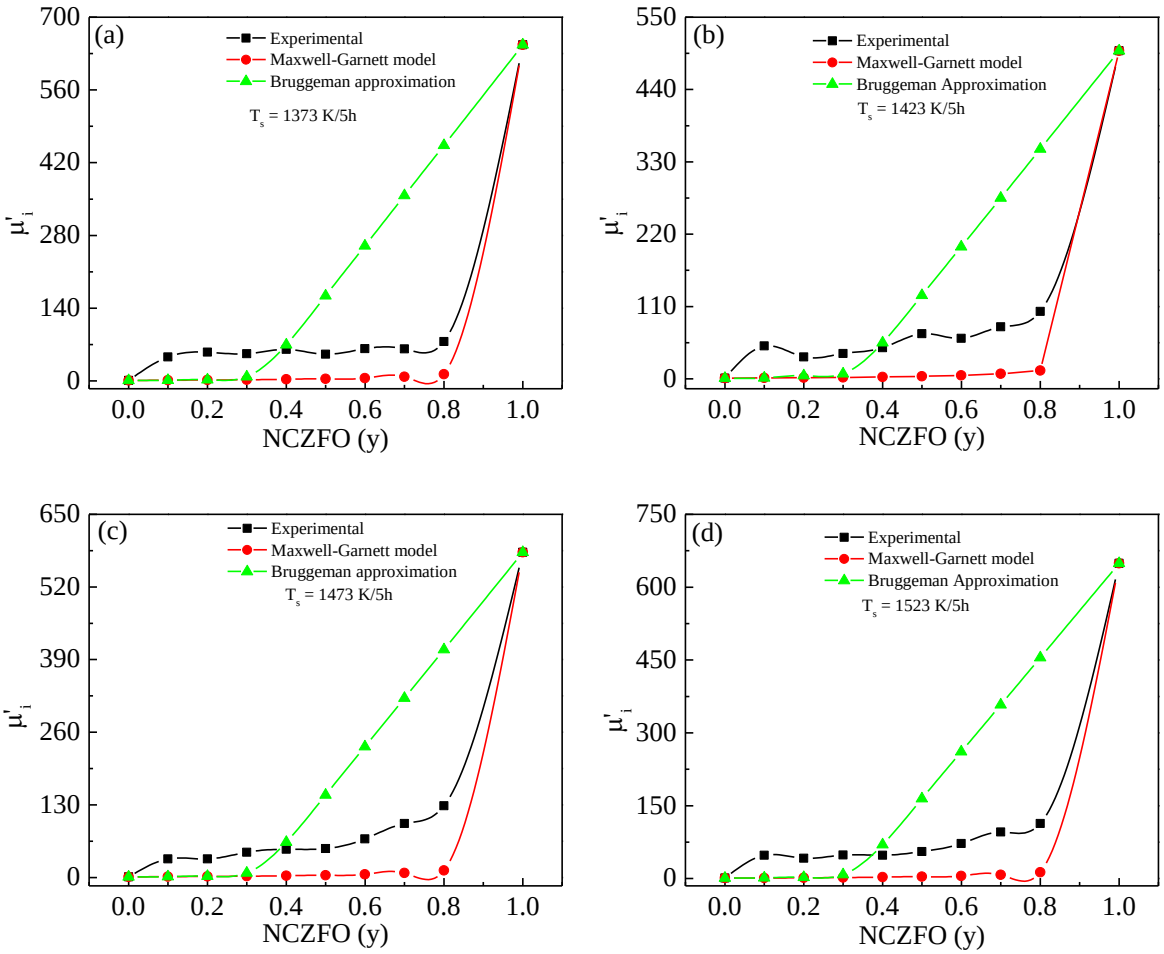

Figure 4.47: Ferrite volume fraction variation of μ_i' of (1-*y*) [BCZTO] + (*y*) [NCZFO] (y = 0.1-1.0) compositie multiferroics at 1 MHz and predicted lines from the Maxwell-Garnett (MG) and Bruggeman-Hanai (BH) equations annealed for 5 h at (a) 1373, (b) 1423, (c) 1473 and, (d) 1523 K.

A possible explanation for the extrinsic properties of windings is that $tan\delta_\mu$ value is strong at lower frequency region and drops at higher frequency region. The value of $tan\delta_\mu$ is progressively reduced to a maximum of 1 MHz, after which it is shown to gradually grow and exhibit a maximum at a specific frequency. The ferromagnetic resonance is thought to be responsible for the peak's existence at a certain frequency [425]. The domain wall's oscillational frequency closely matches applied frequency when resonance occurs. The composite multiferroics show an extremely low value of $tan\delta_\mu$ for all T_s at 0.1 MHz $\leq f \leq$ 10 MHz. For all T_s, the $tan\delta_\mu$ value fluctuates at random to a maximum of y = 0.7. However, the composite y = 0.8 shows a lowest magnitude at 1373 K and a highest magnitude at all T_s except 1373 K. The $tan\delta_\mu$ value is enhanced for additional T_s (1473 and 1523 K) after decreasing at 1423 K. However, with y = 0.8, the value of $tan\delta_\mu$ value progressively improves with rising T_s to a maximum of 1473 K before degrading at 1523 K. Table 4.40-4.43 lists the values of tan at particular frequencies for various T_s.

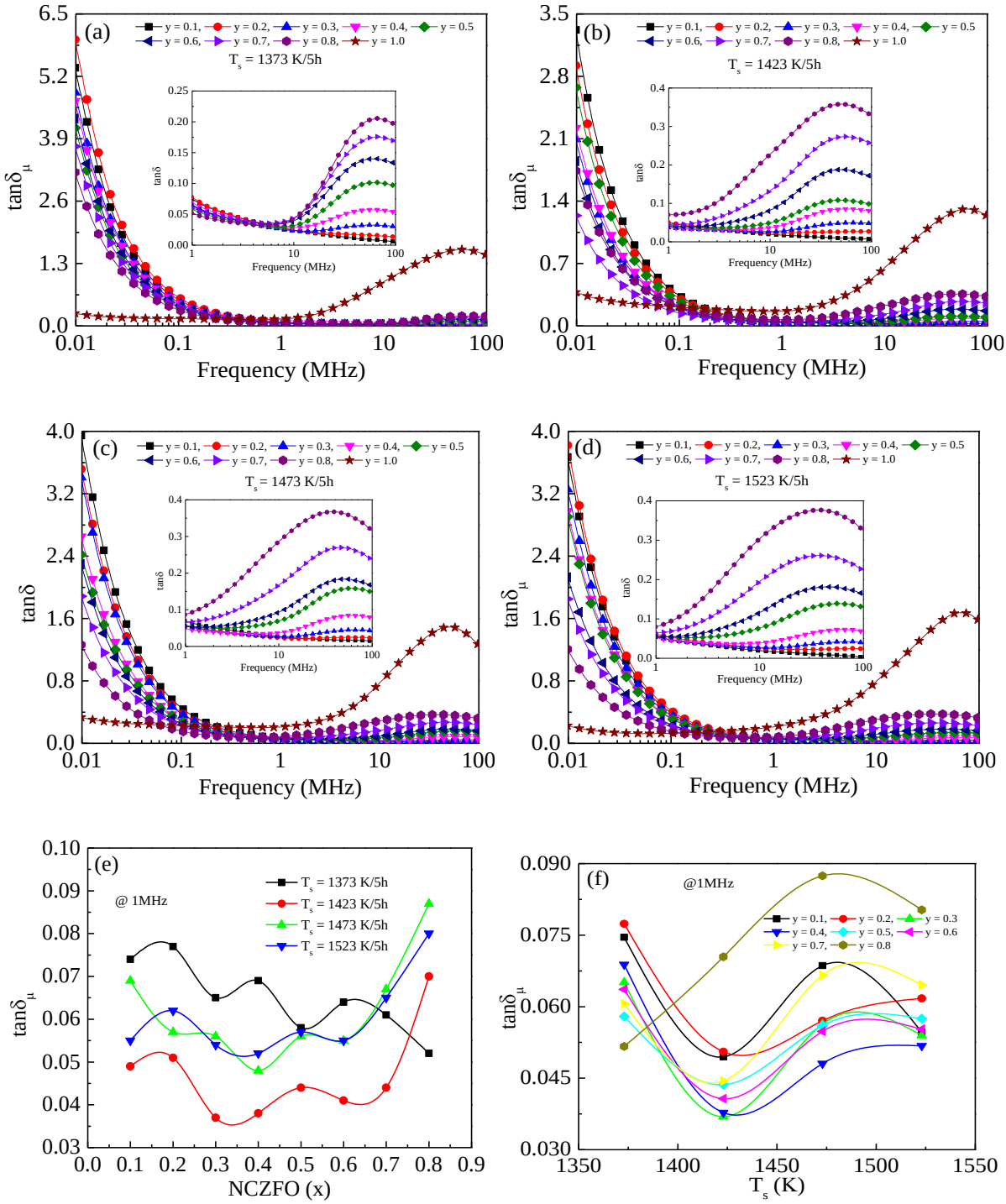

Figure 4.48: Evolution of magnetic loss tangent ($tan\delta_\mu$) with frequency of (1-*y*) [BCZTO] + (*y*) [NCZFO] (*y* = 0.1~1.0) composite multiferroics annealed for 5 h at (a) 1373, (b) 1423, (c) 1473 and, (d) 1523 K, and (e, f) shows composition and T_s dependent $tan\delta_\mu$ at 1 MHz.

4.3.10. Q-factor analysis

Figure 4.49 shows how Q-factor depends on frequency of (1-*y*) [BCZTO] + (*y*) [NCZFO] **(**with *y* = 0.1~0.8) composite multiferroics annealed at: (a) 1373, (b) 1423, (c) 1473 and, (d) 1523 K for 5h. Generally speaking, a material's Q-factor fluctuates as inversely proportionate to its resistivity and is also influenced by a variety of parameters, such as the density, porosity, and grain diameter of the material [426]. The Q-factor rises with frequency, peaks at a certain frequency, and then falls as a result of ferrimagnetic resonance losses. The large grain diameter of the pure NCZFO, which reduces the percentage of grain borders with high resistance, is mostly to blame for the phase's low Q-factor. It is well known that NCZFO has significantly lower resistivity than BCZTO. As a result, the rise in NCZFO concentration supported both an increase in eddy current loss and a decrease in resistivity. Additionally, the relatively large and uniform grain diameter is advantageous for improving residual loss and eddy current loss [427]. The increase in μ_i' value causes the Q-factor peaks to progressively move from a higher frequency domain to a lower frequency domain. The composite multiferroics achieve the maximum Q-factor at 1373 K while having the lowest bulk density. Therefore, microstructure has a far greater impact on Q-factor than bulk density. The fluctuation of Q-factor in relation to NCZFO concentration and T_s at 10 MHz is depicted in Figure 4.49 (e, f). As the NCZFO concentration rises, the Q-factor deviates noticeably, as can be shown in Figure 4.49 (e). Additionally, it is discovered that the T_s, when their NCZFO concentrations vary, have a significant influence on Q-factor. Since big grains often give rise to low Q-factor, these declining properties of the Q-factor may be responsible for the grains' rapid development [258]. A larger concentration of NCZFO phase may have been a major cause in the development of intergranular pores and inhomogeneous grains, which hampered the mobility of the domain wall and increased resistivity, which worsened the Q-factor [428]. The gradually declining Q-factor of the composite multiferroics with rising T_s is seen in Figure 4.49 (f). According to the findings, optimizing the quantity of NCZFO content and maintaining relatively low T_s are

beneficial for raising Q-factor. Table 4.40-4.43 lists the Q-factor values for a selection of T_s at a variety of frequencies.

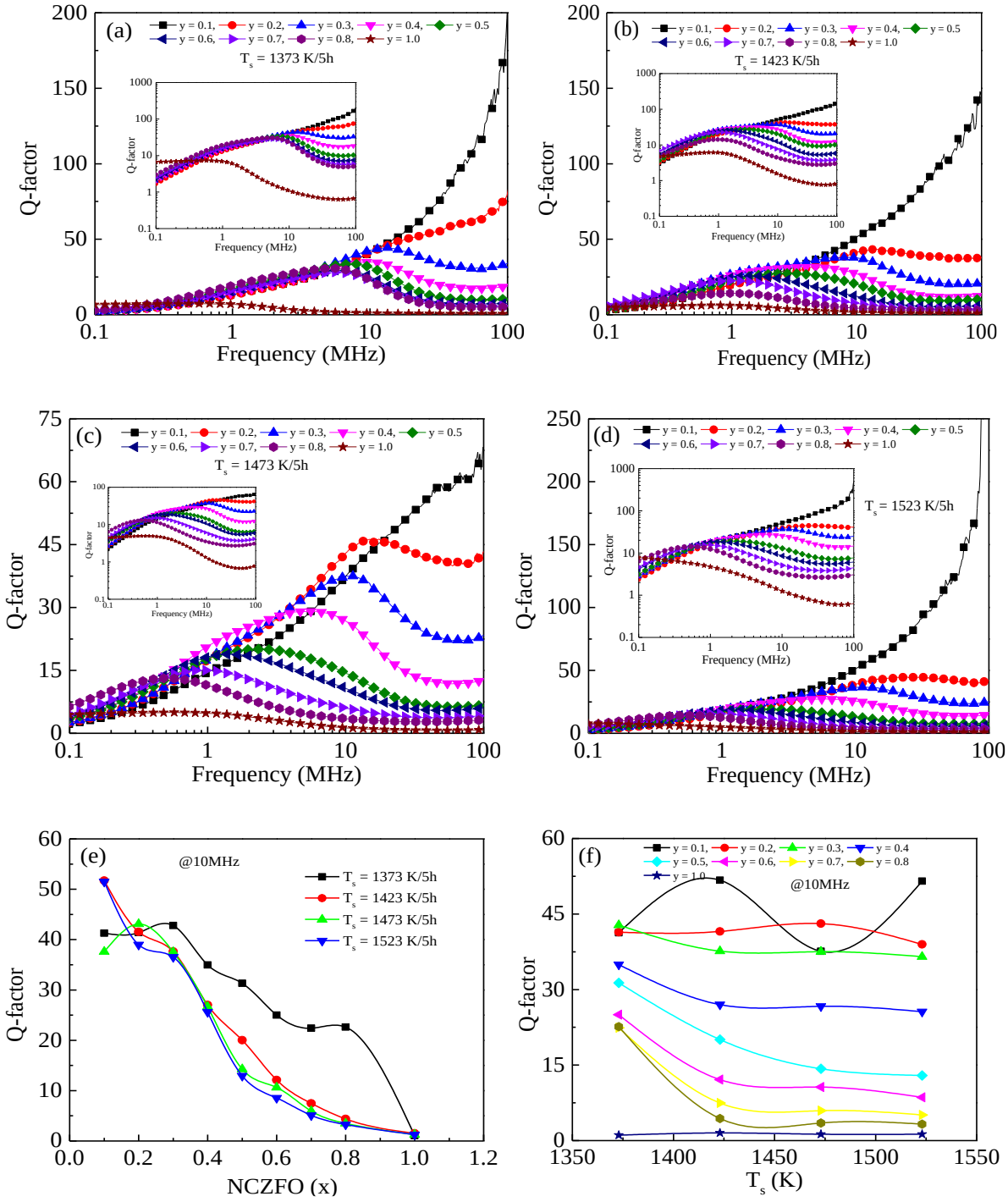

Figure 4.49: Evolution of the Q-factor with frequency of (1-*y*) [BCZTO] + (*y*) [NCZFO] (*y* = 0.1-1.0) composite multiferroics for 5 h annealed at (a)1373, (b) 1423, (c) 1473 and, (d) 1523 K, and (e-f) shows compostion and T_s dependent Q-factor at 10 MHz.

Table 4.40. Magnetic permeability (μ_i'), magnetic loss tangent ($tan\delta_\mu$), Q-factor of (1-*y*) [BCZTO] + (*y*) [NCZFO] (*y* = 0.1-1.0) composite multiferroics at specific frequencies and resonant frequency (f_r) annealed at 1373 K.

T_s	Composition (y)	μ_i'					f_r MHz	$tan\delta_\mu$					Q –factor at				
		10kHz	100kHz	1MHz	10MHz	100MHz		10kHz	100kHz	1MHz	10MHz	100MHz	10kHz	100kHz	1MHz	10MHz	100MHz
1373	0.1	47.6	46.9	46	44.2	43.1		5.29	0.54	0.074	0.024	0.005	0.189	1.86	13.42	41.27	211.71
	0.2	56.7	56.2	55.4	53.4	51.6		5.87	0.59	0.077	0.024	0.012	0.170	1.70	12.92	41.39	82.96
	0.3	53.6	52.7	52.1	50.4	47.8	51.80	4.76	0.49	0.065	0.023	0.029	0.210	2.06	15.36	42.80	34.39
	0.4	63.5	61.9	60.6	58.5	53.8	53.60	4.61	0.48	0.069	0.029	0.052	0.217	2.07	14.53	34.97	19.09
	0.5	52.3	51.9	51.2	49.9	43.5	53.60	4.06	0.41	0.058	0.032	0.095	0.246	2.46	17.27	31.31	10.52
	0.6	64.3	63.2	61.9	60.6	49.9	52.70	4.26	0.44	0.064	0.040	0.131	0.235	2.27	15.71	25.00	7.63
	0.7	64.8	63.3	61.7	60.4	47.6	52.70	3.68	0.39	0.061	0.045	0.166	0.272	2.58	16.50	22.39	6.01
	0.8	78.8	77.1	75.7	74.6	56.7	51.8	3.14	0.33	0.052	0.044	0.194	0.318	3.02	19.35	22.62	5.15
	1.0	891	766	647	301	47.7	72.7	0.26	0.15	0.146	0.930	1.466	0.389	6.67	6.87	1.076	0.68

Table 4.41. Magnetic permeability (μ_i'), magnetic loss tangent ($tan\delta_\mu$), Q-factor of (1-*y*) [BCZTO] + (*y*) [NCZFO] (*y* = 0.1-1.0) composite multiferroics at specific frequencies and resonant frequency (f_r) annealed at 1423 K.

T_s	Composition (y)	μ_i'					f_r MHz	$tan\delta_\mu$					Q –factor at				
		10kHz	100kHz	1MHz	10MHz	100MHz		10kHz	100kHz	1MHz	10MHz	100MHz	10kHz	100kHz	1MHz	10MHz	100MHz
1423	0.1	51.25	50.67	50.09	48.34	46.88		3.26	0.34	0.049	0.019	0.007	0.307	2.98	20.21	51.70	142.58
	0.2	34.88	33.9	33.25	31.98	30.61		2.87	0.31	0.051	0.024	0.027	0.349	3.25	19.78	41.54	37.75
	0.3	39.67	38.93	38.6	37.36	34.63	69.70	2.04	0.21	0.037	0.027	0.048	0.489	4.69	27.09	37.65	20.94
	0.4	48.13	47.64	47.28	45.84	40.20	53.60	2.18	0.22	0.038	0.037	0.080	0.459	4.49	26.48	27.01	12.50
	0.5	70.29	69.32	68.59	66.36	55.54	39.80	2.63	0.27	0.044	0.050	0.097	0.381	3.70	22.92	20.04	10.30
	0.6	64.08	62.72	61.64	59.01	43.80	39.10	1.81	0.20	0.041	0.083	0.169	0.552	5.11	24.58	12.11	5.92
	0.7	83.76	81.30	79	73.22	47.39	35.20	1.21	0.14	0.044	0.134	0.254	0.824	6.97	22.51	7.46	3.93
	0.8	112.68	108	102.64	87.86	49.28	26.10	1.71	0.21	0.070	0.229	0.327	0.584	4.76	14.20	4.37	3.06
	1.0	792.47	623.12	498.76	303.36	53.46	11.70	0.37	0.21	0.165	0.659	1.227	2.672	4.76	6.07	1.52	0.81

Table 4.42. Magnetic permeability (μ_i'), magnetic loss tangent ($tan\delta_\mu$), Q-factor of (1-*y*) [BCZTO] + (*y*) [NCZFO] (*y* = 0.1-1.0) composite multiferroics at specific frequencies and resonant frequency (f_r) annealed at 1473 K.

T_s	Composition (y)	μ_i'					f_r MHz	$tan\delta_\mu$					Q –factor at				
		10kHz	100kHz	1MHz	10MHz	100MHz		10kHz	100kHz	1MHz	10MHz	100MHz	10kHz	100kHz	1MHz	10MHz	100MHz
1473	0.1	37.34	33.87	33.18	31.69	30.96		3.89	0.45	0.069	0.027	0.015	0.257	2.22	14.58	37.60	67.58
	0.2	36.73	33.56	33.25	32.03	31.01		3.45	0.39	0.057	0.023	0.023	0.289	2.56	17.53	43.08	43.30
	0.3	49.14	45.67	44.94	43.41	40.79	59.50	3.36	0.38	0.056	0.027	0.043	0.298	2.65	17.75	37.54	23.33
	0.4	55.07	51.03	50.33	48.64	43.23	56.50	2.60	0.30	0.048	0.037	0.0781	0.384	3.38	20.82	26.67	12.81
	0.5	57.74	53.06	51.63	49.05	39.32	45.00	2.38	0.28	0.056	0.070	0.1479	0.420	3.54	17.84	14.28	6.76
	0.6	74.18	70.68	69.14	64.73	48.92	39.80	2.26	0.25	0.055	0.094	0.1642	0.443	3.97	18.25	10.61	6.09
	0.7	104.67	99.68	96.62	85.15	55.48	28.50	1.86	0.22	0.067	0.168	0.2359	0.538	4.63	15.02	5.94	4.24
	0.8	138.40	133.45	128.31	98.87	55.51	16.00	1.24	0.15	0.087	0.288	0.3150	0.805	6.46	11.44	3.48	3.17
	1.0	984.07	761.04	582.12	316.83	51.91	10.10	0.33	0.23	0.209	0.782	1.2488	3.038	4.44	4.78	1.28	0.80

Table 4.43. Magnetic permeability (μ_i'), magnetic loss tangent ($tan\delta_\mu$), Q-factor of (1-*y*) [BCZTO] + (*y*) [NCZFO] (*y* = 0.1-1.0) composite multiferroics at specific frequencies and resonant frequency (f_r) annealed at 1523 K.

T_s	Composition (y)	μ_i'					f_r MHz	$tan\delta_\mu$					Q –factor at				
		10kHz	100kHz	1MHz	10MHz	100MHz		10kHz	100kHz	1MHz	10MHz	100MHz	10kHz	100kHz	1MHz	10MHz	100MHz
1523	0.1	51.09	48.62	48.23	46.57	45.49		3.62	0.39	0.055	0.019	0.0020	0.276	2.59	18.29	51.51	497.88
	0.2	45.48	42.67	41.99	40.31	38.83		3.77	0.42	0.062	0.026	0.0239	0.265	2.41	16.20	38.99	41.78
	0.3	52.51	49.05	48.46	46.71	43.91	80.20	3.21	0.35	0.054	0.027	0.0398	0.311	2.82	18.53	36.52	25.10
	0.4	51.94	48.66	48.12	46.27	41.60	58.50	2.92	0.32	0.052	0.039	0.0673	0.342	3.10	19.32	25.58	14.86
	0.5	59.92	56.42	55.57	52.42	42.63	41.20	2.85	0.31	0.057	0.077	0.1299	0.351	3.18	17.40	12.92	7.70
	0.6	77.69	73.69	72.12	66.55	49.85	31.70	2.10	0.24	0.055	0.117	0.1622	0.477	4.19	18.09	8.56	6.17
	0.7	103.35	98.48	95.95	82.92	54.39	20.50	1.82	0.21	0.065	0.196	0.2222	0.550	4.72	15.49	5.09	4.50
	0.8	122.43	116.96	113.20	86.48	47.95	13.20	1.19	0.15	0.080	0.305	0.3241	0.842	6.58	12.45	3.28	3.09
	1.0	856.04	789.88	649.01	324.70	47.12	9.30	0.22	0.13	0.211	0.802	1.5695	4.513	7.77	4.74	1.25	0.64

4.4. Exploration of electromagnetic and magnetoelectric traits of (1-*y*) $[Ba_{0.9}Ca_{0.1}Ti_{0.9}Zr_{0.1}O_3]$ + (*y*)$[Ni_{0.25}Cu_{0.13}Zn_{0.62}Fe_{2-x}O_{4-3x/2}]$ system

In this section, the results of the effect of iron-deficient non-stoichiometry (IDNS) dominance on structural, topographical, electric, magnetic, and magnetoelectric properties of (1-*y*) $[Ba_{0.9}Ca_{0.1}Ti_{0.9}Zr_{0.1}O_3]$ (BCTZO) + (*y*) $[Ni_{0.25}Cu_{0.13}Zn_{0.62}Fe_{2-x}O_{4-3x/2}]$ ($NCZFe_{2-x}O_{4-3x/2}$) (where x = 0.00, 0.04, 0.08, 0.12 and y = 0.2, 0.5) multiferroic composites annealed at 1200 ºC are discussed.

4.4.1. Crystallographic characteristics

It is important to do XRPD investigation at room temperature to examine crystal phase provenance, crystal architecture, and extent of crystallinity as well as to determine the crystallite diameter. The quality of the generated ferroelectromagnetic composite ceramics, the unit cell parameters, the subsequent phase formation, and other physical properties were calculated from the XRD data. Figure 4.50 displays the XRPD patterns of the (1-y) [BCZTO] + (y) $[NCZFe_{2-x}O_{4-3x/2}]$ ferroelectromagnetic composite ceramics: (a) x 0.0; 0.04; 0.08; 0.12; y = 0.2 and (b) x = 0.0; 0.04; 0.08; 0.12; y = 0.5. Generally speaking, various variables, including (i) molecular composition, (ii) crystallite diameter, (iii) the X-ray voltage, (iv) step scan and scan duration, (v) the diffraction plane utilized for examination, affect the strength of the diffraction maximum and crystallinity of the specimen [429, 430]. Figure 4.50 (a, b) reveals that the crystallographic planes represented by the solid circle "●" in the XRPD spectra and observed as (100), (110), (111), (200), (210), (211), (220), (300), and (103) resemble to BCZTO phase. Contrarily, the detected (111), (220), (311), (222), (400), (422), (511), (440), (623), and (533) crystallographic planes, designated in the XRPD patterns with an open circle "○" correspond to the $NCZFe_{2-x}O_{4-3x/2}$ phase. As a result, within the constraints of the experiment, the ferroelectromagnetic composite ceramics were successfully created without any additional peaks concerning any foreign phases.

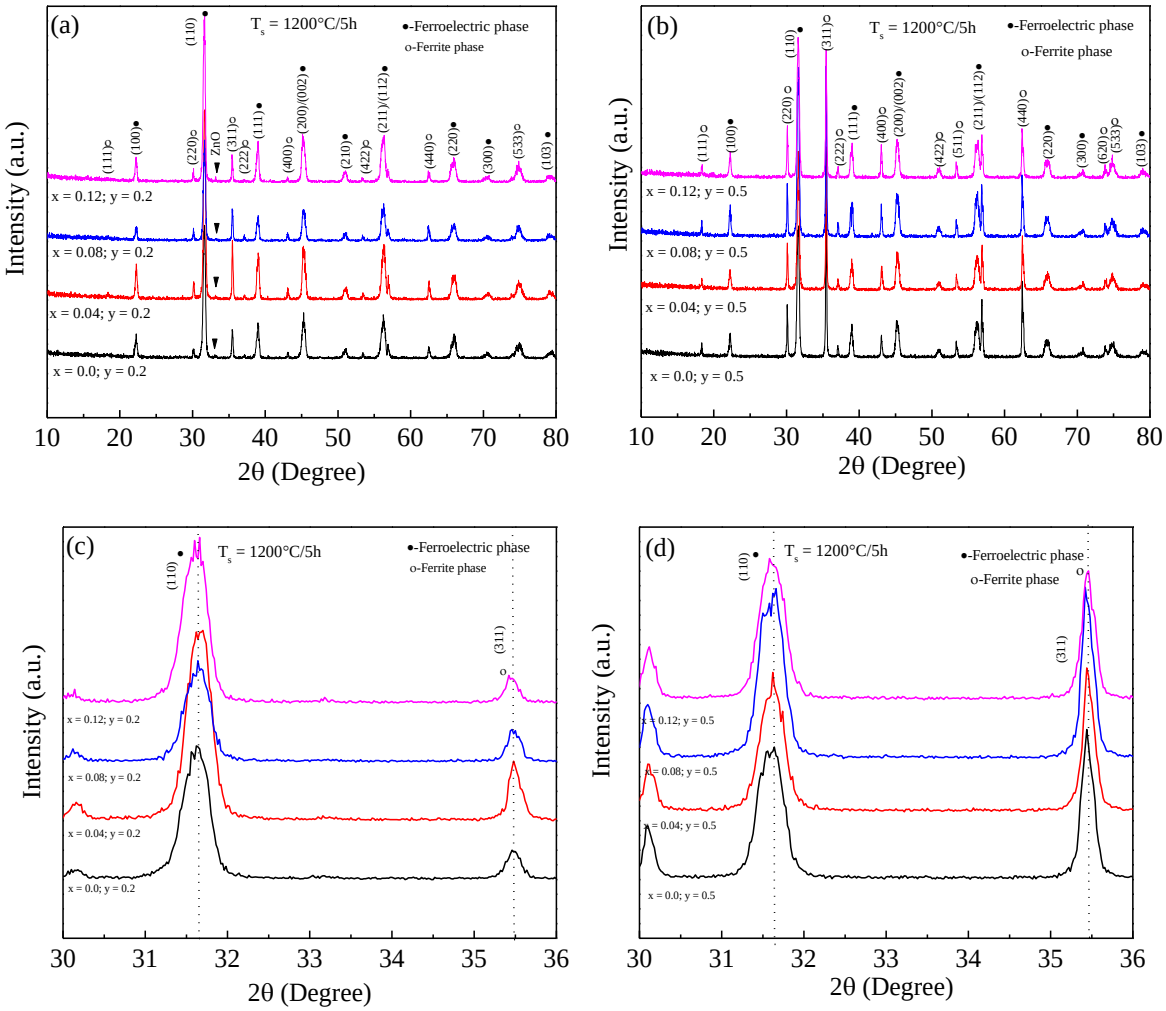

Figure 4.50: XRD profiles for (1-*y*) [BCZTO] + (*y*) [NCZFe$_{2-x}$O$_{4-3x/2}$] (*x* = 0.0; 0.04; 0.08; 0.12; *y* = 0.2, 0.5) ferroelectromagnetic composite ceramics: (a) *x* = 0.0; 0.04; 0.08; 0.12; *y* = 0.2 and (b) *x* = 0.0; 0.04; 0.08; 0.12; *y* = 0.5. Enlarged view of peak (110) corresponding to BCZTO and peak (311) associated with NCZFe$_{2-x}$O$_{4-3x/2}$: (c) *x* = 0.0; 0.04; 0.08; 0.12; *y* = 0.2 and (d) *x* = 0.0; 0.04; 0.08; 0.12; *y* = 0.5, respectively.

The findings suggest that the ferroelectromagnetic composite ceramics have a high crystalline character and lack any indication of observable chemical interaction in the midst of their two component phases when the process of sintering is taking place. A further estimation of the phase progression is provided by the delineation of the principal peaks in the XRPD patterns of the BCZTO and NCZFe$_{2-x}$O$_{4-3x/2}$ phases in Figure 4. 50 (c, d). According to Figure 4.50 (c), the (110) peak shifts from the lower 2θ angle to the greater 2θ angle in x = 0.04 and 0.08 and then back again in y = 0.2, while the (311) peak shifts from the smaller 2θ angle to the greater

2θ angle in x = 0.04 and then back again in x = 0.08 and 0.12 respectively. Instead, the (110) peak progresses to the lower 2θ angle in x = 0.04 and then progresses to the greater 2θ angle in x = 0.08 and finally progresses to the lower 2θ angle in x = 0.12, while the (311) peak progresses to greater 2θ angle in x = 0.04 and then progresses to lower 2θ angle in x = 0.08, and finally progresses to the greater 2θ angle in x = 0.12 and y = 0.5. The shifting of the peaks in the direction of the lower and greaterr 2θ angle, respectively, confirms an escalation and a diminution in the lattice constants. The aforementioned findings show a reciprocal relationship in the midst of the crystal structures of the two distinct phases, which may be partially explained by the lattice stress-strain that both phases have formed on one another. Therefore, it can be predicted that with the current ferroelectromagnetic composite ceramics fabrication method, the two distinct phases' grain border crystal structures will be somewhat altered after being combined, pelletized, and annealed to 1200 °C. The lattice constant and crystallite diameter must be assessed after phase identification of each component phase. Using the well-known Bragg's rule, the distance in the midst of the crystal lattice planes (d_{hkl}) for every diffraction peak of the component phases is quantitatively determined [184]: $2d_{hkl}sin\theta_{hkl} = n\lambda_{Cu-K_\alpha}$, where λ_{Cu-K_α} is the wavelength of 1.5406Å, n is a positive integer, $h, k,$ and l are Miller indices, and θ_{hkl} is the diffraction angle with respect to the (hkl) crystal plane. In order to quantitatively eastimate the lattice constants of the BCZTO and $NCZFe_{2-x}O_{4-3x/2}$ phases the following fomulas were used [183]: $d_{hkl} = 1/\sqrt{\frac{h^2+k^2}{a^2} + \frac{l^2}{c^2}} = \frac{\lambda_{Cu-K_\alpha}}{2sin\theta_{hkl}}$, and $a = d_{hkl}\sqrt{h^2+k^2+l^2} = \frac{\lambda_{Cu-K_\alpha}}{2} \times \sqrt{\frac{(h^2+k^2+l^2)}{sin^2\theta_{hkl}}}$, where $a = b \neq c$ denotes the lattice constants for BCZTO and $a = b = c$ denotes the lattice constants for $NCZFe_{2-x}O_{4-3x/2}$. The computed lattice constants for the $NCZFe_{2-x}O_{4-3x/2}$ and BCZTO phases are shown in Table 4.24. Table 4.24 shows that the $NCZFe_{2-x}O_{4-3x/2}$ phase's lattice constant rises first in x = 0.04, aftewhich drops in x = 0.08, and in the end rises in x = 0.12 at y = 0.2. In contrast, the $NCZFe_{2-x}O_{4-3x/2}$

phase's lattice constant first increases in x = 0.04 and then drops in x = 0.08 before declining in x = 0.12 and y = 0.2. On the other hand, at x = 0.04 the lattice constant (a) of BCZTO first increases and then increases again to a maximum of x = 0.12 in y = 0.2 and 0.5. Comparable to this, the lattice constant (c) increases on rising IDNS level at y = 0.5 and the lattice constant (c) increases on rising IDNS in x = 0.08 and afterwhich rises in x = 0.12 at y = 0.2. Tetragonality (c/a) decreases in x = 0.08 and then rises to a maximum of x = 0.12 when y = 0.2, but afterwhich drops in x = 0.04 and then decreases again when y = 0.5. The lattice anisotropy in BCZTO-$NCZFe_{2-x}O_{4-3x/2}$ ferroelectromagnetic composite ceramics on risng IDNS level is shown by the declining and enhancing patterns in the c/a ratio [431]. The $NCZFe_{2-x}O_{4-3x/2}$ lattice constant changes with BCZTO degree and vice versa in annealed BCZTO/$NCZFe_{2-x}O_{4-3x/2}$ ferroelectromagnetic composite ceramics because the maximum shifts, as seen in Figure 4.50 (c, d). During sintering, there may be a little potential of component ions migrating in the midst of the BCZTO and $NCZFe_{2-x}O_{4-3x/2}$ phases of the ferroelectromagnetic composite ceramics, causing the BCZTO and $NCZFe_{2-x}O_{4-3x/2}$ phases to alternate in their crystal structure and type [432]. We all know that the ionic radius of Ti^{4+} [r_{Ti}^{4+} = 0.605 Å , sixfold coordination number (CN) = 6] and Zr^{4+} (r_{Zr}^{4+} = 0.72 Å , CN = 6) is almost close to those of Fe^{3+} (r_{Fe}^{3+} = 0.645 Å , CN = 6), Ni^{2+} (r_{Ni}^{2+} = 0.69 Å , CN = 6), Cu^{2+} (r_{Cu}^{2+} = 0.73 Å , CN = 6), and Zn^{2+} (r_{Zn}^{2+} = 0.74 Å, CN = 6) and that of Ti^{4+} (r_{Ti}^{4+} = 0.42 Å , CN = 4) and Zr^{4+} (r_{Zr}^{4+}= 0.59 Å , CN = 4) is comparable in size to that of Fe^{3+} (r_{Fe}^{3+} = 0.49 Å , CN = 4), Ni^{2+} (r_{Ni}^{2+} = 0.55 Å , CN = 4), Cu^{2+} (r_{Cu}^{2+} = 0.57 Å, CN = 4), and Zn^{2+} (r_{Zn}^{2+} = 0.60 Å , CN = 4) [344, 432, 433]. Therefore, during sintering, the Fe^{3+}, Ni^{2+}, Cu^{2+}, and Zn^{2+} ions in the $NCZFe_{2-x}O_{4-3x/2}$ phase, of which Fe^{3+} ions are distributed amongst the tetrahedrally and octahedrally coordinated sublattices, while Zn^{2+} ions prefer to occupy oxygen tetrahedron site (tetrahedrally coordinated (A)-site) and Ni^{2+} and Cu^{2+} ions preferably enter the space of oxygen octahedron site (octahedrally coordinated B sublattice), respectively [65, 432, 434], Ti^{4+} and Zr^{4+} must more or less replace these ions. The $NCZFe_{2-x}O_{4-3x/2}$ phase may also develop cation vacancies as a result of the extra positive

charges produced by the substitution of Ti^{4+} and Zr^{4+} ions for Fe^{3+}, Ni^{2+}, Cu^{2+}, and Zn^{2+} ions. As a result, it is assumed that the lattice constant of the $NCZFe_{2-x}O_{4-3x/2}$ phase would decrease as the BCZTO phase intensifies. Since the vacancies of the cation and the replacement of the Ti^{4+} and Zr^{4+} ions with a little sparse ionic radius are achieved with the rise in the component phase content. Similar to this, Ni^{2+} (r_{Ni}^{2+}= 0.69 Å, CN = 6), Cu^{2+} (r_{Cu}^{2+} = 0.73 Å, CN = 6), Zn^{2+} (r_{Zn}^{2+} = 0.74 Å, CN = 6), and Fe^{3+} (r_{Fe}^{3+}= 0.645 Å, CN = 6) ions, each with a slightly greater ionic radius than Ti^{4+} and Zr^{4+}, are substituted for them at the oxygen octahedron of the BCZTO [432, 433]. In other words, even if oxygen vacancies are created in the BCZTO when cations of low charge, such as Ti^{4+} and Zr^{4+}, replace cations of high charge, the lattice constant of BCZTO will decrease with increasing BCZTO phase concentration. Therefore, when the BCZTO content increases, the $NCZFe_{2-x}O_{4-3x/2}$ phase content decreases, resulting in reduced lattice constants for both the BCZTO and $NCZFe_{2-x}O_{4-3x/2}$ phases [432]. As shown in Table 4.24, the lattice constants of the BCZTO and $NCZFe_{2-x}O_{4-3x/2}$ phases are well matched since the $NCZFe_{2-x}O_{4-3x/2}$ phase's lattice constant is almost twice as big as the BCZTO phase's. The component phases' lattice-discrepancy in conjunction with lattice constants $a_{\mathrm{ferroelectric}}(a, (a+c)/2 \text{ and } c)$ of BCZTO phase and a_{ferrite} of $NCZFe_{2-x}O_{4-3x/2}$ phase was calculated employing the relation [435]: $Z = (a_{\mathrm{ferrite}} - 2a_{\mathrm{ferroelectric}}/a_{\mathrm{ferrite}}) \times 100\%$. According to the data, there is a little value lattice difference (< 3%) in the midst of the BCZTO and $NCZFe_{2-x}O_{4-3x/2}$ phases, which is directly related to the efficient strain transfer [436]. The $NCZFe_{2-x}O_{4-3x/2}$ phase's unit cell (the fundamental unit of crystal structure) dimensions increase in x = 004 and then decline in x = 0.08 before increasing again in x = 0.12 and y = 0.2, whereas the cell dimension decreases in x = 0.04 and then rises in x = 0.08 before declining in x = 0.12 and y = 0.5. In BCZTO, the unit cell dimension decreases in x = 0.04 and then increases to x = 0.12 at y = 0.2 and 0.5. The difference in the ionic radii of the components of the component phases may be responsible for the variation in unit cell dimension. Compared to difference in ionic radius in the midst of Ba^{2+} (r_{Ba}^{2+}= 1.35 Å, coordination number (CN) = 6, r_{Ba}^{2+}= 1.61 Å, CN =

12) and Ca^{2+} (r_{Ca}^{2+} = 1.00 Å, CN = 6, r_{Ca}^{2+} = 1.34 Å, CN = 12), Fe^{3+} (r_{Fe}^{3+} = 0.49 Å, CN = 4, r_{Fe}^{3+} = 0.645 Å , CN = 6), Ni^{2+} (r_{Ni}^{2+} = 0.55 Å , CN = 4, r_{Ni}^{2+} = 0.69 Å,CN = 6), Cu^{2+} (r_{Cu}^{2+} = 0.57 Å, CN = 4, r_{Cu}^{2+}= 0.73 Å, CN = 6), and Zn^{2+} (r_{Zn}^{2+} = 0.60 Å, CN = 4, r_{Zn}^{2+} = 0.74 Å, CN = 6) have ionic radii that comaparble to those of Ti^{4+} (r_{Ti}^{4+} = 0.42 Å, CN = 4, r_{Ti}^{4+} = 0.605 Å, CN = 6) and Zr^{4+} (r_{Zr}^{4+} = 0.59 Å , CN = 4, r_{Zr}^{4+} = 0.72 Å , CN = 6), as a result, it may be expected that substituting Ti^{4+} and Zr^{4+} ions with Fe^{3+}, Ni^{2+}, Cu^{2+}, and Zn^{2+} ions will have a minor effect on the unit cell dimensions [344, 437]. An increase in crystallinity is indicated by an increase in peak intensity and a reduction in their full width at half maximum (FWHM). By using the renowned Debye-Scherrer's equation and the strongest diffraction peaks that correspond to (110) for the BCZTO and (311) for the $NCZFe_{2-x}O_{4-3x/2}$, the mean crystallite diameter perpendicular to crystal plane directions, or volume of coherently diffracting domains [438], for the BCZTO and $NCZFe_{2-x}O_{4-3x/2}$ phases were quantitatively calculated. For the BCZTO and $NCZFe_{2-x}O_{4-3x/2}$ phases, the average crystallite diameter perpendicular to crystal plane directions, or the volume of coherently diffracting domains [438], was quantitatively calculated from the XRD peak broadening accounting the strongest diffraction peak corresponding to (110) for the BCZTO phase and the strongest diffraction peak equivalent to (311) for the $NCZFe_{2-x}O_{4-3x/2}$ phase, respectively, utilizing Debye-Scherrer's formula [439]: $D_{SC} = \frac{0.94\times\lambda_{Cu-K_\alpha}}{\Delta(2\theta)\times cos\theta_{hkl}}$, where D_{SC} denotes the mean crystallite diameter and $\Delta(2\theta)$ denotes the width of strongest peaks (110) and (311) equivalent to half maximum height. Table 4.24 shows the values for the computed average crystallite diameter (D_{SC}). Table 4.24 shows that the value of D_{SC} of $NCZFe_{2-x}O_{4-3x/2}$ rises in x = 0.04 and then drops in x = 0.08 before rising again in x = 0.12 and y = 0.2, whilst the IDNS phase enhances with an upturning to a maximum of x = 0.08 and then drops in x = 0.12 and y = 0.5. If y = 0.2, the value of D_{SC} for BCZTO phase decreases in x = 0.12, whereas the IDNS phase enhances with an upturing for x = 0.08 and drops in x = 0.12 and y = 0.5. As a result, it is shown that the D_{SC} values of the component

phases fluctuate arbitrarily with IDNS. This distinctive trait could be caused by the micromorphological faults in the ferroelectromagnetic composite ceramics, e.g., lattice deformation, oxygen vacancies, and cation reallocation [440]. To put it another way, the state of reaction could initially slow the development of grains as IDNS rises and afterwards accelerate up the creation of brand-new nuclei thereby accelerating the creation of particles as IDNS rises even higher, may be correlated with the non-systematic variation of with IDNS [441].

4.4.2. Densification and porosity investigations

In controlling the electromagnetic characteristics of polycrystalline materials, density plays a critical role. Grain growth and densification are connected, according to Lange and Kellet [201]. The diffusion or migration of the grain border controls the development and densification of the grain [442]. The bulk density (ρ_{bulk}) of the ferroelectromagnetic composite ceramics is calculated employing the formula: $\rho_{\text{bulk}} = \frac{\text{Mass of the sample pellet specimen}}{\text{Volume of the pellet specimen}} = \frac{4\times m}{\pi\times D^2\times e}$, where m denotes the mass, D denotes diameter and, e denotes the thickness and presented in Table 4.44-4.45. Figure 4.51 illustrates the impact of IDNS on ρ_{bulk} value: (a) x = 0.0–0.12; y = 0.2 and (b) x = 0.0; 0.04; 0.08; 0.12; y = 0.5. From Table 4.44-4.45 and Figure 4.51, it is clear that the results showed that ρ_{bulk} increases as the IDNS increases to a maximum of x = 0.08 and then drops in x = 0.12 at y = 0.2. On the other hand, when the IDNS increases to x = 0.08, the value of ρ_{bulk} decreases, and if y = 0.5 comes along, it increases in x = 0.12. The sintering process, atomic mass of $NCZFe_{2-x}O_{4-3x/2}$, and heterogeneous architecture of the ferroelectromagnetic composite ceramics may all be responsible for the non-systematic change of ρ_{bulk} value [443]. The increase in ρ_{bulk} value is linked to the reduction in porosity and enhancement of particle diameter. In other words, an increase in ρ_{bulk} value may be attributed to the oxygen ion's acceleration of ionic diffusion [444]. The decrease in molecular mass of the ferroelectromagnetic composite ceramics may be substantiated by the decrease in ρ_{bulk} value

with IDNS [445]. The value of ρ_{bulk} is larger at x = 0.0; 0.04; 0.08; 0.12; y = 0.5 ferroelectromagnetic composite ceramics than at x = 0.0; 0.04; 0.08; 0.12; y = 0.2 ferroelectromagnetic composite ceramics because the value of ρ_{bulk} for $NCZFe_{2-x}O_{4-3x/2}$ is higher than the ρ_{bulk} value for BCZTO. Smit and Wijn's formula [185]: $\rho_{\text{X-ray}}: \frac{Z \times M_W}{N_A \times V}$, where is Z = the number of atoms per unit cell, for BCZTO (Z = 1 and Z = 8 for $NCZFe_{2-x}O_{4-3x/2}$; M = molecular mass; N = Avogadro's number; and V = a^2c and a^3 are the unit cell volume of BCZTO and $NCZFe_{2-x}O_{4-3x/2}$ phases is employed to compute the theoretical density ($\rho_{\text{X-ray}}$) of the component phases. The $NCZFe_{2-x}O_{4-3x/2}$ phase is discovered to have a higher (ρ_{X-ray}) value than the BCZTO phase. The $NCZFe_{2-x}O_{4-3x/2}$ phase is therefore regarded to be denser than the BCZTO phase. The BCZTO phase may experience stress as a result of the $NCZFe_{2-x}O_{4-3x/2}$ phase [446]. The theoretical density (ρ_{X-ray}) of ferroelectromagnetic composite ceramics was calculated employing formula [447]: $\rho_{\text{X-ray}}(\text{composite}) = (1-y)\left[\frac{M_{\text{FE}}}{N_A \times V_{\text{FE}}}\right] + (y)\left[\frac{8 \times M_{\text{F}}}{N_A \times V_{\text{F}}}\right]$, where M_{FE} and M_{F} are the molecular mass, and V_{FE} and V_{F} the are cell volume of the BCZTO and $NCZFe_{2-x}O_{4-3x/2}$ phases. For each of the examined ferroelectromagnetic composite ceramics, the computed values of $\rho_{\text{X-ray}}$ are shown in Table 4.44–4.45. In Figure 4.51, the IDNS-dependent $\rho_{\text{X-ray}}$ value of ferroelectromagnetic composite ceramics is shown. x = 0.0; 0.04; 0.08; 0.12; y = 0.2 in (a) and (b) and x = 0.0; 0.04; 0.08; 0.12; y = 0.5. The $\rho_{\text{X-ray}}$ value changes directly with atomic mass and inversely with the cubic lattice constant. We can see that in y = 0.2 and 0.5, $\rho_{\text{X-ray}}$ value drops with increasing IDNS in Table 4.44-4.45 and Fig. 4.51 (a, b). The discrepancy in density in the midst of the $NCZFe_{2-x}O_{4-3x/2}$ ferrite phase and the BCZTO perovskite phase, as well as the decrease in composition's atomic mass of the ferroelectromagnetic composite ceramics with an upswing of IDNS, account for the lowering trend of $\rho_{\text{X-ray}}$ with an increasing IDNS [448]. Table 4.44-4.45 show that the ρ_{bulk} value is less substantial than the $\rho_{\text{X-ray}}$ value. The mismatch in the midst of the ρ_{bulk} and $\rho_{\text{X-ray}}$ values

of the BCZTO and NCZ$Fe_{2-x}O_{4-3x/2}$ phases, as well as the continuance of pores produced during the sample's fabrication and the sintering procedure, may be responsible for this variance in ρ_{bulk} and $\rho_{\mathrm{X-ray}}$ values [449]. The formula: $\mathrm{P}\ (\%) = \frac{\rho_{\mathrm{X-ray}} - \rho_{\mathrm{bulk}}}{\rho_{\mathrm{X-ray}}} \times 100$ was used to calculate porosity (P %). Calculated porosity for each of the examined ferroelectromagnetic composite ceramics is shown in Table 4.44-4.45. Actually, the porosity may also be impacted by the sintering circumstances and particle diameter distribution [450, 451]. When the grains are large enough, they can decrease the porosity whereas grains that are too tiny can contribute to filling pores or gaps [452]. Figure 4.51 (a, b) depicts the change in porosity with IDNS in x = 0.0; 0.04; 0.08; 0.12; y = 0.2 and x = 0.0; 0.04; 0.08; 0.12; y = 0.5 ferroelectromagnetic composite ceramics. It is generally agrred that porosity (P %) results from the interplay amongst the intragranular (P_{intra}) and intergranular (P_{inter}) porosity, reliant on whether pores are located on grain borders or within component grains [362]. The growth of the grains determines the intergranular porosity (P_{inter}), whilst the T_s and ionic radius determine the intragranular porosity (P_{intra}) [453]. Contrary to intragranular porosity, intergranular porosity has no effect on magnetic permeability [362]. As can be seen from Figure 4.51 (a) and Table 4.44-4.45, the porosity decreases as the IDNS increases in x = 0.08 and afterwhich increases in x = 0.12 and y = 0.2. Conversely, if y = 0.5, the porosity increases in x = 0.04 and then decreases with IDNS to a maximum of x = 0.12. The increase in porosity causes the pores to open up more, the densification to be worse, and the particle adhesion to be inhibited. The decrease in porosity is a sign of smaller pores and increased densification. Due to the reduction in average crystallite diameter, the decline in porosity may also be attributed to the decline in P_{inter} value. In conclusion, the increase in P_{tot} value in x = 0.12 and y = 0.2 and x = 0.04 and y = 0.5 could be supported by the increase in P_{intra} owing to the noticeable increase in the lattice constant, whereas P_{inter} plays an insignificant role as a result of the little reduction in grain diameter [454].

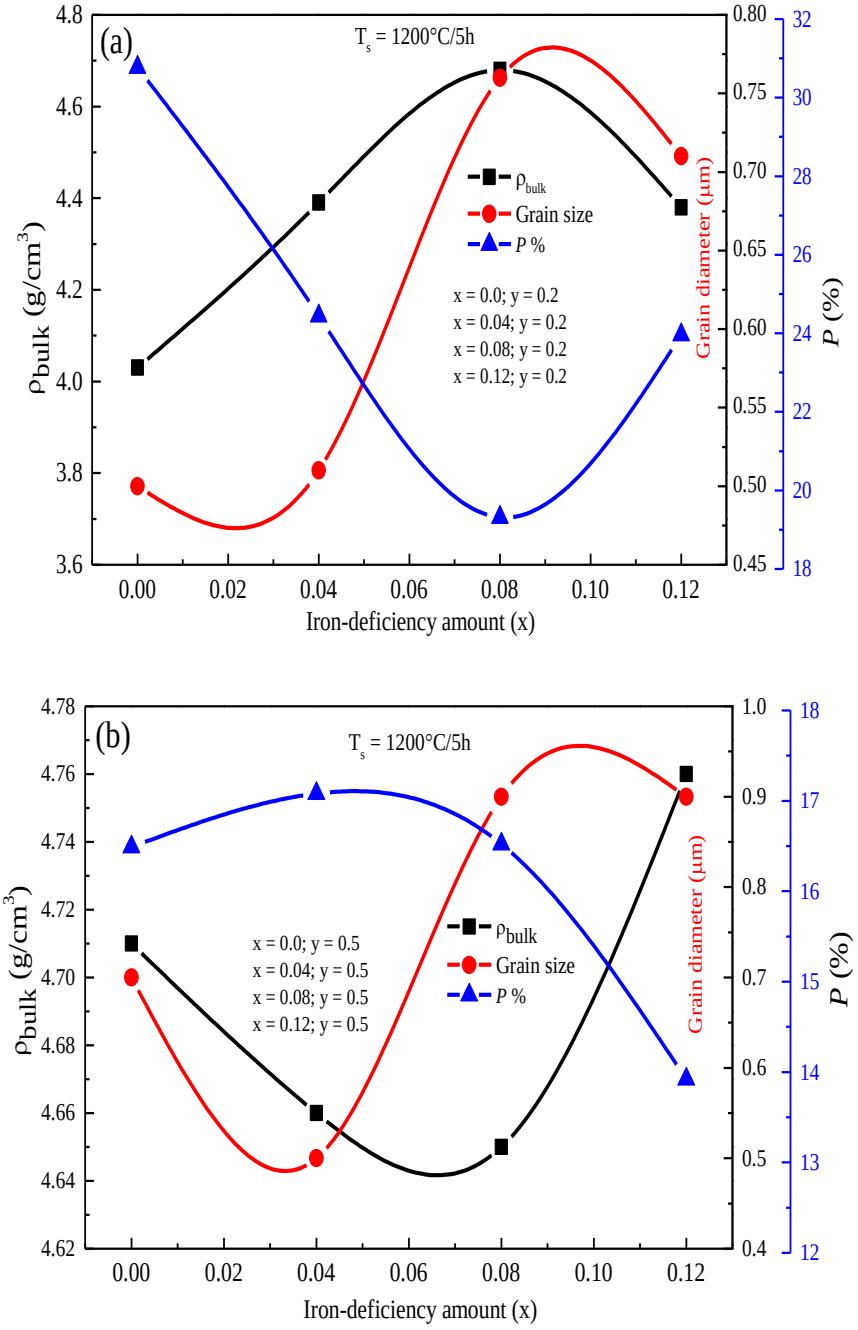

Figure 4.51: Evolution of bulk density, porosity, and grain diameter with IDNS of (1-*y*) [BCZTO] + (*y*) [NCZFe$_{2-x}$O4$_{-3x/2}$] (*x* = 0.0; 0.04; 0.08; 0.12; *y* = 0.2; 0.5) ferroelectromagnetic composite ceramics: (a) *x* = 0.0; 0.04; 0.08; 0.12; *y* = 0.2 and (b) *x* = 0.0; 0.04; 0.08; 0.12; *y* = 0.5.

Table 4.44. Lattice constant (a), cell volume (V), bulk density (ρ_{bulk}), theoretical density (ρ_{X-ray}), porosity (P %), grain diameter (D_{SEM}), and crystallite diameter of the component phases of (1-y) [BCZTO] + (y) [NCZFe$_{2-x}$O$_{4-3x/2}$] (x = 0.0; 0.04; 0.08; 0.12; y = 0.2) ferroelectromagnetic composite ceramics

Composition		Lattice constant (Å)				Unit cell volume (Å^3)		ρ_{bulk} (g/cm^3)	ρ_{X-ray} (g/cm^3)	R. D. (%)	P (%)	D_{SEM} (μm)	(D_{hkl}) (nm)	
		Ferrite phase	Ferroelectric phase			Ferrite phase (a^3)	Ferroelectric phase (a^{2}c)						Ferrite phase	Ferroelectric phase
		a	a	c	c/a									
x	y													
0.0	0.2	8.3867	3.9967	3.9941	0.9993	589.89	63.80	4.03	5.82	69	31	0.50	48.4	24.3
0.04	0.2	8.3937	3.9956	3.9896	0.9985	591.37	63.69	4.39	5.81	76	24	0.51	60.5	27.6
0.08	0.2	8.3887	3.9967	3.9895	0.9982	590.32	63.73	4.68	5.80	81	19	0.76	59.7	26.5
0.12	0.2	8.3977	3.9990	3.9973	0.9996	592.22	63.93	4.38	5.76	76	24	0.71	67.5	26.0

Table 4.45. Lattice constant (a), cell volume (V), bulk density (ρ_{bulk}), theoretical density (ρ_{X-ray}), porosity (P %), grain diameter (D_{SEM}), and crystallite diameter of the component phases of (1-y) [BCZTO] + (y) [NCZFe$_{2-x}$O$_{4-3x/2}$] (x = 0.0; 0.04; 0.08; 0.12; y = 0.5) ferroelectromagnetic composite ceramics

Composition		Lattice constant (Å)				Unit cell volume (Å^3)		ρ_{bulk} (g/cm^3)	ρ_{X-ray} (g/cm^3)	R. D. (%)	P (%)	D_{SEM} (μm)	(D_{hkl}) (nm)	
		Ferrite phase	Ferroelectric phase			Ferrite phase (a^3)	Ferroelectric phase (a^{2}c)						Ferrite phase	Ferroelectric phase
		a	a	c	c/a									
x	y													
0.0	0.5	8.3957	4.0041	3.9934	0.9973	591.79	64.03	4.71	5.64	83	17	0.70	64.5	25.8
0.04	0.5	8.3917	4.0008	3.9844	0.9959	590.95	63.78	4.66	5.62	83	17	0.50	65.0	26.6
0.08	0.5	8.3967	4.0024	3.9916	0.9973	592.01	63.94	4.65	5.57	83	17	0.90	69.7	27.5
0.12	0.5	8.3911	4.0026	3.9969	0.9986	590.82	64.03	4.76	5.53	86	14	0.90	58.1	26.5

4.4.3. Micromorphological investigation

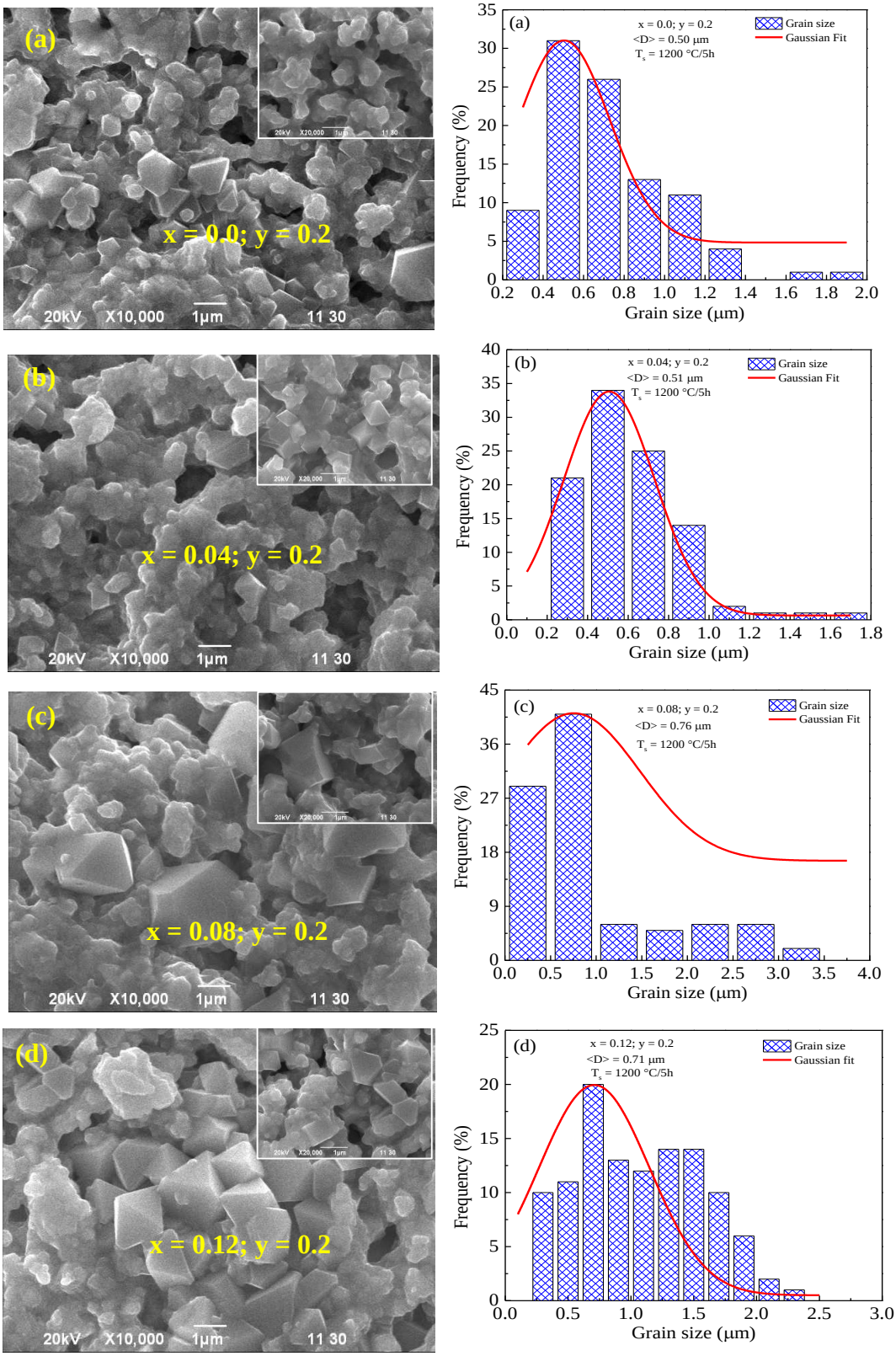

Figure 4.52: Micromorphological structures and histograms of (1-*y*) [BCZTO] + (*y*) [$NCZFe_{2-x}O_{4-3x/2}$] (*x* = 0.0; 0.04; 0.08; 0.12; *y* = 0.2; 0.5) ferroelectromagnetic composite ceramics: (a) *x* = 0, *y* = 0.2, (b) *x* = 0.04, *y* = 0.2, (c) *x* = 0.08, *y* = 0.2, and (d) *x* = 0.12, *y* = 0.2.

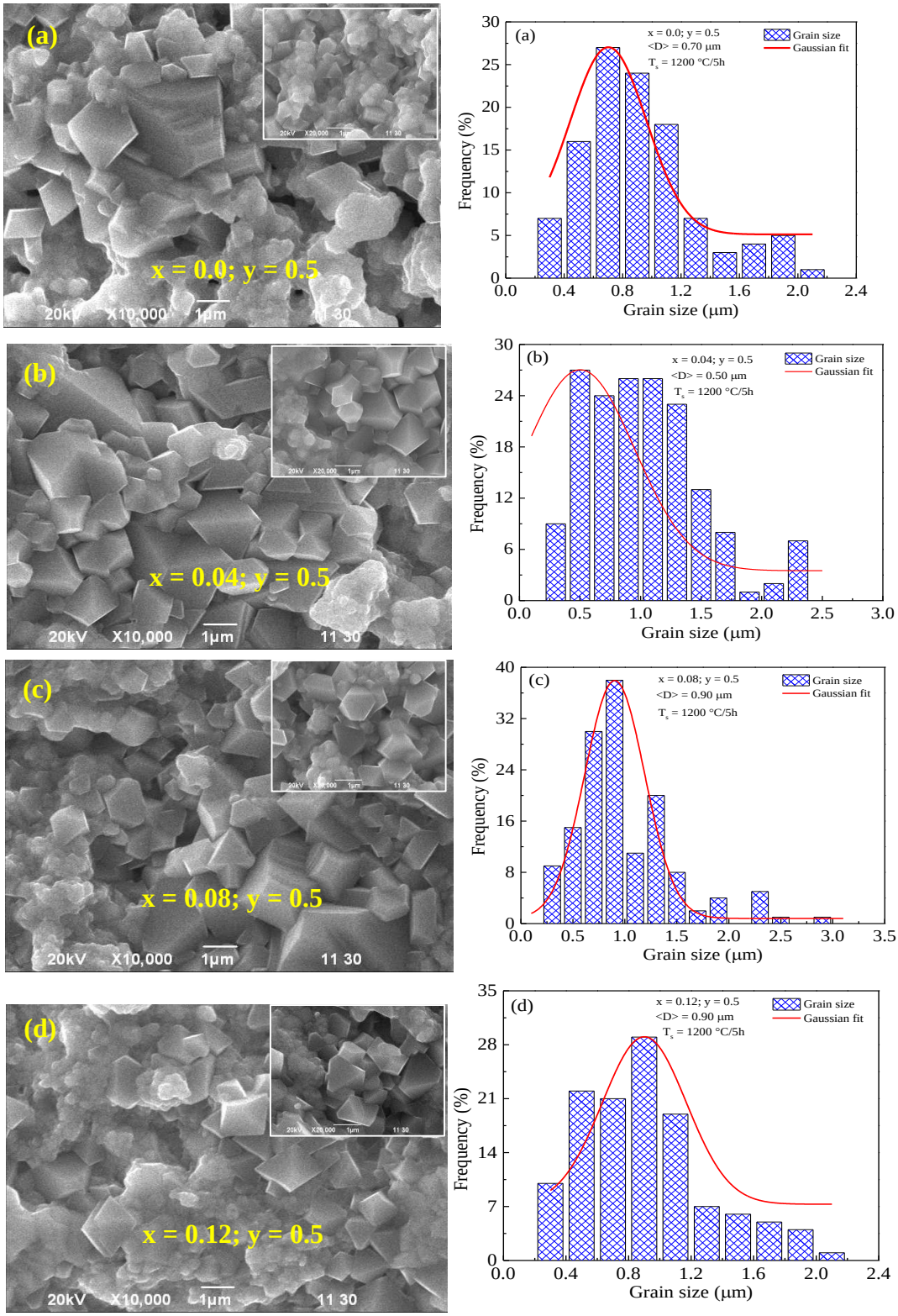

Figure 4.53: Micromorphological structures and histograms of (1-*y*) [BCZTO] + (*y*) [NCZFe$_{2-x}$O$_{4-3x/2}$] (*x* = 0.0; 0.04; 0.08; 0.12; *y* = 0.2; 0.5) ferroelectromagnetic composite ceramics: (a) *x* = 0, *y* = 0.5, (b) *x* = 0.04, *y* = 0.5, (c) *x* = 0.08, *y* = 0.5, and (d) *x* = 0.12, *y* = 0.5.

Ferroelectromagnetic composite ceramics' electromagnetic characteristics are heavily influenced by the microstructure and crystal particle morphology of the crystal particles. Figure 4.52 shows the typical micromorphology of (1-y) [BCZTO] + (y) [$NCZFe_{2-x}O_{4-3x/2}$] ferroelectromagnetic composite ceramics: (a) x = 0.0; y = 0.2, (b) x = 0.04; y = 0.2, (c) x = 0.08; y = 0.2, and (d) x = 0.12; y = 0.2. As opposed to this, Fig. 4.53 shows the micromorphological structures of ferroelectromagnetic composite ceramics: (a) x = 0.0; y = 0.5, (b) x = 0.04; y = 0.5, (c) x = 0.08; y = 0.5, and (d) x = 0.12; y = 0.5. Figures 4.52 (a-d) and 4.53 (a-d) demonstrate that the ferroelectromagnetic composite ceramics have irregular polygonal grains with an uneven distribution and limited pores. The emergence of grains and the continuance of pores immediately influence the dielectric characteristics. The allocation of grains is not properly separated from one another, which makes it challenging to discern BCZTO and $NCZFe_{2-x}O_{4-3x/2}$ grains from SEM pictures [455]. Since the grain diameter heavily depends on the nucleation mechanism and grain growth kinetics at the time of fabrication [456, 457], different grains for various materials are often formed [456, 457]. The development of pores on the surface of ferroelectromagnetic composite ceramics is attributed to a number of factors [458, 459]: (i) the pellet specimen's compaction pressure may not be high enough; and (ii) PVA's intense volatilization and intense burning might result in gases like CO_2 when the the sintering is taking place. Pores are created by the quick expulsion of these gases from the ferroelectromagnetic composite ceramics bodies, and (iii) additional grain borders in the midst of the BCZTO and $NCZFe_{2-x}O_{4-3x/2}$ phases are created during synthesis, which might hamper grain development. Increased grain borders might result in increased pore formation. Both faster grain development at a high T_s and the loss probability of zinc, which is given by the equation [275]: $ZnO \rightarrow Zn + \left(\frac{1}{2}\right) O_2$, may have contributed to the formation of pores since they caused the pores to be trapped inside the grain [276]. Additionally, pores may have been generated by the formation of oxygen vacancies [460]. Because of their magnetic properties and the cohesiveness of the microparticles, the various particles aggregate and form clusters at higher T_s and weaker

Vander Waals interactions [461-463]. Figure 4.52 (a, b) shows how the grain diameter depends on IDNS level in x = 0.0; 0.04; 0.08; 0.12; y = 0.2 and x = 0.0; 0.04; 0.08; 0.12; y = 0.5 ferroelectromagnetic composite ceramics. Table 4.24 and Figure 4.52 (a) show that when the IDNS increases to a maximum of x = 0.08 and then decreases in x = 0.12 and y = 0.2, the grain diameter improves. In contrast, the grain diameter increases until x = 0.04 and then drops till x = 0.12 in y = 0.5. According to a mismatch in the midst of grain growth and grain border diffusion of the component phases, the asymmetrical shift in grain growth has occurred [464]. We note that $D_{SEM} \gg D_{SC}$ in Table 4.44-4.45 and Figure 4.52 (a, b). This is due to the fact that each grain examined by a scanning electron microscope (SEM) is made up of a collection of much smaller crystallites, yet X-rays have a resolution that is much greater [465].

4.4.4. Fourier-transform infrared spectroscopic investigation

Analyzing the location and value of the absorption peak is crucial to comprehend the kind of crystal structure, changes in chemical bonding, and molecular structure in ferroelectromagnetic composite ceramics. The FTIR spectra of the (1-y) [BCZTO] + (y) [$NCZFe_{2-x}O_{4-3x/2}$] ferroelectromagnetic composite ceramics are shown in Figure 4.54 as (a) x = 0.0; 0.04; 0.08; 0.12; y = 0.2 and (b) x = 0.0; 0.04; 0.08; 0.12; y = 0.5, respectively. The FTIR spectrum may be separated into two domains: (i) the domain (4000-1500 cm^{-1}), where we want to find out what functional groups are present in the materials, and (ii) the domain (1500-400 cm^{-1}), where we want to assess the spectral matching/molecular fingerprint [189, 466]. The cation mass, cation-oxygen distance, bonding force, preparation process, grain diameter, and sintering conditions are only a few of the variables that affect how the vibrational bands emerge [467, 468]. Table 4.46 lists the basic bands of each phase along with their assigned positions. Waldron [134] asserts that ferromagnetic substances consistently consist of bonded crystals, demonstrating that they are related to all of their encircling neighbors through identical forces that might be Van der Waal's type, ionic or covalent [134]. Table 4.46 and Figure 4.54 (a, b)

reveal that the FTIR bands were visible in the fingerprint region. The wavenumber band was observed at frequencies of 660-646 cm^{-1} in y = 0.2 and 648-618 cm^{-1} in y = 0.5. These frequencies are typically referred to as higher wavenumber band (ν_1) and correspond to basic stretching of metal-oxygen bonding at tetrahedrally coordinated site ($M_{\text{tetra}} \leftrightarrow O$), while the wavenumber band was observed at frequencies of 503-488 cm^{-1} in y = 0.2 and 496-486 cm^{-1} (known as low frequency (ν_2)) in y = 0.5 that associated with the intrinsic stretching of metal-oxygen bonding at tetrahedrally coordinated site ($M_{\text{octa}} \leftrightarrow O$) [134].

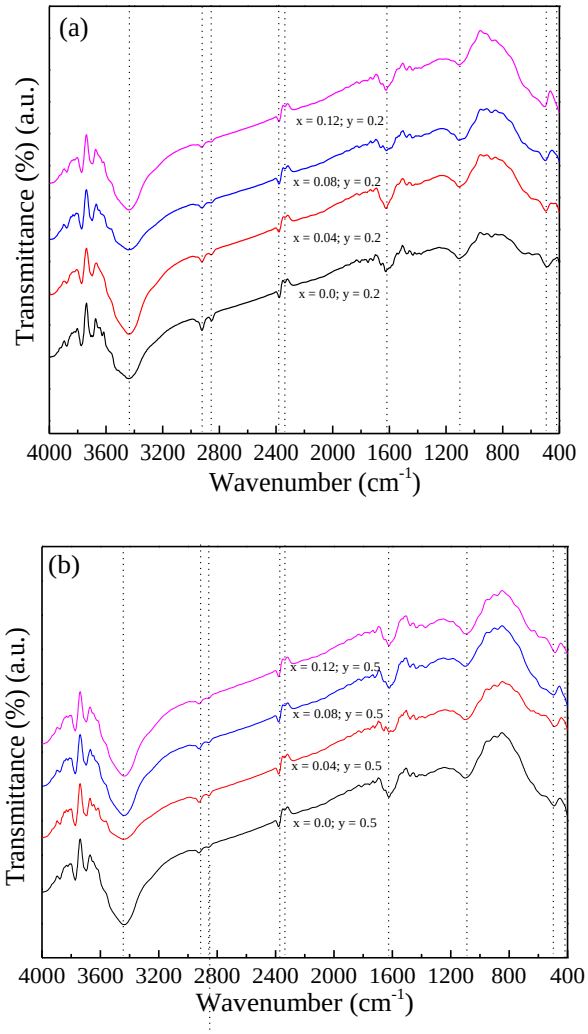

Figure 4.54: FTIR spectra of (1-y) [BCZTO] + (y) [NCZFe$_{2-x}$O$_{4-3x/2}$] ferroelectromagnetic composite ceramics: (a) x = 0.0; 0.04; 0.08; 0.12; y = 0.2 and (b) x = 0.0; 0.04; 0.08; 0.12; y = 0.5.

In y = 0.2 and 0.5, it can be shown that when the IDNS rises, the higher wavenumber band (ν_1) drifts toward the higher frequency side. If y = 0.2, the IDNS rises and the low frequency band (ν_2) advances nearer the higher frequency side. The low frequency band (ν_2), on the other hand, first progresses toward the higher frequency side in x = 0.08, afterwhich gradually progresses to low wavenumber side in x = 0.04 and y = 0.5. The placements and intensities of the two basic bands (ν_1 and ν_2) of the different phases are discovered to differ. The typical metal-oxygen distances, the differing tetrahedrally and octahedrally coordinated bond distances, mass of the cations, the radius of ions, the force constant at the tetrahedrally and octahedrally coordinated sites, the electronegativity, and the the forces that bind may all be used to explain this discrepancy [469, 470]. The discrepancy in bond distance at the A and B sites, as well as the cation's reallocation or transfer amongst the A and B sites in the NCZ$Fe_{2-x}O_{4-3x/2}$ ferrites, may all be used to support the difference in band locations for these materials. From Fig. 4.54 (a, b) and Table 4.46, it can be deduced that the basic bands for BCZTO also exhibit a fingerprint area linked to metal-oxygen bonding, such as Ba-O, Ca-O, Ti-O, and Zr-O [435, 471,472]. The higher wavenumber band (ν_1), which is connected with the metal-oxygen vibrational bonding and is seen to reside in the midst of 445 and 432 cm^{-1} in y = 0.2 and 432-428 cm^{-1} in y = 0.5, is the lattice vibration of the dipole $[(Ba, Ca)^{2+}]$-$[Zr/TiO_3]^{2-}$ [473, 474]. In contrast, the low wavenumber band (ν_2) is found to lie in the midst of 599 and 589 cm^{-1} in y = 0.2 and 602-577 cm^{-1} in y = 0.5. This is supported by the inherent asymmetric and symmetric stretching and bending vibrational modes of the Ti-O and Zr-O ($[TiO_6]^{2-}$ and $[ZrO_6]^{2-}$) octahedron bonding, featuring with its lattice deformation [347, 475]. The high wavenumber band (ν_1) shifts from the low wavenumber side in x = 0.08 to the high wavenumber side in x = 0.12 at y = 0.2. It initially progresses to high wavenumber side in x = 0.04 and afterwhich progresses to low wavenumber side in x = 0.08. The high wavenumber band (ν_1) progresses to low wavenumber side in x = 0.04 at y = 0.5, afterwhich progresses to high wavenumber side in x = 0.08, and finally progresses toward the lower wavenumber side

in x = 0.12. In y = 0.2 and 0.5, the IDNS rises and the low wavenumber band (ν_2) progresses to high wavenumber edge. Therefore, it can be determined that the ferroelectromagnetic composite ceramics were effectively developed. The equation [476]: $k_{t/o} = 4\pi^2 c^2 \nu_{t/o}^2 \mu$ is used to calculate the force constant (k) for Fe/Ti/Zr-O, where ν denotes the wavenumber for the corresponding vibrational frequency of metal-oxygen ions, μ is the reduced mass, and c stands for the speed of light. The equation [290, 477]: $\mu = \left[\frac{M_O \times M_{Fe}}{M_O + M_{Fe}}\right] \times 1.6605 \times 10^{-27}$ kg, where M_O and M_{Fe} are the masses of Fe^{3+} and O^{2-}, was used to calculate the reduced mass (μ) for the $NCZFe_{2-x}O_{4-3x/2}$ phase. The formula [140, 150]: $\mu = \frac{M_O \times [0.9M_{Ti} + 0.1M_{Zr}]}{M_O + [0.9M_{Ti} + 0.1M_{Zr}]} \times 1.6605 \times 10^{-27}$ kg, where, M_O, M_{Ti} and M_{Zr} are the atomic mass of O, Ti, and Zr, was used to determine the reduced mass (μ) of Zr/Ti-O ions for the BCZTO. Table 4.46 contains the calculated force constants for the phases BCZTO and $NCZFe_{2-x}O_{4-3x/2}$. It is evident that K_T value in the $NCZFe_{2-x}O_{4-3x/2}$ phase is bigger than K_O value, suggesting that the band frequency related to the tetrahedrally coordinated (A)-site is larger than that of the octahedrally coordinated (B)-site. Since the IDNS rises in y = 0.2 and 0.5, Table 4.46 shows that the k value for the tetrahedrally coordinated (A)-site increases, but the k value for the octahedrally coordinated (B)-site increases in x = 0.04, then stays steady in x = 0.08, and finally increases in x = 0.12 at y = 0.2. In addition, the k value for the octahedrally coordinated (B)-site rises for x = 0.04, then rises again in x = 0.08, before decreasing in x = 0.12 and y = 0.5. Similar to the BCZTO phase, at y = 0.2 and 0.5, the k value of stretching mode vibration (Zr/Ti-O) rises on rising IDNS level. In contrast, the k value for the Zr/Ti-O bending mode vibration increases in x = 0.04, then drops in x = 0.08, and finally increases in x = 0.12 and y = 0.2. Additionally, the bending vibrational mode (Zr/Ti-O) k value decreases in x = 0.04, rises in x = 0.08, and finally decreases in x = 0.12 and y = 0.5. The increase and decrease in bond length may be used to support the increment and decrease in k that occurs while IDNS is on the rise. According to IDNS observations, the k value fluctuates randomly and is connected with the redistribution of the

cation in the midst of the tetrahedrally and octahedrally coordinated (A and B)-sites [435, 478-480]. According to relation [435, 477]: $r = \left(\frac{17}{k}\right)^{1/3}$, the bond distances ($r$) of the stretching and bending vibration of Fe-O for the $NCZFe_{2-x}O_{4-3x/2}$ and Zr/Ti-O for the BCZTO was determined. Table 4.49 shows the bond lengths that were computed. From Table 4.49, it is noticeable that r value for the tetrahedrally coordinated (A)-site decreases with rising IDNS level in y = 0.2 and 0.5, but r value for the octahedrally coordinated (B)-site decreases in x = 0.04 and then rises somewhat in x = 0.08 before decreasing in x = 0.12 and y = 0.2. Conversely, at x = 0.04, r value of the octahedrally coordinated (B)-site increases. This increase is followed by a fall at x = 0.08 and a last increase at x = 0.12 with y = 0.5. It's possible that a rise in IDNS and an increase or reduction in r will result in changes in the force constant. Table 4.47-4.48 provide a summary of the functional group bands that are assigned to the FEMCC component phases and their corresponding functional group bands.

Table 4.46. FTIR wavenumber bands for the component phases along their assignments and force constants of (1-*y*) [BCZTO] + (*y*) [$NCZFe_{2-x}O_{4-3x/2}$] (*x* = 0.0; 0.04; 0.08; 0.12; *y* = 0.2, 0.5) ferroelectromagnetic composite ceramics

Composition		FTIR wavenumber bands (cm^{-1})											
		$NCZFe_{2-x}O_{4-3x/2}$ phase						BCZTO phase					
		FTIR bands		Assignment		Force constant ($\times 10^5$) (dynes/cm)		FTIR bands		Assignment		Force constant ($\times 10^5$) (dynes/cm)	
x	y	ν_T (cm^{-1})	ν_O (cm^{-1})	ν_T (cm^{-1})	ν_O (cm^{-1})	K_T	K_O	Stretching mode ν_1 (cm^{-1})	Bending mode ν_2 (cm^{-1})	ν_1 (cm^{-1})	ν_2 (cm^{-1})	K_T	K_O
0.0	0.2	645.77	487.99	Due to the intrinsic stretching vibrations of the M-O ions at A-site	Due to the intrinsic stretching vibrations of the M-O ions at the B-site	3.06	1.75	588.93	431.67	Due to the Ti-O or Zr-O stretching vibration of Zr/TiO_6 octahedrally coordinated B-site	Due to the Ti-O-Ti or Zr-O-Zr bending vibration of Zr/TiO_6 octahedrally coordinated B-site	2.51	1.35
0.04	0.2	650.98	497.20			3.11	1.81	597.25	444.85			2.58	1.43
0.08	0.2	658.30	496.57			3.18	1.81	598.26	442.29			2.59	1.41
0.12	0.2	659.68	503.42			3.19	1.86	598.90	444.39			2.59	1.43
0.0	0.5	618.12	491.85			2.80	1.77	576.93	432.40			2.40	1.35
0.04	0.5	618.31	489.92			2.81	1.76	581.42	429.75			2.44	1.33
0.08	0.5	640.00	495.71			3.01	1.80	586.82	432.31			2.49	1.35
0.12	0.5	648.42	486.06			3.08	1.73	601.92	427.64			2.62	1.32

Table 4.47. FTIR wavenumber bands due to the presence of functional groups and their assignments of (1-*y*) [BCZTO] + (*y*) [NCZ$Fe_{2-x}O_{4-3x/2}$] (*x* = 0.0; 0.04; 0.08; 0.12; *y* = 0.2) ferroelectromagnetic composite ceramics

Wavenumber (cm^{-1})				Assignments
x = 0.0; y = 0.2	x = 0.04; y = 0.2	x = 0.08; y = 0.2	x = 0.12; y = 0.2	
3774.69-3439.08	3772.76-3437.15	3772.76-3444.87	3772.76-3437.15	Assigned to O-H stretching vibrations due to physically adsorbed H_2O molecules
2854.65-2922.16	2855.58-2922.16	2858.51-2922.16	2858.51-2924.09	Assigned to C-H stretching vibration
2379.20	2379.20	2379.20	2379.20	Assigned to the asymmetric stretching vibration of free CO_2 absorbed from the atmosphere
1624.06	1624.06	1622.13	1624.06	Assigned to O-H the deformation mode and bending vibration of physically adsorbed water molecules
1435.04	1435.20	1435.20	1435.20	Assigned to the symmetric stretching vibration of C = O
1109.07	1107.14	1107.14	1109.07	Assigned to out of plane bending vibrations of O-H stretching of the absorbed water molecules

Table 4.48. FTIR wavenumber bands due to the presence of functional groups and their assignments of (1-*y*) [BCZTO] + (*y*) [$NCZFe_{2-x}O_{4-3x/2}$] (*x* = 0.0; 0.04; 0.08; 0.12; *y* = 0.5) ferroelectromagnetic composite ceramics

Wavenumber (cm^{-1})				Assignments
x = 0.0; y = 0.5	x = 0.04; y = 0.5	x = 0.08; y = 0.5	x = 0.12; y = 0.5	
3772.76-3437.15	3772.76-3446.79	3772.76-3433.29	3772.76-3433.29	Assigned to O-H stretching vibrations due to physically adsorbed H_2O molecules
2860.43-2924.09	2856.58-2924.09	2858.51-2924.09	2859.20-2926.40	Assigned to C-H stretching vibration
2376.0	2376.0	2376.0	2376.0	Assigned to the asymmetric stretching vibration of free CO_2 absorbed from the atmosphere
1624.06	1622.13	1622.13	1624.06	Assigned to O-H the deformation mode and bending vibration of physically adsorbed water molecules
1438.40	1438.40	1438.40	1438.40	Assigned to the symmetric stretching vibration of C = O
1101.35	1097.5	1101.35	1099.43	Assigned to out of plane bending vibrations of O-H stretching of the absorbed water molecules

Table 4.49. Tetrahedrall and octahedrally coordinated bond lengths of (1-*y*) [BCZTO] + (*y*) [NCZFe$_{2-x}$O$_{4-3x/2}$] (*x* = 0.0; 0.04; 0.08; 0.12; *y* = 0.2; 0.5) ferroelectromagnetic composite ceramics

Composition		Bond-length (Å)			
		NCZFO phase		BCZTO phase	
x	y	Tetrahedrally coordinated site (A-site)	Octahedrally coordinated site (B-site)	Stretching vibration (Zr/Ti-O)	Bending vibration (Zr/Ti-O)
0.0	0.2	1.7711	2.1337	1.8920	2.3265
0.04	0.2	1.7616	2.1099	1.8748	2.2823
0.08	0.2	1.7485	2.1099	1.8723	2.2930
0.12	0.2	1.7467	2.0908	1.8723	2.2823
0.0	0.5	1.8243	2.1257	1.9205	2.3265
0.04	0.5	1.8221	2.1297	1.9099	2.3381
0.08	0.5	1.7809	2.1138	1.8971	2.3265
0.12	0.5	1.7673	2.1419	1.8652	2.3440

4.4.5. Dielectric permittivity analysis

The dispersion and interaction of the component phases determine the multiferroic ferroelectromagnetic composite ceramics' dielectric characteristics. According to Mott's hypothesis [243], the complex permittivity, ε^*, designated as: $\varepsilon^* = \varepsilon' - j\varepsilon''$, where the system's polarization is turned into stored potential energy, creating ionic, electronic, and dipolar polarization, and the real component of the electric permittivity (ε') reveals the dielectric material's great energy storage capacity [481], whereas, the imaginary component (ε'') is directly connected to the energy loss in dielectric materials.

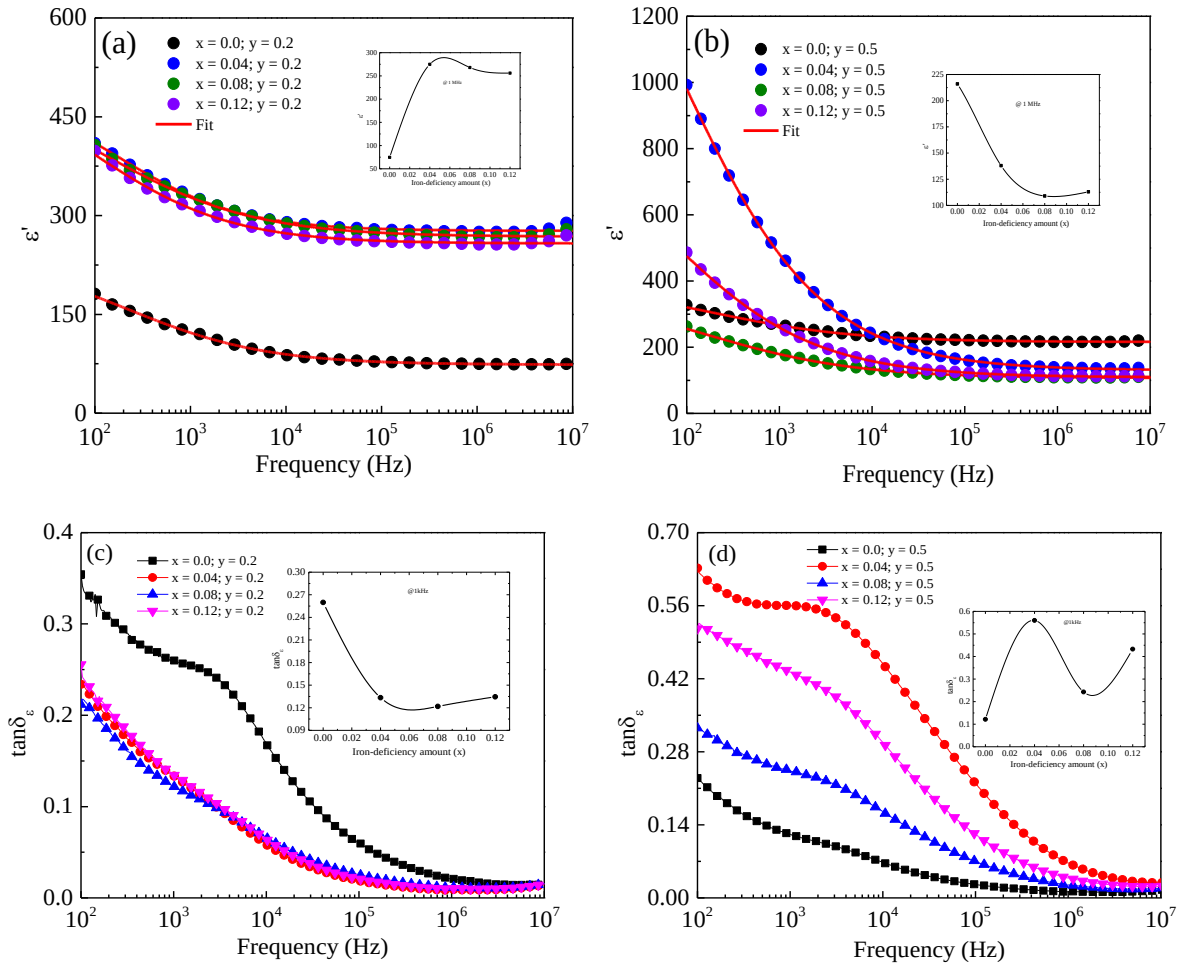

Figure 4.55: Evolution of the real component (ε') of electric permittivity with frequency: (a) x = 0.00-012; y = 0.2 and (b) x = 0.00-012; y = 0.5, and inset shows IDNS dependent ε' at 1 MHz, and (c, d) evolution of the permittivity loss tangent ($tan\delta_\varepsilon$) with frequency and inset shows IDNS dependent $tan\delta_\varepsilon$ at 1 kHz of (1-y) [BCZTO] + (y) [NCZFe$_{2-x}$O$_{4-3x/2}$] composites.

To clarify the mechanism regulating the dielectric characteristics, frequency evolution of ε' of (1-*y*) [BCZTO] + (*y*) [$NCZFe_{2-x}O_{4-3x/2}$] ferroelectromagnetic composite ceramics with various IDNS is shown in Figure 4.55: (a) x = 0.0; 0.04; 0.08; 0.12 and y = 0.2 and (b) x = 0.0; 0.04; 0.08; 0.12 and y = 0.5. On rising frequency to a maximum of 10 kHz, all ferroelectromagnetic composite ceramics display declining behavior that eventually becomes frequency-invariant at higher frequencies, simulating an expected dielectric dispersion. The benefits of electrical polarization with several components might explain this rising trend, which is known as: (i) electronic polarization (EP), (ii) ionic (or atomic) polarization (IP or AP), (iii) dipolar (or orientational) polarization (DP or OP), and (iv) space charge polarization (SCP) [482, 483]. Each polarization's contribution corresponds to a certain frequency. The associated polarization does not play a part in the overall polarization process when the frequency being used is higher than the intended frequencies. In actuality, the lower frequency side exhibits a particularly high effectiveness of the final two polarization processes. The higher frequency side is dominated by the other two polarization processes. In general, EP only occurs in the valence electrons of the outer layer of the atom, progresses at a frequency to a maximum of 10^{16} Hz [484-486], and is reversible as a result of the intense electron's attraction inside the atom's interior layer. In contrast, IP or AP occurs as a result of the interaction in the midst of negative and positive ions and occurs at a frequency of 10^{13} Hz [299, 484-486], and EP has a brief enactment and dissolution time of around 10^{-16}-10^{-15} s [484-486]. Since ions are heavier than electrons, they cannot be polarized fast in this situation. DP or OP generates because of the existence of molecules with persistent electric dipole moments that shift their rotational axis into the applied field's direction and it eventuates to a maximum of 10^{10} Hz [299, 484-486]. The enforcement and disintegration periods for IP are also small with a slight loss of energy and are approximately 10^{-13}-10^{-12} s [484-486]. SCP emerges at frequencies in the midst of 1 and 10^{3} Hz and may last for a few kilohertz and eventually materializes as a result of the charge carriers mobilization (hole and electron) being constrained by the intersection between two materials

or portions of the like material when a strong field is present [484-486]. DP takes longer than EP and IP that respectively take around 10^{-6}-10^{-2} s [484-486]. The dielectric trait, on the contrary hand, has been evaluated at low frequencies and is mainly confirmed through an interfacial SCP determined by the Maxwell-Wagner interfacial polarization, that is put on by the buildup of free charge at the grain/grain border intersections of ferroelectromagnetic composite ceramics or the ferroelectromagnetic composite ceramics /electrodes intersections [487], that agrees with Koop's notion [235, 488], whilst the others are unimportant [299]. According to Koop's idea [235], the ferroelectromagnetic composite ceramics are made up of two layers: the first layer is composed of microscopic crystals or grains that exhibit high conductivity, while the second layer is composed of grain borders that exhibit poor conductivity. The second thin layer is separated from the top layer. Highly conducting grains are very persuasive at higher frequency side compared to poorly conducting grain borders, which are very persuasive at lower frequency side. More ions, including Ba^{2+}, Ba^{3+}, Ca^{2+}, Ca^{3+}, Fe^{2+}, Fe^{3+}, Ni^{2+}, Ni^{3+}, Cu^{1+}, Cu^{2+}, Zn^{2+}, Zn^{3+}, Zr^{3+}, Zr^{4+}, Ti^{3+}, and Ti^{4+}, are affected in our ferroelectromagnetic composite ceramics by the operation of the alternating electric field. Due to the high resistance of the poorly conductive grain borders and interfaces at lower applied frequencies, all ions/charges have the opportunity to collect there. This leads to the development of interfacial space charge polarization and a high ε'value. Since certain of those charges are incapable to accurately detect the fast alteration in frequency of the applied field in accordance with their masses, charge accumulation is reduced at higher applied frequency windows [446, 489]. This is because some of these charges experience hopping in the midst of different ions, which results in a small and constant for ε' value. The Verwey de Bohr mechanism's jumping phenomena might potentially be used to explain dielectric dispersion [434]. In ferroelectromagnetic composite ceramics, the presence of the holes displacement takes place amongst Ba^{2+} and Ba^{3+} ($Ba^{3+} \leftrightarrow Ba^{2+} + e^{+}$ (hole jumping)), Ca^{2+} and Ca^{3+} ($Ca^{3+} \leftrightarrow Ca^{2+} + e^{+}$ (hole jumping)), Ni^{2+} and Ni^{3+} ($Ni^{3+} \leftrightarrow Ni^{2+} + e^{+}$ (hole jumping)), Cu^{2+} and Cu^{1+}

($Cu^{2+} \leftrightarrow Cu^{1+} + e^{+}$ (hole jumping)), Cu^{3+} and Cu^{2+} ($Cu^{3+} \leftrightarrow Cu^{2+} + e^{+}$ (hole jumping)), and Zn^{2+} and Zn^{3+} ($Zn^{3+} \leftrightarrow Zn^{2+} + e^{+}$ (hole jumping)) ions. Along with the electrons Fe^{2+} and Fe^{3+} ($Fe^{2+} \leftrightarrow Fe^{3+} + e^{-}$ (electron jumping)), Zr^{3+} and Zr^{4+} ($Zr^{3+} \leftrightarrow Zr^{4+} + e^{-}$ (electron jumping)), and Ti^{3+} and Ti^{4+} (according to $Ti^{3+} \leftrightarrow Ti^{4+} + e^{-}$ (electron jumping)), additionally, the regional migration of holes along the applied field's direction contribute to the net polarization. Additionally, the achievement of holes is less than the electronic exchange in the midst of Fe^{2+} and Fe^{3+} (according to $Fe^{2+} \leftrightarrow Fe^{3+} + e^{-}$ (electron jumping)), Zr^{3+} and Zr^{4+} ($Zr^{3+} \leftrightarrow Zr^{4+} + e^{-}$ (electron jumping)), and Ti^{3+} and Ti^{4+} ($Ti^{3+} \leftrightarrow Ti^{4+} + e^{-}$ (electron jumping)). Due to their lower mobility and the fact that they have the opposite sign from electrons, holes achieve polarization more quickly than electrons even in a low-frequency frame. In turn, this causes the total polarization to noticeably decline at low-frequency windows and then gradually decline at high-frequency windows (above 1 kHz) [490, 491]. Table 4.50-4.51 and 4.52-4.53 list the values of ε' and ε'' at particular frequencies of the ferroelectromagnetic composite ceramics with x = 0.0; 0.04; 0.08; 0.12; y = 0.2 and x = 0.0; 0.04; 0.08; 0.12; y = 0.5. As shown from Fig. 4.55 (a, b)'s inset in x = 0.0; 0.04; 0.08; 0.12; y = 0.2 and x = 0.0; 0.04; 0.08; 0.12; y = 0.5, ε' value at 1 MHz is graphed against IDNS level to explore the IDNS dependency of ε' for ferroelectromagnetic composite ceramics. From Figure 4.55 (a, b)'s inset, it is recognized that the ε' value rises in x = 0.04 and afterwhich decreases in x = 0.12 and y = 0.2, whilst ε' value reduces with rising IDNS level in x = 0.08 and then rises in x = 0.12 and y = 0.5. The decline in the concentration of the Fe^{2+} ion at the octahedrally coordinated position supports the correlation in the midst of the drop in ε' value and an increase in IDNS. The polarization decreases because the electron exchange in the midst of the ions Fe^{2+} and Fe^{3+}, Zr^{3+} and Zr^{4+}, and Ti^{3+} and Ti^{4+} is hindered. Therefore, the ε' value decreases with an increase in IDNS [492]. Because the value of changes directly with the electrical conductivity's square root, it is possible to attribute the increase in ε' value to the decrease in resistivity in particular [245]. Another possible explanation for the improvement in ε' value with IDNS is the lowering of grain/particle diameter. Additionally,

the low resistivity is caused by the low concentration of Fe^{2+} ions at the octahedrally coordinated site of the $NCZFe_{2-x}O_{4-3x/2}$ phase, which causes ε' value to be greater [493]. The ferroelectromagnetic composite ceramics with x = 0.0; 0.04; 0.08; 0.12; y = 0.2 have a greater value of ε' than the ferroelectromagnetic composite ceramics with x = 0.0; 0.04; 0.08; 0.12; y = 0.5. Since part of the Fe^{3+} ions are transformed into Fe^{2+} ions when the sintering is taking place, the Fe^{2+} ions are given credit for this higher value. The grain-to-grain border ratio is also raised by sintering. As a result, ε' value rises [310]. Contrarily, the $NCZFe_{2-x}O_{4-3x/2}$ phase's conducting character lessens the polarization, resulting in a smaller value of $\varepsilon'$for ferroelectromagnetic composite ceramics with x = 0.0; 0.04; 0.08; 0.12; y = 0.5 than for ferroelectromagnetic composite ceramics with x = 0.0; 0.04; 0.08; 0.12; y = 0.2. Furtherfore, we fitted ε' value using a modified Debye's function [494]: $\varepsilon' = \varepsilon'_{\infty} + \frac{(\varepsilon'_0 - \varepsilon'_{\infty})}{[1+(\omega\tau)^{2(1-\alpha)}]}$ to clarify the electric permittivity's dispersive characteristic that suggests the possibility of more than one charge carriers participating in the permittivity relaxation mechanism., where ε' stands for the real component of the permittivity constant, ε'_{∞} stands for the permittivity constant at higher frequencies (at 10 MHz), ε'_0 stands for the permittivity constant at lower frequencies (at 1 Hz), $\omega\ (= 2\pi f)$ stands for the angular frequency, $\varepsilon'_0 - \varepsilon'_{\infty}$ stands for the dielectric relaxation strength, τ $(\tau = \frac{1}{2\pi f_r})$ stands for the relaxation time, and α stands for the spreading component. Most likely, more than one charge carriers would participate in the dielectric relaxation process given the consistency of the measured and theoretical evidence, which supports the validity of the modified Debye's function [495]. Table 4.54 displays the fitted values for α and τ. Table 4.54 reveals that α in x = 0.04, decreases, then improves in x = 0.08, and in the end reduces in x = 0.12 with y = 0.2 and 0.5. In contrast, at y = 0.2, τ drops as the IDNS increases, but τ improves at x = 0.04, afterwhich drops at x = 0.08, and ultimately rises at x = 0.12 and y = 0.5.

4.4.6. Permittivity loss tangent analysis

One of the crucial concerns in ferroelectromagnetic composite ceramics is the investigation of permittivity loss tangent. Figure 4.55 depicts the development of permittivity loss tangent ($\tan\delta_\varepsilon$) with respect to frequency of (1-*y*) [BCZTO] + (*y*) [$NCZFe_{2-x}O_{4-3x/2}$] ferroelectromagnetic composite ceramics: (c) *x* = 0.0; 0.04; 0.08; 0.12; *y* = 0.2 and (d) *x* = 0.0; 0.04; 0.08; 0.12; *y* = 0.5. Typically, permittivity loss tangent happens when applied ac field's polarization trails behind and is brought by a variety of factors, including grain borders, the existence of free charge carriers), T_s, chemical structure, contaminants, imperfections architectural uniformity, and stoichiometry [496]. The density, on the opposite hand, has a substantial impact on the change in $\tan\delta_\varepsilon$ value, therefore a rise in porosity (lower density) leads to a higher $\tan\delta_\varepsilon$ value. There is no doubt that tan decreases with frequency and becomes constant at the higher frequency side. Unusually poorly conducting grain borders are persuasive at lower frequency side; as a result, $\tan\delta_\varepsilon$ value is high because it takes a lot of energy to move electrons in the midst of Fe^{2+} and Fe^{3+}, Zr^{3+} and Zr^{4+}, and Ti^{3+} and Ti^{4+} ions [497]. To put it another way, if the charge carrier's hopping frequency amongst Fe^{2+} and Fe^{3+}, Zr^{3+} and Zr^{4+}, and Ti^{3+} and Ti^{4+} ions exceed that of the applied field, charge carriers are perfectly able to keep up with rapid changes in the applied field. This causes a higher absorption of electromagnetic waves that are being transmitted, which causes a significant $\tan\delta_\varepsilon$ value to be seen at the lower frequency side [498]. The electrical proactivity of the highly conductive grains at high frequencies necessitates the transfer of a little amount of energy in the midst of the ions of Fe^{2+} and Fe^{3+}, Zr^{3+} and Zr^{4+}, and Ti^{3+} and Ti^{4+}, which results in a low $\tan\delta_\varepsilon$ value [497]. In other words, the charge carriers are incapable to pursue precisely the quick transformation in the field being introduced if their hopping frequency is smaller the applied frequency. As an outcome, propagating electromagnetic waves are scarcely absorbed, and relatively samml $\tan\delta_\varepsilon$ values are observed at higher frequencies [498]. Additionally, it has been demonstrated

that a maximum in $\tan\delta_\varepsilon$ emerges at lower frequencies in x = 0.0 and y = 0.2 and in x = 0.04, 0.08, and 0.12 and y = 0.5 in accordance with Debye-like relaxing mechanisms. Additionally, it has been demonstrated that a maximum in $\tan\delta_\varepsilon$ emerges at lower frequencies in x = 0.0 and y = 0.2 and in x = 0.04, 0.08, and 0.12 and y = 0.5 in accordance with Debye-like relaxing mechanisms. With the aid of the Debye relaxation theory [499, 500], it is possible to analyze this peak's occurrence in $\tan\delta_\varepsilon$ spectra, which is connected to a ferromagnetic resonance effect [499]. This hypothesis states that the loss peak eventuates if the applied frequency and the electron jumping frequency amongst Fe^{2+} and Fe^{3+}, Zr^{3+} and Zr^{4+}, and Ti^{3+} and Ti^{4+} ions coincide [501] and the condition $\omega_{max}\tau = 1$ is satisfied, where ω_{max} $(= 2\pi f_{max})$ refers the angular frequency and τ refers the relaxation. The relaxing time supports the hopping chance per unit time (p) as $\tau = \frac{1}{2p}$ or $\omega_{max} = 2p$ [501]. In this situation, the crystal lattice receives the biggest quantity of electrical energy from the applied field, which results in a quick increase in $tan\delta_\varepsilon$ value. The joint bestowal of electrons and holes further supports the formation of the resonance peak. In this research, the displacement of electrons and the leaping of electrons in the midst of Fe^{2+} and Fe^{3+} ($Fe^{2+} \leftrightarrow Fe^{3+} + e^-$), Zr^{3+} and Zr^{4+} ($Zr^{3+} \leftrightarrow Zr^{4+} + e^-$), and Ti^{3+} and Ti^{4+} ($Ti^{3+} \leftrightarrow Ti^{4+} + e^-$). Additionally, the displacement of holes is supported by the jumping of holes in the midst of Ba^{2+} and Ba^{3+} ($Ba^{3+} \leftrightarrow Ba^{2+} + e^+$), Ca^{2+} and Ca^{3+} ($Ca^{3+} \leftrightarrow Ca^{2+} + e^+$), Ni^{2+} and Ni^{3+} ($Ni^{3+} \leftrightarrow Ni^{2+} + e^+$), Cu^{2+} and Cu^{1+} ($Cu^{2+} \leftrightarrow Cu^{1+} + e^+$), Cu^{3+} and Cu^{2+} ($Cu^{3+} \leftrightarrow Cu^{2+} + e^+$), and Zn^{2+} and Zn^{3+} ($Zn^{3+} \leftrightarrow Zn^{2+} + e^+$). Table 4.50-4.51 and 4.52-4.53 include a list of the values of $\tan\delta_\varepsilon$ at various frequencies. Figure 4.55 (c, d)'s inset shows how $\tan\delta_\varepsilon$ depends on IDNS level at 1 kHz. It is clear that whereas $\tan\delta_\varepsilon$ value improves in x = 0.04 and afterwhich drops on rising IDNS level in x = 0.12 and y = 0.5, $\tan\delta_\varepsilon$ value rises in x = 0.08 and afterwhich drops in x = 0.12 and y = 0.2. The increase and decrease in $\tan\delta_\varepsilon$ value using IDNS may be related to a decrease and increase in resistivity, which results in an improvement and facilitation of $\tan\delta_\varepsilon$ value. Based on the electron theory, thr formula for $\tan\delta_\varepsilon$ is: $\tan\delta_\varepsilon =$

$\sigma_{ac}/2\pi f\varepsilon'\varepsilon_0 = 1/2\pi f\varepsilon'\varepsilon_0\rho_{ac}$, where ρ_{ac} represents the resistivity [443, 502]. According to the aforementioned relationship, $\tan\delta_\varepsilon$ value diminishes as ε' and ρ_{ac} values grow, and vice versa [245]. The $\tan\delta_\varepsilon$ value may be shown to be greater for ferroelectromagnetic composite ceramics with x = 0.0; 0.04; 0.08; 0.12; y = 0.5 than for ferroelectromagnetic composite ceramics with x = 0.0; 0.04; 0.08; 0.12; y = 0.2. This difference in $\tan\delta_\varepsilon$ has developed since ferroelectromagnetic composite ceramics with larger $NCZFe_{2-x}O_{4-3x/2}$ concentration produces large number of charge carriers. At 10 MHz, the small $\tan\delta_\varepsilon$ value of the x = 0.04; y = 0.2 ferroelectromagnetic composite ceramic is 5.04×10^{-5}, whereas that of the x = 0.0; y = 0.5 ferroelectromagnetic composite ceramic is 1.51×10^{-4}. A good quality of the ferroelectromagnetic composite ceramics is shown by the tiny $\tan\delta_\varepsilon$ values.

Table 4.50. Real component (ε') and imaginary component (ε'') of electric permittivity, permittivity loss tangent ($tan\delta$), relative loss factor ($tan\delta/\varepsilon'$), ac conductivity (σ_{ac}), real component (Z') and imaginary component (Z'') of impedance, and real component (M') and imaginary component (M'') of dielectrical modulus of (1-*y*) [BCZTO] + (*y*) [NCZFe$_{2-x}$O$_{4-3x/2}$] (*x* = 0, 0.04; *y* = 0.2) ferroelectromagnetic composite ceramics

Composition		Frequency	ε'	ε''	$tan\delta$	σ_{ac} (Ω^{-1} m^{-1})	$tan\delta/\varepsilon'$	Z' (Ω)	Z'' (Ω)	M'	M''
x	*y*										
0.0	0.2	1 kHz	123	32	0.26	1.80×10^{-6}	2.11×10^{-3}	2.34×10^{6}	9.00×10^{6}	7.60×10^{-3}	1.97×10^{-3}
		10 kHz	88	14.7	0.17	8.38×10^{-6}	1.90×10^{-3}	214745	1.29×10^{6}	1.11×10^{-2}	1.85×10^{-3}
		100 kHz	78.2	4.71	0.06	2.63×10^{-5}	7.71×10^{-4}	9199	152572	1.27×10^{-2}	7.68×10^{-4}
		1 MHz	74.7	1.58	0.02	8.97×10^{-5}	2.84×10^{-4}	334	15759	1.34×10^{-2}	2.84×10^{-4}
		10 MHz	75	1.13	0.02	6.47×10^{-4}	2.01×10^{-4}	23.32	1548	1.33×10^{-2}	2.01×10^{-4}
0.04	0.2	1 kHz	330	44.1	0.13	2.48×10^{-6}	4.04×10^{-4}	418221	3.14×10^{6}	2.97×10^{-3}	3.97×10^{-4}
		10 kHz	290	16.7	0.06	9.53×10^{-6}	1.99×10^{-4}	20626	357863	3.44×10^{-3}	1.98×10^{-4}
		100 kHz	279	5.22	0.02	2.91×10^{-5}	6.71×10^{-5}	714	38152	3.58×10^{-3}	6.71×10^{-5}
		1 MHz	275	2.53	0.01	1.43×10^{-4}	3.34×10^{-5}	35	3820	3.63×10^{-3}	3.34×10^{-5}
		10 MHz	297	4.45	0.01	2.55×10^{-3}	5.04×10^{-5}	5.23	349	3.37×10^{-3}	6.04×10^{-5}

Table 4.51. Real component (ε') and imaginary component (ε'') of electric permittivity, permittivity loss tangent ($tan\delta$), relative loss factor ($tan\delta/\varepsilon'$), ac conductivity (σ_{ac}), real component (Z') and imaginary component (Z'') of impedance, and real component (M') and imaginary component (M'') of dielectrical modulus of (1-*y*) [BCZTO] + (*y*) [NCZFe$_{2-x}$O$_{4-3x/2}$] (*x* = 0.08, 0.12; *y* = 0.2) ferroelectromagnetic composite ceramics

Composition		Frequency	ε'	ε''	$tan\delta$	σ_{ac} (Ω^{-1} m^{-1})	$tan\delta/\varepsilon'$	Z' (Ω)	Z'' (Ω)	M'	M''
x	*y*										
0.08	0.2	1 kHz	328	40	0.12	2.25×10^{-6}	3.71×10^{-4}	428390	3.52×10^{6}	3.00×10^{-3}	3.65×10^{-4}
		10 kHz	288	18.8	0.07	1.07×10^{-5}	2.26×10^{-4}	26128	400770	3.46×10^{-3}	2.26×10^{-4}
		100 kHz	273	6.85	0.03	3.82×10^{-5}	9.19×10^{-5}	1087	43327	3.66×10^{-3}	9.19×10^{-5}
		1 MHz	268	3.23	0.01	1.82×10^{-4}	4.50×10^{-5}	53	4366	3.74×10^{-3}	4.51×10^{-5}
		10 MHz	286	4.52	0.02	2.59×10^{-3}	5.54×10^{-5}	6.39	404	3.50×10^{-3}	5.54×10^{-5}
0.12	0.2	1 kHz	312	41.9	0.13	2.36×10^{-6}	4.31×10^{-4}	453414	3.37×10^{6}	3.15×10^{-3}	4.24×10^{-4}
		10 kHz	272	17.3	0.06	9.86×10^{-6}	2.33×10^{-4}	24501	385945	3.66×10^{-3}	2.32×10^{-4}
		100 kHz	261	5.52	0.02	3.08×10^{-5}	8.11×10^{-5}	876	41371	3.83×10^{-3}	8.12×10^{-5}
		1 MHz	256	2.72	0.01	1.54×10^{-4}	4.14×10^{-5}	44	4152	3.90×10^{-3}	4.13×10^{-5}
		10 MHz	277	4.39	0.02	2.52×10^{-3}	5.72×10^{-5}	6	379	3.60×10^{-3}	5.71×10^{-5}

Table 4.52. Real component (ε') and imaginary component (ε'') of electric permittivity, permittivity loss tangent ($tan\delta$), relative loss factor ($tan\delta/\varepsilon'$), ac conductivity (σ_{ac}), real component (Z') and imaginary component (Z'') of impedance, and real component (M') and imaginary component (M'') of dielectrical modulus of (1-*y*) [BCZTO] + (*y*) [NCZFe$_{2-x}$O$_{4-3x/2}$] (*x* = 0, 0.04; *y* = 0.5) ferroelectromagnetic composite ceramics

Composition		Frequency	ε'	ε''	$tan\delta$	σ_{ac} (Ω^{-1} m^{-1})	$tan\delta/\varepsilon'$	Z' (Ω)	Z'' (Ω)	M'	M''
x	*y*										
0.0	0.5	1 kHz	267	32.5	0.12	$1.83 \times s10^{-6}$	4.56×10^{-4}	479971	3.95×10^{6}	3.69×10^{-3}	4.49×10^{-4}
		10 kHz	233	15.6	0.07	8.93×10^{-6}	2.88×10^{-4}	30307	451082	4.27×10^{-3}	2.87×10^{-4}
		100 kHz	221	5.67	0.03	3.16×10^{-5}	1.16×10^{-4}	1253	48827	4.53×10^{-3}	1.16×10^{-4}
		1 MHz	216	2.68	0.01	1.51×10^{-4}	5.74×10^{-5}	61	4925	4.62×10^{-3}	5.73×10^{-5}
		10 MHz	226	3.44	0.02	1.97×10^{-3}	6.75×10^{-5}	7.10	466	4.30×10^{-3}	6.75×10^{-5}
0.04	0.5	1 kHz	482	270	0.56	1.52×10^{-5}	1.16×10^{-3}	999839	1.79×10^{6}	1.58×10^{-3}	8.85×10^{-4}
		10 kHz	239	107	0.45	6.09×10^{-5}	1.87×10^{-3}	173580	388900	3.48×10^{-3}	1.56×10^{-3}
		100 kHz	160	35.1	0.23	1.96×10^{-5}	1.37×10^{-3}	14859	67912	5.95×10^{-3}	1.30×10^{-3}
		1 MHz	138	9.23	0.07	5.22×10^{-4}	4.83×10^{-4}	540	8102	7.19×10^{-3}	4.79×10^{-4}
		10 MHz	139	4.03	0.03	2.31×10^{-3}	2.09×10^{-4}	23.22	800	7.20×10^{-3}	2.09×10^{-4}

Table 4.53. Real component (ε') and imaginary component (ε'') of electric permittivity, permittivity loss tangent ($tan\delta$), relative loss factor ($tan\delta/\varepsilon'$), ac conductivity (σ_{ac}), real component (Z') and imaginary component (Z'') of impedance, and real component (M') and imaginary component (M'') of dielectrical modulus of (1-*y*) [BCZTO] + (*y*) [NCZFe$_{2-x}$O$_{4-3x/2}$] (*x* = 0.08, 0.12; *y* = 0.5) ferroelectromagnetic composite ceramics

Composition		Frequency	ε'	ε''	$tan\delta$	σ_{ac} (Ω^{-1} m^{-1})	$tan\delta/\varepsilon'$	Z' (Ω)	Z'' (Ω)	M'	M''
x	*y*										
0.08	0.5	1 kHz	180	43.7	0.24	2.46×10^{-6}	1.35×10^{-3}	1.49×10^{6}	6.11×10^{6}	5.25×10^{-3}	1.28×10^{-3}
		10 kHz	133	21.7	0.16	1.24×10^{-5}	1.23×10^{-3}	137971	843101	7.34×10^{-3}	1.20×10^{-3}
		100 kHz	115	8.07	0.07	4.50×10^{-5}	6.10×10^{-4}	7142	101737	8.66×10^{-3}	6.08×10^{-4}
		1 MHz	109	2.73	0.03	1.54×10^{-4}	2.30×10^{-4}	266	10628	9.16×10^{-3}	2.29×10^{-4}
		10 MHz	112	2.10	0.02	1.20×10^{-3}	1.67×10^{-4}	19.03	1019	8.90×10^{-3}	1.66×10^{-4}
0.12	0.5	1 kHz	260	113	0.43	6.34×10^{-6}	1.664×10^{-3}	1.76×10^{6}	4.07×10^{6}	3.24×10^{-3}	1.40×10^{-3}
		10 kHz	156	46.2	0.30	2.64×10^{-5}	1.90×10^{-3}	215671	729584	5.88×10^{-3}	1.74×10^{-3}
		100 kHz	123	14.9	0.12	8.32×10^{-5}	9.89×10^{-4}	12406	101981	8.04×10^{-3}	9.78×10^{-4}
		1 MHz	113	4.33	0.04	2.45×10^{-4}	3.38×10^{-4}	423	11056	8.83×10^{-3}	3.38×10^{-4}
		10 MHz	114	2.59	0.02	1.48×10^{-3}	1.98×10^{-4}	24.44	1081	8.74×10^{-3}	1.98×10^{-4}

Table 4.54. Extracted parameters ε_s', ε_∞', $\Delta\varepsilon$, spreading factor (α) and relaxation time (τ) of (1-*y*) [BCZTO] + (*y*) [NCZFe$_{2-x}$O$_{4-3x/2}$] (*x* = 0.0; 0.04; 0.08; 0.12; *y* = 0.2; 0.5) ferroelectromagnetic composite ceramics.

Composition		Modified Debye function				
		ε_s'	ε_∞'	$\Delta\varepsilon = \varepsilon_s' - \varepsilon_\infty'$	α	$\tau\ (s)$
x	y					
0.0	0.2	181	75	106	0.70	0.75×10^{-3}
0.04	0.2	410	297	113	0.66	0.91×10^{-3}
0.08	0.2	407	286	121	0.72	1.24×10^{-3}
0.12	0.2	398	277	121	0.70	1.62×10^{-3}
0.0	0.5	327	226	101	0.72	0.89×10^{-3}
0.04	0.5	992	139	853	0.72	2.09×10^{-3}
0.08	0.5	262	112	150	0.74	1.07×10^{-3}
0.12	0.5	486	114	372	0.73	2.69×10^{-3}

4.4.7. Electrical conductivity analysis

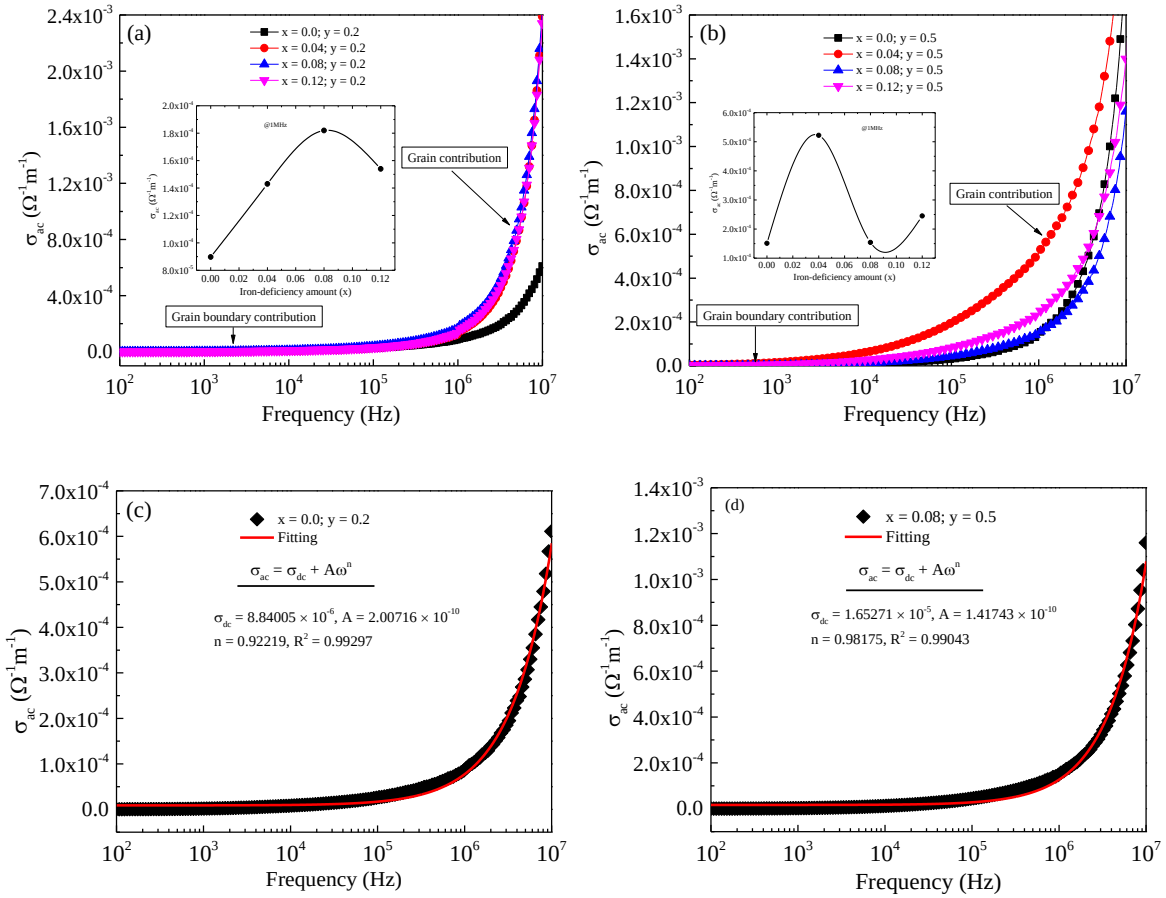

Figure 4.56: Evolution of the ac conductivity (σ_{ac}) with frequency of (1-*y*) [BCZTO] + (*y*) [NCZFe$_{2-x}$O$_{4-3x/2}$] composites: (a) *x* = 0.00-012; *y* = 0.2 and (b) *x* = 0.00-012; *y* = 0.5 and inset shows IDNS dependent σ_{ac} at 1 MHz. (c, d) shows the representative fitted curve of σ_{ac} using Jonscher's power law.

Figure 4.56 investigates and depicts the development of the ac conductivity (σ_{ac}) of (1- y) [BCZTO] + (y) [NCZFe$_{2-x}$O$_{4-3x/2}$] ferroelectromagnetic composite ceramics according to the applied frequency: (a) x = 0.0; 0.04; 0.08; 0.12; y = 0.2 and (b) x = 0.0; 0.04; 0.08; 0.12; y = 0.5. Figure 4.56 (a, b) shows how the dynamical ac spectra may be separated into two distinct groups. (i) The lower frequencies, or frequency-invariant ($\omega \cong 0$) range, are known as the DC conductivity (σ_{dc}), together with relatively small σ_{ac} because of the electrode's polarization impact and uncontrolled diffusion of charge carriers (which relates to the long-distance translational movement) [502]. At higher frequencies, σ_{ac}, also shows frequency dispersion as a result of the enormous improvement in charge carrier's movement (which crelates to the

short-distance translational movement) [503]. Maxwell-Wagner [504] and Koop [235] notions can also be used to explain the shift in σ_{ac}. According to these hypotheses, it can be recognized that ferroelectromagnetic composite ceramics are made up of exceptionally conductive grains that are separated from one another by a thin layer that is not notably conductive. These layers are known as grain borders. According to these models, unremarkably conductive grain borders have electrical proactiveness at low-frequency frequencies that is noticeably stronger than remarkably conductive grain surfaces. In light of this, the Verwey de Bohr mechanism [434] predicts that there is a chance of charge carriers jumping amongst Zr^{3+} and Zr^{4+} ions ($Zr^{3+} \leftrightarrow Zr^{4+} + e^{-}$), Ti^{3+} and Ti^{4+} ions ($Ti^{3+} \leftrightarrow Ti^{4+} + e^{-}$), O^{2-} ions ($O^{2-} \leftrightarrow O^{-} + e^{-}$), and Fe^{2+} and Fe^{3+} ions ($Fe^{2+} \leftrightarrow Fe^{3+} + e^{-}$) and Ba^{3+} and Ba^{2+} ions ($Ba^{3+} \leftrightarrow Ba^{2+} + e^{+}$), Ca^{3+} and Ca^{2+} ions ($Ca^{3+} \leftrightarrow Ca^{2+} + e^{+}$), Ni^{3+} and Ni^{2+} ions ($Ni^{3+} \leftrightarrow Ni^{2+} + e^{+}$), Cu^{2+} and Cu^{1+} ions ($Cu^{2+} \leftrightarrow Cu^{1+} + e^{+}$), Zn^{3+} and Zn^{2+} ions ($Zn^{3+} \leftrightarrow Zn^{2+} + e^{+}$) is incompetent and hence, a continuous plateau zone is formed. The activity unusually conducting grains increases against frequency relative to the borders of less remarkably conductive grains. Accordingly, the charge carrier's jumping probability in the midst of Zr^{3+} and Zr^{4+} ions ($Zr^{3+} \leftrightarrow Zr^{4+} + e^{-}$), Ti^{3+} and Ti^{4+} ions ($Ti^{3+} \leftrightarrow Ti^{4+} + e^{-}$), O^{2-} ions ($O^{2-} \leftrightarrow O^{-} + e^{-}$), and Fe^{2+} and Fe^{3+} ions ($Fe^{2+} \leftrightarrow Fe^{3+} + e^{-}$) and Ba^{3+} and Ba^{2+} ions ($Ba^{3+} \leftrightarrow Ba^{2+} + e^{+}$), Ca^{3+} and Ca^{2+} ions ($Ca^{3+} \leftrightarrow Ca^{2+} + e^{+}$), Ni^{3+} and Ni^{2+} ions ($Ni^{3+} \leftrightarrow Ni^{2+} + e^{+}$), Cu^{2+} and Cu^{1+} ions ($Cu^{2+} \leftrightarrow Cu^{1+} + e^{+}$), Zn^{3+} and Zn^{2+} ions ($Zn^{3+} \leftrightarrow Zn^{2+} + e^{+}$) is eminent. The increase in σ_{ac} at high frequencies was correlated with an increase in the mobility of charge carrier without changing the concentration of net charge carriers [386]. However, the jumping holes can also influence the electrical conductivity. N-type carriers are believed to prevail in the electrical conduction mechanism because the holes jumping is less noticeable than the electron jumping. The frequency-dependent σ_{ac} follows Jonscher's power law as [505]:

$\sigma_{ac}(\omega)(\omega = 0, T) + \sigma_{ac}(\omega) = \sigma_{dc}(\omega = 0, T) + A(T)\omega^{n(T)} = \sigma_{dc}\left(1 + \frac{A(T)\omega^{n(T)}}{\sigma_{dc}}\right) =$

$\sigma_{dc}\left[1 + \left(\frac{\omega}{\omega_h}\right)^{n(T)}\right]$, where σ_{dc} is the DC conductivity, and the term $A(T)\omega^{n}$ $(0 < n < 1)$

describes the frequency dependency of σ_{ac} and the phenomenon of dispersion, where, $\omega\ (=2\pi f)$ denotes the angular frequency, exponent n which weakly relies upon frequency or frequency-invariant, and greatly relies on the materials' inherent characteristics and temperature [506], and also a factor in influencing how strongly mobile ions interact with the lattice and how far the behavior deviates from optimal Debye function [507], A is written as $A(T) = (\pi N^2 e^2)/[6k_B T(2\alpha)]$ possessing unit of $\sigma_{ac}(\omega)$, where e is charge of the electron, N is the number of sites per unit volume where the jumping occurs, k_B denotes the Boltzmann constant, T denotes the temperature, and α denotes the polarizability. The factor (A) declares the magnitude of the material's polarizability and $\omega_h = (\sigma_{dc}/A(T))^{\frac{1}{n}}$ is the frequency used to bridge dc to dispersive conductivity zone when $\omega > \omega_h$ and is known as the charge carrier's jumping frequency [506]. According to Jonscher [508], the energy accumulated in the short-distance correlated motion of charge carriers is the root cause of a value that is higher than zero of n in the dispersive region of σ_{ac}. Ideal ionic-type crystals exhibit coupled ac conduction and DC conduction if $n = 0$ [509]. According to Funke [323], the physical meaning of n is as follows: $n \leq 1$ (Debye-type) shows that the charge carriers give rise to a short-range translatory transfer with a rapid hop which is facilitated by a small polaronic process [319, 508], whilst $n > 1$ (non-Debye type) suggests that the movement is due to a large polaronic process amongst the neighboring sites, which benefits a confined or reorientational jumping without species departing the neighborhood. The jumping frequency, which is determined by by the charged carriers' polaron jumping, is discovered to travel toward the higher frequencies where the slope eventually changes. Inables 4.50-4.51 and 4.52-4.53, the σ_{ac} values for various frequencies are reported. Figure 4.56 (a, b)'s inset displays the dependency of σ_{ac} with IDNS level at 1 MHz for ferroelectromagnetic composite ceramics with x = 0.0; 0.04; 0.08; 0.12; y = 0.2 and x = 0.0; 0.04; 0.08; 0.12; y = 0.5. It is discovered that while the IDNS rises to a maximum of x = 0.08, σ_{ac} improves and afterwhich drops in x = 0.12 and y = 0.2, but

σ_{ac} improves dramatically in x = 0.04 and then descends in x = 0.08 before improving in x = 0.12 and y = 0.5. The ac conductivity is significantly impacted by IDNS, as seen by the data above. The collected data of σ_{ac} were fiited using Jonscher's power law to reveal the measured frequency dispersion and conductivity relaxation as well as to determine the values of σ_{dc}, factor 'A', and exponent 'n'. Table 4.55 lists the extracted parameters. The usual fitted curves of σ_{ac} according to Jonscher's law for the ferroelectromagnetic composite ceramics with x = 0.0, y = 0.2 and x = 0.04, y = 0.5 are shown in Figure 4.56 (c, d). A continuous red line, which indicates the degree of fit, clearly shows how well the fitted curve harmonizes with the measured data. In contrast to σ_{dc}, which improves in x = 0.04 and then lowers in x = 0.08 before enhancing in x = 0.12 and y = 0.5, σ_{dc} ascends as the IDNS rises to a maximum of x = 0.08 and ultimately escalates in x = 0.12 and y = 0.2. This is seen in Table 4.55. The ferroelectromagnetic composite ceramics with small grains contain a significant number of grain borders than grains, which is consistent with the improvement in grain diameter and the augmentation of $\sigma_{dc}$with IDNS. Given that the ferroelectromagnetic composite ceramics with big grains contain a smaller number of grain borders, the decrease in σ_{dc} with IDNS is verified by the decrease in grain diameter. According to Table 4.55, whereas A grows in x = 0.04 and then drops in x = 0.08 before increasing in x = 0.12 and y = 0.5, A increases in x = 0.04 and then drops in x = 0.08 before increasing in x = 0.12 and y = 0.2. It is clear from Table 4.55 that the 'n' numbers range from zero to one (i.e. $0 < n < 1$). We can see from Table 4.55 that n increases in x = 0.12 and y = 0.2 and then decreases with rising IDNS level to a maximum of x = 0.08. On the other hand, n increases in x = 0.08 and aftewhcih decreases in x = 0.12 if y = 0.2. This is in contrast to n declining in x = 0.04 and then increasing in x = 0.08. The growth and decline of charge carrier hopping may be attributed to the increase and decrease in n that accompany an increase in IDNS. So, the hopping of small polarons that are engulfed in limited states supports σ_{ac} [510].

Table 4.55. Extracted parameters from Jonscher's power law: $\sigma_{ac} = \sigma_{dc} + A\omega^n$ of (1-*y*) [BCZTO] + (*y*) [NCZFe$_{2-x}$O$_{4-3x/2}$] (*x* = 0.0; 0.04; 0.08; 0.12; *y* = 0.2; 0.5) ferroelectromagnetic composite ceramics

Composition		From fitting of $\sigma_{ac} = \sigma_{dc} + A\omega^n$				
		$\sigma_{dc}\ (\Omega^{-1}m^{-1})$	$A\ (\Omega^{-1}m^{-1})$	n	χ^2	R^2
x	y					
0.0	0.2	8.84×10^{-6}	2.01×10^{-10}	0.9222	9.65×10^{-11}	0.9930
0.04	0.2	1.78×10^{-6}	1.57×10^{-8}	0.6470	3.37×10^{-12}	0.9960
0.08	0.2	8.79×10^{-7}	2.42×10^{-8}	0.6372	2.17×10^{-12}	0.9986
0.12	0.2	1.79×10^{-6}	1.40×10^{-8}	0.6624	3.26×10^{-12}	0.9968
0.0	0.5	8.49×10^{-7}	1.75×10^{-8}	0.6482	1.44×10^{-12}	0.9987
0.04	0.5	3.50×10^{-5}	8.65×10^{-8}	0.6217	2.59×10^{-9}	0.9873
0.08	0.5	1.65×10^{-5}	1.42×10^{-10}	0.9818	4.30×10^{-10}	0.9904
0.12	0.5	2.46×10^{-5}	2.68×10^{-9}	0.8105	8.01×10^{-10}	0.9891

4.4.8. Impedance spectroscopic analysis

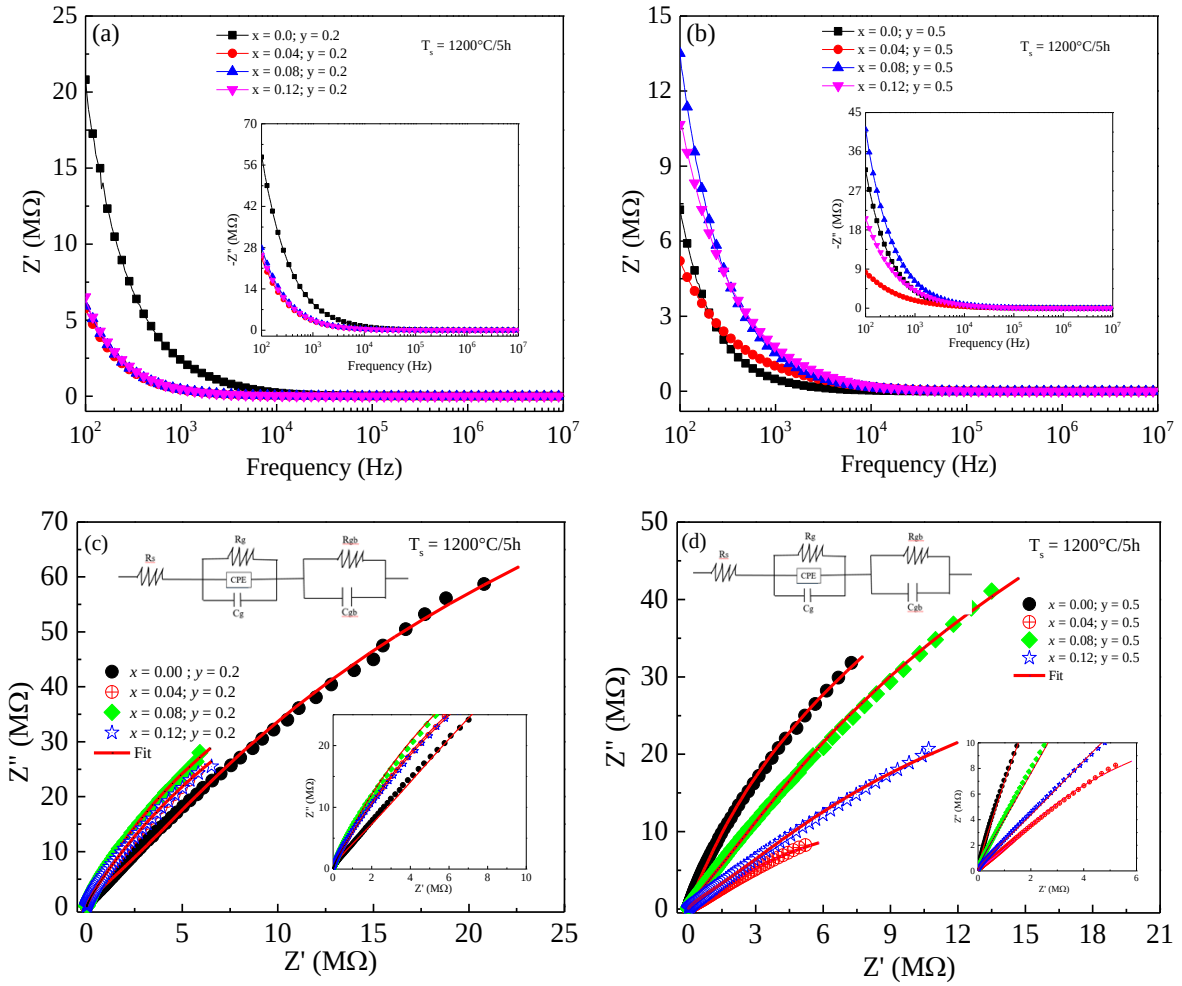

Figure 4.57: (a, b) Evolution of the real component (Z') of impedance with frequency of (1-*y*) [BCZTO] + (*y*) [NCZFe$_{2-x}$O$_{4-3x/2}$] (x = 0.0; 0.04; 0.08; 0.12; y = 0.2, 0.5) and inset shows evolution of the imaginary component (Z'') of impedance, and (c, d) Fitted Nyquist plots and inset shows the the equivalent circuit for fitting.

Figure 4.57 shows how the real component (Z') of impedenace depends on frequency of (1-*y*) [BCZTO] + (*y*) [NCZFe$_{2-x}$O$_{4-3x/2}$] ferroelectromagnetic composite ceramics: (a) x = 0.0; 0.04; 0.08; 0.12; y = 0.2 and (b) x = 0.0; 0.04; 0.08; 0.12; y = 0.5, while how the imaginary component (Z'') depends on frequency is illustarted in the inset of Figure 4.57 (a, b). At lower frequencies, Z' and Z'' values are at their highest value, progressively decreasing to a maximum of 10 kHz before evolving into frequency-independent values that are virtually zero. The proactiveness of extremely resistant grain borders is striking, and all types of polarization are present [511,

512], which is consistent with the large values of Z' and Z'' at the lower frequency side. In other words, because grain borders are proactive, the charge carrier's jumping amongst Zr^{3+} and Zr^{4+} (as reported by $Zr^{3+} \leftrightarrow Zr^{4+} + e^-$), Ti^{3+} and Ti^{4+} ($Ti^{3+} \leftrightarrow Ti^{4+} + e^-$), $O^{2-} \leftrightarrow O^- + e^-$, and Fe^{2+} and Fe^{3+} ($Fe^{2+} \leftrightarrow Fe^{3+} + e^-$) ions (n-type) and Ba^{2+} and Ba^{3+} ($Ba^{3+} \leftrightarrow Ba^{2+} + e^+$), Ca^{2+} and Ca^{3+} ($Ca^{3+} \leftrightarrow Ca^{2+} + e^+$), Ni^{2+} and Ni^{3+} ($Ni^{3+} \leftrightarrow Ni^{2+} + e^+$), Cu^{2+} and Cu^{1+} ($Cu^{2+} \leftrightarrow Cu^{1+} + e^+$), Zn^{2+} and Zn^{3+} ($Zn^{3+} \leftrightarrow Zn^{2+} + e^+$) is low,leading to increased Z' and Z'' values. The decreasing tendency of Z' and Z'' against frequency supports the idea that the relaxation process depends on frequency. The inset of Figure 4.57 (a, b) reveals that Z'' does not display a relaxation maximum in the recorded frequency range. Non-existence of a maximum suggests that the process of dielectric relaxation is absent. With increasing frequency, the characteristics of Z' and Z'' begin to deteriorate, which is a symptom of an increase in charge carrier mobility (the hopping phenomenon) and ac conductivity [513, 514]. The possible reason for the rise in ac conductivity is the quick emancipation of the space charge and subsequent continual diminishing of the barrier features for the space charge movement, are supported by the behavior of Z' and Z'' at higher frequencies, where Z' and Z'' entirely converge to a value that is practically constant and nearly frequency invariant regardless of IDNS level [461, 515]. Based on their characteristics, ferroelectromagnetic composite ceramics may be utilized as low pass filters that only let a certain frequency range to pass while blocking all others [516]. In Table 4.50-4.51 and 4.52-4.53, the Z' and Z'' at various frequencies are listed. Table 4.50-4.51 show that Z' and Z'' at 1 MHz first decrease in x = 0.04; they then increase in x = 0.08; and then, in y = 0.2, they finally plummet in x = 0.12. On the other hand, it can be shown from Table 4.52-4.53 that Z' at 1 MHz rises in x = 0.04, afterwhich drops in x = 0.08, and lastly rises in x = 0.12, but Z'' increases with rising IDNS lelevl in y = 0.5. The drop and rise in Z' and Z'' with rising IDNS level highlight a change in charge carriers' resistance. Figure 4.57 (c, d) depicts the Nyquist plots for the ferroelectromagnetic composite ceramics with (a) x = 0.0; 0.04; 0.08; 0.12; y = 0.2 and (b) x = 0.0; 0.04; 0.08; 0.12; y = 0.5. These plots include showing

Z'' with respect to Z' [517]. The high-frequency Nyquist charts are shown in the inset of Figure 4.57 (c, d). Because there are several relaxation processes in the system, each of which has a distinct relaxation period, Nyquist plots are made up of three successive semicircles that may be drawn at particular frequencies. The second semicircle (at the higher frequencies) is related to the resistance of grain, whilst the first semicircle (at the lower frequencies) is related to the resistance of the grain border [518]. A third semicircle may occasionally occur and be supported by the impedance produced by interfaces or even by electrodes [466]. The semicircular arcs in the graphs do not lie below the center of the Z'-axis, and (i) the graphical depictions do not accomodate any clearly defined semicircles. Such distinctive characteristics may be attributed to superimposed achievements from grain and grain borders as well as potential consequences of a defunct mismatch in the midst of the most relaxed frequencies [519]. We detect depressed semicircles whose centers are below the Z'-axis, and these are associated with the persistence of relaxations other than those of the Debye type [520]. The stress-strain processes that occur at the atomic scale, the borders of grains, atomic impurity distribution, and grain distributions and orientations [521, 522] all provide evidence for the causes of such non-Debye relaxation. In contrast to the semicircular arc, whose radius decreases in x = 0.04 and afterwhich rises in x = 0.08 before in the end ascending in x = 0.12 and y = 0.5, the semicircular arc's radius increases to a maximum of x = 0.08 and then drops in x = 0.12 and y = 0.2. The features of each semicircular arc's radius that increase and decrease with increasing IDNS are directly supported by the advancement and facilitation of resistance-related relaxation consequences, thereby accepting changes in conductivity and relaxation that are also contributing to the observed decline in ac conductivity [523]. The $(R_s)(C_g Q_{gb} R_g)(C_{gb} R_{gb})$ equivalent circuit and ZSimpWin software were used to fit the experimental data, and Table 4.56 shows the extracted parameters. Figure 4.57 (c, d)'s inset shows the comparable electrical circuit model. It is obvious that the fitted and measured data are completely identical. The grain resistance (R_g) is shown in Table 4.56 to increase in x =

0.04 and then diminish with rising IDNS level to a maximum of x = 0.12 and y = 0.2, whilst R_g decreases in x = 0.04 and then escalates in x = 0.08 and ultimately drops in x = 0.5 and y = 0.5. The resistance of grain border, on the other hand, decreases in x = 0.04, escalates in x = 0.08, and finally decreases in x = 0.12 and y = 0.5. The nature of R_g and R_{gb} with rising IDNS level suggests that the potential barrier characteristics are improved and decreased, respectively. Improved electrical transport characteristics were made possible by the potential barrier qualities' improvement and facilitation, while deteriorating electrical transport properties were prevented [524]. The resistance at the grain borders (R_{gb}) is greater than the resistance at the grain (R_g), indicating the creation of surface defects in ferroelectromagnetic composite ceramics, and grain borders control the ac conductivity [525]. According to Table 4.56, the grain capacitance (C_g) for ferroelectromagnetic composite ceramics with x = 0.0; 0.04; 0.08; 0.12; y = 0.2 and x = 0.0; 0.04; 0.08; 0.12; y = 0.5 is greater than the grain border capacitance (C_{gb}). Increased defects and oxygen distribution limit charge carriers within the grains, are evidence of the discrepancy in the midst of the aforementioned parameters [526]. It has been discovered that when y = 0.2, C_g increases to a maximum of x = 0.04 and then drops as the IDNS increases to a maximum of x = 0.12, however and y = 0.5, C_g increases as the IDNS increases to a maximum of x = 0.12. On the other hand, C_{gb} improves in x = 0.04 and then degrades as the IDNS increases to a maximum of x = 0.12 and y = 0.2, whilst C_{gb} falls with rising IDNS level to a maximum of x = 0.12 if y = 0.5. Thus, it might be able to boost and reduce the electronic/ionic faults that allow for larger charge carrier intensification and lessening, leading to, respectively, a reduction and a rise in capacitance with rising and descending IDNS level [526].

Table 4.56. Series resistance (R_s), grain resistance (R_g), grain capacitance (C_g), grain border resistance (R_{gb}), and grain border capacitance (C_{gb}) achieved from the modeling of Nyquist plots with equivalent circuits of (1-*y*) [BCZTO] + (*y*) [NCZFe$_{2-x}$O$_{4-3x/2}$] (*x* = 0.0; 0.04; 0.08; 0.12; *y* = 0.2; 0.5) ferroelectromagnetic composite ceramics.

Composition		R_s (Ω)	R_g (Ω)	CPE (S-sec^n)	n	C_g (F)	R_{gb} (Ω)	C_{gb} (F)
x	y							
0.0	0.2	132.6	1.8×10^{7}	2.19×10^{-6}	0.997	4.84×10^{-8}	1.15×10^{8}	1.12×10^{-11}
0.04	0.2	87.22	3.8×10^{10}	3.04×10^{-11}	1	9.17×10^{-6}	1.92×10^{7}	4.96×10^{-11}
0.08	0.2	1.31	5.12×10^{7}	2.50×10^{-7}	0.02	1.73×10^{-7}	8.82×10^{7}	1.97×10^{-11}
0.12	0.2	1.238	4.2×10^{7}	2.78×10^{-7}	0.02	1.29×10^{-7}	7.36×10^{7}	1.68×10^{-11}
0.0	0.5	198.6	9.5×10^{8}	5.68×10^{-7}	0.04	7.82×10^{-6}	9.91×10^{7}	3.39×10^{-11}
0.04	0.5	227.4	3.1×10^{5}	5.40×10^{-6}	0.01	2.16×10^{-6}	1.02×10^{7}	2.25×10^{-11}
0.08	0.5	352.6	5.6×10^{7}	5.32×10^{-7}	0.79	5.89×10^{-8}	8.35×10^{7}	1.67×10^{-11}
0.12	0.5	270.6	1.4×10^{7}	1.60×10^{-6}	0.81	2.77×10^{-8}	2.90×10^{7}	1.63×10^{-11}

4.4.9. Dielectrical modulus spectroscopic analysis

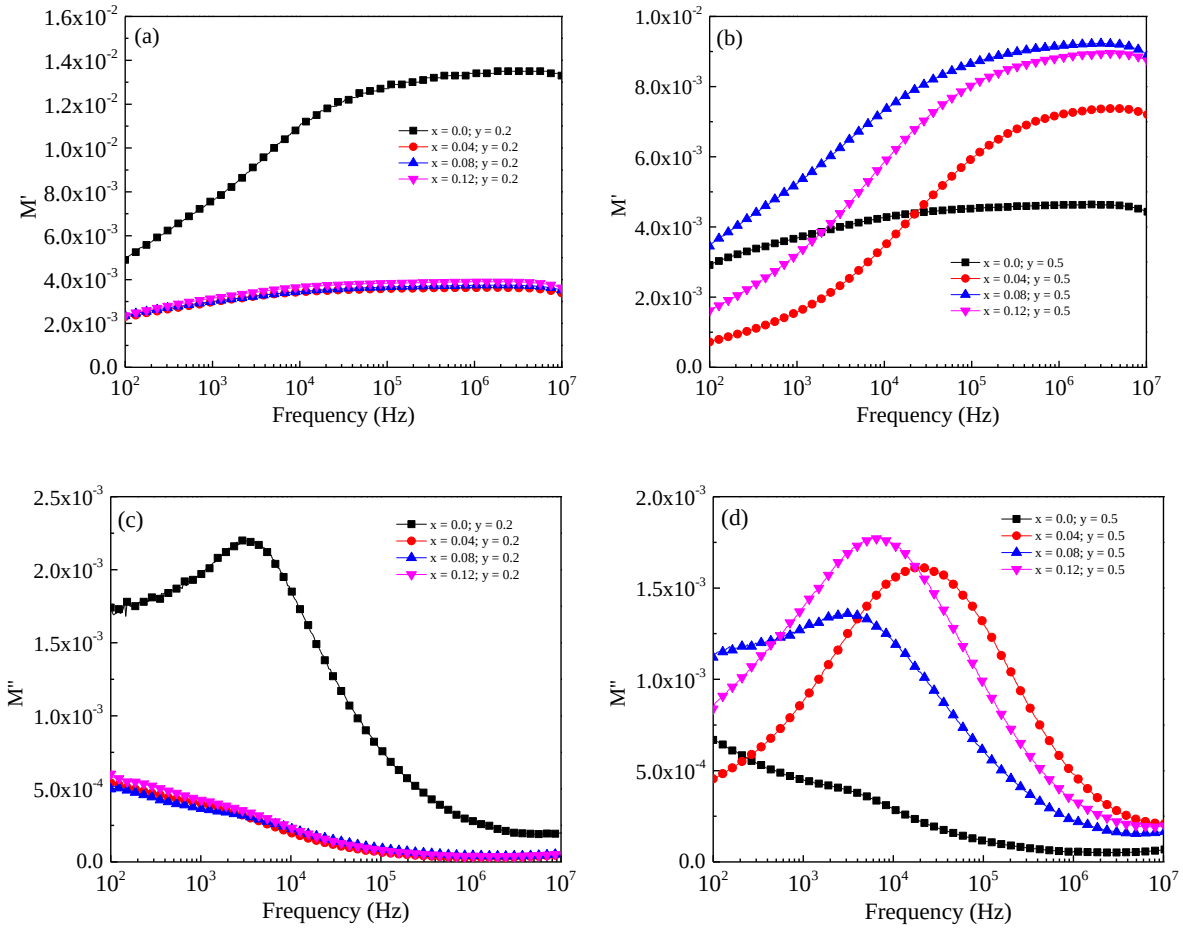

Figure 4.58: Evolution of the real component (M') of dielectrical modulus with frequency: (a) x = 0.0; 0.04; 0.08; 0.12; y = 0.2 and (b) x = 0.0; 0.04; 0.08; 0.12; y = 0.5 and imaginary component of dielectrical modulus (M'') with frequency: (c) x =0.0; 0.04; 0.08; 0.12; y = 0.2 and (d) x = 0.0; 0.04; 0.08; 0.12; y = 0.5 of (1-y) [BCZTO] + (y) [$NCZFe_{2-x}O_{4-3x/2}$] (x = 0.0; 0.04; 0.08; 0.12; y = 0.2; 0.5) ferroelectromagnetic composite ceramics.

Figure 4.58 shows how the real component of dielectrical modulus (M') depends on frequency of (1-y) [BCZTO] + (y) [$NCZFe_{2-x}O_{4-3x/2}$] ferroelectromagnetic composite ceramics: (a) x = 0.0; 0.04; 0.08; 0.12; y = 0.2 and (b) x = 0.0; 0.04; 0.08; 0.12; y = 0.5. It is evident from Figure 4.58 (a, b) that the M' value reaches noticeably smaller value at the lower frequency side. The smaller M' value at lower frequencies suggests insignificant or non-existence or eradication of electrode's polarization and the simplicity of polaron jumping along with minimal electronic polarization [527, 528]. Additionally, for lower frequencies, the smaller M' value reflects the

restoration force's restrictions on the transportability of the charge carrier under the applied field [529]. However, the long-range charge carrier's movement at the lower frequencies controls the electrical conduction phenomena [530]. Due to the short-distance charge carrier's mobility [531] and the M' value is saturating, which is supported by the arrival of the SCP, the M' value at the higher frequency side climbs sharply with frequency, reaches a peak at some frequencies, and then gradually drops. Table 4.50-4.51 and 4.52-4.53 provide a list of the M' values in the ferroelectromagnetic composite ceramics with x = 0.0; 0.04; 0.08; 0.12; y = 0.2 and x = 0.0; 0.04; 0.08; 0.12; y = 0.5 at various frequencies. It can be noticed that M' increases with rising IDNS level to a maximum of x = 0.08 at higher frequencies (10^5 Hz <f <10^7 Hz), and then decreases in x = 0.12 at y = 0.2 and 0.5. Figure 4.58 shows the development of the imaginary component of the dielectrical modulus (M'') with respect to frequency in the ferroelectromagnetic composite ceramics with x = 0.0; 0.04; 0.08; 0.12; and y = 0.2; 0.5. According to Figure 4.58 (c), M'' increases as applied frequency rises, revealing a single asymmetric electrical relaxation peak (M''_{max})) at the electrical relaxation frequency (f_{max}) in x = 0.0. It then gradually decreases with rising frequency in x = 0.04, 0.08, and 0.12 if y = 0.2. In contrast, Figure 4.58 (d) shows that M'' enhances with rising frequency and reveals just one asymmetrical relaxation maxima at f_{max}, and thereafter declines in x = 0.0; 0.04; 0.08; 0.12; y = 0.5. The appearance of the peak demonstrates the occurrence of the electrical conductivity relaxing process in the ferroelectromagnetic composite ceramics. It is evident that when the IDNS level rises in y = 0.2, the M''_{max}' peak shifts toward the lower frequency side. On the other hand, M''_{max} peak shifts from the higher frequency side in x = 0.04 to the lower frequency side in x = 0.08, and lastly shifts back to the higher frequency side in x = 0.12 when y = 0.5. When M''_{max} peak shifts toward the lower and higher frequency sides with rising IDNS level, the relaxation duration also increases and decreases, which suggests a connection amongst the motions of different mobile charge carriers [532]. Additionally, it is recognized that when y = 0.5, the height and breadth of M''_{max} seem to rise with the increase in applied frequency. A

decrease in the capacitance of the ferroelectromagnetic composite ceramics may be responsible for the increase in the height of M''_{max} with frequency [533]. The spreading of the relaxation period with varied time constants (non-Debye type) is confirmed by the broadening (asymmetric) of the peaks [534]. The frequency range under f_{max} displays a range of frequency whereby the electrically charged carriers might successfully jump between a single location to the next, signaling the process of conduction. Conversely, the frequency extent beyond f_{max} favors the spatial containment of the charge carriers within the potential wells and, as consequently, only implements limited movement for the charge carriers within the inside of the potential well. [520]. According to the requirement: $\omega_m \tau_m = 1$, where τ_m is the relaxation period, the peak's frequency range is an early indication of the switch between long-distance to short-distance movement [535]. Table 4.50-4.51 and 4.52-4.53 provide the values of M'' in the ferroelectromagnetic composite ceramics with x = 0.0; 0.04; 0.08; 0.12; y = 0.2 and x = 0.0; 0.04; 0.08; 0.12; y = 0.5 at various frequencies. The full set of M'' attributes, which depend on the charge carrier's hopping in ac conductivity, provide a straightforward validation in IDNS level.

4.4.10. Magnetic permeability and magnetic loss tangent analysis

Figure 4.59 depicts how the real component (μ'_i) of magnetic permeability evolves with frequency of (1-*y*) [BCZTO] + (*y*) [NCZFe$_{2-x}$O$_{4-3x/2}$] ferroelectromagnetic composite ceramics: (a) *x* = 0.0; 0.04; 0.08; 0.12; *y* = 0.2 and (b) *x* = 0.0; 0.04; 0.08; 0.12; *y* = 0.5. Generally speaking, μ'_i is influenced by both intrinsic and extrinsic characteristics, such as density, micromorphology, porosity, particle diameter, and ferrous ions concentration [536]. Examples of intrinsic parameters include magnetization and anisotropy constant. It has previously been stated by Nakamura [330] and Tsutaoka et al. [537] that the μ'_i value of multifunctional materials is connected with the fusion of two distinct magnetization processes, i.e., relaxation-like spin rotation and its dispersion change inversely against frequency, while resonance-like

domain wall's displacement and its dispersion vary directly with the square of the frequency and can be explicited as: $\mu_i' = 1 + \chi_{\mathrm{DW}} + \chi_{\mathrm{Spin}}$, where μ_i' represents the magnetic permeability; χ_{DW} stands for the domain wall's susceptibility; and χ_{Spin} is the inherent rotational susceptibility. χ_{DW} and χ_{Spin} are explicited as: $\chi_{\mathrm{DW}} = \frac{3\pi M_s^2 D_{\mathrm{SEM}}}{4\gamma}$ and $\chi_{\mathrm{Spin}} = \frac{2\pi M_s^2}{K_u}$, where M_s is the saturated magnetization which relies on the number of magnetic atoms, atomic magnetic moment, and temperature of the component material, K_u stands for the net anisotropy constant, D_{SEM} refers for the mean grain diameter, and γ refers the domain wall's energy. Nevertheless, the spin rotation part is dominated by chemical composition, whereas the composition and microstructure both drive the movement of the domain walls [537]. Additionally, it has been noted that, below 500 kHz, domain wall displacement is the primary magnetizing process and significantly contributes to the magentic permeability, whilst domain wall resonance occurs in the midst of 1 and 100 MHz and rotational resonance manifests at the highest frequency of 1 GHz [330, 538-540]. By ignoring spin rotation contributions, Globus and Duplex model have long been mentioned that the μ_i' value due to domain wall's movement changes inversely with the magnetocrystalline anisotropic constant ($K_1 = \frac{M_s H_c}{0.96}$) [541] and directly with the squared M_s and D_{SEM}. In other words, $(\mu_i')_{\mathrm{DW}} \propto \frac{M_s^2 \times D_{\mathrm{SEM}}}{K_1}$. The following elements, including (i) improved mixture of chemicals, (ii) microstructure with large density, (iii) huge grain and lean grain border, and (iv) diminution of the crystallographic anisotropic constant and the magnetostriction, necessary to take into account in order to increase magnetic permeability [208].

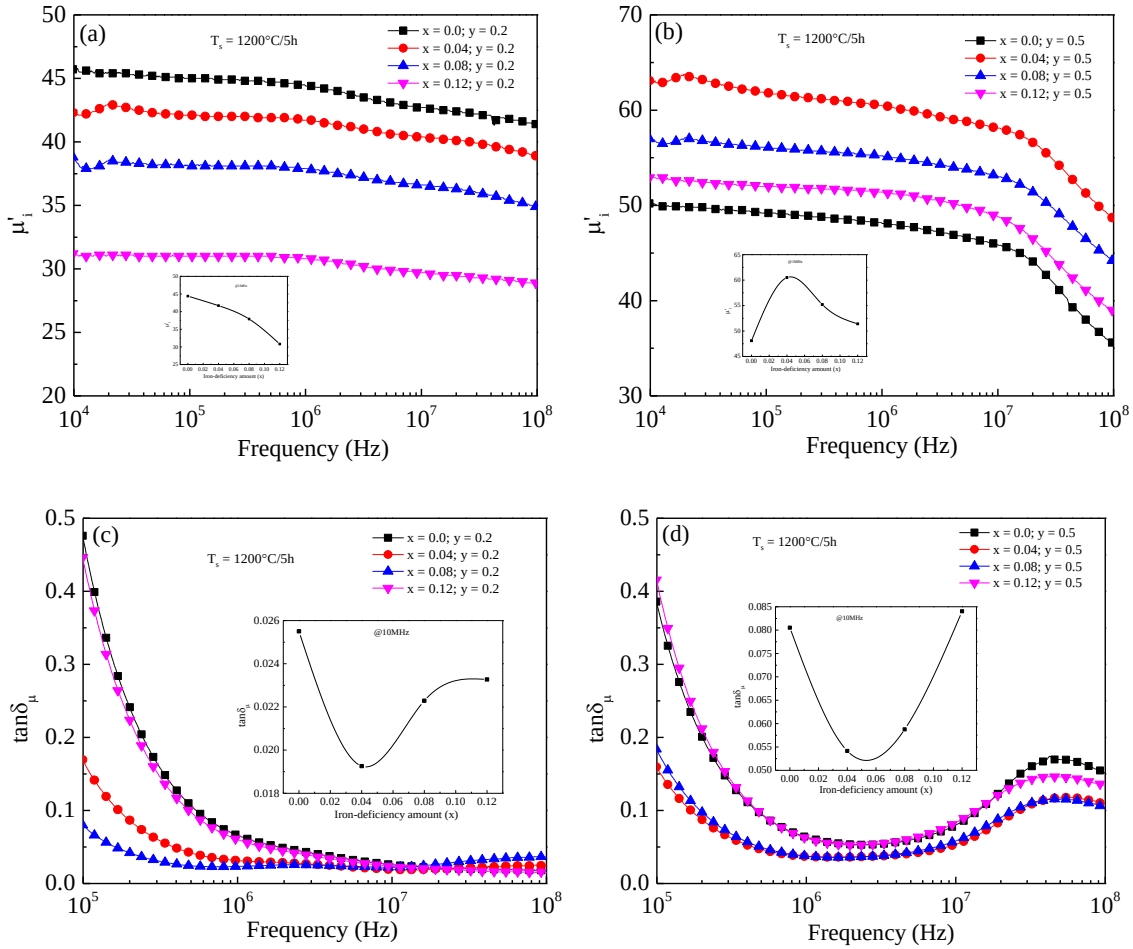

Figure 4.59: Evolution of real component (μ_i') of magnetic permeability with frequency and (inset) IDNS-dependent μ_i' at 1 MHz of (1-*y*) [BCZTO] + (*y*) [NCZFe$_{2-x}$O$_{4-3x/2}$] (*x* = 0.0; 0.04; 0.08; 0.12; *y* = 0.2, 0.5) ferroelectromagnetic composite ceramics: (a) *x* = 0.0; 0.04; 0.08; 0.12; *y* = 0.2 and (b) *x* = 0.0; 0.04; 0.08; 0.12; *y* = 0.5, and evolution of the magnetic loss tangent ($tan\delta_\mu$) with frequency and (inset) IDNS-dependent $tan\delta_\mu$ at 10 MHz: (c) *x* = 0.0; 0.04; 0.08; 0.12; *y* = 0.2 and (d) *x* = 0.0; 0.04; 0.08; 0.12; *y* = 0.5.

The magnetic permeability of magnetic materials has the general characteristic property that it is nearly frequency-invariant, reaches a maximum value at a certain frequency, and then rapidly depreciates through a ferromagnetic relaxing procedure to an extremely small value [542]. As shown in Figure 4.59 (a), the μ_i' value in the current experiment is not particularly steady in x = 0.0; 0.04; 0.08; 0.12; y = 0.2 ferroelectromagnetic composite ceramics across the whole measured frequency domain and steadily decreases as applied frequency increases. In contrast, Figure 4.59 (b) shows that the μ_i' value is nearly steady to a maximum of 10 MHz, but that it

thereafter begins to decline due to the ferromagnetic resonance phenomena. The nonappearance of phase lag amongst the applied frequency and domain wall's movement is attributed to the virtually frequency independent property of the μ_i' value throughout a large-frequency domain [543]. The compositional stability of ferroelectromagnetic composite ceramics is supported by the frequency-invariant μ_i' value. Table 4.57-4.58 and 4.59-4.60 list the μ_i' values for a few frequencies in y = 0.2 and 0.5, respectively. In x = 0.0; 0.04; 0.08; 0.12; y = 0.2 ferroelectromagnetic composite ceramics, the inset of Figure 4.59 (a) demonstrated that μ_i' drops with an ascent in IDNS. Conversely, the inset of Figure 4.59 (b) showed that the μ_i' value rises first in x = 0.04 and then drops with successive increases in IDNS in y = 0.5. Since the value of μ_i' value is exactly proportional to M_s [543], the recognized diminishing tendency in μ_i' value with rising IDNS level might be attributed to the diminution of M_s value. The drop in μ_i' value with IDNS is ascribed to a reduction in saturation magnetization because the reduction of ferrous ions at octahedrally coordinated site reduces the disparity in atomic magnetic moment in the midst of tetrahedrally and octahedrally coordinated sites [544]. Despite the fact that the bulk density and grain diameters rose, the μ_i' value degraded due to the pinning effect as a result of the pores within the grain border growing to be exceedingly big. As IDNS increased in y = 0.2 ferroelectromagnetic composite ceramics, μ_i' value dropped. The μ_i' value at chosen frequencies in the ferroelectromagnetic composite ceramics with x = 0.0; 0.04; 0.08; 0.12; y = 0.2 and x = 0.0; 0.04; 0.08; 0.12; y = 0.5 is shown in Table 4.57-4.58 and 4.59-4.60. Uozumi et al.'s description of the resonant frequency (f_r) [545] states that it follows the following relation [546, 547]: $f_r = \frac{4\rho}{\pi\mu_0\mu_i' D_{\mathrm{SEM}}^2}$, where ρ stands for electrical resistivity and μ_0 for magnetic permeability in air. Since f_r changes inversely with the square of grain diameter, it can be deduced from the relationship above that ferroelectromagnetic composite ceramics with larger grains have lower resonant frequencies. According to Table 4.57-4.58 and 4.59-4.60, the resonant frequency (f_r) is achieved from the maximum of μ_i''value. It is obvious

to see from Figure 4.59 (a) and Table 4.57-4.58 that in y = 0.2, the frequency at which the f_r value may be expected to occur is greater than 100 MHz. In contrast, it is clear from Figure 4.59 (b) and Table 4.59-4.60 that the f_r value escalates in x = 0.04 and afterwhich decreases on rising IDNS level further at y = 0.5. Snoek's law states that the f_r value changes inversely with μ_i' value [334, 548], therefore a decrease in μ_i' value corresponds to an increase in f_r value. Snoek's product [334, 548], that is defined as: $(\mu_i' - 1)f_r = 1/3\pi(\gamma M_s)$, where γ is the gyromagnetic ratio in *x* = 0.0; 0.04; 0.08; 0.12; *y* = 0.2 and *x* = 0.0; 0.04; 0.08; 0.12; *y* = 0.5 ferroelectromagnetic composite ceramics, is shown in Table 4.57-4.58 and 4.59-4.60. In contrast, Table 4.57-4.58 show that Snoek's product increases in x = 0.04 and then drops with rising IDNS level to a maximum of x = 0.12 if y = 0.5. This is because Snoek's product is not present when the f_r value appears away from 100 MHz in ferroelectromagnetic composite ceramics with x = 0.0; 0.04; 0.08; 0.12; y = 0.2. The loss tangent was examined to determine the dissipation of magnetic energy. Figure 4.59 (c, d) show how the magnetic loss tangent ($\tan\delta_\mu$) depends on frequency of the ferroelectromagnetic composite ceramics with (c) *x* = 0.0; 0.04; 0.08; 0.12; *y* = 0.2 and (d) *x* = 0.0; 0.04; 0.08; 0.12; *y* = 0.5. When the domain wall moves laterally relative to the applied field, the $\tan\delta_\mu$value is visible. The $\tan\delta_\mu$ value is expressed as [549]: $\tan\delta_\mu = \tan\delta_e + \tan\delta_h + \tan\delta_c$, where $\tan\delta_e$, $\tan\delta_h$, and $\tan\delta_c$ stand for corresponding eddy current loss tangent, hysteresis loss tangent, and residual loss tangent. According to reports, $\tan\delta_e$, $\tan\delta_h$, and $\tan\delta_c$, respectively, are the primary causes of magnetic loss tangent below 500 kHz [550]. The $\tan\delta_e$ value varies inversely with electrical resistivity and directly with operating frequency squared and average particle diameter [185, 551]. The $\tan\delta_e$ value rises as grain diameter grows because the domain wall may move more readily in larger grains. The $\tan\delta_e$ value becomes important at higher frequencies because changing magnetic fields induce circulating current in the ferroelectromagnetic composite ceramics, which causes energy losses [552]. It is crucial to improve the grain border resistivity in order

to raise the resistivity in order to lower the $\tan\delta_e$ value. In a weakly applied ac field, the $\tan\delta_h$ value has no effect because it alters inversely with the cubic of μ_i' value and directly with the operating frequency, i.e., $\tan\delta_h \propto 1/\mu_i'^3$. On the other hand, $\tan\delta_h$ value is primarily understood by the irreversible domain wall's movement that changes totally with the area of the hysteresis loop [185]. The average grain diameter, saturation magnetization, and magnetic anisotropy constant are viewed as being tightly correlated with the value of μ_i'. In order to lower the $\tan\delta_h$ value at low frequencies, it is therefore necessary to lessen the restriction on domain wall movement [551, 552]. The $\tan\delta_c$ value is consistent with the μ_i'' value, which positively affects the number of ferrous ions in the ferroelectromagnetic composite ceramics. Under low frequency (f <500 kHz), the $\tan\delta_c$ value could often be disregarded. By using a fine-grained sample, it should be able to maximize the complex magnetic permeability at the higher frequency while minimizing the $\tan\delta_c$ value. The IDNS restricts the electron exchange interaction in the midst of Fe^{2+} and Fe^{3+} in the current ferroelectromagnetic composite ceramics. The $\tan\delta_c$ value declines as a result of the electron exchange interaction being hindered by an increase in IDNS level [553]. From Figure 4.59 (c), it can be deduced that $\tan\delta_h$ declines to a maximum of 1 MHz before remaining nearly frequency invariant in x = 0.0; 0.04; 0.08; 0.12; y = 0.2. Furthermore, no discernible ferromagnetic resonant maximum is seen that might have occurred at frequencies greater than 100 MHz. From Figure 4.59 (d), it can be seen that the $\tan\delta_\mu$ value decreases to a maximum of 1 MHz, achieves a lowest value, increases again and achieves the maximum value at a particular frequency (signifying the domain wall's resonant process), drops with a further rise in frequency, and finally drops in ferroelectromagnetic composite ceramics with x = 0.0; 0.04; 0.08; 0.12; y = 0.5. If the frequency of domain wall and applied field harmonize, the loss peak manifests [67]. The $\tan\delta_\mu$ values in ferroelectromagnetic composite ceramics with x = 0.0; 0.04; 0.08; 0.12; y = 0.2 and x = 0.0; 0.04; 0.08; 0.12; y = 0.5 at specific frequencies are reported in Table 4.57-4.58 and

4.59-4.60. The inset of Figure 4.59 (c, d) delineates the alteration in $\tan\delta_\mu$ in the ferroelectromagnetic composite ceramics with x = 0.0; 0.04; 0.08; 0.12; y = 0.2 and x = 0.0; 0.04; 0.08; 0.12; y = 0.5 at a specific frequency (1 MHz) using IDNS. From Figure 4.59 (c)'s inset, it is recognized that $\tan\delta_\mu$ declines as IDNS increases to a maximum of x = 0.04 and then stays constant until x = 0.12 when y = 0.2. In contrast, $\tan\delta_\mu$ is seen to decline in x = 0.04 and then increase on rising IDNS level until x = 0.12 if y = 0.5. These attributes might be attributed to the microstructural change. The relative loss coefficient (RLF) ($RLF = \tan\delta_\mu/\mu_i'$)should be kept as low as feasible in the ferroelectromagnetic composite ceramics' practical applications. Table 4.57-4.58 and 4.59-4.60 displays RLF at certain frequencies in ferroelectromagnetic composite ceramics with x = 0.0; 0.04; 0.08; 0.12; y = 0.2 and x = 0.0; 0.04; 0.08; 0.12; y = 0.5. The smaller grain diameter is assumed to be the cause of the lower RLF values, as shown in Table 4.57-4.58 and 4.59-4.60. The smaller grain diameter implies an improvement in grain borders, which hinders the flow of eddy current [554].

4.4.11. Q-factor analysis

Figure 4.60 shows how the Q-factor evolves with frequency of (1-y) [BCZTO] + (y) [$NCZFe_{2-x}O_{4-3x/2}$] ferroelectromagnetic composite ceramics with (a) x = 0.0; 0.04; 0.08; 0.12; y = 0.2 and (b) x = 0.0; 0.04; 0.08; 0.12; y = 0.5. In the ferroelectromagnetic composite ceramics with x = 0.0; y = 0.2 and x = 0.12; y = 0.2, it can be shown in Figure 4.60 (a) that the Q-factor increases gradually across the accessible frequency range, with the peaks equivalent to the maximum Q-factor being located outside of the experimental frequency. At the higher frequency side, the Q-factor achieves its greatest value and is then aided in x = 0.04; y = 0.2. The Q-factor increases progressively with increasing frequency. There are also two peaks with the values of x = 0.08; y = 0.2. The domain wall oscillations may be responsible for the peak at the lower frequency side, while the precession of electron spins may be responsible for the peak at high frequencies [555, 556]. According to Figure 4.60 (b), the Q-factor rises with increasing applied frequency,

reaches its maximum value, and then starts to fall at the higher frequency side in x = 0.0; 0.04; 0.08; 0.12; y = 0.5. In x = 0.04; y = 0.2 and x = 0.08; y = 0.2, the peak values correlating to the optimal Q-factor shifted toward the lower frequency side with sising IDNS level. In y = 0.5, it was noticed that the peaks equivalent to the highest Q-factor moved toward the lower frequency side on rising IDNS level. When the loss factor ($tan\delta_{\mu}$) is at its lowest, the highest Q-factor manifests. The Q-factor values in x = 0.0; 0.04; 0.08; 0.12; y = 0.2 and x = 0.0; 0.04; 0.08; 0.12; y = 0.5 at specific frequencies are provided in Table 4.57-4.58 and 4.59-4.60. We can see from Table 4.57-4.58 and 4.59-4.60 that the Q-factor increases successively with rising IDNS level to a maximum of x = 0.08 and afterwhich drops in x = 0.12; y = 0.2 at 1 MHz. When y = 0.5 at 1 MHz, the Q-factor first rises in x = 0.04 and then falls with IDNS. Resistivity is increased by the improvement of grain borders. The presence of IDNS significantly raises the resistivity of the ferroelectromagnetic composite ceramics. The x = 0.08 FEMCC displays the highest Q-factor when compared to other ferroelectromagnetic composite ceramics, which is closely related to the presence of substantial magnetic permeability, and increased resistivity leads in a lesser loss tangent. Due to an improvement in the concentration of electronic interaction in the midst of ferrous and ferric ions, the Q-factor rises with IDNS due to an increase in resistivity and a decrease in eddy current loss. As IDNS increases, it is recognized that the optimum Q-factor also increases significantly and shifts toward the higher frequencies. The product ($Q \times f$) in x = 0.0; 0.04; 0.08; 0.12; y = 0.2 and x = 0.0; 0.04; 0.08; 0.12; y = 0.5 at 1 MHz is shown in Table 4.57-4.58 and 4.59-4.60. When y = 0.2, the product ($Q \times f$) grows with rising IDNS level to a maximum of x = 0.08 before declining in x = 0.12; but, if y = 0.5, it rises in x = 0.04 before declining with rising IDNS level to a maximum of x = 0.12.

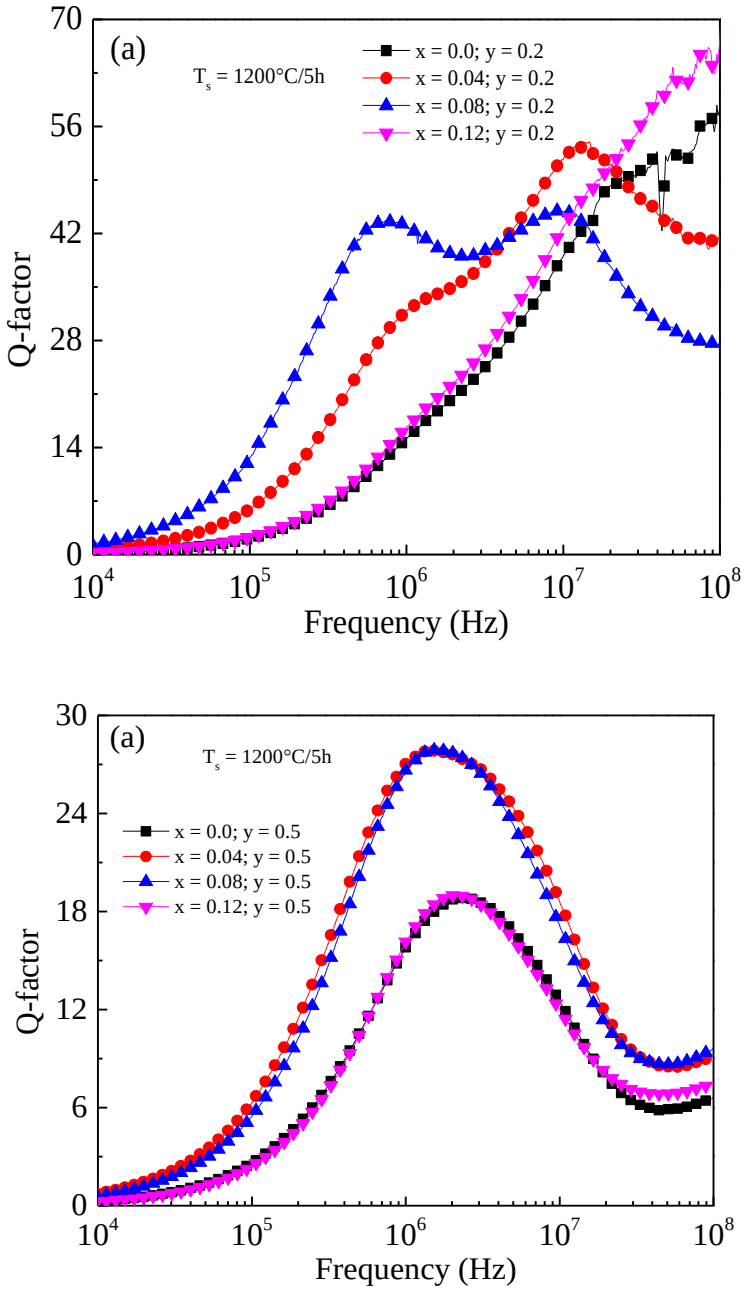

Figure 4.60: Evolution of Q-factor with frequency of (1-*y*) [BCZTO] + (*y*) [NCZFe$_{2-x}$O$_{4-3x/2}$] (*x* = 0.0; 0.04; 0.08; 0.12; *y* = 0.2; 0.5) ferroelectromagnetic composite ceramics: (a) *x* = 0.0; 0.04; 0.08; 0.12; *y* = 0.2 and (b) *x* = 0.0; 0.04; 0.08; 0.12; *y* = 0.5.

Table 4.57. Real component (μ_i') and imaginary component (μ_i'') of magnetic permeability, magnetic loss tangent ($tan\delta$), relative loss factor ($tan\delta_\mu/\mu_i'$), Q-factor at specific frequencies, resonant frequency (f_r), and Snoek's product of (1-*y*) [BCZTO] + (*y*) [$NCZFe_{2-x}O_{4-3x/2}$] (*x* = 0, 0.04; *y* = 0.2) ferroelectromagnetic composite ceramics

Composition		Frequency	μ_i'	μ_i''	$tan\delta$	$tan\delta_\mu/\mu_i'$	Q-factor	$Q \times f$ at 1MHz	f_r (MHz)	Snoek's product ($\mu_i' \times f_r$) at 1 MHz
x	y									
0.0	0.2	10 kHz	45.8	209.0	4.56	9.96×10^{-2}	0.22	15.23	-	-
		100 kHz	45.0	21.0	0.47	1.04×10^{-2}	2.14			
		1 MHz	44.4	2.92	0.07	1.48×10^{-3}	15.23			
		10 MHz	42.7	1.09	0.03	5.97×10^{-4}	39.21			
		100 MHz	41.3	0.67	0.02	3.94×10^{-4}	61.37			
0.04	0.2	10 kHz	42.2	64.5	1.53	3.62×10^{-2}	0.66	31.91	-	-
		100 kHz	42.1	6.96	0.17	3.93×10^{-3}	6.05			
		1 MHz	41.7	1.31	0.03	7.52×10^{-4}	31.91			
		10 MHz	40.4	0.78	0.02	4.77×10^{-4}	51.93			
		100 MHz	38.9	0.96	0.02	6.33×10^{-4}	40.62			

Table 4.58. Real component (μ_i') and imaginary component (μ_i'') of magnetic permeability, magnetic loss tangent ($tan\delta$), relative loss factor ($tan\delta_\mu/\mu_i'$), Q-factor at specific frequencies, resonant frequency (f_r), and Snoek's product of (1-*y*) [BCZTO] + (*y*) [NCZFe$_{2-x}$O$_{4-3x/2}$] (*x* = 0.08, 0.12; *y* = 0.2) ferroelectromagnetic composite ceramics

Composition		Frequency	μ_i'	μ_i''	$tan\delta$	$tan\delta_\mu/\mu_i'$	Q-factor	$Q \times f$ at 1MHz	f_r (MHz)	Snoek's product ($\mu_i' \times f_r$) at 1 MHz
x	y									
0.08	0.2	10 kHz	38.7	26.8	0.69	1.79×10^{-2}	1.44	42.88	-	-
		100 kHz	38.2	2.99	0.08	2.05×10^{-3}	12.78			
		1 MHz	37.9	0.88	0.02	6.15×10^{-4}	42.88			
		10 MHz	36.6	0.82	0.02	6.09×10^{-4}	44.86			
		100 MHz	34.8	1.27	0.04	1.05×10^{-3}	27.41			
0.12	0.2	10 kHz	31.2	136.0	4.36	1.40×10^{-1}	0.23	16.66	-	-
		100 kHz	31.0	13.5	0.44	1.41×10^{-2}	2.29			
		1 MHz	30.8	1.85	0.06	1.95×10^{-3}	16.66			
		10 MHz	29.7	0.69	0.02	7.84×10^{-4}	42.97			
		100 MHz	28.8	0.42	0.01	5.03×10^{-4}	69.04			

Table 4.59. Real component (μ_i') and imaginary component (μ_i'') of magnetic permeability, magnetic loss tangent ($tan\delta$), relative loss factor ($tan\delta_\mu/\mu_i'$), Q-factor at specific frequencies, resonant frequency (f_r), and Snoek's product of (1-*y*) [BCZTO] + (*y*) [$NCZFe_{2-x}O_{4-3x/2}$] (*x* = 0, 0.04; *y* = 0.5) ferroelectromagnetic composite ceramics

Composition		Frequency	μ_i'	μ_i''	$tan\delta$	$tan\delta_\mu/\mu_i'$	Q-factor	$Q \times f$ at 1MHz	f_r (MHz)	Snoek's product ($\mu_i' \times f_r$) at 1 MHz
x	y									
0.0	0.5	10 kHz	50.2	181.0	3.61	7.20×10^{-2}	0.28	15.80	41.9	2015.39
		100 kHz	49.2	18.6	0.38	7.70×10^{-3}	2.64			
		1 MHz	48.1	3.05	0.06	1.32×10^{-3}	15.80			
		10 MHz	45.8	3.69	0.08	1.76×10^{-3}	12.42			
		100 MHz	35.4	5.31	0.15	4.24×10^{-3}	6.67			
0.04	0.5	10 kHz	63.0	83.2	1.32	2.10×10^{-2}	0.76	27.03	44.2	2674.10
		100 kHz	61.8	9.7	0.16	2.54×10^{-3}	6.37			
		1 MHz	60.5	2.24	0.04	6.12×10^{-4}	27.03			
		10 MHz	58.1	3.15	0.05	9.32×10^{-4}	18.47			
		100 MHz	48.5	5.28	0.11	2.24×10^{-3}	9.19			

Table 4.60. Real component (μ_i') and imaginary component (μ_i'') of magnetic permeability, magnetic loss tangent ($tan\delta$), relative loss factor ($tan\delta_\mu/\mu_i'$), Q-factor at specific frequencies, resonant frequency (f_r), and Snoek's product of (1-*y*) [BCZTO] + (*y*) [$NCZFe_{2-x}O_{4-3x/2}$] (*x* = 0.08, 0.12; *y* = 0.5) ferroelectromagnetic composite ceramics

Composition		Frequency	μ_i'	μ_i''	$tan\delta$	$tan\delta_\mu/\mu_i'$	Q-factor	$Q \times f$ at 1MHz	f_r (MHz)	Snoek's product ($\mu_i' \times f_r$) at 1 MHz
x	y									
0.08	0.5	10 kHz	57.2	93.7	1.64	2.86×10^{-2}	0.61	26.64	41.9	2312.88
		100 kHz	56.1	10.1	0.18	3.23×10^{-3}	5.53			
		1 MHz	55.2	2.07	0.04	6.80×10^{-4}	26.64			
		10 MHz	53	3.12	0.06	1.11×10^{-3}	17.02			
		100 MHz	44.1	4.57	0.10	2.35×10^{-3}	9.64			
0.12	0.5	10 kHz	53.0	209.0	3.95	7.45×10^{-2}	0.25	16.15	34.0	1747.60
		100 kHz	52.0	21.3	0.41	7.87×10^{-3}	2.44			
		1 MHz	51.4	3.18	0.06	1.20×10^{-3}	16.15			
		10 MHz	48.8	4.10	0.08	1.72 × 10-3	11.90			
		100 MHz	38.8	5.17	0.13	3.43×10^{-3}	7.51			

4.4.12. Magnetoelectric effect

Figure 4.61 shows how the magnetoelectric response (α_{ME}) of (1-*y*) [BCZTO] + (*y*) [$NCZFe_{2-x}O_{4-3x/2}$] ferroelectromagnetic composite ceramics depends on magnetic field: (a) *x* = 0.0; 0.04; 0.08; 0.12; *y* = 0.2 and (b) *x* = 0.0; 0.04; 0.08; 0.12; *y* = 0.5. The proportion of the component phases, micromorphological development interface borders, electromechanical linking coefficient, piezoelectric and magnetostriction values, magnetic-mechanical-electric interplay, electric permittivity, and resistance of each phase are all significant variables that have an impact on the magnetoelectric response [557, 558]. The interaction of magnetic, mechanical, and electric forces amongst the component phases causes the magnetoelectric effect. Due to its magnetostrictive deformation brought on by spin-orbit interplay, the ferromagnetic phase experiences elastic strain when the magnetic field is triggered. Through the contact, the ferroelectric phase gradually takes on the same elastic strain that was previously present in the ferromagnetic phase. A demonstrably high voltage has been produced in ferroelectromagnetic composite ceramics as a result of the magnetoelectric process brought on by the magnetic field that is applied [559]. The typical type or evidence of the magnetic-mechanical-electric interplay amidst component phases should, in theory, be that α_{ME} improves with rising applied magnetic field, arrives at its maximum value, and then drops with rising applied magnetic field [560]. From Figure 4.61 (a), it can be shown that α_{ME} dramatically improves to a maximum of a certain field and then progressively increases with increasing DC magnetic field in x = 0.0; 0.04; 0.08; 0.12; y = 0.2 ferroelectromagnetic composite ceramics, exhibiting the greatest value of 0.81 mV/cm-Oe. Because of the reduced composition of the $NCZFe_{2-x}O_{4-3x/2}$ and BCZTO phases, which result in a decrease in magnetostriction and piezoelectricity, respectively, this smaller value may be attributed to the combined influence of these two phenomena. According to a theoretical investigation, the reduction of magnetostriction and piezoelectricity results in a reduction in α_{ME} [561]. Additionally, it is important to note that as IDNS increases, α_{ME} improves.

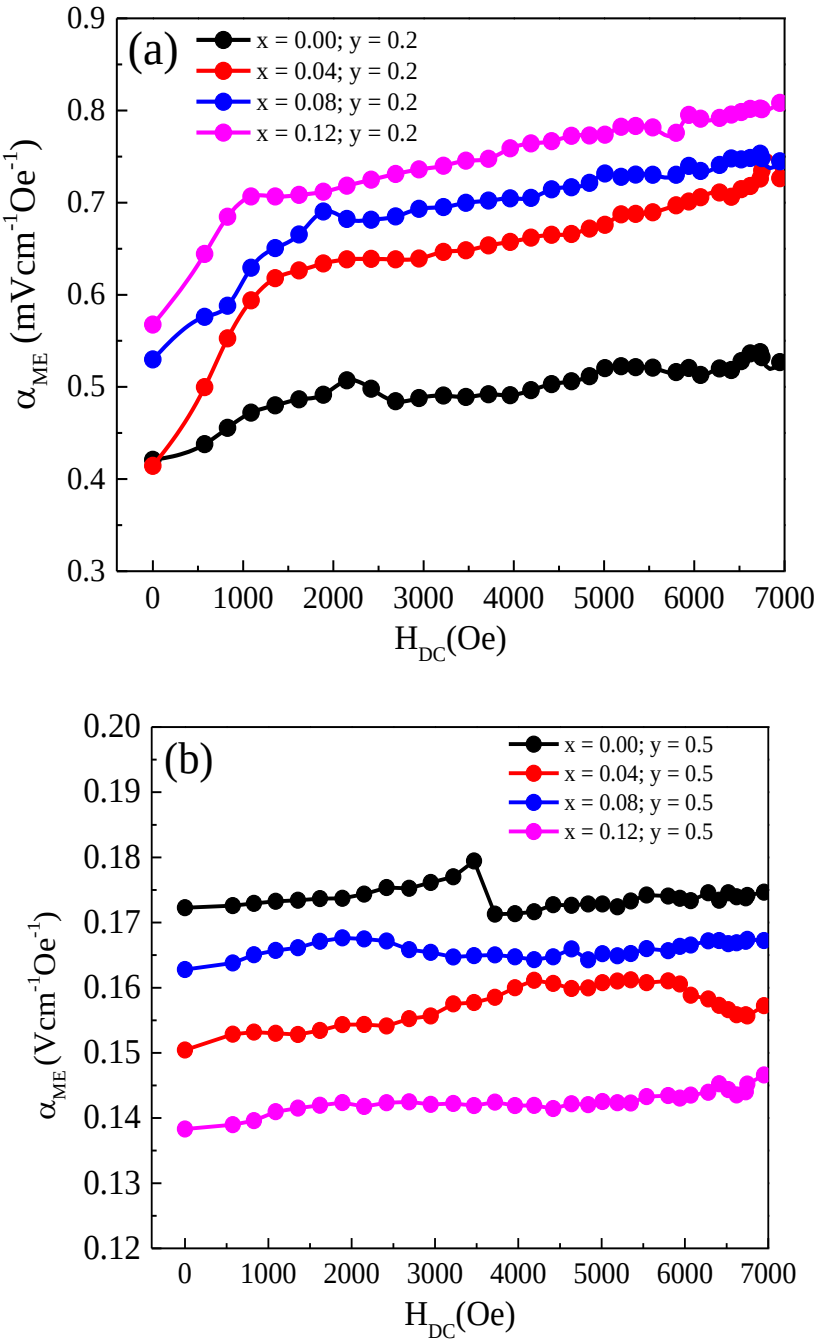

Figure 4.61: Evolution of the magnetoelectric response (α_{ME}) with DC magnetic field of (1-*y*) [BCZTO] + (*y*) [NCZFe$_{2-x}$O$_{4-3x/2}$] (*x* = 0.0; 0.04; 0.08; 0.12; *y* = 0.2, 0.5) ferroelectromagnetic composite ceramics: (a) *x* = 0.0; 0.04; 0.08; 0.12; *y* = 0.2 and (b) *x* = 0.0; 0.04; 0.08; 0.12; *y* = 0.5.

The increase in elastic interactions in the midst of the component phases is credited with causing the first improvement in α_{ME} [453, 562, 563]. According to Figure 4.61 (b), the saturated domain wall movement [564-566], which is attributed to the ferroelectromagnetic

composite ceramics, has the maximum value of 0.17 V/cm-Oe and causes α_{ME} to practically become field invariant in x = 0.0; 0.04; 0.08; 0.12; y = 0.5. The greater $NCZFe_{2-x}O_{4-3x/2}$ concentration in the ferroelectromagnetic composite ceramics has reportedly been shown to have a high magnetostrictive and piezomagnetic coefficient [567]. As a consequence, the $NCZFe_{2-x}O_{4-3x/2}$ phase deforms more when a magnetic field is introduced to the ferroelectromagnetic composite ceramics. This larger deformation is then immediately transferred as a considerable elastic strain to the BCZTO through mechanical linking in the midst of the two phases, improving electrical polarization. A large magnetoelectric output is achieved by this improvement, which also successfully achieves the straightforward alignment of the dipole. According to theory, ferroelectromagnetic composite ceramics with an equal proportion of ferroelectric and ferromagnetic phases should provide the highest magnetoelectric response [568, 569]. In x = 0.0; 0.04; 0.08; 0.12; y = 0.2 and x = 0.0; 0.04; 0.08; 0.12; y = 0.5 ferroelectromagnetic composite ceramics with the change of IDNS, a sizable amount of α_{ME} is seen even at zero field ($H_{dc} = 0$), which might be attributed to the remanence and easy magnetization traits with decreased coercivity [570, 571]. Figure 4.62 shows how the magnetoelectric response (α_{ME}) changes with IDNS, grain diameter, and porosity in (a) x = 0.0; 0.04; 0.08; 0.12; y = 0.2 and (b) x = 0.0; 0.04; 0.08; 0.12; y = 0.5 ferroelectromagnetic composite ceramics. It is evident that the IDNS, grain diameter, and porosity have a significant impact on α_{ME} value. Because increasing porosity lowers the magnetic-mechanical-electrical interplay in the midst of two phases, Petrov et al.'s [572] experimental and theoretical evidence shows that α_{ME} decreases as porosity increases. It can be shown from Figure 4.62 (a, b) that α_{ME} decreases as grain diameter increases. This distinguishing quality is explained by the fact that larger grains are less effective than smaller grains in producing magnetostriction and piezoelectric coefficient [368]. On the other hand, because increased porosity diminishes the magnetic-mechanical-electrical interplay in the midst of two phases, α_{ME} declines with increased porosity [572]. The significant magnetic-mechanical-electric interplay in the midst

of the $NCZFe_{2-x}O_{4-3x/2}$ and BCZTO phases of ferroelectromagnetic composite ceramics may support the improvement in α_{ME}.

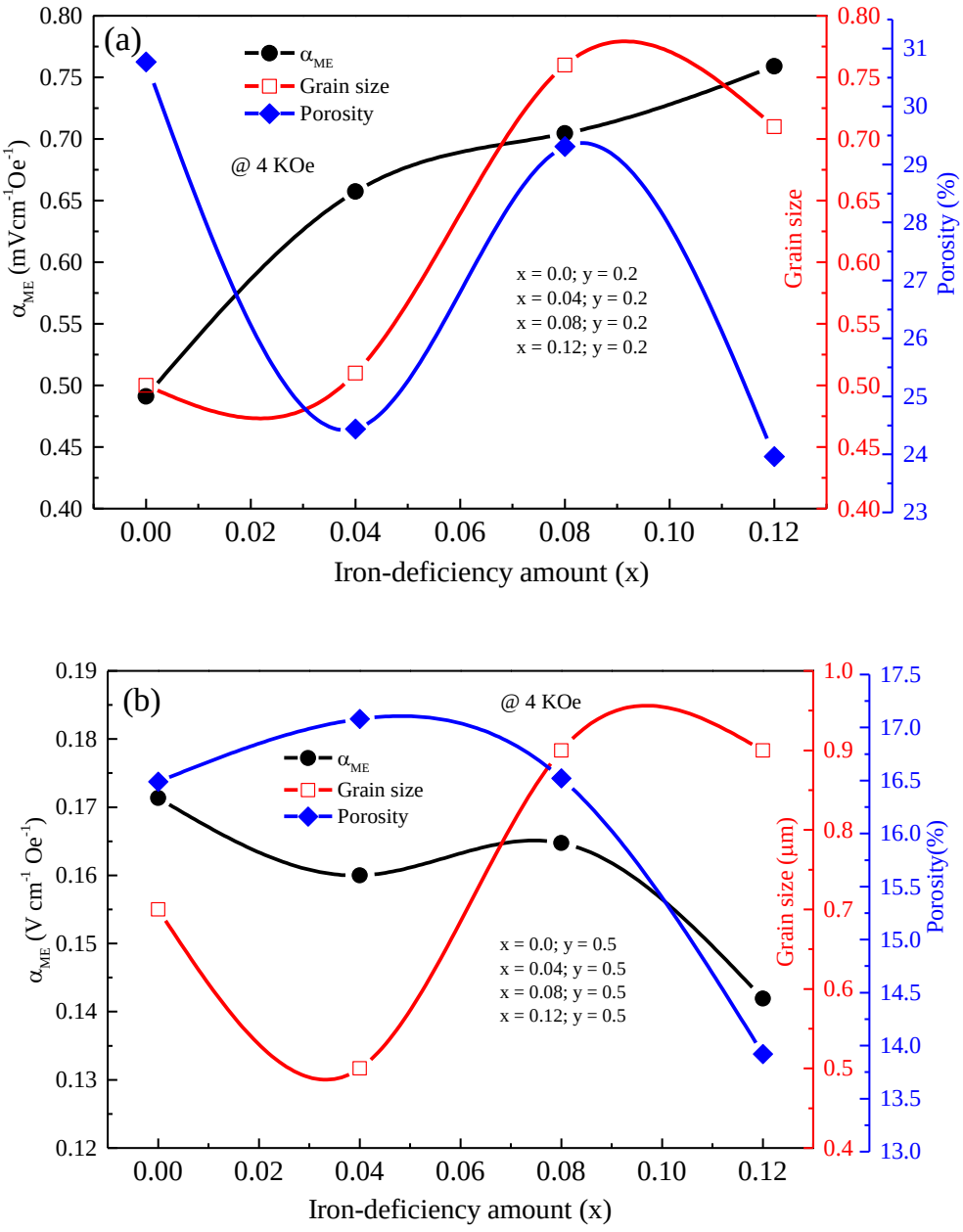

Figure 4.62: Evolution of the magnetoelectric response (α_{ME}), average grain diameter (D_{SEM}), and porosity (P%) with various IDNS at specific DC-applied field (4 kOe) of (1-*y*) [BCZTO] + (*y*) [$NCZFe_{2-x}O_{4-3x/2}$] (*x* = 0.0; 0.04; 0.08; 0.12; *y* = 0.2, 0.5) ferroelectromagnetic composite ceramics: (a) *x* = 0.0; 0.04; 0.08; 0.12; *y* = 0.2 and (b) *x* = 0.0; 0.04; 0.08; 0.12; *y* = 0.5.

Chapter Five: Summary and conclusions

The present research mainly focuses on the sintering temperature and iron-deficient amount dependent structural, microstructural, elastic, electrical and magnetic traits of stoichiometric nickel-copper-zinc ferrites, $Ni_{0.25}Cu_{0.13}Zn_{0.62}Fe_2O_4$ (NCZFO) and non-stoichiometric nickel-copper-zinc ferrites, $Ni_{0.25}Cu_{0.13}Zn_{0.62}Fe_{2-x}O_{4-3x/2}$ ($NCZFe_{2-x}O_{4-3x/2}$) and iron-deficiency non-stoichiometry (IDNS) amount dependent phase structure, microstructure, electric, magnetic, and magnetoelectric traits of (1-*y*) [BCZTO] + (*y*) [NCZFO] ($0 \leq y \leq 1.0$) and (1-*y*) [BCZTO] + (*y*) [$NCZFe_{2-x}O_{4-3x/2}$] (x = 0.0; 0.04; 0.08; 0.12 and y = 0.2; 0.5) ferroelectromagnetic composite ceramics allows us to draw the following conclusions:

5.1. Summary and conclusions

- XRD and FTIR analyses reveal that the stoichiometric NCZFO ferrites possesses spinel skeleton with cubic symmetry. The lattice constant varied in a non-systematic manner with sintering temperature (T_s). Zinc loss from the sample, cation re-allocation in the midst of tetrahedrally and octahedrally coordinated sites, and the oxidation-reduction process all have an impact on how the lattice constant varies with temperature (Ts).
- The crystallite diameter of stoichiometric NCZFO ferrites have been observed to vary non-systematically with T_s. The solid-state diffusion process, which decreases the system's free energy by reducing the particle surface area, has resulted in the particles' consolidation, which has caused the crystallite diameter to grow with T_s. The crystallite diameter was larger at lower T_s than at higher T_s.
- As the T_s rises, the bulk density of stoichiometric NCZFO ferrites drops as the porosity rises. The manifestation of grain development with the elevation of T_s causes the porosities to segregate to the grain borders, which is why the samples appear to be quite dense.

- It is noted that the grain diameter is augmented with elevating T_s, and EDX analysis shows the existence of the component elements in the stoichiometric ratio, according to SEM examination of stoichiometric NCZFO ferrites.
- The elastic moduli, Poisson's ratio, longitudinal, transversal and mean elastic wave velocities, and Debye temperature were assessed. Through the use of the Ledbetter and Datta (LD) and the Hasselman and Fulrath (HF) models, the zero-porosity correction to elastic traits were executed and provide different values for corrected elastic moduli.
- The Maxwell-Wagner-type interfacial polarization causes the dielectric traits of NCZFO ferrites to behave dispersively at lower frequencies, and it is shown to rise with T_s as a result of the partial reduction of Fe^{3+} ions to Fe^{2+} ions.
- According to an analysis of the ac conductivity of NCZFO ferrites, the electrical conduction is discovered to support Jonscher's power law and is controlled by the small polaron-based hopping phenomenon.
- According to Cole-Cole plots, the processes connected to the grain borders in the investigated frequency range are primarily responsible for the capacitative and resistive characteristics of synthesized ferrites. Impedance spectroscopic analysis demonstrates that as T_s is raised, both grain and grain border resistance decrease.
- Due to the improvement in bulk densities and grain diameters, the magnetic permeability of NCZFO ferrites rises with T_s. Along with the rise in T_s, the Q-factor falls and the frequency of resonance moves to lower region of frequency.
- Due to the lack of sample's homogeneity and the existence of intra-granular porosity, the magnetic traits of NCZFO ferrites rapidly decrease with T_s.
- XRD and FTIR analyses confirms the evolution of spinel skeleton with cubic symmetry iron-deficient $NCZFe_{2-x}O_{4-3x/2}$ ferrites. At 1100 °C, the lattice constant increases in linear manner with IDNS amount, however at 1150, 1200, and 1250 °C, it is seen to fluctuate non-linearly.

- The elastic characteristics, longitudinal, transversal, mean elastic wave velocities, and Debye temperature have been computed from FTIR data. Through the use of the HF, LD, and elastic theory (ET) models, the zero porosity correct to elastic traits were executed and provide different values for corrected elastic moduli.
- The agglomeration and irregular grain growth have been seen in $NCZFe_{2-x}O_{4-3x/2}$ ferrites, and agglomerations occur because of the magnetic interplay in the midst of the component grains.
- Because of enhanced densification and the production of Fe^{2+} ions, it is discovered that the dielectric characteristics of $NCZFe_{2-x}O_{4-3x/2}$ ferrites improve with T_s.
- The electrical conductivity study of $NCZFe_{2-x}O_{4-3x/2}$ ferrites suggests that the electrical conduction process obeys Jonscher's universal power expression and is regulated by the charge carrier's hopping amongst the localized states. The power law exponent is observed to vary non-monotonically with increasing T_s and iron-nonstoichiometry amount.
- Cole-Cole plots proclaims that the electrical conduction in $NCZFe_{2-x}O_{4-3x/2}$ ferrites is ascribed to the grain border contribution.
- The alteration of bulk density, porosity, particle diameter, and magnetic anisotropy may be credited for the percieved changes in magnetic permeability and magnetic loss tangent with respect to the IDNS amount.
- XRD and FTIR studies have validated the simultaneousness of distinct phases in (1-*y*) [BCZTO] + (*y*) [NCZFO] ($0 \leq y \leq 1.0$) composites. In composites, the component phases retain their tetragonal structure for BCZTO and cubic structure for NCZFO, respectively. Since the metal's ionic radii in composites change, so do the lattice constants for the component phases in BCZTO-NCZFO composites.
- With rising NCZFO content and T_s, the crystallite diameter of the component phases fluctuates non-systematically. Such changes in crystallite diameter could be associated

with the combined impact of two parameters, such as (1) change in cell volume (the lattice constant) and (2) stress and microstrain that generated from the crystal lattice's imperfections.

- The production of quasi-spherical type micromorphology with generally homogenous grain diameter, negligible voids or pores, and minute agglomeration is revealed by SEM analysis of BCZTO-NCZFO composites. When NCZFO is added to the BCZTO matrix, the uneven grain development is revealed. With increasing NCZFO content, the grain's uneven form has been noticed as a result of NCZFO particles segregating at the grain borders and filling pores in the midst of BCZTO grains.
- Due to space-charge and orientational polarizations, dielectric dispersion is seen at lower frequencies. Due to the dilution effect, the electric permittivity of BCZTO-NCZFO composites is found to decrease as NCZFO concentration increases, whereas the dielectric characteristics are seen to improve when T_s rises. The electric permittivity has been theoretically computed using several models, and comparisons with experimental results have been performed. The ion’s diffusion and contact in the midst of two phases have been perceived to cause a mismatch in the midst of the experimental and calculated values.
- A close coincidence in the midst of the observed electric permittivity and the porosity corrected electric permittivity has been noticed after performing the porosity correction to electric permittivity.
- In a region of low frequency, the conductivity is constant, whereas in a region of high frequency, the conductivity rises as the frequency rises. The electrical conduction mechanism is thought to follow Jonscher's power law and be controlled by the small polaron-based conduction mechanism, according to an examination of the AC conductivity of composites made of BCZTO and NCZFO.

- The existence of both grains and grain borders is indicated by Nyquist plots, and grain borders significantly affect the overall electric characteristics of BCZTO-NCZFO composites.
- It is discovered that the magnetic permeability improves as NCZFO content rises. Theoretically, the magnetic permeability has been calculated via different models, and comparisons with experimental results have been performed. Due to ion diffusion and interplay in the midst of two phases, there is a discrepancy in the midst of the calculated and measured values.
- In (1-y) [BCZTO] + (y) [$NCZFe_{2-x}O_{4-3x/2}$] ferroelectromagnetic composite ceramics, XRD and FTIR investigations supported the simultaneousness of the component phases without having no discernible undesired phase development.
- Lattice constants, average crystallite diameter, and cell volume in BCZTO-$NCZFe_{2-x}O_{4-3x/2}$ composites are observed to fluctuate non-monotonically with increasing IDNS amount.
- SEM analysis of BCZTO-$NCZFe_{2-x}O_{4-3x/2}$ composites demonstrate the production of polyhedral or irregularly shaped grains with minor agglomeration and porosity, as well as IDNS amount.
- According to Koop-Maxwell and Wagner models, the low-frequency dielectric dispersion in BCZTO-$NCZFe_{2-x}O_{4-3x/2}$ composites has been observed due to remarkably conducting grains and weakly conducting grain border.
- The electrical conductivity increases slightly with increasing frequency at lower frequency regime, while raises rapidly at higher frequency regime. In BCZTO-$NCZFe_{2-x}O_{4-3x/2}$ composites, the conductivity follows Jonscher power law with significant dispersion at high frequency region and is controlled through the transfer of charge and hopping of small polaron exchange interplay amongst the adjacent localized sites.

- ❖ The impedance study demonstrated that the phenomena associated with electrical conductivity may be supported by combined effect of highly conducting grain and poorly conducting grain border contributions.
- ❖ It is noticed that the magnetic permeability is enhanced in x = 0.04 before declining upon rising IDNS amount in y = 0.5, after which it is shown to decrease with increasing IDNS amount in y = 0.2.
- ❖ Due to the elastic interplay in the midst of the two phases, which is mediated by strain, a highest magnetoelectric coefficient of 0.17 V $cm^{-1}Oe^{-1}$ has been achieved for the composites at x = 0.0; y = 0.5.

5.2. Recommendations for future Research

Some recommendations for future research are given below:

- ➢ Measurement of Transmission electron micrographs (TEM).
- ➢ Measurement of (P-E) loop measurement to know the ferroelectric properties.
- ➢ Mössbauer spectroscopy to realize cation the allocation in the midst of tetrahedrally coordinated (A) and octahedrally coordinated (B)-sites

References

[1] Vopson, M. M., "Fundamentals of Multiferroic Materials and Their Possible Applications", *Crit. Rev. Solid State Mater. Sci*., 2015, 223-250

[2] Kolozsváry, Z. "The Relationship between Materials Science and the Fourth Industrial Revolution", Acta *Mater. Transylvan*., 2019, 2/1, 1-6.

[3] Whittaker, E. T., "A History of the Theories of Aether and Electricity", Thomas Nelson and Sons, London, 1951

[4] Vaz, C. A. F.; Hoffman, J.; Ahn, C. H.; Ramesh, R., "Magnetoelectric Coupling Effects in Multiferroic Complex Oxide Composite Structures", Adv. Mater., 2010, 22, 2900-2918

[5] Gnewuch, S.; Rodriguez, E. E., "The fourth ferroic order: Current status on ferrotoroidic materials", *J. Solid State Chem*. 2019, 271, 175-190

[6] Schmid, H., "Multi-ferroic magnetoelectrics", *Ferroelectrics*, 1994, 162, 317

[7] Scott, J., "Applications of magnetoelectrics", *J. Mater. Chem*. 2012, 22, 4567-4574

[8] Cheng, Y.; Peng, B.; Hu, Z,; Zhou, Z.; Liu, M., "Recent development and status of magnetoelectric materials and devices", *Phys. Lett. A*, 2018, 382, 3018-3025

[9] Hu, J. M.; Chen, L. Q. (2021), Magnetoelectrics and Multiferroics. In: Coey, M., Parkin, S. (eds.) Handbook of Magnetism and Magnetic Materials. Springer, Cham. p. 595-614

[10] Zhou, Y.; Maurya, D.; Yan, Y.; Srinivasan, G.; Quandt, E.; Priya, S., "Self-Biased Magnetoelectric Composites: An Overview and Future Perspectives", *Energy Harv. Sys*., 2016, 3, 1-42

[11] Pereira, N.; Lima, A. C.; Lanceros-Mendez, S.; Martins, P., "Magnetoelectrics: Three Centuries of Research Heading Towards the 4.0 Industrial Revolution", *Mater*., 2020, 13, 4033

[12] Eerenstein, W.; Mathur, N. D.; Scott, J. F., "Multiferroic and magnetoelectric materials", *Nature*, 2006, 442, 759-765

[13] Martin, L. W.; Crane, S. P.; Chu, Y. H.; Holcomb, M. B.; Gajek, M.; Huijben, M.; Yang, C. H.; Balke, N.; Ramesh, R., "Multiferroics and magnetoelectrics: thin films and nanostructures*", J. Phys.: Condens. Matter.*, 2008, 20, 434220

[14] Röntgen, W. C., "Ueber die durch Bewegung eines im homogenen electrischen Felde befindlichen Dielectricums hervorgerufene electrodynamische Kraft", *Ann. Phys*., 1888, 35, 264-270

[15] Curie, P., "Sur la symétrie dans les phénomènes physiques, symétrie d'un champ électrique et d'un champ magnétique", *J. Phys*., 1894, 393, 118-141

[16] Debye, P., "Remark to some new trials on a magneto-electrical direct effect", Z. Phys., 1926, 36, 300-301

[17] Landau, L. D.; Lifshitz, E. M., *Electrodynamics of Continuous Media* (Addison-Wesley Publishing Company, Inc., Reading, Massachusetts, 1960), p. 119

[18] Dzyaloshinskii, I. E., "On the magneto-electrical effect in antiferromagnets", *J. Exp. Theor. Phys*., 1960, 10, 628-629

[19] Astrov, D. N., "The magnetoelectric effect in antiferromagnetics", *J. Exp. Theor. Phys*., 1960, 11, 708-709

[20] Astrov, D. N., "The magnetoelectric effect in antiferromagnetics", J. Exp. Theoret. Phys., 1960, 38, 948-985

[21] Folen, V. J.; Rado, G. T.; Stalder, E. W., "Anisotropy of the magnetoelectric effect in Cr_2O_3", *Phys. Rev. Lett.*, 1961, 6, 607-608

[22] Rado, G. T.; Folen, V. J., "Observation of the Magnetically Induced Magnetoelectric Effect and Evidence for Antiferromagnetic Domains", *Phys. Rev. Lett.*, 1961, 7, 310-311

[23] Sundaresan, A.; Ter-Oganessian, N. V., "Magnetoelectric and multiferroic properties of spinels", J. Appl. Phys., 2021, 129, 060901

[24] Ascher, E.; Rieder, H.; Schimid, H.; Stössel, H., "Some Properties of Ferromagnetoelectric Nickel-Iodine Boracite", J. Appl. Phys., 1966, 37, 1404-1405

[25] Leung, C. M.; Zhang, S. Y.; Or, S. W.; Ho, S. L.; Lee, K. Y. (2012), *Proceedings of the 1st International Workshop on High-Speed and Intercity Railways*, Springer, Berlin, pp. 319-327

[26] O'Dell, T. H., "The electrodynamics of magneto-electric media", *Phil. Mag*., 1962, 7, 1653-1669

[27] O'Dell, T. H., "The electrodynamics of magneto-electric media", Amsterdam: North-Holland (1970)

[28] Thankachan, R. M.; Balakrishnan, R., Synthesis Strategies of Single-Phase and Composite Multiferroic Nanostructures, In book: Synthesis of Inorganic Nanomaterials: Advances and Key Technologies and Micro and Nano Technologies (2018) pp. 185-211

[29] Buurma, A. J. C.; Blake, E. R.; Palstra, T.; Adem, U., Multiferroic Materials: Physics and Properties, In book: Reference Module in Materials Science and Materials Engineering (2016), pp. 1-17

[30] Van Suchtelen, J., "Product Properties: A New Application of Composite Materials", *Philips Res. Rep*., 1972, 27, 28-37

[31] Van Den Boomgaard, J.; Terrell, D. R.; Born, R. A. J.; Giller, H. F. J. I., "An in situ grown eutectic magnetoelectric composite material", J. Mater. Sci., 1974, 9, 1705-1709

[32] Van Den Boomgaard, J.; Van Run, A. M. J. G.; Van Suchtelen, J., "Magnetoelectricity in piezoelectric-magnetostrictive composites", *Ferroelectrics*, 1976, 10, 295-298

[33] Van den Boomgaard, J.; Born, R. A. J., "A sintered magnetoelectric composite material $BaTiO_3$-Ni(Co, Mn) Fe_2O_4", *J. Mater. Sci.*, 1978, 13, 1538-1548

[34] Nicolenco, A.; de h-Óra, M.; Yun, C.; MacManus-Driscoll, J.; Sort, J., "Perspective: Straingradient effects in nanoscale-engineered magnetoelectric materials", *APL Mater*., 2021, 9, 020903

[35] Cho, J. H.; Jo, W., "A Brief Review on Magnetoelectric Multiferroic Oxides", J. Korean Inst. Electr. Electron. Mater. Eng., 2021, 34,149-166

[36] Hariharan, R., 6-High-sensitivity piezoelectric perovskites for magnetoelectric composites, Hybrid Perovskite Composite Materials: Design to Applications, Woodhead Publishing Series in Composites Science and Engineering (2021) p. 147-167

[37] Harshe, G.; Dougherty, J. P.; Newnham, R. E., "Theoretical modeling of multilayer magnetoelectric composites", *Int. J. Appl. E1ectromagn. Mater*., 1993, 4, 145-154

[38] Harshe, G.; Dougherty, J. P.; Newnham, R. E., "Theoretical modeling of 3-0/O-3 magnetoelectric composites", *Int. J. Appl. E1ectromagn. Mater*., 1993, 4, 161-171

[39] Lopatin, S.; Lopatina, I.; Lisnevskaya, I., "Magnetoelectric PZT/ferrite composite material", *Ferroelectrics*, 1994, 162, 63-68

[40] Wei, H.; Wang, H.; Xia, Y.; Cui, D.; Shi, Y.; Dong, M.; Hu, C.; Ding, T.; Zhang, J.; Ma, Y.; Wang, N.; Wang, Sun, Z. Y.; Wei, R.; Guo, Z., "An overview of lead-free piezoelectric materials and devices", *J. Mater. Chem. C*, 2018, 6, 12446–12467

[41] Shin, D. M.; Hong, S. W.; Hwang, Y H., Recent advances in organic piezoelectric biomaterials for energy and biomedical applications, *Nanomate*r., 2020, 10, 123

[42] Newacheck, S.; Singh, A.; Youssef, G., "On the magnetoelectric performance of multiferroic particulate composite materials", *Smart Mater. Struct*., 2022, 31, 015022

[43] Liu, X. L.; Li, D.; Zhao, H. X.; Dong, X. W.; Long, L. S.; Zheng, L. S., "Inorganic-organic hybrid molecular materials: From multiferroic to magnetoelectric", *Adv. Mater*. 2021, 202004542

[44] Lanceros-Méndez, S.; Martins, P., Magnetoelectric Polymer-Based Composites Fundamentals and Applications (2017) (Wiley-VCH Verlag GmbH & Co. KGaA, Boschstr. 12, 69469 Weinheim, Germany)

[45] Liang, X.; Matyushov, A.; Hayes, P.; Schell, V.; Dong, C.; Chen, H.; He, Y.; Will-Cole, A.; Quandt, E.; Martins, P.; McCord, J.; Medarde, M.; Lanceros-Méndez, S.; van Dijken, S.; Sun, N. X.; Sort, J., "Roadmap on Magnetoelectric Materials and Devices", *IEEE Trans. Magn*., 2021, 57, 21050424

[46] Kumar, A.; Kaur, D. "Magnetoelectric heterostructures for next-generation MEMS magnetic field sensing applications", *J. Alloys Compd*., 2022, 897, 163091.

[47] G. Channagoudra, G.; V. Dayal, V. "Magnetoelectric coupling in ferromagnetic/ferroelectric heterostructures: A survey and perspective*", J. Alloys Compd*., 2022, 928 167181

[48] Bhoi, K.; Mohanty, H. S.; Ravikant, Abdullah, M. F.; Pradhan, D. K.; Babu, S. N.; Singh, A. K.; Vishwakarma, P. N.; Kumar, A.; Thomas, R.; Pradhan, D. K., "Unravelling the nature of magneto-electric coupling in room temperature multiferroic particulate ($PbFe_{0.5}Nb_{0.5}O_3$)-($Co_{0.6}Zn_{0.4}Fe_{1.7}Mn_{0.3}O_4$) composites", *Sci. Rep*., 2021, 11, 3149

[49] Chu, Z.; PourhosseiniAsl, M. J.; Dong, S., "Review of multi-layered magnetoelectric composite materials and devices applications", *J. Phys. D: Appl. Phys*., 2018, 51, 243001

[50] Reyes-Montero A.; Pardo, L.; Lopez-Juarez, R.; González, A.; Cruz, M.; Villafuerte-Castrejón, M.E., "Lead-free $Ba_{0.90}Ca_{0.10}Ti_{0.90}Zr_{0.10}O_3$ piezoelectric ceramics processed below 1300ºC", *J. Alloys Compd*., 2014, 584, 28-33.

[51] Herrera-Pérez G., O. Solis-Canto, G. Silva-Vidaurri, et al., "Multiplet structure for perovskite-type $Ba_{0.90}Ca_{0.10}Ti_{0.90}Zr_{0.10}O_3$ by core-hole spectroscopies", *J. Appl. Phys*., 2020, 128, 064106; doi: 10.1063/5.0014496.

[52] Reyes-Montero, A.; Pardo, L.; López-Juárez, R.; González, A. M.; Rea-López, S. O.; Cruz M. P.; and Villafuerte-Castrejón, M. E., "Sub-10μm grain size, $Ba_{1-x}Ca_xTi_{0.90}Zr_{0.10}O_3$ (x = 0.10 and x = 0.15) piezoceramics processed using a reduced thermal treatment", *Smart Mater. Struct*., 2015, 24, 065033.

[53] Reyes-Montero, A.; Rubio-Marcos, F.; Pardo, L.; del Campo, A.; López-Juárez R., and Castrejón, M. E., "Electric Field Effect on the microstructure and properties of $Ba_{0.90}Ca_{0.10}Ti_{0.90}Zr_{0.10}O_3$ (BCTZ) lead-free ceramics", *J. Mater. Chem. A*, 2018. **6**(13), 5419-5429.

[54] Herrera-Pérez, G.; Reyes-Montero, A.; Campos-Venegas, K.; Gómez-Bartres, R.; Canche-Tello, J.; Montero-Cabrera, M. E.; Plaisier, J. R.; Eichert, D.; Reyes-Rojas A.; and Fuentes-Cobas, L. E., "Structural, Micro-structural and Electronic Structure Evolution in Polycrystalline Perovskite Electro-Ceramics Based on $Ba_{1-x}Ca_xTi_{0.90}Zr_{0.10}O_3$ (x = 0, 0.1, 0.125, 0.15, 0.175, 0.2) *Microsc. Microanal*., 2018. 24(S1), 392-393.

[55] Herrera-Pérez, G.; Morales D.; Paraguay-Delgado, C. F.; Hurtado-Macias, A.; Borja Urby, R.; Tapia-Padilla, G.; Reyes-Rojas, A.; Fuentes-Cobas, L. E., "Low loss Electron Energy Spectroscopy

Characterization of Electronic Structure and Piezo-response of $Ba_{0.90}Ca_{0.10}Ti_{0.90}Zr_{0.10}O_3$ Nanocrystals", *Microsc. Microanal.*, 22 (Suppl 3), 2016.

[56] Herrera-PérezaG; Isaí Castillo-Sandoval, Oscar Solís-Cantoc, Gabriela Tapia-Padilla, Armando Reyes-Rojas, Luis Edmundo Fuentes-Cobas, "Local piezo-response for lead-free $Ba_{0.90}Ca_{0.10}Ti_{0.90}Zr_{0.10}O_3$ electro-ceramic by switching spectroscopy", *Materials Research*., 2018; 21(2): e20170605.

[57] Herrera-Pérez, G.; Reyes-Montero, A.; Canche-Tello, J.; MonteroCabrera, M. E.; Fuentes-Montero, M. E.; Plaisier, J. R.; Eichert, D.; Reyes-Rojas, A.; Fuentes-Cobas, L. E.," Effects of local distortion on the electrical properties of lead-free perovskite-type electro-ceramics $Ba_{1-x}Ca_xTi_{0.9}Zr_{0.1}O_3$, IOP Conf. Series: J. Phys. Conf. Series, 2019, 1221, 012005.

[58] Sujatha, Ch.; Venugopal Reddy K.; Sowri Babu, K.; Rama Chandra Reddy A.; Rao, K. H., "Effect of sintering temperature on electromagnetic properties of NiCuZn ferrite", *Ceram. Int.*, 2013, 39, 3077-3086.

[59] Gholizadeh, A.; Jafari, E., "Effects of sintering atmosphere and temperature on structural and magnetic properties of Ni-Cu-Zn ferrite nano-particles: Magnetic enhancement by a reducing atmosphere", *J. Magn. Magn. Mater*., 2017, 422, 328-336

[60] Murthy, S. R., Low temperature sintering of NiCuZn ferrite and its electrical, magnetic and elastic properties, *J. Mater. Sci. Lett*., 2002, 21, 657-660

[61] Su, H.; Tang, X.; Zhang, H.; Jia, L.; Zhong, Z., "Influences of iron-deficiency on electromagnetic properties of low-temperature-fired NiCuZn ferrite", *J. Magn. Magn. Mater*., 2010, 322 (13), 1779-1783

[62] Murbe, J.; Topfer, J., "Low temperature sintering of sub-stoichiometric Ni–Cu–Zn ferrites: Shrinkage, microstructure and permeability," *J. Magn. Magn. Mater*., 2012, 324, 578-583.

[63] Khan, Z. H.; Mahbubur Rahman, M.; Sikder, S. S.; Hakim, M. A.; Saha, D. K., "Complex permeability of Fe-deficient Ni-Cu-Zn ferrites", *J. Alloys Compd*., 2013, 548, 208-2015.

[64] Chen, L.; Yu, Z.; Yang, Y.; Rongdi Guo, R.; Jiang, X.; Sun, K.; Wu, C.; Lan, Z., "Effects of Fe-deficiency on magnetic properties and Brillouin function characteristics for NiCuZn ferrites", *J. Magn. Magn. Mater*., 2015, 387, 1–5.

[65] Sun, K.; Pu, Z.; Yang, Y.; Chen, L.; Yu, W.; Wu, C.; Jiang, X.; Lan, Z.," Rietveld refinement, microstructure and ferromagnetic resonance linewidth of iron-deficiency NiCuZn ferrites", *J. Alloys Compd*., 2016, 681, 139-145.

[66] Priese, C.; Töpfer, J., "Phase Formation, Microstructure and Permeability of Fe-Deficient Ni-Cu-Zn Ferrites, (I): Effect of Sintering Temperature", *Magneto chemistry*, 2021, 7, 118.

[67] Bahiraei, H.; Ong, C. K., "The role of iron ions on microstructural and magnetic properties of MgCuZn ferrites prepared by sol-gel auto-combustion process", Mater. Res. Bull., 2019, 111, 195-201

.

[68] Wang, Y.; Pu, Y., Tian, Y.; Li, X.; Wang, Z.; Shi, Y.; Zhang, J.; Zhang, G., "Enhanced magnetoelectric properties of the laminated $Ba_{0.90}Ca_{0.10}Ti_{0.90}Zr_{0.10}O_3/Co_{0.8}Ni_{0.1}Zn_{0.1}Fe_2O_4$ composites", *J. Alloys Compd*., 2017, 696, 1307-1313.

[69] Wang, Y.; Pu, Y.; Shi, Y.; Cui, Y., "Ferroelectric, magnetic, magnetoelectric properties of the $Ba_{0.90}Ca_{0.10}Ti_{0.90}Zr_{0.10}O_3/CoFe_2O_4$ laminated composites", *J Mater Sci: Mater Electron*, 2017, 28, 11125-11131.

[70] Li, W.; Wu, H.; Ao, H.; Zeng, Z.; Gao, R.; Cai, W.; Fu, C.; Deng, X.; Chen, G.; Wang, Z.; Lei, X., "Dielectric, ferroelectric, magnetic and multiferroic properties of $xNi_{0.15}Cu_{0.25}Zn_{0.6}Fe_2O_4$-(1-x) $Ba_{0.85}Ca_{0.15}Zr_{0.1}Ti_{0.9}O_3$ composite ceramics", *Applied Physics A*, 2021, 127:915.

[71] Tanna, A. R.; Srinivasan, S. S.; Joshi, H. H., "Enhancement in magnetoelectric properties of lead-free multiferroic composite through high-energy mechanical milling", *J. Mate. Sci: Mater. Electron*., 2020, 31(12), 9306-9320.

[72] Rani, J.; Yadav, K. L.; Prakash, S., "Dielectric and magnetic properties of $x$$CoFe_2O_4$-(1-$x$) [$0.5Ba(Zr_{0.2}Ti_{0.8})O_3$-$0.5(Ba_{0.7}Ca_{0.3})TiO_3$] composites", *Mater. Res. Bull*., 2014, 60, 367.

[73] Negi, N. S.; Kumar, R.; Sharma, H., Shah, J.; Kotnala, R. K., "Structural, multiferroic, dielectric and magnetoelectric properties of (1-x) $Ba_{0.85}Ca_{0.15}Ti_{0.90}Zr_{0.10}O_3$ - $x$$CoFe_2O_4$ lead-free composites", *J. Magn. Magn. Mater*., 2018, 456, 292.

[74] Praveen, J. P.; Monaji, V. R.; Kumar, S. D.; Subramanian, V.; Das, D., "Enhanced magnetoelectric response from lead-free $(Ba_{0.85}Ca_{0.15})(Zr_{0.1}Ti_{0.9})O_3$- $CoFe_2O_4$ laminate and particulate composites", *Ceram. Int.*, 2018, 44, 4298.

[75] Praveen, J. P.; Reddy, M. V.; Kolte, J.; Kumar, S. D.; Subramanian, V.; Das, D., "Synthesis, characterization, and magneto-electric properties of (1-x) BCZT-xCFO ceramic particulate composites", *Int. J. Appl. Ceram. Technol*., 2017, 14, 200.

[76] Naveed-Ul-Haq, M.; Shvartsman, V.V.; Salamon, S.; Wende, H.; Trivedi, H.; Mumtaz, A.; Lupascu, D.C., "A new (Ba, Ca) (Ti, Zr)O_3 based multiferroic composite with large magnetoelectric effect", *Sci. Rep*., 2016, 6, 32164.

[77] Mane, S. M.; Pawar, S. A.; Patil, D. S.; Kulkarni, S. B.; Tayade, N. T.; Shin, J. C., "Magnetoelectric, magnetodielectric effect and dielectric, magnetic properties of microwave-sintered lead-free $x(Co_{0.9}Ni_{0.1}Fe_2O_4)$-(1-x)[$0.5(Ba_{0.7}Ca_{0.3}TiO_3)$-$0.5(BaZr_{0.2}Ti_{0.8}O_3)$] particulate multiferroic composite", *Ceram. Int*. 2020, 46, 3311-3323.

[78] Jain, A.; Panwar, A. K.; Jha, A. K.; Sharma, Y., "Improvement in dielectric, ferroelectric and ferromagnetic characteristics of $Ba_{0.9}Sr_{0.1}Zr_{0.1}Ti_{0.9}O_3$-$NiFe_2O_4$ composites", *Ceram. Int*., 2017, 43, 1025b3-10262.

[79] Jain, A.; Panwar, A. K.; Jha, A. K., "Significant enhancement in structural, dielectric, piezoelectric and ferromagnetic properties of $Ba_{0.9}Sr_{0.1}Zr_{0.1}Ti_{0.9}O_3$-$CoFe_2O_4$ multiferroic composites", *Mater. Res. Bull*., 2018, 100, 367-376.

[80] Sowmya, N. S.; Srinivas, A.; Reddy, K. V. G.; Praveen, J. P.; Das, D.; Kumar, S. D.; Subramanian, V.; Kamat, S.V., "Magnetoelectric coupling studies on (x) (0.5BZT-0.5BCT)-(100-x) $NiFe_2O_4$ [x = 90-70 wt%] particulate composite", *Ceram. Int*., 2017, 43, 2523-2528.

[81] Naveed-Ul-Haq, M.; Shvartsman, V.V.; Trivedi, H.; Salamon, S.; Webers, S.; Wende, H.; Hagemann, U.; Schroder, J.; Lupascu, D.C., "Strong converse magnetoelectric effect in (Ba,Ca)(Zr,Ti)O_3 - $NiFe_2O_4$ multiferroics: A relationship between phase-connectivity and interface coupling", *Acta Mater*., 2018, 144, 305-313.

[82] Rani, J.; Kushwaha, V. K.; Kolte, J.; Tomy, C. V., "Structural, dielectric and magnetoelectric studies of [$0.5Ba(Zr_{0.2}Ti_{0.8})O_3$-$0.5(Ba_{0.7}Ca_{0.3})TiO_3$]-$Ni_{0.8}Zn_{0.2}Fe_2O_4$ multiferroic composites", *J. Alloys Compd*., 2017, 696, 266-275.

[83] Sadhana, K.; Praveena, K.; Ramana; murthy, S., "Magnetic properties of $xNi_{0.53}Cu_{0.12}Zn_{0.35}Fe_{1.88}O_4$ + (1-x) $BaTiO_3$ nanocomposites", *J. Magn. Magn. Mater*., 2010, 322, 3729-3736.

[84] Ling, W.; Zhang, H.; Song, Y.; Liu, Y.; Li, Y.; Su, H., "Low-temperature sintering and electromagnetic properties of ferroelectric–ferromagnetic composites", *J. Magn. Magn. Mater*., 2009, 321(18), 2871-2876.

[85] Lin, Y.; Zhu, Z.; Yang, H., "Low-Temperature Sintering and Electromagnetic Properties of NiCuZn/$BaFe_{0.5}Nb_{0.5}O_3$ Composites", *Mater.Manu. Pro.*, 2011, 26(4), 632–635.

[86] Qi, X.; Zhou, J.; Yue, Z.; Gui, Z.; Li, L., "Investigation of magnetic properties of $Ni_{0.2}Cu_{0.2}Zn_{0.6}Fe_{1.96}O_4$–$BaTiO_3$ composites", *J. Magn. Magn. Mater*., 2004, 269(3), 352-358.

[87] Su, H.; Zhang, H.; Tang, X.; Jing, Y.; Zhong, Z., "Dielectric and magnetic properties of low-temperature fired NiCuZn-$BaTiO_3$ composites", *J. Magn. Magn. Mater*., 2009, 321(18), 2763-2766.

[88] Su, L.; Liu, P.; He, Y.; Zhou, J.; Cao, L.; Liu, C.; Zhang, H., "Electrical and magnetic properties of low-temperature sintered $xBa_{0.6}Sr_{0.4}TiO_3$ + (1-x) $Ni_{0.2}Cu_{0.2}Zn_{0.62}O(Fe_2O_3)_{0.98}$ composite ceramics", *J. Alloy. Compd*., 2010, 494, 330-335.

[89] Jia, L.; Li, T.; Zhang, H.; Zhong, H.; Liu, Y.; Xue, G., "Electromagnetic properties of low-temperature co-fired xPZT+(1- x) NiCuZn–ferrite composites", *J. Magn. Magn. Mater*., 2009, 321(18) 2936–2940.

[90] Yang, H.; Wang, H.; He, L.; Yao, X., "Low-temperature sintering and electromagnetic properties of $Ba(Zn_{1/3}Nb_{2/3})O_3$/NiCuZn ferrite composites", *J. Phys. Chem. Sol*.,2012, **73**, 454-459.

[91] Yang, H.; Lin, Y.; Zhu, J.; Wang, F., "A low loss low-temperature sintered ferrite dielectric composite thick film for high-frequency application, *Curr. Appl. Phys*, 2010, 10, 1148-1151.

[92] Sadhana, K.; Praveena, K.; Bharadwaj, S.; Murthy, S.R., "Microwave-Hydrothermal synthesis of $BaTiO_3$ + $NiCuZnFe_2O_4$ nanocomposites", *J. Alloys Compd*., 2009, 472, 484-488.

[93] Liu, X.; Gao, F.; Liu, J.; Tian, C., "Low-temperature cofiring behavior of $ZnTiO_3$ dielectrics/NiZnCu ferrite composites", *J. Alloys Compd*., 2009, 470, 269-272.

[94] Lin, Y.; Zhang, J.; Yang, H.; Tong Wang, "Excellent piezoelectric and magnetoelectric properties of the $(K_{0.45}Na_{0.55})_{0.98}Li_{0.02}(Nb_{0.77}Ta_{0.18}Sb_{0.05})O_3/Ni_{0.37}Cu_{0.20}Zn_{0.43}Fe_{1.92}O_{3.88}$ laminated composites", *J. Alloys Compd*., 2017, 692, 86-94.

[95] Yang, H.; Yang, Y.; Lu, L.; Lin, Y., "Low-temperature sintering and properties of $Bi_4Ti_3O_{12}$-$Ni_{0.37}Cu_{0.20}Zn_{0.43}Fe_{1.92}O_{3.88}$ composites", *J. Alloys Compd*., 2013, 555, 402-404.

[96] Yang, H.; Yang, Y.; Lin, Y.; Zhu, J.; Wang, F., "Low-Temperature Sintering and Electromagnetic Properties of NiCuZn/$CaTiO_3$ Composites" *J. Electron. Mater*., 2012, 41, 701-705.

[97] Hsiang, H. I.; Chen, T. H., "Dielectric and Magnetic Properties of Low-Temperature-Fired Ferrite-Dielectric Composites", *J. Am. Ceram. Soc*., 2008, 91, 2043-2046.

[98] Hsiang, H. I.; Chen, T. H., "Electrical properties of low-temperature-fired ferrite–dielectric composites", *Ceram. Int.*, 2009, 35, 2035-2039.

[99] Peng, T. M.; Hsu, R.T.; Jean, J. H., "Low-Fire Processing and Properties of Ferrite1Dielectric Ceramic Composite", *J. Am. Ceram. Soc*., 2006, 89, 2822-2827.

[100] Ling, W. W.; Zhang, H. W.; He, Y.; Li, Y. X.; Wang, Y.Y.; Prog., "Magnetic and dielectric properties of low temperature fired ferrite/ceramic composite materials", *Nat. Sci.: Mater. Int*.,2011, 21, 21-26.

[101] Ling, W.; Ma, W.; Xu, C.; Chen, Z., "Influence of oxygen annealing on electromagnetic properties of low temperature fired ferrite/ceramic composite materials", *Adv. Mater. Res*., 2013, 721, 215-218.

[102] Spaldin, N. A.; Sephardim, R., History of Ferroelectrics-A Crystallography Perspective, arXiv: 2018.13776v1 [cond-mat. mrtl-sci]]

[103] Maraj, M.; Wei, W.; Peng, B.; Sun, W., "Dielectric and Energy Storage Properties of $Ba_{1-x}Ca_xZr_yTi_{1-y}O_3$ (BCZT): A Review", *Materials*, 2019, 12, 3641

[104] Fu, D.; Itoh, M., "Role of Ca off-centering in tuning the ferroelectric phase transitions in Ba (Zr, Ti)O_3 system", arXiv preprint arXiv: 1503.00406, 2015.

[105] Mitsui, T.; Westphal, W. B., "Dielectric and X-Ray Studies of $Ca_xBa_{1-x}TiO_3$ and $Ca_xSr_{1-x}TiO_3$*", Phys. Rev*., 1961, 124, 1354-1359

[106] Villafuerte-Castrejón, M. E.; Morán, E.; Reyes-Montero, A.; Vivar-Ocampo, R.; Peña-Jiménez, J. A.; Rea-López, S. O.; Pardo, L., "Towards lead-free piezoceramics: Facing a Synthesis Challenge", *Materials.* 9 (2016)

[107] Liu, W.; Ren, X., "Large piezoelectric effect in Pb-free ceramics", *Phys. Rev. Lett*., 2009, 103, 257602

[108] Acosta, M.; Khakpash, N.; Someya, T.; Novak, N.; Jo, W.; Nagata, H.; Rossetti, G. A., Rodel, J., "Origin of the large piezoelectric activity in (1-x)$Ba(Zr_{0.2}Ti_{0.8})O_3$-x$(Ba_{0.7}Ca_{0.3})TiO_3$ ceramics", *Phys. Rev. B*, 2015, 91, 104108

[109] Jaffe, B., Cook, W. R. and Jaffe, H., *Piezoelectric ceramics*, Academic Press; London, New York, 1971

[110] Keeble, D. S.; Benabdallah, F.; Thomas, P. A.; Maglione, M.; Kreisel, J., "Revised structural phase diagram of $(Ba_{0.7}Ca_{0.3}TiO_3)$-$(BaZr_{0.2}Ti_{0.8}O_3)$", *Appl. Phys. Lett*., 2013, 102, 092903

[111] Damjanovic, D.; Biancoli, A.; Batooli, L.; Vahabzadeh, A.; Trodahl, J., "Elastic, dielectric and piezoelectric anomalies and Raman spectroscopy of 0.5$Ba(Ti_{0.2}Zr_{0.8})O_3$-0.5$(Ba_{0.7}Ca_{0.3})TiO_3$", *Appl. Phys. Lett*., 2012, 100, 192907

[112] Dahiya, R. S.; Valle, M., "Robotic Tactile Sensing", Springer Science and Business Media LLC, 2013

[113] Patel, I., (2011), Advances in Ceramics-Electric and Magnetic Ceramics, Bioceramics, Ceramics and Environment, Chapter: Ceramic Based Intelligent Piezoelectric Energy Harvesting Device, IntechOpen book, edited by Costas Sikalidis. DOI: 10.5772/19189

[114] Wu, J., "Perovskite lead-free piezoelectric ceramics", *J. Appl. Phys*., 2020, 127, 19090

[115] Holler, F. J. S., Douglas, A., Crouch, Stanley, R., (2007) Principles of instrumental analysis, 6th edn. Cengage Learning, p 9. ISBN 978-0-495-01201-6

[116] Wu, J., Advances in Lead-Free Piezoelectric Materials, Springer Nature Singapore Pte Ltd. (2018)

[117] Rödel, J.; Li, J. F., "Lead-free piezoceramics: Status and perspectives", MRS Bull., 2018, 43, 576-580

[118] Buchanan, R. C., Ceramic Materials for Electronics (3eds.) CRC press, 2004, p. 1-7

[119] Kasap, S. O., Principles of Electronic Materials and Devices (4th eds.), McGraw-Hill (2017)

[120] Bain, A. K.; Chand, P., Ferroelectrics: Principles and Applications, First Edition. (2017) Wiley-VCH Verlag GmbH & Co. KGaA.

[121] Raihan, R.; Rabbi, F.; Vadlamudi, V.; Reifsnider, K., "Composite Materials Damage Modeling Based on Dielectric Properties", *Mater. Sci. Appl*., 2015, 6, 1033-1053

[122] Yattinahalli, S. S.; Kapatkar, S. B.; Mathad, S. N., "Structural and Mechanical Properties of a Nano Ferrite", *Adv. Sci. Focus*, 2014, 2, 42-46

[123] Wu, M. M.; Wen, L.; Tang, B. Y.; Peng, L. M.; Ding, W. J., "First-principles study of elastic and electronic properties of $MgZn_2$ and $ScZn_2$ phases in Mg-Sc-Zn alloy", *J. Alloy. Compd*., 2010, 506, 412-417

[124] Wei, Q.; Zhang, Q.; Zhang, M., "Crystal structures and mechanical properties of Ca_2C at high pressure", *Mater*., 2016, 9, 570

[125] Chandekar, K. V.; Shkir, M.; AlFaify, S., "A structural, elastic, mechanical, spectroscopic, thermodynamic, and magnetic properties of polymer coated $CoFe_2O_4$ nanostructures for various applications", *J. Mol. Struct*., 2020, 1205, 127681

[126] Wooster, W. A., "Physical properties and atomic arrangements in crystals", *Rep. Prog. Phys*., 1953, 16, 62-82

[127] Frantsevich, I. N.; Voronov, F. F.; Bokuta, S. A., Elastic Constants and Elastic Moduli of Metals and Insulators Handbook, edited by I.N. Frantsevich (Naukova Dumka, Kiev, 1983), pp. 60–180

[128] Pugh, S. F., "XCII. Relations between the elastic moduli and the plastic properties of polycrystalline pure metals", *Philos. Mag.*, 1954, 45, 823-843

[129] Sharma, P. U.; Modi, K. B., "Effect of Fe^{3+} substitution on elastic properties of yttrium iron garnet", *Phys. Scr*., 2010, 81, 015601

[130] Hasselman, D.; Fulrath, R. M., "The effect of a small fraction of spherical porosity on the elstic moduli of glass", *J. Am. Ceram. Soc*., 1964, 47, 52-53.

[131] Ledbetter, H.; Datta, S. K., "Effective wave speeds in a SiC-particle-reinforced Al composite", J. Acoust. Soc. Am., 1986, 79(2), 239-248

[132] Rice, R. W., *Treatise on Material Science and Technology* ed. R. K. Mac Crane (New York: Academic) 11 **(**1977**)** p 199

[133] Modi, K. B.; Pathak, T. K.; Vasoya, N. H.; Lakhani, V. K.; Baldha, G. J.; Jha, P. K., "X-ray Debye temperature of mechanically milled $Ni_{0.5}Zn_{0.5}Fe_2O_4$ spinel ferrite", *Indian J. Phys*., 2011, 85, 411-420

[134] Waldron, R. D., "Infrared Spectra of Ferrites", *Phys. Rev*., 1955, 99, 1727-1735

[135] Anderson, O. L., "A simplified method for calculating the Debye temperature from elastic constants*", J. Phys. Chem. Solids*, 1963, 24, 909-917

[136] Khedri, H.; Gholizadeh, A., "Experimental comparison of structural, magnetic and elastic properties of $M_{0.3}Cu_{0.2}Zn_{0.5}Fe_2O_4$ (M = Cu, Mn, Fe, Co, Ni, Mg) nanoparticles", *Appl. Phys. A*, 2019, 125, 709

[137] Coey, J. M. D.; College, T.; Dublin, J. M. D., Magnetism and Magnetic Materials (Cambridge University Press, UK, 2010)

[138] Zhang, S., Electric-Field Control of Magnetization and Electronic Transport in Ferromagnetic/Ferroelectric Heterostructures, Springer Theses, DOI: 10.1007/978-3-642-54839-0_1

[139] Zhao, Q.; Yan, Z.; Chen, C.; Chen, J., "Spinels: Controlled Preparation, Oxygen Reduction/Evolution Reaction Application, and Beyond", *Chem. Rev*., 2017, 117, 10121-10211

[140] Olowoyo, J. O.; Kriek, R. J., "Recent Progress on Bimetallic-Based Spinels as Electrocatalysts for the Oxygen Evolution Reaction", *Small*, 2022, 18, 2203125

[141] Patil, A. D.; Patange, S. M.; Dighe, P. M.; Shaikh, S. F.; Rana, A. H. S.; Pandit, B.; Jadhav, S. S., "Tuning the structural, optical and magnetic properties of NiCuZn ($Ni_{0.4}Cu_{0.3}Zn_{0.3}Fe_2O_4$) spinel ferrites by Nb_2O_5 additive", *Ceram. Int*., 2022, 48, 27039-27050

[142] Khomskii, D., "Classifying multiferroics: Mechanisms and effects", *Physics*, 2009, 2, 20

[143] Khomskii, D. I., "Multiferroics: Different ways to combine magnetism and ferroelectricity", *J. Magn. Magn. Mater*., 2006, 306, 1-8

[144] Efremov, D. V.; Van den Brink, J.; Khomskii, D. I., "Bond- versus site-centred ordering and possible ferroelectricity in manganites", *Nat. Mater*., 2004, 3, 853-856

[145] Fiebig, M.; Lottermoser, T.; Meier, D.; Trassin, M., "The evolution of multiferroics", *Nat. Rev. Mater*., 2016, 1, 1-14

[146] Sergienko, I. A.; Dagotto, E., "Role of the Dzyaloshinskii-Moriya interaction in multiferroic perovskites", *Phys. Rev. B*, 2006, 73, 5

[147] Lottermoser, T.; Meier, D., "A short history of multiferroics", *Phys. Sci. Rev*., 2020, 6, 1-11

[148] Gruyter, D., Multiferroics: Fundamentals and Applications, Andrés Cano, Dennis Meier, Morgan Trassin (Eds.) (2021) p. 5

[149] Jena, A. K.; Chelvane, J. A.; Mohanty, J., "Simultaneous improvement of piezoelectric and magnetic properties in diamagnetic ion modified $BiFeO_3$ film", *J. Alloys Compd.*, 2019, 805, 1168-1174

[150] Liu, Y.; Tan, G.; Guo, M.; Chai, Z.; Lv, L.; Xue, M.; Ren, X.; Li, J.; Ren, H.; Xia, A., "Multiferroic properties of La/Er/Mn/Co multi-doped $BiFeO_3$ thin films", *Ceram. Int.*, 2019, 45, 11765-11775

[151] Wang, Y.; Guo, Z.; Jia, Q.; Dong, J.; Zhang, J.; Chen, D., "Effect of Nd/Mn substitution on the structure and magnetic properties of nano-$BiFeO_3$", *J. Alloys Compd.*, 2019, 786, 385-393

[152] Lu, J.; Qiao, L. J.; Fu, P. Z.; Wu, Y. C., "Phase equilibrium of Bi_2O_3-Fe_2O_3 pseudo-binary system and growth of $BiFeO_3$ single crystal", *J. Cryst. Growth*, 2011, 318, 936-941

[153] Hu, J. M.; Chen, L. Q., Magnetoelectrics and Multiferroics, Chapter 12, in Handbook of Magnetism and Magnetic Materials (2021) Springer, Edited by J. M. D. Coey, S. S. P. Parkin

[154] Reddy, V. A.; Pathak, N. P.; Nath, R., "Particle size dependent magnetic properties and phase transitions in multiferroic $BiFeO_3$ nano-particles", *J. Alloys Compd.*, 2012, 543, 206-212

[155] Newnham, R. E., "Composite Electroceramics", *Ferroelectrics*, 1-32 (1986)

[156] Srinivasan, G.; Priya, S.; Sun, N. X., Composite Magnetoelectrics: Materials, Structure and Applications, Woodhead Publishing Series in Electronic and Optical Materials (Elsevier) (2015) pp.108

[157] Bhimasankaram, T.; Suryanarayana, S. V.; Prasad, G., "Piezoelectric polymer composite materials", Current Sci., 1998, 74, 967-976

[158] Kopyl, S.; Surmenev, R.; Surmeneva, M.; Fetisov, Y.; Kholkin, A., "Magnetoelectric effect: principles and applications in biology and medicine-a review", *Mater. Today Bio*., 2021, 12, 100149

[159] Uchino, K., Piezoelectric Composites, Reference Module in Materials Science and Materials Engineering (2022)

[160] Zygmunt, S.; Dariusz, B., "Multiferroic materials for sensors, transducers and memory devices", *Arch. Acoust*., 2008, 33, 243-260

[161] Uchino, K., Ferroelectric Devices (2010) by Taylor & Francis Group, LLC

[162] Hu, J. M.; Duan, C. G.; Nan, C. W.; L. Q. Chen, L. Q., "Understanding and designing magnetoelectric heterostructures guided by computation: progresses, remaining questions, and perspectives", *NPJ Comp. Mater*. (2017)

[163] Khojah, R.; Xiao, Z.; Panduranga, M. K.; Bogumil, M.; Wang, Y.; Goiriena-Goikoetxea, M.; Chopdekar, R. V.; Bokor, J.; Carman, G. P.; Candler, R. N.; Carlo, D. D., "Single-Domain Multiferroic Array-Addressable Terfenol-D (SMArT) Micromagnets for Programmable Single-Cell Capture and Release", *Adv. Mater*. 2021, 2006651

[164] Pradhan, D. K.; Kumari, S.; Rack, P.D., "Magnetoelectric Composites: Applications, Coupling Mechanisms, and Future Directions", Nanomater., 2020, 10, 2072

[165] Leung, C. M.; Li, J.; Viehland, D.; Zhuang, X., "A review on applications of magnetoelectric composites: from Heterostructural uncooled magnetic sensors, Energy harvesters to Highly efficient power converters", *J. Phys. D: Appl. Phys*., 2018, 51, 263002

[166] Vopsaroiu, M.; Blackburn, J.; Cain, M. G., "Emerging Technologies and Opportunities Based on the Magnetoelectric Effect in Multiferroic Composites", *Mater. Res. Soc. Symp. Proc.*, 2009, 1161, 1161-I05-04

[167] Rivera, J. P., "A short review of the magnetoelectric effect and related experimental techniques on single phase (multi-) ferroics", *Eur. Phys. J. B*, 2009, 71, 299-313

[168] Rivera, J. P., "On definitions, units, measurements, tensor forms of the linear magnetoelectric effect and on a new dynamic method applied to Cr-Cl boracite", *Ferroelectrics*, 1994, 161, 165-180

[169] Wang, K. F.; Liu, J. M.; Ren, Z. F., "Multiferroicity: the coupling between magnetic and polarization orders", *Adv. Phys*., 2009, 58, 321-448

[170] Kharchenko, N. F., "The linear magneto-optic effect as a manifestation of a higher order magnetoelectric effect", Ferroelectrics, 1994, 162, 173-189

[171] Gupta, R.; Kotnala, R. K., "A review on current status and mechanisms of room temperature magnetoelectric coupling in multiferroics for device applications", *J. Mater. Sci*., 2022, 57, 12710-12737

[172] Brown, W. F.; Hornreich, R. M.; Shtrikman, S., "Upper Bound on the Magnetoelectric Susceptibility", *Phys. Rev*., 1968, 168, 574

[173] Fiebig, M., "Revival of the magnetoelectric effect", *J. Phys. D Appl. Phys*., 2005, 38, R123-R152

[174] Lawes, G.; Srinivasan, G., "Introduction to magnetoelectric coupling and multiferroic films", *J. Phys. D Appl. Phys*., 2011, 44, 243001

[175] Srinivasan, G., "Magnetoelectric composites", *Ann. Rev. Mater. Res*., 2010, 40, 153-178

[176] Vopson, M. M.; Fetisov, Y. K.; Caruntu, G.; Srinivasan, G., "Measurement Techniques of the Magneto-Electric Coupling in Multiferroics", *Materials* 2017, 10, 963

[177] Mao, Q.; Wu, J.; Hu, Z.; Xu, Y.; Du, Y.; Hao, Y.; Guan, M.; Wang, C.; Wang, Z.; Zhou, Z.; Dong, S.; Ren, W.; Liu, M.; Jiang, Z., "Magnetoelectric devices based on magnetoelectric bulk composites", *J. Mater. Chem. C*, 2021, 9, 5594

[178] Tyagi, A. K.; R. S. Ningthoujam, R. S., Handbook on Synthesis Strategies for Advanced Materials, Volume-I: Techniques and Fundamentals, Indian Inst. Met. Series, Springer (2021) P. 1-49

[179] Tilley, R. J. D., Understanding Solids, John Wiley & Sons Ltd (2013), p. 213

[180] Kang, S. J. L., Sintering: Densification, Grain Growth and Microstructure (Elsevier Science, 2004)

[181] Tanaka, H.; Yamamoto, A.; Shimoyama, J.; Ogino, H.; K. Kishio, K., "Strongly connected *ex situ* MgB_2 polycrystalline bulks fabricated by solid-state self-sintering", *Supercond. Sci. Technol*., 2012, 25, 115022

[182] Warren, B. E., *X-ray Diffraction*, Addison-Wesley Publishing Company, Massachusetts, 1968.

[183] Cullity, B. D., *Elements of X-ray Diffraction*: Addison-Wesley Publishing, 1956.

[184] Kittel, C., *Introduction to solid state physics*, 7th ed., John Wiley & Sons Inc., New York, 1996.

[185] Smit, J.; Wijn, *Ferrites*, *Philips technical library*, The Netherlands, 1959, 278.

[186] Salunkhe, A. B.; Khot, V. M.; Phadatare, M. R.; Thorat, N. D.; Joshi, R. S.; Yadav, H. M.; Pawar, S. H., "Low temperature combustion synthesis and magnetostructural properties of Co-Mn nanoferrites", *J. Magn. Magn. Mate*r., 2014, 352, 91-98

[187] Bharti, M. K.; Chalia, S.; Thakur, P.; Sridhara, S. N.; Sharma, P. B.; Thakur, A., "Microstructural Analysis and Effect of Spin-Canting on Magnetic Attributes of Single-Phase Polycrystalline Cobalt Ferrite Nanoparticles", *J. Supercond. Nov. Magn*., 2022, 35, 571-579

[188] Michelson, A. A, "On the application of interference methods to spectroscopic measurements", The London, Edinburgh, and Dublin Philosophical Magazine and Journal of Science, 1891, 31, 338-346

[189] Smith, B. C., Fundamentals of Fourier Transform Infrared Spectroscopy, CRC Press, Taylor & Francis Group, 2011

[190] Griffiths, P. R.; J.A. De Haseth, Fourier transform infrared spectrometry, John Wiley & Sons, 2007

[191] http://emicroscope.blogspot.com/2011/03/scanning-electron-microscope-sem-how-it.html

[192] Stokes, D. J., Principles and Practice of Variable Pressure/Environmental Scanning Electron Microscopy (VP-ESEM), Wiley & Sons, 2008

[193] Halliday, D; Resnick, R., Walker, J., *Fundamentals of Physics*, John Wiley & Sons, 2011.

[194] Foner, S., “Versatile and Sensitive Vibrating Sample Magnetometer”, Rev. Sci. Instrum., 159, 30, 548-557

[195] Dodrill, B.; Lindemuth, J. R., Vibrating Sample Magnetometry, Magnetic Measurement Techniques for Materials Characterization, V. Franco, B. Dodrill edited, Springer (2021) p. 15-18.

[196] Grössinger, R., “Characterization of hard magnetic materials”, *J. Elec. Eng*., 2008, 59, 15-20

[197] Duong, G. V.; Groessingera, R.; Schoenharta, M.; Bueno-Basques, D., “The lock-in technique for studying magnetoelectric effect”, *J. Magn. Magn. Mater*., 2007, 316, 390-393

[198] Sutka, A.; Gross, K.; Mezinskis, G.; Bebris, G.; Knite, M., “The effect of heating conditions on the properties of nano-and microstructured Ni-Zn ferrite”, *Phys. Scr*., 2011, 83, 025601.

[199] Coble, R.; Gupta T., *Sintering and Related Phenomena*, Gordon and Breach, New York, 1976, 423.

[200] Kang, S. L., *Sintering: densification, grain growth and microstructure*, Elsevier Butterworth-Heinemann, Burlington, MA, 2005.

[201] Lange, R. F.; Kellet, B.J., “Thermodynamics of densification: II, grain growth in porous compacts and relation to densification”, *J. Am. Ceram. Soc*., 1989, 72, 735–741.

[202] Yadav, R. S.; Kuřitka, I.; Vilcakova, J.; Urbánek, P.; Machovsky, M.; Masař, M.; Holek, M., “Structural, magnetic, optical, dielectric, electrical and modulus spectroscopic characteristics of $ZnFe_2O_4$ spinel ferrite nanoparticles synthesized via honey-mediated sol-gel combustion method”, *J. Phys. Chem. Sol*., 2017, 110, 87-99.

[203] Yadav, R. S.; Kuřitka, I.; Havlica, J.; Hnatko, M.; Alexander, C.; Masilko, J.; Kalina, L.; Hajdúchová, M.; Rusnak, J.; Enev, V., “Structural, magnetic, elastic, dielectric and electrical properties of hot-press sintered $Co_{1-x}Zn_xFe_2O_4$ (x = 0.0, 0.5) spinel ferrite nanoparticles”, *J. Magn. Magn. Mater*., 2018, 447, 48–57.

[204] Malyshev, A.; Petrova, A.; Surzhikov, A.; Sokolovskiy, “Effect of sintering regimes on the microstructure and magnetic properties of LiTiZn ferrite ceramics”, *Ceram. Int.*, 2019, 45, 2719-2724.

[205] Ahmed, Y.; Hessien, M.; Rashad, M.; Ibrahim, “Nano-crystalline copper ferrites from secondary iron oxide (mill scale)”, *J. Magn. Magn. Mater*., 2009, 321(3), 181-187.

[206] Wada, Y.; Nishimatsu, S., “Grain growth mechanism of heavily phosphorus-implanted polycrystalline silicon” *J. Electrochem. Soc*., 1978, 125, 1499–1504.

[207] Liu, J.; Mei, Y.; Liu, W.; Li, X.; Hou, F.; Lu, G., “Effects of sintering temperature on properties of toroid cores using NiZnCu ferrites for power applications at > 1 MHz”, *J. Magn. Magn. Mater*., 2018, 454, 6-12.

[208] Kalarus, J.; Kogias, G.; Holz, D.; Zaspalis, “High permeability-high frequency stable MnZn ferrites”, *J. Magn. Magn. Mater*., 2012, 324, 2788-2794.

[209] Al-Hilli, M.F.; Li, S.; Kassim, “Gadolinium substitution and sintering temperature dependent electronic properties of Li-Ni ferrite”, *Mater. Chem. Phys*., 2011, 128, 127–132.

[210] Paik, J. G.; Lee, M. J.; Hyun, S., “Reaction kinetics and formation mechanism of magnesium ferrites”, *Thermochim. Acta*, 2005, 425, 131–136.

[211] Oumezzine, E.; Hcini, S.; Hlil, E.K.; Dhahri, E.; Oumezzine, M., “Effect of Ni-doping on structural, magnetic and magnetocaloric properties of $La_{0.6}Pr_{0.1}Ba_{0.3}Mn_{1-x}Ni_xO_3$ nanocrystalline manganites synthesized by Pechini sol-gel method”, *J. Alloys Compd*., 2014, 615, 553–560.

[212] Costa, A.; Tortella, E.; Morelli, M.; Kiminami, R., “Synthesis, microstructure and magnetic properties of Ni-Zn ferrites”, *J. Magn. Magn. Mater*., 2003, 256, 174-182.

[213] Ravinder, D., "Effect of sintering temperature on electrical conductivity of mixed lithium–cadmium ferrites", *Mater. Lett*., 1999, 40(4), 198-203.

[214] Tong, G.; Guan, J.; Zhang, Q., "Goethite hierarchical nanostructures: Glucose-assisted synthesis, chemical conversion into hematite with excellent photocatalytic properties", *Mater. Chem. Phys*., 2011, 127, 371-378.

[215] Labde, B.; Sable, M. C.; Shamkuwar, N. R., "Structural and infra-red studies of $Ni_{1+x}Pb_xFe_{2-2x}O_4$ system", *Mater. Lett*., 2003, 57, 1651-1655.

[216] Evans, B. J.; Hafner, S. S. "Mössbauer resonance of Fe^{57} in oxidic spinels containing Cu and Fe", *J. Phys. Chem. Solid*., 1968, 29, 1573-1588.

[217] Naik, M. M.; Naik, H. B.; Nagaraju, G.; Vinuth, M.; Vinu, K.; Rashmi, S. K., "Effect of aluminium doping on structural, optical, photocatalytic and antibacterial activity on nickel ferrite nanoparticles by sol-gel auto-combustion method", *J. Mater. Sci.: Mater. Electron*., 2018, 29, 20395-20414.

[218] Naveenkumar, A.; Kuruva, P.; Shivakumara, C.; Srilakshmi, C., "Mixture of fuels approach for the synthesis of $SrFeO_{3-\delta}$ nanocatalyst and its impact on the catalytic reduction of nitrobenzene", *Inorg. Chem*., 2014, 53, 12178-12185.

[219] Xiao, S. H.; Jiang, W. F.; Li, L.Y.; Li, X. J., "Low-temperature auto-combustion synthesis and magnetic properties of cobalt ferrite nanopowder", *Mater. Chem. Phys*., 2007, 106(1), 82–87.

[220] Liu, Y.; Zhang, Y.; Feng, J.D.; Li, C.F.; Shi, J.; Xiong, R., "Dependence of magnetic properties on crystallite size of $CoFe_2O_4$ nanoparticles synthesised by auto-combustion method", *J. Exp. Nano Sci.*, 2009, 4, 159-168.

[221] Reddy, C. V.; Prabhakar Vattikuti, S.; Ravikumar, R.; Moon, S. J.; Shim, J., "Influence of calcination temperature on $Cd_{0.3}Co_{0.7}Fe_2O_4$ nanoparticles: Structural, thermal and magnetic properties", *J. Magn. Magn. Mater*., 2015, 394, 70-76.

[222] Meiorin, C.; Muraca, D.; Pirota, K. R.; Aranguren; M. I., Mosiewicki, M. A., "Nanocomposites with superparamagnetic behavior based on a vegetable oil and magnetite nanoparticles", *Eur. Polym. J*., 2014, 53, 90-99.

[223] Zaki, H.; Dawoud H. A., "Far-infrared spectra for copper-zinc mixed ferrites", *Phys. B*, 2010, 405, 4476-4479.

[224] Yadav, R.S.; Havlica, J.; Masilko, J.; Kalina, L.; Wasserbauer, J.; Hajdúchová, M.; Enev, V.; Kuřitka, I.; Kožáková, Z, "Effects of annealing temperature variation on the evolution of structural and magnetic properties of $NiFe_2O_4$ nanoparticles synthesized by starch-assisted sol–gel auto-combustion method", *J. Magn. Magn. Mater*., 2015, 394, 439-447.

[225] Mazen, S.; Abdallah, M.; Nakhla, R.; Zaki, H.; Metawe, F., "X-ray analysis and IR absorption spectra of Li-Ge ferrite", *Mater. Chem. Phys*., 1993, 34, 35-40.

[226] Patange, S.; Shirsath, S.E.; Lohar, K.; Algude, S.; Kamble, S.; Kulkarni, N., et al. "Infrared spectral and elastic moduli study of $NiFe_{2-x}Cr_xO_4$ nanocrystalline ferrites", *J. Magn. Magn. Mater.*, 2013, 325, 107-111.

[227] Amer, M.; Meaz, T.; Mostafa, A.; El-Kastawi, M.; Ghoneim, A., "Characterization and spectral studies of Co^{3+}-doped $Cd_{0.4}Mn_{0.6}Fe_2O_4$ ferrites", *JCI*, 2014, 40(1) 241-8.

[228] Mazen S.; Mansour, S.; Dhahri, E.; H.; Elmosalami, T., "The infrared absorption and dielectric properties of Li-Ga ferrite", *J. Alloys Compd*., 2009, 470(1-2), 294-300.

[229] Amer, M.; Meaz, T.; Attalah, S.; Ghoneim, A., "Structural phase transition of as-synthesized Sr-Mn nanoferrites by annealing temperature", *J. Magn. Magn. Mater*., 2015, 393, 467-78.

[230] Patange, S.; Shirsath, S.E.; Jadhav, S.; Hogade, V.; Kamble S.; Jadhav K.J., "Elastic properties of nanocrystalline aluminum substituted nickel ferrites prepared by co-precipitation method", *J. Mol. Struct*., 2013, 1038, 40-44.

[231] Bhaskar, A.; Murthy, S.R., "Effect of sintering temperatures on the elastic properties of Mn (1%) added MgCuZn ferrites", *J. Magn. Magn. Mater*., 2014, 355, 100-103.

[232] Tatarchuk, T. R.; Paliychuk, N.D.; Bououdina, M.; Al-Najar, B.; Pacia, M.; Macyk, W.; Shyichuk, A., "Effect of cobalt substitution on structural, elastic, magnetic and optical properties of zinc ferrite nanoparticles", *J. Alloys Compd*., 2018, 731, 1256-1266.

[233] Mohamed, M. B.; Wahba, A.M., "Structural, magnetic, and elastic properties of nanocrystalline Al-substituted $Mn_{0.5}Zn_{0.5}Fe_2O_4$ ferrite", *Ceram. Int*., 2014, 40, 11773-11780.

[234] Saafan, S.; Meaz, T.; Ghazzawy, E.H.; Nimr M.K.; Ayad, M.; Bakr, M., "AC and DC conductivity of NiZn ferrite nanoparticles in wet and dry conditions", *J. Magn. Magn. Mater*., 2010, 322, 2369-2374.

[235] Koops, C. G., "On the dispersion of resistivity and dielectric constant of some semiconductors at audio frequencies", *Phys. Rev*., 1951, 83, 121-124.

[236] Kouki, N.; Hcini, S.; Aldawas, R.; Boudard, M., "Structural, Infrared, Magnetic, and Electrical Properties of $Ni_{0.6}Cd_{0.2}Cu_{0.2}Fe_2O_4$ Ferrites Synthesized Using Sol-Gel Method Under Different Sintering Temperatures", *J. Supercond. Nov. Magn*., 2019, 32, 2209-18.

[237] Zaspalis, V.; Tsakaloudi, V.; Kogias, G., "MnZn-ferrites: targeted material design for new emerging application products", *EPJ Web Conf.*, 2014, 75, 04004.

[238] Praveena, K.; Sadhana, K.; Matteppanavar, S.; Liu, H.L., "Effect of sintering temperature on the structural, dielectric and magnetic properties of $Ni_{0.4}Zn_{0.2}Mn_{0.4}Fe_2O_4$ potential for radar absorbing", *J. Magn. Magn. Mater*., 2017, 423, 343-352.

[239] Raghavender, A.; Shirsath, S.E.; Kumar, K.V., "Synthesis and study of nanocrystalline Ni-Cu-Zn ferrites prepared by oxalate-based precursor method", *J. Alloys Compd*., 2011, 509, 7004-7008.

[240] Kumar, G. R.; Venudhar, Y.; Raghavender, A.; Kumar, K.V., "Electrical properties of copper substituted nickel ferrites", *J. Korean Phys. Soc*., 2012, 60, 1082-1086.

[241] Rao, P.V.S.; Anjaneyulu, T.; Reddy, M.R., "Annealing Temperature Dependent Structural and Magnetic Properties of Ni-Cu-Zn Nanoferrites", *J. Korean Phys. Soc*., 2018, 72, 593–598.

[242] Reddy, M. P.; Venkata Ramana, M.; Madhuri, W.; Sadhana, K.; Siva Kumar, K.; Ramakrishna Reddy, R.R., "Effects of sintering temperature on structural and electromagnetic properties of MgCuZn ferrite prepared by microwave sintering", *Adv. Appl. Ceram*., 2015, 114, 326–332.

[243] Mott, N. F., Davis, E.A., *Electronic processes in non-crystalline materials*: Oxford university press, 2012.

[244] Anupama, M.; Rudraswamy, B.; Dhananjaya, N., "Investigation on impedance response and dielectric relaxation of Ni-Zn ferrites prepared by self-combustion technique", *J. Alloys Compd*., 2017, 706, 554-561.

[245] Kambale, R.; Shaikh, P.; Bhosale, C.; Rajpure, K.; Kolekar, Y.D., "Dielectric properties and complex impedance spectroscopy studies of mixed Ni-Co ferrites", *Smart Mater. Struct*., 2009, 18, 085014.

[246] Kambale, R., Shaikh, P., Kamble, S., Kolekar, Y., "Effect of cobalt substitution on structural, magnetic and electric properties of nickel ferrite", *J. Alloys Compd*., 2009, 478, 599-603.

[247] Amer, M.; Matsuda, A.; Kawamura, G.; El-Shater, R.; Meaz, T.; Fakhry, F., "Structural, magnetic, vibrational and optical studies of structure transformed spinel Fe^{2+}-Cr nano-ferrites by sintering process", *J. Alloys Compd*., 2018, 735, 975-985.

[248] Sun, K.; Lan, Z.; Yu, Z.; Jiang, X.; Huang, J., "Phase formation, grain growth and magnetic properties of NiCuZn ferrites", *J. Magn. Magn. Mater*., 2011, 323, 927-932.

[249] Kannan, Y.; Saravanan, R.; Srinivasan, N.; Ismail, I., "Sintering effect on structural, magnetic and optical properties of $Ni_{0.5}Zn_{0.5}Fe_2O_4$ ferrite nano particles", *J. Magn. Magn. Mater.*, 2017, 423, 217-225.

[250] Ali, N. J.; Rahman, J.; Chowdhury, M.A., "The influence of the addition of CaO on the magnetic and electrical properties of Ni-Zn ferrites", *Jpn. Soc. Appl. Phys*., 2000, 39, 3378–3381.

[251] Beitollahi, A.; Hoor, M., "Effect of sintering temperature on the microstructure and high-frequency magnetic properties of $Ni_{0.467}Zn_{0.07}Co_{0.015}Fe_{0.511}O_4$ ferrite", *J. Mater. Sci.: Mater. Electron*., 2003, 14, 477-482.

[252] Verma, A.; Goel, T.; Mendiratta, R.G., "Frequency variation of initial permeability of NiZn ferrites prepared by the citrate precursor method", *J. Magn. Magn. Mater*., 2000, 210, 274-278.

[253] Koh, J. G., "Studies of the magnetic properties of Ni-Zn-Cu ferrite and its synthesis by using metal nitrate salts", *J. Korean Phys. Soc*., 2004, 44, 1504-1508.

[254] Kim, C. W.; Koh, J. G., "Study of the physical properties of NiCuZn-ferrite and its synthesis by using thermal decomposition of metal nitrate salts", *J. Korean Phys. Soc*., 2002, 41, 364–370.

[255] Su, H.; Zhang, H.; Tang, X.; Jing, Y.; Liu, Y., "Effects of composition and sintering temperature on properties of NiZn and NiCuZn ferrites", *J. Magn. Magn. Mater*., 2007, 310, 17-21.

[256] Dimri, M. C.; Verma, A.; Kashyap, S.C.; Dube, D.; Thakur, O.; Prakash, C., "Structural, dielectric and magnetic properties of NiCuZn ferrite grown by citrate precursor method", *Mater. Sci. Eng., B*, 2006, 133, 42-48.

[257] Wu, X.; Yan, S.; Liu, W.; Feng, Z.; Chen, Y.; Harris, V., "Influence of particle size on the magnetic spectrum of NiCuZn ferrites for electromagnetic shielding applications", *J. Magn. Magn. Mater*., 2016, 401, 1093-1096.

[258] Lin, Q.; Yuan, G.; He, Y.; Wang, L.; Dong, J.; Yu, Y., "The influence of La-substituted $Cu_{0.5}Co_{0.5}Fe_2O_4$ nanoparticles on its structural and magnetic properties", *Mater. Des*., 2015, 78, 80.

[259] Yang, A.; Chinnasamy, C.; Greneche, J.; Chen, Y.; Yoon, S.D.; Hsu, K.; Vittoria, C.; Haris, V.G., "Large tunability of Néel temperature by growth-rate-induced cation inversion in Mn-ferrite nanoparticles", *Appl. Phys. Lett*., 2009, 94, 113109.

[260] Gabal, M. A.; Al Angari, Y., "Low-temperature synthesis of nanocrystalline NiCuZn ferrite and the effect of Cr substitution on its electrical properties", *J. Magn. Magn. Mater*., 2010, 322, 3159.

[261] Han, Q.; Ji D.; Tang, G.; Li, Z.; Hou, X.; Qi W.; Liu, S.; Bian, R., "Estimating the cation distributions in the spinel ferrites $Cu_{0.5-x}Ni_{0.5}Zn_xFe_2O_4$ ($0.0 \leq x \leq 0.5$)", *J. Magn. Magn. Mater*., 2012, 324, 1975.

[262] Thomas, J. J.; Shinde, A.; Krishna, P.; Kalarikkal, N., "Cation distribution and micro level magnetic alignments in the nanosized nickel zinc ferrite", *J. Alloys Compd*., 2013, 546, 77.

[263] Ghasemi, A.; Ekhlasi, S.; Mousavinia, "Effect of Cr and Al substitution cations on the structural and magnetic properties of $Ni_{0.6}Zn_{0.4}Fe_{2-x}Cr_{x/2}Al_{x/2}O_4$ nanoparticles synthesized using the sol–gel auto-combustion method", *J. Magn. Magn. Mater*., 2014, 354, 136.

[264] Lwin, N.; Fauzi, M.A.; Sreekantan, S.; Othman, R.; Thant, A.A., "Effect of iron- Deficiency on Structural and Magnetic Properties in Low Temperature Synthesized Mg-Mn Ferrite", *Int. J. Nanosci*., 2011, 10(06), 1257-63.

[265] Ahamad, H.; Rewatkar, K.; Meshram, N.; Dhoble, S.J., "Synthesis and study of Co doped Ni-Cd ferro-spinels by microwave assisted sol-gel auto-combustion method", *J. Ferroelectrics*, 2020, 555, 146.

[266] Stokes, A.; Wilson, A., "The diffraction of X rays by distorted crystal aggregates-I.", *Phys. Soc*., 1994, 56, 174.

[267] Siraj, K.; Khaleeq-ur-Rahman, M.; Hussain, S.; Rafique, M., Anjum, "Effect of deposition temperature on structural, surface, optical and magnetic properties of pulsed laser deposited Al-doped CdO thin films", *J. Alloys Compd*., 2011, 509, 6756.

[268] Angadi, V. J.; Rudraswamy, B.; Sadhana, K.; Murthy, S.R.; Praveena, "Effect of Sm^{3+}–Gd^{3+} on structural, electrical and magnetic properties of Mn–Zn ferrites synthesized via combustion route", *J. Alloys Compd*., 2016, 656, 5.

[269] Kakade, S.; Kambale, R.; Ramanna, C.; Kolekar, "Crystal strain, chemical bonding, magnetic and magnetostrictive properties of erbium (Er^{3+}) ion substituted cobalt-rich ferrite ($Co_{1.1}Fe_{1.9-x}Er_xO_4$)", *RSC Adv*., 2016, 6, 33308.

[270] Bouhadouza, N.; Rais, A.; Kaoua, S.; Moreau, M.; Taibi, K.; Addou, "Structural and vibrational studies of $NiAl_xFe_{2-x}O_4$ ferrites ($0 \leq x \leq 1$)", *Ceram. Int*., 2015, 41, 11687.

[271] Naik P. P.; Tangsali, R.; Meena, S.; Yusuf, "Influence of rare earth (Nd_{+3}) doping on structural and magnetic properties of nanocrystalline manganese-zinc ferrite", *Mater. Chem. Phys*., 2017, 191, 215.

[272] Yan, Z.; Luo, "Effects of CeZn co-substitution on structure, magnetic and microwave absorption properties of nickel ferrite nanoparticles", *J. Alloys Compd*., 2017, 695, 1185.

[273] Mohammed, K.; Al-Rawas, A.; Gismelseed, A.; Sellai, A.; Widatallah, H.; Yousif, A., et al. "Infrared and structural studies of $Mg_{1-x}Zn_xFe_2O_4$ ferrites, *Phys. B Condens. Matter*, 2012, 407, 795.

[274] Somvanshi, S. B.; Jadhav, S.A.; Khedkar, M.V.; Kharat, P.B.; More, S.; Jadhav, "Structural, thermal, spectral, optical and surface analysis of rare earth metal ion (Gd^{3+}) doped mixed Zn–Mg nano-spinel ferrites", *Ceram. Int*., 2020, 46, 13170.

[275] Sainamthip, P.; Amarakoon, "Role of zinc volatilization on the microstructure development of manganese zinc ferrites", *J. Am. Ceram. Soc*., 1988, 71, 644.

[276] Zulkimi, M. M. M.; Hashim, M.; Ismail, I.; Kanagesan, S.; Mustaffa, M.S., Zawawi, M. K. I. M., "Trends of Parallel Microstructure and Magnetic Properties Evolution in $Co_{0.5}Zn_{0.5}Fe_2O_4$", *J. Supercond. Nov. Magn*., 2014, 27, 1903.

[277] Valenzuela, R., *Magnetic ceramics* (Cambridge University Press, Cambridge, 1994).

[278] Wang, X.; Zhang, D.; Wang, G.; Jin, L.; Li, J.; Liao, Y.; H. Zhang, H.; Wang, S., "Synthesis of V_2O_5-Doped and low-sintered NiCuZn ferrite with uniform grains and enhanced magnetic properties", *Ceram. Int*., 2020, 46, 10652.

[279] Yang, Y.; Zhang, H.; Li, J.; Gan, G.; Wang, G.; Wen, D., "Enhanced grain-boundary diffusion on power loss of low-temperature-fired NiCuZn ferrites for high-frequency power supplies", *Appl. Phys. A*, 2018, 124, 785.

[280] Xu, F.; Liao, Y.; Zhang, D.; Zhou, T.; Li, J.; Gan, G.; Zhang, H., "Synthesis of highly uniform and compact lithium zinc ferrite ceramics via an efficient low temperature approach", Inorg. Chem., 2017, 56, 4512.

[281] Su, H.; Tang, X.; Zhang, H.; Jing, Y.; Bai, F.; Zhong, "Low-loss NiCuZn ferrite with matching permeability and permittivity by two-step sintering process", *J. Appl. Phys*., 2011, 109, 07A501.

[282] Mechi, N.; Mallah, A.; Hcini, S.; Bouazizi, M.L.; Boudard, M.; Dhahri, A., "Effects of Sintering Temperature on Microstructural, Magnetic, and Impedance Spectroscopic Properties of $Ni_{0.4}Cd_{0.3}Zn_{0.3}Fe_2O_4$ Ferrites", *J. Supercond. Nov. Magn*., 2020, 33, 1547.

[283] Rana, K.; Thakur, P.; Sharma, P.; Tomar, M.; Gupta, V.; Thakur, A., "Improved structural and magnetic properties of cobalt nanoferrites: influence of sintering temperature", *Ceram. Int*., 2015, 41, 4492.

[284] Prasad, B.B.V.S.V.; Ramesh, K.; Srinivas, A., "Structural, morphological and magnetic properties of divalent copper-substituted Co-Zn Nanoferrites", *Int. J. Mod. Phys. B*, 2018, 32, 1850172.

[285] Akhtar, K.; Gul, M.; Haq, I.U.; Khan, R.A.; Khan, Z.U.; Hussain, A., "Synthesis and characterization of uniform fine particles of pure and chromium-substituted manganese ferrite with low dielectric losses", *Ceram. Int*., 2016, 42, 18064.

[286] Tang, G. D.; Shang, Z. F.; Zhang, X. Y.; Xu, J.; Li, Z. Z.; Li, C. M.; zhen, W. H.; Qi, L. L.; Lang., "Evidence from infrared spectra for the magnetic moment directions of CR cations in the spinel ferrites", Phys. B Condens. Matter, 2015. 463, 26-29.

[287] Khalaf, K. A.; Al-Rawas, A.; Gismelseed, A.; Al-Ruqeishi, M.; Al-Ani, S.; Al-Jubouri, A., "Effects of Zn substitution on structure factors, Debye-Waller factors and related structural properties of the $Mg_{1-x}Zn_xFeNiO_4$ spinels", *Adv. Mater*., 2019, 8, 70.

[288] Kumar, A.; Singh, A.; Yadav, M.; Arora, M.; Pant, R., "Finite size effect on Ni doped nanocrystalline $Ni_xZn_{1-x}Fe_2O_4$ ($0.1 \leq x \leq 0.5$)", *Thin Solid Films*, 2010, 519, 1056.

[289] Lakshmi, Ch.; Sridhar, S.L.N.; Govindraj, G.; Bangarraju, S.; Potukuchi, D.M., "Structural, magnetic and dielectric investigations in antimony doped nano-phased nickel-zinc ferrites", *Phys. B*, 2015, 459, 97.

[290] Tatarchuk, T.; Myslin, M.; Mironyuk, I.; Bououdina, M.; Pędziwiatr, A.T.; Gargula, R.P.; Kurzydło, "Synthesis, morphology, crystallite size and adsorption properties of nanostructured Mg-Zn ferrites with enhanced porous structure", *J. Alloys Compd*., 2020, 819, 152945.

[291] Holz, D.; Pagana, A.; Tsakaloudi, V.; Kogias, G.; Zaspalis, V., "Fundamentals of the Densification Mechanism of NiCuZn-Ferrites", *J. Jpn. Soc. Powder Metall*., 2014, 61, S75.

[292] Galperin, Y.M., *Introduction to Modern Solid-State Physics*, Department of Physics, Oslo, 2001, 1048, 45-75.

[293] El-Ghazzawy, E.H., "Effect of heat treatment on structural, magnetic, elastic and optical properties of the co-precipitated $Co_{0.4}Sr_{0.6}Fe_2O_4$", *J. Magn. Magn. Mater*., 2020, 497(1), 166017.

[294] Mazen, S.; Elmosalami, *Structural and elastic properties of Li-Ni ferrite*, International Scholarly Research Notices, 2011.

[295] Algude, S.; Patange, S.; Shirsath, S.E.; Mane, D.; Jadhav, K.M., "Elastic behaviour of Cr^{3+} substituted Co-Zn ferrites", *J. Magn. Magn. Mater*., 2014, 350, 39.

[296] Shamgani, N.; Gholizadeh, A., "Structural, magnetic and elastic properties of $Mn_{0.3-x}Mg_xCu_{0.2}Zn_{0.5}Fe_3O_4$ nanoparticles", *Ceram. Int*., 2019, 45, 239.

[297] Patil, V.; Shirsath, S.E.; More, S.; Shukla, S.; Jadhav, K.M., "Effect of zinc substitution on structural and elastic properties of cobalt ferrite", *J. Alloys Compd*., 2009, 488, 199.

[298] El-Ghazzawy; Amer, E., "Structural, elastic and magnetic studies of the as-synthesized Co_{1-x} $Sr_xFe_2O_4$ nanoparticles", *J. Alloys Compd*., 2017, 690, 293-303.

[299] Beyranvand, M.; Gholizadeh, A., "Structural, magnetic, elastic, and dielectric properties of $Mn_{0.3-x}Cd_xCu_{0.2}Zn_{0.5}Fe_2O_4$ nanoparticles", *J. Mater. Sci*., 2020, 31, 5124.

[300] Pawar, R. A.; Patange, S. M.; Tamboli, Q. Y.; Ramanathan, V.; Shirsath, S. E., "Spectroscopic, elastic and dielectric properties of Ho^{3+} substituted Co-Zn ferrites synthesized by sol-gel method", *Ceram. Int*., 2016, 42, 16096.

[301] Anis-ur-Rehman, M.; Asghar, M., "Variation in structural and dielectric properties of co-precipitated nanoparticles strontium ferrites due to value of pH", *J. Alloys Compd*., 2011, 509, 435-9.

[302] Watawe, S. C.; Sarwade, B. D.; Bellad, S. S.; Sutar, B. D.; Chougule, B. K., "Microstructure, frequency and temperature-dependent dielectric properties of cobalt-substituted lithium ferrites", *J. Magn. Magn. Mater*., 2000, 214(1), 55-60.

[303] Frey, E.; Kroy, K., "Brownian motion: a paradigm of soft matter and biological physics", *Ann. Der Phys*., 2005, 14, 20.

[304] Gawas, U.; Kothawale, M.; Pednekar, R.; Meena, S.; Prasad, N.; Alla, S.K., "Investigation of resistivity, magnetic susceptibility and dielectric properties of nanocrystalline Ni-Mn-Zn ferrites", *J. Supercond. Nov. Magn*., 2017, 30, 1287.

[305] Ansari, M. M. N.; Khan, S.; Ahmad, N., "Structural, electrical transport and magnetic properties of Nd^{3+} substituted Mn-Cu nanoferrites", *J. Alloys Compd*., 2020, 831, 154778.

[306] Shirsath, S. E.; Jadhav, S. S.; Toksha, B.; Patange, S.; Jadhav, S., "Remarkable influence of Ce^{4+} ions on the electronic conduction of $Ni_{1-2x}Ce_xFe_2O_4$", *Scripta Materialia*, 2011, 64(8), 773-6.

[307] Guo, R.; Yu, Z.; Yang, Y.; Sun, K.; Wu, C.; Liu, H.; Li, L., "Effects of iron deficiency content on electromagnetic performance of LiZn ferrites", *J. Supercond. Nov. Magn*., 2017, 30, 1767.

[308] Siva Ram Prasad, M.; Prasad, B.; Rajesh Babu, "Magnetic, structural and dc electrical resistivity studies on the divalent cobalt substituted Ni-Zn ferrite system", *Int. J. Mod. Phys. B*, 2015, 29, 1550067.

[309] Chen, K.; Li, G.; Gao, F.; Liu, J.; Liu, J.; Zhu, J., "Conducting grain boundaries in the high-dielectric-constant ceramic $CaCu_3Ti_4O_{12}$", *J. Appl. Phys*., 2007, 101, 074101.

[310] Qayoom, M.; Bhat, R.; Shah, K.A.; Pandit, A.H.; Firdous, A.; Dar, G.N., "Modified solution combustion synthesis of nickel-doped magnetite nanoparticles and the influence of annealing on their optical, electrical, and magnetic properties", *J. Electron. Mater*., 2020, 49, 1215.

[311] Jagadeeshwaran, C.; Murugaraj, "Investigation on structural, optical, and electrical properties for sintered Mg-Zn aluminate systems", *J. Mater. Sci*., 2020, 31, 6744.

[312] Peng, L.; Li, L.; Zhong, X.; Hu, Y.; Tu, X.; Wang, R., "Magnetic, electrical, and dielectric properties of La-Cu substituted Sr-hexaferrites for use in microwave LTCC devices", *J. Alloys Compd*., 2016, 665, 31.

[313] Rezlescu, N.; Rezlescu, E., "Dielectric properties of copper containing ferrites", *J. Phys. Stat. Sol*., 1974, 23, 575.

[314] Böttger, H.; Bryksin, V.V., *Hopping Conduction in Solids*, Akademie-Verlag, Berlin, 1985.

[315] Parida, K.; Das, S.; Mahapatra, P.; Choudhary, R., "Relaxor behavior and impedance spectroscopic studies of chemically synthesized $SrCu_3Ti_4O_{12}$ ceramic", *Res. Bull*., 2019, 111, 7.

[316] Ray, A.; Basu, T.; Behera, B.; Kumar, M.; Thapa, R.; Nayak, P., "Role of Gd-doping in conduction mechanism of BFO-PZO nanocrystalline composites: experimental and first-principles studies", *J. Alloys Compd*., 2018, 768, 198.

[317] Kamran, M.; Anis-ur-Rehman, M., "Enhanced transport properties in Ce doped cobalt ferrites nanoparticles for resistive RAM applications", *J. Alloys Compd*., 2020, 822, 153583.

[318] Atif, M.; Idrees, M.; Nadeem, M.; Siddique, M.; Ashraf, M.W., "Investigation on the structural, dielectric and impedance analysis of manganese substituted cobalt ferrite i.e., $Co_{1-x}Mn_xFe_2O_4$ $(0.0 \leq x \leq 0.4)$", *RSC Adv*., 2016, 6, 20876.

[319] Gholizadeh, A., Beyranvand, M. "Investigation on the structural, magnetic, dielectric and impedance analysis of $Mg_{0.3-x}Ba_xCu_{0.2}Zn_{0.5}Fe_2O_4$ nanoparticles", *Phys. B*, 2020, 584, 412079.

[320] Yue, Z.; Zhou, J.; Li L.; Wang, X.; Gui, Z., "Effect of copper on the electromagnetic properties of Mg-Zn-Cu ferrites prepared by sol–gel auto-combustion method", *Mater. Sci. Eng. B*, 2001, 86, 64.

[321] Pike, G. F., "AC conductivity of scandium oxide and a new hopping model for conductivity", *Phys. Rev. B*, 1972, 6, 1572.

[322] Elliott, S. R., "A theory of ac conduction in chalcogenide glasses", *j. Philos. Mag*., 1977, 36, 1291.

[323] Funke, K., Jump relaxation in solid electrolytes. Prog. *Solid State Chem*., 1993, 22, 111.

[324] Sekulic, D. L.; Lazarevic, Z. Z.; Sataric, M. V.; Jovalekic, C. D.; Romcevic, N. Z., "Temperature-dependent complex impedance, electrical conductivity and dielectric studies of MFe_2O_4 (M = Mn, Ni, Zn) ferrites prepared by sintering of mechanochemical synthesized nanopowders", *J. Mater. Sci*., 2015, 26, 1291.

[325] Mott, N. F., "Conduction in non-crystalline materials: III. Localized states in a pseudogap and near extremities of conduction and valence bands", *Philos. Mag*., 1969, 19, 835.

[326] Lahouli, R.; Massoudi, J.; Smari, M.; Rahmouni, H.; Khirouni, K.; Dhahri, E.; Bessais, L., "Investigation of annealing effects on the physical properties of $Ni_{0.6}Zn_{0.4}Fe_{1.5}Al_{0.5}O_4$ ferrite", *RSC Adv*., 2019, 9, 19949.

[327] Mansour, S.; Al-Hazmi, F.; Abdo, M.A., "Relaxation time enhancement of cobalt zinc nanoferrites via Cr^{3+} doping", *J. Alloys Compd*., 2019, 792, 626.

[328] Ray, A.; Basu, T.; Behera, B.; Gavali, D.S.; Thapa, R.; Vajandar, S.; Nayak, P., "Structural, dielectric, electrical properties of Nd doped double perovskite ceramics and variation of density of states upon doping", *Mater. Chem. Phys*., 2020, 239, 122250.

[329] Petrović, M. V.; Grigalaitis, R.; Dzunuzovic, A.; Bobić, J.; Stojanović, B.; Šalaševičius, R.; Banys, J., "Positive influence of Sb doping on properties of di-phase multiferroics based on barium titanate and nickel ferrite", *J. Alloys Compd*., 2018, 749, 1043.

[330] Nakamura, T., "Low-temperature sintering of NiZnCu ferrite and its permeability spectra", *J. Magn. Magn. Mater*., 1997, 168, 285-291.

[331] Globus, A.; Duplex, P.; Guyot, M., "Determination of initial magnetization curve from crystallites size and effective anisotropy field", *IEEE Trans. Magn*., 1971, 7, 617.

[332] Sattar, A. A.; El-Sayed, H.; El-Shokrofy, K.; Eltabey, M. M., "Improvement of the Magnetic Properties of Mn-Ni-Zn Ferrite by the Non-magnetic Al^{3+} Ion Substitution", *J. Appl. Sci*., 2005, 5, 162.

[333] Prasad, B. B. V. S. V.; Ramesh, K.V.; Srinivas, A. "Physical, structural, morphological, magnetic and electrical properties of $Co_{0.5-x}Ni_xZn_{0.5}Fe_2O_4$ nanocrystalline ferrites", Ceramics International. *Ceram. Int*., 2019, 45, 4549.

[334] Nakamura, "Snoek's limit in high-frequency permeability of polycrystalline Ni-Zn, Mg-Zn, and Ni-Zn-Cu spinel ferrites", *J. Appl. Phys*., 2000, 88, 348-353.

[335] Lathiya, P.; Kreuzer, M.; Wang, J., "RF complex permeability spectra of Ni-Cu-Zn ferrites prepared under different applied hydraulic pressures and durations for wireless power transfer (WPT) applications", *J. Magn. Magn. Mater*., 2020, 499, 166273.

[336] Mustaffa, M. S.; Hashim, M.; Azis, R.; Ismail, I.; Kanagesan, S.; Zulkimi, M. M., "Magnetic phase-transition dependence on nano-to-micron grain-size microstructural changes of mechanically alloyed and sintered $Ni_{0.6}Zn_{0.4}Fe_2O_4$", *J. Supercond. Nov. Magn.*, 2014, 27, 1451.

[337] Verma, A.; Goel, T.; Mendiratta, R.; Gupta, R., "High-resistivity nickel–zinc ferrites by the citrate precursor method", *J. Magn. Magn. Mater*., 1999, 192, 271.

[338] Peng, Z.; Fu, X.; Ge, H.; Fu, Z.; Wang, C.; Qi, L., "Effect of Pr^{3+} doping on magnetic and dielectric properties of Ni-Zn ferrites by "one-step synthesis", *J. Magn. Magn. Mater*., 2011, 323, 2513.

[339] Thakur, A.; Mathur, P.; Singh, M., "Study of dielectric behaviour of Mn–Zn nano ferrites", *J. Phys. Chem. Solids*, 2007, 68, 378.

[340] Guinier, A., "X-Ray diffraction in crystals, imperfect crystals and amorphous bodies, ed. by WH Freeman and Co.", *J San Francisco*, 1963.

[341] Modi, K.; Shah, S.; Pujara, N.; Pathak, T.; Vasoya, N.; Jhala, I.G., "Infrared spectral evolution, elastic, optical and thermodynamic properties study on mechanically milled $Ni_{0.5}Zn_{0.5}Fe_2O_4$ spinel ferrite", *J. Mol. Struct*., 2013, 1049, 250.

[342] Humbe, A. V.; Kharat, P. B.; Nawle, A. C.; Jadhav, K. M., "Nanocrystalline $Ni_{0.70-x}Cu_xZn_{0.30}Fe_2O_4$ with $0 \leq x \leq 0.25$ prepared by nitrate-citrate route: structure, morphology and electrical investigations", *J. Mater. Sci. Mater. Electron*., 2018, 29, 3467.

[343] Bangruwa, J. S.; Kumar, S.; Chauhan, A.; Kumar, P.; Verma, V., "Magnetism N. Modified magnetic and electrical properties of perovskite-spinel multiferroic composites", *J. Supercond. Nov. Magn*., 2019, 32, 2559.

[344] Shannon, R. D., crystal physics, diffraction, theoretical, crystallography g. "Revised effective ionic radii and systematic studies of interatomic distances in halides and chalcogenides", *Acta Cryst. A*, 1976, 32, 751.

[345] Verma, K.; Singh, M.; Kotnala, R.; Goyal, N., "Magnetic field control of polarization/capacitance/voltage/resistance through lattice strain in $BaTiO_3$-$CoFe_2O_4$ multiferroic nanocomposite", *J. Magn. Magn. Mater*., 2019, 469, 483.

[346] Hammad A. B. A.; Darwish A.G.; El Nahrawy, A.M., "Identification of dielectric and magnetic properties of core shell $ZnTiO_3$/$CoFe_2O_4$ nanocomposites", *Appl. Phys. A*, 2020, 126, 504.

[347] Ramesh, T.; Rajendar, V.; Murthy, S.R., "$CoFe_2O_4$-$BaTiO_3$ multiferroic composites: role of ferrite and ferroelectric phases on the structural, magneto dielectric properties", *J. Mater. Sci. Mater. Electron*., 2017, 28, 11779-11788.

[348] Islam, R. A.; Priya, S., "Synthesis of high magnetoelectric coefficient composites using annealing and aging route", *Int. J. Appl. Ceram. Technol*., 2006, 3, 353.

[349] Wang, L.; Yu, G.; Zhu, C.; Lv, F.; Liu, F.; Kong., "Preparation and investigation of structure, magnetic, and dielectric properties of (1-x) $Bi_2Fe_4O_9$-x$MgFe_2O_4$ bicomponent ceramics", *J. Mater. Sci. Mater. Electron*., 2019, 30, 20556.

[350] Mendelson, M. I., "Average grain size in polycrystalline ceramics", *J. Am. Ceram. Soc*., 1969, 52, 443.

[351] Shen, J.; Bai, Y.; Zhou, J.; Li, L., "Magnetic properties of a novel ceramic ferroelectric–ferromagnetic composite", *J. Am. Ceram. Soc*., 2005, 88, 3440.

[352] Bai, Y.; Xu, F.; Qiao, L.; Zhou, J.; Li, L., "The static and hyper-frequency magnetic properties of a ferromagnetic–ferroelectric composite", *J. Magn. Magn. Mater*., 2009, 321(3), 148.

[353] Kumar, Y.; Yadav, K.; Shah, J.; Kotnala, R.K, "Structural, dielectric, magnetic and magnetoelectric properties of (x) $Bi_{0.5}Na_{0.5}TiO_3$-(1-*x*) $Ni_{0.2}Co_{0.8}Fe_2O_4$ composites", *Mater. Res. Express*, 2016, 3, 065701.

[354] Kavanloui, M., Hashemi, B., "Effect of B_2O_3 on the densification and magnetic properties of Li-Zn ferrite", *Mater. Des*., 2011, 32, 4257.

[355] Qin, X.; Wu, H.; Xu, R.; Gao, R.; Wang, Z.; Chen, G.; Cai, W., "Study on magnetoelectric properties of $Ni_{0.5}Zn_{0.5}Fe_2O_4$/$Ba_{0.8}Sr_{0.2}TiO_3$ composite ceramics based on Bi_2O_3 as combustion aid", *J. Mater. Sci. Mater. Electron*., 2020, 31, 4073.

[356] Zheng, Y.; Jia, L.; Xu, F.; Wang, G.; Shi, X.; Zhang, H., "Microstructures and magnetic properties of low temperature sintering NiCuZn ferrite ceramics for microwave applications", *Ceram. Int*., 2019, 45, 22163.

[357] Salunkhe, S.; Jigajeni, S.; Sutar, M.; Tarale, A.; Joshi, P.B., "Magnetoelectric and magnetodielectric effect in CFMO-PBT nanocomposites", *J. Phys. Chem. Solid*., 2013, 74, 388.

[358] Qi, X.; Zhou, J.; Li, B.; Zhang, Y.; Yue, Z.; Gui, Z.; Li, L., "Preparation and spontaneous polarization–magnetization of a new ceramic ferroelectric–ferromagnetic composite", *J. Am. Ceram. Soc*., 2004, 87, 1848.

[359] Samad, R.; Want, R.B., "Magnetic, and Magnetoelectric Properties of Yttrium-Containing $BaY_{0.025}Ti_{0.9625}O_3$-$SrFe_{12}O_{19}$ Composite", *J. Electron. Mater*., 2018, 47, 2143.

[360] Ansari, M. M. N.; Khan, S.; Ahmad, "Effect of R^{3+}(R= Pr, Nd, Eu and Gd) substitution on the structural, electrical, magnetic and optical properties of Mn-ferrite nanoparticles", *J. Magn. Magn. Mater*., 2018, 465, 81.

[361] Kigery, W. D.; Bowen, H. K.; Uhlmann, D. R., *Introduction of Ceramics*, Wiley, New York, 1975, *p.* 458.

[362] Kumar, S.; Shinde, T.; Vasambekar, P., Engineering High Permeability: Mn-Zn and Ni-Zn Ferrites. *Int. J. Appl. Ceram. Technol*., 2015, 12, 851.

[363] Patankar, K.; Nipankar, R.; Mathe, V.; Mahajan, R.; Patil, S.A., "Role of sintering on magneto-electric effect in $CuFe_{1.8}Cr_{0.2}O_4$-$Ba_{0.8}Pb_{0.2}Ti_{0.8}Zr_{0.2}O_3$ composite ceramics", 2001, *Ceram. Int*., 27, 853.

[364] Maxwell, J. C., *Electricity and magnetism*: Dover New York, 1954.

[365] Mani, A. D.; Soibam, "Comparative studies of the dielectric properties of (1−x) $BiFeO_3$-x$Ni_{0.8}Zn_{0.2}Fe_2O_4$ (x = 0.0, 0.2, 0.5, 0.8, 1.0) multiferroic nanocomposite with their single phase $BiFeO_3$ and $Ni_{0.8}Zn_{0.2}Fe_2O_4$", 2017, *Phys. B*, 507, 21.

[366] Curecheriu, L. P.; Buscaglia, M. T.; Buscaglia, V.; Mitoseriu, L.; Postolache, P.; Ianculescu, A.P.; Nanni, "Functional properties of $BaTiO_3$-$Ni_{0.5}Zn_{0.5}Fe_2O_4$ magnetoelectric ceramics prepared from powders with core-shell structure", *J. Appl. Phys*., 2010, 107, 104106.

[367] Jiang, N.; Yang, Y.; Zhou, J.P.; Yang, J.; Liu, P., "Microstructure and microwave-frequency electromagnetic properties of $Ni_{0.4}Zn_{0.6}Fe_2O_4$/$Ba_{0.6}Sr_{0.4}TiO_3$ composites", *Ceram. Int*., 2016, 42, 15585.

[368] Belavi, P.; Naik, L.; Kotnala, R.; Mathe, V.L., "Structural, electrical and magnetic properties of NCCF+ BTO ME composites", *Int. J. Sci. Eng. Res*., 2013, 4, 43-53.

[369] Jonscher, A.; Meca, F.; Millany, H., "Charge-carrier contributions to dielectric loss", *J. Phys. C Solid State Phys*., 1979, 12, L293.

[370] Upadhyay, S.; Kumar, D.; Parkash, O., "Effect of composition on dielectric and electrical properties of the $Sr_{1-x}La_xTi_{1-x}Co_xO_3$ system", *Bull. Mater. Sci*., 1996, 19, 513.

[371] Pandey, R.; Meena, B.R.; Singh, A.K., "Structural and dielectric characterization on multiferroic *x*$Ni_{0.9}Zn_{0.1}Fe_2O_4$/(1-*x*) $PbZr_{0.52}Ti_{0.48}O_3$ particulate composite", *J. Alloys Compd*., 2014, 593, 224.

[372] Bibes, M.; Barthélémy, A., Towards a magnetoelectric memory. *Nat. Mater*., 2008, 7, 425.

[373] Zhang, R. F.; Deng, C. Y.; Ren, L.; Li, Z.; Zhou., "Dielectric, ferromagnetic and maganetoelectric properties of $BaTiO_3$-$Ni_{0.7}Zn_{0.3}Fe_2O_4$ composite ceramics", *Mater. Res. Bull*., 2013, 48, 4100.

[374] Schileo, G.; Pascual-Gonzalez, C.; Alguero, M.; Reaney, I.M.; Postolache, P.; Mitoseriu, L.; Mitoseriu, K.; Reichmann, A.; Feteira, "Yttrium iron garnet/barium titanate multiferroic composites", *J. Am. Ceram. Soc*., 2016, 99, 1609.

[375] Looyenga, H., "Dielectric constants of heterogeneous mixtures", Physica, 1965, 31, 401-406.

[376] Yang, R. B.; Hsu, S. D.; Lin, C. K., "Frequency-dependent complex permittivity and permeability of iron-based powders in 2-18 GHz", *J. Appl. Phys*., 2009, 105, 07A527.

[377] Hossain, M. E.; Liu, S. Y.; O'Brien, S.; Li, J., "Modeling of high-k dielectric nanocomposites", *Acta Mech*., 2014, 225, 1197.

[378] Tian, W.; Xiao, B.; Chen, Z.; Tang, Y.; Ma, N.; Wang, Z.; Du, P., "A tri-phase percolative ceramic composite with high initial permeability and composition-independent giant permittivity", *RSC Adv*., 2019, 9, 30641.

[379] Paiva, D.; Silva, M.; Ribeiro, T.; Vasconcelos, I.; Sombra, A.; Góes, J., "Novel magnetic–dielectric composite ceramic obtained from $Y_3Fe_5O_{12}$ and $CaTiO_3$", *J. Alloys Compd*., 2015, 644, 763.

[380] Ciomaga, C. E.; Airimioaei, M.; Turcan, I.; Lukacs, A.V.; Tascu, S.; Grigoras, M.; Lupu, N.; Banys, J.; Mitoseriu, L., "Functional properties of percolative $CoFe_2O_4$-$PbTiO_3$ composite ceramics", *J. Alloys Compd*., 2019, 775, 90.

[381] Venet, M.; Santa-Rosa, W.; da Silva, P.S.; M'Peko, J.C.; Ramos P.; Amorín, H., "Selection and optimization of a $K_{0.5}Na_{0.5}NbO_3$-based material for environmentally-friendly magnetoelectric composites", *J. Materials*, 2020, 13, 731.

[382] Rushman, D.; Strivens M.A., The effective permittivity of two-phase systems, *Proc. Phys. Soc*., 1947, 59, 1011.

[383] Pahuja, P.; Sharma, R.; Singh, V.; Tandon, R. P., "Novel method of synthesis of multiferroic nickel cobalt ferrite-barium strontium titanate composite system", *J. Appl. Ceram. Technol*., 2015, 12, E156.

[384] Loyau, V.; Wang, G.Y.; Bue M.L.; Mazaleyrat, F., "An analysis of Mn-Zn ferrite microstructure by impedance spectroscopy, scanning transmission electron microscopy and energy dispersion spectrometry characterizations", *J. Appl. Phys*., 2012, 111, 053928.

[385] Mangalaraja, R.; Ananthakumar, S.; Manohar, P.; Gnanam, F.D., "Dielectric behavior of $Ni_{1-x}Zn_xFe_2O_4$ prepared by flash combustion technique", *Mater. Lett*., 2003, 57, 1151.

[386] Kolekar, Y.; Sanchez, L.; Ramana, C.V., "Dielectric relaxations and alternating current conductivity in manganese substituted cobalt ferrite", *J. Appl. Phys*., 2014, 115, 144106.

[387] Rahaman, M.; Aldalbahi, A.; Govindasami, P.; Khanam, N.P.; Bhandari, S.; Feng, P.; Altalhi, T., "A new insight in determining the percolation threshold of electrical conductivity for extrinsically conducting polymer composites through different sigmoidal models", *Polymers*., 2017, 9, 527.

[388] Verwey, E.; De Boer, F.; Van Santen, J. H., Cation arrangement in spinels, *J. Chem. Phys*., 1948, 161, 1091.

[389] Devan, R.; Chougule, B.K., "Effect of composition on coupled electric, magnetic, and dielectric properties of two-phase particulate magnetoelectric composite", *J. Appl. Phys*., 2007, 101, 014109.

[390] Selvasekarapandian, S.; Vijayakumar, M., "The ac impedance spectroscopy studies on $LiDyO_2$", *Mater. Chem. Phys*., 2003, 80, 29.

[391] Kaushal, A.; Olhero, S.; Singh, B.; Fagg, D.P.; Bdikin, I.; Ferreira, M.F. J., "Impedance analysis of $0.5Ba(Zr_{0.2}Ti_{0.8})O_3$-$0.5(Ba_{0.7}Ca_{0.3})TiO_3$ ceramics consolidated from micro-granules", *Ceram. Int*., 2014, 40, 10593-10600.

[392] James, A.; Srinivas, K., "Low temperature fabrication and impedance spectroscopy of PMN-PT ceramics", *Mater. Res. Bull*., 1999, 34, 1301.

[393] Hafsia, A. B.; Rammeh, N.; Farid, M.; Khitouni, M., "Electrical conductivity and dielectric study of $LaBaFe_{0.5}Zn_{0.5}MnO_{6-\delta}$ compound", *Ceram. Int*., 2016, 42, 3673-3680.

[394] Kumar, N.; Shukla, A.; Kumar, N.; Choudhary, R. N. P., "Effects of milling time on structural, electrical and ferroelectric features of mechanothermally synthesized multi-doped bismuth ferrite", Appl. Phys. A, 2020, 126, 181.

[395] Mohamed, M. B.; Wang, H.; Fuess, H., "Dielectric relaxation and magnetic properties of Cr doped $GaFeO_3$", *J. Phys. D Appl. Phys*., 2010, 43, 455409.

[396] Rahaman, M. N., *Ceramic Processing and Sintering*, Marcel Dekker, New York, 1995.

[397] Ahmed, M.; Mansour, S.; Abdo, M.A., "Electrical properties of Cu substituted Co nano ferrite", *Phys. Scr*., 2012, 86, 025705.

[398] Ciomaga, C. E.; Maria Neagu, A.; Valentin Pop, M.; Airimioaei, M.; Tascu, S.; Schileo, G.; Galassi, C.; Mitoseriu, L., "Ferroelectric and dielectric properties of ferrite-ferroelectric ceramic composites", *J. Appl. Phys*., 2013, 113, 074103.

[399] Macdonald, J. R., "Note on the parameterization of the constant-phase admittance element", *Solid State Ion*., 1984, 13, 147.

[400] Barick, B.; Mishra, K.; Arora, A.; Choudhary, R.; Pradhan, D.K., "Impedance and Raman spectroscopic studies of $(Na_{0.5}Bi_{0.5})\ TiO_3$", *J. Phys. D Appl. Phys*., 2011, 44, 355402.

[401] Bhasin, T.; Agarwal, A.; Sanghi, S.; Kotnala, R.; Shah, J.; Yadav, M., "Study of crystal structure, dielectric, magnetic and magnetoelecrtic properties of $xCoFe_2O_4$-(1-x) $Na_{0.5}Bi_{0.5}TiO_3$ composites", *Ceram. Int*., 2018, 44, 7629.

[402] Shah, J.; Kotnala, R.K., "Induced magnetism and magnetoelectric coupling in ferroelectric $BaTiO_3$ by Cr-doping synthesized by a facile chemical route", *J. Mater. Chem. A*, 2013, 1, 8601.

[403] Vasoya, N.; Jha, P. K.; Saija, K.; Dolia, S.; Zankat, K.; Modi, K .B., "Electric Modulus, Scaling and Modeling of Dielectric Properties for Mn^{2+}-Si^{4+}Co-substituted Mn-Zn Ferrites", *J. Electron. Mater*., 2016, 45, 917.

[404] Provenzano, V.; Boesch, L.; Volterra, V.; Moynihan, C.; Macedo, P. B., "Electrical relaxation in $Na_2O_3SiO_2$ glass", *J. Am. Ceram. Soc*., 1972. 55(10), 492-496.

[405] Hodge, I.; Ingram, M.; West, A. R., "A new method for analysing the ac behaviour of polycrystalline solid electrolytes", *J. Electroanal. Chem*., 1975, 58, 429.

[406] Charguia, R.; Hcini, S.; Boudard, M.; Dhahri, A., "Microstructural properties, conduction mechanism, dielectric behavior, impedance and electrical modulus of $La_{0.6}Sr_{0.2}Na_{0.2}MnO_3$ manganite", *J. Mater. Sci.: Mater. Electron*., 2019, 30, 2975-2984.

[407] Prakash, B. S.; Varma, K. B. R., "Microstructural and dielectric properties of donor doped (La^{3+}) $CaCu_3Ti_4O_{12}$ ceramics", *J. Mater. Sci.: Mater. Electron*., 2006, 17, 899-907.

[408] Sahoo, P.; Panigrahi, A.; Patri, S.; Choudhary, R. N. P., "Impedance spectroscopy of $Ba_3Sr_2DyTi_3V_7O_{30}$ ceramic", *Bull. Mater. Sci*., 2010, 33, 129-134.

[409] Liu, J.; Duan, C. G.; Yin, W. G.; Mei, W. N.; Smith, R. W.; Hardy, J. R., "Dielectric permittivity and electric modulus in $Bi_2Ti_4O_{11}$", *J. Chem. Phys*., 2003, 119, 2812.

[410] Kumar, N.; Shukla, A.; Kumar, N.; Choudhary, R. N. P., "Structural, electrical and magnetic properties of eco-friendly complex multiferroic material: $Bi(Co_{0.35}Ti_{0.35}Fe_{0.30})O_3$", *Ceram. Int*., 2019, 45, 822-831.

[411] Tang, R.; Jiang, C.; Qian, W.; Jian, J.; Zhang, X.; Wang, H.; Yang, H., "Dielectric relaxation, resonance and scaling behaviors in $Sr_3Co_2Fe_{24}O_{41}$ hexaferrite", *Sci. Rep*; 2015.

[412] Pradhan, D. K.; Choudhary, R.; Rinaldi, C.; Katiyar, R. S., "Effect of Mn substitution on electrical and magnetic properties of $Bi_{0.9}La_{0.1}FeO_3$", *J. Appl. Phys*., 2009, 106, 024102.

[413] Khalid, A.; Abbas, S. K.; Mustafa, G.; Atiq, S.; Hussain, S. S.; Anwar, M. S.; Naseem, S., "Analysis of dielectric dispersion and magnetoelectric coupling in $BiFeO_3$ and $NiFe_2O_4$ nanocomposites", *Ceram. Int*., 2019, 45, 24453-24460.

[414] Ai, L.; Jiang, J.; Li, L., "Frequency-dependent dielectric and electric modulus properties of Li-Ni-Sm-Fe-O spinel embedded in conducting polymer", *J. Mater. Sci.: Mater. Electron*., 2010, 21, 206-210.

[415] Gao, L.; Wang, X.; Wang, H.; Lei, Q., "Improvement of dielectric performance and interfacial polarization of polyvinylidene fluoride composites with $CaCu_3Ti_4O_{12}$@ Ni hybrid nanofibers", *J. Mater. Sci.: Mater. Electron*., 2018, 29, 10600-10613.

[416] Mizouri, F.; Abdelmoula, N.; Mezzane, D.; Khemakhem, H., "Compounds. Impedance spectroscopy and conduction mechanism of multiferroic $Bi_{0.8}(Ba_{0.9}Ca_{0.1})_{0.8}Fe_{0.8}(Ti_{0.9}Sn_{0.1})_{0.8}O_3$", *J. Alloys Compd*., 2018, 763, 570-580.

[417] Gerhardt, R., "Impedance and dielectric spectroscopy revisited: distinguishing localized relaxation from long-range conductivity", *J. Phys. Chem. Sol*., 1994, 55, 1491-1506.

[418] Zahi, S.; Hashim, M.; Daud, A.R., "Synthesis, magnetic properties and microstructure of Ni-Zn ferrite by sol-gel technique", *J. Magn. Magn. Mater*., 2007, 308, 177.

[419] Zahi, S.; Daud, A.; Hashim, A.R., "A comparative study of nickel-zinc ferrites by sol-gel route and solid-state reaction", *J. Mater. Chem. Phys*., 2007, 106, 452.

[420] Verma, A.; Goel, T.; Mendiratta, R.; Kishan, P., "Magnetic properties of nickel–zinc ferrites prepared by the citrate precursor method", *J. Magn. Magn. Mater*., 2000, 208, 13-19.

[421] Polder, D., *Ferrite materials*, Inst. Electron. Eng. Part II, 1950, 97(56): *p*. 246-256.

[422] Zheng, H.; Dong, Y.; Wang, X.; Weng, W.; Han, G.; Ma, N., "Super high threshold percolative ferroelectric/ferrimagnetic composite ceramics with outstanding permittivity and initial permeability", *Chem. Int. Ed. Engl*., 2009, 48, 8927.

[423] Nan, C. W., Physics of inhomogeneous inorganic materials. Prog., *Mater. Sci*., 1993, 37, 1.

[424] Paterson, J.; Devine, R.; Phelps, A. D. R., "Complex permeability of soft magnetic ferrite/polyester resin composites at frequencies above 1 MHz", *J. Magn. Magn. Mater*., 1999, 196-1997, 394-396.

[425] Qi, X.; Zhou, J.; Yue, Z.; Gui, Z.; Li, L.; Buddhudu, S., "A ferroelectric ferromagnetic composite material with significant permeability and permittivity", *Adv. Funct. Mater*., 2004, 14, 920.

[426] Yue, Z.; Zhou, J.; Li, L.; Gui, Z., "Effects of MnO_2 on the electromagnetic properties of NiCuZn ferrites prepared by sol-gel auto-combustion", *J. Magn. Magn. Mater*., 2001, 233, 224-229.

[427] Zhao, Q.; Zhang, H.; Li, J.; Xu, F.,; Liao, Y.; Liu, C.; Su, H., "Low-temperature sintering synthesis and electromagnetic properties of NiCuZn/$BaTiO_3$ composite materials", *J. Alloys Compd*., 2019, 788, 44-49.

[428] Bahiraei, H.; Ong, C. K., "Microstructural and electromagnetic study of low temperature fired nano crystalline MgCuZn ferrite with Bi_2O_3 addition", *Ceram. Int*., 2017, 43, 4780-4784.

[429] Zhou, B.; Zhang, Y. W.; Liao, C. S.; Yan, C. H.; Chen, L.Y.; Wang, S.Y., "Rare-earth-mediated magnetism and magneto-optical Kerr effects in nanocrystalline $CoFeMn_{0.9}RE_{0.1}O_4$ thin films", *J. Magn. Magn Mater.*, 2004, 280, 327-333.

[430] Hussain, K.; Amin, N.; Arshad, M. I., "Evaluation of structural, optical, dielectric, electrical, and magnetic properties of Ce^{3+} doped $Cu_{0.5}Cd_{0.25}Co_{0.25}Fe_{2-x}O_4$ spinel nano-ferrites", 2021, *Ceram. Int*., 47, 3401-3410.

[431] Si, S.; Deng, H.; Wang, T.; Zheng, D.; Yang, P.; Chu, J., "Structural, optical, and enhanced multiferroic properties of $x$$CoFe_2O_4$-(1-$x$)$K_{0.5}Bi_{0.5}TiO_3$ ferrite-ferroelectric composites", *J. Mater. Sci.: Mater. Electron*., 2020, 31, 10639-10648.

[432] Zheng, H.; Li, L.; Xu, Z.; Weng, W.; Han, G.; Ma, N.; Du, P., "Ferroelectric/ferromagnetic ceramic composite and its hybrid permittivity stemming from hopping charge and conductivity inhomogeneity", *J. Appl. Phys*., 2013, 113, 044101.

[433] Dean, J. A., Lange's Handbook of Chemistry (McGraw-Hill Professional, Columbus, 1998), Sec. 4, 430-434.

[434] Verwey, E. J. W., Heilmann, E. L., "Physical properties and cation arrangement of oxides with spinel structures I. Cation arrangement in spinels", *J. Chem. Phys*., 1947, 15, 174-180.

[435] Singh, M.; Singh, J.; Kumar, M.; Kumar, S., "Investigations on multiferroic properties of lead free (1-x) BCZT-xCZFMO based particulate ceramic composites", *Solid State Sci.*, 2020, 108, 106380.

[436] Tiwari, S.; Vitta, S., "Magnetoelectric and magnetodielectric coupling and microwave resonator characteristics of $Ba_{0.5}Sr_{0.5}Nb_2O_6/CoCr_{0.4}Fe_{1.6}O_4$ multiferroic composite", Sci. Rep., 2018, 8, 11619.

[437] Chen, J.; Deng, H.; Zheng, D.; Pan, Y.; Si, S.; Zhang, Y.; Yang, P.; Chu, J., "Band gap narrowing and electrical properties of (1-x) $BaTiO_{3-x}SrFe_{0.5}Nb_{0.5}O_3$ lead-free ceramics", *J. Mater. Sci.: Mater. Electron*., 2021, 32, 10151-10159.

[438] Maksoud, M. I. A. A.; El-Sayyad, G. S.; Abokhadra, A.; Soliman, L. I.; El-Bahnasawy, H. H.; Ashour, A. H., "Influence of Mg^{2+} substitution on structural, optical, magnetic, and antimicrobial properties of Mn-Zn ferrite nanoparticles", *J. Mater. Sci.: Mater. Electron*., 2020, 31, 2598-2616.

[439] Patterson, A. L., *The Scherrer formula for X-ray particle size determination*, Phys.Rev., 1939, 56, 978-982.

[440] Feng, J.; Xiong, R.; Cheng, L.; Liu, Y., "Effect of chromium substitution on structural and magnetic properties of nickel-cobalt ferrite nanoparticles synthesized by co-precipitation method", *J. Supercond. Nov. Magn.*, 2017, 30, 3513-3521.

[441] Hong, Y.; Zhou, W.; Cheng, Z.; Huang, H.; Wu, Z.; Liao, S.; Luo, G., "Magnetic, electrical, and structural properties of Mg^{2+}-doped nickel–zinc ferrite prepared by sol–gel–SHS method", *J. Mater. Sci.: Mater. Electron*., 2020, 31, 16975-16982.

[442] Wang, X.; Li, Y.; Chen, Z.; Zhang, H.; Su, H.; Wang, G.; Liao, Y.; Zhong, Z., "Low-temperature sintering and ferromagnetic properties of $Li_{0.35}Zn_{0.30}Mn_{0.05}Ti_{0.15}Fe_{2.15}O_4$ ferrites co-fired with Bi_2O_3-MgO mixture", *J. Alloys Compd*., 2019, 797, 566-572.

[443] Ashiq, M. N.; Bibi, N.; Malana, M.A., "Effect of Sn-Ni substitution on the structural, electrical and magnetic properties of mixed spinel ferrites", *J. Alloys Compd*., 2010, 490, 594-597.

[444] Thakur, A.; Thakur, P.; Hsu, J. H., "Novel magnetodielectric nanomaterials with matching permeability and permittivity for the very-high-frequency applications", *Scr. Mater*., 2011. 64, 205-208.

[445] Musa, M. A.; Azis, R. S.; Dong, X.; Osman, N. H.; Hassan, J.; Muhammad, F. D.; Mokthar, N.., "Influence of aluminum substitution on microstructural, electrical, dielectric, and electromagnetic properties of sol-gel synthesized yttrium iron garnet (YIG)", *AIP Adv*. 2020. 10(4) 045128.

[446] ElGendy, L., Ghani, A. A., Darwish, A. S., Sattar, A. A., "Synthesis, microstructure analysis, electrical and magnetic properties of $Ni_{0.5}Mg_{0.5}Fe_2O_4$-$BaTiO_3$ Nano-composites", Appl. Phys. A, 2021,127, 1-14.

[447] Ansaree, Md. J.; Kumar, U.; Upadhyay, S., "Structural, dielectric and magnetic properties of particulate composites of relaxor ($BaTi_{0.85}Sn_{0.15}O_3$) and ferrite ($NiFe_2O_4$) synthesized by gel-combustion method", *J. Electroceram.*, 2018, 40, 257-269.

[448] Dastagiri, S.; Lakshmaiah, M. V.; Naidu, K. C. B., "Defect dipole polarization mechanism in low-dimensional Europium substituted $Al_{0.8}La_{0.2}$ TiO_3 nanostructures", Physica, 2020, E 120, 114058.

[449] Yang, Y.; Liu, X.; Jin, D., "Influence of heat treatment temperatures on structural and magnetic properties of $Sr_{0.50}Ca_{0.20}La_{0.30}Fe_{11.15}Co_{0.25}O_{19}$ hexagonal ferrites", *J. Magn. Magn. Mater*., 2014, 364, 11-17.

[450] Dar, K. M. A.; Batoo, M.; Verma, V.; Siddiqui, W. A.; Kotnala, R.K., "Synthesis and characterization of nano-sized pure and Al-doped lithium ferrite having high value of dielectric constant", *J. Alloys Compd*., 2010, 493, 553-560.

[451] Yan, W.; Li, N.; Han, B. Q., High-strength, lightweight spinel refractories, Am. Ceram. Soc. Bull., 2005, 84, 1-3.

[452] Yan, W.; Li, N.; Liu, G.; Han, B. Q.; Xu, J., "Effect of particle size on microstructure and strength of porous spinel ceramics prepared by pore-forming in situ technique", *Bull. Mater. Sci*., 2011, 34, 1109-1112.

[453] Kingery, W. J. J. W. and Sons, Introduction to Ceramics 2nd ed., 1976, 449-468

[454] Agami, W. R.; Ashmawy, M. A., "Structural, physical, and magnetic properties of nanocrystalline manganese-substituted lithium ferrite synthesized by sol-gel autocombustion technique", 2020, *Appl. Phys. A*, 126, 563.

[455] Pahuja, P.; Prakash, C.; Tandon, R. P., "Comparative study of magnetoelectric composite system $Ba_{0.95}Sr_{0.05}TiO_3$-$Ni_{0.8}Co_{0.2}Fe_2O_4$ with ferrite prepared by different methods", *Ceram. Int.* 2014, 40, 5731-5743

[456] Cao, M. S., Science and Technology of ultrafine preparation, Harbin Institute of Technology Press, Harbin (1998).

[457] Jain, A.; Wang, Y.G.; Wang, N.; Li, Y.; Wang, F. L., "Influence of individual phases on the magnetoelectric coupling and electromechanical response in (1-*x*)$Ba_{0.83}Ca_{0.10}Sr_{0.07}TiO_{3-x}BiFeO_3$ (*x*=0–0.30) multiferroic composites", *J. Magn. Magn. Mater*., 2020, 495, 165905.

[458] Bai, L.; Gao, R.; Zhang, Q.; Xu, Z.; Wang, Z.; Fu, C.; Chen, G.; Deng, X.; Luo, X.; Cai, W.., "Strong magnetic properties and enhanced coupling effect by tailoring the molar ratio in $BaTiO_3/Co_{0.5}Mg_{0.3}Zn_{0.2}Fe_2O_4$ composite ceramics", *J. Mater. Sci.: Mater. Electron*., 2019, 30, 11563-11575.

[459] Wang, Z.; Gao, R.; Chen, G.; Deng, X.; Cai, W.; Fu, C., "Dielectric, ferroelectric and magnetoelectric properties of in-situ synthesized $CoFe_2O_4/BaTiO_3$ composite ceramics", Ceram. Int., 2020, 46, 9154-9160.

[460] Si, S.; Deng, H.; Wang, T.; Yang, P.; Chu, J., "Structural phase transition, optical bandgap, interband electronic transition, and improved magnetism in bivalent Ca-, Sr-, Pb-, and Ba-doped $BiFeO_3$ ceramics", *J. Mater. Sci. Mater. Electron*., 2020, 31, 8464-8471.

[461] Kharrat, A. B. J.; Moutiab, N.; Khirouni, K.; Boujelben, W., "Investigation of electrical behavior and dielectric properties in polycristalline $Pr_{0.8}Sr_{0.2}MnO_3$ manganite perovskite", *Mater. Res. Bull*., 2018, 105, 75-83.

[462] Achary, P. G. R.; Behera, S.; Choudhary, R. N. P.; Parida, S. K., "Structural, dielectric and electrical properties of cerium-modified strontium manganite ceramics", 2021, *J. Mater. Sci.: Mater. Electron*., 32, 5738-5754.

[463] Ghodake, J. S.; Kambale, R. C.; Shinde, T.J.; Maskar, P.K.; Suryavanshi, S.S., "Magnetic and microwave absorbing properties of Co^{2+} substituted nickel–zinc ferrites with the emphasis on initial permeability studies", *J. Magn. Magn. Mater*., 2016, 401, 938-942.

[464] Xu, F.; Zhang, H.; Xie, F.; Liao, Y.; Li, Y.; Li, J.; Jin, L.; Yang, Y.; Gan, G.; Wang, G.; Zhao, Q., "Investigation of grain boundary diffusion and grain growth of lithium zinc ferrites with low activation energy", *J. Am. Ceram. Soc*., 2018, 101, 5037-5045.

[465] Bouzayen, M.; Dhahri, R.; Benali, A.; Chaabouni, S.; Khirouni, K.; Costa, B. F. O., "Synthesis and investigation of oxygen deficiency effect on electric properties of $La_{0.75}Ba_{0.10}Sr_{0.15}FeO_{2.875-\delta}$ (δ= 0.00, 0.125 and 0.25) ferrites", *J. Mater. Sci.: Mater. Electron*., 2020, 32, 13000-13013.

[466] Rafiq, M. A.; Zaman, T. U.; Ishfaq, H. A.; Maqbool, A.; Waqar, M.; Muhammad, Q. K.; Anjum, A.; Waris, A., "Exploring the conduction mechanism of multiferroic SrM-BCZT composite", *Ceram. Int*., 2020, 46, 2489-2499.

[467] Gholizadeh, A., "A comparative study of the physical properties of Cu-Zn ferrites annealed under different atmospheres and temperatures: Magnetic enhancement of $Cu_{0.5}Zn_{0.5}Fe_2O_4$ nanoparticles by a reducing atmosphere", *J. Magn. Magn. Mater*., 2018, 452, 389.

[468] Patil, S. A.; Mahajan, V. C.; Ghatage, A. K.; Lotke, S. D., "Structure and magnetic properties of Cd and Ti/Si substituted cobalt ferrites", *Mater. Chem. Phys*., 1998, 57, 86-91.

[469] Hankare, P. P.; Patil, R. P.; Garadkar, K. M.; Sasikala, R.; Chougule, B.K., "Synthesis, dielectric behavior and impedance measurement studies of Cr-substituted Zn-Mn ferrites. Mater", *Res. Bull*., 2011, 46, 447-452.

[470] Hcini, F.; Hcini, S.; Alzahrani, B.; Zemni, S.; Bouazizi, M. L., "Effect of Cr substitution on structural, magnetic and impedance spectroscopic properties of $Cd_{0.5}Zn_{0.5}Fe_{2-x}Cr_xO_4$ ferrites", *Appl. Phys. A*, 2020, 126, 362.

[471] Perry, C.; Khanna, B.; Rupprecht, G., Infrared studies of perovskite titanates, *Phys. Rev*., 1964, 135, A408.

[472] Wang, Z. M.; Zhao, K.; Guo, X.L.; Sun, W.; Jiang, H.L.; Han, X.Q.; Tao, X.T.; Cheng, Z.X.; Zhao, H.Y.; Kimura, H., "Crystallization, phase evolution and ferroelectric properties of sol–gel-synthesized $Ba(Ti_{0.8}Zr_{0.2})O_{3-x}$ ($Ba_{0.7}Ca_{0.3}$) TiO_3 thin films", *J. Mater. Chem. C*., 2013, 1, 522-530.

[473] Devi, C. S.; Kumar, G. S.; Prasad, G., "Spectroscopic and electrical studies on Nd^{3+}, Zr^{4+} ions doped nano-sized $BaTiO_3$ ferroelectrics prepared by sol-gel method", *Spectrochim. Acta. A Mol. Biomol. Spectrosc*., 2015, 136, 366-372.

[474] Liang, S.; Zhun, J.; Zheng, M.; Zhang, P.; Sun, P.; Wang, Z.; Zhu, X., "Microstructure and electrical properties of $(Na_{0.5}K_{0.5})_{1-2x}Mg_xNbO_3$-$Bi_{0.5}Na_{0.5}TiO_3$ lead-free piezoelectric ceramics", *Ceram. Int.*, 40, 2014, 2763-2768.

[475] Bisen, S.; Khan, M.; Mishra, A., "Tailoring effect of large polaron hopping in the conduction mechanism of Ca-modified $BaTiO_3$ system", *J. Mater. Sci.: Mater. Electron*., 2020, 31, 9212-9223.

[476] Kumar, S.; Sreenivas, K., "Effects of dl-alanine fuel and annealing on auto-combustion derived $MgFe_2O_4$ powder with low carbon content and improved magnetic properties", *Appl. Phys. A*, 2021, 127, 165.

[477] Verma, P.; Roy, P. K., "Effect of Gd substitution on the dielectric and magnetic properties of BSFO-based multiferroic system", *J. Mater. Sci.: Mater. Electron*., 2020, 31, 13028-13039.

[478] Khirade, P. P.; Shankar D.; Birajdar, Raut, Jadhav, A.V.; K.M., "Multiferroic iron doped $BaTiO_3$ nanoceramics synthesized by sol-gel auto combustion: influence of iron on physical properties", *Ceram. Int.*, 2016, 42, 12441-12451.

[479] Kumar, K. A.; Bhowmik, R., "Micro-structural characterization and magnetic study of $Ni_{1.5}Fe_{1.5}O_4$ ferrite synthesized through coprecipitation route at different pH values", *Mater. Chem. Phys*., 2014, 146, 159-169.

[480] Hanani, Z.; Ablouh, E. H.; Amjoud, M.; Mezzane, D.; Fourcade, S.; Gouné, M., "M.'barek Amjoud, D. Mezzane, S. Fourcade and M. Gouné", *Ceram. Int.*, 2018, 44, 10997-11000.

[481] Raut, A. V.; Khirade, P. P.; Humbe, A.; Jadhav, S. A.; Shengule, D. R., "Structural, electrical, dielectric and magnetic properties of Al^{3+} substituted Ni-Zn ferrite", *J. Supercond. Nov. Magn*., 2016, 29, 1331-1337.

[482] Hegab, N. A.; Afifi, M. A.; Atiya, H. E.; Farid, A. S., "Ac conductivity and dielectric properties of amorphous $Se_{80}Te_{20-x}Ge_x$ chalcogenide glass film compositions", *J. Alloys Compd*., 2009, **477**, 925-930.

[483] Barsoum, M., Fundamental of Ceramics (McGraw-Hill, New York, 1997), 543.

[484] Liu, S.; Bo Shen, Hao, H.; Zhai, J., "Glass-ceramic dielectric materials with high energy density and ultra-fast discharge speed for high power energy storage applications", *J. Mater. Chem*., 2019, C**7**, 15118.

[485] Badr, A. M.; Elshaikh, H.A.; Ashraf, I. M.; Mod. J., "Impacts of temperature and frequency on the dielectric properties for insight into the nature of the charge transports in the Tl_2S layered single crystals", J. Mod. Phys., 2011, 2, 12-25.

[486] Sharma, N.; Patial, B. S.; Thakur, N., "On the dielectric study and AC conductivity measurements of Sb additive Se-Te chalcogenide alloys", *Appl. Phys. A*, 2016, 122, 209.

[487] Lataoui, R.; Triki, A.; Hcini, S.; Zemni, S.; Dhahri, J.; Kanoun, O., "Structural, morphological and dielectric analyses of $La_{1-x}Sr_xFeO_3$ solid solutions", *Appl. Phys. A*, 2021, 127, 721.

[488] Wagner, K. W., "Erklärung der dielektrischen nachwirkungsvorgänge auf grund maxwellscher vorstellungen", *Archiv f. Elektrotechnik*, 1914, 2, 371-387.

[489] Sheoran, N.; Kumar, A.; Kumar, V.; Chahar, M. A. "Banerjee, Structural and multiferroic properties of $BiFeO_3/MgLa_{0.025}Fe_{1.975}O_4$ nanocomposite synthesized by sol-gel auto combustion route", *J. Mater. Sci.: Mater. Electron.*, 2020, 31, 2777-2788.

[490] Jabez, S.; Mahalakshmi, S.; Nithiyanantham, S., "Frequency and temperature effects on dielectric properties of cobalt ferrite", *J. Mater. Sci.: Mater. Electron*., 2017, 28, 5504-5511.

[491] Dabas, S.; Chaudhary, P.; Kumar, M.; Shankar, S.; Thakur, O. P., "Structural, microstructural and multiferroic properties of $BiFeO_3$-$CoFe_2O_4$ composites", *J. Mater. Sci.: Mater. Electron*., 2019, 30, 2837-2846.

[492] Ishaque, M.; Islam, M.U.; Azhar Khan, M.; Rahman, I.Z.; Genson, A.; Hampshire, S., "Structural, electrical and dielectric properties of yttrium substituted nickel ferrites", *Physica B*, 2010, 405, 1532-1540.

[493] Kakade, S. G.; Kambale, R. C.; Kolekar, Y. D.; Ramana, C. V., "Dielectric, electrical transport and magnetic properties of Er^{3+} substituted nanocrystalline cobalt ferrite", J. Phys. Chem. Solid., 2016. 98, 20-27.

[494] Atif, M.; Rafique, T.; Atta Ur Rehman; Wahab, H.; Khalid, W.; Ali,Z.; Nadeem, M., "Effect of cation distribution on the structural and dielectric properties of $Ni_{0.5-x}Co_xZn_{0.5}Fe_2O_4$ ($0.0 \leq x \leq 0.5$) ferrites", J. Mater. Sci.: Mater. Electron., 2020, 31, 10970-10980.

[495] Routray, K. L.; Saha, S.; Behera, D., "Rare-earth (La^{3+}) substitution induced changes in the structural, dielectric and magnetic properties of nano-$CoFe_2O_4$ for high-frequency and magneto-recording devices", *Appl. Phys. A*, 2019, 125, 328.

[496] Yadav, R. S.; Kuřitka, I.; Vilcakova, J.; Havlica, J.; Masilko, J.; Kalina, L.; Tkacz, J.; Švec, J.; Enev, V.; Hajdúchová, M., "Impact of grain size and structural changes on magnetic, dielectric, electrical, impedance and modulus spectroscopic characteristics of $CoFe_2O_4$ nanoparticles synthesized by honey mediated sol-gel combustion method", Adv. *Nat. Sci.: Nanosci. Nanotechnol*, 2017, 8, 045002.

[497] Jacob, B. P.; Thankachan, S.; Xavier, S.; Mohammed, E.M., "Dielectric behavior and AC conductivity of Tb^{3+} doped $Ni_{0.4}Zn_{0.6}Fe_2O_4$ nanoparticles", *J. Alloys Compd*., 2012, 541, 29-35.

[498] Murugesan, C.; Okrasa, L.; Chandrasekaran, G., "Structural, Chandrasekaran, Structural, AC cnductivity, impedance and dielectric study of nanocrystalline MFe_2O_4 (M=Mg, Co or Cu) spinel ferrites", *J. Mater. Sci.: Mater. Electron.*, 2017, 28, 13168-13175.

[499] Liu, J.; Duan, C. G.; Yin, W. G.; Mei, W. N.; Smith, R. W.; Hardy, J. R., "Large dielectric constant and Maxwell-Wagner relaxation in $Bi_{2/3}Cu_3Ti_4O_{12}$", *Phys. Rev. B*, 2004, 70, 144106.

[500] Hashim, M.; Alimuddin, Kumar, S.; Ali, S.; Koo, B.H.; Chung, H.; Kumar, R., "Structural, magnetic and electrical properties of Al^{3+} substituted Ni-Zn ferrite nanoparticles", *J. Alloys Compd*., 2012, 511, 107-114.

[501] Mohanty, H. S.; Kumar, A.; Sahoo, B.; Kurliya, P. K.; Pradhan, D. K., "Impedance spectroscopic study on microwave sintered (1-x) $Na_{0.5}Bi_{0.5}TiO_3$-x $BaTiO_3$ ceramics", *J. Mater. Sci.: Mater. Electron*., 2018, 29, 6966-6977.

[502] Ramo, S.; Whinnery, J. R.; Duzer, T. V., Fields and Waves in Communication Electronics (Wiley, New York, 1984).

[503] Vasoya, N. H.; Prafulla K. Jha, Saija, K. G.; Bhalodia, J. A.; Modi, K. B., "Master curve generation and modeling of ac conductivity for $Mn_{0.7+x}Zn_{0.3}Si_xFe_{2-2x}O_4$ spinel ferrite system", *J. Adv. Dielect*., 2017, **7**, 1750022.

[504] Lopez, G. P.; Silvetti, S. P., "Effect of milling time on Fe/SiO2 system prepared by mechanical alloying", *Physica B*, 2004, 354, 141-144.

[505] Hadded, A.; Massoudi, J.; Dhahri, E.; Khirouni, K.; Costa, B. F. O., "Structural, optical and dielectric properties of $Cu_{1.5}Mn_{1.5}O_4$ spinel nanoparticles", *RSC Adv*., 2020, 10, 42542.

[506] Karmakar, A.; Majumdar, S.; Giri, S., "Polaron relaxation and hopping conductivity in $LaMn_{1-x}Fe_xO_3$", *Phys. Rev. B*, 2009, 79, 094406.

[507] Venkataraman, B. H.; Varma, K. B. R., "Frequency-dependent dielectric characteristics of ferroelectric $SrBi_2Nb_2O_9$ ceramics", *Solid State Ionics*, 2004, 167, 197-202.

[508] Jonscher, A. K., Dielectric relaxation in solids, *J. Mater. Sci*. 16, 2037-2060 (1981)

[509] Radoń, A.; Hawełek, Ł.; Łukowiec, D.; Kubacki, J.; Włodarczyk, P., "Dielectric and electromagnetic interference shielding properties of high entropy (Zn, Fe, Ni, Mg, Cd) Fe_2O_4 ferrite", *Sci. Rep*., 2019, 9, 20078.

[510] Alder, D.; Feinleib, J., "Electrical and optical properties of narrow-band materials", *Phys. Rev*. *B*, 1970, **2**, 3112-3134.

[511] Dar, M. A.; Majid, K.; Batoo, K. M.; Kotnala, R. K., "Dielectric and impedance study of polycrystalline $Li_{0.35-0.5X}Cd_{0.3}Ni_XFe_{2.35-0.5X}O_4$ ferrites synthesized via a citrate-gel auto combustion method", *J. Alloys Comp*., 2015, 632, 307-320.

[512] Azam, A.; Ahmed, A. S.; Chaman, M.; Naqvi, A. H., "Investigation of electrical properties of Mn doped tin oxide nanoparticles using impedance spectroscopy", *J. Appl. Phys*., 2010, 108, 094329.

[513] Halder, S.; Dey, A.; Sil, S.; Ray, P. P., "Study of AC conductivity and dielectric behaviour of hydrothermally synthesised molybdenum disulphide", *J. Mater. Sci.: Mater. Electron.*, 2021, 32, 168-181.

[514] Rhimi, T.; Leroy, G.; Duponchel, B.; Khirouni, K.; Guermazi, S.; Toumi, M., "AC and DC conductivity study of LiH_2PO_4 compound using impedance spectroscopy Ionics", 2018, 24, 1305-1312.

[515] Raddaoui, Z.; Lahouli, R.; Kossi, S.E.L.; Dhahri, J.; Khirouni, K.; Taibi, K., "Effect of oxygen vacancies on dielectric properties of $Ba_{(1-x)}Nd_{(2x/3)}TiO_3$ compounds", *J. Alloys Compd*., 2018, 771, 67-78.

[516] Benali, M.; Benali, A.; Bejar, M.; Dhahri, E.; Graca, M. P. F.; Valente, M. A.; Sanguino, P.; Costa, B. F. O., "Effect of annealing temperature on structural, morphological and dielectric properties of $La_{0.8}Ba_{0.1}Ce_{0.1}FeO_3$ perovskite", *J. Mater. Sci.: Mater. Electron*., 2020, 31, 16220-16234.

[517] Issaoui, H.; Benali, A.; Bejar, M.; Dhahri, E.; Costa, B. F. O.; Graca, M. P. F.; Valente, M. A., "Effect of Bi-substitution into the A-site of multiferroic $La_{0.8}Ca_{0.2}FeO_3$ on structural, electrical and dielectric properties", 2020, *RSC Adv*., 10, 16132.

[518] Singh, L.; Kim, W. I.; Sin, B. C.; Ullah, A.; Woo, S. K.; Lee, Y., "Study of dielectric, AC-impedance, modulus properties of $0.5Bi_{0.5}Na_{0.5}TiO_3$-$0.5CaCu_3Ti_4O_{12}$ nano-composite synthesized by a modified solid state method", *Mater. Sci. Semicond. Process*., 2015, 31, 386-396.

[519] Verma, K.; Sharma, S., "Impedance spectroscopy and dielectric behavior in barium strontium titanate-nickel zinc ferrite composites", *Phys. Stat. Sol. B*., 2012, 249, 209-216.

[520] Chawla, A.; Singh, A.; Singh, M.; Malhi, P.S., "Small polaron hopping-assisted electrical conduction and relaxation in BCT and Mn-doped BCT samples", *J. Asian Ceram. Soc.*, 2019, **7**, 558-568.

[521] Sahoo, S.; Hajra, S.; De, M.; Choudhary, R. N. P., "Resistive, capacitive and conducting properties of $Bi_{0.5}Na_{0.5}TiO_3$-$BaTiO_3$ solid solution", 2018, *Ceram. Int*. 44, 4719-4726.

[522] Gouitaa, N.; Lamcharfi, T.; Bouayad, M.; Abdi, F.; Hadi, N., "Impedance, modulus and conductivity studies of Fe^{3+} doped BaTiO 3 ceramics prepared by solid state method", *J. Mater. Sci.: Mater. Electron*., 2018, 29, 6797-6804.

[523] Umapathy, G.; Senguttuvan, G.; John Berchmans, L.; Sivakumar, V., "Structural, dielectric and AC conductivity studies of Zn substituted nickel ferrites prepared by combustion technique", *J. Mater. Sci.: Mater. Electron*., 2016, 27, 7062-7072.

[524] Khammassi, F.; Cherif, W.; Sales, A. J. M.; Riahi, K.; Graça, M. P. F.; Dammak, M., "Conduction Mechanism and Dielectric Properties of Polycrystalline $La_{0.53}Ca_{0.47}Mn_{0.5}Cr_{0.5}O_3$", *J. Supercond. Nov. Magn.*, 2021, 34, 497-505.

[525] Selmi, A.; Hcini, S.; Rahmouni, H.; Omri, A.; Bouazizi, M. L.; Dhahri, A., "Synthesis, structural and complex impedance spectroscopy studies of $Ni_{0.4}Co_{0.4}Mg_{0.2}Fe_2O_4$ spinel ferrite Phase Transitions", 2017, 90, 942-954.

[526] Javed, M.; Khan, A. A.; Ahmed, M. S.; Khisro, S. N.; Khan, M. N.; Bilkees, R.; Kazmi, J.; Mohamed, M. A., "Temperature dependent impedance spectroscopy and electrical transport mechanism in sol-gel derived $MgCr_2O_4$ spinel oxide", *Physica B*, 2020, 599, 412377.

[527] Shovon, O. G.; Rahaman, Md. D.; Tahsin, S., Akther Hossain, A. K. M.,, "Synthesis and characterization of (100-x)$Ba_{0.82}Sr_{0.03}Ca_{0.15}Zr_{0.10}Ti_{0.90}O_3$ + (x) $Mg_{0.25}Cu_{0.25}Zn_{0.5}Mn_{0.05}Fe_{1.95}O_4$ composites with improved magnetoelectric voltage coefficient", *J. Alloys Compd*., 2018, 735, 291-311.

[528] Khan, M. Z.; Gul, I. H.; Baig, M. M.; Khan, A. N., "Comprehensive study on structural, electrical, magnetic and photocatalytic degradation properties of Al^{3+} ions substituted nickel ferrites nanoparticles", *J. Alloys Compd*., 2020, 848, 155795.

[529] Hajra, S.; Sahu, M.; Purohit, V.; Choudhary, R.N.P., "Dielectric, conductivity and ferroelectric properties of lead-free electronic ceramic 0.6Bi $(Fe_{0.98}Ga_{0.02})O_3$-0.4$BaTiO_3$", Heliyon, 2019, 5, 01654.

[530] Parida, R. K.; Pattanayak, D.K.; Parida, B.N., "Impedance and modulus analysis of double perovskite Pb_2BiVO_6", *J. Mater. Sci. Mater. Electron*., 2017, 28, 16689-16695.

[531] Yadav, R. S.; Kuřitka, I.; Vilcakova, J.; Havlica, J.; Kalina, L.; Urbánek, P.; Machovsky, M.; Skoda, D.; Masař, M., "Influence of Gd^{3+}-substitution on structural, magnetic, dielectric and modulus spectroscopic characteristics of $ZnFe_2O_4$ spinel ferrite nanoparticles", *J. Mater. Sci.: Mater. Electron*., 2018, 29, 15878-15893.

[532] Khan, M. Z.; Gul, I. H.; Malik, A., "Improved Electrical Properties Displayed by Mg^{2+}-Substituted Cobalt Ferrite Nano Particles, Prepared Via Co-precipitation Route", *J. Supercond. Nov. Magn*., 2020, 33, 3133-3144.

[533] Deepti, P. L.; Patri, S. K.; Choudhary, R. N. P.; Das, P. S., "Dielectric, impedance and modulus spectroscopy of Ta-based layered perovskite, Phase Transitions", 2019, 92, 642-656.

[534] Prasad, K.; Priyanka Chandra, K. P.; Kulkarni, A. R., "Structural and electrical properties of lead-free perovskite ceramic: $Ba(In_{1/2}Nb_{1/2})O_3$", *J. Non-Cryst. Solids*, 2011, 357, 1209-1217.

[535] Kaiser, M., "Magnetic and electric modulus properties of In substituted Mg-Mn-Cu ferrites", *Mater. Res. Bull*., 2016, 73, 452-458.

[536] Bahiraei, H.; Shoushtari, M.Z.; Gheisari, K.; Ong, C.K., "The effect of non-magnetic Al^{3+} ions on the structure and electromagnetic properties of MgCuZn ferrite", *J. Magn, Magn. Mater*., 2014, 371, 29-34.

[537] Tsutaoka, T., Ueshima, M.; Tokunaga, T., "Frequency dispersion and temperature variation of complex permeability of Ni-Zn ferrite composite materials", *J. Appl. Phys*., 1995, 78, 3983-3991.

[538] Rado, G. T., Wright R. W., and Emerson, W. H., "Ferromagnetism at very high frequencies. III. Two mechanisms of dispersion in a ferrite", Phys. Rev., 1950, 80, 273-280.

[539] Tsutaoka, T., "Frequency dispersion of complex permeability in Mn-Zn and Ni-Zn spinel ferrites and their composite materials", *J. Appl. Phys*., 2003, 93, 2789-2796.

[540] Su, H.; Zhang, H.; Tang, X.; Jing, Y., "Influence of microstructure on permeability dispersion and power loss of NiZn ferrite", 2008., *Appl. Phys*. 103, 093903.

[541] Zhang, Y. G.; Huang, Y.J.; Luo, D.M., Magnetic Materials (Institute of Electronmunication and Engineering Publishing House, Chengdu, 1988)

[542] Babu, K. R.; Rao, K. R.; Babu, B. R., "Effect of Cu and Cation Redistribution on Structural and Magnetic Properties of Co-Mg Nanoferrite", J. Supercond. Nov. Magn., 2017, 30, 2621-2630.

[543] Singh, A. K.; Goel, T. C.; Mendiratta, R. G.; Thakur, O. P.; Prakash, C., "Magnetic properties of Mn-substituted Ni-Zn ferrites", J. Appl. Phys., 2002, 92, 3872-3876.

[544] Zhong, H.; Xiao, Z.; Yang, J.; Jiao, X.; Wang, H.; Shi, Y., "Electromagnetic properties of Nb_2O_5 substituted ferroelectric-ferromagnetic composite ferrite", *J. Mater. Sci.: Mater. Electron*., 2013, 24, 1116-1120.

[545] Uozumi, G., Watanabe, M., Nakayama, R., Igarashi, K., & Morimoto, K., "Properties of soft magnetic composite with evaporated MgO insulation coating for low iron loss", *Mater. Sci. Forum*, 2007, 534-536, 1361-1364.Trans Tech Publications Ltd.

[546] Ďáková, L.; Füzer, J.; Dobák, S.; Kollár, P.; Fáberová, M.; Strečková, M.; Bureš, R.; Hadraba, H., "The Influence of $NiZnFe_2O_4$ Content on Magnetic Properties of Supermalloy Type Material", *Acta Phys. Pol. A*, 2017, 131, 813-815.

[547] Mazaleyrat, F.; Varga, L. K., "Ferromagnetic nanocomposites", *J. Magn. Magn. Mater*., 2000, 215-216, 253-259.

[548] Snoek, J. L., "Dispersion and absorption in magnetic ferrites at frequencies above one Mc/s", Physica (Amsterdam), 1948, 14, 207-217.

[549] Peng, Y.; Wu, X.; Chen, Z.; Liu, W.; Wang, F.; Wang, X.; Feng, Z.; Chen, Y.; Harris, V.G., "$BiFeO_3$ tailored low loss M-type hexaferrite composites having equivalent permeability and permittivity for very high frequency applications" *J. Alloy. Comp*., 2015, 630, 48-53.

[550] Nien, H. H.; Huang, C. K.; Wang, M.Y.; Lin, C. W.; Changchien, S. K., "Estimation of eddy-current loss for MnZn ferrite cores", Advanced Materials Research Adv. Mater. Res. 2012, 382, 204-209.

[551] Guo, Y.; Zhu, J.; Li, H., "Structure, electromagnetic and dielectric properties of Ti-substituted lithium-zinc ferrite", *J. Mater. Sci.: Mater. Electron*., 2021, 32, 8354-8365.

[552] Azis, R. S.; Mustaffa, M. S.; Shahrani, N. M. M. "Sintering Temperature Effect on Microstructure and Magnetic Evolution Properties with Nano-and Micrometer Grain Size in Ferrite Polycrystals", Sintering Technology-Method and Application, ed. By Malin Liu (IntechOpen, 2018), Chapter 3, 45-61 http://dx.doi.org/10.5772/intechopen.78638

[553] Yang, P.; Qi, H.; Liu, Z.; Fu, X.; Peng, Z., "Microstructure, magnetism, and high-frequency performance of polycrystalline $Ni_{0.5}Zn_{0.5}Sm_{0.025}Ho_xFe_{1.975-x}O_4$ ferrites", *J. Am. Ceram. Soc*., 2019, 102, 7469-7479.

[554] Jahanbin, T.; Hashim, M.; Mantori, K. A., "Comparative studies on the structure and electromagnetic properties of Ni-Zn ferrites prepared via co-precipitation and conventional ceramic processing routes", *J. Magn. Magn. Mater*. 2010, 322, 2684-2689.

[555] Kang, S. H.; Han-III Yoo, "The effect of nonstoichiometry (δ) on the magnetic properties of $(Mg_{0.22}Mn_{0.07}Fe_{0.71})_{3-\delta}O_4$ ferrite", *J. Appl. Phys*., 2000, 88, 4754-4757.

[556] Rado, G. T.; Wright, R. W.; Emerson, W. H., "Ferromagnetism at very high frequencies. IV. Temperature dependence of the magnetic spectrum of a ferrite", *A. Terris*, *Phys. Rev*., 1052, 88, 909-915.

[557] Li, S. B.; Wang, C.B.; Shen, Q.; Zhang, L.M., "Multiferroic properties of (1-x) BCZT-xLCMO laminated composites", *Ceram. Int*., 2018, 44, 231-235.

[558] Negi, N. S.; Bala, K.; Sharma, P.; Kotnala, R. K., "Multiferroic and magnetoelectric properties of $MnFe_2O_4/(Pb_{0.8}Sr_{0.2})TiO_3$", *composite films* Phil. Mag., 2017, 97, 269-283.

[559] Kumar, A. S.; Lekha, C. S. C.; Vivek, S.; Nandakumar, K.; Anantharaman, M. R.; Nair, S. S., "Effect of $CoFe_2O4$ weight fraction on multiferroic and magnetoelectric properties of (1-x) $Ba_{0.85}Ca_{0.15}Zr_{0.1}Ti_{0.9}O_3$-$xCoFe_2O_4$ particulate composites", *J. Mate. Sci.: Mater. Electron*., 2019, 30, 8239-8248.

[560] Wang, L. G.; Wang, X.X.; Zhu, C.M.; Yu, G.B.; Zhao, Y.T.; Huang, Z.H.; W.J. Kong, F.C. Liu, F.Z. Lv, "Influences of annealing temperature on dielectric, magnetic and magnetoelectric coupling properties of $0.7Bi_{0.5}Na_{0.5}TiO_{3-0.3}$ $NiFe_2O_4$ ceramics", *J. Magn. Magn. Mater*., 2020, 494, 165773.

[561] Nan, C. W., Magnetoelectric effect in composites of piezoelectric and piezomagnetic phases, *Phys. Rev. B*, 1994, 50, 6082-6088.

[562] Praveen, J. P.; Monaji, V.R.; Chandrakala, E.; Indla, S.; kumar, S.D.; Subramanian, V.; Das, D., "Enhanced magnetoelectric coupling in Ti and Ce substituted lead free CFO-BCZT laminate composites", *J. Alloy. Compd*., 2018, 750, 392-400.

[563] Khomeriki, R.; Chotorlishvili, L.; Tralle, I.; Berakdar, J., "Positive-negative birefringence in multiferroic layered metasurfaces", *Nano Lett*., 2016, 16, 7290-7294.

[564] Padmapriya D., Dhayanithi D., Rahul M.T., N. Kalarikkal, Giridharan N. V., "Study of room-temperature magnetoelectric coupling in (1-*x*)$BaTiO_3$ and (*x*)$NiFe_2O_4$ multiferroic composites", *Appl. Phys. A*, 2021, 127, 293.

[565] Dhanalakshmi, B.; Kollu, P.; Barnes, C.H.; Rao, B.P.; Rao, P.S., "Multiferroic and magnetoelectric studies on BMFO-NZFO nanocomposites", *Appl. Phys. A*, 2018, 124, 396.

[566] Woldu, T.; Raneesh, B.; Hazra, B.K.; Srinath, S.; Saravanan, P.; Reddy, M. R.; Kalarikkal, N., "A comparative study on structural, dielectric and multiferroic properties of $CaFe_2O_4$/$BaTiO_3$ core-shell and mixed composites", *J. Alloys Compd*., 2017, 691, 644-652.

[567] Liu, S.; Yan, S.; Luo, H.; Yao, L.; Li, Y.; He, J.; He, L.; Huang, S.; Deng, L., "Magnetoelectric Effect in Cofired Lead-Free Laminated ($Bi_{0.5}Na_{0.5}TiO_3$-$Bi_{0.5}K_{0.5}TiO_3$)/($Ni_{0.8}Zn_{0.2}$) Fe_2O_4 Composites", *Phys. Stat. Sol. A*, 2017, 214, 1700533.

[568] Bas, J. A.; Calero, J. A.; Dougan, M. J., "Sintered soft magnetic materials. Properties and applications", *J. Magn. Magn. Mater*., 2003, 254, 391-398.

[569] Srinivas, S.; Li, J. Y.; Zhou, Y. C.; Soh, A. K., "The effective magnetoelectroelastic moduli of matrix-based multiferroic composites", *J. Appl. Phys*., 2006, 99, 043905.

[570] Zhou, Y.; Yang, S. C.; Apo, D.J.; Maurya, D.; Priya, S., "Tunable self-biased magnetoelectric response in homogenous laminates", *Appl. Phys. Lett*., 2012, 101, 232905.

[571] Dhakal, T.; Mukherjee, D.; Hyde, R.; Mukherjee, P.; Phan, M.H.; Srikanth, H.; Witanachchi, S., "Magnetic anisotropy and field switching in cobalt ferrite thin films deposited by pulsed laser ablation", *J. Appl. Phys.*, 2010, 107, 053914.

[572] Petrov, V., Srinivasan, G., Laletsin, U., Bichurin, M. I., Tuskov, D. S., Paddubnaya, N., "Magnetoelectric effects in porous ferromagnetic-piezoelectric bulk composites: experiment and theory", 2007, 75 (17) 174422.

List of publications

The present these is based on the following research contributions:

i) Journal:

1. **Sharifa Nasrin**, Subrin Mostafa Khan, M. A. Matin, M. N. I. Khan, A. K. M. Akther Hossain, Md. D. Rahaman, **"Synthesis and deciphering the effects of sintering temperature on structural, elastic, dielectric, electric and magnetic properties of magnetic $Ni_{0.25}Cu_{0.13}Zn_{0.62}Fe_2O_4$ ceramics**", Journal of Materials Science: Materials in Electronics, 30 (2019) 10722-10741.

2. **Sharifa Nasrin**, Most. Sharmin, A. K. M. Akther Hossain and Md. D. Rahaman, **"Fabrication and unravelling the impact of iron-deficiency amount on crystal structure, micromorphology, elastic and electromagnetic properties $Ni_{0.25}Cu_{0.13}Zn_{0.62}Fe_{2-x}O_{4-3x/2}$ ferrites under different sintering temperatures",** Journal of Materials Science: Materials in Electronics, 32 (2021) 4592-4628.

3. **Sharifa Nasrin**, Most. Sharmin, M. A. Matin, A. K. M. Akther Hossain, Md. D. Rahaman, "**Study the impact of sintering temperature on electromagnetic properties of (1-y) $[Ba_{0.9}Ca_{0.1}Zr_{0.1}Ti_{0.9}O_3]$ + (y) $[Ni_{0.25}Cu_{0.13}Zn_{0.62}Fe_2O_4]$ composites",** Applied Physics A 127 (2021) 59.

4. **Sharifa Nasrin**, Tabassum Haque Joyee, A.K.M. Akther Hossain, and Md. D. Rahaman, "**Exploring the influence of iron-deficient non-stoichiometric dominance on the crystal structure, morphological, electromagnetic and magnetoelectric characteristics of (1-*y*) $[Ba_{0.90}Ca_{0.10}Ti_{0.90}Zr_{0.10}O_3]$ + (*y*) $[Ni_{0.25}Cu_{0.13}Zn_{0.62}Fe_{2-x}O_{4-3x/2}]$ composites**", Journal of Materials Science: Materials in Electronics 33 (2022) 5411-5455.

ii) Published Abstracts/Presentations:

1. **Sharifa Nasrin**, M. A. Matin, M. N. I. Khan, M. N. Hossain, and A.K.M. Akther Hossain, Md. D. Rahaman, "**Effect of sintering temperature on structural, elastic, electric and magnetic properties of $Ni_{0.25}Cu_{0.13}Zn_{0.62}Fe_2O_4$ spinel ferrite**", "National conference on Physics -2019" organized by Bangladesh Physical Society in Department of Physics, the University of Dhaka on 07-09 February 2019.

2. M. N. Hossain, M. A. Matin**,** M. A. Hakim**,** M. N. I. Khan, Manifa Noor, M. A. Al Mamun, M. T. Morshed, **Sharifa Nasrin**, and M. F. Islam **"Synthesis and characterization of yttrium iron garnet nanoparticles doped with Gadolinium and Chromium",** "National conference on Physics -2019" organized by Bangladesh Physical Society in Department of Physics, the University of Dhaka on 07-09 February 2019.

3. **Sharifa Nasrin**, M. A. Matin, A.K.M. Akther Hossain, and Md. D. Rahaman, "**Electromagnetic Properties of (1-y) $[0.5(Ba_{0.8}Ca_{0.2})TiO_3$-$0.5Ba(Ti_{0.8}Zr_{0.2})O_3]$ + (y) $[Ni_{0.25}Cu_{0.13}Zn_{0.62}Fe_2O_4]$ Composites**", "National Conference on Electronics and Informatics-2019", Atomic Energy Centre, Dhaka on 04-05 December 2019.

4. **Sharifa Nasrin**, M. A. Matin, and A.K.M. Akther Hossain, Md. D. Rahaman, **"Deciphering the effect of sintering temperature on the electromagnetic properties of (1-y) [0.5($Ba_{0.8}Ca_{0.2}$)TiO_3-0.5Ba($Ti_{0.8}Zr_{0.2}$)O_3] + (y) [$Ni_{0.25}Cu_{0.13}Zn_{0.62}Fe_2O_4$] particulate composites"** "International conference on Physics-2020", Atomic Energy Center, Dhaka, 05-07 March 2020.

5. **Sharifa Nasrin**, A.K.M. Akther Hossain, and Md. D. Rahaman, **"Study the structural and electromagnetic properties of (1-y) [$Ba_{0.9}Ca_{0.1}Zr_{0.1}Ti_{0.9}O_3$] + (y) [$Ni_{0.25}Cu_{0.13}Zn_{0.62}Fe_2O_4$] composites",** Sixth Conference (virtual) of Bangladesh Crystallographic Association, 15-16 January 2021.

6. Roksana Parvin, A.A. Momin, **Sharifa Nasrin**, and A.K.M. Akther Hossain, "**Mixed Polaron Hopping Type AC Conductivity in 0.8BST + 0.2LCCZFO Multiferroic Composites: Analysis and Interpretation"** Sixth Conference (virtual) of Bangladesh Crystallographic Association, 15-16 January 2021.

7. **Sharifa Nasrin**, Tabassum Haque Joyee, A.K.M. Akther Hossain, and Md. D. Rahaman, **"Study on the iron-deficient non-stoichiometry driven electromagnetic and magnetoelectric properties of multiferroic composites",** National conference (virtual) on Physics-2021, Organized by Bangladesh Physical Society, 06-07 August 2021.

8. **Sharifa Nasrin**, A.K.M. Akther Hossain, and Md. D. Rahaman, "**Preparation and exploration on structural, electromagnetic and magnetoelectric properties of the iron-deficient multiferroic composites**", International Conference on Electronics and Informatics 2021, Atomic Energy Center, Dhaka, 27-28 November 2021.